THÈSE

Présentée à

L'UNIVERSITÉ DE POITIERS

Pour l'obtention du Grade de

DOCTEUR DE L'UNIVERSITE DE POITIERS

ÉCOLE NATIONALE SUPERIEURE D'INGENIEURS DE POITIERS
(Diplôme National - Arrêté du 25 mai 2016)

École Doctorale : Sciences et Ingénierie des Systèmes, Mathématiques, Informatique (SISMI)

Secteur de Recherche : Génie Électrique

Présentée par :

Daniela Yassuda Yamashita

****

Hierarchical Control for Building Microgrids

****

Directeur de Thèse : Prof. Jean-Paul Gaubert
Co-directeur de thèse : Prof. Ionel Vechiu

Soutenue le 28 avril 2021 devant le jury composé de :

Delphine RIU
Professeur à l'Université Grenoble Alpes INP, Ense3, G2Elab (rapportrice)

Manuela SECHILARIU
Professeur à l'Université de Technologie de Compiègne, AVENUES (rapportrice)

Florence OSSART
Professeur à Sorbonne Université, GeePs (examinatrice)

Ignacio HERNANDO GIL
Enseignant chercheur à l'ESTIA, ESTIA-Recherche (examinateur)

Ionel VECHIU
Professeur à l'ESTIA, ESTIA-Recherche (directeur de thèse)

Jean-Paul GAUBERT
Professeur à l'Université de Poitiers, LIAS (directeur de thèse)

Alain ROCHEUX
Ingénieur à H2Gremm (invité)

Etienne OUSS
Ingénieur de recherche EDF (invité)

Thèse préparée au sein des laboratoires ESTIA Institute of Technology et LIAS

Abstract

Representing more than one-third of global electricity consumption, buildings undergo the most important sector capable of reducing greenhouse gas emissions and promote the share of Renewable Energy Sources (RES). The integrated RES and electric energy storage system in buildings can assist the energy transition toward a low-carbon electricity system while allowing end-energy consumers to benefit from clean energy. Despite its valuable advantages, this innovative distributed Building MicroGrid (BMG) topology requires significant changes in the current electric grid, which is highly dependent on grid energy policies and technology breakthroughs.

The complexity of designing a robust Energy Management System (EMS) capable of managing all electric components inside the microgrid efficiently without harming the main grid stability is one of the greatest challenges in the development of BMG. To mitigate the harmful effects of unpredictable grid actors, the concept of self-consumption has been increasingly adopted. Nonetheless, further technical-economic analysis is needed to optimally manage the energy storage systems to attain higher marks of self-consumption.

Facing these issues, the purpose of this doctoral thesis is to propose a complete framework for designing a building EMS for microgrids installed in buildings capable of maximising the self-consumption rate at minimum operating cost. Among all possible control architectures, the hierarchical structure has proved effective to handle conflicting goals that are not in the same timeframe. Hence, a Hierarchical Model Predictive (HMPC) control structure was adopted to address the uncertainties in the power imbalance as well as the trade-off between costs and compliance with the French grid code.

Considering that buildings are not homogeneous and require solutions tailored to their specific conditions, the proposed controller was enhanced by two data-driven modules. The first data-driven algorithm is to handle inaccuracies in HMPC internal models. Without needing to tune any parameter, this algorithm can enhance the accuracy of the battery model up to three times and improve up to ten times the precision of the hydrogen storage model. This makes the building EMS more flexible and less dependent on pre-modelling steps.

The second data-oriented algorithm determines autonomously adequate parameters to HMPC to relieve the trade-off between economic and energy aspects. Relying only on power imbalance data analysis and local measurements, the proposed hierarchical controller determines which energy storage device must run daily based on the estimation of the annual self-consumption rate and the annual microgrid operating cost. These estimations decrease microgrid expenditure because it avoids grid penalties regarding the requirements of annual self-consumption and reduces the degradation and maintenance of energy storage devices.

The proposed EMS also demonstrated being capable of exploiting the potentials of shifting in time the charging of batteries of plug-in electric vehicles. The simulation confirmed that the proposed controller preferably charges electric vehicles' batteries at periods of energy surplus and discharges them during periods of energy deficit, leading the building microgrid to reduce grid energy exchange. The results also showed that electric vehicle batteries' contribution depends on the size of the vehicle parking, their arrival and departure time, and the building's net power imbalance profile. In conclusion, through simulations using the dataset of both public and residential buildings, the proposed hierarchical building EMS proved its effectiveness to handle different kinds of energy storage devices and foster the development of forthcoming building microgrids.

Keywords: Hierarchical Model Predictive Control, Building MicroGrid, Hydrogen storage system, Li-ion batteries, Electric Vehicles, Data-driven algorithms, optimization, Renewable energy sources.

Résumé

Représentant plus d'un tiers de la consommation mondiale d'électricité, les bâtiments sont le secteur énergétique majeur pour promouvoir l'usage des énergies renouvelables. L'installation à la fois de sources d'énergie renouvelable et d'un système de stockage d'énergie électrique dans les bâtiments peut favoriser la transition énergétique vers un système électrique à faible émission de carbone, tout en permettant aux consommateurs d'énergie finaux de bénéficier d'une énergie propre. Malgré tous ces avantages, cette topologie innovante et distribuée d'un Micro-réseau dédié au Bâtiment (MB) nécessite des changements importants dans le réseau actuel, qui dépend des politiques énergétiques et d'avancement technologiques.

La conception d'un Système de Gestion de l'Energie (EMS) capable de gérer efficacement les composants électriques du micro-réseau sans menacer la stabilité du réseau principal est un obstacle au développement des MB. Pour atténuer les effets néfastes introduits par des acteurs d'énergie imprévisibles, le concept d'autoconsommation est de plus en plus adopté. Néanmoins, une analyse technico-économique plus approfondie est nécessaire pour piloter d'une manière optimale des systèmes de stockage d'énergie afin d'atteindre des indices d'autoconsommation plus élevés.

Face à ces enjeux, le but de ce doctorat est de proposer un EMS pour les micro-réseaux installés dans les bâtiments afin de maximiser leur taux d'autoconsommation à un coût d'exploitation minimum. Parmi les architectures de contrôle, la structure hiérarchique s'est avérée efficace pour gérer des objectifs contradictoires qui ne sont pas dans la même échelle de temps. Ainsi, une structure de contrôle Hiérarchique à Modèle Prédictif (HMPC) a été adoptée pour remédier aux incertitudes liées aux déséquilibres de puissance ainsi qu'établir un compromis entre la réduction du coût de fonctionnement et le respect du code de l'énergie français.

Considérant que les bâtiments ne sont pas homogènes et nécessitent des solutions adaptées à leur besoin, le contrôleur proposé a été couplé à deux modules fonctionnant à base d'analyse de données. Le premier algorithme consiste à gérer les inexactitudes dans les modèles internes de l'HMPC. Sans avoir besoin de régler aucun paramètre, cet algorithme améliore la précision du modèle de batteries jusqu'à trois fois et augmente jusqu'à dix fois la précision du modèle de stockage d'hydrogène, réduisant ainsi la dépendance de l'EMS aux étapes de modélisation.

Le deuxième algorithme détermine de manière autonome les paramètres de l'HMPC et facilite le compromis entre les aspects économiques et énergétiques. S'appuyant uniquement sur l'analyse des données de déséquilibre de puissance et des mesures, le contrôleur hiérarchique spécifie quel dispositif de stockage d'énergie doit fonctionner quotidiennement en fonction de l'estimation du taux d'autoconsommation et du coût de fonctionnement du micro-réseau. Ces estimations diminuent les dépenses annuelles du micro-réseau en évitant la pénalisation en ce qui concerne les exigences d'autoconsommation et en réduisant la dégradation et l'entretien des systèmes de stockage d'énergie.

L'EMS proposé s'est également révélé capable de charger de préférence les batteries des véhicules électriques en période de surplus d'énergie et les décharger pendant les périodes de déficit pour réduire les échanges d'énergie avec le réseau principal. Les résultats ont aussi montré que la contribution des batteries de véhicules électriques dépend de la taille du parc de véhicules, de leur temps de connexion et du profil de déséquilibre de puissance. En conclusion, à travers les simulations utilisant le dimensionnement réel d'un bâtiment public et résidentiel, l'EMS hiérarchique s'est avéré efficace pour gérer de nombreux dispositifs de stockage d'énergie et contribuer à l'essor de micro-réseaux dédiés aux bâtiments à l'avenir.

Mots clés : Contrôle Hiérarchique par Modèle Prédictif, Micro-réseau dédié aux Bâtiments, Système de Stockage d'Hydrogène, Batteries Li-ion, Véhicules Electrique, Algorithmes basés sur les données, Optimisation, Sources d'Energie Renouvelables.

Acknowledgments

I would like to express my gratitude to my supervisors, Prof. Dr. Ionel Vechiu and Prof. Dr. Jean-Paul Gaubert, for the continuous support of my Ph.D. thesis. Thanks to them, I had the opportunity to come to France and contribute to the latest research in the domain of building microgrids. Particularly, I am very grateful to Prof. Dr. Ionel Vechiu for his valuable guidance throughout this research. He has always been very patient in teaching me how to present the research work as concise and clear as possible. He gave me valuable remarks in the manuscript that were crucial for improving the research. Additionally, he has always encouraged me to go further, by proposing me new opportunities and new visions of thinking. I would like also to thank Prof. Dr. Jean-Paul Gaubert for his commitment with all administrative issues related to the SISMI Doctorate School and for his kindness in explaining me the main aspects of being a researcher.

During the thesis, I also had the opportunity to meet incredible people, such as all Ph.D. students and researchers at ESTIA Institute of Technology. I would like to thank them for all discussions that we had either professionally or casually. I am especially thankful to Samuel Jupin who not only gave me valuable insights during the early stages of the hierarchical building energy management system design but also helped me to improve my French skills and learn more about the French culture.

I am extremely grateful to my parents who have encouraged me to pursue the studies and my dreams. Even separated by the second largest ocean, they supported me all along this journey. They offered me all the moral motivations necessary to complete this Ph.D. thesis. I also would like to thank my twin brother, Rodrigo Yassuda Yamashita, who ever since has helped me in all situations.

Finally, I would like to thank my partner, Raphael de Brito Tamaki, for his patience in listening to all my debriefings concerning my Ph.D. thesis and his valuable recommendations. He helped me to conduct my Ph.D. thesis not only through our extensive discussions but also through his friendship. Certainly, without him, I would not be capable of achieving this goal.

Table of contents

Hierarchical Control for Building Microgrids **1**

Acknowledgments **4**

Overview of building microgrids **14**

Chapter 1 A literature review of the advantages and barriers of building microgrids **42**

1.1 Introduction 42

1.2 Building MicroGrid demonstrators and the state of energy management strategies 44

1.3 Requirements for building microgrid control systems 46

1.3.1 Power-sharing [100 ms – 1s]: 46

1.3.2 Thermal control and resident comfort [10 min – 1h]: 46

1.3.3 Voltage and frequency regulation [1ms – 1s] 46

1.3.4 Power dispatch and electricity market trading [1min – 1h]: 47

1.3.5 Elastic loads and demand response [more than 1h]: 48

1.3.6 Power quality enhancement concerning the grid code [1ms – 1 min]: 48

1.3.7 Grid faults and island detection [1ms – 1s]: 49

1.4 Hierarchical control structure 49

1.4.1 Hierarchical control topologies 53

1.5 Details of hierarchical control layers 55

1.5.1 Primary control layer 55

1.5.2 Secondary control layer 59

1.5.3 Tertiary control layer 59

1.6 Integration of building microgrid into the current electricity market 60

1.6.1 Traditional electricity market elements 60

1.6.2 Trends in the electricity market for building MicroGrids 65

1.6.3 Main strategies to trade on the electricity market 67

1.7 Review of the main energy management algorithms 67

1.7.1 Voltage and frequency regulation 68

1.7.2 Optimal power dispatch 69

1.7.3 Comparison of the advantages and disadvantages of the main energy management algorithms 73

1.8 Barriers and perspectives for building microgrids 74

1.9 Conclusions 75

Chapter 2 Modelling of the building microgrid simulator in MATLAB Simulink **77**

2.1 Introduction 77
2.2 Modelling of the DC bus and the main grid 78
2.3 Modelling of the PVs power generation and building power consumption 81
2.3.1 Modelling of photovoltaic panels power generation 82
2.3.2 Modelling of building power consumption 83
2.4 Modelling of the day-ahead electricity price 85
2.5 Modelling of energy storage devices and their ancillary devices 85
2.5.1 Modelling of Lithium-ion batteries 85
2.5.2 Modelling of hydrogen energy storage system 90
2.6 Conclusion 102
Chapter 3 Description of the hierarchical control structure 103
3.1 Introduction 103
3.2 The fundamental concepts of Model Predictive Control strategy 104
3.3 Linear models for predicting the Building MicroGrid states 107
3.3.1 Modelling of building raw net power imbalance and electricity price evolution 107
3.3.2 Modelling of energy storage devices 108
3.4 Hierarchical Model Predictive Control 121
3.4.1 Economic Model Predictive Control 121
3.4.2 Tracking Model Predictive Control 123
3.4.3 Common constraints in the hierarchical MPC structure 124
3.5 Power-sharing Module 128
3.6 Conclusion 133
Chapter 4 Real-time model identification 134
4.1 Introduction 134
4.2 Detail of the RTMI algorithm for batteries 135
4.2.1 Step 1: Classification of data measurements by temperature interval 137
4.2.2 Step 2: Updating the values of the batteries model parameters 140
4.2.3 Step 3: Identification of the limits for charging and discharging the batteries 144
4.2.4 Evaluation of the performance of RTMI of batteries model 146
4.3 Detail of the RTMI algorithm for hydrogen energy storage energy 150
4.3.1 Dynamic identification of the parameter linking the stack current and $\Delta LoHk$ 151
4.3.2 Linear regression between current and power 154
4.3.3 Evaluation of the performance of RTMI of hydrogen energy storage system 158

4.4 Conclusions 159

Chapter 5 The MicroGrid cost estimator 160

5.1 Introduction 160

5.2 Estimation of the expected annual building microgrid cost 161

5.2.1 Electricity cost 161

5.2.2 Costs due to the degradation of energy storage devices 161

5.2.3 Grid reward for self-consuming electricity 164

5.2.4 Grid penalization for not attaining the marks of self-consumption 166

5.2.5 Summary of the estimation of the building microgrid operation cost 166

5.3 Details of the algorithm for estimating the annual self-consumption rate 167

5.3.1 Classification of prediction data using k-means algorithm 167

5.3.2 The estimation of the average behaviour of the hierarchical MPC 171

5.3.3 Integration of the annual expected self-consumption rate into the formulation of the Economic Model Predictive Control 174

5.4 Initialisation of the microgrid cost estimator algorithm 175

5.5 Validation of the microgrid cost estimator algorithm 176

5.5.1 Validation of the estimation of the annual self-consumption rate 176

5.5.2 Validation of the estimation of the annual microgrid operating cost 183

5.6 Conclusion 189

Chapter 6 Simulation results 191

6.1 Introduction 191

6.2 The input parameters and conditions of simulation tests 191

6.3 The conventional hierarchical model predictive controller and the rule-based controller 192

6.4 The metrics for comparison and overview of the simulation cases 193

6.5 Comparison between RB, HMPC, and HMPC-kmeans 195

6.5.1 Impact of installing an energy storage system 195

6.5.2 Impact of hydrogen ESS capital costs 201

6.5.3 Impact of operating the hydrogen ESS at a nominal power rate 205

6.5.4 Impact of power imbalance prediction data error 207

6.6 Performance of the power-sharing module and potentials of exploring the batteries of electric vehicles 210

6.6.1 Performance of the Power-sharing module 210

6.6.2 Potentials of exploring the batteries of electric vehicles 218

6.6.3 Directives to adapt the MG cost estimator to operate with the electric vehicles 222
6.7 Conclusion 224
Chapter 7 Conclusions and perspectives 228
List of publications 234
Appendix 235
I. Calculation of hydrogen utilisation rate in PEMFC 235
II. Analytical equations for calculating the linear parameters of the hydrogen chain linear model 236
III. Dynamic average algorithm 238
IV. Calculation of the premium for self-consuming electricity (additional income) 238
V. Absolute values of the simulation of Chapiter 6 239
References 241

Abbreviations

BEMS	Building Energy Management System
BMG	Building MicroGrid
CACM	Capacity Allocation & Congestion Management
CCDG	Community Controllable Distributed Generator
CHC	Centralized Hierarchical Control
CSC	Current Sources Converters
DER	Distributed Energy Resources
DG	Distributed Generator
DHC	Distributed Hierarchical Control
DSM	Demand-Side Management
DSO	Distributed System Operators
EMPC	Economic Model Predictive Controller
EMS	Energy Management System
ESS	Energy Storage System
GA	Genetic Algorithm
GenCom	Generator Companies
HMPC	Hierarchical Model Predictive Control
HVAC	Heating Ventilation and Air Conditioning
HHC	Hybrid Hierarchical Control
KPI	Key Performance Indicators
LoH	Level-of-hydrogen
LSE	Local Services Entities
MAS	Multi-Agent System
MG	Microgrid
MGC	Microgrid Community
MILP	Mixed-Integer Linear Programming
MINLP	Mixed-Integer Non-Linear Programming
MO	Market Operator
MPC	Model Predictive Control
MPPT	Maximum Power Point Tracking
NEMO	Nominated Electricity Market Operator
NZEB	Net-Zero Energy Building
O&M	Operation and Maintenance
PCC	Point of Common Coupling
PEV	Plug-in Electric Vehicle
PI	Proportional Integral
PSM	Power Sharing Module
PSO	Particle Swarm Optimisation
PV	Photovoltaic panel
PWM	Pulse Width Modulation
RB	Rule-based controller
RES	Renewable Energy Source
RTMI	Real-Time Model Identification
SoC	State-of-Charge
SPOF	Single Point Of Failure
TMPC	Tracking Model Predictive Controller
v&f	Voltage and Frequency
VSC	Voltage Source Converter
WT	Wind Turbine

Acronyms and Indexes

P	– power (W) or pressure (Pa)
E	– Energy (Wh)
π	– Price (€) or Geometric plan
δ	– Binary variable [0 or 1]
i_t	– Integral of current (Ah)
T	– Temperature (K or °C)
t	– Time (h or s)
ID	– Identification number of an electric vehicle
η	– Efficiency of energy storage systems (%)
f	– Function
Δ	– Variation between time k and $k-1$
ω	– Weight
v	– Voltage (V)
i	– Current (A)
C	– Capital cost (€)
k	– Index of time (h)
$pevs$	– All electric vehicles in the parking
pev_{ID}	– Electric vehicle with ID number
bat	– Lithium-ion batteries
fc	– Fuel cell stack
els	– Electrolyser
$tank$	– Hydrogen tank
ref	– Reference
nom	– Nominal value
$meas$	– Measurement
$comp$	– Compressor
avg	– Average
sc	– Self-Consumption
$inst$	– Installation

Variables

P_{imb}
Raw net power imbalance (W)

P_{grid}^{import}
Power imported from the grid (W)

$P_{grid,k}^{injected}$
Power injected into the grid (W)

P_{els}
Power consumed by the electrolyser (W)

P_{fc}
Power produced by the fuel cells (W)

P_{bat}^{dis}
Power used to discharge batteries (W)

P_{bat}^{ch}
Power used to charge the batteries (W)

P_{pevs}^{dis}
Power used to discharge electric vehicle parking (W)

P_{pevs}^{ch}
Power used to charge electric vehicle parking (W)

P_{bat}
Power reference to operate batteries (W)

P_{pevs}^{ref}
Power reference to operate electric vehicle parking (W)

P_{pv}
Photovoltaic power generation (W)

P_{cons}
Building power consumption (W)

P_{comp}
Power consumed by the hydrogen compressor (W)

SoC_k^{pevs}
Average SoC of the electric vehicle parking (%)

$\delta_{pev_{ID},k}$
Boolean variable indicating whether the electric vehicle of ID number is plugged to the building microgrid

$Q_{pev_{ID}}$
Capacity of the electric vehicle of ID number (Ah)

$Q_{pevs,k}$
Capacity of electric vehicle parking at instant k (Ah)

N_{PEV}
Number of charging stations

LoH_k
Level of hydrogen stored in the tank (%)

n_k^{pevs}
Number of electric vehicles plugged at the microgrid

$t_{arrival}$
Estimated arrival time of an electric vehicle (h)

$t_{departure}$
Estimated departure time of an electric vehicle (h)

$t_{pevID,k}^{connection}$
Time that the electric vehicle ID stay connected to the building microgrid (h)

$t_{pevID,k}^{minCharge}$
Minimum time needed to fully charge the electric vehicle ID (h)

$\delta_{pev_{ID}}^{available}$
Boolean variable indicating whether the owner of electric vehicle ID has authorized the discharge of its vehicle's batteries

δ_{pevs}^{ch}
Integer variable indicating whether electric vehicle parking is charging

$n_k^{arrival}$
Number of electric vehicle arrivals at instant k

$n_k^{departure}$
Number of electric vehicle departures at instant k

η_{dis}^{pev}
Discharging efficiency of electric vehicle's batteries (%)

η_{ch}^{pev}
Charging efficiency of electric vehicle's batteries (%)

P_{pevs}^{MAX}
Electric vehicle parking maximum discharging power rate (W)

P_{pevs}^{MIN}
Electric vehicle parking maximum charging power rate (W)

$i_{t,k}^{pevs}$
Energy stored in the aggregation of electric vehicles (Ah)

$i_{t_k}^{arrival}$
Energy stored at the electric vehicles when plugged to the building microgrid at instant k (Ah)

$i_{t_k}^{departure}$
Energy stored at the electric vehicles when disconnected from the building microgrid at instant k (Ah)

$v_{pevs,k}$
Average voltage at all electric vehicles' batteries [V]

P_{pv}^{inst}
Photovoltaic nominal power installation (W)

$i_{t,k}^{bat}$
Energy stored in Lithium Batteries (Ah)

Q_{nom}^{bat}
Lithium-ion batteries nominal capacity (Ah)

Q_{bat}
Lithium-ion batteries maximum capacity (Ah)

$P_{dc,k}$
Lithium-ion batteries power reference when they are discharging at instant $k-1$ and charging at instant k (W)

$P_{cc,k}$
Lithium-ion batteries power reference when they are charging at instant $k-1$ and k (W)

$P_{cd,k}$
Lithium-ion batteries power reference when they are charging at instant $k-1$ and discharging k (W)

$P_{dd,k}$
Lithium-ion batteries power reference when they are discharging at instant $k-1$ and k (W)

$\delta_{cc,k}$
Integer variable indicating whether batteries were charging at $k-1$ and k

$\delta_{dc,k}$
Integer variable indicating whether batteries were discharging at $k-1$ and charging at k

$\delta_{dd,k}$
Integer variable indicating whether batteries were discharging at $k-1$ and k

$\delta_{cd,k}$
Integer variable indicating whether batteries were charging at $k-1$ and discharging at k

$\delta_{k}^{lastCharge}$
Dummy integer variable to indicate whether the batteries were charging at instant k

T_{cell}
Cell temperature (°C)

η_{ch}^{bat}
Charging efficiency of Lithium-ion battery pack (%)

η_{dis}^{bat}
Discharging efficiency of Lithium-ion battery pack (%)

v_{nom}^{bat}
Lithium-ion batteries nominal voltage

P_{bat}^{MIN}
Lithium-ion batteries maximum discharging power (W)

P_{bat}^{MAX}
Lithium-ion batteries maximum charging power (W)

$\alpha_{\varepsilon}, \beta_{\varepsilon}, \gamma_{\varepsilon}$
Parameters defining the intermediary linear model of batteries model, where $\varepsilon = \{cc, dc, dd, cd\}$ is the sequence status of charging and discharging of batteries

θ_{ε}
Parameters defining the final linear model of batteries model, where $\varepsilon = \{cc, dc, dd, cd\}$ is the sequence status of charging and discharging of batteries

T_{class}
Temperature class used to determine the linear model of batteries in real-time

T_s
Time sample of the model (the unit depends on the model application)

T_s^{EMPC}
Time stamp of economic model predictive controller (h)

T_s^{TMPC}
Time stamp of tracking model predictive controller (h)

N_h^{EMPC}
Horizon of the economic model predictive controller (h)

N_h^{TMPC}
Horizon of the tracking model predictive controller (h)

f_{pevs}
Linear function to predict the energy stored in the electric vehicle parking

f_{bat}
Linear function to predict the energy stored in Lithium-ion battery pack

f_{els}
Linear function to predict hydrogen consumed by the electrolyser

f_{fc}
Linear function to predict hydrogen produced by fuel cell

$\dot{n}_{H_2}^{els}$
Hydrogen flow production (mol s^{-1})

$\dot{n}_{H_2}^{fc}$
Hydrogen flow consumption (mol s^{-1})

$N_{cells}^{els}, N_{cells}^{fc}$
Number of cells in the electrolyser or fuel cell stack

$A_{cells}^{els,fc}, A_{cells}^{els,fc}$
Fuel cell or electrolyser membrane active area (cm^2)

F
Faraday constant (A s mol^{-1})

R
Ideal gas constant (m^3 Pa K^{-1} mol^{-1})

$n_{H_2,k}^{tank}$
Number of moles in the hydrogen tank (mol)

$\boldsymbol{T_{tank}}$
Temperature of the hydrogen tank (K)

$\boldsymbol{V_{tank}}$
Hydrogen tank volume (m^3)

$\boldsymbol{\Delta P_{tank,k}}$
Hydrogen tank pressure variation between k and $k-1$ (Pa)

$\boldsymbol{n_{H_2}^{max}}$
Maximum number of moles that the hydrogen tank can store (mol)

$\boldsymbol{\beta_{Faraday}^{els}}$
Angular coefficient linking the current in electrolyser with the tank's pressure variation ($\Delta P_{tank,k}$) (Pa A^{-1})

$\boldsymbol{\beta_{Faraday}^{fc}}$
Angular coefficient linking the current in fuel cell with the tank's pressure variation ($\Delta P_{tank,k}$) (Pa A^{-1})

$\boldsymbol{\beta_{els}^{zone_i}}$
Linear coefficient linking the current and power consumed by the electrolyser if it is in power zone $i \in \{1,2,3\}$ (A)

$\boldsymbol{\alpha_{els}^{zone_i}}$
Angular coefficient linking the current and power consumed by the electrolyser if it is in power zone $i \in \{1,2,3\}$ (A W^{-1})

$\boldsymbol{\beta_{fc}^{zone_i}}$
Linear coefficient linking the current and power in fuel cell if it is in power zone $i \in \{1,2,3\}$ (A)

$\boldsymbol{\alpha_{fc}^{zone_i}}$
Angular coefficient linking the current and power in fuel cell if it is in power zone $i \in \{1,2,3\}$ (A W^{-1})

$\boldsymbol{P_{fc,k}^{zone_i}}$
Power generated by the fuel cell if it is in power zone $i \in \{1,2,3\}$ (W)

$\boldsymbol{\delta_{fc,k}^{zone_i}}$
Boolean variable indicating whether the fuel cell is operating in power zone $i \in \{1,2,3\}$

$\boldsymbol{\delta_{els,k}^{zone_i}}$
Boolean variable indicating whether the electrolyser is operating in power zone $i \in \{1,2,3\}$

$\boldsymbol{P_{fc}^{MAX}}$
Fuel cell maximum power rate (W)

$\boldsymbol{P_{els}^{MAX}}$
Electrolyser maximum bearable power rate (W)

$\boldsymbol{x_{H_2}}$
Nominal composition of hydrogen in the fuel flow (%)

$\boldsymbol{NC_{fc}}$
Number of oscillations in the fuel cell current density

$\boldsymbol{\pi_{bat}^{deg}}$
Amortized battery degradation cost (€)

$\boldsymbol{\pi_{els,k}^{deg}}$
Amortized fuel cell degradation cost (€)

$\boldsymbol{\pi_{sc,k}}$
Annual reward for self-consuming electricity (€)

$\boldsymbol{\pi_{grid}}$
Electricity expenses (€)

$\boldsymbol{\pi_{elec}}$
Electricity price (€/Wh)

$\boldsymbol{\pi_{sc,k}^{pen}}$
Penalisation for not attaining the required marks of annual self-consumption rate (€)

$\boldsymbol{t_{reOpt}}$
Time in which the re-optimisation of the Economic Model Predictive is triggered (h)

$\boldsymbol{P_{grid,k}^{meas}}$
Time in which the re-optimisation of the Economic Model Predictive happened (h)

$\boldsymbol{\Delta P_{grid}^{thr}}$
Power exchanged with the grid measured by the smart meter every hour (W)

$\boldsymbol{\varepsilon_{grid,k}}$
Predefined threshold of the error between the estimated ($P_{grid}^{import} + P_{grid}^{export}$) and real power exchanged with the grid ($P_{grid,k}^{meas}$) (%)

$\boldsymbol{d_{bat}}$
Degradation rate of batteries (Ah Wh^{-1})

$\boldsymbol{d_{fc}}$
Degradation rate of fuel cell (V Wh^{-1})

$\boldsymbol{d_{els}}$
Degradation rate of electrolyser (V Wh^{-1})

$\boldsymbol{\tau_{sc}}$
Self-Consumption rate (%)

$\boldsymbol{\tau_c}$
Coverage or Self-Sufficient rate (%)

$\boldsymbol{\beta_{grid}^{EMPC}}$
Cost function weight of Economic Model Predictive Control to penalise grid energy exchange (€/Wh)

$\boldsymbol{\beta_{fcDeg}^{EMPC}}$
Cost function weight of Economic Model Predictive Control to penalise fuel cell degradation (€/Wh)

$\boldsymbol{\beta_{elsDeg}^{EMPC}}$
Cost function weight of Economic Model Predictive Control to penalise electrolyser degradation (€/Wh)

$\boldsymbol{n}_{K_{today}}^{\boldsymbol{future}}$
Estimated number of times the k-means class K_{class} is likely to be repeated until the end of the year

$\boldsymbol{n}_{K_{tomorrow}}^{\boldsymbol{future}}$
Estimated number of times the k-means class $K_{tomorrow}$ is likely to be repeated until the end of the year

$\mathbb{C}_{\boldsymbol{K}}$
Centroid of the k-means class K

$\boldsymbol{\beta}_{\boldsymbol{sc}}^{\boldsymbol{const}}, \boldsymbol{\beta}_{\boldsymbol{sc}}^{\boldsymbol{today}}, \boldsymbol{\beta}_{\boldsymbol{sc}}^{\boldsymbol{tomorrow}}$
Parameters of for estimating the annual self-consumption rate

$\boldsymbol{\beta}_{\boldsymbol{maxInjected}}^{\boldsymbol{EMPC}}$
Cost function weight of Economic Model Predictive Control to reduce the maximum power injected (€/W)

$\boldsymbol{\beta}_{\boldsymbol{batDeg}}^{\boldsymbol{EMPC}}$
Cost function weight of Economic Model Predictive Control to penalise batteries degradation (€/Wh)

$\boldsymbol{\beta}_{\boldsymbol{scPen}}^{\boldsymbol{EMPC}}$
Cost function weight of Economic Model Predictive Control to avoid disrespecting the minimum index of self-consumption required by the grid code (€)

Overview of building microgrids

1 General introduction

Energy is essential for the modern economy and is of great importance for the needs of society. Despite its relevance, the energy sector is consolidated over an unsustainable system that meets 70% of primary energy demand with fossil fuel [1]. Consequently, it has grown the awareness about environment protection and has incited the development of more durable alternatives for energy generation. In this context, Renewable Energy Sources (RESs) play a fundamental role to pave the way toward the transformation of the global energy sector from fossil-based to zero-carbon energy.

This energetic transition depends on policy-based incentives and restructuring in all branches of the energy sector. The fast energy transitioning scenario, well in line with the Paris Agreement signed in 2016, plans to reduce in 90% the carbon emission produced from electricity by 2050 [2]. To attain this target, significant efforts are needed to expand the integration of RESs into the current electrical grid and shift the energy mix toward low-carbon sources based on solar and wind energy.

Unlike traditional fuel power plants, RESs are non-dispatchable units that cannot be fully controlled due to power production uncertainties induced by their dependency on weather conditions. Without any dispatchable unit, in the form of Energy Storage System (ESS), RESs represent a thread for grid stability, especially due to fluctuations in their energy generation [3], [4]. In front of this problem, by approaching final energy consumers to power generation units, Building MicroGrids (BMGs) have emerged as a suitable grid topology for hedging these uncertainties and fostering RESs breakthrough [5]–[8].

This innovative grid structure – in which distributed RESs and ESS are installed near to power consumption – enables to connect the second largest sector consumer of energy to the generation sector directly, without needing long and expensive transmission lines. Being a part of a larger distributed grid architecture, the interest of BMGs is to promote the use of renewables while beneficiating from the potential of natural and clean sources of energy that are usually not exploited. By installing roof-top PhotoVoltaic (PV) panels, buildings can profit from free solar energy and become active prosumers (i.e. both producers and consumers of energy) in the current electricity market.

This new configuration allows buildings to either import or inject energy into the external grid, which can reduce their electricity expenditure. However, without any grid regulation for limiting their energy injection, BMGs will increase the grid management complexity, especially due to the subtle rise of unpredictable grid actors [9]. To maintain grid stability, stringent requirements concerning BMG energy import and injection have been designed.

Although the grid code for individual prosumers is still under development [9], [10], it is of primary interest of grid operators to dispose of faithful estimations concerning the daily power imbalance to supply the energy demand as efficiently as possible. Therefore, the grid restructuring for adapting forthcoming BMGs to the current power grid consists of simplifying the role of market operators by introducing the concept of self-consumption of PV electricity [11]. This grid regulation aims at reducing

the total amount of energy injected into the grid, by prioritizing the consumption of the electricity generated locally over its injection into the public power grid. Therefore, the power consumed directly from either the on-site PV power system or the local ESSs defines the self-consumed energy, which is a key indicator for assessing the energetic autonomy of PV-coupled systems.

An important aspect constraining BMGs to become a large market player is the economics of the investment. Various support schemes have been needed to make PV coupled with ESS cost-efficient and compensate for the trade-off between local electricity production costs and the savings made by avoiding purchasing electricity. To economically encourage both the installation of PVs in buildings and the consumption of renewable energy locally, a mechanism of reward and penalty based on the amount of self-consumed energy has been established in many countries worldwide, including in France [12]. However, it is needed further analysis to verify whether this policy is aligned to make BMGs affordable and sustainable for the near future.

The foremost challenge faced by BMGs lies in the complexity of respecting the strict grid code regarding self-consumption while keeping the whole system profitable and durable. Within this context, hierarchical control has proved suitable for handling multiple and conflicting requirements simultaneously so that it can satisfactorily adapt to building environments. Therefore, the focus of this Ph.D. thesis resides in the design of a hierarchical Energy Management System (EMS) capable of handling electrical and economic hurdles arisen from the integration of PVs and hybrid ESSs into non-residential (e.g. public) and residential buildings. The French grid reward for fostering high marks of self-consumption, the degradation costs of ESSs, along with the potentials of exploiting batteries of Plug-in Electric Vehicles (PEV) on behalf of the BMG are the central topics of this study.

2 Thesis outline

The main objective of this doctoral thesis is to propose a novel hierarchical control architecture to optimise the power flow among BMG resources, considering the fluctuations in the daily electricity price, the unstable load demand, and the stochasticity of renewable energy generation. The purpose of this research work is to identify and propose a feasible solution for the main barriers of the real implementation of BMGs not only from a technical perspective but also from economic standpoints. Intending to establish a solid background about the advantages and challenges of BMGs, Chapter 1 comprehends a detailed literature review on the main hierarchical control algorithms for BMGs. This chapter, which is also available in the format of a journal paper [13], enumerates the paramount requirements for BMG control systems and outlines some insights for forthcoming building prosumers.

All this piecewise knowledge built from the deeper understanding and critical analysis of the most recent scientific literature on the topic of hierarchical control for BMGs allowed to identify the Model Predictive Control (MPC) algorithm as the most suitable control strategy for tackling the major BMG feasibility problems. Therefore, in the scope of this thesis, the performance of a hierarchical MPC controller was assessed through simulations in MATLAB Simulink® using real sizing of a public and a residential BMG. In this regard, Chapter 2 provides a detailed description of the mathematical modelling of the BMG electrical components used for emulating the real behaviour of a medium-size

DC-AC BMG, including the PV arrays, the hydrogen ESS, the Lithium-ion batteries, and the parking of plug-in electric vehicles. Chapter 2 also details the input parameters of the whole system, evidencing the modelling of both the electricity price evolution and the building power imbalance profile.

Chapter 3 details the proposed hierarchical control architecture based on the concatenation of two MPCs synchronized with two data-driven algorithms and one power sharing module. The first versions of the hierarchical controller were published in [14] and [15], whereas the final version is detailed in [16]. This chapter deals with the definition of equality and inequality constraints, which are essential for BMGs to respect the restriction in total energy injection and total electricity purchase imposed by the grid code. A brief overview of the objectives and responsibilities of each control unit in the BMG operation is the focus of this chapter, which aims to provide a global comprehension of the whole hierarchical control by stating the most important features concerning its operation.

Subsequently, in Chapter 4 and Chapter 5, further details about the operation of the two data-driven algorithms are described. These two MPC extension modules aim at enhancing the BMG flexibility by reducing human intervention when designing the microgrid EMS. The essence of these data-oriented approaches consists of learning from the BMG past behaviour to improve future actions. In this view, Chapter 4 presents the first data-driven module [15], which addresses ESS model inaccuracy issues, which is one of the utmost weakness of MPC. The robustness of the proposed real-time module was evaluated under scenarios that consider imprecisions in manufacturing parameters, temperature variation, and ageing effects of batteries and just manufacture parameter imprecisions of hydrogen ESS.

Afterwards, Chapter 5 explains how the MPC cost function was designed to attain, at minimum operation cost, the marks of self-consumption required by local grid regulators [16]. The weights of the MPC cost function are updated dynamically thanks to strong data processing implemented by the second data-driven module. The core of this algorithm lies in classifying the daily net power imbalance data of the previous year into four classes sharing a common portion of data and calculating the likelihood of attaining the grid requirement concerning self-consumption rate and the corresponding operation cost.

In Chapter 6, the flexibility of the designed cost function together with the resilience of the whole hierarchical control architecture was assessed by analysing its performance when dealing with different datasets, distinct intensities of prediction data error and diverse BMG installed devices. Part of this thoughtful analysis is also available in [16]. The sensitivity of the controller to the variation in the ESS capital cost was also evaluated to verify the economic viability of hydrogen ESS and batteries. Additionally, considering that one of the greatest challenges of the design of a reliable EMS for hybrid ESS is the trade-off between the use of batteries and hydrogen ESS, the proposed cost function was assessed when either a single or hybrid ESS is installed in the BMG. The effectiveness of the proposed control regarding all these aspects was compared to a well-established rule-based controller and a hierarchical MPC using a simplified cost function. Last but not least, the potentials of exploiting the batteries of PEV to reduce the grid energy dependence were also assessed with the purpose to take full advantages of PEV parking without damaging the total welfare of PEV's owners. The main results of this analysis are under consideration for publication in a conference paper.

The last chapter outlines the theoretical, methodological, and practical relevance of this thesis and points out some directives for further research on the topic of energy management in building microgrids.

Chapitre 1 État de l'art sur les avantages et les obstacles des micro-réseaux dédiés aux bâtiments

Les micro-réseaux dédiés aux bâtiments (BMG) sont apparus comme une alternative avantageuse pour faire face aux problèmes environnementaux et sont susceptibles d'apporter du service au réseau de distribution d'électricité. Cependant, les incertitudes au niveau de la production et de la consommation, ainsi que les exigences strictes imposées par le code de l'énergie restreignent le développement à grande échelle des BMG. La conception d'un système de gestion de l'énergie (EMS), qui soit à la fois conforme aux exigences du réseau principal de distribution ainsi qu'économiquement avantageux, représente aujourd'hui un défi conséquent au développement des BMG.

Pour répondre au mieux à autant d'exigences liées au BMG, la structure de contrôle hiérarchique a été de plus en plus adoptée. L'intérêt principal de cette topologie est qu'elle permet de gérer plusieurs objectifs parfois contradictoires et qui ne sont pas sur la même échelle de temps. Le contrôle hiérarchique appliqué à la gestion de flux de puissance vise principalement à attribuer de manière optimale les références de puissance à chaque dispositif électrique installé dans le micro-réseau.

Dans les environnements des BMG, l'objectif principal est de maximiser l'exploitation des Sources d'Energie Renouvelable (RES) et de minimiser la dépendance énergétique vis-à-vis du réseau principal, tout en évitant les mesures non désirables, telles que la coupure des sources d'énergie ou la non-alimentation des certaines charges. Notamment, sans aucun Système de Stockage d'Energie (ESS), le bilan de puissance ne peut être satisfait que par l'achat d'électricité au réseau principal. Néanmoins, cela ne constitue pas forcément une configuration plus rentable, puisque l'insertion de ESS peut conduire à une réduction des dépenses d'achats d'électricité.

Afin d'appréhender les problématiques liés aux BMG, en englobant l'installation de RES couplées à des ESS dans les bâtiments, ce chapitre propose une étude approfondie de la littérature sur les algorithmes de contrôle appliqués à l'environnement des BMG. Cet état de l'art représente une aide et un support à la conception d'un système complet de gestion d'énergie d'un bâtiment en détaillant chaque niveau de contrôle dans une structure hiérarchique. Il fournit un ensemble de notions importantes pour comprendre le domaine des réseaux intelligents, des systèmes de gestion de l'énergie et des exigences du marché de l'électricité, ce qui est fondamental pour favoriser non seulement le développement de BMG, mais aussi de multiples projets durables.

Afin de vérifier l'état de développement des BMG actuel, la section 1.2 analyse quelques études scientifiques se reportant aux démonstrateurs réels des BMG. En analysant les approches majoritaires et récentes pour rendre les bâtiments plus durables et énergétiquement efficients à l'avenir, il a été constaté que les démonstrateurs employant les RES et les ESS migrent du stade de recherche et développement à la pleine accessibilité du marché. La complexité de la conception d'un EMS est une des principales causes empêchant l'essor de BMG. Dans le but de réduire cette complexité, la plupart des EMS destinés aux BMG sont configurés de manière hiérarchique, en superposant les contrôleurs locaux des convertisseurs de puissances à un contrôleur central dédié à la gestion du flux de puissance.

Pour identifier les freins au développement de BMG, la section 1.3 résume les principaux cahiers des charges pour la conception et la mise en œuvre d'un EMS. La régulation de la fréquence et de la tension, la détection d'erreurs de conformité vis-à-vis du standard pour la qualité d'énergie, la gestion de la réponse à la demande, le contrôle thermique et la gestion optimale du flux de puissance ont été soulignés comme les exigences majeures auxquelles le contrôleur hiérarchique doit répondre. Il est notable que toutes ces tâches doivent être accomplies en parallèle, même si elles ne sont pas sur la même échelle de temps. En raison de la réponse rapide des convertisseurs de puissance, la régulation de la fréquence et de la tension, le partage de la puissance et la détection du fonctionnement en mode îloté doivent être satisfaits presque instantanément (quelques millisecondes). D'autre part, toutes les notions liées aux problèmes de la qualité de l'énergie peuvent être traitées sur une fenêtre de quelques millisecondes à une minute. Par ailleurs, la répartition de l'énergie peut être examinée en quelques minutes, tandis que l'optimisation économique et la participation au marché d'électricité sont généralement déployées toutes les minutes à une heure.

Face à cette variation temporelle, l'architecture hiérarchique est considérée comme une configuration appropriée pour des applications dans les BMG car elle permet de contrôler plusieurs variables presque indépendamment, grâce à sa structure intrinsèque en cascade. En vue de comprendre plus en détail la structure hiérarchique, la section 1.4 explique les trois topologies les plus usitées et décrites dans la littérature, à savoir la structure centralisée, distribuée ou la combinaison des deux, formant les structures hybrides. Ensuite, dans la section 1.5, les trois couches constituant le contrôle hiérarchique sont détaillées, notamment le contrôle primaire, secondaire et tertiaire.

Bien qu'elle ne soit pas totalement standardisée, la commande primaire est divisée en deux : une boucle interne chargée de réguler la tension et le courant à la sortie des convertisseurs de puissance, et la boucle externe chargée d'assurer le partage de la puissance. Les principaux thèmes qui font encore l'objet de recherches pour la boucle interne demeurent l'amélioration de la réponse transitoire, la réduction des déséquilibres de tension, de fréquence et des harmoniques, et l'élaboration d'algorithmes de contrôle capables de fonctionner en modes micro-réseau connecté ou déconnecté. Concernant la boucle externe, le partage de la puissance est généralement mis en œuvre de manière distribuée par des stratégies de *droop control*, en raison des exigences de communication à faible bande passante et grâce à leur flexibilité concernant la connexion et déconnexion des dispositifs composant le BMG. En plus des architectures distribuées, des structures centralisées, telles que les méthodes « maître-esclave », et concentrées, ont également été envisagées pour des raisons de moindre déviation de la tension et de la fréquence.

A propos des couches de contrôle supérieures, la commande secondaire est chargée de corriger les écarts de tension et de fréquence qui n'ont pas été résolus par la commande primaire. D'autre part, le contrôle tertiaire définit les références des puissances active et réactive optimales de chaque dispositif électrique distribué, ainsi que la quantité d'énergie que le BMG a besoin d'échanger avec le réseau externe pour satisfaire l'équilibre de la puissance entre la consommation et la production d'électricité. Pour une meilleure performance, la commande tertiaire peut considérer des données de prévision économiques et météorologiques dans sa prise de décision. Les commandes secondaire et tertiaire composent l'EMS du micro-réseau et en fonction du niveau des ressources de calcul, elles peuvent

embarquées différents types d'algorithmes de contrôle qui se différencient par leur complexité et performance. La section 1.7 explique les stratégies de commande existantes pour le bon fonctionnement du BMG et fournit une comparaison approfondie des algorithmes de gestion d'énergie.

Classés entre métaheuristique, déterministe, modèle prédictif, intelligence artificielle et stochastiques, les algorithmes de gestion du flux de puissance ont été détaillés en prenant soin de démontrer comment ils sont exploités dans le contexte des micro-réseaux. Les algorithmes les plus répandus dans chacune de ces catégories ont été comparés selon cinq critères, à savoir : capacité à considérer les prédictions, complexité du calcul, dépendance à la précision des modèles mathématiques, flexibilité concernant l'expansion du BMG et robustesse face aux incertitudes. Cette comparaison a permis d'identifier le Contrôle par Modèle Prédictif (MPC) comme l'approche la plus appropriée pour les BMG, grâce à sa robustesse, simplicité et capacité à prendre en compte les données de prédiction.

Sachant que les BMG sont une architecture de réseau innovante, l'analyse de la littérature conduite dans ce chapitre vise aussi à fournir une compréhension détaillée de la façon dont les BMG seront intégrés dans le réseau électrique actuel, permettant ainsi la transition énergétique. Dans ce contexte, la section 1.6 détaille le réseau électrique européen traditionnel et présente les configurations possibles pour connecter les BMG au marché électrique existant.

Finalement, la section 1.8 décrit les perspectives de BMG sur un avenir proche. De nombreuses projections sur le devenir des BMG existent, mais des cadres concrets pour l'architecture de réseaux électriques où les BMG pourraient s'intégrer ont besoin d'être établis. Les détails sur l'interopérabilité entre les bâtiments, la définition des protocoles de communication des bâtiments et la structure de la gestion de la demande sont des thématiques de recherche qui restent encore ouvertes et qui suscitent de l'intérêt. En se basant sur la littérature, il existe une tendance à la multi-coopération entre les bâtiments d'une même communauté pour atteindre des indices d'autoconsommation plus élevés. Ce mécanisme de régulation peut réduire l'instabilité du réseau et promouvoir l'utilisation d'énergies renouvelables. Pourtant, la définition des incitations économiques pour les services de réseau offerts par le BMG et les offres contractuelles avec d'autres acteurs du marché de l'électricité sont en cours d'élaboration.

Il ressort également de cette étude bibliographique la nécessité de concevoir un EMS plus flexible, capable de s'adapter à différentes configurations. Il est nécessaire de concevoir un contrôleur hiérarchique capable d'inclure facilement de nouveaux dispositifs électriques et de s'adapter automatiquement aux changements de l'environnement, sans avoir besoin de restructurer l'ensemble du contrôleur avec des tests exhaustifs. Dans ce contexte, les algorithmes dotés du traitement des données, comme les approches d'intelligence artificielle, sont envisageables pour les bâtiments. De plus, les systèmes de gestion de l'énergie de bâtiments doivent être capables de gérer la production d'électricité stochastique des énergies renouvelables en tenant compte des prévisions de données. Des algorithmes comme le contrôle prédictif et les stratégies basées sur des scénarios ont démontré leur capacité à couvrir ces risques.

À cet égard, cette thèse contribue à la conception d'un EMS hiérarchique pour optimiser le flux d'énergie dans des BMG publics et résidentiels équipés de panneaux photovoltaïques et d'un système de stockage d'énergie hybride, y compris des batteries, de stockage de l'hydrogène et des véhicules électriques. Cette nouvelle stratégie de contrôle combine les atouts du contrôle par modèle prédictif et

du traitement des données pour améliorer en permanence les performances du contrôleur. Les chapitres suivants détailleront le contrôle hiérarchique proposé dans le but de rendre possible l'intégration de BMG au réseau électrique.

Chapitre 2 Modélisation et simulateur d'un micro-réseau dédié aux bâtiments sous MATLAB Simulink

Ce chapitre décrit la modélisation et le simulateur associé élaboré sous la plateforme logicielle MATLAB-Simulink® pour émuler le comportement d'un Micro-Réseau dédié aux Bâtiments (BMG), principalement alimenté par des panneaux photovoltaïques et qui interagissent avec un agrégateur de réseau communautaire. Le BMG et son système hiérarchique de gestion de l'énergie s'appuient sur un système de stockage hybride composé par des batteries Lithium-ion et d'une chaîne d'hydrogène pour minimiser les importations et les exportations d'énergie du réseau, et donc maximiser le taux d'autoconsommation. En plus des stockages d'énergie statiques, les batteries des véhicules électriques (PEV) peuvent aussi supporter la demande énergétique du BMG. Les PEV peuvent être aussi déchargées pour couvrir la consommation du bâtiment à condition qu'elles soient complétement chargées avant leur départ prévu.

Le modèle du BMG implémenté sous MATLAB-Simulink® a été élaboré en envisageant un équilibre entre la précision des composants électriques distribués et la charge de calcul. Ce modèle est suffisamment complexe pour tenir compte de la dynamique principale du système et est suffisamment simple pour conduire à un temps de simulation raisonnable. Dans ce contexte, la section 2.2 décrit certaines simplifications adoptées pour réduire le temps de simulation. Ainsi, les effets transitoires induits par la commutation des interrupteurs de puissance dans les convertisseurs et l'impact de l'impédance de ligne du bus DC sur la qualité de l'énergie ont été présumés inexistants. Ces simplifications supposent que le BMG est connecté à un réseau principal puissant, capable de supporter le BMG indépendamment des puissances active et réactive nécessaires pour assurer l'équilibre de ces dernières au sein du BMG. Par conséquent, le convertisseur de puissance AC-DC reliant le BMG au réseau externe est considéré idéal.

Ensuite, dans la section 2.3 la modélisation de la production d'électricité et de la consommation sont détaillées. Sachant que l'énergie produite par les panneaux photovoltaïques et consommée par le bâtiment sont des variables stochastiques qui ne sont pas contrôlées directement par l'EMS, le comportement temporel de ces variables a été modélisé à l'aide d'un ensemble de données prédéfinit qui est lu à partir de fichiers CSV (*Comma-Separated-Variable*). Puisque l'objectif du BEMS développé est d'atteindre les indices d'autoconsommation imposés par le code de l'énergie français indépendamment des fluctuations du déséquilibre de puissance, la fidélité de la puissance générée et consommée avec le BMG réel n'est pas critique.

Comme le BMG en question est un micro-réseau connecté au réseau principal, la section 2.4 démontre comment l'interaction entre le BMG et l'agrégateur de réseau communautaire est établie. La demande de puissance du bâtiment est indirectement contrôlée par un mécanisme d'un signal de réponse à la demande provenant de l'agrégateur. En conséquence, le prix de l'électricité journalier est envoyé au contrôleur central du bâtiment pour réduire la consommation d'énergie aux heures pleines. Afin d'émuler ce phénomène, le prix journalier de l'électricité basé sur les tarifs d'Enedis® (opérateur de distribution français) de 2018 sont lus périodiquement à partir d'un fichier CSV. L'objectif d'inclure le prix de l'électricité dans le système de gestion de l'énergie est de faire réagir le contrôleur en fonction

des signaux de réponse à la demande de l'agrégateur communautaire, ainsi que d'estimer les dépenses annuelles avec l'électricité.

Pour détailler l'implémentation des modèles de systèmes de stockage – y compris les batteries Lithium-ion, véhicules électriques, électrolyseur et pile à combustible – la section 2.5 fournit toutes les connaissances permettant de comprendre comment les paramètres intrinsèques à chaque modèle doivent être réglés pour être conformes au dimensionnement du BMG. Pour émuler sous MATLAB-Simulink® le comportement réel des batteries Lithium-ion, le bloc existant sous Simulink® a été utilisé. Ce modèle mathématique a été validé par des résultats expérimentaux rapportés dans la littérature, et il admet hypothèses, telle que le manque de mémoire, la résistance interne constante et l'absence d'autodécharge. Malgré ces simplifications, ce modèle englobe les principales caractéristiques électriques et thermiques pour l'analyse de flux de puissance. Par conséquent, ce modèle a été adopté pour émuler le comportement des batteries installés dans le BMG et des batteries des véhicules électriques.

En particulier, pour se rapprocher le plus possible de l'environnement d'un BMG réel, les effets de température et de vieillissement du modèle Simulink® ont été activés pour la batterie du BMG. En revanche, les batteries des véhicules électriques ne tiennent pas compte ni des effets de la température, ni du vieillissement. De plus, contrairement aux batteries du BMG, les batteries des véhicules électriques ne sont pas connectées en permanence au BMG. Leur connexion au BMG dépend de l'heures d'arrivée et de départ des véhicules émulées par des interrupteurs commandés à l'aide d'un signal lu à partir d'un fichier CSV.

Dans l'objectif d'atteindre un modèle précis pour évaluer les aspects technico-économiques de l'installation d'un système de stockage en hydrogène au sein d'un bâtiment, la section 2.5.2 détaille le dimensionnement et l'implémentation sous Simulink® de l'électrolyseur, du compresseur, du réservoir de gaz d'hydrogène et de la pile à combustible. Parmi les types d'électrolyseur et de pile à combustible existants, la technologie en utilisant une Membrane d'Echange de Protons (PEM) s'avère plus adaptée à être couplée aux sources d'énergie renouvelable, grâce à son temps de réponse plus rapide et à son taux de dégradation plus faible lorsqu'elle est soumise à de puissance intermittente. À cet égard, le stockage à hydrogène implémenté sous Simulink® utilise la technologie PEM.

L'ajustement du dimensionnement de la pile à combustible et de l'électrolyseur consiste à empiler plusieurs cellules en série. Cette modularité constitue un avantage majeur de ces composants, leur permettant d'être utilisés dans différentes applications sans affecter énormément leur processus d'installation ou de maintenance. A partir d'un modèle prédéfini existant dans la libraire SimPowerSystem de MATLAB Simulink®, le nombre de cellule empilé dans la pile à combustible a été modifié pour arriver à la puissance nominale désirée. Il est important de souligner que ce modèle prédéfini est basé sur une courbe de polarisation d'une pile à combustible réelle existante sur le marché.

D'autre part, comme le modèle de l'électrolyseur dans MATLAB-Simulink® n'existe pas encore, un modèle simplifié a été conçu en s'appuyant sur des courbes de polarisation d'une cellule réelle pour cinq températures différentes. Malgré sa simplicité, ce modèle prend en compte les pertes liées au processus de séchage et de désoxydation de l'hydrogène ainsi que le potentiel d'activation de la cellule.

Ce modèle comporte donc les principales fonctionnalités pour permettre une analyse précise du flux de puissance.

Considérant que le système de gestion de l'énergie développé dans cette thèse de doctorat spécifie l'usage de systèmes de stockage selon leur durée de vie estimée et leur coût d'installation et d'achat, la dégradation des systèmes de stockage nécessite d'être modélisée. Cependant, le modèle de la pile à combustible existant sous Simulink® ne considère pas la réduction de la tension due à la dégradation des membranes. En raison de cette problématique, la perte graduelle d'efficacité de la conversion de l'entropie du gaz d'hydrogène en électricité a été modélisée à partir des résultats d'un test de durabilité de la membrane polymère pendant 1000 heures de fonctionnement sur différents modes d'opération.

D'après ces résultats, la chute de tension est plus intense lors de leur fonctionnement pendant de longues périodes et avec une densité de courant supérieure à 1 A/cm^2. En effet, de longues interruptions de fonctionnement de la pile à combustible ou de l'électrolyseur permettent à la membrane de se régénérer et de ce fait ralentissent sa dégradation. Par conséquent, les modèles de la pile à combustible et l'électrolyseur ont été améliorés en ajoutant un module émulant la perte d'efficacité de la réaction chimique de l'électrolyse due à la dégradation des membranes de cellules.

Pour rendre le simulateur du BMG plus complet, certains dispositifs auxiliaires ont aussi été modélisés. Le modèle du réservoir d'hydrogène a été conçu en utilisant la formule de Beattie-Bridgeman, dans laquelle le niveau d'hydrogène stocké dépend du nombre de moles d'hydrogène stocké, la température et la pression du gaz. D'autre part, la puissance consommée par le compresseur a été prise en compte dans le bilan de puissance afin d'inclure la dépense d'électricité supplémentaire à cause des dispositifs auxiliaires dans le coût d'exploitation du micro-réseau.

Malgré toutes ces simplifications, l'émulateur de BMG implémenté inclut les effets de vieillissement des batteries, piles à combustible et électrolyseurs, le profil annuel de déséquilibre de puissance interne d'un bâtiment, l'évolution journalier du prix de l'électricité et le fonctionnement principal d'un parc de véhicules électriques. En outre, l'ensemble du BMG a été modélisé sur la base de tests expérimentaux rapportés dans la littérature, en tenant compte du dimensionnement réel d'un bâtiment résidentiel et non résidentiel typiques de taille moyenne. Tous ces aspects conduisent à rendre cet émulateur BMG en totale adéquation pour l'étude des flux de puissance et l'analyse technico-économique, qui sont les principaux objectifs de cette thèse de doctorat. L'émulateur de BMG couvre les aspects fondamentaux pour évaluer les capacités de la structure hiérarchique de gestion de l'énergie proposée, qui sera détaillée dans le chapitre suivant.

Chapitre 3 Description de la structure du contrôle hiérarchique

Ce chapitre vise à donner un aperçu global de l'ensemble du Système de Gestion d'Energie (EMS) hiérarchique en décrivant chaque module de commande et ses principales caractéristiques. L'EMS développé vise à optimiser le fonctionnement d'un Micro-Réseau dédié aux Bâtiments (BMG) tout en respectant le code de l'énergie concernant l'autoconsommation. Le rôle principal de l'EMS est donc de gérer le flux de puissance interne au BMG pour satisfaire la demande énergétique du bâtiment en utilisant autant que possible les ressources installées et en réduisant la dépendance énergétique vis-à-vis du réseau externe.

En effet, en cas d'excès de puissance, l'EMS dispose de quatre options : produire et stocker de l'hydrogène à travers l'électrolyseur, charger les batteries statiques, recharger les véhicules électriques ou injecter le surplus dans le réseau principal. D'autre part, en cas de déficit énergétique interne, l'EMS retient également quatre alternatives : produire de l'électricité grâce aux piles à combustible, décharger les batteries statiques, décharger les véhicules électriques ou importer de l'énergie du réseau. Au vu du grand nombre de solutions possibles pour satisfaire l'équilibre de puissance entre génération et consommation, l'EMS développé s'appuie sur les atouts d'une structure de Contrôle par Modèle Prédictif (MPC) et sur l'analyse intensive de données pour assurer l'optimalité de la gestion du flux de puissance du BMG sur des critères non seulement énergétique mais aussi économique.

A cet égard, l'échange d'énergie avec le réseau principal est supervisé en permanence par un compteur intelligent situé à proximité du convertisseur AC-DC reliant le BMG au réseau principal. Le compteur intelligent collecte les données de la production d'énergie issue des panneaux solaires, la consommation du bâtiment et l'énergie totale importée et exportée. En plus, chaque Système de Stockage d'Energie (ESS) possède des capteurs qui transmettent les mesures de la tension et du courant directement à l'EMS du bâtiment. Toutes ces données collectées sont traitées par le contrôleur hiérarchique pour améliorer en permanence la performance du BMG.

L'EMS hiérarchique proposé est donc divisé en cinq unités de contrôle fonctionnant au synchronisme, à savoir deux MPC, deux modules pilotés par des données et un Module de Partage de Puissance (PSM). Les deux MPC en cascade avec l'aide des modules pilotés minimisent les coûts d'exploitation du système tout en garantissant que le BMG fonctionne en sécurité. Ils calculent les références des puissances destinées à chaque ESS, y compris les batteries Lithium-ion, l'électrolyseur, la pile à combustible et le parc de voitures électriques. Leurs buts consistent aussi à maintenir le bilan de puissance interne et à respecter la limitation physique de chaque composant électrique.

Élaborée comme une structure de MPC économique (*Economic MPC* ou EMPC), la couche de contrôle supérieure minimise les coûts de fonctionnement du BMG en déterminant à la fois les références d'état de charge des batteries (SoC_{ref}) et la référence de niveau d'hydrogène du réservoir (LoH_{ref}) à transmettre au MPC inférieur. L'EMPC est également chargé d'envoyer la planification d'échange journalière d'énergie avec le réseau principal à l'agrégateur communautaire. Cette planification est essentielle pour permettre aux agrégateurs de maintenir la stabilité du réseau et de garantir des contrats rentables concernant les prix de l'électricité locaux. Dans le but de réduire les

charges de calcul, l'EMPC est réactualisé au moins une fois par jour, ce qui amène cette couche de contrôle à être la plus lente dans toute la structure du contrôle hiérarchique.

En parallèle, une technique de suivi associée au MPC (*Tracking MPC* –TMPC ou suivi du MPC) détermine les références de puissance pour chaque ESS afin de poursuivre les trajectoires des références de SoC_{ref} et LoH_{ref} déterminées par le MPC supérieur. Contrairement à l'EMPC, le TMPC est une unité de contrôle plus souple qui a moins de contraintes. Puisque le prix de l'électricité et les données de prédiction de déséquilibre de puissance ne varient pas énormément dans 24 heures, l'EMPC n'a pas besoin d'être optimisé toutes les heures. Par conséquent, le TMPC, qui a un horizon de prédiction plus court coopère avec l'EMPC. Cette couche de contrôle inférieure est mise à jour toutes les heures et son rôle principal est de garantir que les contraintes impliquant l'équilibre de puissance et la sécurité des ESS ne sont pas violées.

Afin de réduire à la fois la complexité de la modélisation mathématique des MPC et la charge de calcul, les niveaux supérieurs du contrôleur hiérarchique considèrent le parc de voitures électriques comme une unique batterie conséquente dont la capacité varie en fonction du nombre de PEV branchées. Au lieu d'estimer l'énergie stockée dans chaque PEV, la structure du MPC à deux niveaux estime l'énergie totale stockée dans tout le parc de voitures. Par conséquent, les consignes de charge et de décharge de chaque PEV sont assurées par le module PSM. Cet algorithme complémentaire à la structure du MPC hiérarchique spécifie la portion de puissance qui doit être destinée à chaque PEV branchée pour garantir qu'elles sont complètement chargées avant leur heure de départ prévue.

La prédiction des états futurs du BMG est embarquée sur les deux MPC à travers des équations linéaires sous la forme d'une représentation d'espace d'états. L'utilisation de modèles linéaires permet de réduire la complexité du problème d'optimisation sans impacter drastiquement les performances du contrôleur. De plus, les modèles linéaires permettent d'exploiter l'algorithme MILP (*Mixed-Integer Linear Programming*) de la librairie CPLEX, un solveur de haute performance développé par IBM®.

Comme le rôle des MPC est de gérer le flux d'énergie interne du bâtiment, il est essentiel de concevoir des modèles mathématiques fiables pour estimer l'énergie totale stockée, ainsi que l'énergie totale générée et consommée en interne. De plus, dans la mesure où le MPC supérieur met en œuvre une optimisation économique, les fluctuations du prix de l'électricité journalier doivent également être estimées. Par conséquent, ce chapitre décrit également comment la prédiction du déséquilibre de puissance du bâtiment, l'évolution du prix de l'électricité et la prédiction de l'énergie stockée dans les dispositifs de stockage d'énergie ont été implémentées.

L'estimation du déséquilibre de puissance et du prix de l'électricité sont construits à partir des mêmes données utilisées dans le simulateur Simulink explicité dans le Chapitre 2. Par conséquent, ces deux types de données sont interprétés par l'EMS comme des vecteurs de résolution sur un horizon d'une heure qui sont mis à jour périodiquement. Ainsi, l'EMPC et le TMPC ne calculent ni l'estimation concernant la consommation électrique du bâtiment, ni la production d'électricité photovoltaïque, ni le prix de l'électricité. Cette simplification considère que l'agrégateur communautaire traite les données de prévisions météorologiques et du marché d'électricité pour tous les bâtiments appartenant au même cluster. Par conséquent, à chaque heure, l'agrégateur communautaire envoie aux MPC la production d'électricité des panneaux photovoltaïques et le prix de l'électricité estimé pour les périodes suivantes.

De même, il est supposé que la consommation électrique du bâtiment acquise par le compteur intelligent est traitée par un module interne qui envoie aux deux MPC la consommation électrique estimée pour les périodes à venir.

Concernant la modélisation des ESS, l'énergie stockée à chaque instant dans l'horizon des MPC est estimée à partir des modèles basés sur les réservoirs d'énergie. À cet égard, les batteries des PEV, la batterie statique du BMG et le stockage en hydrogène sont modélisés par des équations linéaires reliant l'énergie future stockée à leur puissance fournie au BMG.

En se basant sur les valeurs moyennes de la tension, la capacité et l'état de charge de toutes les batteries des PEV branchées à la station de recharge, ainsi que les créneaux estimés de connexion et déconnexion de chaque PEV, les MPC calculent la quantité d'énergie disponible dans tout le parc des voitures électriques pour les périodes correspondant à leur horizon de prédiction. Une des particularités de la modélisation de PEV est que leur état de charge est maintenu la plupart du temps faiblement contraint, sauf au moment de leur heure de départ, où il est forcé à être complétement chargé. Les MPC ont été formulés de cette manière pour permettre aux batteries des PEV de prendre en charge des besoins énergétiques du BMG sous la condition d'être chargées avant de se déconnecter.

Par ailleurs, les modèles conventionnels des batteries et du réservoir d'hydrogène rapportés dans la littérature ont été modifiés afin d'améliorer la précision de l'estimation de leur état de charge. En conséquence, le nouveau modèle linéaire des batteries Lithium-ion prend en compte l'efficacité et la tension distinctes lors de la commutation entre la charge et la décharge. Par conséquent, les modèles de batteries contiennent plus de dégrée de liberté, ce qui peut améliorer la précision de son état de charge. Avec le même propos, le modèle linéaire du stockage en hydrogène a été rectifié pour faire face au comportement non-linéaire de la production et consommation en cas de fonctionnement loin de la puissance nominale de l'électrolyseur et de la pile à combustible. Pour de plus amples informations, le Chapitre 4 détaille les avantages et les inconvénients de ces nouvelles approches de modélisation.

Pour améliorer la flexibilité du contrôleur, l'EMS s'adapte en fonction des mesures de données en continu grâce aux deux modules pilotés par les données. Expliqué plus en détail respectivement dans les Chapitre 4 et 5, le premier est le module d'Identification en Temps Réel des Modèles (ITRM), tandis que le second est l'Estimateur des Coûts du Micro-Réseau (ECMR). Ces deux modules fonctionnent uniquement sur la base des données de mesures de façon qu'ils ne nécessitent aucun réglage de paramètres. L'algorithme ITRM corrige les inexactitudes dans les modèles internes au MPC en ajustant en temps réel les matrices de représentation d'états internes au MPC, alors que l'ECMR détermine les paramètres optimaux pour la fonction coût des MPC afin de faciliter le compromis entre la maximisation du taux d'autoconsommation annuel et la minimisation du coût de fonctionnement.

En conclusion, dans le but de fournir une compréhension globale de l'EMS hiérarchique développé, ce chapitre décrit les équations linéaires composant les modèles de prédiction et indique comment les intégrer dans le MPC hiérarchique à deux niveaux. En outre, une brève introduction de la fonction de coût des deux MPC a été fournie, ainsi que leurs signaux d'entrée et de sortie pour interagir avec d'autres modules complémentaires dans l'architecture hiérarchique, y compris les unités basées sur l'analyse de données. Dans les chapitres suivants, les deux modules fonctionnant à partir de l'analyse de données seront détaillés.

Chapitre 4 Identification en Temps Réel de Modèles

Les Systèmes de Stockage d'Energie (ESS) sont des éléments clés pour permettre la conception de Micro-Réseaux dédiés aux Bâtiments (BMG), principalement pour faire face au comportement stochastique des sources d'énergie renouvelable et pour être en mesure de compenser le décalage des pics de consommation et d'injection d'énergie. Cependant, des inexactitudes dans les modèles mathématiques des ESS dues à des effets de température et de vieillissement peuvent réduire les performances d'une structure de Contrôle par Modèle Prédictif (MPC). Bien que l'architecture MPC a prouvé sa robustesse contre des perturbations environnementales même avec l'exploitation d'un modèle simplifié. Toutefois, il demeure des interrogations sur l'évaluation de ses performances face aux dérives physiques, telles que la température, le vieillissement des appareils électriques et l'imprécision des paramètres du modèle.

Pour faire face à ces incertitudes, il existe plusieurs techniques pour mieux estimer les paramètres intrinsèques des batteries, de pile à combustible et de l'électrolyseur. Dans le cas des batteries, l'équation d'Arrhenius ou des modèles élaborés à partir de spécifications techniques sont généralement adoptés. Concernant le stockage hydrogène, les modèles basés sur la structure physique des Membrane d'Echange de Protons (PEM) peuvent aboutir à un modèle très précis, mais ils demeurent trop complexes pour être intégrés dans la prédiction associée au MPC car ils nécessitent un grand nombre de paramètres qui sont généralement inconnus ou difficiles à mesurer. En revanche, dans la littérature des modèles d'électrolyseur PEM simples sont aussi largement employés, tels que ceux basés sur des équations logarithmiques simplifiées. Toutefois, les paramètres de ces modèles sont statiques et valables pour une température unique et donc sujets à des imprécisions pour un fonctionnement à long terme. De plus, ces types de modélisation nécessitent une calibration préalable du modèle, ce qui peut conduire à des incertitudes sur toute la durée de vie des ESS.

Dans cette perspective, visant à renforcer la robustesse du MPC, un algorithme basé sur l'analyse de données de mesures a été conçu pour l'Identification en Temps Réel des Modèles (ITRM) des batteries Lithium-ion et du stockage de l'hydrogène. Cet algorithme vise à renforcer le MPC hiérarchique à deux niveaux (HMPC) décrit dans le Chapitre 3 avec une estimation d'état plus précise. Dans l'objectif de tirer profit au maximum des ressources du BMG sans les surexploiter, l'objectif de l'algorithme ITRM est de parfaire la prédiction de l'énergie stockée dans le pack de batteries et le réservoir d'hydrogène en continu et automatiquement sans exiger un modèle mathématique complexe. Il est à noter que l'ITRM ne gère pas l'imprécision du modèle des batteries des véhicules électriques (PEV) car il est considéré qu'un module similaire est embarqué dans chaque PEV de manière que la station de recharge de PEV fournisse des valeurs précises concernant les paramètres de ces batteries.

Afin de valider l'algorithme ITRM dédié aux modèles de batteries, des simulations sur une année complète sur MATLAB-Simulink® d'un BMG équipé par des panneaux photovoltaïques et des batteries Lithium-ion ont été conduites. Dans l'intention de prouver la robustesse de l'algorithme face à des imprécisions des paramètres provenant des spécifications techniques, des incertitudes ayant trait aux valeurs de la capacité réelle des batteries (Q) ont été ajoutées au niveau du contrôleur MPC. Par ailleurs, des scénarios avec deux niveaux de vieillissement des batteries ont été évalués, notamment quand les

batteries sont neuves et quand les batteries sont à la moitié de leur vie, représentant une dégradation de 10% de leur capacité nominale.

Les résultats montrent que, dans tous ces cas d'études, l'erreur cumulative de la prédiction de l'état de charge des batteries en utilisant le MPC doté du module ITRM est 2 à 3 fois plus faible qu'en utilisant un MPC avec une modélisation classique dont les paramètres sont statiques. De plus, il a été constaté que l'erreur cumulative du MPC classique est deux fois plus important lorsque la capacité des batteries est surestimée. En revanche, avec le module ITRM, les erreurs cumulées sont maintenues sous contrôle dans tous les scénarios envisagés.

Cette robustesse supplémentaire introduite par l'algorithme ITRM conduit le contrôleur à avoir une performance uniforme même en présence d'imprécisions sur la capacité et le niveau de dégradation des batteries. Avec une différence inférieure à 1%, l'algorithme ITMR a démontré sa capacité à assurer presque les mêmes taux d'autoconsommation (τ_a) et de couvertures (τ_c) annuelles malgré l'existence d'erreurs paramétriques. Comparé avec la modélisation classique des batteries, l'algorithme ITRM a assuré des valeurs des taux τ_a et τ_c toujours plus élevés, atteignant même un écart jusqu'à 3%. Ces résultats reflètent l'habilité du module ITRM à identifier les capacités réelles des batteries en évitant ainsi leur sous-exploitation. En contrepartie, le MPC classique n'est pas robuste contre les incertitudes sur la valeur de Q, puisque τ_a et τ_c sont réduis quand les batteries sont sous-estimées. De manière similaire, τ_a et τ_c sont augmentés quand elles sont surestimées.

Comme l'algorithme ITMR met à jour en permanence les limites inférieure et supérieure de l'état de charge des batteries, le MPC doté de l'algorithme ITMR garantit une vitesse de dégradation quasi constante. En revanche, le MPC classique dégrade plus les batteries dans le scénario où leurs paramètres sont mal dimensionnés. En effet, avec l'approche classique de modélisation, sur une durée d'une année d'exploitation, les batteries ont été dégradées de 13% plus vite dans le cas du scénario où les batteries sont à la moitié de leur durée de vie par rapport au cas où elles sont neuves. La raison sous-jacente à ce phénomène réside dans le fait que le MPC classique ne surveille pas la profondeur de décharge (*Depth of Discharge* (DoD) en anglais) des batteries, elles vont donc être déchargées comme si elles n'étaient pas dégradées. Par conséquent, la DoD est plus importante avec le MPC classique, il en va de même du taux de dégradation des batteries.

Au-delà de la régulation de la profondeur de décharge, la température des cellules est un des facteurs le plus impactant sur l'état de santé des batteries, ce qui exige une régulation de leur température. Par ailleurs, en utilisant l'algorithme ITMR, les variations des températures des cellules des batteries sont indirectement surveillées à travers la classification par niveau de température (T_{class}) implémentée intrinsèquement. Avec le traitement des données de mesures de la tension et de l'intégrale du courant, l'indice de classe T_{class} représente une image de la variation de la température. Cette information peut être utilisée par le contrôleur MPC afin de réguler la température des batteries et ainsi prolonger leur durée de vie.

En conclusion, les résultats ont démontré qu'une meilleure estimation de l'état de charge et de la capacité des batteries, permet au contrôleur d'avoir plus d'informations concernant les variations de température des cellules et d'agir sur la dégradation de la capacité. Il a été constaté une corrélation entre la profondeur de décharge des batteries et les taux de couverture et d'autoconsommation du bâtiment.

Tous ces renseignements fournis par ce nouvel algorithme permettent au contrôleur de prendre des décisions plus fiables, spécialement pour trouver un bon compromis entre l'autonomie énergétique des bâtiments et le niveau de dégradation des batteries. Les prochaines étapes consistent à utiliser les estimations de la variation de la température et de la capacité pour ralentir la dégradation des batteries.

Concernant le stockage de l'hydrogène, l'algorithme ITRM améliore l'estimation du niveau de l'hydrogène du réservoir grâce à un processus itératif. En s'appuyant uniquement sur des mesures instantanées de la pression du réservoir, du courant et de la tension aux bornes de l'électrolyseur et de la pile à combustible, l'algorithme ITRM évalue les paramètres constituant la représentation d'état du modèle de la chaîne complète du stockage de l'hydrogène présenté au Chapitre 3. Cet algorithme est implémenté à partir de deux processus de réglage itératifs. Le premier consiste à déterminer les coefficients angulaires reliant le courant aux bornes de l'électrolyseur et de la pile à combustible à la variation de pression du réservoir. La deuxième partie de l'algorithme consiste à identifier les paramètres reliant le courant circulant dans les empilements des cellules et la puissance active correspondante.

Afin d'évaluer la performance de l'algorithme développé, le fonctionnement des piles à combustible et des électrolyseurs a été simulé sur un horizon de 10 jours. Les résultats de simulations montrent que, depuis les premières heures de fonctionnement, l'algorithme ITRM a identifié un modèle linéaire plus précis que le modèle linéaire classique trouvé dans la littérature. À long terme, l'algorithme ITRM augmente jusqu'à dix fois la précision de l'estimation du niveau d'hydrogène par rapport à l'approche traditionnelle de modélisation. A plus forte raison, la performance de l'algorithme ITRM serait plus importante si le modèle classique comportait des erreurs sur certains paramètres des modèles de la pile à combustible et de l'électrolyseur.

Comme étapes futures, il est prévu d'améliorer l'algorithme ITRM dédié au stockage de l'hydrogène en compensant la variation de température du système par la division en classes de température telle que celle mise en œuvre dans le cas de l'algorithme ITRM des batteries. De plus, la robustesse de l'algorithme contre les oscillations de température ambiante et le bruit de mesure doit être évaluée avant de l'implémenter dans de systèmes réels.

Chapitre 5 L’estimateur des coûts du micro-réseau

L'une des plus grandes faiblesses de la structure de Contrôle par Modèle Prédictif (MPC) est sa dépendance à une définition fiable de la fonction coût. Lorsqu'il s'agit d’un système comportant un Système de Stockage d’Energie (ESS) hybride, la fonction coût du MPC est généralement conçue comme une fonction multi-objective. Le compromis entre l’usage des batteries et la mise en fonctionnement du stockage hydrogène est souvent géré par des facteurs de pondération dans la fonction coût du MPC qui sont réglés par une approche d’ajustement manuel. Ces facteurs de pondération sont souvent attribués suivant un ordre de priorité pour réduire, en toutes circonstances, les importations et les exportations totales d'énergie et en privilégiant l'utilisation des batteries sur le stockage hydrogène. Cela diminue clairement la généralité du contrôleur et peut empêcher le MPC d'atteindre ses objectifs si ces facteurs de pondération dans la fonction coût ne sont pas bien réglés ou en cas de variations inattendus dans le système.

Pour résoudre ce problème, dans la littérature, la fonction multi-objective définissant la fonction coût du MPC peut être normalisée en convertissant chaque terme de la fonction coût dans la même unité physique, telle que la monnaie locale pour les optimisations économiques. Pour déterminer une utilisation équilibrée du ESS hybride, le coût de dégradation des batteries, des électrolyseurs et des piles à combustible ainsi que le prix de l'électricité sont souvent intégrés. Néanmoins, ces optimisations se limitent à l’horizon du MPC et ne tiennent compte ni de la saisonnalité au cours de l’année, ni des objectifs à long terme, comme l’exigence relative au taux d’autoconsommation annuel des bâtiments.

Pour remédier à cette faiblesse d'une structure MPC, l'Estimateur des Coûts du Micro-Réseau (ECMR) a été conçu pour ajuster quotidiennement la fonction objective de la couche de contrôle supérieure de la structure MPC Hiérarchique (HMPC) en fonction de l'analyse de données. Sans avoir besoin de régler aucun paramètre, l'objectif de cet algorithme est de faciliter le compromis entre la maximisation du taux d'autoconsommation annuel et la minimisation du coût d'exploitation total du micro-réseau dédié au bâtiment (BMG). L’ECMR permet également au Système de Gestion de l’Energie (EMS) du bâtiment d’équilibrer l’utilisation des batteries et du stockage en hydrogène, à travers l'estimation de leur durée de vie et l'évaluation de leurs capacités à réduire l'injection du BMG et à maximiser le revenu total du BMG.

En analysant à la fois les données de prédiction du déséquilibre de puissance journalier et celles de l'année précédente, l’algorithme ECMR estime le comportement moyen de l’EMS hiérarchique lorsqu'il est soumis à des conditions similaires de déséquilibre de puissance quotidien. Ce comportement moyen permet à l'ECMR de calculer à la fois le coût annuel du BMG attendu et le taux d'autoconsommation annuel attendu. Le coût de fonctionnement annuel définit la fonction coût du MPC économique (EMPC) qui est minimisée au moins une fois par jour. De manière similaire, l’estimation du taux d'autoconsommation annuel est intégrée dans la formulation de l’EMPC via une contrainte d'inégalité, le forçant à être supérieur à l’indice requis par le code de l’énergie français.

Dans le but de décrire le fonctionnement principal de l'ECMR, le calcul permettant d’estimer le coût annuel du BMG est détaillé dans la section 5.2, tandis que l'algorithme pour estimer le taux d'autoconsommation annuel est exposé dans la section 5.3. Les critères envisageables pour estimer les

coûts de fonctionnement annuels du BMG sont décomposés en quatre grandes catégories, à savoir les charges avec l'achat de l'électricité, le coût amorti de l'installation et l'achat des dispositifs de stockage, le complément de rémunération selon le taux d'autoconsommation annuel versé par la Commission de Régulation de l'Energie (CRE) français et la pénalité virtuelle pour forcer le BMG à respecter la restriction d'injection d'énergie dans le réseau principal.

En vue d'exploiter le BMG à un coût minimal, mais en même temps de garantir les indices annuels d'autoconsommation imposées par la CRE, l'ECMR estime aussi le taux d'autoconsommation annuel attendu en utilisant à la fois les données de prévision de l'année précédente et le comportement moyen du HMPC. Le processus d'estimation comprend trois étapes principales qui sont mises en œuvre une fois par jour. Premièrement, les données de prédiction passées sont classées en quatre groupes à l'aide de l'algorithme k-means. Deuxièmement, la moyenne des variables du contrôle HMPC est attribuée à chacune de ces classes k-means, ce qui permet de calculer le taux d'autoconsommation annuel attendu. Enfin, le taux d'autoconsommation annuel estimé est intégré dans l'horizon de l'EMPC.

Comme l'ECMR est un algorithme itératif qui évolue avec le temps, les estimations actuelles du coût de fonctionnement total du BMG et du taux d'autoconsommation annuels reposent sur l'estimation de l'itération précédente et des mesures de données récentes. Pour cette raison, la section 5.4 décrit le processus d'initialisation de l'algorithme ECMR avec des valeurs fiables. Cette initialisation vise à s'assurer que l'algorithme fonctionne correctement depuis les premiers jours d'activité.

La validation et les performances de l'algorithme proposé sont démontrées dans la section 5.5. Pour vérifier si les estimations du coût de fonctionnement et du taux d'autoconsommation annuels sont correctement mises en œuvre, ces deux valeurs estimées ont été comparées aux valeurs réelles atteintes par le BMG après une simulation sur une durée d'un an. Les simulations analysées dans ce chapitre comportent les cas avec un BMG équipé par un système de stockage hybride et non hybride. Par conséquent, les capacités du pack de batteries et du système de stockage hydrogène à réduire les dépenses totales du BMG et d'augmenter le taux d'autoconsommation ont été évaluées.

Afin de vérifier la flexibilité de l'algorithme développé, l'ECMR a été soumis à plusieurs configurations de fonctionnement du BMG. Au-delà des différents types de ESS installés, les cas avec différents profils de consommation comme ceux d'un bâtiment résidentiel et public typiques ont été évaluées. De plus, il a été recherché la sensibilité de cet algorithme lorsqu'il existe des aides incitatives pour investir sur ces éléments de stockage. A cet égard, les scénarios pour lesquels l'investissement dans ces systèmes de stockage en hydrogène est subventionné et non subventionné ont aussi été analysés. Également, la précision et la robustesse de l'algorithme face à des imprécisions des données de prédiction provenant de l'agrégateur du réseau communautaire font aussi partie des cas d'études investigués dans ce chapitre.

Les résultats des simulations démontrent que l'ECMR pour tous ces scénarios est capable de prévoir le taux d'autoconsommation annuel avec une erreur moyenne inférieure à 2% dans les bâtiments résidentiels et publics. De même, l'ECMR informe le HMPC des dépenses annuelles de BMG depuis les premiers jours de fonctionnement avec une précision de l'ordre de 10%. Grâce au processus interactif de l'algorithme ECMR, l'estimation du coût de fonctionnement s'améliore progressivement permettant l'EMS d'avoir un aperçu sur quelle est la source majeure de ses dépenses. Cette vision

financière globale du BMG conduit l'EMS à prendre, en ayant plus de connaissances, des décisions plus judicieuses surtout quand il s'agit de l'usage des ESS.

Toutes ces informations amène l'HMPC sur des décisions plus appropriées afin d'exploiter correctement les dispositifs électriques installés dans le BMG. Dans le chapitre suivant, les aspects énergétiques et économiques de l'ensemble du système hiérarchique de gestion énergétique des bâtiments seront évalués. Le contrôleur hiérarchique proposé sera comparé à d'autres stratégies conventionnelles trouvées dans la littérature, telles qu'un contrôleur *rule-based* et un HMPC sans l'algorithme ECMR.

Il est important de souligner que l'algorithme ECMR n'est pas encore capable d'estimer l'impact que le parc de voitures électriques a sur le coût annuel de fonctionnement du BMG et sur le taux l'autoconsommation. En conséquence, une extension future de ce travail examinera les potentiels d'exploitation des batteries de véhicules électriques en les incluant dans l'algorithme ECMR. En outre, comme l'analyse de la capacité de l'algorithme ECMR a été évaluée sur des simulations avec des données de prédiction perturbées par du bruit blanc dont la moyenne est nulle, il est nécessaire de vérifier la robustesse de cet algorithme lorsqu'il est soumis à d'autre types de perturbations. Parmi les faiblesses constatées de l'algorithme et comme suggestion pour son amélioration, le temps de réponse de l'ECMR doit être perfectionné pour lui permettre de s'adapter aux changements brusques du système, tels que la prise en compte des modifications comportementales sur les jours de vacances ou l'augmentation inattendue de la consommation d'énergie.

Chapitre 6 Résultats des simulations

Des Systèmes de Stockage d'Energie (ESS) hybrides sont désormais usuellement intégrés dans les Micro-Réseaux dédiés aux Bâtiments (BMG) afin d'atténuer les effets négatifs engendrés par l'imprévisibilité des Sources d'Energies Renouvelables (RES). La combinaison de ESS à long et à court terme est en mesure d'améliorer la capacité d'un BMG pour satisfaire sa demande énergétique à partir des RES, augmentant ainsi le taux d'autoconsommation. Cependant, la conception des Systèmes de Gestion de l'Energie (EMS) pour les micro-réseaux équipés par des ESS hybrides est plus complexe que pour les systèmes constitués d'un seul type de ESS. Les autres freins identifiés qui limitent l'essor des BMG sont la rentabilité de l'installation de ESS dans les bâtiments et les modalités de les mettre à profit pour garantir des indices élevés d'autoconsommation avec un coût minimal.

Face à ces enjeux, une structure de Contrôle Hiérarchique basée sur Modèle Prédictif (HMPC) à deux niveaux enrichis de deux modules pilotés par l'analyse de données a été conçue. En combinant les atouts de l'Identification en Temps Réel des Modèles (ITRM) présentée au Chapitre 4 et de l'Estimateur des Coûts du Micro-Réseau (ECMR) expliqué au Chapitre 5, cette stratégie de contrôle innovante vise à augmenter la flexibilité du contrôleur de flux de puissance en lui permettant de s'adapter automatiquement à différentes installations de stockage d'énergie (hybrides ou non hybrides) et différents types de bâtiments (résidentiels ou publics).

Dans ce contexte, ce chapitre vise donc à évaluer la performance de l'ensemble du EMS hiérarchique développé sous différentes configurations. Comme le contrôleur hiérarchique doté de l'ECMR n'inclut pas encore les effets des batteries disponibles dans le parc de Véhicules Electriques (PEV), les résultats de simulation exposés dans ce chapitre sont divisés en deux parties. La première évalue les performances de l'ECMR en mettant en évidence sa capacité à gérer un ESS hybride de façon à satisfaire le taux d'autoconsommation requis à un coût de fonctionnement minimum. D'autre part, le deuxième volet de ce chapitre traite du potentiel d'utilisation des batteries des PEV en faveur du BMG. En plus d'évaluer l'efficacité du Module de Partage de Puissance (PSM) présenté au Chapitre 3, il estime les capacités de l'EMS proposé à tirer parti du PEV pour augmenter le taux d'autoconsommation annuel tout en s'assurant que les véhicules électriques soient chargées avant leur heure de départ.

Dans la première partie du chapitre, grâce à des simulations utilisant l'ensemble des données d'un bâtiment public et résidentiel, le HMPC doté de l'IRTM et l'ECMR a été confronté à un algorithme de contrôle *rule-based* simplifié issu de la littérature et un HMPC conventionnel sans l'ECMR. Les simulations ont été réalisées sous la plateforme logicielle MATLAB-Simulink® pour évaluer quatre aspects importants de ces trois contrôleurs, à savoir les impacts de l'installation du ESS, des coûts d'investissement du stockage d'hydrogène, de la limitation d'utilisation du stockage de l'hydrogène autour de sa puissance nominale et des erreurs dans les données de prédiction.

Compte tenu de tous ces scénarios de simulation, le HMPC proposé – nommé HMPC-kmeans – identifie le ESS le plus adapté à opérer quotidiennement pour garantir le taux d'autoconsommation requis avec un coût minimum. Par rapport au contrôleur *rule-based*, le contrôleur élaboré réduit le coût du fonctionnement total du BMG jusqu'à 5% dans les bâtiments résidentiels et jusqu'à 9% dans les bâtiments non résidentiels au cours de la première année d'exploitation. Pour souligner l'importance de

prendre en considération non seulement les aspects énergétiques mais aussi économiques dans l'optimisation du flux d'énergie et de démontrer une stratégie réalisable pour résoudre ce problème, ce contrôleur détermine automatiquement un équilibre entre coût, profit et autonomie énergétique. Il a été comparé à un autre HMPC qui contient une fonction de coût qui maximise uniquement le taux d'autoconsommation. Bien que la stratégie proposée garantisse un taux d'autoconsommation de 5% à 17% inférieur au HMPC conventionnel, elle a satisfait le taux d'autoconsommation requis avec un coût d'exploitation annuel inférieur de 1% à 7%.

Les résultats ont également révélé que le complément de rémunération pour l'autoconsommation accordé par la Commission de Réseau de l'Energie (CRE) français n'est pas suffisant pour encourager l'utilisation des piles à combustible et des électrolyseurs avec leur coût d'investissement actuel. Le stockage de l'hydrogène reste actuellement trop coûteux pour être rentable dans une architecture de BMG. Puisque l'HMPC proposé définit les variables de contrôle qui maximisent le taux d'autoconsommation annuel attendu et minimisent le coût d'exploitation annuel prévu, il ne sollicite les piles à combustible et les électrolyseurs que lorsque cela est strictement nécessaire. En conséquence, le stockage d'hydrogène est presque inutilisé dans le scénario où le micro-réseau peut satisfaire les exigences minimales du taux d'autoconsommation avec uniquement des batteries.

En revanche, le contrôleur *rule-based* et le HMPC conventionnel exploitent la chaîne de l'hydrogène autant que possible pour maximiser le taux d'autoconsommation, mais ils ignorent les aspects économiques, ce qui entraîne des coûts de fonctionnement plus élevés. Il est important de souligner que même si ce résultat a été obtenu dans le scénario de la politique du réseau français, il peut être transposé dans d'autres pays. Sur la base des résultats obtenus, trois scénarios possibles pour rentabiliser l'utilisation des piles à combustible ont été suggérés, ces réflexions peuvent servir pour d'autres applications visant à encourager l'autoconsommation dans les bâtiments.

En outre, il a été vérifié que le fait de contraindre l'utilisation du stockage en hydrogène autour de leur puissance nominale limite la capacité du BMG à atteindre un taux d'autoconsommation annuel plus élevé. En raison des variations du déséquilibre de puissance, il est difficile de déterminer un seuil de puissance minimum optimal pour faire fonctionner les piles à combustible et les électrolyseurs, sans dégrader la rentabilité du système. Par conséquent, rendre l'utilisation de la chaîne hydrogène sans limitations fortes permet non seulement au BMG d'augmenter le taux d'autoconsommation jusqu'à 6.5% et de réduire les coûts totaux jusqu'à 7%, mais aussi de réduire la complexité de la conception du contrôleur.

Dans la deuxième partie de ce chapitre, les potentiels liés à l'utilisation des batteries de PEV pendant les phases où elles sont raccordées au BMG ont été évalués. Comme l'HMPC doté par l'ECMR dans cet ensemble de simulation a été désactivé, les potentiels d'exploitation de leurs batteries en faveur du BMG ont été déterminés en utilisant un HMPC simplifié qui minimise l'échange d'énergie avec le réseau principal et ignore les aspects économiques. Considérant également les profils de consommation d'un bâtiment résidentiel et public typiques, les simulations réalisées avec des PEV visent à évaluer l'impact d'associer un parc de véhicule dans un bâtiment et la contribution de cet ensemble à l'augmentation du taux annuel d'autoconsommation. Les résultats de simulation montrent que la coopération entre les trois niveaux de commande de la structure de contrôle hiérarchique (HMPC à deux niveaux avec le module

PSM) permet de réduire la complexité de la conception du contrôleur MPC et garantit un niveau de charge à plus de 75% même en cas d'inexactitude sur la prédiction des données.

En plus de la réduction sur la complexité de la conception du contrôleur, la combinaison d'unités de commande fonctionnant avec des horizons longs et courts a permis au contrôleur d'utiliser les batteries de PEV pour réduire la dépendance énergétique vis-à-vis du réseau. Cette stratégie diminue l'injection d'énergie annuelle jusqu'à 7% dans les bâtiments résidentiels et jusqu'à 32% dans les bâtiments publics, par rapport au scénario où seulement des batteries sont installées. À travers six scénarios de simulation différents, le HMPC proposé parvient bien à charger de préférence les véhicules électriques pendant les périodes de surplus et de les décharger pendant le déficit énergétique.

Néanmoins, du fait du profil déséquilibré de puissance, du dimensionnement des packs de batteries et des profils quotidiens de connexion et de déconnexion des véhicules électriques, la recharge des PEV à partir d'énergies renouvelables est saturée à 10% de la production annuelle d'énergie photovoltaïque (soit 13 MWh/an) dans les bâtiments résidentiels et environ 12% (soit 16 MWh/an) dans les bâtiments publics. Cela signifie qu'environ 10% à 14% de la demande totale d'énergie du parc de 20 véhicules sont alimentés en énergie renouvelable, alors que seulement 4% à 8% avec 40 véhicules. Ainsi, avec l'élargissement du parc des PEV, le taux d'autoconsommation annuel est saturé à 72% dans les bâtiments résidentiels et à 89% dans les bâtiments publics. Le parc des PEV entraîne également une augmentation considérable de l'énergie totale achetée au réseau. En fonction du nombre de PEV, il est constaté une augmentation de l'achat total d'énergie au réseau d'environ 17 MWh/an pour un parc de 4 véhicules et jusqu'à 209 MWh/an pour un parc de 40 véhicules, soit une augmentation d'environ 5% et 61% de la consommation électrique annuelle du bâtiment, respectivement.

Dans les travaux futurs, l'évaluation de la performance du HMPC proposé avec des erreurs de données de prédiction plus importants est envisageable. Dans ce chapitre, les simulations avec une imprécision des données ont été limitées aux bruits centrés sur zéro. Cela signifie que la moyenne du déséquilibre annuel de la puissance dans le cas idéal et dans le scénario avec erreur de prédiction des données sont très proches. Comme l'ECMR repose sur le comportement moyen du HMPC et que la classification k-means est basée sur des valeurs moyennes, le contrôleur hiérarchique proposé reste très robuste face aux erreurs avec la moyenne autour de zéro. Pour mieux évaluer les performances de l'EMS élaboré, il est nécessaire de l'expertiser lorsqu'il est soumis à une erreur avec biais. Cela vérifiera la robustesse du contrôleur et sa capacité à gérer des événements qui se rapprochent d'applications réelles.

Toujours dans les perspectives, l'impact et la contribution des PEV sur le taux d'autoconsommation annuel et les dépenses annuelles du BMG doivent être intégrés dans l'algorithme de l'ECMR. Par exemple, l'utilisation du tableau des horaires avec les heures d'arrivée et de départ prévues ainsi que l'estimation de l'état de charge initial des batteries des PEV sont fondamentales pour prévoir l'énergie annuelle nécessaire à la charger et la décharger les PEV. Dans ce chapitre, certaines directives pour estimer leur impact sur les dépenses totales du BMG et le taux annuel d'autoconsommation ont été fournies, mais il est nécessaire de le développer davantage pour le rendre opérationnel dans des applications réelles.

Chapitre 7 Conclusions et perspectives

La recherche menée dans cette thèse de doctorat vise à fournir une analyse approfondie pour permettre aux Sources d'Energie Renouvelables (RES) d'être intégrées dans le mix énergétique des bâtiments. L'installation à la fois de panneaux photovoltaïques (PV) et des Systèmes de Stockage d'Energie (ESS) dans les environnements des bâtiments peut favoriser la transition énergétique vers un système électrique à basse émission de carbone, d'autant plus que les bâtiments représentent aujourd'hui plus de 40% de l'énergie électrique consommée dans le monde. Cette topologie de réseau innovante, identifiée sous le vocable de Micro-Réseau dédié aux Bâtiments (BMG), permet de bénéficier d'énergie décarbonée tout en permettant aux consommateurs d'énergie finaux de devenir des acteurs actifs dans le réseau électrique. Cependant, des efforts importants sont nécessaires pour restructurer l'ensemble du réseau électrique centralisé, basé principalement sur des combustibles fossiles, vers un système électrique distribué et vers une émission de carbone voisine de zéro.

L'un des plus grands défis est de concevoir un Système de Gestion d'Energie (EMS) fiable capable de gérer tous les composants électriques à l'intérieur du micro-réseau afin qu'il fonctionne efficacement sans menacer la stabilité du réseau principal. Dans ce contexte, une revue de la littérature sur les exigences primordiales pour la construction de BMG et sur les stratégies de contrôle les plus pertinentes pour aborder ces paradigmes ont été discutées dans le Chapitre 1. Cette analyse sur la structure du contrôle hiérarchique pour les BMG a permis d'identifier que l'amélioration de la robustesse face à l'imprévisibilité des déséquilibres de puissance et la définition de règles bien établies pour l'interopérabilité entre les petits prosommateurs et le réseau principal sont les principaux verrous qui limitent le développement des RES dans les bâtiments.

Parmi les solutions possibles pour interconnecter les BMG au réseau électrique, les concepts d'agrégateur communautaire et de taux d'autoconsommation sont apparus comme une approche viable qui évite des changements radicaux dans la structure actuelle du réseau. Par rapport à la nouvelle configuration pair-à-pair, la division du réseau en groupes énergétiques gérées par un agrégateur communautaire local est une approche plus conservatrice, car son fonctionnement est similaire au marché traditionnel de l'électricité mais avec une capacité plus petite. Ainsi, certaines fonctionnalités déjà bien implémentées dans le réseau électrique traditionnel peuvent être adaptées à cette nouvelle architecture.

Outre le dilemme dans la construction d'une topologie de réseau appropriée pour les futurs BMG, certaines restrictions se rajoutent au niveau de leur EMS. La plupart des stratégies de contrôle rapportées dans la littérature ont été développées pour gérer le flux d'énergie d'un système électrique avec un dimensionnement de micro-réseau spécifique. Cependant, plusieurs types de bâtiments existent, tels que les bâtiments résidentiels, industriels, commerciaux et publics. Par conséquent, leur profil de consommation d'énergie diffère considérablement les uns des autres, ainsi que le dimensionnement de leurs dispositifs électriques. Ainsi, les BMG seraient plus facilement répandus si leur EMS était plus flexible et plus simple à concevoir. Dans cette optique les composants électriques pourraient être simplement raccordés au micro-réseau sans nécessiter une étape de préréglage laborieuse.

En comparant les stratégies de contrôle les plus pertinentes pour gérer l'optimisation du flux d'énergie – y compris les algorithmes de contrôle déterministe, métaheuristique, stochastique, prédictif et d'intelligence artificielle – la structure de Contrôle par Modèle Prédictif (MPC) a été identifiée comme étant l'approche la plus appropriée pour gérer les principaux obstacles des BMG mentionnés ci-dessus. La capacité à prendre en compte les données de prédiction et les optimisations périodiques sur une fenêtre glissante sont les principaux atouts d'une structure MPC, ce qui lui confère un grand intérêt pour des applications académiques et industrielles. Le principal avantage de l'utilisation de la structure MPC est l'inclusion de données de prévision dans son processus de prise de décision. En outre, par rapport à d'autres algorithmes, le MPC constitue une structure de contrôle intuitive qui est très robuste avec une mise en œuvre aisée, car elle repose généralement sur des modèles linéaires simples.

Sur cette base, le Chapitre 3 a fourni une démarche complète pour concevoir un MPC hiérarchique prêt à être implémenté dans des BMG réels. Tout ce travail qui détaille la globalité du contrôleur hiérarchique, conforme au code d'énergie français concernant le taux d'autoconsommation, constitue l'une des contributions de cette thèse. Bien que ce contrôleur soit basé sur le code d'énergie français, il est transposable à d'autres applications en modifiant quelques paramètres ou en incluant d'autres contraintes d'égalité et d'inégalité en suivant un raisonnement similaire à celui détaillé au Chapitre 3.

Afin de résoudre les principaux obstacles identifiés au Chapitre 1, le contrôleur élaboré se décompose principalement sur deux couches MPC en cascade couplé avec deux modules fonctionnant à partir d'analyse de données, nommés modules : Identification en Temps Réels des Modèles (ITRM) et Estimateur des Coûts du Micro-réseau (ECMR). Présentées respectivement au Chapitre 4 et au Chapitre 5, ces deux unités de contrôle complémentaires visent à améliorer la flexibilité de la structure MPC pour favoriser l'autoconsommation. Grâce à ces deux modules annexes, le EMS du bâtiment s'adapte selon des mesures de données en continu pour atteindre ses objectifs le plus efficacement possible sans exiger des étapes de conception rigoureuses ou de nombreuses interventions humaines.

Le module ITRM fait face aux incertitudes introduites par l'imprécision de la modélisation des ESS. En effet, l'une des faiblesses du MPC réside dans la forte dépendance aux fiabilités des modèles internes qui doivent généralement être préréglés lors de tests exhaustifs. Au contraire, ce module ITRM a été conçu pour identifier automatiquement les paramètres qui permettent au MPC de prédire l'état de charge des batteries Li-ion et le niveau d'hydrogène du réservoir plus précisément. À l'aide de simulations d'un BMG développé sous MATLAB-Simulink® (Chapitre 2), l'algorithme ITRM s'est avéré plus précis que les approches de modélisation conventionnelles présentes dans la littérature. Il améliore l'estimation de l'état de charge des batteries jusqu'à trois fois et augmenter jusqu'à dix fois la précision de l'estimation du niveau d'hydrogène stocké dans le réservoir.

L'amélioration du modèle interne du MPC fournie par l'algorithme ITRM permet également au contrôleur de prendre des décisions plus fiables et d'éviter la surexploitation des systèmes de stockage d'énergie. Par rapport à la méthode de modélisation conventionnelle, le ITRM dégrade 13% moins les batteries lorsqu'elles opèrent au milieu de leur cycle de vie. En effet, le module ITRM modifie les limites d'état de charge maximum et minimum des batteries à des valeurs correspondant à la même profondeur de décharge quel que soit leur niveau de dégradation ou l'amplitude des imprécisions des paramètres. Les résultats de la simulation ont montré que le module ITRM permettait également d'estimer les

variations de température des cellules des batteries, ce qui constitue un paramètre très profitable pour retarder le taux de dégradation des batteries et prolonger leur durée de vie. De plus, une corrélation a été établie entre la profondeur de décharge des batteries et les taux de couverture et d'autoconsommation du bâtiment : plus la profondeur de décharge est importante, plus les taux de couverture et d'autoconsommation sont élevés. Toutes ces informations fournies par le nouvel algorithme permettent au MPC de trouver un compromis entre l'autonomie énergétique des bâtiments et le niveau de dégradation des batteries.

Concernant le stockage de l'hydrogène, l'algorithme ITRM gère le comportement non linéaire du flux d'hydrogène dans les électrolyseurs et les piles à combustible en temps réel. Cependant, il ne compense pas encore les variations de température comme le fait l'ITRM pour les batteries. Par conséquent, lors des étapes suivantes, il est nécessaire d'inclure la température dans l'algorithme ITRM via la division en classes de température sur un principe équivalent au cas des batteries. De plus, la robustesse de l'algorithme ITRM par rapport aux variations de température ambiante et aux bruits de mesure doit être évaluée avant de l'implémenter dans des applications réelles.

Le deuxième module d'extension du MPC a été conçue pour déterminer automatiquement des pondérations adéquates pour la fonction coût du MPC de niveau hiérarchique plus élevé. S'appuyant uniquement sur la prédiction des données de déséquilibre de puissance et des mesures locales, ce module complémentaire définit également des paramètres de contraintes clés qui garantissent que le BMG satisfait le taux d'autoconsommation annuel requis à un coût de fonctionnement minimum. Puisque les aspects économiques et énergétiques sont parfois des objectifs contradictoires qui sont difficiles à équilibrer, l'ECMR conçu détermine de manière autonome les paramètres adéquats pour le MPC hiérarchique afin de faciliter le compromis entre ces deux objectifs antinomiques.

Malheureusement, la maximisation de l'énergie auto-consommée n'implique pas nécessairement la configuration la plus rentable pour les BMG. En raison des profils de production et de consommation d'énergie inhérents aux bâtiments, l'augmentation du taux d'autoconsommation nécessite une utilisation plus intensive des ESS. Néanmoins, selon la simulation réalisée au Chapitre 6, avec un contrôleur simplifié *rule-based*, l'utilisation de ESS apparaîtrait trop onéreuse, car les batteries représentent environ 12% du coût d'exploitation annuel total du micro-réseau, alors qu'un ESS hybride se situerait à environ 25%. Dans ce contexte, en France, un mécanisme de récompense et de pénalisation tend à se mettre en place pour inciter les bâtiments à installer des ESS afin d'atteindre des indices d'autoconsommation plus élevé. Néanmoins, une analyse plus approfondie est nécessaire pour vérifier si cette politique énergétique est avantageuse avec les coûts actuels et futurs des équipements constituant le BMG.

Dans le but de fournir une analyse technico-économique et de proposer une stratégie réaliste pour prendre en compte à la fois les aspects énergétiques et économiques dans l'optimisation du flux de puissance du BMG sans avoir besoin d'ajuster aucun paramètre, la performance de l'ECMR a été évaluée en la comparant à un contrôleur *rule-based* et à un MPC hiérarchique conventionnel. A travers les simulations conduites, le contrôleur hiérarchique doté de l'ECMR peut déterminer quel ESS doit être utilisé quotidiennement en se basant uniquement sur l'estimation du taux d'autoconsommation annuel et des coûts annuels de fonctionnement du micro-réseau. En plus de réduire la complexité de la

conception du contrôleur, l'analyse en temps réel mise en œuvre par l'ECMR diminue les dépenses totales du bâtiment car elle évite la pénalisation du réseau en ce qui concerne le taux d'autoconsommation annuel et réduit la dégradation et la maintenance des dispositifs de stockage d'énergie. Bien que le contrôleur hiérarchique proposé garantisse un taux d'autoconsommation de 5% à 17% inférieur au MPC hiérarchique conventionnel, la stratégie proposée satisfait le taux d'autoconsommation requis avec un coût d'exploitation annuel inférieur de 1% à 7%.

Les résultats de simulation du Chapitre 6 mettent également en évidence que la politique actuelle pour l'autoconsommation en France ne suffit pas à valoriser une installation incluant un stockage d'hydrogène. Le coût d'investissement élevé des piles à combustible, la faible efficacité de la conversion de l'hydrogène et les coûts élevés d'exploitation et de maintenance du stockage d'hydrogène sont les principaux facteurs qui limitent la rentabilité dans les installations dédiées aux bâtiments. Trois scénarios possibles pour rendre l'utilisation des piles à combustible avantageuse ont été suggérés sur la base de trois mécanismes : l'augmentation du prix de l'électricité, la réduction du coût d'investissement de la pile à combustible et l'augmentation du complément de rémunération dû au taux d'autoconsommation. Ces trois scénarios peuvent être utiles pour des projets visant à promouvoir l'autoconsommation et l'utilisation du stockage d'hydrogène dans les bâtiments.

Enfin, les possibilités de décalage dans le temps de la charge des batteries des véhicules électriques (PEV) pour réduire la dépendance énergétique du réseau principal ont été évaluées dans la dernière section du Chapitre 6. Les PEV sont des charges élastiques qui doivent être satisfaites dans un créneau prédéfini. Par conséquent, pour favoriser l'autoconsommation, il est primordial de charger les PEV en période de surplus d'énergie et de les décharger pendant les périodes de déficit énergétique. En combinant les atouts du MPC et du Module de Partage de Puissance (PSM) décrit au Chapitre 3, l'ensemble du contrôleur hiérarchique garantit que plus de 99% des véhicules électriques rechargeables disposent d'un état de charge des batteries supérieur à 75%.

L'un des avantages de la conception d'une unité de commande supplémentaire pour gérer les particularités du parc des PEV est la réduction de la complexité de conception du MPC hiérarchique. Au lieu d'estimer l'état de charge de chaque véhicule électrique rechargeable, les deux MPC en cascade n'estiment que l'énergie moyenne stockée dans tout le parc. C'est la mission du PSM de déterminer quelle quantité d'énergie doit être adressée à chaque PEV pour les recharger avant leur départ. En plus de simplifier la conception du contrôleur, cette coopération du PSM avec le MPC hiérarchique sollicite les batteries des véhicules électriques rechargeables pour réduire la dépendance énergétique au réseau principal, en raison de la diminution de l'injection annuelle d'énergie jusqu'à 7% dans les bâtiments résidentiels et jusqu'à 32% dans les bâtiments publics, par rapport au scénario où seules des batteries sont installées.

Néanmoins, en raison du net déséquilibre de puissance, du dimensionnement des packs batteries, et des profils quotidiens de connexion et de déconnexion des véhicules électriques, la recharge des véhicules électriques à partir d'énergies renouvelables est saturée. Ainsi, avec l'élargissement du parc des PEV, le taux d'autoconsommation annuel est saturé à 72% dans les bâtiments résidentiels et à 89% dans les bâtiments publics. Le parc des PEV entraîne également une augmentation conséquente de l'énergie totale achetée sur le réseau. En fonction du nombre de PEV, cette étude révèle une

augmentation de l'achat total d'énergie du réseau d'environ 5% pour un parc de 4 véhicules et de 61% pour un parc de 40 véhicules.

En conclusion, les principales contributions du système hiérarchique de gestion énergétique des bâtiments développé au cours de cette thèse peut être résumé par les six points énoncés ci-dessous :

- Maximisation du taux d'autoconsommation à moindre coût suivant le code d'énergie français.
- Analyse technico-économique de l'accessibilité du marché des systèmes de stockage d'énergie à l'hydrogène.
- Évaluation périodique du taux de dégradation des batteries, électrolyseurs et piles à combustible.
- Identification en temps réel du modèle des systèmes de stockage d'énergie.
- Estimation de l'autoconsommation annuelle et du coût de fonctionnement du bâtiment à travers le traitement des données de déséquilibre de puissance.
- Evaluation des potentialités d'exploitation des batteries de véhicules électriques rechargeables pour favoriser l'autonomie énergétique des micro-réseaux dédiés aux bâtiments.

Les suggestions pour de nouvelles recherches découlent principalement des limites de l'échelle du BMG. L'élargissement de l'analyse technico-économique au contexte de l'autoconsommation collective serait un développement judicieux. L'installation de ESS dans les bâtiments pourrait être plus accessibles dans le scénario où plusieurs micro-réseaux dédiés aux bâtiments partageraient les mêmes ressources électriques. En plus de réduire le coût d'investissement total par bâtiment, la coopération entre les bâtiments voisins pourrait atteindre un indice élevé du taux d'autoconsommation, puisque le degré de liberté de l'ensemble du système augmente. De plus, il est nécessaire d'extrapoler l'analyse menée en simulation à des systèmes réels. Une analyse plus approfondie est nécessaire pour traiter les problèmes éventuels liés au délai des communications, aux limitations des ressources de calcul, aux bruits de mesures et à la résilience aux défauts. Il est donc essentiel que les recherches futures prennent en compte toutes les particularités techniques et économiques des applications réelles pour accroître l'intégration des sources d'énergie renouvelables au sein des bâtiments dans un futur proche.

Chapter 1 A literature review of the advantages and barriers of building microgrids

1.1 Introduction

Building MicroGrids (BMGs) have emerged as an advantageous alternative for tackling environmental issues while enhancing the electricity distribution system [5]–[8]. However, uncertainties in power generation, electricity prices, and power consumption, along with stringent requirements imposed by the grid code restrain the wide development of BMGs. This is because BMGs create a complex environment that struggles the design of a unique Building EMS (BEMS) capable of being simultaneously compliant with power quality standards [17] and economically advantageous when trading in the electricity market [18], [19].

However, few studies deal with the electricity market trade and the current grid code concerning BMGs. Most of them deal with each BMG concern separately without considering any possible conflicting objectives when they are put together. To tackle as many BMG requirements as possible, the hierarchical control structure has been increasingly adopted [20]–[23]. The main interest of the hierarchical control structure is that it makes it possible to handle multiple objectives that are sometimes conflicting and not on the same time scale.

The hierarchical control architecture has proved suitable for handling some important MG trade-offs. For instance, it can determine a balance in increasing active power injection without degrading the islanded MG frequency [24] or assuring the safe power-sharing while keeping the level of voltage unbalance within the standard boundaries [25]. The division of multiple hierarchical layers also enables to maximize the profit made from the electricity market while ensuring the power balance [26]. It also determines a worthy compromise for reducing the building power consumption without penalizing its residents' comfort [27]–[31].

The hierarchical control aims at optimally assigning each dispatchable unit inside the BMG with power references. In BMG environments, its primary purpose is to maximize the RESs exploitation and minimize the power dependency on the main utility [3], [8], [32], [33] while avoiding unsought measures such as renewable sources curtailment [34] and load shedding [35]. Notably, without any dispatchable unit, the power balance cannot be satisfied except by purchasing electricity from the main grid.

From the economic perspective, the inclusion of dispatchable units in the form of batteries reduces the electricity expenditure, leading to a more affordable configuration [3], [4]. For this reason, in the literature, the fundamental and most common approach in BMGs is to install and manage an appropriate ESS, which might include batteries, flywheels, and supercapacitors as detailed and reviewed in [36].

Consequently, most of the EMSs incorporates constraints regarding the State of Charge (SoC) of ESSs as long as a factor for enhancing their lifetime in their objective functions, as studied in [18], [37], [38].

Generally, the energy management in a BMG is conceived with a unique ESS and with a horizon of one day-ahead. For instance, in [39], [40] fuzzy logic was employed in a PV-battery MG, whilst in [41], [42] a ruled-based to manage a WT-PV-battery system was used. On the other hand, in [43] a Multi-Agent System (MAS) structure with Particle-Swarm Optimization (PSO) algorithm and fuzzy logic was conceived to coordinate a BMG considering the internal comfort while reducing expenses. Likewise, [38], [44] used metaheuristic methods with a small MG, whereas the authors of [45] employed stochastic algorithms to tackle uncertainties of electricity prices and power generation.

Based on the load profile, hybrid ESSs are also envisaged in BMGs, as highlighted in [46]. Despite less common in BMGs, supercapacitors and batteries can be designed to reduce the stochastic power generation of RES, soften fast peak of consumption and regulate the frequency when operating in island mode [47], whereas fuel cells can be suitable to handle seasonal power variability [48]. There are many strategies to manage hybrid ESS, such as MPC for managing fuel cell and batteries [37], [49]–[51], PSO [52] and Genetic Algorithm (GA) [18], [53].

Some studies also consider the batteries of Plug-in Electric Vehicles (PEVs) in MG energy management, such as [49], [54] and [55]. Particularly, in [49] and [55] a two-stage controller was used to ensure the MG stability in the first stage and economic dispatch in the second one. Similarly, in [8] a hierarchical MPC was designed to use the PEV batteries to compensate for the power imbalance between the generation and consumption, under the condition to charge the PEV batteries at the end of the working day and considering their aleatory arrival and departure time.

Aiming at covering the most relevant BMGs concerns to allow RESs coupled with ESSs to be installed in buildings, this chapter creates an extensive literature survey about the most important control algorithms applied to the BMG environment. This review assists the design of a complete building energy management system by detailing each control level in a hierarchical control structure adapted for buildings. It provides a solid basis for comprehension on the field of smart grids, energy management systems, and electricity market requirements, which will be straightforward to foster not only the development of BMGs but also multiple sustainable projects worldwide.

This chapter is structured as follows. Section 1.2 presents some relevant BMGs demonstrators around the world. Section 1.3 lists the most important BMG control requirements. Section 1.4 explains the three most common hierarchical control structures found in the literature. Section 1.5 details each hierarchical control layer by stating their responsibilities in BMG operation. Section 1.6 details how BMGs should be adapted to the current electricity market. Section 1.7 explains the existing command strategies for BMG regulation and provides an extensive comparison of the most usual energy management algorithms in MGs. Section 1.8 clarifies BMG perspectives for the near future. Finally, Section 1.9 concludes this chapter.

1.2 Building MicroGrid demonstrators and the state of energy management strategies

International directives worldwide have conducted researches aiming for new technologies to pave the way toward sustainable buildings with high thermal and electrical efficiencies, also known as Net-Zero Energy Building (NZEB) plan [56], [57]. A successful path aiming at NZEB requirements accomplishment should be accompanied by technology breakthrough following the well-defined priority order highlighted in [56] and illustrated in Fig. 1.1.

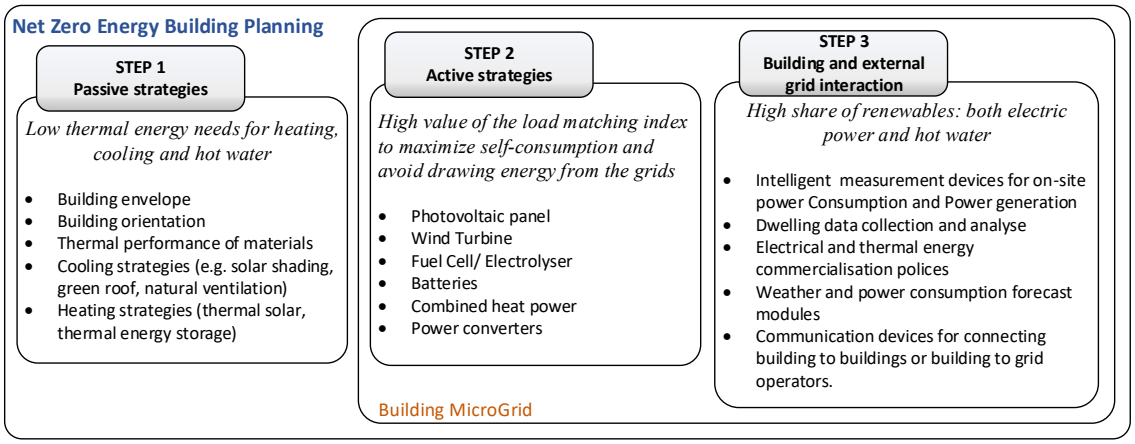

Fig. 1.1: Recommended steps toward NZEBs and their respective requirements regarding device installation and technology breakthrough.

Targeting to make all new buildings NZEB within the next decades, many demonstrators have been built all around the world. In [58], more than 400 buildings were analysed by pointing out their main features to attain the NZEB requirements. Analogously, authors of [59] summarized 74 academic papers that refer to real NZEBs, whereas [60] analysed 600 real NZEBs found in web platforms like Zero Carbon Hub [61] by dividing them into five clusters depending on temperature, ownership and site location.

However, real NZEB energy management strategies lie much more on thermal efficiency by implementing passive solutions rather than active methods with on-site power generation. Passive strategies, which comprehend thermal insulation and natural lighting architectures, are cheaper and faster measures to improve building efficiency, because energy demand for thermal control represents 59% of total building energy demand, as depicted in Fig. 1.2 [1]. According to [56], on-site electricity generation through RES combined with ESS exploitation is essential to accomplish NZEB requirements. Otherwise, the buildings will not reach the expected rates for electric self-consumption and self-coverage [11] in one year.

Real implementations with active solutions are mainly focused on building-integrated PVs as pictured in Fig. 1.3, in which their energy surplus is either fed directly into the grid (photovoltaic systems) or stored in thermal collectors (thermal-solar systems) as those mentioned in [58], [62]. In these studies, electric ESSs are not usually considered due to the complexity of its energy management algorithms, expensive installation cost, and the necessity of additional power converters. Demonstrators

employing both RESs and ESSs are transitioning from the research and development stage to full market accessibility.

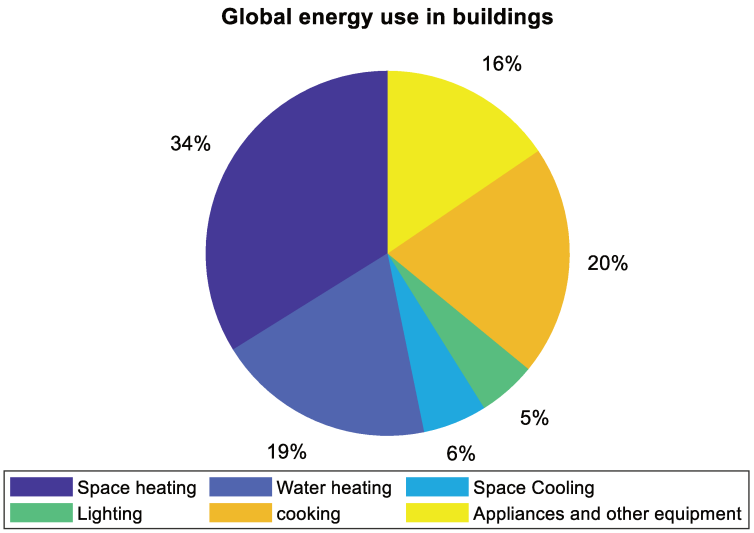

Fig. 1.2: Buildings end-use energy consumption, 2017. Data collected from the International Energy Agency report of 2019 [1].

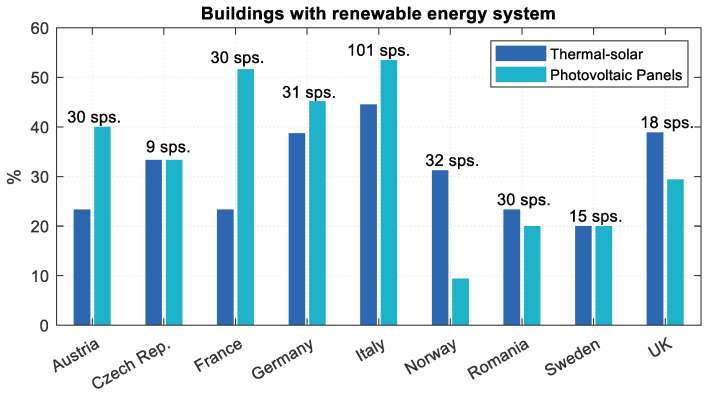

sps. = Sample buildings

Fig. 1.3: Real Net-Zero Energy Buildings in Europe with active energy efficiency solutions. Source ZEBRA [58].

Although most of BMGs are usually reported either in the laboratory [30], [39], [41], [49], [51] or demonstrator scale, as the Pixel Building in Australia [63] or Pearl River Tower in China [64], some companies start offering residents the possibility to install their home batteries. Companies like EDF [65] and Naked Solar [66] started integrating electric ESS into buildings, but it is still too expensive for being broadly implemented. Some relevant real BMGs testbeds with electric ESS exist [31], [41], [64], [67]–[69], where most of their BEMS are conceived hierarchically, by superposing local controllers of ESS and RES with a central EMS for managing BMG power flow. Seen that most of the BEMS of BMG demonstrators tend to be structured hierarchically, in this chapter a comprehensive review of hierarchical energy management algorithms for BMGs equipped with electric ESS will be presented.

1.3 Requirements for building microgrid control systems

Developing a suitable controller for BMGs is one of the most significant challenges for buildings to become active prosumers (both producers and consumers) in the current electricity market [7], [9], [28] and achieve the targets defined for NZEBs. The main difficulty faced by BEMS is to manage multiple variables that are not on the same time scale. To understand the main control objectives related to hierarchical control for BMGs, the most relevant requirements are detailed underneath, highlighting their respective usual time frame.

1.3.1 *Power-sharing [100 ms – 1s]:*

The power-sharing difficulty consists of optimally assigning each Distributed Generator (DG) with its respective active and reactive power (in AC MGs) so that the load demand is satisfied without overloading a specific DER and without degrading the MG bus voltage and frequency ($v\&f$) levels. The power-sharing is usually implemented in a distributed way by droop control strategies, because of low-bandwidth communication requirements and high flexibility concerning plug-and-play MG devices [23], [70]–[74]. A comprehensive review of droop control strategies is summarized in [75].

Besides distributed architectures, centralized structures have also been envisaged due to more accurate power-sharing results and less voltage and frequency ($v\&f$) deviations. Master-slave [76], [77], and concentrate methods [78] are the most usual centralized power-sharing strategies found in the literature. Further discussion about power-sharing control algorithms is detailed in paragraph 1.5.1.

1.3.2 *Thermal control and resident comfort [10 min – 1h]:*

Controlling Heating, Ventilating, and Air-Conditioning (HVAC) systems can enhance the whole efficiency of buildings and reduce the cost of purchasing electricity from the main grid while keeping residential comfort, as studied in [27], [30], [79]. Generally, the indoor comfort is evaluated based on the Predictive Mean Vote index and controlled respecting the ASHRAE [80] or EN15251 standards. However, conceiving a real building thermal model may be cumbersome, which leads to simplified resistance-capacitance models [27], [50] or other thermodynamic models [30], [55]. Another approach is to use software assistants (e.g. EnergyPlus and TRNSYS) to simulate complex thermal dynamics of an entire building [79]. Alternatively, grey-box models, which consider real data and theoretical models, have also been studied [81].

1.3.3 *Voltage and frequency regulation [1ms – 1s]*

According to [7], BMGs can be modelled in different scales depending on their electric capacity, operating either as independent building (i.e. residential buildings with a capacity of 1kW – 10kW), a community or high-capacity building also known as nanogrids (i.e. commercial building with a capacity higher than 10kW). Depending on its size, the grid-connected building/community MG can offer some ancillary services to the grid for $v\&f$ regulation at the Point of Common Coupling (PCC).

In [41], it is studied a scenario where a residential community in Thailand could offer active power as ancillary service to the main grid by optimizing the power dispatch among different houses and

employing load shedding to match the active power demand. Likewise, [27] proposed a different electricity market structure in which the main grid interacts with both individual buildings and community residences to promote load following and power imbalance service to respect the grid constraints at PCC. Alternatively, [82] used MPC and perturb & observation to estimate the MG's energy capacity to participate in the ancillary service market for grid frequency support in a commercial building.

However, when connected to weak grids, such as isolated communities forming an off-grid system, the fact of ensuring the power-sharing among DGs will not necessarily ensure the *v&f* regulation at the MG common bus. Due to the cross-correlation between active/reactive power and voltage/current, there will often be a voltage deviation between the voltage reference and the measured one at common bus. A detailed review of the main strategies to properly regulate the $v\&f$ is summarized in [83] and in Section 1.7.

1.3.4 *Power dispatch and electricity market trading [1min – 1h]:*

The BMGs prime interest is to exploit as much as possible RESs and trade in the electricity market only in emergency situations to achieve the autonomy indicators of self-consumption and self-coverage [11] imposed by regional grid regulations. Consequently, PV panels and WTs are normally controlled via MPPT algorithms to extract the maximum power whatever the weather conditions [84], [85]. As a result, the power dispatch in BMGs is concentrated on the coordination of their ESSs, Demand-side management (DSM) and determining the amount of energy to be exchanged with the main grid.

Depending on the BMG's electrical architecture, the power dispatch must be designed differently. For instance, contrary to DC and AC BMGs, the EMS of hybrid BMGs must manage the power flow between AC and DC buses through bidirectional AC-DC power converters to guarantee power quality in both buses [86]. Likewise, there are differences in the power dispatch when connected or disconnected from the main grid. In off-grid buildings, batteries are mainly used to assure power quality inside the MG. Meanwhile, in grid-connected systems, ESSs are normally used to shift the peak demand according to some demand-response incentives. Moreover, when connected to the grid, the BMG can rely on external grids to satisfy its demand, by participating in the electricity market [10], [26], [87], [88]. A more detailed explanation about building interaction with external grids is discussed in section 1.5.3.

When multiple sorts of ESSs (i.e. hybrid systems), and dispatchable and non-dispatchable units are installed inside the BMG, there are numerous ways of satisfying the load demand depending on how the BEMS coordinates the DGs. Nonetheless, all possible solutions are not necessarily considered as optimal in terms of economic or environmental aspects. In this case, the power dispatch can be formulated as an optimisation problem that considers the cost of each DG, the fatigue of energy storage systems, as studied in [32], [37], [89], and/or the gas emissions as investigated in [38], [48]. Power dispatch optimisation lies in a multi-objective problem that is usually solved using the Pareto frontier to determine the best compromises among various possible solutions [54]. A critical review of different EMS methods for power dispatch in MGs and existing algorithms are summarised in [90] and Section 1.7.

1.3.5 *Elastic loads and demand response [more than 1h]:*

Energy demand is classified either as elastic or inelastic one [91]. The inelastic demands are those that need to be supplied immediately, such as lighting and domestic equipment (e.g. televisions and computers). Consequently, they cannot be controlled by BEMS directly. Meanwhile, elastic demands have energy requirements that are to be met within a certain deadline, such as dishwashers, water heaters, air conditioners, and PEVs [8], [27], [29], [92], [93]. This kind of load can be curtailed or shifted to satisfy the power balance. Alternatively, the implementation of demand response programs can be used to maintain the system reliability and enhance BMG flexibility during peak-load periods by either financial incentives or education programs as reviewed in [94].

Table 1.1: Collection of electrical standards for building microgrid control design.

Standard	Building Application	Description	Ref.
IEC 61851	Electric vehicle	Information about household Electric Vehicle charging station for voltage levels up to 250V for single-phase systems and 480 V for three-phase systems.	[95]
IEC 60364-1	Human Safety	Recommendations for design and verification of electrical installation of nominal voltages up to 1000 VAC or 1500 VDC to guarantee the safety of persons against life dangers.	[96]
IEEE 2030.10	DC off-grid energy providers	Rules for low DC voltage bus of 48V destinated for isolated communities, providing recommendations for DC power management and communication protocols.	[97]
IEEE 1547	Microgrid connection with the main grid	Rules for integrating distributed resources (< 10 MVA) to the grid in a safe manner, such as unintentional island tolerances, the procedure for MG reconnection, power quality requirements, and the correct voltage, frequency, and phase angle at PCC.	[98]
IEC 61000 and IEEE Std115	Electromagnetic Compatibility	Information about power quality boundaries for AC and DC buses. For instance, voltage unbalance is limited to 3%.	[99]
IEEE Std 1709	Medium Voltage Direct Current bus	Power quality recommendations for DC bus between 1,5kV to 35kV, such as maximum acceptable ripple and DC voltage tolerances.	[100]
ISO 52016-1	Building Energy Thermal Efficiency	Some important response time for HVAC to BMG to respect building thermal zone standards as ASHRAE, such as estimation of the energy need for heating and cooling.	*
ISO 52000-1/ ISO 52003-1/ ISO 52010-1/ ISO 52016-1/ ISO 52018-1	Energy performance of buildings	Some indicators for assessing the energy performance in buildings. These standards help to define NZEB.	*
IEEE 2030.7	Energy Management System	Functions for the control level associated with the proper operation of the EMS that is common to all microgrids, regardless of topology, configuration, or jurisdiction.	[101]
IEC 61850	Power Utility Automation	Rules for the communication between BMG and substation as long as between intelligent devices inside BMG.	[102]

*These standards need to be purchased to have full access.

1.3.6 *Power quality enhancement concerning the grid code [1ms – 1 min]:*

The control design of BMGs must respect electrical standards to guarantee both inhabitants' safety and grid power quality. In [96], some important BMG standards were enumerated and discussed, while [99] summarized the main relevant electrical indicators that the controller must monitor in DC MGs. In AC MGs, the load-MG coupling must respect the constraints of power quality defined by standards, considering harmonic generation [103], [104], voltage unbalance [105], [106], $v\&f$ regulation [107]–

[109]. A collection of the main electrical standards applied in Europe, and that is essential for BMG controller design are summarized in Table 1.1. Depending on BMG capacity, different standards may be considered, as summarized in [96] and detailed in Table 1.2.

Power quality burden and the number of power converters are reduced in DC BMGs, whereas grid synchronization and frequency regulation are major concerns in AC BMGs. Consequently, DC BMGs are usually deployed in remote areas or low capacity buildings [41], [42]. However, their reliability is reduced when connecting to the main grid since they rely only on the interlinking bidirectional converter, contrary to multiple inverters in AC BMGs. Therefore, hybrid coupled MGs have been envisaged for grid-connected buildings [6], [31], [110], because they can include both the simplicity of DC buses and the high flexibility and reliability of AC buses when connecting to the main utility.

Table 1.2: Typical voltage level in DC and AC bus of building microgrids.

BMG topology	**BMG application**	**Voltage Level**	**Tolerance Level and the most important standard**
AC	Any traditioinal grid-connected BMG (i.e. hybrid or AC BMGs)	230 V / 400 V	Voltage amplitude: $\pm 5\%$ Frequency: ± 0.2Hz* (IEEE 1547)
DC	Off-grid remote home	48 V	Maximum Current: 5A (IEEE 2030.10 and IEC 60038)
	Grid-connected residence, commercial building	380V – 400V	DC level at the supply terminals: $\pm 10\%$ DC drop at equipment terminal: $\pm 4\%$ (IEC 60038)
	Industrial application, commercial building	1500V ($\pm 750V$)	DC level: $\pm 10\%$ Ripple: $\pm 5\%$ (IEEE Std 1709)

*Depend on the duration of frequency deviation and other temporal issues.

1.3.7 *Grid faults and island detection [1ms – 1s]:*

When a grid fault happens, the MG must disconnect from the main grid to avoid damage to electrical devices and possible disturbances to the main grid. In this context, grid-connected MGs must be capable of detecting grid faults and continue to operate in island mode [107]. Consequently, grid-connected MGs are also designed with either passive [111] or active islanded detection systems [112] as well as dedicated control algorithms for regulating the electrical transients when commuting between operation modes [110].

Some efforts have been made to propose a single controller for both grid-connected and off-grid configurations. For instance, the fuzzy logic controller was proposed in [113] to predict increases in current and voltage and limiting the power supply of DERs. In [110], a pre-synchronization system based on angle compensation was proposed as an alternative to the conventional phase lock loop, allowing a single control for a master-slave converter topology [114] to be used when operating in either islanded or grid-connected modes. As a consequence, island detection becomes less critical, and the transient response is enhanced once the commutation between controllers is no longer required.

1.4 Hierarchical control structure

After recognizing the major requirements of a BMG, it is noteworthy that all these concerns must be accomplished in parallel, even though they are not on the same time scale as illustrated in Fig. 1.4.

For instance, due to the fast response of power converters, the frequency and voltage regulation, power-sharing, and island detection must be satisfied almost instantaneously (some milliseconds). On the other hand, depending on the power quality issue, it might be treated from some milliseconds to one minute. Additionally, power dispatch can be dealt with within a few minutes, whilst economic dispatching and market participation are usually deployed from every few minutes to one hour.

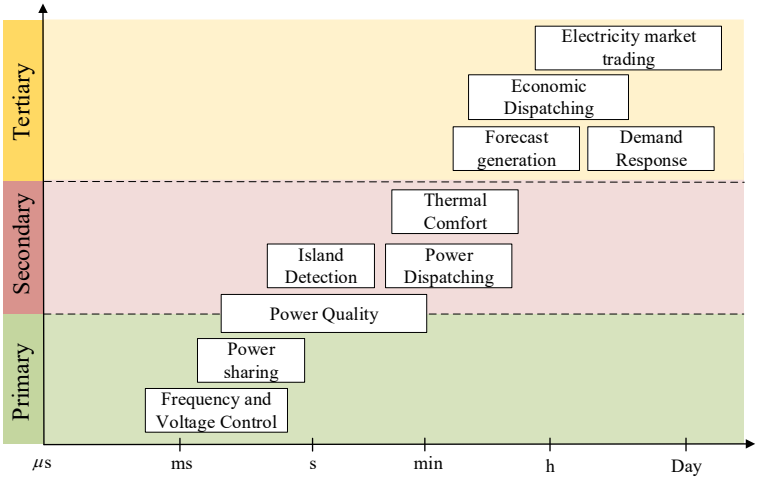

Fig. 1.4: Different timescale of the main microgrid control functions.

The smartness of hierarchical control lies in dividing a complex problem into different time-based chunks (e.g. k_1, k_2, k_3 and k_4 in) that are interconnected by exchanges of some variables from lower to upper hierarchical levels (or *vice-versa*) that are normally fulfilled via an external wireless-communication or direct communication-link protocols [100]. A summary of the communication technology that is applicable in building environments is detailed in Table 1.3 for wired communication and Table 1.4 for wireless communication, whereas the advantages and disadvantages of each of these types of communication links are summarized in Table 1.5.

Table 1.3: Wired communication technology used for building energy management systems.

Communication Protocols					**Application**	
Type	**Technology**	**Indoor range (m)**	**Data rate**	**Frequency band**	**Type**	**Hierarchical control level**
Serial	RS-232/ RS-422/ RS-485	**	2.4 kbps	NA	Smart Building, Smart home	Secondary
Ethernet	Ethernet IEEE 802.3	**	Up to 1Gbps	NA	Smart Building, Smart Home, Smart Cities	Primary, Secondary, Tertiary (communication between buildings)
Bus-based	Modbus	**	9 – 19.2 kbps	NA	Smart Building, Smart Home	Primary, Secondary
	Profibus	**	9.6 – 12 Mbps	NA	Smart Building, Smart Home	Primary, Secondary
	CANBus	**	up to 1 Mbps	NA	Smart Building, Smart Home	Primary, Secondary
Power Line	PLC	**	20 – 200 kbps	NA	Smart Building, Smart Home	Primary, Secondary

Wired communications are more expensive than wireless ones, but they are more robust against cyberattacks and possess lower delays. Therefore, wireless communication is more suitable for large environments on the scale of cities. On the other hand, wired ones are more convenient for small systems, such as in size from a single building to a neighbourhood. The communication protocol must be chosen following control design requirements concerning latency and baud rate as outlined in the IEC6185 standard (Table 1.1) and Table 1.6, respectively.

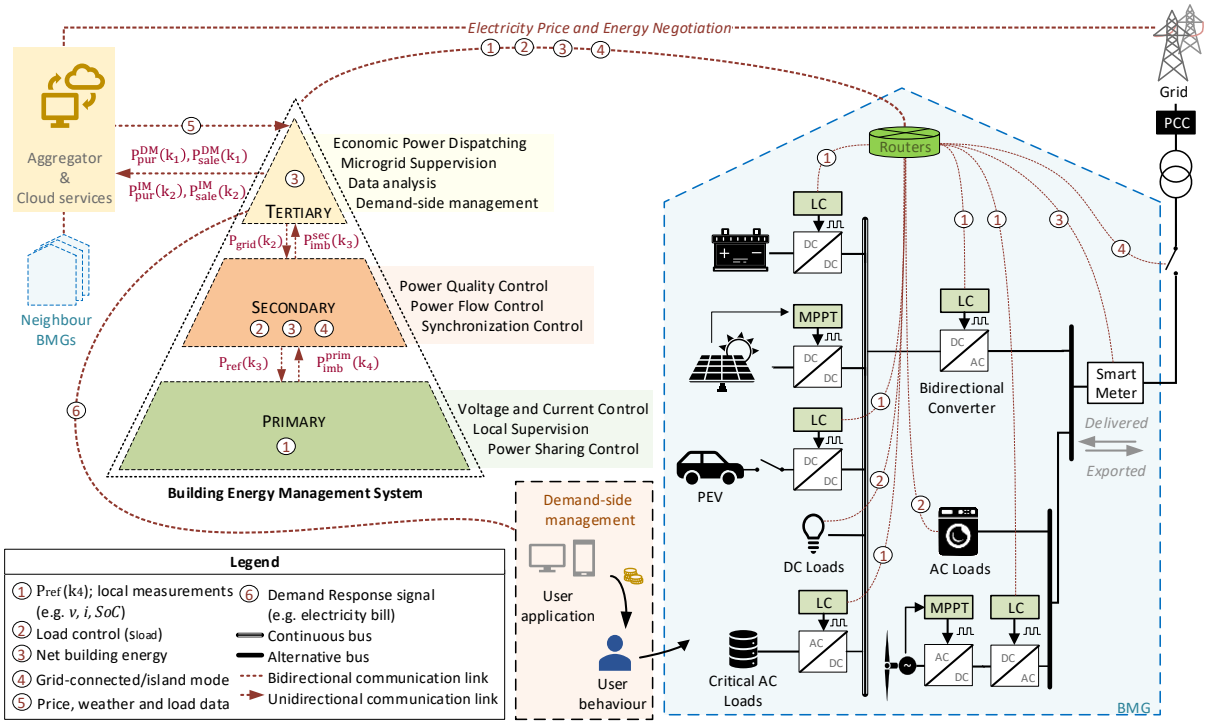

Fig. 1.5 : Scheme of a typical hierarchical control architecture for a hybrid grid-connected BMG.

Table 1.4: Wireless communication technology used for building energy management systems.

Communication Protocols					**Application**	
Type	Technology	Indoor range (m)	Data rate	Frequency band	Type	Hierarchical control level
Wireless Local Area Network (WLAN)	Bluetooth	<10	25 Mbps	2.4 GHz	Smart home	Primary
	WiFi	70	54 Mbps	2.4 – 5 GHz	Smart Building, Smart Home, Smart Cities	Primary, Secondary and Tertiary (communication between buildings)
	ZigBee	up to 20	250 kbps	2.5 GHz	Smart Building, Smart Home	Primary and Secondary
	LiFi	10	1 Gbps	Hundreds of Tera Hz	Smart Building, Smart Home	Primary and Secondary
Cellular networks	3G	Entire GMS coverage area	200 kbps	2.4 GHz	Smart Cities	Tertiary (communication between buildings)
	4G	Entire GMS coverage area	100 Mbps to 1 Gbps	0.7 – 2.6 GHz	Smart Cities	Tertiary (communication between buildings)

Table 1.5: Advantages and disadvantages of wired and wireless communications in building microgrids.

Technology	Advantage	Disadvantage	Common communication architectures
Wired	Robust against cyber attack High reliability High bandwidth	Cannot operate well in decentralize configuration (except when using Ethernet) Expensive implementation (except for Power-Line Communication) Difficult of expanding the network The number of connected devices is limited to physical connections High risk of SPOF	Enhanced Performance Architecture (EPA) used in Supervisory Control and Data Acquisition (SCADA) communication. Further explanation about EPA: [102]. Studies that used SCADA: [30], [116], [117]
Wireless	Self-healing property Self-organization property Can operate in decentralized or centralized configurations Cheap implementation A large number of devices can be connected.	Not robust against cyber attack	Software-Defined Network (SDN) with OpenFlow protocol [115] SDN based on cloud data analysis [115] Peer-to-peer overlays: [9]

Table 1.6: Network requirement depending on building microgrid application. Table modified from [102].

Building Microgrid Message Type	**Hierarchical Control Layer**			**Baud rate**
	Primary	Secondary	Tertiary	
Demand response		x	x	14 – 100 kbps
Distributed Energy Resources and Storage	x	x		9.6 – 56 kbps
Energy Management System		x		9.6 – 100 kbps

Therefore, through external communication, the exchangeable variables among hierarchical levels are employed to ensure the power balance (P_{grid}, P_{imb}^{sec} and P_{imb}^{prim}) or to optimal assign power references (P_{ref}) toward distributed Local Controllers (LC) of each power converter, as shown in Fig. 1.5. The BEMS can also implement DSM through demand-response mechanisms to shift the load demand by determining equipment on/off signals (s_{load}) or indirectly control the building power imbalance by changing its dwellings' behavior through financial incentives [94].

Demand-response incentives are usually based on the analysis of real-time building net energy that was collected by the building smart meter and processed remotely with the huge amount of other forecasted data coming from cloud services [118], [119] or building community aggregator [26], [27]. Consequently, data collection modules, such as smart connected devices (e.g. smart meters, and sensors), also known as Internet of Things (IoT) components along with weather and load forecast data analysis plays an important hole in BEMS [118], [119].

The hierarchical control is regulated by relying on local measurements acquired by the primary control at PCC or common bus, which comprise voltages and currents at each converter output. Notably, the hierarchical control scheme depicted in Fig. 1.5 is a simplified architecture that can be enhanced by adding sharing variables like total harmonic distortion [103] or voltage unbalance factor [105] to address power quality issues or temperature sensor signals to regulate HVAC system [27], [30], [79]. In the literature, different hierarchical control approaches are presented such as the traditional PI-hierarchical control [120], hierarchical multiagent system [121], [122], hierarchical predictive control [49], [123] and stochastic hierarchical control [26], [124].

1.4.1 *Hierarchical control topologies*

Depending on the MG size, communication, and computer technology, a hierarchical control MG can be designed by either centralized, distributed fashion [125] or a combination of both, forming the hybrid MGs [126]. As will be explained in the following three paragraphs, the hierarchical control classification is based on how the secondary control layer, also known as the supervisory control system, is conceived.

1.4.1.1. Centralized hierarchical control

Centralized Hierarchical Control (CHC) consists of one master control entity and other slave low levels – see Fig. 1.6a. It relies on huge data storage systems and high-performance computers to construct a dedicated central controller that communicates extensively with the controlled units. Therefore, CHC enables high computational cost algorithms to be used. For instance, [26], [127] managed MG uncertainties through a CHC in which multiple scenarios were analyzed before performing the optimal power dispatch. Correspondingly, [18], [38], [128] employed metaheuristic algorithms with the calculation of Pareto optimal solutions in a multi-objective cost function. To reduce the computational demand for CHC architecture, cloud services empowered with data science techniques and vast forecast databases have also been envisaged in BMG environments as reviewed in [118], [119], but security aspects restrain industries from embracing cloud computing technologies.

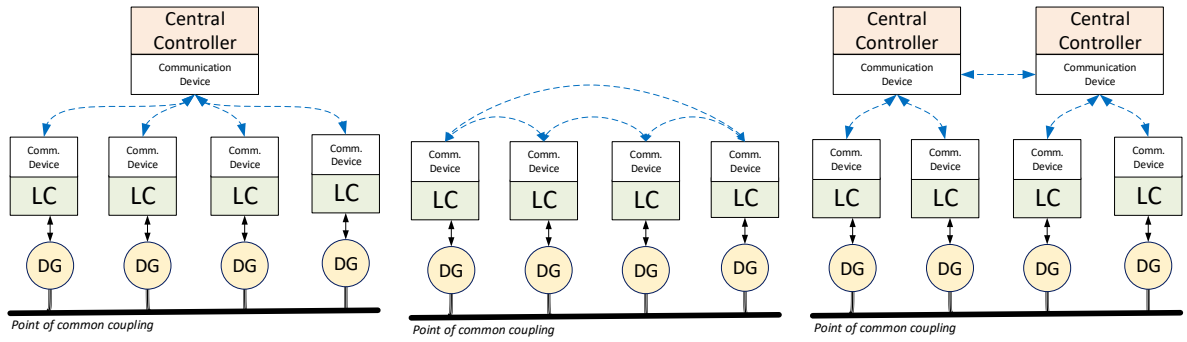

(a) Centralized microgrid (b) Distributed microgrid (c) Hybrid microgrid

Fig. 1.6: Conventional topologies in the microgrid control architecture based on the communication disposition [129].

The main advantage of CHC is that it holds the control intelligence that considers the MG as a whole. Consequently, it does not depend on the complex Consensus Algorithm [121] to build global knowledge of the MG, making the design of centralized BEMS easier than distributed architectures. Therefore, relying on trustworthy state variables allows simple algorithms to be used in MG energy management, such as fuzzy logic [39], [130], and rule-based [42], [88].

MGs covering extensive geographic areas, such as the agglomeration of multiple BMGs, make centralized MG control architectures infeasible due to extensive communication and computational costs. Nonetheless, in small environments such as hospitals, schools, and small communities, centralized MG can be suitable. Another drawback of CHC is the weakness against Single Point Of Failure (SPOF) in communication, which can lead to a complete collapse of centralized systems, while

only an occasional and transient loss of performance in distributed architectures [103], [131]. In this context, Software Defined Networks have been emerging as a promising communication architecture to improve the robustness of CHC in BMGs regarding self-healing properties when in contingency situations and to enhance its reliability by reducing the amount of data transfer, as reviewed in [115] and implemented in an MG testbed in [132].

1.4.1.2. Distributed hierarchical control

In Distributed Hierarchical Control (DHC), illustrated in Fig. 1.6b, each LC actuates individually in each DER, without relying on any command coming from a central controller as in CHC. Each individual best-evaluated solution is determined locally based on local measurements and the sharing of information among all the MG's LC through peer-to-peer communication, standardized by IEC 61968 (for a single BEMS) and IEC61850 (for interoperability between BMGs). In this kind of topology, full knowledge of MG state variables is built based on average consensus algorithm. Due to incomplete information about the overall MG status and delays caused by consensus algorithm, centralized topologies have a higher performance than distributed ones [133].

Massive research has been conducted in an attempt to improve the performance of distributed architectures through consensus algorithm [131], [134], to achieve information awareness comparable to that of centralized controllers. There are different strategies to implement DHC. For instance, in [40], the voltage regulator uses a noise-resilient voltage observer to estimate the global average voltage which is used to adjust the local voltage set point to provide global voltage regulation through consensus algorithm, while in [92] Mult-Agent System (MAS) was used to manage an isolated multi-generation MG using partial load shedding optimally.

1.4.1.3. Hybrid hierarchical control

Hybrid Hierarchical Control (HHC) is a combination of distributed and centralized controllers, as depicted in Fig. 1.6c. Local and global optimizations work in cooperation to achieve the MG's optimal point of operation. The local controllers are organized in groups so that the central controller's intelligence is split into smaller computation resources. HHC implementation is more complex than CHC since coordination among central controllers is mandatory to build the overall MG knowledge, but delay time in communication is less harmful than in DHCs. Similar to DHCs, the likelihood of SPOF in HHC is lower than fully centralized controllers, because each central controller can also operate independently in the case of contingency situations. Therefore, the scalability, flexibility, robustness, and cost of investment of HHC are more advantageous than DHC and CHC in large environments [126].

In the context of BMGs, the HHCs were evaluated for managing BMG communities when importing and exporting energy among multiple prosumers under the peer-to-peer electricity market concept. In [135], the IEEE 14-bus was divided into three communities that trade electricity amongst each other to reduce energy exchange with the external grid. Similarly, in [136], the power flow inside each household equipped with PV array and batteries is managed through a central controller to maximize its self-consumption rate, while peer-to-peer control configuration coordinates the energy trade with neighbouring microgrids and the external community grid in a distributed manner.

1.5 Details of hierarchical control layers

Notably, a single controller is not capable of solving all BMG concerns simultaneously. Hence, the hierarchical architecture is considered a suitable configuration to be used in BMGs because it allows multiple variables to be controlled almost independently thanks to its inherent cascade structure [72], [125]. It usually has three control levels – namely primary, secondary, and tertiary control – in which each one holds a dedicated responsibility regarding the overall MG interest as depicted in Fig. 1.5 with further details below.

1.5.1 *Primary control layer*

The primary control layer sends control at intervals of several milliseconds to the power electronic devices to stabilize the $v\&f$ at MG internal buses, perform islanding detection, accomplish power-sharing among different DERs and address some of the power quality issues. Since DERs are physically distributed, and the control is based mainly on local measurements, communication in this control layer tends to be minimal or inexistent. Despite not being totally standardized, the primary control is divided in two: an inner loop responsible for regulating the output voltage and current of power converters, and the outer loop in charge of ensuring safe and correct power-sharing.

1.5.1.1. Inner loop control

The inner control loop of the primary controller is responsible for interacting directly with power converters, either in grid forming or grid following configurations [114], [137]. Generally, in islanded connected mode the converters are set up as grid-forming mode in which they can be represented as Voltage Source Converter (VSC) so that the output current and voltage are usually regulated by two Proportional Integral (PI) controllers in cascade: the first PI voltage controller generates the current reference for the second PI current loop – see Fig. 1.7. On the contrary, in grid-connected mode, the power converters operate in a grid-feeding mode where they are commanded as Current Sources Converters (CSC) and power references are assigned with the aim to achieve converters' desired point of operation [114], as shown in Fig. 1.8.

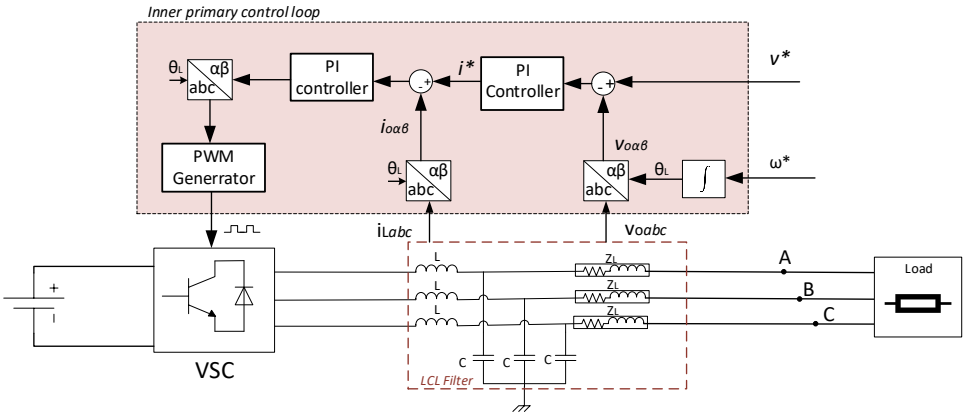

Fig. 1.7: Common inner primary control loop in island mode.

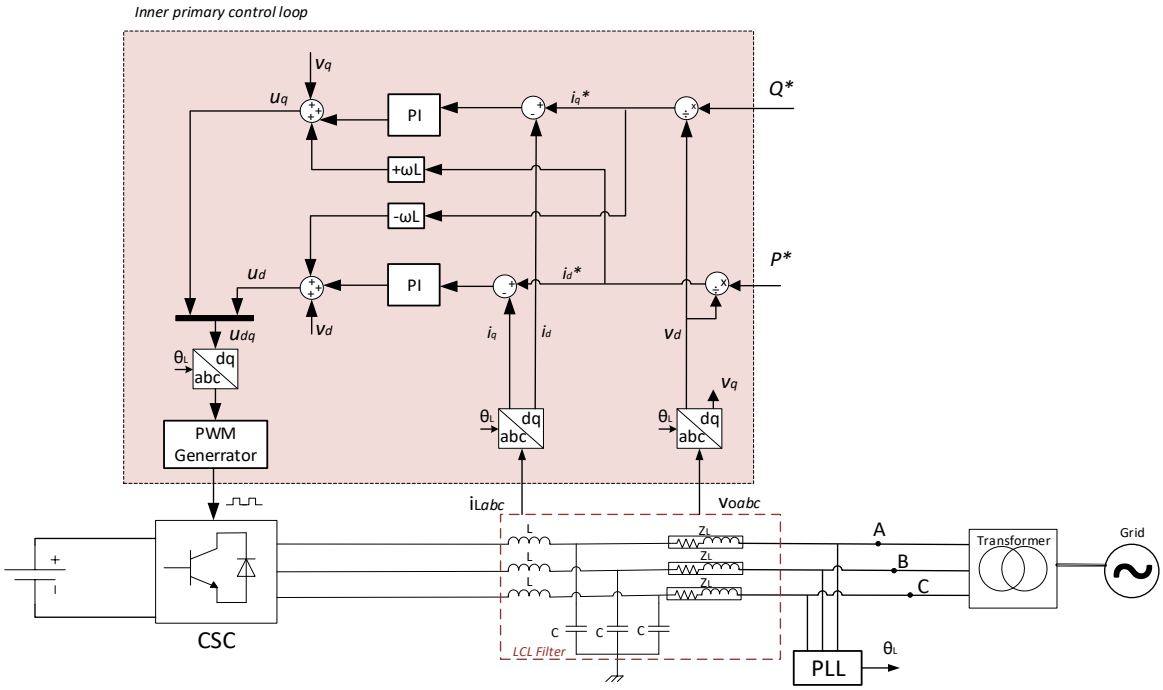

Fig. 1.8: Common inner primary loop in grid-connected mode.

Although the inner loop has been exhaustively studied in the literature [75], [107] to the point that normally the converters have already been equipped with built-in output current and voltage controllers that are predefined by the manufacturer, a great deal of research is still being conducted. The main topics that are still subject to research are improving the robustness against topological uncertainties, enhancing transient response [73], reducing unbalances [138]–[140] and harmonics [104], [103], developing control schemes plans capable of operating in both grid and islanded modes [113] and providing a smooth transition for MG operation modes [141].

Different power converter architectures associated with innovative inner control loops have been also investigated to facilitate the interconnection of RES and batteries into the main grid [138]–[140], [142], [140], [139]. Particularly, in [138], a three-level four-legs Neutral-Point Clumped (NPC) inverter was proposed as a single interface to both a hybrid ESS and RES. This new topology associated with a second-order sliding model controller proved to be more performant than classic PI controllers, especially considering AC-side harmonics, unbalances voltages and power flow accuracy. Voltages and currents unbalance arisen from the connection of monophasic devices, i.e. electric vehicles, batteries and RES, can be reduced by increasing the degree of freedom of classic three-phases power converters, either using four-leg power converters [139] or three-level NPC topology [140], [142], or by combining both [138].

Moreover, alternative methods to generate adequate digital signals for the converter's power transistors have been developed. With the MPC adopted in [143], [144], the limitations of PWM have been overcome since the output of the MPC generates the control of the power switches directly. This novel strategy allows the inclusion of various constraints and multiple objective functions, improving converter flexibility and reliability. Alternatively, PI controllers can also be substituted by proportional-resonant controllers to reduce the harmonic current circulation and improve the transient behaviour of

current control loops [92]. Additionally, robust controls can also be used to improve the transient response and robustness against any minor disturbances in terms of frequency like in [145], [145] that used H-infinity control.

1.5.1.2. Power-sharing control

The power-sharing control aims at assigning the power reference (voltage and current couple) of each DERs connected at the common bus in order to respect the physical constraint of each MG equipment while satisfying the power quality requirement concerning the $v\&f$ regulation. A simple equivalent model of a distributed system of two converters connected in parallel to supply a single charge is represented in Fig. 1.9. Basically, the power-sharing module has to determine the values of the current I_1 and I_2 to satisfy the load demand without overloading any converter. The power-sharing control is classified based on its communication aspect as either master-slave, concentrated, or distributed approaches [146]. The main advantages and disadvantages of each topology are summarised in Table 1.7 based on five relevant criteria.

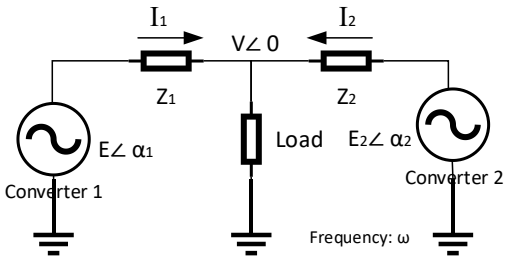

Fig. 1.9: Equivalent model of two inverters connected in parallel to supply a common load.

Table 1.7: Comparison of power-sharing topologies.

Criteria	**Topology**		
	Master-slave	Concentrated	Distributed
Robust against SPOF	✗	✗	✓
Consider constraints	✓	✓	✗
Computational cost (low)	✗	✗	✓
Communication bandwidth (low)	✗	✗	✓
High accuracy & transient response	✓	✓	✗
Reference	[76], [77], [110]	[78], [131]	[23], [70]–[74], [147]

In the master-slave control, also known as communication-based control, the highest capacity DG is usually chosen as master (i.e. operation in VSC) which controls the common bus voltage and handles transient during system disturbances, whereas the slave inverters (i.e. operation in CSC) follow the master to ensure power-sharing. On the other hand, in concentrated power-sharing techniques, the current sharing module measures the total current being consumed by the load (i_{load}) at the PCC and determines throughout a central module the reference current of each DG, typically the average current calculated as i_{load}/N, where N is the total number of DGs connected to the common bus. Finally, distributed control, also called the non-communication-based approach, requires that each DG unit regulates the output voltage and current while sharing active and reactive power. Among these topologies, distributed control based on droop is generally implemented because compared to other

power-sharing strategies, it is more reliable and more flexible since it coordinates parallel-connected inverters of each DG unit based only on local sensed voltage and current at the PCC, and, therefore, it is considered suitable for the BMG environment.

In the droop control method, the active and reactive power flow is controlled by the droop characteristics with the help of local sensed voltage and current at the PCC. However, depending on the dominant characteristic of the line impedance, the relation between active/reactive power and frequency/voltage changes [75], as depicted in Table 1.8, where P_K, Q_K, m_K and n_K are the real active power output, real reactive power output, frequency droop coefficient, and voltage droop coefficient of the Kth inverter, respectively.

Table 1.8: Relation between droop control parameters and line impedance.

$\boldsymbol{Z_0}$	$\boldsymbol{Z = jX}$	$\boldsymbol{Z = R}$
$\boldsymbol{P}$	$P = \frac{EV}{X} sin\alpha$	$P = \frac{EV\ cos\alpha - V^2}{R}$
$\boldsymbol{Q}$	$Q = -\frac{EV\ cos\alpha - V^2}{R}$	$Q = -\frac{EV}{X} sin\alpha$
Droops	$\omega = \omega^* - m_k Q_k$ $E = E^* - n_k P_k$	$\omega = \omega^* + m_k P_k$ $E = E^* + n_k Q_k$

Typically, in grid-connected mode, due to large synchronous generators, the line impedance tends to be inductive dominant. However, in a small and isolated environment, it tends to be predominantly resistive. Therefore, the droop characteristic changes with the line impedance which can bring instability to the power-sharing, that can be overcome by introducing virtual impedances as a feed-forward control loop [25], [72], [103]. Virtual impedance is equivalent to the series impedance of a synchronous generator. Nonetheless, instead of being mainly resistive, virtual impedances can be chosen arbitrary, ensuring the droop characteristics and consequently enhancing the robustness of the system against the line impedance uncertainties. In contrast to real impedance, virtual impedances presents no power losses, and thus it can emulate a real resistance without compromising the efficiency [148].

The main drawbacks of the droop control comprehend its slow transient response, its strong correlation between the output voltage/current and active/reactive power, its low dynamics at the time of disturbances compared to other methods. As highlighted in [75], [146], power-sharing with the conventional droop control always has a trade-off between $v\&f$ regulation and load sharing. This conflict is due to the droop coefficients which determine the active and reactive power references based on the frequency and voltage sensed at the common bus. Variants of the traditional droop control were developed to tackle but not eliminate this trade-off, such as adaptative droop controls [75], [146], [147], robust droop control strategy [74] and online droop parameter determination based on output active and reactive power [71]. Another approach is to add a secondary control layer that changes the set-points of the units using low-bandwidth communication as proposed by [24], [149].

In contrast, communication-based approaches can handle power-sharing and MG $v\&f$ deviation better than droop control strategies. Although the cross-correlation between active/reactive power and frequency/voltage still exists, it is decoupled through the division of converter roles in the case of master-slave strategies and strong data share among the MG units in the concentrated methods. This

enables the primary centralized controller to determine accurate current and voltage references. They also allow embedding complex algorithms to reduce harmonic circulation and unbalance voltage easier than droop control approaches [83], [150]. Nevertheless, they are dependent on high-bandwidth communication links and are prone to SPOF because they contain no system redundancy. Although these methods are more expensive than droop control and sometimes impracticable in large environments, they can ensure power-sharing accurately without needing an additional secondary control layer or adaptative strategies, and thus, can be suitable for BMGs.

1.5.2 *Secondary control layer*

The secondary control is responsible for correcting the voltage and frequency deviations that have not been solved by the primary control. This control layer is also considered as a moderator between the third layer and the primary layer, correcting any power mismatch between the optimization upper reference signals and real MG measurements as stated in [39]. The optimal power references coming from the upper layer are not necessarily compatible with the instantaneous power available in the real system on account of differences in the time scale. As a result, the secondary level tries to follow the upper reference by sending modified power references to DERs to keep the MG reliable and economically efficient while avoiding voltage and current violations [18]. In this context, secondary control can also be formulated as a redundant optimization problem to achieve greater accuracy in the final result [44].

When the secondary control layer is designed to calculate optimal power references toward the primary control, it assumes a partial role of BEMS, which is responsible for sending switch-on or turn-off commands (s_{load} in Fig. 1.5) to each programmable load and set-points for dispatchable DER for the next periods. The BEMS takes its decisions based on its inputs that include the battery SoC, prediction of non-dispatchable generators, weather forecast, DERs maintenance costs, energy price estimations, and operational limits of electrical components. Since the value of signals for load curtailment decisions, the operation state of generator units, and the PV disconnection decisions are discrete variables and reactive and active power outputs of generators and bus voltage magnitudes are continuous variables, the BEMS becomes a complex optimization problem. This kind of problem is normally written as an MINLP that can be simplified into a MILP [151], by using Taylor series first-order expansion and replacing non-linear variables by linear ones. However, other studies considered the energy management problem as a MILP model directly as in [54], [152], and [39]. Further details about the secondary control algorithms are outlined in Section 1.7.

1.5.3 *Tertiary control layer*

Tertiary control layer is the highest and slowest control level in the hierarchical control. It defines the optimal active and reactive power references of each DG, and how much energy and at which price the MG is willing to trade with the electricity market to satisfy the power balance between load consumption and power generation, by considering economical and meteorological prediction data [55]. Like the secondary control layer, it also performs energy management, but in slower time samples on its constraints and objective functions. Although the power dispatch in the secondary layer is more

concentrated on power quality and $v\&f$ regulation, the power dispatch in the tertiary control focuses on BMG economic aspects, highlighting electricity market participation, management of spinning reserves, and ancillary services [153].

To perform the optimal economic power dispatch, the tertiary control layer relies on accurate prediction data. In the literature, there are two different main approaches to estimate them: either by artificial neural network techniques as used in [40] or by autoregressive-moving-average model [8], [45]. However, innovative approaches have been used in MG predictions, such as Grey prediction [92]. It has low computation costs since it combines mathematical RES models [153] with historical data.

Therefore, the tertiary control level is endowed with powerful optimization algorithms, such as those mentioned and discussed in Section 1.7. Moreover, this control layer incorporates thoughtful strategies to deal with the nuances of the electricity market. For that reason, in the following section, a comprehensive definition and survey of the electricity market are detailed.

1.6 Integration of building microgrid into the current electricity market

Aiming at providing a detailed comprehension of how BMGs will be integrated into the current electrical grid, this section explains the traditional European electrical grid and presents possible configurations for connecting BMGs to the existent electricity market. In subsection 1.6.1, the traditional electricity market elements are described, while in subsection 1.6.2, it is outlined the trends for adapting BMGs into the electricity market. Finally, the common strategies for optimization of electricity trading are discussed in subsection 1.7.2.

1.6.1 *Traditional electricity market elements*

The traditional electrical grid is composed of three parts, namely the generation, transmission, and distribution sectors, as illustrated in Fig. 1.10. The generation sector is composed of high capacity power producers, such as gas, nuclear, WT, or PV power plants. Subsequently, the Nominated Electricity Market Operator (NEMO i.e. composed of Wholesale Market and Market Operator), the utility transmission and the retail market embody the transmission sector. Finally, the distribution sector delivers electricity to final consumers. This structure represents not only competition among the generation in the wholesale market but also complete competition among final sales of electricity in the retail market. Retail energy marketers buy and sell electricity from the wholesale market and sell it to residential and small commercial customers, leading the opportunity of small consumers to choose the distribution and transmission utility according to the price and quality of the final energy product [154], [155].

For further information, the papers [4],[156] and [37] explain how MOs determine the marginal clearing prices for Load Service Entities (LSEs), also known as the actors of the retail electricity market. A detailed explanation of the European electricity market is provided in [157].

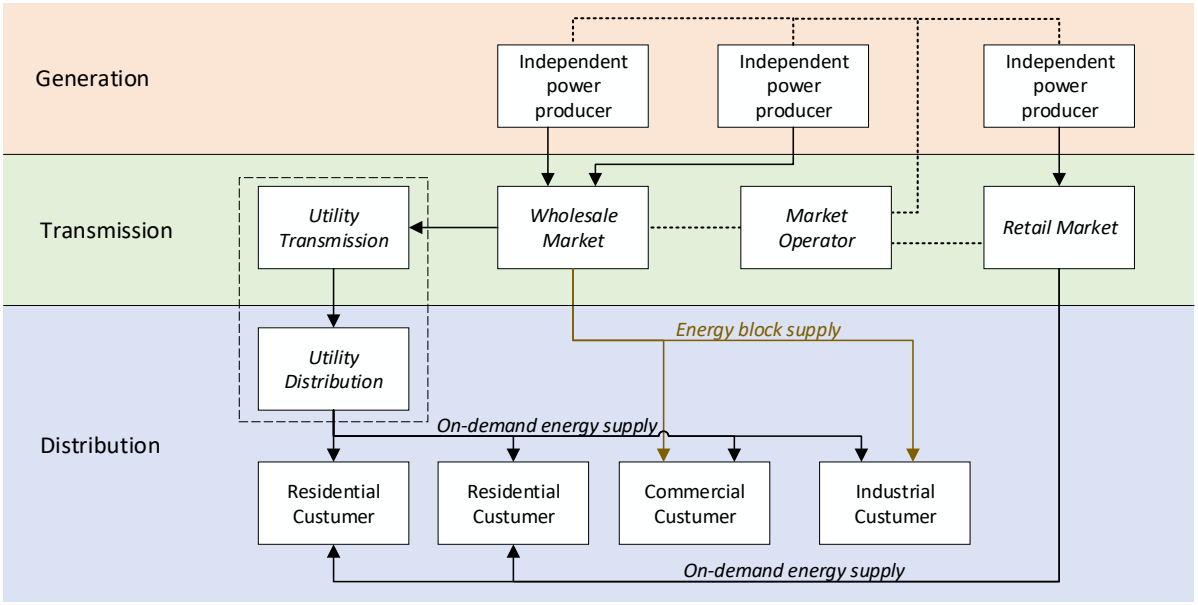

Fig. 1.10: Traditional electricity market scheme.

The electricity market trading involves both the NEMO and the LSE, commonly known as suppliers and customers. In the European grid, the NEMO is a market operator designated by the competent authorities of the European Union Member State to participate in single day-ahead coupling and single intraday coupling [158]. Market Operators are entities that manage energy trade in specific areas. For instance, the spot market in Germany, France, the United Kindom, the Netherlands, Belgium, Austria, Switzerland and Luxembourg are operated by EPEX SPOT. Meanwhile, OMIE manages the spot market on the Iberian Peninsula, and Nord Pool Spot operates in the Nordic countries. Fig. 1.11 details some important market operators and participants in Central Western Europe, Iberian Peninsula and Nordic and Baltic regions [158].

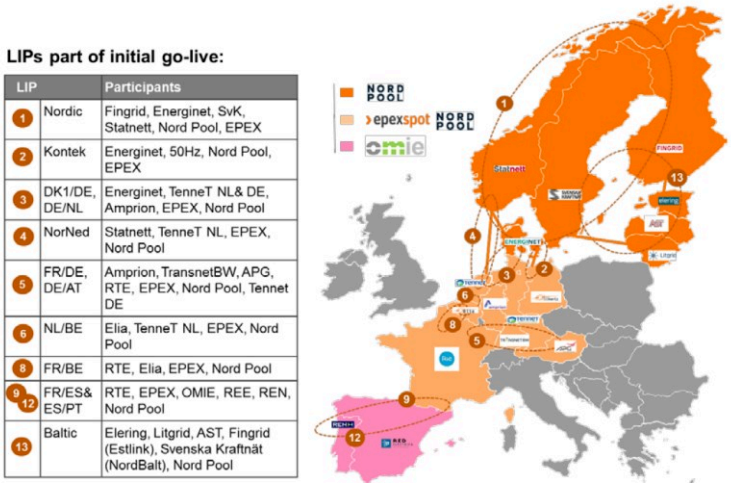

Fig. 1.11: Location and zone of actuation of some market participants in Europe. Figure retrieved from [158]. Obs.: LIPs (Local Implementation Projects).

The main responsibilities of NEMOs comprehend proposing for price coupling and the continuous trading matching through dedicated algorithms. These algorithms define a common set of requirements

for the price coupling and continuous trading matching, in accordance with Art. 37 of Capacity Allocation & Congestion Management (CACM) [159]. NEMOs are also in charge of proposing a harmonized maximum and minimum clearing prices to be applied in all bidding zones [19], [160], [161] which participate in single day-ahead and single intraday couplings in accordance with Art. 41 and Art. 54 of CACM.

Meanwhile, Load Serving Entity (LSE) is the industry term for an electricity company. In means a company or other organization that supplies electricity to a customer. In many cases, it is the same company that distributes electricity too. The objective of the LSE is to obtain the optimal demand bid that ensures the maximum payoff for customers. The LSE controls the output of the storage units/DGs to gain higher profit. The optimal demand bids consist of determining optimal schedules of the commitment and generation of the DGs/storage units owned by the LSEs. Although different market operators exist worldwide, most electricity markets are similar and can roughly be classified into three major markets [153], named daily market [162], intraday market [163] and ancillary service [164] markets.

1.6.1.1. Daily electricity market

Daily market, also called pool market, is in charge to match the whole energy that will be consumed on the following day with the forecast load demand. It handles electricity transactions for the following day through the presentation of 24 h planning for selling and purchasing electricity. To accomplish it, the market operator receives one day before ($D - 1$) the offers of each energy production entity – also called Load Serving Entity (LSE) – specifying the total amount of energy (E_{offer}) with its respective prices (c_{offer}) that are expected to be produced in each programming period (typically 1 hour), as well as the load prediction data. Additionally, the market operator receives supply offers from generator companies (GenCom), that, contrary to LSE, do not have a dedicated load to be supplied.

Afterwards, on the morning of the day D, when the dispatch will take place, the market operator receives the demand bids and possibly supply offers of each LSE as well as supply offers of each GenCom. Gathering all this piece of information from several power producers and generator companies, the market operator decides based on elaborated market clearing software and on determinist algorithms (for instance Euphemia algorithm in Europe) [157] how much energy each entity must produce, taking into account the energy price, number of penalties and the quality of the dispatched energy. The market-clearing software determines the hourly dispatch schedules to minimize the cost of purchasing energy and ancillary services requirement.

Thereafter, the market operator transmits to each power producer the cleared energy with the cleared cost, establishing in this manner a commitment between the MOs and power producers. However, it is noteworthy that in the daily market the electricity trade is only with active power. As a consequence, the reactive power is not considered in this type of market. As further detailed in section 1.6.1.3, reactive power is traded into the ancillary service market, also known as secondary reserve market.

In summary, the electricity day-ahead market operation can be modeled through the definition of three main units: the market operator, the generation companies (or GenCom), and LSE. The interaction amongst these three units can be defined by three main steps [156]:

- ***Step 1: in the day D -1:***

As shown in Fig. 1.12, in the day $D-1$, the forecast load consumption is shared between market operator and LSEs so that the market operator gathers the load prediction data from all LSEs on its responsibility. As a response, the market operator publishes the forecasted zonal load data for that day, which is the predicted power consumption that LSEs can supply. With this information, each LSE determines the estimated local power imbalance and calculates the optimal bid (i.e. price and amount of energy to be traded) for the next day (day D).

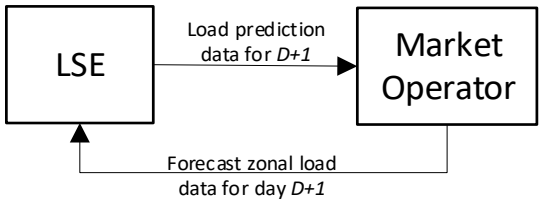

Fig. 1.12: First step of the daily electricity market energy allocation.

- ***Step 2: in the morning of the day D (before gate closes):***

As illustrated in Fig. 1.13, both the LSE and GENCO send their optimal bids to the market operator. Remarkably, the LSE, which detain its load demand, send to market operator the demand bids in case of purchasing energy and supply offers when the LSE generate more energy than consumed. In contrast, the GENCOs present to market operator only their supply offers, because they do not need to supply an internal load, consequently they will never buy electricity from MOs. Once received all the demand and supply bids, the electricity market gate closes, and no more electricity market unit can make proposals in the day-ahead market.



Fig. 1.13:Second step of the daily electricity market energy allocation.

- ***Step 3: before the day D begins:***

Gathering all this piece of information, the market operator will run the market-clearing software and determines the dispatch schedules for each electricity market unit, by building a unit commitment with the MOs – see Fig. 1.14. This commitment is sealed by bilateral contracts [165].



Fig. 1.14: Third step of the daily electricity market energy allocation.

1.6.1.2. Intraday electricity market

Unfortunately, the perfect match between consumption and production is not always satisfied only with the day-ahead market. For this reason, intraday markets are opened all along the day with the intention to solve these discrepancies and ensure a reliable energy dispatch toward the load. As in the

day-ahead electricity market, in the intraday market, the energy producers (i.e. LSE or GENCO) transmit their offers to the market operator. Subsequently, as a response, the market operator cleared the bids by defining the unit commitment and bilateral contracts.

Once the proposal was accepted, by the market operator and a commitment was fixed, the energy producer must fulfil it strictly; otherwise, it will suffer penalties. In front of this scenario, the energy producer has to be wise enough to take into account all these particularities in order to offer an optimal proposal (E_{offer} and c_{offer}) to MOs, avoiding penalties and maximizing its revenue [166]. Intraday markets are an implicit cross-zonal capacity allocation mechanism which collects orders for each bidding zone from wholesale market participants and matches them continuously into contracts to deliver electricity while respecting cross-zonal capacity and allocation constraints [163]. The biggest constraint for trading in intraday markets is that the LSE or GENCO have had traded into the day-ahead market [37], [163], [166]. This restriction is taken place to avoid eventual speculation in the electricity market so that to implicitly regulate the price of energy to the final consumer.

Moreover, the Capacity Allocation and Congestion Management (CACM) imposes another measure to avoid speculation in the electricity market by forcing the intraday energy price to be always higher than the daily market price [159]. In this way, intraday market participation is not economically advantageous, leading power producer to propose to the market operator reliable bids and load power consumption in the day-ahead electricity market. Certainly, with more trustworthy information received from the power producer one day-ahead, market operators can easily regulate the power balance between load and producer.

Table 1.9 shows the type of products offered in the electricity market in different market areas [158]. It is remarkable that hourly products are available in all the market areas, whereas the 15-min product is present only in Germany and Austria. Moreover, 30-min commitment can be made only in France and Germany. Specifically, in the Iberian peninsula, the intraday market is opened six times per day but with schedules of 30-minutes [167].

Table 1.9: Specific product availability in different market areas. Table retrieved from [158].

	German	**Austria**	**France**	**Netherland and Belgium**	**Nordics and Baltics**	**Iberia**
Size	Min vol. Increment 0.1 MW					
Price Tick	EUR 0.1 / 0.01 per MWh					
Price Range	-9 999 €/MWh to 9 999 €/MWh					
15-min	✗	✗				
30-min	✗		✗			
Hourly	✗	✗	✗	✗	✗	✗
User defined blocks	✗	✗	✗	✗	✗	

1.6.1.3. Ancillary services market

The purpose of the ancillary service market, or secondary reserve market, is to maintain the generation-demand balance by correcting deviations to fill the gap between forecasted and actual energy consumption [82], [164]. One of the biggest problems in MG power management is keeping the balance between demand consumption and power generation. Even though intraday markets can mitigate most

of the existent power imbalance, the ancillary services handle the power imbalance issue by increasing or reducing power generation to meet short term fluctuations in the costumers' load. Contrary to the daily and intraday market that trade active power, the ancillary services are those that considered reactive power too. Among all the ancillary services available in the electricity market, spinning reserves, non-spinning reserves, supplemental reserves, automatic generation control and black start units are the most common types.

The spinning reserves usually are the generators that are disconnected from the grid but are already turning at the same frequency and phase as the electric current on the grid so that the connection to the grid can be made at any moment when additional power is needed. On the other hand, non-spinning reserves comprehends generators that are not synchronized to the grid frequency but can run and inject power into the grid within 10 minutes if requested [82], [164].

As mentioned before, for reasons of grid stability, when a MG fault occurs, and the MG control cannot handle it properly to maintain the MG connected, the standard imposes that the MG be disconnected to the main grid and starts operating in islanded mode [107]. Nevertheless, in extreme cases, if the fault lasts and endangers the safe operation of stand-alone MG's electrical devices, all the internal DGs must be shutdown. In this situation, to restart the MG after the grid fault, it must purchase black start ancillary services, which provide the needed power to start the MG generators.

1.6.2 *Trends in the electricity market for building MicroGrids*

According to [10], [166], the structure of the current electricity market is not totally suited to make the investment in renewable energy profitable. Consequently, the electricity market standardization is still being designed and may change over the coming years. Nowadays, many countries have adopted feed-in-tariff policies, in which the risk of the uncertain and competitive electricity market is hedged by long-term contracts to foster RESs development. However, as stated in [166], this is a temporary measure that does not incite major changes to lead RESs worthwhile and to adapt to the current electricity market.

Hence, different branches of research have been conducted to provide the means for BMGs equipped with RESs to participate in the electricity market broadly. One tendency is to consider that smart buildings will be centrally organized throughout a common aggregator, which is responsible for trading electricity with wholesale markets and offer the final electricity price for all its dependent BMGs structured into a so-called MG Community (MGC) [9], [26], [27], [41], [116], [168] as depicted in Fig. 1.15. This structure can reduce the risk of price oscillation for small prosumers and enhance the profit of both consumers and aggregators [168].

It is essential to highlight that MGCs with an aggregator is similar to the current electricity market but with small power capacity. The aggregator of multiple BMGs works as an interface between NEMO and LSE in the traditional electricity market. In the BMG context, NEMO is the unit with which the community aggregator will negotiate electricity purchase or sell, by offering optimal bids. On the other hand, the LSE in the traditional electricity market is analogous of the tertiary control layer in the hierarchical control for BMG, because its role is to determine an optimal schedule to each DG to maintain the MG power balance and maximize the profit.

Basically, prosumers send to the aggregator their forecast load consumption for one day-ahead, as well as their electricity bid (purchase or sell). Thereafter, the aggregator buys (or sells) electricity from the market operator at wholesale market prices and sells to (or purchase from) prosumers in the MGC at retail market prices. The authors of [168] and [88] proposed an algorithm to determine the optimal retail price based on the wholesale electricity price to improve the profit of aggregators without harming prosumers' revenue. In addition to trading electricity with the main grid, MGC allows neighbouring prosumers to exchange electricity among themselves, as studied in [26] and [87], in which the BMG can purchase either from the main utility at wholesale prices or from the MGC at lower retail prices.

Another grid topology is studied in [9], [26], [116], in which it is considered that individual prosumers could use the common infrastructure installed inside the MGC, such as Community ESS (CESS) and Community Controllable Distributed Generator (CCDG) at different prices. The community aggregator interacts with Distributed System Operators (DSOs) to trade electricity and offer some ancillary services to the main grid, that is transmitted to final consumers through a demand-response signal, as studied in [27] and [41]. Depending on the building capacity (e.g. commercial buildings), it can trade in the electricity market directly, without an aggregator, as discussed in [55].

Unlike these structures, [9], [135], [136] made a business plan for the early concept of peer-to-peer electricity trading by evaluating the possibility of direct interaction between market participants without considering a third party's involvement, in other words, without an aggregator, as illustrated in Fig. 1.16. In a more microscopic perspective, authors of [57] structured a framework of individual building interaction with external grids based on the concept of NZEB in which weighting factors are determined to define a unique measure for many types of energy carriers inside a building, coming from PV arrays, batteries, electric vehicles, combined heat power, gas, and hot water.

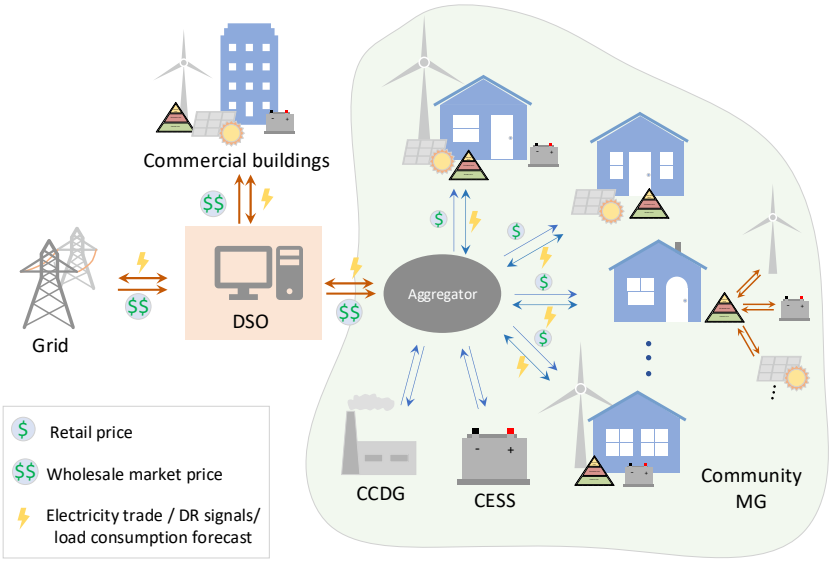

Fig. 1.15: Diagram of the tendency structure of a community microgrid supervised by an aggregator.

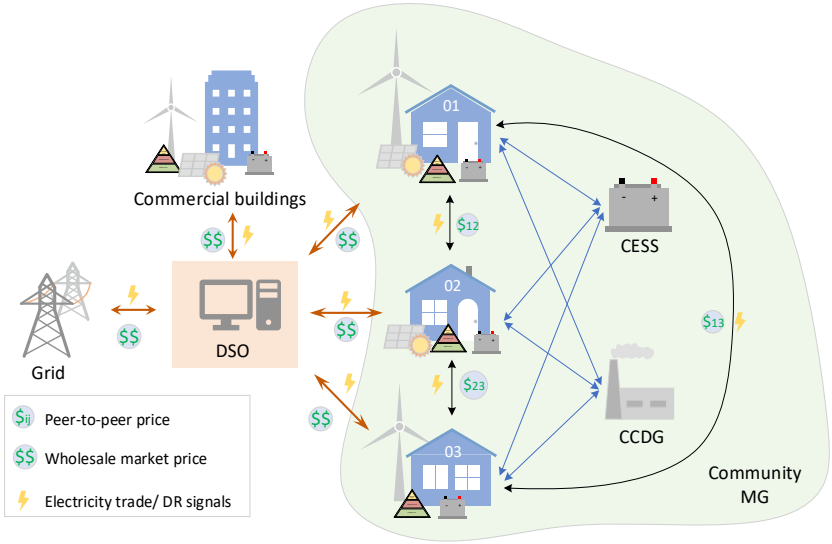

Fig. 1.16: Diagram of the tendency structure of a community microgrid based on the peer-to-peer concept.

1.6.3 *Main strategies to trade on the electricity market*

Concerning BMGs inside a CMG, many studies model the electricity market throughout a fixed electricity price profile with a time step of one hour, like [8], [39], [44], [45], [53], [55], [169]. To optimally trade on the electricity market, centralized tertiary control is envisaged, which considers daily electricity prices and receives the load consumption and power generation to estimate any power imbalance throughout the day to be covered by the electricity market exchanges. One simple and safe way to interact with the electricity market is to achieve a high index of self-consumption by penalizing any electricity trade as adopted in [19], in which no profit is made by selling electricity, since it is sold at a minimum price and purchased at a maximum price. In [169], an MPC controller was designed to formulate optimal bids toward the Spanish electricity market to reduce economic penalties by minimizing the deviation between power production and power committed in the electricity pool. Since the electricity market is a competitive environment in which MOs and local power producers wish to maximize their own revenue, [156] implemented competitive MAS empowered with Q-learning in a complex bus with hourly time-varying load data profile. Contrary to most studies, in [124] the three electricity markets were modelled in a virtual WT power plant, concluding that the MG could make more profit trading with the imbalance settlement and on ancillary services markets than on daily and intraday markets. Another well-clarified approach to participate in the daily and intraday electricity markets is to structure a tertiary cascade level divided into different time scales as proposed in [37], in which the errors introduced by a long prediction horizon were reduced.

1.7 Review of the main energy management algorithms

This section details the main algorithms for $v\&f$ regulation in the secondary control and discusses the main algorithms for power dispatch in both secondary and tertiary control levels. All these algorithms are summarized in Table 1.10, where they were grouped into five different categories:

metaheuristic, deterministic, predictive control, artificial intelligence, and stochastic & robust algorithms.

Table 1.10: Summary of secondary and tertiary control algorithms.

	Control Layer	**Category**	**Algorithm**	**References**
v & f **regulation**	Secondary Control	Deterministic	PI controller	[47], [73], [120]
			Fuzzy Logic	[113], [170], [171]
		Predictive Control	MPC	[109], [172], [173]
Power dispatch	Secondary and Tertiary Control	Metaheuristic	Genetic Algorithm	[18], [38], [53]
			Particle Swarm Optimization	[52], [89], [128], [174], [175]
			Ant Colony Optimization	[44], [176]
			Simulated annealing	[177]–[179]
			Differential evolution	[180]–[182]
		Deterministic	Fuzzy Logic	[40], [43], [130]
			Rule based	[41], [42], [92]
		Predictive Control	MPC	[37], [49]–[51], [117], [183]–[186]
		Artificial intelligence	Reinforcement learning	[88], [187]–[190]
		Stochastic & Robust	Scenario generation	[26], [45], [127], [191], [192]

1.7.1 *Voltage and frequency regulation*

1.7.1.1. Deterministic algorithms

Deterministic algorithms for $v\&f$ regulation are characterized by low computational costs and ease of implementation. In the literature, PI controllers and fuzzy logic are the most common deterministic approaches. For instance, the PI controller is adopted in [47], [73], [120], in which the MG bus voltage is measured, and small $v\&f$ corrective variations are sent back to the primary control to regulate them in the primary control layer.

Concerning fuzzy logic, [113] and [170] proposed a fuzzy-based control capable of determining the small frequency and voltage step corrections to improve the performance of droop control, diminishing any mismatch in the common bus without heavy communication links. Likewise, in [171], voltage control is conceived based on the combination of fuzzy control with gain-scheduling techniques to achieve both power-sharing and energy management. However, the foremost drawback of fuzzy control is that it is too dependent on pre-defined knowledge of the system plant and experimental procedure to design the most suitable membership functions, which may reduce its flexibility and robustness.

1.7.1.2. Predictive control

Model predictive control for $v\&f$ regulation is generally conceived centrally. In [172], a centralized MPC coordinates reactive power and regulates the MG voltage in a critical load bus voltage. Similarly, in [173], a two-level MPC was designed, including a Voltage MPC for autonomous operation to regulate the capacitor voltage of an AC-DC converter and a Power MPC for the grid-connected mode to maintain

the DC bus voltage stable while exchanging reactive power with the main grid. However, not only is centralized MPC envisaged to improve the quality of $v\&f$ but also distributed MPC. In [109], a distributed MPC was implemented in an isolated MG, in which the frequency regulation and economic costs were formulated as a unique objective function.

1.7.2 *Optimal power dispatch*

1.7.2.1. Metaheuristic

Being usually nature-inspired, metaheuristic algorithms are categorised as a pseudo-random approach that apply search space strategies to find an optimal solution for an optimisation problem. These strategies consist of finding a balance between exploitation and exploration, or intensification and diversification. This equilibrium is necessary to reduce the computation cost to identify the region in the search space containing the optimal solutions (diversification or exploration), while avoiding wasting time with regions that have already been explored and do not provide the highest quality solution (intensification or exploitation) [193].

Among metaheuristic approaches, Genetic Algorithm (GA), which is inspired by Darwin's theory of survival of the fittest, is commonly applied to BEMS optimization. It has the advantage that it can escape from local minima, but its complexity increases with the number of parameters. For instance, in [38], minimization of the cost of power generation and maximization of the useful life of lead-acid batteries in a standalone WT-PV-diesel-battery MG system were achieved through the solution of a multi-objective optimization problem using the non-dominated sorting genetic algorithm.

One of the biggest challenges faced by GA is in the mutation and crossover steps that violate constraints. To overcome this, the authors of [18] proposed a priority-based initialization of the GA population and simulated binary crossover strategy with a semi-probabilistic mutation method to reduce the number of constraint violations. Alternatively, still concerning the constraints using GA, some studies used non-linear penalties in the objective function to reduce the complexity of optimization like in [53].

Another metaheuristic optimization algorithm is Particle Swarm Optimisation (PSO). It consists of an evolutionary agent-based technique that simulates the social behaviour of how a swarm moves in search of food. Among the advantages of PSO, fast interaction and convergence, ease of implementation, and few parameters to be tuned can be highlighted. However, PSO can be disadvantageous when the objective function has many dimensions because it tends to fall into local minima due to loss of diversity. To tackle its drawbacks, the traditional PSO, which relies on fixed particle velocity limits, inertia, memory, and cooperation weights, has been replaced by a modified PSO that considers dynamic and diverse velocity to speed up the search process [174].

Evolutionary PSO [175], Adaptive PSO [52] and hybrid-PSO [174] are innovative alternatives to traditional PSO that modify the intrinsic PSO parameters based on mutation, bad experiences and stochastic approaches to improve the diversity of searching process and enhance the likelihood of finding the global minimum. In [89], PSO was designed to determine the day-ahead power flow of a community MG considering battery degradation and it was demonstrated that the algorithm could

reduce the MG operation costs under scenarios with electricity price variations and data forecast inaccuracy.

Similarly, Ant Colony Algorithm (ACA) is based on the behaviour of ants while searching for food. Each ant leaves a pheromone trail on the path from the nest to food. This pheromone evaporates with time so that the other ants can reach the food by following the shortest paths marked with strong pheromone quantities. The study in [176] used ACA to determine optimal power dispatching in an MG while achieving minimum power loss and increment the load balance factor of radial distribution networks with distributed generators. In [44], multi-layer ACA was implemented in a two-stage EMS model aimed at minimizing operating costs for island MG, in which the first layer deals with hourly day-ahead scheduling, whereas the second layer carries out five-minute real-time scheduling.

The ACA can find the global solution if the parameters are well-tuned. Since the pheromone evaporates and ants move pseudo-randomly depending on the amount of pheromone, the ant colony can adapt to noise and changes in the environment thanks to their tracking of pheromone. ACA is characterized by its simplicity because only a few parameters need to be set up to implement ACA, such as the number of ants, pheromone decay, and pheromone update parameters. The biggest disadvantage of ACA is – like most metaheuristic methods – the theoretical convergence time and its probabilistic distribution are uncertain, so the prior analysis is not possible.

Many other metaheuristic algorithms are also used in MG power dispatches, such as Simulated Annealing [177]–[179], Differential Evolution, Gravitational Search [194] and Artificial Bee Colony-based Algorithm [195]. For instance, in [180]–[182], the Differential Evolution approach was used to solve the optimal power flow problem with multiple and competing objectives, like economic and environmental issues.

1.7.2.2. Deterministic

Due to the complexity of power management, fuzzy logic can be an easy but not necessarily optimal solution to the schedule battery charge and discharge according to the weather forecast, electricity prices, and SoC of batteries as proposed by the authors of [40]. Fuzzy logic is also used in thermal comfort because of its simplicity, as in [43], which implemented hierarchical centralized MAS with a user interface to improve the internal comfort of residents using both fuzzy logic and PSO while reducing MG operating costs and minimizing electricity purchases from the main utility. An interesting review on fuzzy logic and its hybrid approaches used in the context of MGs can be found in [196].

Contrary to metaheuristic algorithms, deterministic approaches such as fuzzy-logic and rule-based [41], [42], [92] methods are not considered optimization algorithms [42] because the energy management in these cases is solved based on *a priori* rules or membership functions to choose the best action and estimate the parameters' values, which require a lot of empirical plant knowledge, leading to a complicated design step. However, some studies tried to use metaheuristic algorithms like GA to adjust the fuzzy logic parameters [130].

1.7.2.3. Predictive control

Hierarchical MPC for power dispatch is usually divided into two stages. The upper stage performs the economic MPC that is responsible for computing economic optimization [51], by managing electricity purchases and sales to the power grid, maximize the use of renewable energy sources and control the use of batteries. In contrast, the lower stage, generally implemented as a tracking MPC, is responsible for ensuring MG's stability by trying to follow the optimal references calculated in the upper level while regulating the $v\&f$ [183]. In [49], a two-stage EMS using MPC was implemented in a grid-tied MG, which uses batteries of electric vehicles to ensure MG stability in the first stage and economic dispatch in the second stage.

The difficulty of multilayer MPC is to manage different constraints and calculate the optimal references because, in practice, the optimal reference may be infeasible due to stringent constraints. To avoid this situation, slack variables can be introduced in the constraints or scaling the multiple objectives into priorities so that the constraints of the objective function with the lowest priority are more likely to be violated than important objective functions. Alternatively, in [50], the authors coordinated a modular multiparametric MPC by exploiting the hierarchical levels of all MPC critical regions. This modular MPC for an office BMG was designed to achieve two different objectives. The first objective was to maintain temperature comfort in an energy-optimal way, and the second objective was to maintain the cost-optimal energy balance of the MG.

The weakness of MPC is its dependence on trustful modelling and cost function definition. When dealing with hybrid ESS, the MPC's objective function is usually designed as a multi-objective one, as in [117], [184], [185]. Weights are usually assigned following a priority order with the purpose of reducing, in all circumstances, the total imports and exports of grid energy and prioritizing the use of batteries over the hydrogen chain. This clearly diminishes the generality of the controller and might prevent the MPC to accomplish its objectives if these weights are not well-tuned or under unexpected changes in the plant model. To overcome this problem, weights are usually normalised and converted to the same physical unit, such as the local currency for economic optimisations, as adopted in [37], [186]. To determine balanced weights, the degradation cost of batteries, electrolysis and fuel cell, as well as the electricity price are often integrated

1.7.2.4. Artificial intelligence

A powerful method to handle uncertainties is artificial-intelligence approaches because they can adapt according to disturbances in the environment. reinforcement learning is an artificial-intelligence-based method that has been envisaged for EMS for MGs. Reinforcement learning is a non-supervised learning algorithm that drives the learning based on rewards or penalties evaluated on a sequence of actions taken in response to the environment dynamic. The main interest aspect of this method is that the controller results are improved over time because both the reward function and possible future scenarios are updated based on past experiences.

In [187], Q-learning-based control with scenario construction was used to coordinate battery charging and discharging in a grid-connected MG based on past data. The results demonstrated that over the years, the performance of the MG was improved if new scenarios are no longer revealed. Other

studies also proved that Q-learning could be enlarged in a future horizon, allowing more trustworthy decisions to be taken concerning load consumption and power generation fluctuations, as in [188], where the charging and discharging of batteries in a PV microgrid was decided based on 3-steps-ahead of a Q-learning algorithm using the Markov decision process.

To increase the time horizon without increasing the computational cost burden, distributed and cooperative reinforcement learning with a linear and dynamic approximation of Q values was proposed in [189]. If the horizon is not enlarged because of high computational costs, the actions are discretized and are normally predicted one step before, resulting in oscillating control signals that can be harmful to batteries durability, for instance. To mitigate this problem, fuzzy logic combined with Q-learning functions is used to provide a good approximation of Q-learning functions allowing them to be employed in continuous state-space problems and to smooth the control actions, as used in [190] in which a distributed MG through MAS with reinforcement learning using the fuzzy-Q learning approach was implemented. The potential advantages of this method are that the dynamic and iterative estimation of Q values make the control system model-free and independent of a large amount of previous data because it depends only on the instantaneous reward function and the Q value of the previous iteration.

1.7.2.5. Stochastic

Stochastic algorithms are those that deal with stochastic problems that, by definition, comprise random variables [193]. This category of algorithm strongly depends on the probabilistic structure of the model and usually relies on the expected values and variance of random variables that describe the system. They address optimisation problems that contain uncertain information about the real system and target to take the best action considering many possible scenarios.

In the context of BMGs, the uncertainties in the power generation of renewable sources of energy is a huge obstacle to lead BEMS robust and cost-efficient. In this context, stochastic-optimization-based algorithms can incorporate these uncertainties in the control model, leading to a more efficient control strategy. In [127], two-stage secondary Mixed-Integer Linear Programming (MILP) stochastic programming optimization is proposed to handle the uncertainties of PV and WT generation and regulate the $v\&f$ of an islanded MG. In the first stage, random scenario generations using the Monte-Carlo Simulation and Roulette Wheel Mechanism and scenario reduction by eliminating low probable and similar scenarios were conceived. Afterwards, in the second stage, the optimisation algorithm based on the MILP model is executed based on the probabilistic scenarios in the first stage. Similarly, in [26], the power balance mismatch provoked by the uncertainties on electricity price, electricity load, and RESs power generation were mitigated through a stochastic analysis using the mean-variance Markowitz theory so that multiple scenarios were analysed before performing the optimal power dispatch. The results demonstrated that day-ahead scheduling and real-time dispatch have more energy surplus and fewer shortages when including risk hedging parameters.

In scenario-based stochastic approaches, the computational cost is the main concern, because the system's uncertainties are modelled by calculating many possible scenarios. Moreover, they are based on the expected values of the scenario with the highest probability, which does not guarantee that a contingency out of the considered scenarios may occur. In this perspective, robust approaches usually

consider the worst-case instead of the most likely scenario to calculate optimal unit commitment and power dispatch in MG. Although robust strategies cannot always guarantee the optimal cost, especially in non-contingency scenarios, in comparison to stochastic methods, it can ensure compliance with security levels as long as achieve comparable MG operation cost [191]. In [45], [192], besides generating multiple scenarios through the Mont-Carlo simulation, the conditional value of risk was also considered in the objective function of the economic dispatch to avoid making decisions with a high risk of unprofitably.

1.7.3 *Comparison of the advantages and disadvantages of the main energy management algorithms*

As stated in section 1.7.1 and 1.7.2, there are many strategies to deal with all the challenges concerning BMGs. For the sake of simplicity, the most usual algorithm for each category presented in Table 1.10 was compared in Table 1.11 based on the following five important criteria:

I. Ability to consider predictions.
II. Calculation complexity.
III. Model dependency.
IV. Flexibility concerning MG expansion.
V. Robustness against uncertainties.

Table 1.11: Comparison of building energy management systems algorithms

Category	Algorithm	I	II	III	IV	V
Metaheuristic	Genetic Algorithm	•	••	••	•••	••
Deterministic	Fuzzy Logic	•	•	••••	••	••
Predictive control	MPC	•••••	••	••	•••	••••
Artificial intelligence	Q-learning	•••	•••	•	••••	•••••
Stochastic & Robust	CVar	••	••••	•••	•••	••••

Legend: • very low ••••• very high

As shown in Table 1.10, metaheuristic algorithms tend to have a low model dependency, and low computation cost in the case of minor MG optimization, but it can neither consider predictions nor face uncertainties [18]. Although fuzzy logic and other deterministic algorithms have simple design control step, they are mostly based on empirical system knowledge. Consequently, they are prone to fail when the system changes or unexpected disturbances occur [40].

Meanwhile, MPC has been increasingly adopted in the industry due to its simplicity and robustness against external disturbances and changes in the environment. Since it considers past control variables and plant state predictions to forecast MG behaviour and anticipate control actions and only the first sample is applied to the real plant, even with a basic model, the MPC has demonstrated robust and efficient against small disturbances with slight model inaccuracy [40]. Despite not being well-proven yet, since MPC is dependent on mathematical models, its performance can be reduced if the model changes over the years due to the aging of components or drastic changes in the external environment.

In this context, Q-learning has emerged as a suitable algorithm to adapt and learn from the environment to improve its algorithm automatically. This can reduce the model's dependency and enhance MG flexibility [189]. However, long-term horizons, such as those used in MPC approaches, are unfeasible due to the exponential increase of state variables. Moreover, another potential drawback

of this method is the convergence of time and robustness against drastic changes in the system because the required time to achieve MG efficient point of operation is long or even undetermined in advance. As a result, in the first algorithm iterations, reinforcement learning with the scenario generation approach cannot take optimal decisions because of the lack of past information, unless some past data were used to teach the Q-learning agents how to proceed in each situation. Finally, stochastic algorithms face uncertainties in predictions to hedge risks and increase MG benefits. However, this strategy needs high computational resources because of multiple scenario optimizations [127].

1.8 Barriers and perspectives for building microgrids

BMGs tend to bring more flexibility to the electrical grid, but bulk changes in both occupant behaviour, electricity operation system, and governmental policies are mandatory to boost the future implementation of BMGs. Although many studies were conducted to strive for RES penetration on electricity market throughout BMGs, many concerns must still be addressed to bring BMGs into line with the current electricity market and electrical grid standards, notably:

- dealing with power generation uncertainties
- fostering the plug-in-play aspect of BMG devices
- defining demand-response mechanisms to allow BMGs to respond to grid needs
- defining the rules of energy exchange between BMGs and the external grid

Thanks to technological breakthroughs in communication and IoT devices, real-time data collection has played an important role in dealing with these challenges [118]. Precise data forecasts, scenario generation, and artificial-intelligent models based on historical data are promising techniques for designing a BEMS. Algorithms like MPC, reinforcement learning, and stochastic-based algorithms can handle BMG uncertainties and improve the robustness of a MG system. On the other hand, they are heavily dependent on faithful databases to achieve high performance, which can be a serious disadvantage when considering computation costs. Hence, BMGs will tend to be structured around aggregators capable of supporting them with cloud services that offer high computational resources [119].

The major controversies of data sharing between the community aggregator and buildings are data privacy and data compatibility, which are not yet well-defined. Particularly, broadcasting weather prediction data among buildings in the same community can be promising since it is independent of data ownership. However, other building data types are more sensitive concerning cyberattacks, but it has been overcome by advanced cryptography algorithms [94]. Therefore, it is necessary to define which data will be shared, at which rate, and under which protocol. Otherwise, it will be difficult to design a BEMS capable of being connected to other buildings and capable of adapting to the constraints of the real system.

Another barrier faced by BEMS design is the lack of an accurate definition of automated demand-response programs to allow BMGs to respond continuously to external grid needs. The difficulty of defining demand-response mechanisms is to achieve a harmonic integration between the main grid and BMGs that is beneficial for both sides [94]. For instance, it is not yet standardized how buildings will

be rewarded for offering reactive/active power or for reducing power consumption. This standardization will only be achieved with synchronism between government policies, communication technology, and electricity grid players. However, some designs of future demand-response programs for buildings exist in the literature. The raw electricity price's dissemination among BMGs can entail harmful grid instability, leading to the development of other demand-response variables for improving grid flexibility through DSM, such as load shaping [27][41]. In this context, automatic HVAC controlling and ESS management [79], [197] are promising mechanisms to allow BMGs to be properly rewarded for supporting the external grid.

Furthermore, there is a lack of clear rules concerning the energy exchange between buildings and the external grid. The definition of an architecture capable of synchronizing multiple buildings inside a grid is still under discussion. The trade-off between peer-to-peer and aggregator structures must be clarified. Peer-to-peer configuration can enhance grid flexibility, but its feasibility in prototypes considering its stability, reliability and its limitation concerning communication delay needs to be evaluated. Most business plans for peer-to-peer BMGs architectures are limited to simulations [9], [136], [198]. On the other hand, energy exchange moderated by a community aggregator is more conservative than peer-to-peer configurations because its operation is like the traditional electricity market but with a smaller capacity. Therefore, the experience of traditional electricity markets can be adapted for this new configuration.

Exploiting BMGs concept in the long term, BMGs are key elements for the next energy system step evolution toward smart energy systems [199], also known as the energy internet, in which intelligent sensing and cloud computing will allow different infrastructure sectors to be interconnected to enhance the overall energy system's efficiency. Combining BMGs, district heating, and cooling mechanisms with transportation framework through data sharing and data analysis, the concept of a completely renewable energy system can be envisaged for the near future as concluded in [200]. In [57], [201] proposed a multi-energy market bidding strategy for trading both electricity, natural gas, and heat energy, instead of only active and reactive power. In [199], it was proved that with multi-energy conversion, buildings could be more flexible to the grid's needs by implementing peak shifting through energy conversion. In this way, the BEMS has to manage both electrical and thermal storage to match power generation with power consumption. Therefore, future buildings will be both thermal and electric efficient by relying on advanced BEMS algorithms empowered with strong data processing and multiple power exchanges among neighbouring BMGs.

1.9 Conclusions

Dividing the building microgrid controller into hierarchical levels leads to a more robust system, which can reduce the impact of control delays and disturbances. Each control level holds a specific responsibility, but its design depends on the size of the building, the microgrid operating mode (grid-connected or isolated), the architecture of interconnection of multiple buildings with the external grid, and available computation resources. Depending on all these aspects, the energy management system is devised differently.

This chapter identifies some directives to assist the building controller design considering standards, communication protocols, building architectures, and types of energy management algorithms. Moreover, a comprehensive review of recent studies in hierarchical control for building microgrids is discussed, highlighting the functionalities in each control level as well as the nuances of the electricity market.

Many projections about the future of building microgrids have been created, but concrete frameworks for building architectures inside the grid should be established. Details about interoperability among buildings, the definition of building communication protocols, and the structuration of demand-side management are topics that still opened to research. Based on the literature, there is a tendency for multi-cooperation among buildings inside the same community to achieve high marks of self-consumption. This business model can reduce grid instability and promote the use of renewables. Still, the definition of economic incentives for grid services offered by building microgrids and contractual bids with other electricity market players are under development.

The grid regulation by means of self-consumption supervision can reduce the grid instability inherent to the unpredictable power generation of renewable energy sources. In this context, ESS are key elements for attaining a high portion of internal load matching from renewable energy generated locally and consequently enhance the building energy autonomy indexes. As pointed out in this literature review, the combination of short- and long-term ESS has been envisaged for real BMG implementation to tackle the seasonality of renewable energy source. A battery bank is usually designed to absorb the transients in the power balance, whereas hydrogen ESS is more suitable for smooth peak shaving. However, hybrid ESS increases the complexity of the BMG energy management, which calls for powerful strategies to keep the entire system economic and energetic efficiency.

The review indicates the necessity of designing a more flexible energy management system capable of adapting to different configurations. It is necessary to design a hierarchical controller capable of including new microgrid devices easily and adapting to changes in the environment automatically, without needing to restructure the entire controller with exhaustive tests. In this context, algorithms empowered with data processing, such as artificial-intelligence approaches, are promising for buildings. Moreover, building energy management systems must be capable of handling the stochastic power generation of renewables by considering data forecasts. Algorithms like predictive control and scenario-based strategies have demonstrated their ability to hedge these risks.

In this regard, this thesis contributes to the design of a hierarchical EMS to optimise the power flow of public and residential building microgrids equipped with roof-top PV arrays and hybrid energy storage system, including batteries, hydrogen ESS and electric vehicles. This novel control strategy combines the strengths of MPC and data processing to improve the performance of the controller continuously. The following chapters will detail the proposed hierarchical control with the purpose to make feasible the integration of real building microgrids into the electrical grid.

Chapter 2 Modelling of the building microgrid simulator in MATLAB Simulink

2.1 Introduction

This chapter describes the simulation model designed in MATLAB Simulink® to emulate the behaviour of a BMG primarily supplied by roof-top PV arrays that interacts with a community aggregator. As illustrated in Fig. 2.1, the BMG together with its hierarchical energy management system counts on a hybrid ESS composed of batteries and a hydrogen chain to minimize grid energy imports and exports, and therefore maximize the energy self-consumption. Based on the power consumption and power generation annual profile, the sizing of the BMG electrical piece of equipment was determined by Valorem®, a French company specialized in renewable energy production facilities [202]. The key results of this sizing analysis are reported in Table 2.1.

In addition to the BMG sizing yield from Valorem® analysis, the parking of Plug-in Electric Vehicles (PEVs) can support the BMG needs by discharging them to supply the building demand under the condition to be completed charged within a pre-defined schedule. In the following sections, each electrical component, along with the DC bus and the main grid modelling, will be detailed.

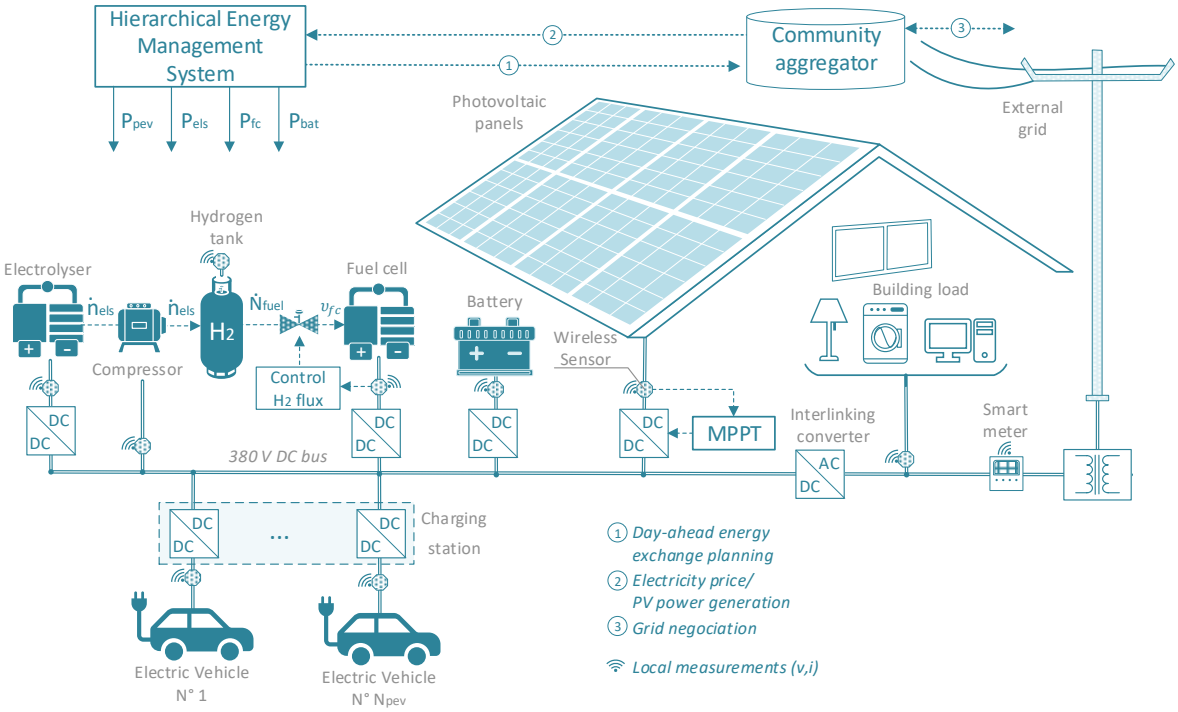

Fig. 2.1: Hierarchical energy management system for optimizing the power flow of a grid-connected building microgrid.

Table 2.1: Sizing of the building microgrid.

Equipment	Description
Photovoltaic panels	Peak power at 1000 W/m^2: 107 kWc
Lithium-ion batteries	Nominal capacity: 167 Ah Nominal Voltage: 720V Nominal discharge current: 70A Maximum power rate: 60 kW
Electric Vehicle parking	Number of vehicles ($\boldsymbol{N_{PEV}}$): 4* Nominal Voltage ($\boldsymbol{v_{nom}^{pev}}$): 400 V Maximum power rate: 7 kW Nominal capacity ($\boldsymbol{Q_{nom}^{pev}}$): 130 Ah
PEM Electrolyser	Nominal power: 25 kW Hydrogen production ($\boldsymbol{\varsigma_{els}}$): 4.18 kWh/Nm^3 Maximum power rate: 30 kW
PEM Fuel cell	Nominal power: 20 kW Hydrogen consumption ($\boldsymbol{\varsigma_{fc}}$): 0.63 Nm^3/kWh Maximum power rate: 48 kW
Hydrogen compressor	Nominal power consumption: 1kW
Hydrogen tank	Maximum pressure: 30 bars @ 80°C Maximum hydrogen mass: 18 kg Volume ($\boldsymbol{V_{tank}}$): 224 Nm^3
Grid	Maximum grid power exchange: 100 kW DC bus voltage: 380 V

* Different number of electric vehicles were also analysed in Chapter 6.

2.2 Modelling of the DC bus and the main grid

Aiming at reducing the simulation time without compromising the accuracy of the power flow analysis of the BMG, the power converters were considered ideal, and the DC bus model was simplified. Given that the focus of this thesis is to propose a hierarchical Building Energy Management System

(BEMS) capable of operating the BMG at minimum cost while satisfying the grid requirements concerning self-consumption, the transitory effects induced by power converters and impedance lines impact the power flow minimally to the point that they can be neglected. This assumption is reasonable because their dynamic is much faster than the sampling time of the BEMS. Power converters are mainly ruled by Pulse-Width Modulation (PWM), which ranges from some microseconds to some milliseconds [203], whereas the input data of the BEMS are usually discretized in one-hour resolution [41], [42][45].

This simplification can be interpreted as an overestimation of the performance of the secondary and primary layers in the hierarchical architecture. In other words, the switching states of the transistors in power converters are assumed instantaneous, and power quality issues are presumed inexistent. This hypothesis assumes that the main grid is strong enough to provide the active and reactive power that the BMG needs to maintain its power balance. Consequently, the voltage and frequency at the PCC and at the internal DC bus are regulated perfectly by the local controllers (i.e. primary and secondary controllers) of the interlinking DC-AC converter, connecting the BMG to the main grid.

With the support of the stiff main grid, the power assigned by the BEMS for the ESSs (i.e. batteries (P'_{bat}), PEVs (P'_{pevs}), fuel-cell stacks (P'_{fc}) and electrolysers (P'_{els}) and ancillary systems (i.e. power consumed by the hydrogen compressor P'_{comp}) are followed by the lower and faster control layers perfectly. On the other hand, the power generated by PVs (P'_{pv}) and building power consumption (P'_{load}) are uncontrolled by the BEMS because they are governed by meteorological conditions and dwellings' behaviour. Finally, the interlinking DC-AC converter is controlled to cover the remaining BMG power imbalance. Consequently, the power exchanged with the grid is a linear combination of P'_{bat}, P'_{pevs}, P'_{fc}, P'_{els} P'_{load} and P'_{comp} as specified in equation (2.1).

$$P_{grid} = P'_{load} - P'_{fc} + P'_{els} - P'_{bat} + P'_{comp} - P'_{pv} - P'_{pevs} \tag{2.1}$$

In this case, the external grid together with the interlinking converter are considered robust enough to supply the power demand of the BMG independently on the rate and intensity required. In this way, the DC bus of the grid-connected BMG was modelled as illustrated in Fig. 2.2.

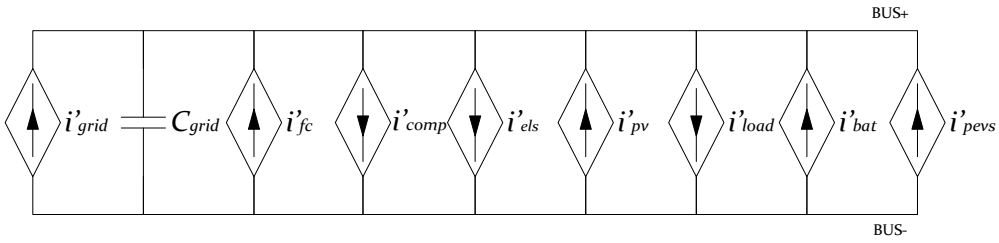

Fig. 2.2: Model of the DC bus.

Each electrical component connected to the DC bus is modelled as a source of current from the grid's point of view. The bus capacitor C_{grid} enables to emulate the DC bus voltage fluctuation. To keep the DC voltage constant, the current flowing through C_{grid} must be zero. Therefore, by balancing the current of loads, PVs, ESSs, and the external grid, the common bus voltage is maintained constant at V_{BUS}. This balancing must respect the Kirchhoff's law, as detailed in equation (2.2).

$$i'_{grid} = i'_{load} - i'_{fc} + i'_{els} - i'_{bat} + i'_{comp} - i'_{pv} - i'_{pevs} \tag{2.2}$$

The PVs and ESSs are interfaced by ideal power converters modelled as shown in Fig. 2.3, whereas the building loads are connected directly to the AC bus through the built-in AC-DC power converter embedded in each building electrical piece of equipment. The dynamics of AC-DC converters of the building loads are also neglected to the point that they are modelled as a single controlled-current source that withdraws from the PCC the current of intensity i'_{load}.

Depending on how the Distributed Generator (DG) (i.e. batteries, fuel cells, electrolysers, electric vehicle batteries and PVs) were modelled, the power converters must be chosen as either a current-controller source (Fig. 2.3a) or a voltage-controlled source (Fig. 2.3b). This is because the power converters must interface the DGs that are modelled either as a current source for non-dispatchable DGs or as voltage sources for dispatchable DGs. Therefore, photovoltaic panels [84] are modelled as a current source, whereas batteries [204], fuel-cell stacks [205], and electrolysers [206], [207] are modelled as voltage sources.

The power consumed or generated on the DG side is reflected in the bus side almost identically. Due to the power loss in the power converters, the power flowing in the DC bus is worth P'_{DG} and is scaled from the original power delivered from the DG (P_{DG}) by a factor named η_{DG}. This factor η_{DG} corresponds to the efficiency of the power converter connecting the DG to the BMG bus. The notation DG refers to all distributed generators connected to the common bus, including PVs and ESSs. Therefore, the subset $DG = \{pv, fc, els, bat, pevs\}$ refers to PV arrays, fuel-cells stacks, electrolysers, batteries, and PEVs, respectively.

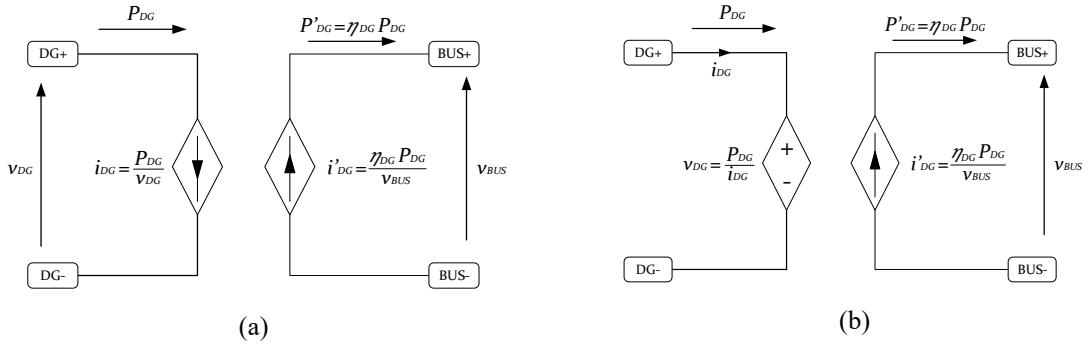

Fig. 2.3: Ideal model of power converters. (a) Current-based model. (b) Voltage-based model

According to [208], the efficiency in power converters ranges from 95% to 99% depending mainly on the ripple current and transistors switching frequency. Therefore, the dynamic of power converters is modelled as a constant in between the range of $0.95 < \eta_{DG} \leq 0.99$. This enables to couple the power in the DG side (P_{DG}) with the power delivered to the bus (P'_{DG}) following the equation (2.3).

$$P'_{DG} = \eta_{DG} \cdot P_{DG} \tag{2.3}$$

From the DG side, the current flowing through the DG (i_{DG}) depends on both their assigned power (P_{DG}), their internal impedance (Z_{DG}) and their internal voltage (v'_{DG}), as illustrated in Fig. 2.4. The output voltage v_{DG} is calculated using the voltage mesh analysis, resulting in the equation (2.4).

$$v_{DG} = v'_{DG} - Z_{DG} \cdot i_{DG} \tag{2.4}$$

The power reference P_{DG} is either directly determined by the BEMS in the case of the ESSs (P_{bat}, P_{fc}, P_{els} and P_{pevs}) or indirectly set up by solar irradiation (P_{pv}). Considering the ESSs (i.e. direct power assignation), the voltage (v'_{DG}) and current (i_{DG}) are defined respecting their operating point defined by P_{DG} and DG's inherent dynamic established by the relationship between v'_{DG} and i_{DG}. On the other hand, the indirect assignation of P_{pv} is defined by the incremental conductance MPPT algorithm [84], in which the voltage v_{pv} is set up to track the maximum PV generated power given the irradiation intensity.

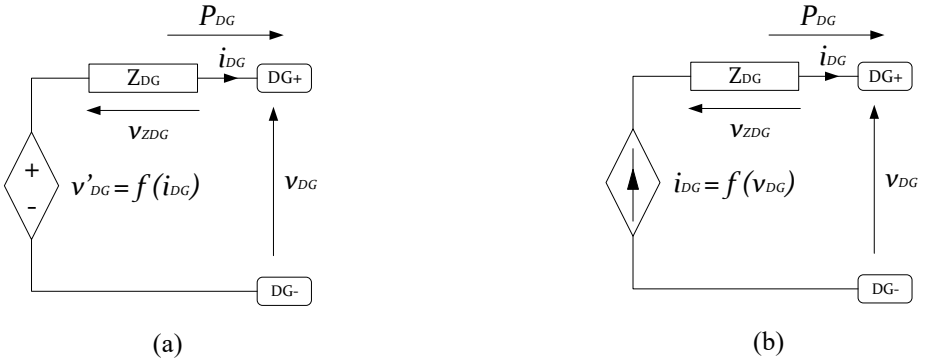

Fig. 2.4: Simplified model of distributed generators. (a) Voltage-controlled source model that is suitable for batteries, electrolysers, and fuel-cell stacks. (b) Current-controlled source model that is suitable for photovoltaic panels.

However, in both the direct and indirect power assignations, the DGs were modelled as either a controlled-voltage source (Fig. 2.4a) or a controlled-current source (Fig. 2.4b). The function f links v'_{DG} to i_{DG} in voltage-controlled sources or i_{DG} to v_{DG} in current-controlled sources, and depends on each type of DG. Notably, a function f depending only on i_{DG} or v_{DG} is a simplified mathematical formulation for simulating the real behaviour of a DG. In more complex formulas, the temperature, the level of degradation, the level of energy storage in ESS, and other external and/or inherent factors can also be considered to improve the accuracy of the model. Some of these elements were investigated through simulations and will be further detailed in following sections.

2.3 Modelling of the PVs power generation and building power consumption

As mentioned in the previous section, the power generated by the PVs and consumed by the building are stochastic variables that are uncontrolled by the EMS directly. In this regard, the PVs power generation and the building power consumption were modelled using a predefined dataset read from Comma-Separated-Variable (CSV) files. Since the objective of the developed BEMS is to attain the required marks of self-consumption independently on the fluctuations in the power imbalance, the fidelity of the generated and consumed power with the real BMG is not critical. The next two subsections further discuss the modelling of PVs power generation and building power consumption.

2.3.1 *Modelling of photovoltaic panels power generation*

The PV arrays were modelled using real profiles of PV power generation for Bidart city, where the future BMG will be placed. However, different geographical areas can be easily considered by following the procedure explained in this subsection. The solar profiles were constructed using solar irradiation and temperature data procured from Joint Research Centre platform for photovoltaic geographical study [209]. Using the latitude and longitude coordinates of Bidart (43.4392° N, 1.5901° W), it was retrieved the one-hour resolution irradiation (I) and temperature (T) profiles of 2016, as shown in Fig. 2.5.

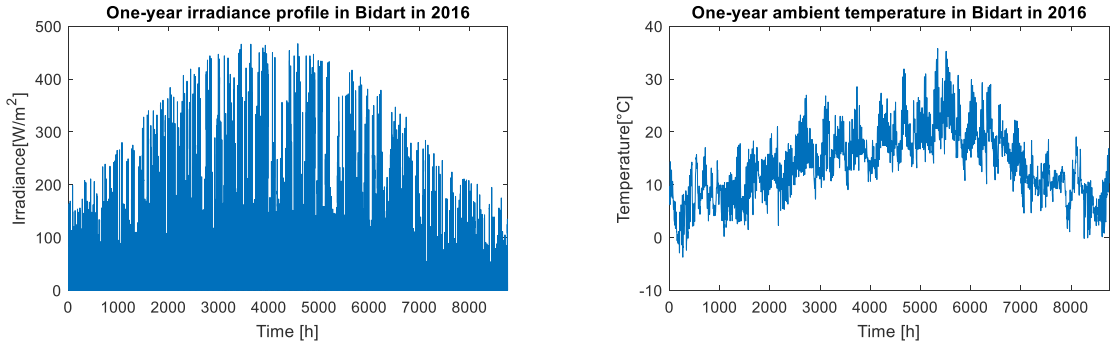

Fig. 2.5: Solar irradiance and ambient temperature in Bidart in 2016, from January to December.

As shown in Fig. 2.6, to determine the corresponding estimated power generated, these meteorological data were set up as input for the PV mathematical model [84] of technical specification shown in Table 2.2. The P-V characteristic of this PV array is shown in Fig. 2.7, in which it is possible to visualise the maximum power delivered by PVs under different intensities of solar irradiation at the ambient temperature of 25°C.

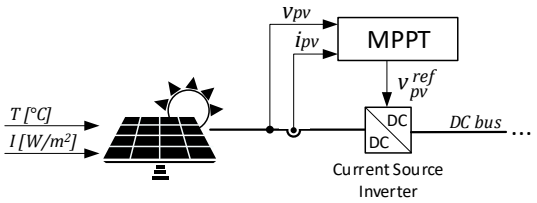

Fig. 2.6: Photovoltaic panel controlled by Maximum Power Point Tracking algorithm.

Table 2.2: Technical specifications of the photovoltaic array.

Parameter	**Value**
Maximum power per cell	75 W
Short circuit current per cell	4.8 V
Open circuit voltage per cell	21.7 V
Number of cells in series	25
Number of cells in parallel	110
Diode Quality factor	1.99

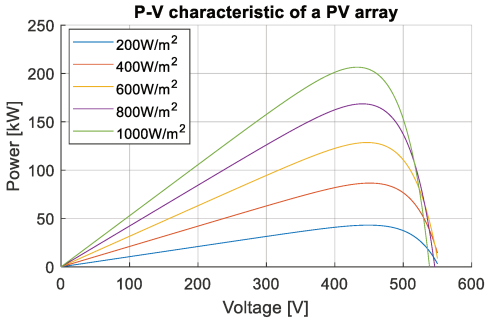

Fig. 2.7: P-V characteristic of the photovoltaic array at 25°C.

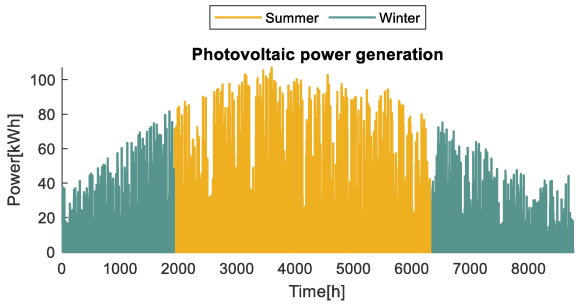

Fig. 2.8: Photovoltaic power generation during an entire year, from January to December.

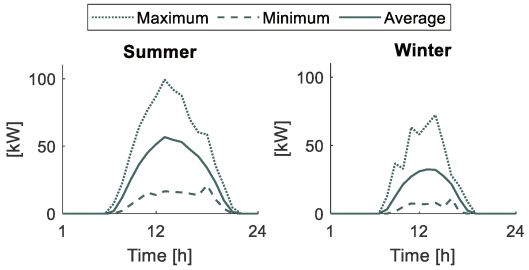

Fig. 2.9: Maximum, minimum and average photovoltaic power generation profiles during summer and winter periods.

As discussed in section 2.2, the PV arrays connects to the DC bus through a power converter modelled as a current source. Driven by an incremental conductance MPPT algorithm [84], the PV panels of sizing specified in Table 2.2 generate the power illustrated in Fig. 2.8, considering the irradiation and temperature profiles of Fig. 2.5. Therefore, the PV panels have a yearly maximum power generation of 107 kW. Additionally, the PV array average generation is up to 50kW during the summer and up to 25kW during the winter, as specified in Fig. 2.9.

2.3.2 *Modelling of building power consumption*

Similar to the PV power generation modelling, the building power consumption was designed using the estimated power consumption of a medium-sized building through a controlled-current source driven by CSV files. Since the objective of this thesis is to conceive a generic BEMS for any type of buildings, the power consumption under study mimics the behaviour of a non-residential (i.e. public) and a residential building. The power consumption profile of a public building was estimated from an existing building of ESTIA Institute of Technology, whereas the data of a typical residential building was scaled from [210]. Remarkably, in both cases, the building demand is about 25% more elevated during the winter than in summer days due to heating devices. Moreover, weekends and holidays were considered for conceiving the non-residential dataset, whereas only weekends were taken into account in the residential one, as shown in Fig. 2.10.

The annual power consumption is conceived by linearly scaling the power profiles of Fig. 2.10 from summer to winter. In this manner, it is obtained the annual profiles depicted in Fig. 2.11 for residential buildings and Fig. 2.12 for public ones. For further details, Table 2.3 provides the annual energy

consumed in both types of buildings and, the average energy consumed during holidays, working days and weekends.

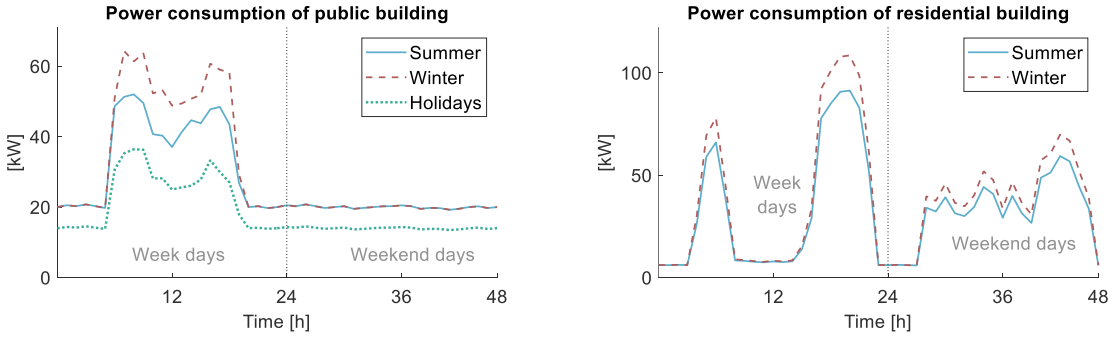

(a) (b)

Fig. 2.10: Daily power consumption profile. (a) Public building. (b) Residential

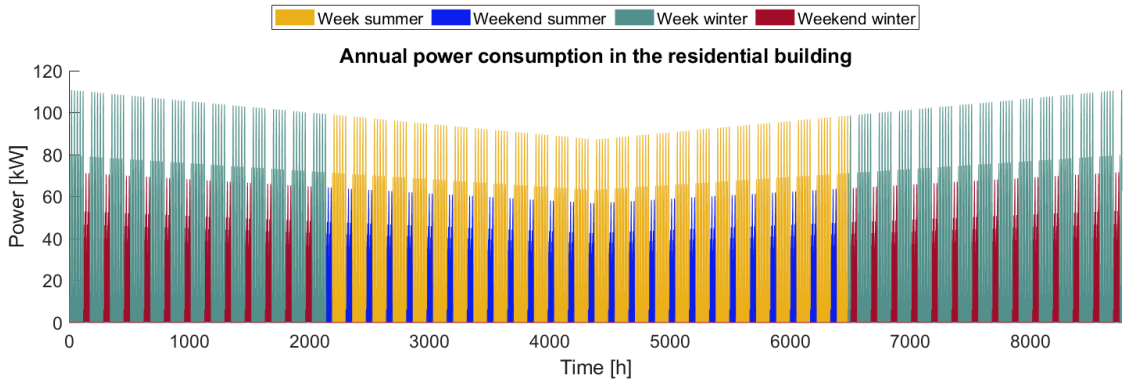

Fig. 2.11: Annual power consumption in the residential building from January to December.

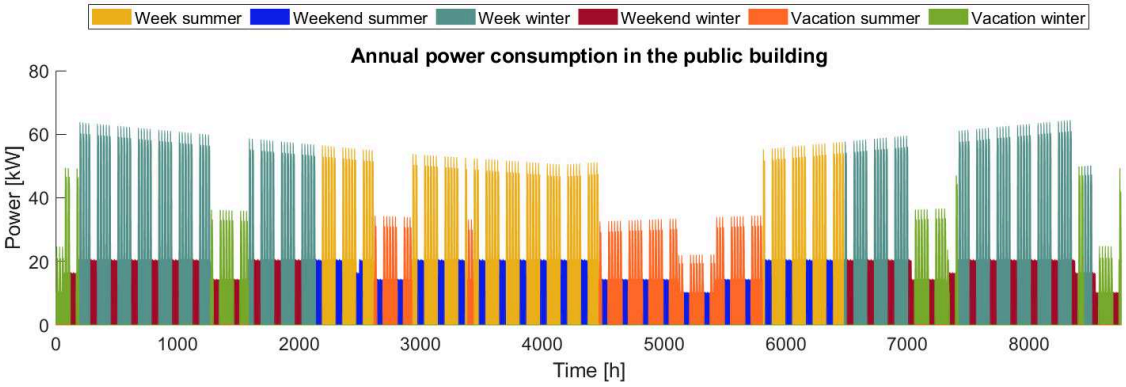

Fig. 2.12: Annual power consumption in the public building from January to December.

Table 2.3: Energy consumption in residential and public buildings categorized into weekend, week and holidays.

		Public building	**Residential building**
Annual energy consumption (MWh)		241.9	307.2
Average energy consumption in summer day* (kWh)	Weekend	59.2	108.1
	Week	179.2	286.9
	Vacation	67.2	–
Average energy consumption in winter day (kWh)**	Weekend	62.02	120.0
	Week	245.3	326.4
	Vacation	49.7	–

*From April to September
**From January to March and from October to December

2.4 Modelling of the day-ahead electricity price

To interconnect the BMG to the main electric grid, the power demand is indirectly controlled through a mechanism of demand response signal coming from the community grid aggregator [9]. Consequently, the ongoing electricity price is sent to the central building controller to reduce the power consumption in peak hours. Therefore, the electricity price from 7 AM to 8 PM is about 30% more expensive than off-peak periods, as shown in Fig. 2.13. In this manner, purchasing electricity is more expensive when most neighbouring BMGs will have a surplus of energy to foster the self-consumption.

In this study, the daily electricity price was determined based on the Enedis® (French distribution operator) tariffs of 2018, and it was considered equal all along the year. Although these tariffs may change in the future, it will not harm the generality of the study conducted in this thesis. Since the objective of including the electricity price in the designed energy management system is to make the controller reacts according to the community aggregator demand-response signals, the exact value of electricity price is not very prominent.

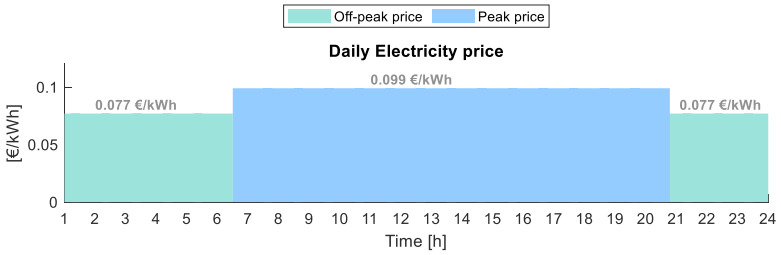

Fig. 2.13: Daily electricity price sent by the community aggregator.

2.5 Modelling of energy storage devices and their ancillary devices

Energy storage devices are dispatchable DGs that are modelled in Simulink® as controlled-voltage sources. The subsections 2.5.1.1, 2.5.1.2 and 2.5.2.1 describe how the built-in Simulink® models were set up to emulate the real behaviour of Lithium-ion batterie pack, Electric Vehicle batteries and fuel-cell stacks. On the other hand, since electrolysers, hydrogen tank and hydrogen compressor Simulink® model do not exist yet, their electrical behaviour was conceived based on mathematical models found in the literature that were validated through experimental results. The developed models are detailed in subsections 2.5.2.2, 2.5.2.3 and 2.5.2.4, respectively.

2.5.1 *Modelling of Lithium-ion batteries*

To emulate in MATLAB Simulink® the real behaviour of Lithium-ion batteries, the built-in Simulink® block *Battery* has been used. This mathematical model was validated through experimental results reported in [204], and it assumes that:

- The internal resistance is constant during the charge and discharge cycles and does not vary with the current amplitude.

- The parameters of the model are derived from discharge characteristics and assumed to be the same for charging.
- The capacity of the battery does not change with the amplitude of the current.
- The self-discharge of the battery is not represented.
- The battery has no memory effect.

Despite these simplifications, this model englobes the main electrical and thermal characteristics for power flow analysis. Therefore, this model was adopted to emulate the behaviour of both the BMG Lithium-ion battery pack and the Plug-in Electric Vehicles (PEV) batteries. The particularity of each of these type of batteries is further detailed in subsections 2.5.1.1 and 2.5.1.2.

2.5.1.1. Building MicroGrid battery pack

To approach as much as possible to real BMG environment, the temperature and ageing effects of the Simulink® block *Battery* were activated. For this reason, the input variable T_a referring to ambient temperature is necessary in this type of model. Although T_a was kept constant (at 25°C) under all the scenarios studied in this thesis, by activating the temperature effects, the cell temperature (T_{cell}) of batteries varies depending on the intensity of current and insulate thermal coupling (thermal capacitance C_{th} and thermal resistance R_{th}). Therefore, T_a can be interpreted as a disturbance in the T_{cell}, which will impact the battery output voltage. The papers [211] and [204] provide a deep understanding of the correlation between the battery output voltage, cell temperature and ambient temperature.

The integral of current (i_t in Ah) is the energy retrieved from batteries along their entire life, and it is calculated using equations (2.5) and (2.6). Following equation (2.6), the term $\Delta i_{t,k}$ is the total batteries charged or discharged energy within the Simulink time sample ($T_s = 60s$). Conversely, the SoC, defined by (2.7), is the percentage of energy stored in the batteries regarding the maximum batteries' capacity (Q).

$$i_{t,k+1} = i_{t,k} + \Delta i_{t,k}\ [Ah] \tag{2.5}$$

$$\Delta i_{t,k} = \int_{k}^{k+T_s} i\ dt\ [Ah] \tag{2.6}$$

$$SoC_{k+1} = 100 \cdot \left(1 - \frac{i_{t,k+1}}{Q}\right)\ [\%] \tag{2.7}$$

Considering the parameter configuration, the Simulink battery model was set up to be in accordance with the BMG sizing defined by Valorem® and reported in Table 2.1. For that, the default parameters of the Simulink Lithium-ion battery model – that is explained in the paper [204] – were modified by scaling them according to the number of cells in parallel (N_{par}) and in series (N_{ser}). Therefore, all voltage parameters are multiplied by N_{ser}, all current parameters are multiplied by N_{par}, all capacity parameters are multiplied by N_{par}, and all resistance parameters are multiplied by N_{ser}/N_{par}. These relationships are summarized in equations (2.8) – (2.11).

$$\text{Voltage parameters [V]: } V_{pack} = V_{bat}^{cell} \cdot N_{ser} \tag{2.8}$$

$$\text{Current parameters [A]: } I_{pack} = I_{bat}^{cell} \cdot N_{par} \tag{2.9}$$

$$\text{Capacity parameters [Ah]: } Q_{pack} = C_{bat}^{cell} \cdot N_{par} \tag{2.10}$$

$$\text{Resistance parameters [Ω]: } R_{pack} = R_{bat}^{cell} \cdot \frac{N_{ser}}{N_{par}} \tag{2.11}$$

The values of N_{ser} and N_{par} depends on the selected cell battery and the desired battery pack sizing defined by its nominal capacity Q_{bat}^{nom} and nominal voltage V_{bat}^{nom}. According to the sizing requirements of Table 2.1, $V_{bat}^{nom} = 720V$ and $Q_{bat} = 167Ah$. Since a single battery cell voltage (V_{bat}^{cell} of the default values of Simulink battery model [204]) is worth 7.2V, and a single battery cell capacity is equal to 5.4Ah, it results in 100 cells in series ($N_{ser} = 100$) and 31 cells in parallel ($N_{par} = 31$). As a result, the four tabs of the Simulink block *Battery* – General parameters, Discharge, Temperature, Ageing tabs – is set up as specified in Table 2.4, which results in the discharge curves in Fig. 2.14. Notably, the current intensities of 6.5A, 13A, 32.5A and 75A were chosen arbitrarily to cover the range of power that the BMG can assign to the battery pack which is up to 60kW as specified in Table 2.1.

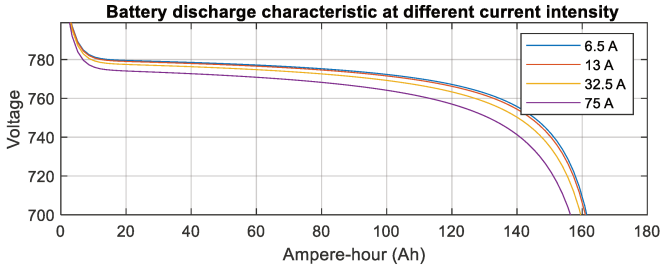

Fig. 2.14: Discharge curve of the building microgrid battery pack at a cell temperature of 20°C and zero cycles (new battery pack) implemented in Simulink. Battery output voltage *vs* integral of current.

Table 2.4: Setup parameters of the building microgrid battery packs, where $N_{ser} = 31$ and $N_{par} = 100$ [204].

Category	Parameter	Value
General parameters	Nominal Voltage (V) @ T_1	7.2· N_{ser}
	Rated capacity (Ah) @ T_1	5.4· N_{par}
	Battery Response time (s)	30
Discharge	Maximum Capacity (Ah) @ T_1	5.4· N_{par}
	Cut-off Voltage (V) @ T_1	5.4· N_{ser}
	Fully charged Voltage (V) @ T_1	8.3807· N_{ser}
	Nominal discharge current (A) @ T_1	2.3478· N_{par}
	Internal Resistance (Ω) @ T_1	0.0133· N_{ser}/N_{par}
	Capacity (Ah) at nominal voltage @ T_1	4.8835· N_{par}
	Exponential zone [Voltage (V), Capacity (Ah)] @ T_1	[7.7788· N_{ser}, 0.2653· N_{par}]
Temperature	Nominal ambient temperature (°C) (T_1)	20
	Second ambient temperature (°C) (T_2)	-30
	Maximum capacity voltage @ T_2	4.8· N_{par}
	Initial discharge voltage (V) @ T_2	7.1· N_{ser}
	Voltage at 90% maximum capacity (V) @ T_2	5.655· N_{ser}
	Exponential zone [Voltage (V), Capacity (Ah)] @ T_2	[6.58· N_{ser}, 1· N_{par}]
	Thermal resistance, cell-to-ambient	0.0019
	Thermal time constant, cell-to-ambient	500000
	Heat loss difference [charge vs. discharge]	0
Ageing	Ageing model sampling time (s)	60
	Ambient temperature (Ta1) (°C)	25
	Capacity at EOL (End Of Life) (Ah) @ Ta1	0.8· 5.4 · N_{par}
	Internal resistance at EOL (Ω) @ Ta1	0.013333·2· N_{ser}/N_{par}
	Charge current (nominal, maximum) [Ic(A), Icmax(A)] @ Ta1	[2.3478, 3]· N_{par}
	Discharge current (nominal, maximum) (Id(A), Idmax(A)) @ Ta1	[2.5, 10]· N_{par}
	Cycle life at 100% DoD, Ic and Id (Cycles) @ Ta1	1500
	Cycle life at 25% DoD, Ic and Id (Cycles) @ Ta1	10500
	Cycle life at 100% DoD, Ic and Idmax (Cycles) @ Ta1	1000
	Cycle life at 100% DoD, Icmax and Id (Cycles) @ Ta1	1400
	Ambient temperature (Ta2) (°C)	45
	Cycle life at 100% DoD, Ic and Id (Cycles) @ Ta2	950

The parameters in *Discharge* tab refers to key voltage-capacity couples that compose the discharge curve at nominal temperature (T_1), which was set up as 20°C. The parameters in *Temperature* tab describe how the cell temperature impacts the cell voltage. The Simulink battery model linearly interpolates two discharge curves at different temperatures (T_1 and T_2) to emulate the voltage variation due to temperature. For this reason, a second discharge curve at a second temperature (typically $T_2 < T_1$) is needed to configure the *Temperature* tab. Since at lower temperatures the batteries' efficiency is lower [212], the voltage parameters of *Temperature* tab must be strict smaller than the parameters of *Discharge* tab.

Finally, the *Ageing* tab contains the parameters that enables to emulate the degradation of batteries over time. The Simulink batteries' degradation is modelled based on the number of charging discharging cycles, its Depth of Discharge (DoD), and cell temperature [213], [214]. The batteries' life reduces faster with deeper DoD and at higher temperatures. Furthermore, the batteries degradation rate is directly correlated to the number of charging-discharging cycles [213]. With the batteries' usage, the maximum batteries' capacity reduces gradually up to attain its End of Life (EoL), which was set up as 80% of the initial maximum capacity [213].

2.5.1.2. Electric vehicle batteries

The PEVs batteries were also modelled using the built-in Simulink® block *Battery* to emulate the batteries of the electric vehicle Zoe of Renault® with technical specification reported in Table 2.1. The setup of the battery Simulink® model is the same as this implemented for the BMG battery pack described in section 2.5.1.1, which resulted in the parameters specified in Table 2.5. It is important to highlight that the PEV batteries consider neither the temperature nor the ageing effects.

Table 2.5: Setup parameters of the plug-in electric vehicle battery packs.

Category	Parameter	Value
General parameters	Nominal Voltage (V)	400
	Rated capacity (Ah)	130
	Battery Response time (s)	30
Discharge	Maximum Capacity (Ah)	130
	Cut-off Voltage (V)	300
	Fully charged Voltage (V)	465.6
	Nominal discharge curves (Ah)	56.5
	Internal Resistance (Ω)	0.030769
	Capacity (Ah) at nominal voltage	117.56
	Exponential zone [Voltage (V), Capacity (Ah)]	[432.2, 6.4]

However, contrary to the BMG battery packs, the PEVs batteries are not connected all the time to the BMG. Their connection to the BMG depends on the PEVs arrival and departure time emulated by switches controlled by a Boolean signal called PEV_{ON}. As illustrated in Fig. 2.15, when PEV_{ON} is one, the PEV battery pack is connected to the DC BMG bus, and it responds to the power references determined by the BEMS (i.e. variable from P_{pev1} to P_{pevN} in Fig. 2.15). On the other hand, when PEV_{ON} is zero, the PEV battery pack is disconnected to the DC BMG bus, and it is discharged/charged up to SoC_{initN}^{ref} by an internal controller named *PEV SoC emulator*.

By means of a proportional controller, the *PEV SoC Emulator* resets the PEV's SoC to SoC_{init}^{refN} to prepare PEV batteries to be reconnected in the next day. The main purpose of this intermediary block is to emulate the arrival of PEVs batteries with different SoC.

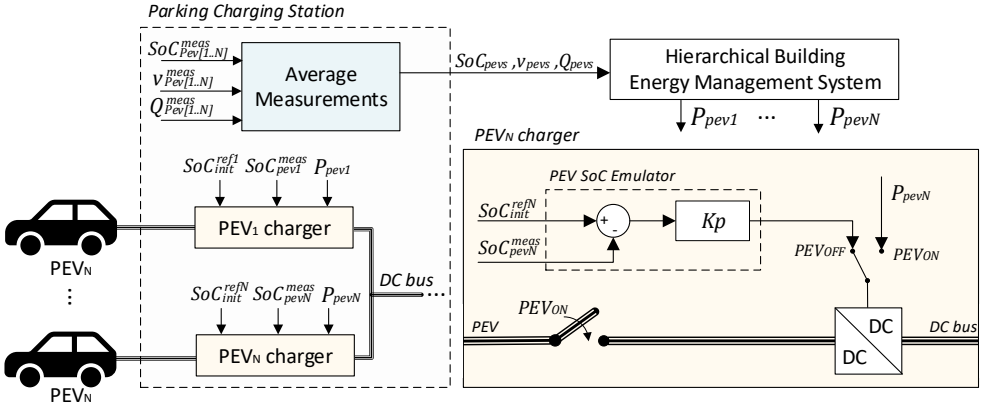

Fig. 2.15: Schematic of the parking of electric vehicles implemented in Simulink.

The graphs of Fig. 2.16 show the PEV batteries SoC evolution during two days of simulation, considering that PEV battery connects to the BMG at 8h with SoC=40% and are charged while

connected. Remarkably, at 18h and 42h the PEV is disconnected (i.e. Connection is OFF) and then the batteries start discharging up to $SoC_{init}^{refN} = 40\%$ in order to reset its SoC for the next connection.

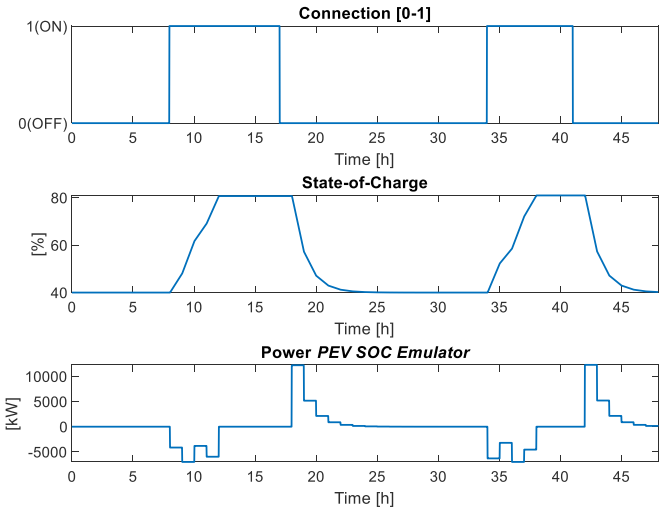

Fig. 2.16: Temporal curves of the plug-in electric vehicle emulator designed in Simulink®.

Remarkably, the *Parking Charging Station* in Fig. 2.15 measures the average status of the PEV parking, by sending to the central hierarchical BEMS the average maximum capacity of all PEVs (Q_{pevs}), the average SoC (SoC_{pevs}) and the average voltage (v_{pevs}). These three average values are calculated following the equations (2.12) – (2.14). Notably, each PEV is identified by an ID number ranging from 1 to N_{PEV}, where N_{PEV} is the number of charging stations installed in the BMG. The term n_k^{pevs} refers to the total number of PEVs that are plugged and available to support the BMG at instant k. Instead of sending the status of each PEV, only the average values are transmitted to the central BEMS to reduce the computation cost of the BMG power flow optimiser. These average status of the PEV parking is necessary because, as further detailed in Chapter 3, from the point of view of the BEMS, the PEV parking is seen as a huge battery of capacity Q_{pevs}, voltage v_{pevs} and state-of-charge SoC_{pevs}.

$$Q_{pevs,k} = \frac{1}{n_k^{pevs}} \sum_{ID=1}^{N_{PEV}} Q_{pev_{ID}} \tag{2.12}$$

$$v_{pevs,k} = \frac{1}{n_k^{pevs}} \sum_{ID=1}^{N_{PEV}} v_{pev_{ID}} \tag{2.13}$$

$$SoC_{pevs,k} = \frac{1}{n_k^{pevs}} \sum_{ID=1}^{N_{PEV}} SoC_{pev_{ID}} \tag{2.14}$$

2.5.2 *Modelling of hydrogen energy storage system*

In recent years, hydrogen-based storage systems have become an important long-term seasonal ESS for enabling the energy transition, on account of its high energy capacity (300 – 1200 Wh/kg) and its nearly to zero self-discharging rate [36], [48]. In particular, despite power fluctuations, Proton Exchange Membrane (PEM) technology for electrolysis and fuel cells can be coupled with RESs, thanks

to its faster response time and lower degradation rate when subjected to intermittent power rate than other technologies [215]. In this regard, the designed hydrogen ESS in Simulink uses PEM technology that follows the sizing of Table 2.1.

The power-to-power hydrogen ESS includes three main parts: hydrogen producer device, hydrogen consumer device, and the hydrogen reservoir, as shown in Fig. 2.1. By means of water electrolysis chemical reaction happening in PEM Electrolyser (PEME) cells, electricity and water are converted into heat, oxygen gas and hydrogen gas, as specified in equations (2.15) – (2.17) [206]. As shown in left scheme of Fig. 2.17, the electrons pass through the electrical circuit attached to the electrolyser, while protons pass through the membrane dividing the anode and cathode. Subsequently, the protons arriving through the PEME membrane at the cathode combine with the electrons arriving through the ancillary electrical circuit, generating hydrogen in the gaseous form.

$$\text{Complete electrolysis chemical reaction: } H_2O \rightarrow H_2 + \frac{1}{2}O_2 \tag{2.15}$$

$$\text{Anode}: \ H_2O \rightarrow 2H^+ + \frac{1}{2}O_2 + 2e^- \tag{2.16}$$

$$\text{Cathode: } 2H^+ + 2e^- \rightarrow H_2 \tag{2.17}$$

The hydrogen produced in the cathode side of the PEME is pushed into the hydrogen tank by using a hydrogen compressor [216]. The compressor adapts the difference of pressure between the PEME cathode and the hydrogen reservoir pressure, enabling the hydrogen to flow inside the tank. The stored hydrogen can be used later to generate electric power according to the BMG needs by regulating the operating pointing of PEM Fuel Cells (PEMFC) and the outlet hydrogen flow.

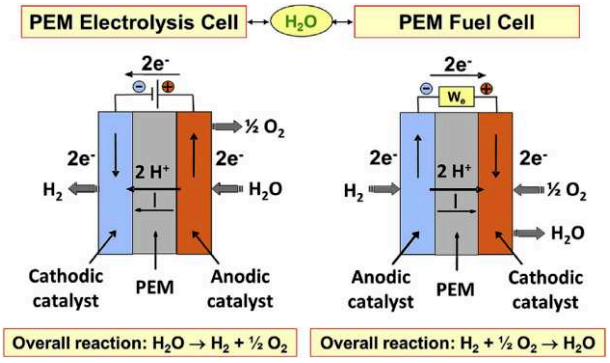

Fig. 2.17: Summary of chemical reaction in cathode and anode sides of Proton Exchange Membrane Electrolysis cell and Proton Exchange Membrane fuel cells. [217].

The PEMFC converts into electricity the chemical energy of the combustion of hydrogen with oxygen, producing water, electricity and heat, as specified in equations (2.18) – (2.20) [206]. As illustrated in the right scheme of Fig. 2.17, the electro-oxidation of the hydrogen happens in the anode side, while the electro-reduction of oxygen in the cathode side. The regulation of the outlet hydrogen throughput is assured by setting up the position of a mechanical valve located in between the tank and the anode of PEMFC, whereas the operating point of PEMFC is assured by controlling its DC-DC power converter. One important remark to assure high PEMFC electrochemical efficiency is that the PEMFC hydrogen utilisation rate (named U_{H_2}) must be regulated to make PEMFC consume all the

hydrogen flowing throughout the cells. In this way, all hydrogen crossing PEMFC is used to generated power, avoiding wasting of resources.

$$\text{Complete combustion chemical reaction: } H_2 + \frac{1}{2}O_2 \rightarrow H_2O \tag{2.18}$$

$$\text{Anode}: \ H_2 \rightarrow 2H^+ + 2e^- \tag{2.19}$$

$$\text{Cathode:} \frac{1}{2}O_2 + 2H^+ + 2e^- \rightarrow H_2O \tag{2.20}$$

The elementary electrochemical behaviour of a power-to-power hydrogen ESS emulated in MATLAB Simulink® is shown in Fig. 2.18. Each of its components will be further detailed in the following subsections.

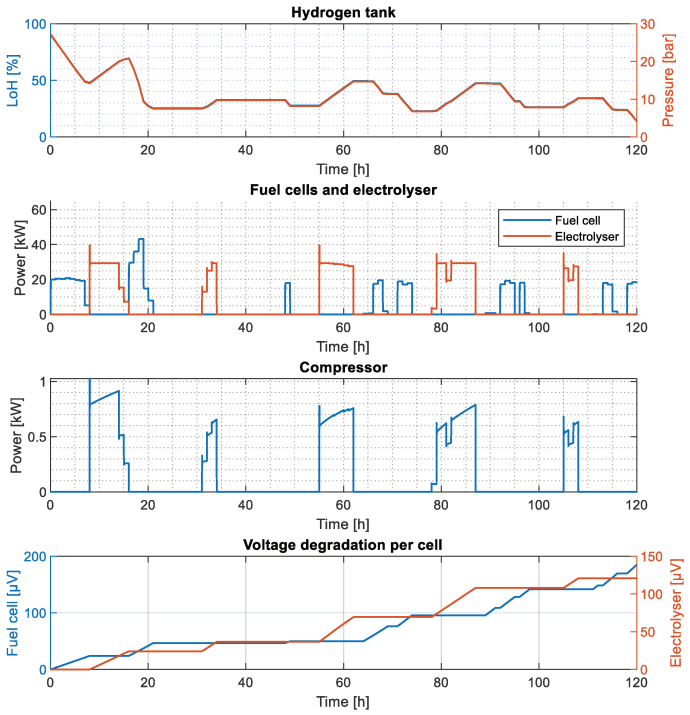

Fig. 2.18: Dynamic of hydrogen tank, electrolysers, fuel cells, compressor and PEM membrane degradation modelled in MATLAB Simulink.

2.5.2.1. Modelling of fuel-cell stacks

The built-in MATLAB Simulink® *Fuel cell Stack* block was used to emulate the real behaviour of a PEMFC of sizing specified in Table 2.1. The setup of its intrinsic parameters follows a similar procedure to configure the inherent parameters of Lithium-ion batteries explained in section 2.5.1. The desired fuel cell sizing of nominal power 20 kW was accomplished by tuning the values of *Fuel cell Stack* pre-set model *PEMFC – 50 kW – 625 Vdc*. This pre-set model was chosen as the basis for the setup of the final model because, among all the Simulink pre-set models, its sizing is the closest one to the desired nominal power and nominal voltage. It is important to highlight that this Simulink pre-set model is based on a predetermined polarization curve and parameters for a particular fuel cell stack found on the market.

The sizing adjustment of a PEMFC consists of stacking multiple PEMFC cells (i.e. N_{cell}) in series [205], as shown in Fig. 2.19. This modularity is the greatest advantage of PEMFC, enabling it to be employed in a different environment and simplifying its maintenance. Therefore, starting from the pre-set *PEMFC -50 kW – 625 Vdc* stack, the number of cells in series was modified to set it up as a 20kW PEMFC.

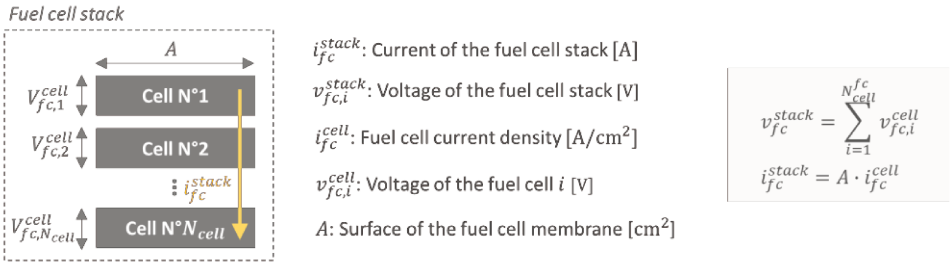

Fig. 2.19: Composition of the Fuel cell stack.

As shown in Fig. 2.19, when concatenating multiple PEMFC cells in series to compose a PEMFC stack, the stack voltage v_{fc}^{stack} is the sum of each cell potential following equation (2.21). Considering that all PEMFC cells are identical, the voltage stack can be approximated to the number of cells times the potential of a single cell, as also shown in (2.21).

$$v_{fc}^{stack} = \sum_{i=1}^{N_{cell}^{fc}} v_{fc,i}^{cell} \cong N_{cell}^{fc} \cdot v_{fc}^{cell} \tag{2.21}$$

On the other hand, the current i_{fc}^{stack} flowing across the cells is dependent on the electrolysis chemical reaction happening in each PEMFC cell. The hydrogen flowing through the cells will combine with oxygen coming from the cathode liberating two electrons that will create the current i_{fc}^{stack}. The Faraday's law of electrolysis in equation (2.22) associates the hydrogen consumption in mol/s with the current traversing the cells, where A is the active area in cm², i_{fc}^{cell} is the current density in A/cm², z is the number of moving electrons ($z = 2$) and F is the Faraday constant in A s/mol ($F = 96485$ As/mol) [205]. Since the PEMFC cells are connected in series, the current flowing is the same in all cells. This leads the hydrogen consumption by the PEMFC stack ($\dot{n}_{H_2cons}^{stack}$) to be proportional to the number of cells in series, as specified in (2.23).

$$\dot{n}_{H_2cons}^{cell} = \frac{A \cdot i_{fc}^{cell}}{z \cdot F} \tag{2.22}$$

$$\dot{n}_{H_2cons}^{stack} = \sum_{i=1}^{N_{cell}^{fc}} \dot{n}_{H_2cons,i}^{cell} = N_{cell}^{fc} \cdot \dot{n}_{H_2cons}^{cell} \tag{2.23}$$

The complexity of the electrolysis chemical reaction is embedded in the PEMFC cell polarization curve of PEMFC specified by the manufacture. This polarization curve links the current density i_{fc}^{cell} (in A/cm²) to the voltage of a single cell (in V). The allure of the PEMFC polarization curve depends on the membrane characteristic, such as width, porosity size and humidification [206], [218]. Moreover, the polarization curve varies according to hydrogen and oxygen concentration in the anode and cathode sides and the cell temperature [206], [218].

The built-in Simulink *Fuel cell Stack* model is based on the polarization curve of the stack, instead of a single cell. Therefore, from the datasheet, the real behaviour of the PEMFC stack can be emulated by fitting the polarization curve of the model to the manufacture's one, by tuning parameters like stack nominal voltage, stack nominal current, stack maximum power rate and the number of cells. To set it up to 20kW while keeping the same electrochemical characteristic of the PEMFC cells of the Simulink pre-set model, these parameters must be set up in harmony to avoid changing the original cell polarization curve.

Therefore, if the number of cells was multiplied by a scalar variable named k_{fc}, all voltage parameters must be multiplied by k_{fc} too. Furthermore, it is needed to assure that each cell of the final model will consume the same quantity of hydrogen per cell of the pre-set model. Therefore, the airflow rate must also be multiplied by k_{fc} to prevent changing the oxygen concentration, and consequently, keeping the same hydrogen consumption rate per cell. On the other hand, all other parameters must be maintained constant.

Since the nominal power of the pre-set model is worth $P_{nom}^{preset} = I_{nom}^{preset} \cdot V_{nom}^{preset} = 50\text{kW}$, the value of k_{fc} can be determined by using equation (2.24), in which P_{fc}^{nom} is the desired nominal power which is equal to 20kW. Therefore, $k_{fc} = \frac{2}{5}$, which leads to the set of parameters specified in Table 2.6. The pre-set and final PEMFC stack characteristic curves are shown in Fig. 2.20.

$$k_{fc} = \frac{P_{fc}^{nom}}{P_{fc}^{preset}} \tag{2.24}$$

Table 2.6: Simulink fuel cell model parameters.

Parameter	**Value**	
	Pre-set model 50kW	**Final model 20kW**
Voltage at 0A*	900V	360V
Voltage at 1A*	895V	358V
Nominal current (I_{fc}^{NOM})	80A	80A
Nominal Voltage*	625V	250V
Maximum current	280A	280A
Maximum voltage*	430V	172V
Number of cells*	900	360
Stack efficiency	55%	55%
Operating temperature	65°C	65°C
Nominal airflow rate*	2100 lpm	840 lpm
Nominal fuel supply pressure	1.5 bar	1.5 bar
Nominal air supply pressure	1.0 bar	1.0 bar
Nominal composition of hydrogen in the fuel flow (x_{H_2})	99.95%	99.95%
Nominal composition of oxygen in the oxidant flow (air)	21%	21%
Nominal composition of water in the oxidant flow (air)	1%	1%

***Parameters that need to be multiplied by $k_{fc} = \frac{2}{5}$ to pass from sizing of 50kW to 20kW.**

The PEMFC model interacts with the hydrogen tank model by sharing the fuel flow rate signal, named v_{fc} as shown in the schematic of Fig. 2.1. All friction loss in the pipe is neglected, making the fuel flow rate traversing the PEMFC equal to the reservoir outlet flow rate. The local controller of

PEMFC regulates both the DC-DC converter and the tank hydrogen valve set points to assure that the PEMFC consumes all the hydrogen crossing the PEMFC cells.

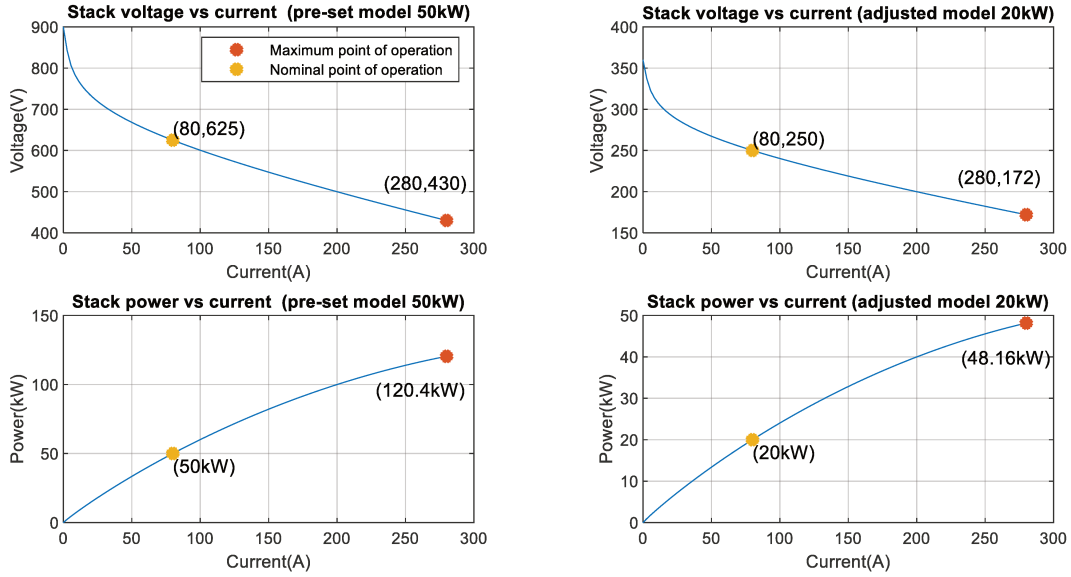

(a) (b)

Fig. 2.20: Fuel cell stack characteristic curves of the pre-set model. (a) Nominal power of 50kW. (b) Nominal power of 20kW.

This set point regulation is assured by the block *H_2 flux control* shown in Fig. 2.1. The *H_2 flux control* measures the current flowing across the PEMFC and determines the output fuel flow rate ($\dot{N}_{fuel}$ in l/min) for the hydrogen tank valve. In the developed Simulink model, the valve dynamic was also neglected, making the $\dot{N}_{fuel}$ determined by *H2 flux controller* equal to the hydrogen flowing through the PEMFC (υ_{fc}).

The block *H2 flux control* controls the hydrogen flow by implementing the equation (2.25), which calculates the value of $\dot{N}_{fuel} = \upsilon_{fc}$ that makes the hydrogen utilization U_{H_2} equal to 100%. Notably, R is the ideal gas constant, T_{fc} is the PEMFC temperature, F is the Faraday constant, x_{H_2} is the nominal composition of hydrogen in the fuel flow, and P_f is the nominal fuel supply pressure. All these variables are in the SI system (International System of Units). The full reasoning for deducting (2.25) is described in Appendix I on page 235.

$$\dot{N}_{fuel} = \frac{60000 \cdot R \cdot T_{fc} \cdot N_{cell} \cdot i_{fc}^{stack}}{2 \cdot F \cdot x_{H_2} \cdot P_f} \; [l/min] \tag{2.25}$$

Since one of the objectives of this thesis is to analyse the advantages and disadvantages of installing hydrogen ESS in BMGs considering both the economic and energy aspects, the built-in Simulink *Fuel Cell Stack* block was enhanced by adding a module called *Fuel Cell Degradation per Cell* for emulating the PEMFC loss of efficiency due to cell degradation. This module, shown in Fig. 2.21, permits to emulate the PEMFC degradation rate that is essential to assess their operating cost based on their End of Life (EoL).

The degradation of hydrogen ESS can be estimated from experimental curves provided by the manufactures, in which the voltage offset is used for assessing the EoL of PEMFC and PEME [215]. Generally, fuel cells and electrolysers must be replaced when they lost 10% of their efficiency, representing 10% of voltage offset for the same operation condition [219]. According to [220], the degradation rate in electrolysers and fuel cells is around $3\,\frac{\mu V}{h}$ per each cell at nominal operation.

Since fuel cells Simulink® model does not consider the voltage degradation, this phenomenon was modelled based on [215], in which the voltage drop is more intense when operating them for long periods and with a density of current above 1 A/cm^2. However, the current density in A/cm^2 is unknown in the built-in Simulink *Fuel Cell Stack* model because the active area is not considered in the model. In front of this problem, instead of modelling the cell degradation based on the current density, it was considered the normalized PEMFC called i_{fc}^{norm} calculated as in (2.26), where I_{fc}^{NOM} is the PEMFC nominal current. This assumption is realistically because a density of current of 1A/cm^2 usually corresponds to the nominal operation of PEMFC.

$$i_{fc}^{norm} = \frac{i_{fc}}{I_{fc}^{NOM}} \tag{2.26}$$

As a result, the modified Simulink *Fuel Cell Stack* internal model for emulating the PEMFC voltage degradation is shown in Fig. 2.21. It receives as input the fuel cell current i_{fc} and calculates Δv_{fc}^{cell} corresponding to the voltage offset per cell of the original PEMFC cell voltage $v_{fc}^{cell,original}$. Therefore, depending on the number of cells of the PEMFC stack (N_{cell}^{fc}), the output voltage v_{fc} can be calculated. The PEMFC degradation cell reduces gradually the efficiency of hydrogen combustion, which means that for the same delivered electric power, the hydrogen consumption will be more elevated. According to equation (2.22), the hydrogen consumption per cell depends on the PEMFC current (i_{fc}). Therefore, the voltage offset Δv_{fc} must reduce $v_{fc}^{cell,original}$ to mimic this loss of efficiency, following the equation (2.27).

$$v_{fc} = N_{cell}^{fc} \cdot \left(v_{fc}^{cell,original} - \Delta v_{fc}^{cell}\right) \tag{2.27}$$

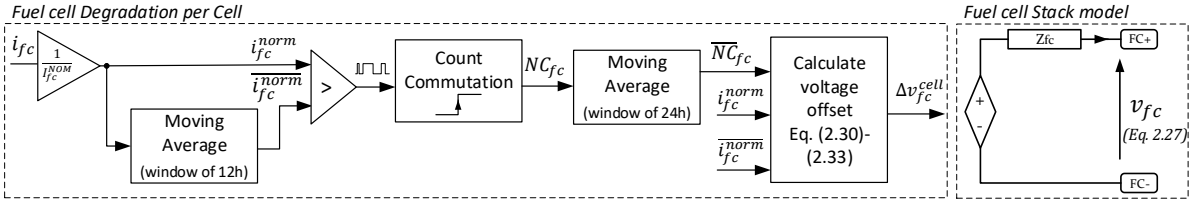

Fig. 2.21: Schematic of the modified built-in *Fuel cell Stack* Simulink model to emulate the fuel cell degradation.

Based on the results of [215] that is reported in Table 2.7, the degradation rate depends on the mode of operation of PEMFC. Notably, long breaks of 6 hours (mode D) led to almost full recovery of cells degradation, while continuous operation at high density of current (mode B) resulted in fast pace of degradation. Furthermore, long cycling intervals of 6 h (mode D) resulted in less degradation than shorter cycling intervals of 10 min (mode E). Therefore, aiming to emulate similar behaviour, the block

Fuel Cell Degradation per Cell was designed. This block calculates the voltage degradation per cell (Δv_{fc}^{cell}) based on:

- the average value of the i_{fc}^{norm} ($\overline{i_{fc}^{norm}}$),
- the average value of the number of PEMFC current density oscillation ($\overline{NC_{fc}}$).

Table 2.7: Comparison of the observed degradation in the durability test of 1000 hours reported in [215] and the designed model in Simulink.

Mode of operation	**Voltage degradation rate (mV)**	
	Experimental results of paper [215]	Designed model in Simulink
A: Constant power rate (1 A/cm2)	0	3
B: Constant power rate (2 A/cm2)	196	200
C: Dynamic power rate (2 ↔1 A/cm2) 6 hour each	66	77
D: Dynamic power rate (2 ↔0 A/cm2) 6 hour each	16	9
E: Dynamic power rate (2 ↔0 A/cm2) 10 min each	50	63

Remarkably, $\overline{i_{fc}^{norm}}$ was calculated using the moving average formula (2.28) over a sliding window of 12 hours, corresponding to $N_{s1} = \frac{12 \cdot 3600}{T_s}$ samples, where $T_s = 60s$ is the sampling time of the discrete Simulink simulation. Similarly, $\overline{NC_{fc}}$ was calculated using the moving average of equation (2.29) within a sliding window of 24 hours, corresponding to $N_{s2} = \frac{24 \cdot 3600}{T_s}$ samples.

$$\overline{i_{fc,k}^{norm}} = \frac{1}{N_{s1}} \cdot \sum_{i=k-N_s}^{k} i_{fc,i}^{norm} \tag{2.28}$$

$$\overline{NC_{fc,k}} = \frac{1}{N_{s2}} \cdot \sum_{i=k-N_s}^{k} NC_{fc,i} \tag{2.29}$$

The number of oscillation in the current density (NC_{fc}) is calculated by counting the number of times that i_{fc}^{norm} crossed $\overline{i_{fc}^{norm}}$ (rising edge) within a window of 24 hours – see Fig. 2.21 and Fig. 2.22. This counting algorithm is implemented through a function named *Count Commutation* illustrated in Fig. 2.21. Subsequently, by using $\overline{NC_{fc}}$, $\overline{i_{fc}^{norm}}$, and i_{fc}^{norm} the voltage offset per cell Δv_{fc}^{cell} is calculated using equations (2.30) – (2.33). Notably, Δv_{fc}^{cell} is divided into three main components, called v_1, v_2 and v_3, corresponding respectively to:

- the constant voltage degradation (v_1)
- the voltage degradation due to intensity of current density (v_2)
- the voltage degradation due to the frequency of commutation (v_3)

In this manner, the voltage offset per cell Δv_{fc}^{cell} at instant k is calculated by adding the degradation of each of these components (v_1, v_2 and v_3) if the current flowing through the PEMFC is nonzero, following equations (2.30) – (2.33). The values of the constant variables a_0, a_1, a_2, a_3, a_4 and a_5 were tuned by trial and error to approach Δv_{fc}^{cell} to the experimental results of Table 2.7, obtaining the values shown Table 2.8. The evolution in time of $\overline{i_{fc}^{norm}}$, i_{fc}^{norm}, $\overline{NC_{fc}}$, NC_{fc} and Δv_{fc}^{cell} under the five operation

modes (A to E) are shown in Fig. 2.22. Comparing the results after 1000 hours of simulation (Table 2.7), the degradation rate is close to the experimental results of [215].

Table 2.8: Parameters of the Fuel Cell Degradation per Cell model.

a_0	a_1	a_2	a_3	a_4	a_5
$\frac{T_s \cdot 3e-6}{3600}$	$\frac{T_s \cdot 55e-6}{3600}$	$\frac{T_s \cdot 85e-6}{3600}$	$\frac{T_s \cdot 60e-6}{3600}$	$\frac{T_s \cdot 3.2e-6}{3600}$	$\frac{T_s \cdot 15e-6}{3600}$

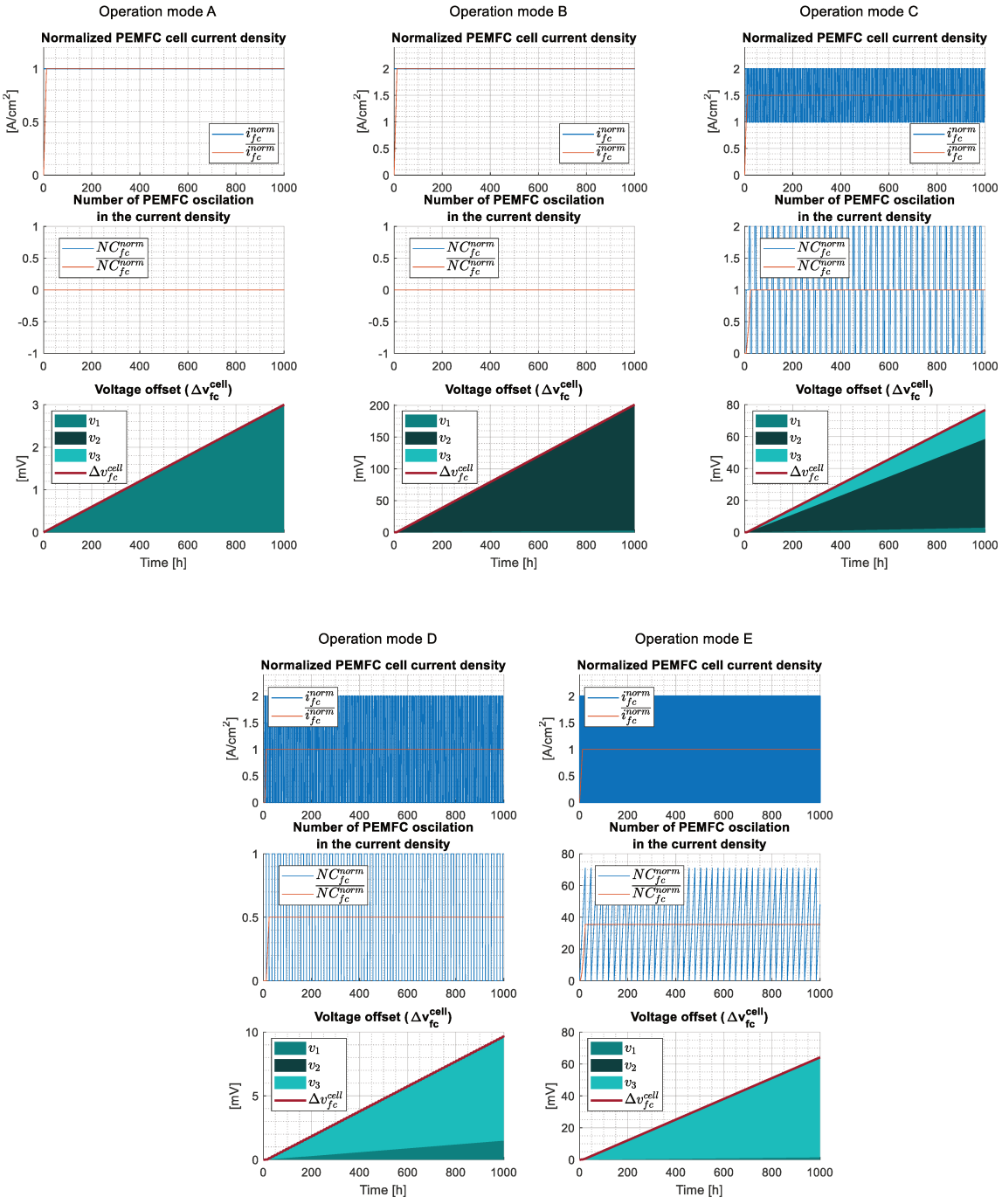

Fig. 2.22: Voltage offset of PEMFC under different operation modes.

$$\Delta v_{fc,k}^{cell} = v_{1,k} + v_{2,k} + v_{3,k} \tag{2.30}$$

$$v_{1,k} = \begin{cases} v_{1,k-1} + a_0, & if\ i_{fc}^{norm} \neq 0 \\ v_{1,k}, & otherwise \end{cases} \tag{2.31}$$

$$v_{2,k} = \begin{cases} v_{2,k} + a_1 \cdot \left(\overline{i_{fc}^{norm}} - 1\right) + a_2 \cdot \left(\overline{i_{fc}^{norm}} - 1\right)^2 + a_3 \cdot \left(\overline{i_{fc}^{norm}} - 1\right)^3, if\ i_{fc}^{norm} > 1 \\ v_{2,k}, \quad otherwise \end{cases} \tag{2.32}$$

$$v_{3,k} = \begin{cases} v_{3,k} + a_4 \cdot \overline{NC_{fc,k}} + a_5, & if\ i_{fc}^{norm} \neq 0 \\ v_{3,k}, & otherwise \end{cases} \tag{2.33}$$

In Fig. 2.22, it is possible to observe that low (below or equal to 1 A/cm^2) and constant current density, like in the operation mode A, the voltage offset is low and equal to 3 µV/h. At low density current, there is only the constant degradation rate of fuel cells, corresponding to the offset voltage component v_1. When the current density is elevated (2 A/cm^2), corresponding to the operating mode B, the degradation rate increases to 200 µV/h mostly due to the intensity of current density or the voltage component v_2.

Conversely, oscillating operation of PEMFC with current intensity above 1 A/cm^2, like the operation mode C, leads the degradation rate to decrease to around 77 µV/h. On the other hand, the slow commutation between idle and non-idle mode, as in the operation mode D, the degradation rate dropped to 9 µV/h .This is because long breaks in the operation of PEMFC enables the membrane to recovery, which as consequence reduces the degradation rate. However, fast commutations between idle and non-idle modes increases the degradation rate from 9 µV/h to 63 µV/h. Therefore, according to [215], to extend the lifetime of PEMFC, it is recommended its intermittent operation, rather than continuous operation. This result demonstrates that PEMFC is an adequate technology to be coupled with fluctuating renewable energy.

2.5.2.2. Modelling of electrolysers

Since the electrolyser model in MATLAB Simulink does not exist yet, a simplified model of the PEME was designed based on [207]. The simplified Simulink model uses a lookup table with the polarization curve of a PEME cell, correlating v_{els}^{cell} to i_{els}^{cell} at five different temperatures, namely 40°C, 50°C, 60°C, 70°C and 80°C. These curves was replicated from [207] to Fig. 2.23, in which the polarization curve of the PEME was based on experimental tests.

Similar to PEMFC, PEME sizing can be adjusted by stacking multiple PEME stacks up to arrive to the desire rate power. Therefore, the voltage of PEME stack is the sum of all PEME cell potential, as defined in (2.34). Since the cells are stacked in series, the current consumed by all PEME cells are the same and it is dependent on the current density (in A/cm^2) and the active area A (in cm^2), as defined in (2.35). The excitation of PEME stacks by electricity triggers the electrolysis chemical reaction that generate hydrogen as final product. The hydrogen production rate in mol/s follows the Faraday's law of electrolysis in (2.36).

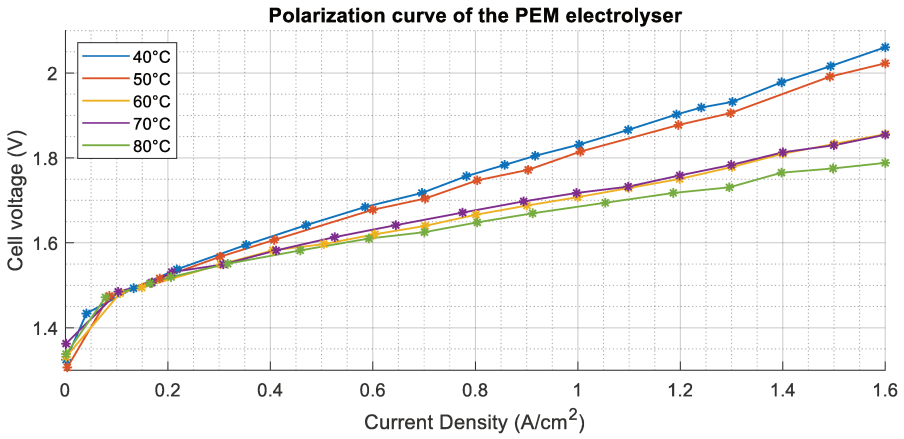

Fig. 2.23: Polarization curve of the electrolysers cell based on [207].

To increase the efficiency of PEME, it is more advantageous to have a high hydrogen production per cell for small current consumption. Knowing that the total cell current consumption is calculated by multiplying the current density (in A) times the active area A (in A/cm^2), as defined in (2.35) and following the Faraday's law of electrolysis in (2.36), the active area in PEME must be large and the number of cells as small as possible. Controversially, in PEMFC, it is convenient to have a small active area to reduce hydrogen consumption and many PEMFC cells to increase the stack voltage potential.

$$\boldsymbol{v_{els}^{stack} = \sum_{i=1}^{N_{cell}^{els}} v_{els,i}^{cell} \cong N_{cell}^{els} \cdot v_{els}^{cell}} \quad \textbf{(2.34)}$$

$$I_{els} = A \cdot i_{els}^{cell} \quad (2.35)$$

$$\dot{n}_{els}^{(ideal)} = \frac{N_{cell}^{els} \cdot A \cdot i_{els}^{cell}}{2F} \quad (2.36)$$

Remarkably, Faraday's law of electrolysis in (2.36) is the ideal hydrogen production in gaseous form that is mixed with water and oxygen. The process of dryer and deoxidizer introduce additional losses which are mathematically compensate by multiplying the ideal Faraday's equation by η_{els}, as shown in (2.37) [207]. Moreover, the electrolysis chemical reaction happens only if the cell overpotential (v_{els}^{cell}) is above the activation overpotential (v_{act}^{cell}). The v_{act}^{cell} represents the cell voltage for which the activation energy required to transfer an electron from an electrode to an anolyte is surpassed, triggering the electrolysis process [206], [207].

$$\dot{n}_{els}^{(ideal)} = \dot{n}_{els} = \begin{cases} \dfrac{\eta_{els} \cdot N_{cell}^{els} \cdot A \cdot i_{els}^{cell}}{2F}, if\ v_{els}^{cell} > v_{act}^{cell} \\ 0, \quad otherwise \end{cases} \quad (2.37)$$

Therefore, the sizing of the PEME consisted of determining the number of cells N_{cell}^{els}, the active area A, the cell activation overpotential v_{act}^{cell} and hydrogen production efficiency η_{els}. To obtain a PEME stack of 25kW and hydrogen production of 4.18 kWh/Nm^3, N_{cell}^{els}, A, v_{act}^{cell} and η_{els} were setup as 26 cells, 500 cm^2, 1.4V and 90%.

Similar to the PEMFC, the degradation rate of PEME was emulated using the results of [215]. Therefore, the same degradation block per cell used in PEMFC (Fig. 2.21) was incorporated into the

PEME Simulink® schematic. Since the active area is equal to $A = 500\ cm^2$, the input parameter of this block is the current density $i_{els}^{cell} = I_{els}/A$, rather than the normalized current. Furthermore, contrary to PEMFC, the loss of efficiency in PEME is represented by a positive offset in the original cell PEME voltage ($v_{els}^{cell,original}$). According to equation (2.37), the hydrogen production per cell depends on the PEME current (i_{els}). Therefore, the voltage offset Δv_{fc}^{cell} must increase $v_{fc}^{cell,original}$ to increase the electric power consumption for the same hydrogen production, following the equation (2.38).

$$v_{els} = N_{cell}^{els} \cdot \left(v_{els}^{cell,original} + \Delta v_{els}\right) \tag{2.38}$$

2.5.2.3. Modelling of the hydrogen tank

The hydrogen tank in MATLAB Simulink is also inexistent. Therefore, the hydrogen tank model was conceived based on the Beattie-Bridgeman formula specified in (2.39) [216].

$$P_{tank} = \frac{{n_{tank}}^2 R T_{tank}}{{V_{tank}}^2}\left(1 - \frac{c_n}{V_{tank}{T_{tank}}^3}\right)\left[\frac{V}{n_{tank}} + B_0\left(1 - \frac{b_n}{V_{tank}}\right)\right] - \frac{A_0\left(1 - \frac{a_n}{V}\right){n_{tank}}^2}{{V_{tank}}^2} \tag{2.39}$$

Where,

- n_{tank} is the total number of moles in the tank $[mol]$
- A_0, B_0, a_n, b_n et c_n are the coefficient of Beattie-Bridgeman for the hydrogen.
  - $A_0 = 0.02\ [Pa \cdot m^3 \cdot mol^{-2}]$
  - $B_0 = 2.0960e-05\ [m^3 \cdot mol^{-1}]$
  - $a_n = -0.00506e-3\ [m^3 \cdot mol^{-1}]$
  - $b_n = -0.04359e-3\ [m^3 \cdot mol^{-1}]$
  - $c_n = 0.0504e1\ [m^3 \cdot K^3 \backslash bulllet\ mol^{-1}]$
- V_{tank} is the volume of the tank $[m^3]$
- T_{tank} is the temperature of the gas in the tank $[K]$
- R is the ideal gas constant $[m^3 \cdot Pa \cdot K^{-1} \cdot mol^{-1}]$

The total number of moles stored inside the tank ($n_{tank,k}$) at instant k is calculated using the theorem of conservation of mass, following equation (2.40), where T_s is the sampling time in seconds of the Simulink discrete simulation in seconds, $\dot{n}_{els}$ is the hydrogen production rate of PEME in mol/s and $\dot{n}_{fc}$ is the hydrogen consumed by the PEME in mol/s.

$$n_{tank,k} = n_{tank,k-1} + T_s \cdot \dot{n}_{els} - T_s \cdot \dot{n}_{fc} \tag{2.40}$$

To calculate the Level of Hydrogen (LoH) of the tank in percentage, it is necessary to estimate the maximum capacity of the reservoir. Based on the technical specification of Table 2.1, the hydrogen tank can store 18 kg at 30 bars at 80°C. Therefore, the tank temperature is setup as 80°C (or 253.15K). Knowing that the molar mass of hydrogen is 2 g/mol, the maximum number of moles n_{tank}^{max} is equal to 9000 moles. Finally, using Beattie-Bridgeman equation in (2.39), the tank volume V_{tank} is 9 m^3.

2.5.2.4. Modelling of the hydrogen compressor

The hydrogen compressor delivers hydrogen from the PEME cathode to the hydrogen reservoir, adjusting the inlet and outlet pressures. The model used to estimate the power consumed by the compressor was based on equation (2.41) [216].

$$P_{comp} = 2\dot{n}_{els}\frac{\gamma RT}{\gamma - 1}\left[\left(\frac{P_{tank}}{\sqrt{P_{cat}P_{tank}}}\right)^{\frac{\gamma-1}{\gamma}} - 1\right]\frac{1}{\eta_{comp}} \tag{2.41}$$

Where,

- $\dot{n}_{H_2}$ is the flow rate of hydrogen [mol/s]
- R is the constant of an ideal gas $[m^3 \cdot Pa \cdot K^{-1} \cdot mol^{-1}]$
- T is the gas temperature [K]
- $\eta_{comp} = 0.95$ is the compressor efficiency
- γ is the polytropic index. As the process is considered isentropic (adiabatic and reversible process of an ideal gas), $\gamma = C_p C_v$.
- $C_p = 14.32$ specific heat of hydrogen at CNTP (20 ° C and 1 atm) at constant pressure
- $C_v = 10.16$ specific heat of hydrogen at CNTP (20 ° C and 1 atm) at constant volume

Therefore, knowing the gas flowing $\dot{n}_{els}$, the pressure of the cathode of the PEME (P_{cat}) and the pressure of the hydrogen tank (P_{tank}), it is possible to calculate the power P_{comp} consumed by the compressor in W. Remarkably, the pressure P_{cat} is maintained constant by ancillary devices, keeping it equal to 1 bar [207], which is near to the atmospheric pressure.

2.6 Conclusion

This chapter presents a balanced MATLAB Simulink® model between accuracy of distributed electrical components and computation burden. The BMG model is complex enough to consider the major system dynamics and is simple enough not to demand long-run simulations. To reduce the simulation time, simplifications in power converters, DC bus and main grid dynamics were adopted. The transitory effects induced by transistors switching in power converters and the impact of DC-bus impedance lines on the BMG power quality were presumed inexistent. This simplification assumes that the BMG is connected to a stiff main grid that can support the BMG independently on the active and reactive power required to assure the BMG internal power balance. In this view, the interlinking AC-DC power converter connecting the BMG to the external grid is considered ideal.

Despite these simplifications, the designed BMG emulator includes the ageing effects of batteries, fuel cells and electrolysers, the annual internal power imbalance profile of a medium-sized building, the daily electricity price evolution and the main functioning of a parking of plug-in electric vehicles. Furthermore, the entire BMG was modelled based on experimental tests reported in the literature, considering the real sizing of a typical medium-sized residential and non-residential building. All these aspects lead the designed BMG emulator adequate for power flow and technical-economic analysis, which are the focus of this Ph.D. thesis. The BMG emulator covers the fundamental aspects to assess the capabilities of the proposed hierarchical energy management strategy, which will be further detailed in the following chapter.

Chapter 3 Description of the hierarchical control structure

3.1 Introduction

This chapter aims at providing a global overview of the whole hierarchical BEMS by describing each control module and its main features to optimise the operation of the BMG while respecting the grid code concerning the self-consumption. The role of the BEMS is to manage the MG power flow to supply the building energy demand using as much as possible the resources installed in the building and reducing the energy dependency on the external grid.

To accomplish it, the energy exchange with the external grid is continuously supervised by a smart meter located near to the bidirectional interlinking DC-AC converter connecting the BMG to the main grid, as shown in Fig. 3.1 and Fig. 2.1. The smart meter collects the building raw net power imbalance ($P_{imb,k}$), the total energy imported ($P_{grid,k}^{import}$) and exported ($P_{grid,k}^{injected}$), defined by (3.1) – (3.3), respectively. Moreover, each ESS possesses sensors that transmit voltage and current measures directly to the central BEMS. The hierarchical controller processes all these valuable data to assess the BMG performance continuously.

$$P_{imb,k} = P_{pv,k} - P_{cons,k} \tag{3.1}$$

$$P_{grid,k}^{import} = P_{imb,k}, if\ P_{imb,k} \geq 0 \tag{3.2}$$

$$P_{grid,k}^{injected} = P_{imb,k}, if\ P_{imb,k} \leq 0 \tag{3.3}$$

Basically, in the case of power excess ($P_{imb,k} > 0$), the BEMS has four options: produce and store hydrogen by means of electrolysis (P_{els}), charge the batteries (P_{bat}^{ch}), charge the electric vehicles (P_{pevs}^{ch}) or inject the surplus into the main grid ($P_{grid}^{injected}$). Similarly, when there is an internal energy deficit ($P_{imb,k} < 0$) the BEMS also detains four alternatives: produce electricity through the fuel cells (P_{fc}), discharge the batteries (P_{bat}^{dis}), discharge the electric vehicles (P_{pevs}^{dis}) or import energy from the grid (P_{grid}^{import}).

The proposed hierarchical BEMS is divided into five control units working synchronously, notably two Model Predictive Controllers (MPC), two data-driven modules and one Power Sharing Module (PSM), as shown in Fig. 3.1. Notably, P_{bat}, P_{els} and P_{fc} are calculated by the two-level Hierarchical MPC (HMPC) and sent directly to the local controllers of their power converters (i.e. real system), whereas the power reference of plug-in electric vehicles (P_{pevs}^{ref}) is pre-processed by the PSM. Additionally, to improve the flexibility of the MG system, the EMS adapts itself according to continuous data measurements, thanks to the two data-driven modules. The first one is the Real-Time

Model Identification (RTMI) unit for handling the imprecision of ESS modelling, whereas the second one is the MG cost estimator to update the MPCs cost function weights and constraints parameters.

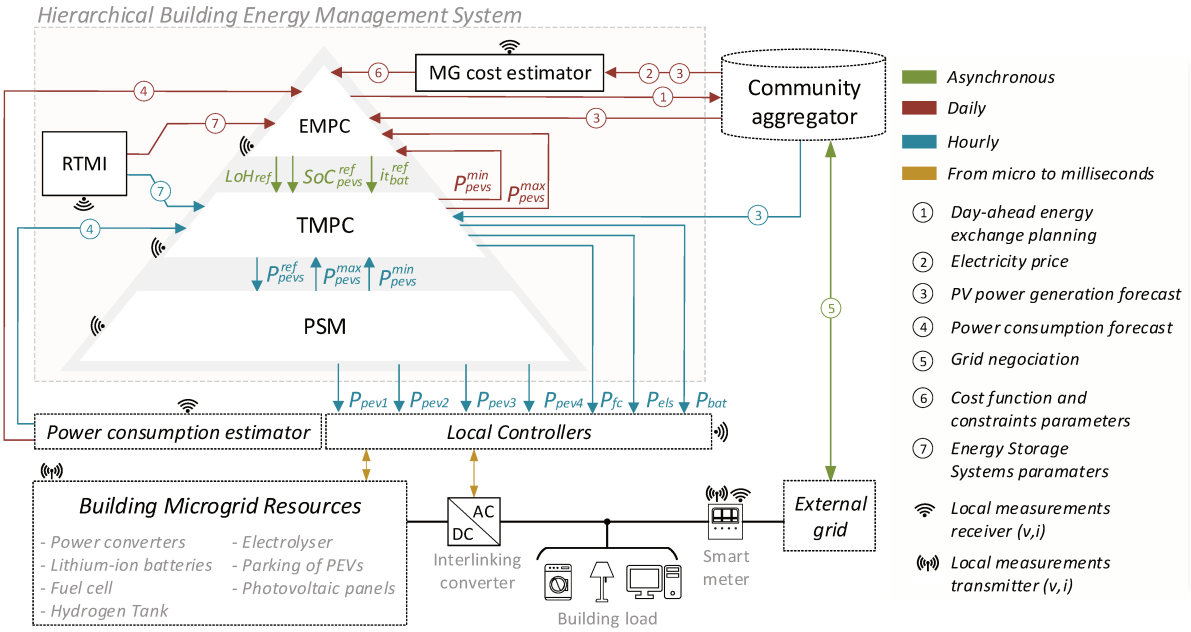

Fig. 3.1: Hierarchical energy management system for optimisation of the power flow of a building microgrid.

Aiming at providing a great understanding of the proposed hierarchical control, this chapter is structured as follows. Firstly, the fundamental concepts of the traditional MPC strategy are explained in subsection 3.2. Afterwards, in subsection 3.2, the BMG linear models used in both EMPC and TMPC prediction are detailed. Thereafter, in subsection 3.4, it is described the constraints and the main properties of both EMPC and TMPC. Section 3.5 discusses the main components of the algorithm that implements the power-sharing among multiple PEVs. Finally, section 3.6 concludes the chapter by summarizing the proposed hierarchical controller.

3.2 The fundamental concepts of Model Predictive Control strategy

Model predictive control designates a control strategy group that explicitly employs the mathematical model of a process to obtain the sequence of control signals that minimise an objective function projected to the future [221]. The predictive control structure is based on three main concepts:

- Prediction of the future states of the system based on a mathematical model over a predefined period composed of N samples called horizon;
- Optimisation of an objective function to determine the best control sequence that offers the highest welfare over the entire horizon; and
- Receding strategy based on periodic re-optimisations over a sliding window comprehending the horizon. Only the first control signal is implemented at each re-optimisation, while the rest of the sequence is discarded.

This process involves many advantages that lead this control strategy to be an attractive solution for industrial and academic issues. Thanks to the receding strategy assured by periodic re-optimisations

within the sliding window, the MPC introduces a feed-forward control loop to compensate the disturbances. Moreover, depending on the time stamp of the re-optimisations and the optimiser type, MPC can easily deal with multivariable system and complex constraints. Furthermore, by considering prediction data in its decision-making process, the MPC can anticipate future actions, improving its robustness against external disturbances.

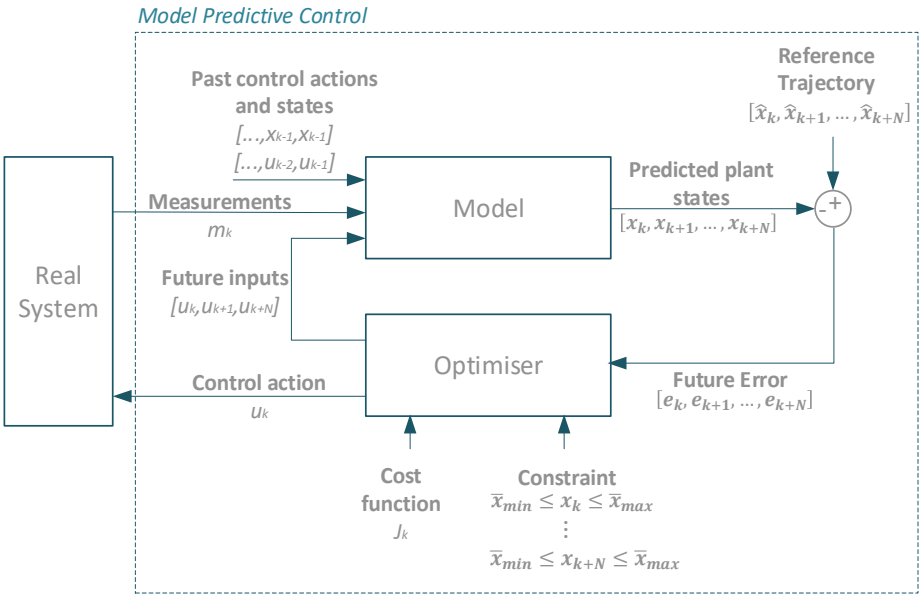

Fig. 3.2: Structure of the model predictive control algorithm.

As illustrated in Fig. 3.2, the MPC strategy is an iterative algorithm that involves the processing of both measurements, prediction data (embedded in the predicted plant states) and the mathematical model of the plant. The mathematical model of the plant allows estimating its predicted states for the upcoming periods inside the horizon N, namely $x_k, x_{k+1}, \dots, x_{k+N}$. This estimation uses the future actions $u_k|k \in [k, k+N]$ calculated by the optimiser, as well as the MPC past actions $u_k|k \in [0, k-1]$ and current measurements m_k.

To be compliant with the MPC structure, the most usual technique for modelling the real system is through state-space representation for p inputs and n state variables, as defined in (3.4). Therefore, the dynamic of the plant can be represented by a set of parameters comprehending the matrix A and B.

$$x_{k+1} = A \cdot x_k + B \cdot u_k \tag{3.4}$$

Where,

- x_k is the state vector, in which $x_k \in \mathcal{R}^n$
- u_k is the control vector, in which $u_k \in \mathcal{R}^p$
- A is the state matrix, in which $\dim(A) = n \times n$
- B is the input matrix, in which $\dim(B) = n \times p$

Although this modelling approach requires linear models, it is largely employed in the literature because of its simplicity and satisfactory performance [37], [117], [184]–[186]. In the MPC process, the use of simplified linear models guarantees an acceptable accuracy because the current measurements

at instant k – called vector m_k – are used to correct the predicted model states for instant k. This allows to enhance the accuracy of the next states estimation ($x_k|k \in [k+1; k+N]$) at each iteration.

Therefore, at each MPC sampling time, the state x_0, referring to the current time $k = 0$, is updated using $m_{k=0}$. If the state $x_0(i)$ is observable, the measure $m_0(i)$ is assigned directly to $x_0(i)$, as defined in (3.5). Notably, the notation i refers to the ith element of the vector x_0 or m_0. However, if the state $x_0(i)$ is non-observable, the state $x_0(i)$ is updated through an observer, which is a mathematical model – named function f_{obs} – that enables to estimate the value of the real state at instant $k = 0$, as specified in (3.6).

$$x_0(i) = m_0(i), i \in [0, n] \tag{3.5}$$

$$x_0(i) \cong f_{obs}(m_0) \tag{3.6}$$

Once updated the current plant states (x_0), the upcoming states are calculated using the recurrence equation (3.4). Hence, the state estimation for future periods is calculated following (3.7).

$$\begin{gathered} x_1 = A \cdot x_0 + B \cdot u_0 \\ x_2 = A \cdot x_1 + B \cdot u_1 \\ \cdots \\ x_N = A \cdot x_{N-1} + B \cdot u_{N-1} \end{gathered} \tag{3.7}$$

By replacing the estimation of one state (e.g. x_1) in the next state (e.g. x_2) and repeating this process along the entire horizon N, the state estimation within the horizon can be determined only using the current state x_0 and future control actions $u_k, \dots, u_{k+N}$, as specified in (3.8).

$$\begin{bmatrix} x_1 \\ x_2 \\ \vdots \\ x_N \end{bmatrix} = x_0 \cdot \begin{bmatrix} A \\ A \\ \vdots \\ A \end{bmatrix} + \begin{bmatrix} B & 0 & \cdots & 0 \\ AB & B & \cdots & 0 \\ \vdots & \vdots & & \vdots \\ A^{N-1}B & A^{N-2}B & \cdots & B \end{bmatrix} \cdot \begin{bmatrix} u_0 \\ u_1 \\ \vdots \\ u_N \end{bmatrix} \tag{3.8}$$

The prediction of the future plant states permits MPC to assess how far it is from making the real system to accomplish a specific objective. For instance, the position estimation in a road allows evaluating the accuracy of a self-driving car to follow a trajectory. Similarly, the position estimation of the encoder in the motor axis can assist a robotic arm catching an object. In the context of BMGs, the estimation of the available energy stored in ESS allows optimising the BMG power flow.

Consequently, by evaluating the error between the desire plant behaviour described by a reference trajectory $\hat{x}_k, \hat{x}_{k+1}, \dots, \hat{x}_{k+N}$ and the estimated plant states $x_k, x_{k+1}, \dots, x_{k+N}$, it is possible to determine corrective actions $u_k, \dots, u_{k+N}$ that lead the real system to approach to this reference trajectory. These control actions are determined through an optimiser that usually tries to minimize a cost function J_k that refers to the quadratic error e_k, defined by (3.9).

$$J_k = e_k = \sum_{i=k}^{k+N} (\hat{x}_i - x_i)^2 \tag{3.9}$$

This optimisation often must respect some boundary constraints, as outlined in (3.10). The choice of the optimiser is arbitrary and depends on how J_k and its constraints were designed. For instance, it

can be a quadratic optimiser, linear programming or even a metaheuristic algorithm, like genetic algorithm and particle swarm optimisation.

$$[u_k, \dots, u_{k+N}] = \arg\left(\min_{[u_k,\dots,u_{k+N}]} J_k\right)$$

Subject to:

$$x_{min,k} \leq x_k \leq x_{max,k} \tag{3.10}$$

$$\dots$$

$$x_{min,k+N} \leq x_{k+N} \leq x_{max,k+N}$$

Following (3.10), the optimiser will determine the sequence of action $u_k, \dots, u_{k+N}$ covering the entire prediction horizon N. Nonetheless, only the first control action u_k is sent to the real system, while the other $N-1$ control actions is rejected. Finally, at the next iteration, a new measurement m_k is acquired and the whole MPC process is repeated.

3.3 Linear models for predicting the Building MicroGrid states

In the context of this thesis, the MPC structure was adopted to optimise the power flow among the electrical resources installed in the building. The entire BMG predicted states are estimated through linear equations in the form of state-space representation. The employment of linear models allows reducing the complexity of the optimisation problem without impacting the performance of the controller drastically. Furthermore, linear models enable exploiting the Mixed-Integer Linear Programming (MILP) framework of CPLEX, a high-performance mathematical programming solver developed by IBM®.

Since the role of MPC is to manage the building internal power flow, it is essential to conceive trustful mathematical models to estimate the total energy stored inside the BMG, as well as the total energy generated and consumed internally. Moreover, since the upper MPC implements an economic optimisation, fluctuations in electricity price along the day also need to be estimated. Consequently, the prediction of the future states of the BMG is divided into two categories, namely the prediction of the raw building net power imbalance and the electricity price evolution, and the prediction of the energy stored in the energy storage devices.

3.3.1 *Modelling of building raw net power imbalance and electricity price evolution*

The estimation of the raw net power imbalance and the day-ahead electricity price are constructed from the same data employed in the Simulink simulator described in section 2.3 and section 2.4, respectively. Therefore, both the raw net power imbalance and the electricity price were modelled as one-hour resolution streaming vectors that are read by the Hierarchical MPC (HMPC) periodically.

Hence, the EMPC and TMPC compute neither the estimation concerning the building power consumption, nor photovoltaic power generation, nor the day-ahead electricity price. Indeed, these prediction data are received by the central EMS directly from adjunct modules. In this way, the HMPC does not need to perform any data treatment to estimate them.

This simplification considers that the community aggregator processes the weather and electricity market forecast data for all buildings belonging to the same neighbourhood. Consequently, at each hour, the community aggregator sends to HMPC the estimated PV power generation ($P_{pv,k}$) and the electricity price ($\pi_{elec,k}$) for the next periods. Similarly, it is assumed that building power consumption ($P_{cons,k}$) acquired by the smart meter is processed by an internal module – identified as *Power consumption estimator* in Fig. 3.1– that sends to the HMPC the estimated power consumption for the upcoming periods.

3.3.2 *Modelling of energy storage devices*

The energy storage devices assume reservoir-based models for estimating their remaining energy. In this regard, PEVs batteries, BMG battery pack, and the hydrogen chain are modelled through linear equations linking the expected future energy stored (i.e. SoC_{k+1}^{pevs}, $i_{t,k+1}^{bat}$, and LoH_{k+1}) to their power supplied to the BMG ($P_{els,k}$, $P_{bat,k}^{ch}$, $P_{bat,k}^{dis}$ or $P_{fc,k}$), as specified in equations (3.11) – (3.13). Remarkably, f_{pevs}, f_{bat} and f_{H_2} are linear functions that will be further detailed in the following three subsections.

$$SoC_{k+1}^{pevs} = SoC_{k}^{pevs} + f_{pevs}(P_{pevs,k}^{ch}, P_{pevs,k}^{dis}) \tag{3.11}$$

$$i_{t,k+1}^{bat} = i_{t,k}^{bat} + f_{bat}(P_{bat,k}^{ch}, P_{bat,k}^{dis}) \tag{3.12}$$

$$LoH_{k+1} = LoH_{k} + f_{els}\left(P_{els,k}\right) - f_{fc}\left(P_{fc,k}\right) \tag{3.13}$$

3.3.2.1. Linear function for modelling electric vehicle batteries

The linear function f_{pevs} enables HMPC to estimate the total energy stored in the batteries of all electric vehicles connected to the building charging station. The formulation of f_{pevs} was designed based on the paper [8], in which the PEV parking seems like a huge battery with capacity dependent on the number of PEVs plugged into the BMG.

When the PEV is connected to the BMG, its batteries must be fully charged up to SoC_{pev}^{max} before its departure, and it can be discharged to supply the BMG energetic needs if its owner has authorised it. Therefore, to estimate the total charge stored in PEV parking – namely i_t^{pev} – that is exploitable by the BMG, it is used the estimated number of available PEVs at instant k, namely n_k^{pevs}. Remarkably the relation between battery charge ($i_{t,k}^{pevs}$) and battery state-of-charge (SoC_k^{pevs}) is defined by (3.14).

$$i_{t,k}^{pevs} = SoC_{k}^{pevs} \cdot Q_{pevs,k} \tag{3.14}$$

The estimation of n_k^{pevs} is implemented through the connection and disconnection schedule of each PEV. It is considered that as soon as a PEV is plugged into the charging station, the next departure time is provided by the user. In this way, it is possible to estimate the total number of PEVs available and the period that they will remain plugged into the BMG. This information is interpreted by the HMPC as a table containing the estimated arrival ($t_{arrival}$) and departure time ($t_{departure}$) of each PEV, as well as their discharge permission ($\delta_{pev_{ID}}^{available}$) along the entire MPC horizon. The variable $\delta_{pev_{ID}}^{available}$

is fundamental to set up adequate constraints to avoid the controller discharging the PEVs that are not allowed to be discharged. This table also allows HMPC to determine the number of PEVs plugged at instant k (n_k^{pevs}), the number of arrivals ($n_k^{arrival}$), and departures ($n_k^{departure}$).

Table 3.1: Example of connection and disconnection schedule of plug-in electric vehicles in a parking.

Identification Number (ID)	**Available to be discharged ($\delta_{pev_{ID}}^{available}$)**	**Arrival time ($t_{arrival}$)**	**Departure time ($t_{departure}$)**
1	True	9h	18h
2	True	7h	17h
3	False	9h	18h
4	True	8h	11h
4	True	14h	16h

For instance, if the PEV schedule table is as this shown in Table 3.1 for a horizon of one-day ahead, it is obtained n_k^{pevs}, $n_k^{arrival}$ and $n_k^{departure}$ represented in Fig. 3.3. Notably, n_k^{pevs} is calculated by means of an auxiliary variable named $\delta_{pev_{iD},k}$, which is a binary variable that is worth 1 when the pev_{ID} is plugged at instant k, and 0 otherwise, as defined in (3.15). Therefore, n_k^{pevs} is calculated using (3.16). Following similar reasoning, the number of PEV arrivals is calculated using (3.17), while the number of departures is determined using (3.18).

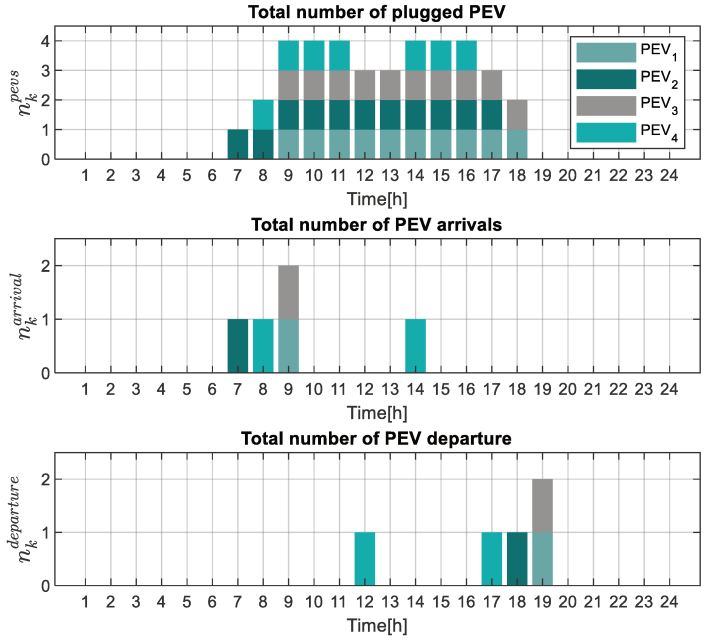

Fig. 3.3: Estimated number of plug-in electric vehicles connected to the building microgrid constructed from the arrival and departure schedule.

$$\delta_{pev_{ID},k} = \begin{cases} 1, & t_{arrival} \leq k \leq t_{departure} \\ 0, & otherwise \end{cases} \tag{3.15}$$

$$n_k^{pevs} = \sum_{ID=1}^{N_{PEV}} \delta_{pev_{ID},k} \tag{3.16}$$

$$n_k^{arrival} = \begin{cases} n_k^{pev} - n_{k-1}^{pev}, & if\ n_k^{pev} > n_{k-1}^{pev} \\ 0, & otherwise \end{cases} \tag{3.17}$$

$$n_k^{departure} = \begin{cases} n_{k-1}^{pev} - n_k^{pev}, & if\ n_k^{pev} < n_{k-1}^{pev} \\ 0, & otherwise \end{cases} \tag{3.18}$$

From this piecewise information together with the average SoC ($SoC_{pevs,k}$), voltage ($v_{pevs,k}$), and nominal capacity ($Q_{pevs,k}$) provided by the charging station (equations (2.12) – (2.14), respectively), the PEV parking charge at instant k ($i_{t_k}^{pevs}$ in Ah) can be estimated by summing up all PEV charge of each vehicle ($i_{t_k}^{pev_{ID}} \cdot \delta_{pev_{ID},k}$), as defined in (3.19). Since all PEVs batteries has the same technical specification[1], $Q_{pevs,k}$ is constant and equal to $Q_{pev_{ID}}$ for all $ID \in [1, N_{PEV}]$, where N_{PEV} is the number of charging stations.

$$i_{t_k}^{pevs} = \sum_{ID}^{N_{PEV}} \delta_{pev_{ID},k} \cdot i_{t_k}^{pev_{ID}} = SoC_{pevs,k} \cdot Q_{pevs,k} \cong n_k^{pev} \cdot SoC_{pevs,k} \cdot Q_{pevs,ID} \tag{3.19}$$

Once calculated the total charge at instant k, the linear model to estimate the remaining energy for upcoming periods can be expressed by (3.20), in which the efficiency when charging (η_{ch}^{pev} in %) and discharging (η_{dis}^{pev} in %) them are taken into account. Notably, T_s is the sampling time of the model in hours, $P_{pevs,k}^{ch}$ is the PEVs charging power and $P_{pevs,k}^{dis}$ is the PEVs discharging power.

$$i_{t_{k+1}}^{pevs} = i_{t_k}^{pevs} - \frac{\eta_{ch}^{pev} \cdot T_s}{v_{pevs,k}} \cdot P_{pevs,k}^{ch} - \frac{T_s}{v_{pevs,k} \cdot \eta_{dis}^{pev}} \cdot P_{pevs,k}^{dis} + i_{t_k}^{arrival} - i_{t_k}^{departure} \tag{3.20}$$

Remarkably, the PEVs cannot be charged and discharged at the same time. Consequently, $P_{pevs,k}^{ch}$ and $P_{pevs,k}^{dis}$ are complementary variables that are controlled through Mixed Logic Dynamic (MLD) constraints [37] and an integer variable, namely δ_{pevs}^{ch} that equals 1 when PEVs are charging and 0 otherwise. Therefore, δ_{pevs}^{ch} must be limited by the inequality constraint (3.21), whereas $P_{pevs,k}^{ch}$ and $P_{pevs,k}^{dis}$ by (3.22) and (3.23), where P_{pevs}^{MIN} and P_{pevs}^{MAX} are the maximum charging and discharging power rate, respectively. Since the powers $P_{pevs,k}^{ch}$ and $P_{pevs,k}^{dis}$ refer to the entire PEV parking, P_{pevs}^{MIN} and P_{pevs}^{MAX} are dependent on the number of PEVs connected at instant k (n_k^{pev}) and the SoC of each PEV, as defined in (3.24) and (3.25). As the PSM supervises each PEV individually, it has a more accurate estimation of the PEV capacity. Consequently, $P_{pevs,1}^{MIN}$ and $P_{pevs,1}^{MAX}$, referring to the first element in the MPC horizon ($k = 1$) are updated by the PSM.

$$0 \leq \delta_{pevs,k}^{ch} \leq 1, \qquad \delta_{pevs}^{ch} \in \mathbb{Z} \tag{3.21}$$

$$P_{pevs,k}^{MIN} \cdot \delta_{pevs,k}^{ch} \leq P_{pevs,k}^{ch} \leq 0 \tag{3.22}$$

$$0 \leq P_{pevs,k}^{dis} \leq P_{pevs,k}^{MAX} \cdot \left(1 - \delta_{pevs,k}^{ch}\right) \tag{3.23}$$

$$P_{pevs,k}^{MIN} = n_k^{pev} \cdot P_{pev_{ID}}^{MIN}, \qquad \forall\ ID \in [1, N_{PEV}]\ and\ k \in [2, N] \tag{3.24}$$

$$P_{pevs,k}^{MAX} = \sum_{ID=1}^{N_{PEV}} P_{pev_{ID}}^{MAX} \cdot \delta_{pev_{ID}}^{available} \cdot \delta_{pev_{ID},k} \tag{3.25}$$

[1] All plug-in electric vehicles are a Zoe of Renault®.

It is important to highlight that the equation (3.20) considers the PEV battery charge obtained ($i_{t_k}^{arrival}$) and lost ($i_{t_k}^{departure}$) when a PEV is connected or disconnected. When a PEV arrives at instant k in the BMG, it brings with it its battery charge, named $i_{t_k}^{arrival}$. Likewise, when a PEV disconnects from the BMG, its batteries charge – namely $i_{t_k}^{departure}$ – is departed with the PEV.

To empower HMPC to predict this behaviour, the estimated number of arrivals ($n_k^{arrival}$) and departures ($n_k^{departure}$) are used. Therefore, the battery charge arrived from all new PEVs connection ($i_{t_k}^{arrival}$) is estimated by using equation (3.26). The term $\widehat{SoC}_{pevs,k}^{arrival}$ is the average estimation of the state-of-charge of all PEVs arrived at instant k.

$$i_{t_k}^{arrival} = n_k^{arrival} \cdot Q_{pevs} \cdot \widehat{SoC}_{pevs,k}^{arrival} \tag{3.26}$$

Similarly, the total battery charge lost by the BMG due to a PEV departure ($i_{t_k}^{departure}$) is calculated using the equation (3.27). This equation considers that the SoC of all PEV available in the parking is shared among all PEVs equally, which means that the departure of $n_k^{departure}$ PEVs correspond to a proportion of the average charge of all PEVs. This assumption is reasonable because the Power Sharing Module, detailed in section 3.5, assures equitable state-of-charge among all PEVs.

$$i_{t_k}^{departure} = \frac{n_k^{departure}}{n_k^{pevs}} \cdot i_{t_k}^{pevs} \tag{3.27}$$

From equations (3.11), (3.20) – (3.27), f_{pevs} is expressed by equation (3.28), whereas the state representation for estimating SoC_{k+1}^{pev} is defined by (3.29).

$$\begin{aligned} f_{pevs}\left(P_{pevs,k}^{ch}, P_{pevs,k}^{dis}\right) &= -\underbrace{\frac{\eta_{ch} \cdot T_s}{v_{pevs,0} \cdot Q_{pevs,0}}}_{\alpha_{pevs}} P_{pevs,k}^{ch} - \underbrace{\frac{T_s}{v_{pevs,0} \cdot Q_{pevs,0} \cdot \eta_{dis}}}_{\beta_{pevs}} P_{pevs,k}^{dis} + \underbrace{n_k^{arrival} \cdot \widehat{SoC}_{pevs,k}^{arrival}}_{\gamma_{pevs,k}} \\ &\quad - \underbrace{\frac{n_k^{departure}}{n_k^{pevs} \cdot Q_{pevs,0}}}_{\theta_{pev,k}} SoC_k^{pevs} \end{aligned} \tag{3.28}$$

$$\begin{aligned} \underbrace{\begin{bmatrix} SoC_1^{pevs} \\ SoC_2^{pevs} \\ \vdots \\ SoC_N^{pevs} \end{bmatrix}}_{x_{pevs,k+1}} &= \underbrace{-\begin{bmatrix} \alpha_{pevs} & \beta_{pevs} & 0 & \cdots & \cdots & \cdots & 0 & 0 \\ \alpha_{pevs}(1-\theta_{pev,0}) & \beta_{pevs}(1-\theta_{pev,0}) & \alpha_{pevs} & \beta_{pevs} & 0 & \cdots & 0 & 0 \\ & & \vdots & & & \ddots & 0 & 0 \\ \alpha_{pevs}(1-\theta_{pev,0})^{N-1} & \beta_{pevs}(1-\theta_{pev,0})^{N-1} & \alpha_{pevs}(1-\theta_{pev,0})^{N-2} & \beta_{pevs}(1-\theta_{pev,0})^{N-2} & \cdots & \cdots & \alpha_{pevs} & \beta_{pevs} \end{bmatrix}}_{A_{pevs,k}} \\ &\quad \cdot \underbrace{\begin{bmatrix} P_{pevs,0}^{ch} \\ P_{pevs,0}^{dis} \\ P_{pevs,1}^{ch} \\ P_{pevs,1}^{dis} \\ \vdots \\ P_{pevs,N}^{ch} \\ P_{pevs,N}^{dis} \end{bmatrix}}_{u_{pevs,k}} + \underbrace{\begin{bmatrix} SoC_0^{pevs} \cdot (1-\theta_{pev,0}) - \sum_{i=0}^{0} \gamma_{pev,i} \\ SoC_0^{pevs} \cdot (1-\theta_{pev,0}) - \sum_{i=0}^{1} \gamma_{pev,i} \\ \vdots \\ SoC_0^{pevs} \cdot (1-\theta_{pev,0}) - \sum_{i=0}^{N} \gamma_{pev,i} \end{bmatrix}}_{x_{pevs,0}} \end{aligned} \tag{3.29}$$

Where,

- $v_{pevs,0}$ is the average voltage of the all PEV batteries at the current time that is provided by the charging station.
- $Q_{pevs,0}$ is the average capacity of the all PEV batteries at the current time that is provided by the charging station.
- SoC_0^{pevs} is the average state-of-charge of the all PEV batteries at the current time that is provided by the charging station.

3.3.2.2. Linear function for modelling battery pack

The linear function f_{bat} considers the distinct efficiency and voltage when commuting between charging and discharging of batteries [204]. According to the mathematical model of Li-ion batteries validated with experimental data [204], [211], the voltage when discharging them is defined by (3.30), while the voltage when charging them is ruled by (3.31).

$$v_{dis} = E_0(T_{cell}) - K(T_{cell}) \cdot \frac{Q_{bat}(T_{amb})}{Q_{bat}(T_{amb}) - i_t^{bat}} \cdot (i^* + i_t^{bat}) + A \cdot \exp(-B \cdot i_t^{bat}) - C \cdot i_t^{bat} - R \cdot i \tag{3.30}$$

$$v_{ch} = E_0(T_{cell}) - K(T_{cell}) \cdot \frac{Q_{bat}(T_{amb})}{i_t^{bat} + 0.1 \cdot Q_{bat}(T_{amb})} \cdot i^* - K(T_{cell}) \cdot \frac{Q_{bat}(T_{amb})}{Q_{bat}(T_{amb}) - i_t^{bat}} + A \cdot \exp(-B \cdot i_t^{bat}) - C \cdot i_t^{bat} - R \cdot i \tag{3.31}$$

Where,

- $E_0$is battery constant voltage (V).
- T_{cell} is the cell temperature (°C).
- T_{amb} is the ambient temperature (°C).
- $i_t^{bat} = \int i \, dt$ is the actual battery charge (Ah).
- i^* is the filtered current (A).
- Q_{bat} is the battery maximum capacity (Ah).
- R is the internal resistance (Ω).
- A is the exponential zone amplitude (V).
- B is the exponential zone time constant inverse $(Ah)^{-1}$.
- C is nominal discharge curve slope, in V/Ah. For lithium-ion batteries with less pronounced discharge curves (such as lithium iron phosphate batteries), this parameter is set to zero.

Unfortunately, in the literature [37], [49], [123], this voltage variation when charging and discharging batteries is neglected. A common approach to estimate the state-of-charge of batteries ($SoC_{bat,k+1}$) is through the equation (3.32). In this formulation, T_s is the sampling time of the discrete model, whereas Q_{nom}^{bat}, v_{nom}^{bat}, η_{ch}^{bat} and η_{dis}^{bat} are constant parameters that are usually retrieved in the manufacture's technical specification, referring to the batteries nominal capacity in Ah, the batteries nominal voltage, the efficiency when charging and discharging them, respectively.

$$SoC_{bat,k+1} = SoC_{bat,k} + \frac{\eta_{ch}^{bat} \cdot T_s}{Q_{nom}^{bat} \cdot v_{nom}^{bat}} \cdot P_{bat,k}^{ch} + \frac{T_s}{Q_{nom}^{bat} \cdot v_{nom}^{bat} \cdot \eta_{dis}^{bat}} \cdot P_{bat,k}^{ch} \tag{3.32}$$

However, according to equations (3.30) and (3.31), the batteries voltage is not constant, and it is far from the nominal voltage (v_{nom}), depending on their operation. Indeed, it is dependent on many external and intrinsic factors, including the total energy stored (i_t^{bat}), the temperature and the direction of the flowing current (i.e. charging or discharging). Therefore, the small differences in the voltage due to the current direction, defined by (3.33), introduces some inaccuracies when estimating $SoC_{bat,k+1}$ for long prediction horizons through the classical model of (3.32). Besides this voltage drop, the variation of the battery voltage when they are fully charged ($i_t^{bat} = 0$) and fully discharged ($i_t^{bat} = Q$) also impacts the SoC estimation when employing the model of equation (3.32).

$$\begin{aligned} |v_{dis} - v_{ch}| = \Bigg| & K(T_{cell}) \frac{Q_{bat}(T_{amb})}{Q_{bat}(T_{amb}) - i_t^{bat}} (i^* + i_t^{bat}) \\ & - K(T_{cell}) \frac{Q_{bat}(T_{amb})}{i_t^{bat} + 0.1 \cdot Q_{bat}(T_{amb})} \cdot i^* \Bigg| \end{aligned} \tag{3.33}$$

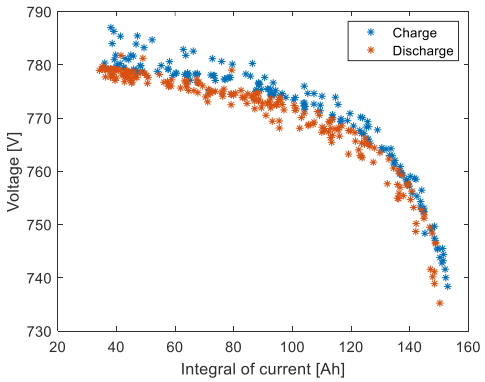

Fig. 3.4: Battery voltage variation when charging and discharging and under different stored energy (integral of current).

To verify the intensity of this voltage variation, a one-month simulation in MATLAB Simulink® of the Lithium-ion battery of size explained in section 2.5.1.1 was conducted, resulting in the data points shown in Fig. 3.4. It is possible to verify that the voltage gap when charging and discharging them can be up to 10V, whereas the voltage offset when they are charged to $SoC = 80\%$ and discharged to $SoC = 10\%$ can attain up to 50V.

Representing from 0.5% to 7% of the voltage gap regarding the nominal voltage (720V), this voltage variation may reduce the accuracy of the SoC estimation. As explained briefly in section 2.5.1, the SoC is calculated using (3.34) – (3.36). Therefore, the energy stored in the batteries is dependent on the current flowing through the battery cells. Consequently, the voltage gap of (3.32) and the voltage drop depending on i_t (Fig. 3.4) will result in different variations of SoC for the same delivered power (P_{bat}^{ch} and P_{bat}^{dis}).

$$i_{t,k+1}^{bat} = i_{t,k}^{bat} + \Delta i_{t,k}^{bat} \; [Ah] \tag{3.34}$$

$$\Delta i_{t,k}^{bat} = \int_k^{k+T_s} i \; dt \; [Ah] \tag{3.35}$$

$$SoC_{k+1}^{bat} = 100 \cdot \left(1 - \frac{i_{t,k+1}^{bat}}{Q_{bat}(T_{amb})}\right) [\%] \tag{3.36}$$

For this reason, a new method for modelling the SoC is proposed. Firstly, to tackle the different voltages when charging and discharging batteries, the power assigned to the battery packs was divided into four variables, named $P_{cd,k}$ and $P_{dd,k}$ when the batteries are discharged ($P_{bat,k}^{dis}$), and $P_{dc,k}$ and $P_{cc,k}$ when they are charged ($P_{bat,k}^{ch}$), at time k. The indexes $\varepsilon = \{cd, dd, cc, dc\}$ indicate the sequence of charge (c) and discharge (d), at time $k-1$ and k, making each of these variables dependent on the current and previous batteries states. Consequently, the total batteries power ($P_{bat,k}$) is the sum of these four variables, as defined in (3.37).

$$P_{bat,k} = \underbrace{P_{cc,k} + P_{dc,k}}_{P_{bat,k}^{ch}} + \underbrace{P_{cd,k} + P_{dd,k}}_{P_{bat,k}^{dis}} \tag{3.37}$$

Remarkably, the status ε is unique for each time k. In other words, either $P_{cc,k}$, $P_{dc,k}$, $P_{cd,k}$ or $P_{dd,k}$ are non-null. The selection of ε is controlled by MLD constraints and binary variables, namely $\delta_{cc,k}$, $\delta_{dc,k}$, $\delta_{dd,k}$ and $\delta_{cd,k}$. For the sake of simplicity, these four binary variables are noted as $\delta_{\varepsilon,k}$, in which is worth 1 when the battery is active under the status ε and 0 otherwise, as defined in (3.38). Therefore, the inequality constraints (3.39) – (3.44) for all $k \in [0, N]$, where N is the size of MPC horizon, must be integrated in the MILP formulation. Notably, P_{bat}^{MIN} and P_{bat}^{MAX} are the maximum power rate when charging and discharging the batteries, respectively.

$$0 \leq \delta_{\varepsilon,k}, \leq 1\,, \qquad \delta_{\varepsilon,k} \in \mathbb{Z};\ \varepsilon = \{cd, dd, cc, dc\} \tag{3.38}$$

$$0 \leq \delta_{cc,k} + \delta_{dc,k} + \delta_{dd,k} + \delta_{cd,k} \leq 1 \tag{3.39}$$

$$\delta_{cc,k} \cdot P_{bat}^{MIN} \leq P_{cc,k} \leq 0 \tag{3.40}$$

$$\delta_{dc,k} \cdot P_{bat}^{MIN} \leq P_{dc,k} \leq 0 \tag{3.41}$$

$$0 \leq P_{dd,k} \leq \delta_{dd,k} \cdot P_{bat}^{MAX} \tag{3.42}$$

$$0 \leq P_{cd,k} \leq \delta_{cd,k} \cdot P_{bat}^{MAX} \tag{3.43}$$

$$P_{bat}^{MIN} \leq P_{bat,k} \leq P_{bat}^{MAX} \tag{3.44}$$

The direction of the battery current is measured by the sensors continuously and sent to the HMPC periodically. Consequently, the HMPC knows whether the batteries were charged or discharged at instant $k-1$. This knowledge is saved in an auxiliary binary variable defined by (3.45) and named $\delta_k^{lastCharge}$, which is equal 1 when the batteries were charging at instant $k-1$, and 0 otherwise. Remarkably, idle status (i.e. zero current) will not impact the last value of $\delta_k^{lastCharge} \forall k \in [0, N]$.

$$0 \leq \delta_k^{lastCharge} \leq 1, \qquad \delta_k^{lastCharge} \in \mathbb{Z} \tag{3.45}$$

Therefore, $\delta_{\varepsilon,0}$ constraints are set as in (3.46) and (3.47), for the first value of the HMPC horizon ($k = 0$).

$$\text{If battery is discharged at k} - 1\text{: } \delta_{cc,0} = 0;\ \delta_{cd,0} = 0; 0 \le \delta_{dd,0} \le 1; 0 \le \delta_{dc,0} \le 1 \tag{3.46}$$

$$\text{If battery is charged at k} - 1\text{: } 0 \le \delta_{cc,0} \le 1; 0 \le \delta_{cd,0} \le 1; \delta_{dd,0} = 0;\ \delta_{dc,0} = 0 \tag{3.47}$$

The value of $\delta_{\varepsilon,k}$ for upcoming periods ($k \in [1, N]$) depends on the action $P_{bat,k}$, and therefore, the value of $\delta_{\varepsilon,k-1}$, as defined in (3.48) – (3.52).

$$\delta_{cc,\mathrm{k}} \le \delta_k^{lastCharge} \tag{3.48}$$

$$\delta_{cd,\mathrm{k}} \le \delta_k^{lastCharge} \tag{3.49}$$

$$\delta_{dd,\mathrm{k}} \le 1 - \delta_k^{lastCharge} \tag{3.50}$$

$$\delta_{dc,\mathrm{k}} \le 1 - \delta_k^{lastCharge} \tag{3.51}$$

$$\delta_k^{lastCharge} = \delta_{k-1}^{lastCharge} - \delta_{cd,\mathrm{k}-1} - \delta_{dc,\mathrm{k}-1} \tag{3.52}$$

Based on equations (3.34) – (3.36), the new model calculates the variation of energy stored (Δi_t) from the actions of control variables $P_{cd,k}$, $P_{dd,k}$, $P_{cc,k}$ and $P_{dc,k}$, as defined in (3.53). Moreover, to diminish the SoC estimation error due to voltage variation according to the level of stored energy (i_t^{bat}), i_t^{bat} is also included in the formulation. The parameters α_ε, β_ε and γ_ε does not have a direct physical meaning, but they are tuned dynamically by the Real-Time Model Identification (RTMI) module that will be detailed in Chapter 4 on page 134.

$$\begin{aligned}\Delta i_{t,k} = {} & \alpha_{cc}P_{cc,k} + \beta_{cc}i_{t,k-1}^{bat} + \gamma_{cc}\delta_{cc,k} + \\ & \alpha_{cd}P_{cd,k} + \beta_{cd}i_{t,k-1} + \gamma_{cd}\delta_{cd,k} + \\ & \alpha_{dd}P_{dd,k} + \beta_{dd}i_{t,k-1} + \gamma_{dd}\delta_{dd,k} + \\ & \alpha_{dc}P_{dc,k} + \beta_{dc}i_{t,k-1} + \gamma_{dc}\delta_{dc,k}\end{aligned} \tag{3.53}$$

An interpretation of this equation can be easily understood from the discharge curve of batteries shown in Fig. 3.5. Considering that the battery current state is defined by an integral of current $i_{t,k}^{bat}$, therefore the voltage associate to it corresponds to v_k. If the control action $P_{bat,k}$ is applied to the batteries, the next state will be $i_{t,k+1}^{bat}$ and v_{k+1}. Therefore, the integral of current between k and $k+1$ will be the same given that the control variable (P_{bat}^{dis}) and the battery current states are the same ($i_{t,k}$ and v_k).

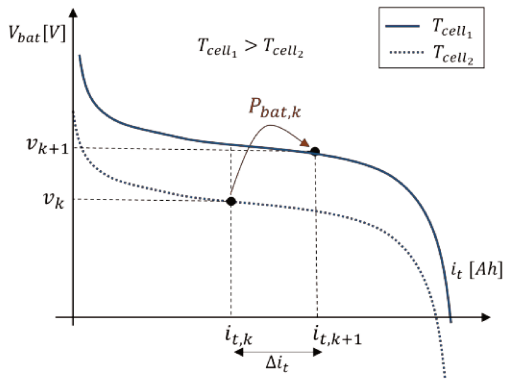

Fig. 3.5: Discharge curve of battery with variations of temperature.

Remarkably, the equation (3.53) is an equality equation defined by three variables, notably Δi_t, P_{bat} and i_t^{bat}. Therefore, it can be interpreted as the sum of four plans – namely π_ε – that are active according to the variable $\delta_{\varepsilon,k}$. In Fig. 3.6 only the active plan π_ε at instant k is illustrated, in which four key points, namely A, B,C and D, are represented. These four points covers the feasible space of battery operation, in which their values are shown in Table 3.2, where:

- i_t^{MIN} is the minimum value of the integral of current (Ah).
- i_t^{MAX} is the maximum value of the integral of current (Ah).
- $P_{bat}^{MAX} > 0$ is the maximum discharging power rate of the batteries (W).
- $P_{bat}^{MIN} < 0$ is the maximum charging power rate of the batteries (W).

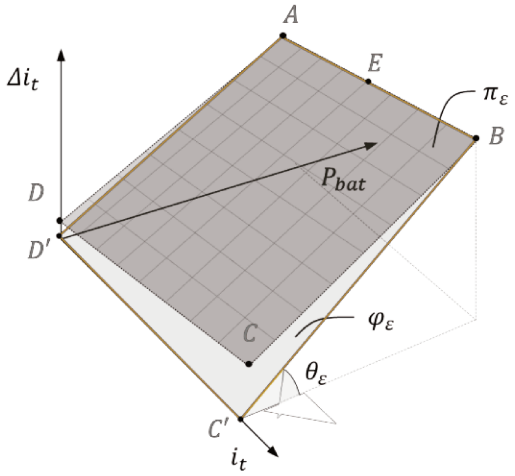

Fig. 3.6: Perspective of the linear model of the battery pack.

Table 3.2: Coordinates of key points for the batteries linear model.

Point	$\boldsymbol{i_t}$	$\boldsymbol{P_{bat}}$	$\boldsymbol{\Delta i_t}$
A	$i_t^A = i_t^{MIN}$	$P_{bat}^A = P_{bat}^{MAX}$ if discharging* $P_{bat}^A = P_{bat}^{MIN}$ if charging**	$\Delta i_t^A = \alpha_\varepsilon P_{bat}^A + \beta_\varepsilon i_t^{MIN} + \gamma_\varepsilon \delta_\varepsilon$
B	$i_t^B = i_t^{MAX}$	$P_{bat}^B = P_{bat}^{MAX}$ if discharging* $P_{bat}^B = P_{bat}^{MIN}$ if charging**	$\Delta i_t^B = \alpha_\varepsilon P_{bat}^B + \beta_\varepsilon i_t^{MAX} + \gamma_\varepsilon \delta_\varepsilon$
C	$i_t^C = i_t^{MAX}$	$P_{bat}^C = 0$	$\Delta i_t^C = \beta_\varepsilon i_t^{MAX} + \gamma_\varepsilon \delta_\varepsilon$
D	$i_t^D = i_t^{MIN}$	$P_{bat}^D = 0$	$\Delta i_t^D = \beta_\varepsilon i_t^{MIN} + \gamma_\varepsilon \delta_\varepsilon$
E	$i_t^E = \frac{i_t^{MIN} + i_t^{MAX}}{2}$	$P_{bat}^E = P_{bat}^{MAX}$ if discharging* $P_{bat}^E = P_{bat}^{MIN}$ if charging**	$\Delta i_t^E = \frac{\Delta i_t^A + \Delta i_t^B}{2}$ $= \alpha_\varepsilon P_{bat}^E + \beta_\varepsilon \frac{(i_t^{MIN} + i_t^{MAX})}{2} + \gamma_\varepsilon \delta_\varepsilon$
C'	i_t^{MAX}	0	$\Delta i_t^{C'} = 0$
D'	i_t^{MIN}	0	$\Delta i_t^{D'} = 0$

*$\varepsilon = \{cd, dd\}$ **$\varepsilon = \{dc, cc\}$

According to the values of Table 3.2 and the illustration of Fig. 3.6, the plan π_ε does not cross the $\vec{\imath}_t$ axis, which makes the batteries model inaccurate for low powers. Therefore, the equation (3.53) was modified to force Δi_t to be equal to zero when the battery is in idle operation ($P_{bat} = 0$). In this way, the new model is represented by the plan φ_ε in Fig. 3.6, which is defined by the points C',D' and E. Notably, the point E is the median point of the segment $\overline{AB}$, which lead the coordinate for Δi_t^E to be the average value of Δi_t^A and Δi_t^B. Therefore, the batteries final model is represented by equation (3.54), in which θ_ε is calculated using (3.55) when discharging and (3.56) when charging the batteries.

$$\Delta i_{t,k} = \theta_{cc} P_{cc,k} + \theta_{cd} P_{cd,k} + \theta_{dc} P_{dc,k} + \theta_{dd} P_{dd,k} \tag{3.54}$$

$$\theta_{\varepsilon} = \alpha_{\varepsilon} + \frac{1}{P_{bat}^{MAX}} \cdot \left(\gamma_{\varepsilon} + \frac{(i_t^{MAX} + i_t^{MIN}) \cdot \beta_{\varepsilon}}{2} \right), \text{if } \varepsilon = [cd, dd] \tag{3.55}$$

$$\theta_{\varepsilon} = \alpha_{\varepsilon} + \frac{1}{P_{bat}^{MIN}} \cdot \left(\gamma_{\varepsilon} + \frac{(i_t^{MAX} + i_t^{MIN}) \cdot \beta_{\varepsilon}}{2} \right), \text{if } \varepsilon = [cc, dc] \tag{3.56}$$

As a result, the recurrence equation that enables HMPC to predict the batteries state of charge is defined by (3.57), which lead f_{bat} to be expressed by (3.58). Therefore, in the state space representation, the SoC estimation is assured by (3.59).

$$i_{t,k+1}^{bat} = i_{t,k}^{bat} + \theta_{cc} P_{cc,k} + \theta_{cd} P_{cd,k} + \theta_{dc} P_{dc,k} + \theta_{dd} P_{dd,k} \tag{3.57}$$

$$f_{bat}(P_{bat}) = \theta_{cc} P_{cc,k} + \theta_{cd} P_{cd,k} + \theta_{dc} P_{dc,k} + \theta_{dd} P_{dd,k} \tag{3.58}$$

$$\underbrace{\begin{bmatrix} i_{t,1}^{bat} \\ i_{t,2}^{bat} \\ \vdots \\ i_{t,N}^{bat} \end{bmatrix}}_{x_{bat,k+1}} = \underbrace{\begin{bmatrix} \theta_{cc} & \theta_{cd} & \theta_{dc} & \theta_{dc} & 0 & 0 & 0 & 0 & \cdots & 0 & 0 & 0 & 0 \\ \theta_{cc} & \theta_{cd} & \theta_{dc} & \theta_{dc} & \theta_{cc} & \theta_{cd} & \theta_{dc} & \theta_{dc} & \cdots & 0 & 0 & 0 & 0 \\ & & & \vdots & & & & & \ddots & 0 & 0 & 0 & 0 \\ \theta_{cc} & \theta_{cd} & \theta_{dc} & \theta_{dc} & \theta_{cc} & \theta_{cd} & \theta_{dc} & \theta_{dc} & \cdots & \theta_{cc} & \theta_{cd} & \theta_{dc} & \theta_{dc} \end{bmatrix}}_{A_{bat,k}} \cdot \underbrace{\begin{bmatrix} P_{cc,0} \\ P_{cd,0} \\ P_{dc,0} \\ P_{dd,0} \\ \vdots \\ P_{cc,N} \\ P_{cd,N} \\ P_{dc,N} \\ P_{dd,N} \end{bmatrix}}_{u_{bat,k}} + \underbrace{\begin{bmatrix} i_{t,0}^{bat} \\ i_{t,0}^{bat} \\ \vdots \\ i_{t,0}^{bat} \end{bmatrix}}_{x_{bat,0}} \tag{3.59}$$

3.3.2.3. Linear function for modelling the hydrogen chain

Concerning the hydrogen chain, f_{els} and f_{fc} were divided into three ranges of power, named zone1, zone2 and zone3, referring to small, medium and large power rates. This division is necessary because, if operating outside the nominal power, the current – which is the image of the hydrogen flowing across the cells – is non-linear with the power, as shown in Fig. 3.7. Faraday's law, defined in (3.60), links the current (i_{els} and i_{fc} in A) and the hydrogen flowing ($\dot{n}_{H_2}^{els}$ and $\dot{n}_{H_2}^{fc}$ in mol/s), which is constant when operating near the nominal conditions (~1A/cm²). In this equation, $N_{cells}^{els,fc}$ is the number of cells in electrolysers or fuel cell stack, F is the Faraday constant.

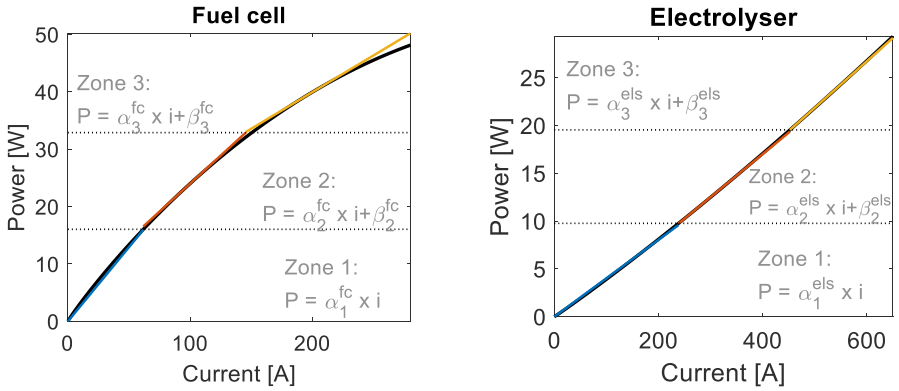

Fig. 3.7: Fuel cell and electrolyser power in function of their current.

$$\dot{n}_{H_2}^{els,fc} = \frac{N_{cells}^{els,fc}}{2 \cdot F} \cdot i_{els,fc}\ [mol/s] \tag{3.60}$$

In this study, it was assumed that the temperature regulation of the entire hydrogen chain is perfectly controlled by ancillary services, in a way that the electrolysers, the tank and the fuel cells temperatures are constant. Therefore, the number of moles stored in the tank is proportional to the tank pressure, as defined in (3.61). Consequently, $\dot{n}_{H_2,k}^{els}$ and $\dot{n}_{H_2,k}^{fc}$ can be estimated by the variation of pressure, as specified in (3.62) and (3.63).

$$\frac{n_{H_2,k}^{tank}}{P_{tank,k}} = \frac{V_{tank}}{R \cdot T_{tank}} \cong constant \tag{3.61}$$

$$\dot{n}_{H_2,k}^{els} = \frac{n_{H_2,k}^{tank} - n_{H_2,k-1}^{tank}}{T_s} = \left(\frac{V_{tank}}{R \cdot T_{tank}}\right) \cdot \frac{P_{tank,k} - P_{tank,k-1}}{T_s}, if\ P_{tank,k} > P_{tank,k-1} \tag{3.62}$$

$$\dot{n}_{H_2,k}^{fc} = \frac{n_{H_2,k}^{tank} - n_{H_2,k-1}^{tank}}{T_s} = \left(\frac{V_{tank}}{R \cdot T_{tank}}\right) \cdot \frac{P_{tank,k} - P_{tank,k-1}}{T_s}, if\ P_{tank,k} < P_{tank,k-1} \tag{3.63}$$

As a result, Faraday's law of (3.60) can be rewritten in function of the tank pressure, instead of the number of moles, as shown in (3.64).

$$\Delta P_{tank,k} = \left(\frac{R \cdot T_{tank}}{V_{tank}}\right) \cdot \frac{N_{cells}^{els,fc}}{2 \cdot F} \cdot T_s \cdot i_{els,fc} = \beta_{Faraday}^{els,fc} \cdot i_{els,fc} \tag{3.64}$$

Due to the non-linearity between current and power, a unique line for representing the tank inlet and outlet hydrogen flow, as proposed in most of the studies in the literature [37], [117], may result in a non-accurate model. In front of this problem, a new linear model based on the intensity of power is proposed. This novel linear model divides the power reference assigned to electrolysers (P_{els}) and fuel cells (P_{fc}) into three operating zones, which yields six zonal variables, named "zonal powers", as defined in (3.65) and (3.66).

$$P_{fc,k} = P_{fc,k}^{zone1} + P_{fc,k}^{zone2} + P_{fc,k}^{zone3} \tag{3.65}$$

$$P_{els,k} = P_{els,k}^{zone1} + P_{els,k}^{zone2} + P_{els,k}^{zone3} \tag{3.66}$$

The zonal powers for the fuel cells are defined as $P_{fc}^{zone1}, P_{fc}^{zone1}$ and P_{fc}^{zone2}, whereas for the electrolysers, they are called $P_{els}^{zone1}, P_{els}^{zone1}$ and P_{els}^{zone2}. The selection of these zonal powers is assured by MLD constraints and binary variables defined by (3.67) and (3.68), namely $\delta_{fc}^{zone1}, \delta_{fc}^{zone2}$ and δ_{fc}^{zone3} for the fuel cells; and $\delta_{els}^{zone1}, \delta_{els}^{zone2}$ and δ_{els}^{zone3} for the electrolysers. Each zonal power belongs to a range of power, as defined in the inequality constraints (3.69) – (3.74), where EPS is a small value, typically of order of 10^{-3}. Notably, EPS is added to these inequality constraints to prevent mathematical singularities.

$$0 \leq \delta_{fc,k}^{zone1}, \delta_{fc,k}^{zone2}, \delta_{fc,k}^{zone3} \leq 1, \qquad \delta_{fc,k}^{zone1}, \delta_{fc,k}^{zone1}, \delta_{fc,k}^{zone1} \in \mathbb{Z} \tag{3.67}$$

$$0 \leq \delta_{els,k}^{zone1}, \delta_{els,k}^{zone2}, \delta_{els,k}^{zone3} \leq 1, \qquad \delta_{els,k}^{zone1}, \delta_{els,k}^{zone1}, \delta_{els,k}^{zone1} \in \mathbb{Z} \tag{3.68}$$

$$0 \leq P_{fc,k}^{zone1} \leq \frac{1}{3} \cdot P_{fc}^{MAX} \cdot \delta_{fc,k}^{zone1} \tag{3.69}$$

$$\left(\frac{1}{3}\cdot P_{fc}^{MAX}+EPS\right)\cdot\delta_{fc,k}^{zone2}\le P_{fc}^{zone2}\le\frac{2}{3}\cdot P_{fc}^{MAX}\cdot\delta_{fc,k}^{zone2} \tag{3.70}$$

$$\left(\frac{2}{3}\cdot P_{fc}^{MAX}+EPS\right)\cdot\delta_{fc,k}^{zone3}\le P_{fc}^{zone3}\le P_{fc}^{MAX}\cdot\delta_{fc,k}^{zone3} \tag{3.71}$$

$$0\le P_{els,k}^{zone1}\le\frac{1}{3}\cdot P_{els}^{MAX}\cdot\delta_{fc,k}^{zone1} \tag{3.72}$$

$$\left(\frac{1}{3}\cdot P_{els}^{MAX}+EPS\right)\cdot\delta_{els,k}^{zone2}\le P_{els}^{zone2}\le\frac{2}{3}\cdot P_{els}^{MAX}\cdot\delta_{els,k}^{zone2} \tag{3.73}$$

$$\left(\frac{2}{3}\cdot P_{els}^{MAX}+EPS\right)\cdot\delta_{els,k}^{zone3}\le P_{els}^{zone3}\le P_{els}^{MAX}\cdot\delta_{els,k}^{zone3} \tag{3.74}$$

To avoid loss of efficiency and guarantee that only one zonal power is non-null at each time k, the electrolysers and the fuel cells must operate in a complementary fashion. Therefore, the inequality constraint (3.75) must be integrated into HMPC design. In other words, either the fuel cell, the electrolysers or neither one is active at instant k.

$$0\le\delta_{fc,k}^{zone1}+\delta_{fc,k}^{zone2}+\delta_{fc,k}^{zone3}+\delta_{els,k}^{zone1}+\delta_{els,k}^{zone2}+\delta_{els,k}^{zone3}\le 1 \tag{3.75}$$

Operating the electrolyser and fuel cells at a specific power (i.e. P_{els} and P_{fc}) inducts a corresponding current flowing i_{els} and i_{fc}, as shown in curves of Fig. 3.7. To enhance the model accuracy, the non-linear curve is split into three power zones, resulting in three linear functions selected according to the states of the binary variables, as defined in equations (3.76) – (3.81). Notably, the parameters α_{fc}^{zone1}, α_{fc}^{zone2}, α_{fc}^{zone3}, β_{fc}^{zone2}, β_{fc}^{zone3}, α_{els}^{zone1}, α_{els}^{zone2}, α_{els}^{zone3}, β_{els}^{zone2}, and β_{els}^{zone3} can be either analytically determined by following the Appendix II or identified in real-time by the RTMI module that will be further detailed in Chapter 4.

$$P_{fc,k}^{zone1}=\alpha_{fc}^{zone1}\cdot i_{fc,k} \tag{3.76}$$

$$P_{fc,k}^{zone2}=\alpha_{fc}^{zone2}\cdot i_{fc,k}+\beta_{fc}^{zone2}\cdot\delta_{fc}^{zone2} \tag{3.77}$$

$$P_{fc,k}^{zone3}=\alpha_{fc}^{zone3}\cdot i_{fc,k}+\beta_{fc}^{zone3}\cdot\delta_{fc}^{zone3} \tag{3.78}$$

$$P_{els,k}^{zone1}=\alpha_{els}^{zone1}\cdot i_{els,k} \tag{3.79}$$

$$P_{els,k}^{zone2}=\alpha_{els}^{zone2}\cdot i_{els,k}+\beta_{els}^{zone2}\cdot\delta_{els}^{zone2} \tag{3.80}$$

$$P_{els,k}^{zone3}=\alpha_{els}^{zone3}\cdot i_{els,k}+\beta_{els}^{zone3}\cdot\delta_{els}^{zone3} \tag{3.81}$$

By rearranging equations (3.76) – (3.81), it is obtained (3.82) for calculating the fuel cells current and (3.83) for estimating the electrolyser current.

$$i_{fc,k}=\frac{P_{fc,k}^{zone1}}{\alpha_{fc}^{zone1}}+\frac{P_{fc,k}^{zone2}}{\alpha_{fc}^{zone2}}+\frac{P_{fc,k}^{zone3}}{\alpha_{fc}^{zone3}}-\frac{\beta_{fc}^{zone2}\cdot\delta_{fc,k}^{zone2}}{\alpha_{fc}^{zone2}}-\frac{\beta_{fc}^{zone3}\cdot\delta_{fc,k}^{zone3}}{\alpha_{fc}^{zone3}} \tag{3.82}$$

$$i_{els,k}=\frac{P_{els,k}^{zone1}}{\alpha_{els}^{zone1}}+\frac{P_{els,k}^{zone2}}{\alpha_{els}^{zone2}}+\frac{P_{els,k}^{zone3}}{\alpha_{els}^{zone3}}-\frac{\beta_{els}^{zone2}\cdot\delta_{els,k}^{zone2}}{\alpha_{els}^{zone2}}-\frac{\beta_{els}^{zone3}\cdot\delta_{els,k}^{zone3}}{\alpha_{els}^{zone3}} \tag{3.83}$$

Based on the modified Faraday's law of (3.64), the equation for predicting the variation of hydrogen stored in the tank, namely ΔLoH_k, can be calculated using (3.84), where T_s is the sampling time of the

discrete model in seconds and $n_{H_2}^{max}$ is the maximum number of mols that the hydrogen reservoir can store.

$$\begin{aligned}\Delta LoH_k = f_{els}(P_{els,k}) - f_{fc}(P_{fc,k}) &= \frac{T_s \cdot \dot{n}_{H_2,k}^{els} - T_s \cdot \dot{n}_{H_2,k}^{fc}}{n_{H_2}^{max}} \\ &\cong \frac{T_s \cdot \beta_{Faraday}^{els} \cdot i_{els,k} - T_s \cdot \beta_{Faraday}^{fc} \cdot i_{fc,k}}{P_{H_2}^{max}} \ [\%]\end{aligned} \tag{3.84}$$

The $n_{H_2}^{max}$ is dependent on the tank volume (V_{tank}), temperature (T_{tank}) and its maximum bearable pressure (P_{tank}^{max}). Finally, by replacing (3.82) and (3.83) into (3.84), the variation of hydrogen stored in the tank due to PEME and PEMFC power can be estimated through (3.85).

$$\begin{aligned}\Delta LoH_k = &\underbrace{\frac{T_s \cdot \beta_{Faraday}^{els}}{P_{H_2}^{max}}\left(\frac{P_{els,k}^{zone1}}{\alpha_{els}^{zone1}} + \frac{P_{els,k}^{zone2}}{\alpha_{els}^{zone2}} + \frac{P_{els,k}^{zone3}}{\alpha_{els}^{zone3}} - \frac{\beta_{els}^{zone2} \cdot \delta_{els,k}^{zone2}}{\alpha_{els}^{zone2}} - \frac{\beta_{els}^{zone3} \cdot \delta_{els,k}^{zone3}}{\alpha_{els}^{zone3}}\right)}_{f_{els}(P_{fc,k})} \\ &- \underbrace{\frac{T_s \cdot \beta_{Faraday}^{fc}}{P_{H_2}^{max}}\left(\frac{P_{fc,k}^{zone1}}{\alpha_{fc}^{zone1}} + \frac{P_{fc,k}^{zone2}}{\alpha_{fc}^{zone2}} + \frac{P_{fc,k}^{zone3}}{\alpha_{fc}^{zone3}} - \frac{\beta_{fc}^{zone2} \cdot \delta_{fc,k}^{zone2}}{\alpha_{fc}^{zone2}} - \frac{\beta_{fc}^{zone3} \cdot \delta_{fc,k}^{zone3}}{\alpha_{fc}^{zone3}}\right)}_{f_{fc}(P_{els,k})}\end{aligned} \tag{3.85}$$

Consequently, in state-space representation, the LoH_{k+1} along the horizon N can be estimated through (3.86).

$$\underbrace{\begin{bmatrix} LoH_0 \\ LoH_1 \\ \vdots \\ LoH_N \end{bmatrix}}_{x_k^{fc,els}} = \underbrace{\begin{bmatrix} \vec{a}_{fc} & \vec{a}_{els} & 0 & 0 & \cdots & 0 & 0 & 0 \\ \vec{a}_{fc} & \vec{a}_{els} & \vec{a}_{fc} & \vec{a}_{els} & 0 & \cdots & 0 & 0 \\ & & \vdots & & & \ddots & \vdots & \vdots \\ \vec{a}_{fc} & \vec{a}_{els} & \vec{a}_{fc} & \vec{a}_{els} & \vec{a}_{fc} & \cdots & \vec{a}_{fc} & \vec{a}_{els} \end{bmatrix}}_{A_{fc,els}} \cdot \underbrace{\begin{bmatrix} \vec{u}_{fc,0} \\ \vec{u}_{els,0} \\ \vec{u}_{fc,1} \\ \vec{u}_{els,1} \\ \vdots \\ \vec{u}_{fc,N} \\ \vec{u}_{els,N} \end{bmatrix}}_{u_{fc,els}} + \underbrace{\begin{bmatrix} LoH_0 \\ LoH_0 \\ \vdots \\ LoH_0 \end{bmatrix}}_{x_0^{fc,els}} \tag{3.86}$$

Where,

- $\vec{u}_{fc,k}$ is a vector containing the control variables of fuel cells.
- $\vec{u}_{els,k}$ is a vector containing the control variables of electrolysers.
- $\vec{a}_{fc}$ is a vector containing the parameters of the fuel cells model.
- $\vec{a}_{els}$ is a vector containing the parameters of the electrolyser model.
- LoH_k^{MIN} is the minimum level of hydrogen that can be stored in the tank at instant $k \in [0, N]$.
- LoH_k^{MAX} is the maximum level of hydrogen that can be stored in the tank at instant $k \in [0, N]$.
- LoH_0 is the level of hydrogen at the current time. It is estimated by the HMPC using the pressure measures, by the relation[2] $LoH_0 = \frac{P_{tank,k}}{P_{tank}^{MAX}}$.

The control vectors $\vec{u}_{fc,k}$ and $\vec{u}_{els,k}$ are defined by (3.87) and (3.88), whereas the parameter vectors $\vec{a}_{fc}$ and $\vec{a}_{els}$ is structure as in (3.89) and (3.90), respectively.

[2] This equation considers that the tank temperature is constant, and it is deducted from the ideal gas law.

$$\vec{u}_{fc,k} = \left[P_{fc,k}^{zone1} \quad P_{fc,k}^{zone2} \quad P_{fc,k}^{zone3} \quad \delta_{fc,k}^{zone2} \quad \delta_{fc,k}^{zone3}\right]^T \tag{3.87}$$

$$\vec{u}_{els,k} = \left[P_{els,k}^{zone1} \quad P_{els,k}^{zone2} \quad P_{els,k}^{zone3} \quad \delta_{els,k}^{zone2} \quad \delta_{els,k}^{zone3}\right]^T \tag{3.88}$$

$$\vec{a}_{fc} = \frac{T_s \cdot \beta_{Faraday}^{fc}}{n_{H_2}^{max}} \cdot \left[\frac{1}{\alpha_{fc}^{zone1}} \quad \frac{1}{\alpha_{fc}^{zone1}} \quad \frac{1}{\alpha_{fc}^{zone1}} \quad -\frac{\beta_{fc}^{zone2}}{\alpha_{fc}^{zone2}} \quad -\frac{\beta_{fc}^{zone3}}{\alpha_{fc}^{zone3}}\right] \tag{3.89}$$

$$\vec{a}_{els} = \frac{T_s \cdot \beta_{Faraday}^{els}}{n_{H_2}^{max}} \cdot \left[\frac{1}{\alpha_{els}^{zone1}} \quad \frac{1}{\alpha_{els}^{zone1}} \quad \frac{1}{\alpha_{els}^{zone1}} \quad -\frac{\beta_{els}^{zone2}}{\alpha_{els}^{zone2}} \quad -\frac{\beta_{els}^{zone3}}{\alpha_{els}^{zone3}}\right] \tag{3.90}$$

3.4 Hierarchical Model Predictive Control

The proposed two-level hierarchical model predictive controller was designed to minimise the operating costs of BMG, while maintaining the safe operation of its electrical devices even under stochasticity in the raw net power imbalance. Formulated as an Economic MPC (EMPC), the upper control level minimises the BMG operation cost by determining both the batteries charge references for battery packs ($i_{t_{bat}}^{ref}$), State-of-Charge references for electric vehicle batteries (SoC_{pevs}^{ref}), and the tank Level of Hydrogen reference (LoH_{ref}) to be forward to the lower MPC, as shown in Fig. 3.2.

Additionally, the EMPC is updated daily to send the day-ahead energy planning to the community aggregator. This piecewise information is essential for enabling aggregators to maintain grid stability and assure profitable grid contracts concerning the local electricity price [168]. Simultaneously, the lower level, designed as Tracking MPC (TMPC), determines the power references for batteries pack, electric vehicles, electrolyser and fuel cells (P_{bat}, P_{pevs}, P_{els}, P_{fc}, respectively) that follow both $i_{t_{bat}}^{ref}$, SoC_{pevs}^{ref} and LoH_{ref}. The following subsections describe the main features of EMPC, TMPC and the common constraints that must be integrated into their formulation.

3.4.1 *Economic Model Predictive Control*

The objective of EMPC is to guarantee the BMG operation at minimum cost. To reach this objective, the EMPC minimises the estimated annual BMG expenditure over a horizon of two-days ahead ($N_h^{EMPC} = 48h$), considering:

- the total electricity cost ($\pi_{grid,k}$),
- the total ESS degradation cost ($\pi_{bat,k}^{deg} + \pi_{els,k}^{deg} + \pi_{fc,k}^{deg}$),
- the annual financial reward for self-consuming electricity ($\pi_{sc,k}$); and
- the penalisation for not attaining the required marks of annual self-consumption rate ($\pi_{sc,k}^{pen}$).

Therefore, the EMPC optimises at least once a day ($T_s^{EMPC} = 24h$) the cost function defined by (3.91) and determine the $i_{t_{ref}}^{bat}$, LoH_{ref} and SoC_{pev}^{ref} to be sent to the lower MPC. Each of these costs is updated daily based on the parameters coming from the MG cost estimator module that is further detailed in Chapter 5.

$$i_{t_{ref}}^{bat}, LoH_{ref}, SoC_{pev}^{ref} = arg\left(\min_{u_{EMPC}} J_k^{EMPC}\right) = arg\left(\min_{i_{t_{ref}}^{bat}, SoC_{pev}^{ref}, LoH_{ref}} \sum_{k=1}^{N_h^{EMPC}=48} \pi_{grid,k} + \pi_{els,k}^{deg} + \pi_{fc,k}^{deg} + \pi_{bat,k}^{deg} - \pi_{sc,k} + \pi_{sc,k}^{pen}\right) \quad (3.91)$$

The EMPC also supervises the performance of TMPC. Every hour, EMPC assesses the accuracy of $i_{t_{ref}}^{bat}$, LoH_{ref} and SoC_{pevs}^{ref} tracking by comparing the imported and exported energy measurements provided by the smart meter ($P_{grid,k}^{meas}$) and those calculated by EMPC ($P_{grid,k}$). Therefore, the gap between $P_{grid,k}^{meas}$ and $P_{grid,k}$ can be due to either imprecisions in $i_{t,k+1}^{bat}$ and LoH_{k+1} model estimation or on account of unexpected raw net power imbalance variation ($P_{pv,k} - P_{cons,k}$).

To soften the effects of this stochasticity, the absolute difference between $P_{grid,k}$, and $P_{grid,k}^{meas}$ is supervised by the EMPC hourly. This error in the power imbalance estimation, named $\varepsilon_{grid,k}$ is calculated using (3.92), where $P_{pv}^{capacity}$ is the maximum power that the PV panels can generate. In the BMG understudy, $P_{pv}^{capacity}$ is worth 100 kW.

$$\varepsilon_{grid,k} = \frac{\left|P_{grid,k} - P_{grid,k}^{meas}\right|}{P_{pv}^{capacity}} \quad (3.92)$$

If $\varepsilon_{grid,k}$ is higher than a predefined threshold – named ΔP_{grid}^{thr} – the EMPC determines new $i_{t_{ref}}^{bat}$, LoH_{ref} and SoC_{pev}^{ref}. This asynchronous re-optimisation process uses the updated prediction data $P_{pv,k}$ provided by the aggregator, and $P_{cons,k}$ calculated by the *Power consumption estimator*. However, instead of using all data comprising the entire horizon, it uses a reduced horizon, as illustrated in Fig. 3.8. The reduced horizon comprehends the data prediction of the period between the time where the absolute error surpasses ΔP_{grid}^{thr} – named t_{reOpt} – and the end of the original horizon, being equal to $N_h^{EMPC} - t_{reOpt}$.

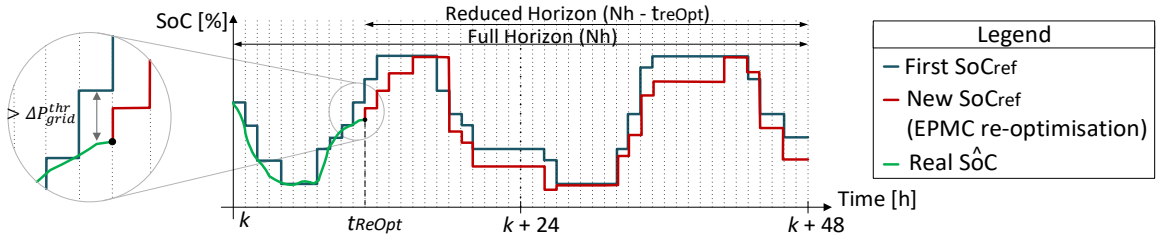

Fig. 3.8: Re-optimisation of EMPC using the reduced horizon.

The schematic of Fig. 3.9 summarizes the EMPC operation by highlighting its interaction with the other control modules in the hierarchical control structure. Remarkably, the EMPC interacts with the community aggregator, the RTMI module, the MG cost estimator, the TMPC layer, the PSM and the real BMG, through the BMG sensors and the smart meter. The RTMI module updates the matrixes A_k and B_k of the EMPC model, referring to the parameters of hydrogen ESS, Li-ion battery pack and PEV batteries. Furthermore, RTMI module determines the maximum and minimum boundaries of batteries pack ($i_{t_{bat}}^{max}$ and $i_{t_{bat}}^{min}$) that are used in the EMPC inequalities constraints. On the other hand, the MG

cost estimator determines both the cost function J_k^{EMPC} and calculates $A'_{EMPC,k}$ and $B'_{EMPC,k}$ and $C'_{EMPC,k}$ that define some equality constraints. The PSM sends to the EMPC the maximum PEV power exploitable by the BMG for the next hour, whereas the charging station sends the connection schedule table of the PEV parking. The EMPC processes the prediction data $P_{pv,k}$ and $P_{cons,k}$, by integrating them in both equality and inequality constraints.

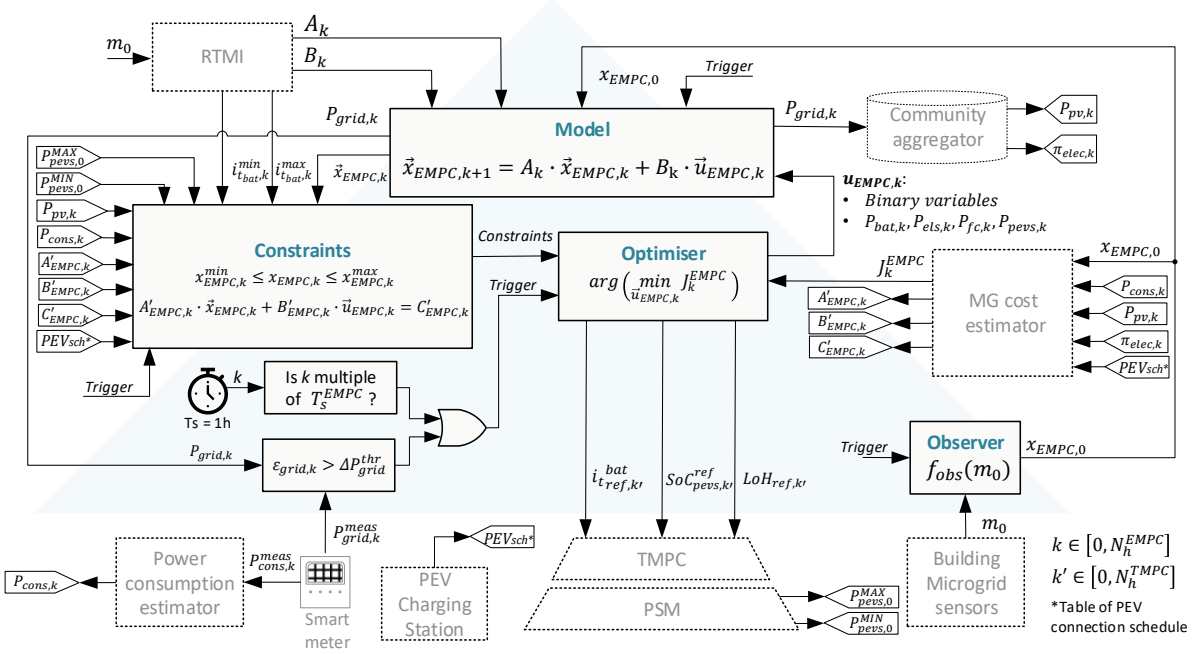

Fig. 3.9: Detail of the economic model predictive controller.

3.4.2 *Tracking Model Predictive Control*

Parallelly to EMPC, the TMPC determines corrective power references for batteries, fuel cells and electrolysers to track $i_{t_{ref}}^{bat}$, LoH_{ref} and SoC_{pev}^{ref} determined by EMPC. For this, TMPC optimises the cost function defined by (3.93) at a cadence of one hour ($T_s^{TMPC} = 1h$). The purpose of TMPC is to keep the safe operation of the BMG regarding the maximum and minimum boundaries; as well as the power balance, without raising the computation cost. Instead of optimising hourly the cumbersome cost function defined by (3.91), it optimises (3.93) that possess a short horizon of only 6 hours ahead.

$$P_{bat}, P_{fc}, P_{els}, P_{pevs} = \arg\left(\min_{P_{bat},P_{fc},P_{els},P_{pevs}} J_k^{TMPC}\right)$$

$$= \arg\left(\min_{P_{bat},P_{fc},P_{els},P_{pevs}} \sum_{k=1}^{N_h^{TMPC}=6} \underbrace{\left(\frac{N_h^{TMPC}-k-1}{SoC_{pev,k}^{MAX}}\right)^2 \left(SoC_{pev}^{ref} - SoC_{pev,k}\right)^2}_{\substack{Electric\ Vehicle \\ state-of-charge\ tracking}} \right. \tag{3.93}$$

$$\left. + \underbrace{\left(\frac{N_h^{TMPC}-k-1}{i_{t,k}^{MAX}}\right)^2 \left(i_{t_{ref}}^{bat} - i_{t,k}^{bat}\right)^2}_{\substack{Battery\ charge \\ tracking}} + \underbrace{\left(\frac{N_h^{TMPC}-k-1}{LoH_{max}}\right)^2 \left(LoH_{ref,k} - LoH_k\right)^2}_{\substack{Tank\ level-of-hydrogen \\ tracking}} \right)$$

The cost function of TMPC is composed of three terms that are normalised to make the error of each reference tracking between 0 and 1. For this reason, each quadratic error (i.e. $\left(SoC_{pev}^{ref} - SoC_{pev,k}\right)^2$, $\left(i_{t_{ref}}^{bat} - i_{t,k}^{bat}\right)^2$ and $\left(LoH_{ref,k} - LoH_k\right)^2$) is divided by its maximum value (i.e. $SoC_{pev,k}^{MAX}$, $i_{t,k}^{MAX}$ and LoH_{max}). Additionally, aiming to give more importance to the instantaneous reference than the upcoming references, the quadratic errors are multiplied by the term $\left(N_h^{TMPC} - k - 1\right)^2$, where N_h^{TMPC} is the TMPC horizon and k is the time within the horizon window.

The TMPC is a simplified MPC formulation that interacts with EMPC, RTMI, PSM, the PEV charging station, the aggregator, power consumption estimator and the real BMG, as illustrated in Fig. 3.10.

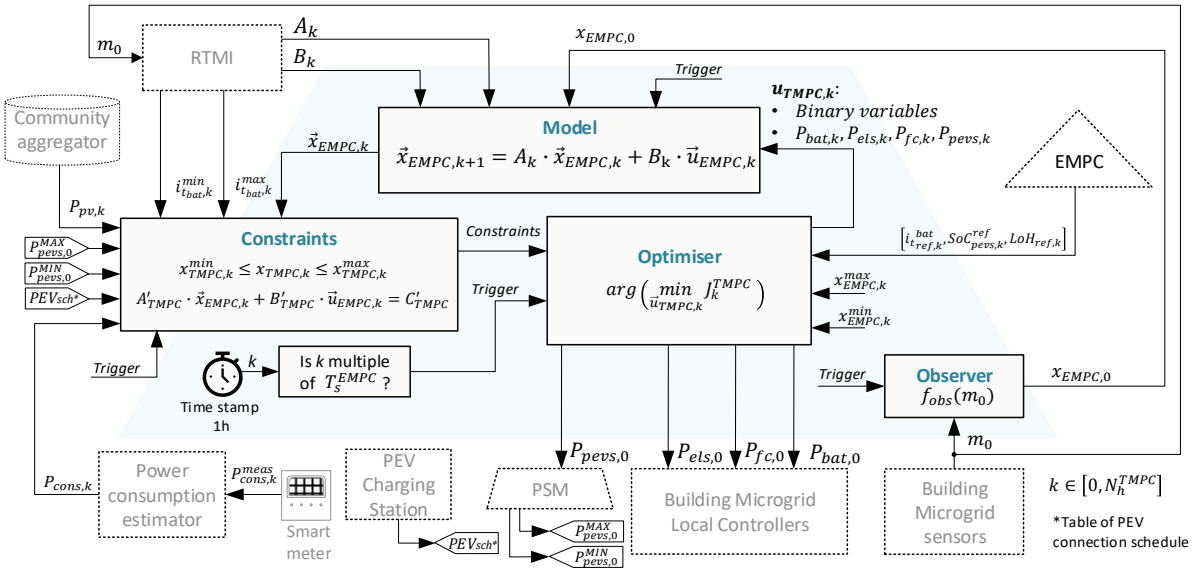

Fig. 3.10: Detail of the tracking model predictive controller.

3.4.3 *Common constraints in the hierarchical MPC structure*

The EMPC and TMPC hold almost the same architecture and are quietly similar regarding their constraints. This is because the constraints of the two MPC layers must assure:

- The power balance among the building microgrid resources,
- The maximum and minimum storage capacity of each ESS (i.e. LoH, SoC_{pevs} and i_t^{bat}),
- The maximum and minimum power rate of both the interlinking AC-DC power converter and each ESS,
- The charge of ESS only from energy generated locally; and
- The discharge of ESS to only supply the local energy demand.

Notably, the first three sets of constraints are to keep the safe operation of the BMG and avoid damages in its electrical devices, whereas the last two requirements are imposed to the HMPC to respect the grid code with respect the building microgrids in France [222]. The French grid regulators impose the restriction in charging and discharging of ESS to encourage the consumption of the PV power generated locally and avoid injecting it directly to the grid. Consequently, this implicitly fosters self-

consumption and prevents the BMG from using its resources to only take advantage of fluctuations in the electricity price. The next four subsections explain the design of these five groups of constraints that need to be integrated into both EMPC and TMPC.

3.4.3.1. Constraints to guarantee the power balance

To ensure the power balance at each sampling time k, the equality constraint (3.94) is integrated into both MPCs, where the future states of ESS and the raw net power imbalance described in previous sections are used. In this formulation, P_{comp} refers to the power consumed by the compressor that is turned on whenever the electrolyser is operating. The non-linear dynamic of the compressor was neglected to the point that P_{comp} is considered as a constant parameter. Since the power consumed by the compressor is very small compared to the power of other BMG electrical components ($P_{comp} \leq 1kW$), this simplification will not harm drastically the accuracy of the HMPC predictions.

$$\begin{aligned} 0 = \underbrace{P_{pv,k} - P_{cons,k}}_{\substack{Prediction\ data \\ section\ 3.3.1}} + \underbrace{P^{ch}_{pevs,k} + P^{dis}_{pevs,k}}_{\substack{PEV\ power\ references \\ Determined\ by\ MPC \\ section\ 3.3.2.1}} + \underbrace{P_{cc,k} + P_{dc,k} + P_{dd,k} + P_{cd,k}}_{\substack{Batteries\ power\ references \\ Determined\ by\ MPC \\ section\ 3.3.2.2}} \\ + \underbrace{P^{zone1}_{els,k} + P^{zone2}_{els,k} + P^{zone3}_{els,k}}_{\substack{Electrolyser\ power\ references \\ Determined\ by\ MPC \\ section\ 3.3.2.3}} + \underbrace{P^{zone1}_{fc,k} + P^{zone2}_{fc,k} + P^{zone3}_{fc,k}}_{\substack{Fuel\ cells\ power\ references \\ Determined\ by\ MPC \\ section\ 3.3.2.3}} \\ - P_{comp} \underbrace{\left(\delta^{zone1}_{els,k} + \delta^{zone2}_{els,k} + \delta^{zone3}_{els,k}\right)}_{\substack{Determined\ by\ MPC \\ section\ 3.3.2.3}} - \underbrace{P^{injected}_{grid,k} - P^{impoted}_{grid,k}}_{\substack{Determined \\ by\ MPC}} \end{aligned} \tag{3.94}$$

3.4.3.2. Constraints to respect the ESS capacity

To respect the maximum and minimum storage capacity of each ESS, the constraints (3.95) – (3.97) are integrated into the MILP formulation of the HMPC. Remarkably, these inequality constraints were deducted from the ESS state-space representation expressed in (3.29), (3.59) and (3.86), respectively.

$$SoC^{min}_{pevs,k} - x_{pevs,0} \leq A_{pevs,k} \cdot u_{pevs,k} \leq SoC^{max}_{pevs,k} - x_{pevs,0}, \qquad \forall k \in [1, N] \tag{3.95}$$

$$i^{min}_{t_{bat},k} - x_{bat,0} \leq A_{bat,k} \cdot u_{bat,k} \leq i^{max}_{t_{bat},k} - x_{bat,0}, \qquad \forall k \in [1, N] \tag{3.96}$$

$$LoH^{min}_{k} - x^{fc,els}_{0} \leq A_{fc,els} \cdot u_{fc,els} \leq LoH^{max}_{k} - x^{fc,els}_{0}, \qquad \forall k \in [1, N] \tag{3.97}$$

The parameters $SoC^{min}_{pevs,k}$ and $SoC^{max}_{pevs,k}$ are dynamic boundaries that depend on the total number of PEVs plugged at instant k (n^{pevs}_{k}), as defined in (3.98) and (3.99), where SoC^{min}_{pevID} and SoC^{max}_{pevID} are the minimum and maximum state-of-charge that the pev_{ID} accepts, respectively. The values of SoC^{min}_{pevID} and SoC^{max}_{pevID} are transmitted by the PEV charging station and it is considered that all PEVs have the same technical specification. Therefore, $SoC^{min,max}_{pevID} = SoC^{min,max}_{pevID+1}, \forall\, pevID \in [0, N_{PEV} - 1]$. To guarantee that the PEV batteries are charged before their departure, the time at which any PEV is planning to disconnect from the BMG ($n^{departure}_{k} \neq 0$), $SoC^{min}_{pevs,k}$ is adjusted to force that its batteries are fully charged, following equation (3.100).

$$SoC^{min}_{pevs,k} = n^{pevs}_{k} \cdot SoC^{min}_{pevID} \cdot Q_{pevID} \tag{3.98}$$

$$SoC_{pevs,k}^{max} = n_k^{pevs} \cdot SoC_{pevID}^{max} \cdot Q_{pevID} \tag{3.99}$$

$$SoC_{pevs,k}^{min} = SoC_{pevs,k}^{max}, \qquad if\ n_k^{departure} \neq 0 \tag{3.100}$$

Similarly, the dynamic boundaries $i_{t_{bat},k}^{min}$ and $i_{t_{bat},k}^{max}$ in equation (3.96) are the minimum and maximum charge that the batteries pack can support. These values are calculated by the RTMI module that will be detailed in Chapter 4. Finally, LoH_k^{min} and LoH_k^{max} refer to the minimum and maximum LoH that the hydrogen tank can bear, respectively. These values are deducted from the manufacturer's technical specification of the hydrogen tank.

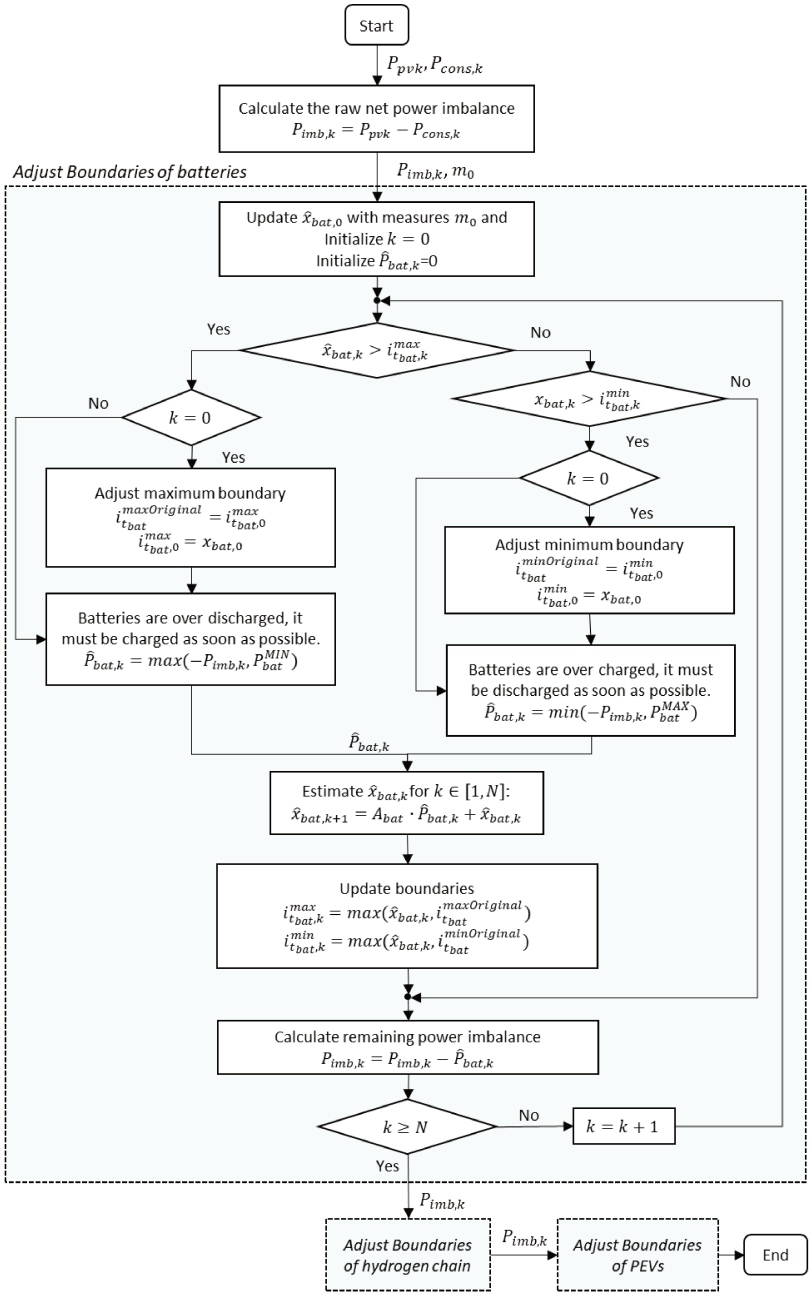

Fig. 3.11: Algorithm for updating the boundaries of the capacity of ESS when they are outside their feasible zone.

To avoid MILP optimiser errors, these maximum and minimum boundaries are slightly adjusted if HMPC realises that the real values of SoC^{pev}, LoH and i_t^{bat} have exceeded their limits. The algorithm to modify the boundaries is detailed in Fig. 3.11, in which the batteries boundaries are adjusted firstly, followed by hydrogen ESS and PEV batteries.

In other words, as illustrated in Fig. 3.12 in the case of batteries ($i_{t,k}^{bat}$), if their charge at $k = 0$ is smaller than its minimum boundary ($i_{t,0}^{bat} < i_{t_{bat},0}^{min}$) or greater than its maximum boundary ($i_{t,0}^{bat} > i_{t_{bat},0}^{max}$), the boundaries are adjusted. The new boundaries are modified to force $i_{t,k}^{bat}$ to return as soon as possible to the safe zone ($i_{t_{bat},k}^{min} \leq i_{t,k}^{bat} \leq i_{t_{bat},k}^{max}$). Consequently, this boundary update depends on the raw net power imbalance ($P_{imb,k} = P_{pv,k} - P_{cons,k}$) and the batteries pack model defined by (3.59).

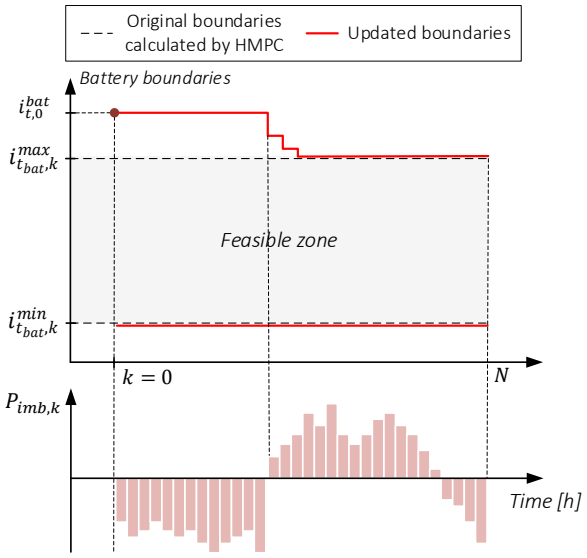

Fig. 3.12: Example of the adjustment of the batteries boundaries to keep their operation inside the feasible zone.

3.4.3.3. Constraints to respect the maximum power rate of BMG electrical devices

Aiming at respecting the physical limitations of ESS concerning their power rate, the inequality constraints (3.21) – (3.23) must be integrated in the HMPC constraints to assure the safe operation of the PEV parking, whereas the equations (3.39) – (3.44) must be considered when operating batteries. Finally, the inequality constraints (3.69) – (3.74) ensure the secure operation of fuel cells and electrolysers. Concerning the interlinking AC-DC power converters, the maximum power injected and exported to the external grid must be limited to respect its physical limits. For these, the MDL constraints (3.101) – (3.103) must be included in the HMPC.

$$0 \leq \delta_{grid}^{injected} \leq 1, \qquad \delta_{grid}^{injected} \in \mathbb{Z} \tag{3.101}$$

$$\delta_{grid}^{injected} \cdot P_{grid}^{MIN} \leq P_{grid,k}^{injected} \leq 0 \tag{3.102}$$

$$0 \leq P_{grid,k}^{import} \leq P_{grid}^{MAX} \cdot \left(1 - \delta_{grid}^{injected}\right) \tag{3.103}$$

3.4.3.4. Constraint to respect the grid code concerning the charging and discharging of ESS

To limit the charge and discharge of ESS to be compliant to the French grid code, the constraints (3.104) and (3.105) must be embedded in both control layers. Consequently, the energy used to charge the ESS comes only from PV arrays surplus, whereas ESS discharge is limited to supply the power deficit and charge PEVs. Notably, the PEVs are not limited to be charged according to the power surplus because it is a building load that can be charged with the energy coming from the external grid. On the other hand, they can be discharged only to supply the local power consumption. For that reason, they can be discharged only when there is power deficit.

$$\left|\max\left(P_{bat}^{MIN}+P_{els}^{MIN},-P_{surplus,k}\right)\right| \le P_{cc,k}+P_{dc,k}+P_{els,k}^{\text{zone1}}+P_{els,k}^{\text{zone2}}+P_{els,k}^{\text{zone3}} \le 0 \tag{3.104}$$

$$\begin{aligned} 0 \le P_{dd,k}+P_{cd,k}+P_{fc,k}^{\text{zone1}}+P_{fc,k}^{\text{zone2}}+P_{fc,k}^{\text{zone3}}+P_{pevs,k}^{dis} \\ \le \left|\max\left(P_{bat}^{MAX}+P_{els}^{MAX}+P_{pevs}^{MAX},P_{deficit,k}-P_{pevs,k}^{ch}\right)\right| \end{aligned} \tag{3.105}$$

Where,

- $P_{deficit,k}$ is the raw deficit of energy at instant k (W), defined by (3.106).
- $P_{surplus,k}$ is the raw surplus of energy at instant k (W) defined by (3.107).
- P_{bat}^{MAX} and P_{bat}^{MIN} are the maximum and minimum power rate of the batteries pack (W).
- P_{fc}^{MAX} and P_{fc}^{MIN} are the maximum and minimum power rate of the fuel cell stack (W).
- P_{els}^{MAX} and P_{els}^{MIN} are the maximum and minimum power rate of the electrolysers (W).
- P_{pevs}^{MAX} and P_{pevs}^{MIN} are the maximum and minimum power rate of the PEV parking (W).

$$E_{deficit,k}=\begin{cases}P_{pv,k}-P_{cons,k} \Leftrightarrow P_{pv,k}<P_{cons,k}\\ 0 \Leftrightarrow P_{pv,k}\ge P_{cons,k}\end{cases} \tag{3.106}$$

$$E_{surplus,k}=\begin{cases}P_{pv,k}-P_{cons,k} \Leftrightarrow P_{pv,k}>P_{cons,k}\\ 0 \Leftrightarrow P_{pv,k}\le P_{cons,k}\end{cases} \tag{3.107}$$

3.5 Power-sharing Module

As in [8] and defined in equation (3.95), to reduce computation burden, the two MPC in cascade estimate the total energy stored in the aggregation of PEV rather than individual PEV. Consequently, neither EMPC nor TMPC have any information about the SoC of each PEV, but only the average SoC of the entire EV parking, named $SoC_{pev,k}$. To assure that all PEVs are fully charged before their scheduled departure, EMPC and TMPC modify the boundaries of $SoC_{pev,k}$ (i.e. $SoC_{pevs,k}^{min}$ and $SoC_{pevs,k}^{max}$) so that to force both to be 80% when any PEV are planning to disconnect to the BMG, as defined in (3.100). However, due to the incomplete information about the SoC of each PEV, the complete charging of individual PEV cannot be always guaranteed with only HMPC power assignation. Especially when PEVs connect at a different time or when they arrive with different level of SoC, the equal power-sharing of the power references determined by HMPC (i.e. $\left(P_{pevs}^{ch}+P_{pevs}^{dis}\right)/n_k^{pevs}$) cannot guarantee that all PEV are charged before their departure time. Therefore, aiming to take full advantages of PEV's batteries despite unpredictability in the user's behaviour, the hierarchical MPC operates together with PSM, as shown in Fig. 3.13.

To ensure that all PEVs are fully charged before their scheduled departure time, the PSM determines the portion of $P^{ref}_{pevs,k} = P^{ch}_{pevs,k} + P^{dis}_{pevs,k}$ that will be assigned for each PEV, as well as the maximum charging ($P^{MIN}_{pevs,k+1}$) and discharging power rate ($P^{MAX}_{pevs,k+1}$) for the next period. Notably, as explained in section 3.3.2.1, $P^{MIN}_{pevs,k+1}$ and $P^{MAX}_{pevs,k+1}$ are transmitted to the TMPC in order to update the PEV power boundaries (equations (3.24) and (3.25)) to enable TMPC to better optimise the power flow at $k+1$. This avoids losing performance because adjusting the power boundaries according to the real PEV parking capacity prevents TMPC from charging PEVs that are already fully charged or discharging PEVs that are already empty. As illustrated in Fig. 3.14, it shares $P^{ref}_{pevs,k}$ among each available PEV according to their state-of-charge ($SoC_{pev_{ID},k}$) and their estimated remaining time connected to the BMG ($t^{connection}_{pev_{ID}}$).

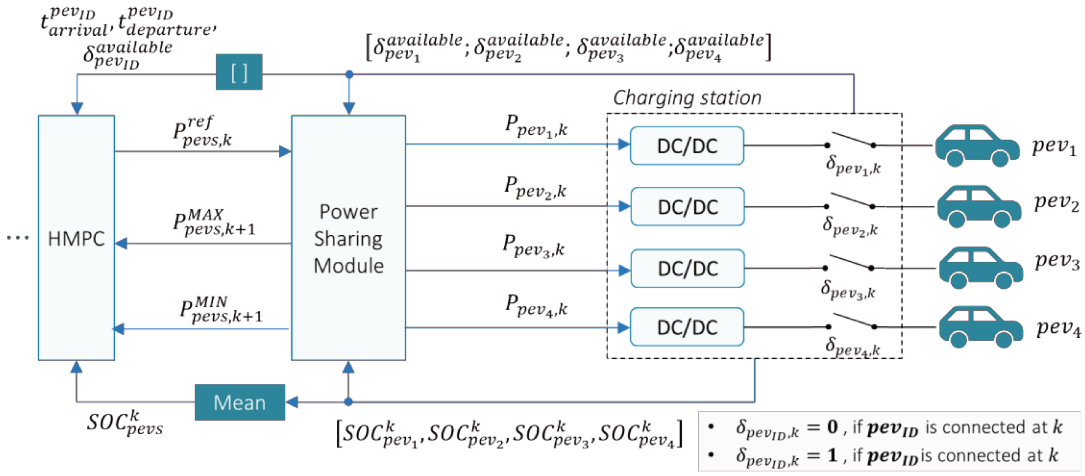

Fig. 3.13: Detail of the power-sharing module.

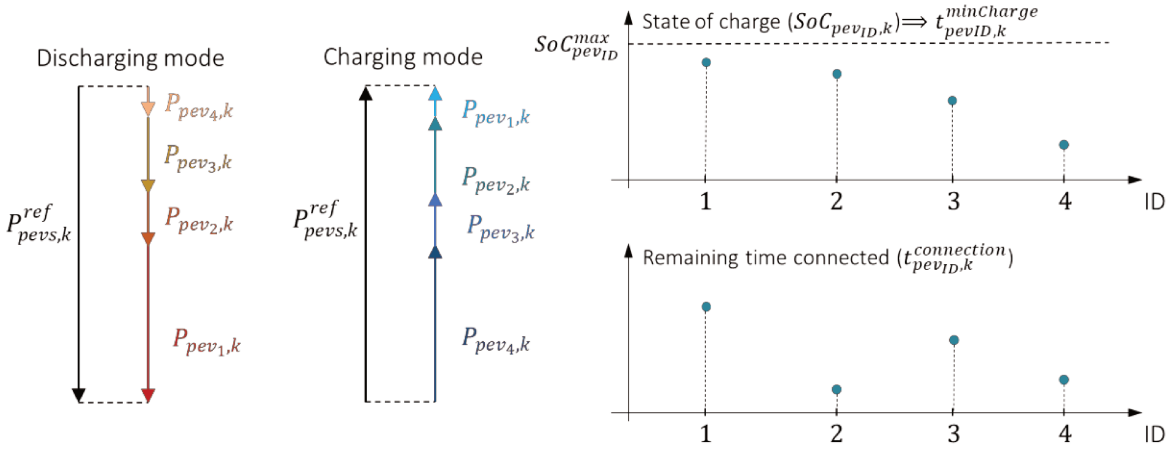

$$\omega_{pev_{ID},k} = \begin{cases} \dfrac{1}{t^{connection}_{pevID,k} - t^{minCharge}_{pevID,k}}, if\ charging \\ t^{connection}_{pevID,k} - t^{minCharge}_{pevID,k}, if\ discharging \end{cases} \qquad \omega_{norm,k} = \sum_{ID=1}^{N_{PEV}} \omega_{pev_{ID},k} \qquad P_{pev_{ID},k} = \frac{\omega_{pev_{ID},k}}{\omega_{norm,k}} P^{ref}_{pevs,k}$$

Fig. 3.14: Principal formulas and mechanisms to share the power among all PEVs connected according to their state of charge and remaining time connected to the building microgrid.

The power-sharing algorithm is composed of five steps that are detailed below. The flow chart in Fig. 3.15 summarizes the PSM algorithm.

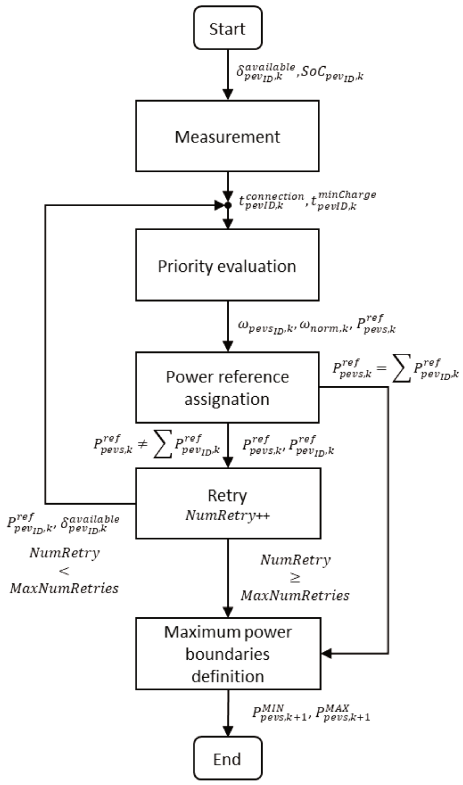

Fig. 3.15: Summary of the power-sharing module algorithm.

1. **Measurement:**
   - Verify the availability of all PEVs plugged to the BMG at instant k ($\delta^{available}_{pev_{ID},k}$) that is provided by the BMG charging station.
   - Measure the state-of-charge of each available PEV at instant k ($SoC_{pev_{ID},k}$).
   - Calculate the estimated time that each PEV will remain connected to the BMG ($t^{connection}_{pevID,k}$), following equation (3.108).

$$t^{connection}_{pevID,k} = t^{departure}_{pevID,k} - t_{current} \tag{3.108}$$

   Where, $t^{departure}_{pevID,k}$ is the next departure time of $pevID$ in the next 24 hours, and $t_{current}$ is the current time of the day. Therefore, $0 \leq t^{departure}_{pevID,k} \leq 24$ and $t^{departure}_{pevID,k} \in \mathbb{Z}$.

   - Calculate the minimum time needed to fully charge each PEV ($t^{minCharge}_{pevID,k}$), using (3.109). Notably, $t^{minCharge}_{pevID,k}$ corresponds to the time that $SoC_{pev_{ID},k}$ will reach $SoC^{max}_{pev_{ID}}$ if pev_{ID} is charged at maximum power rate $P^{MIN}_{pev_{ID}}$.

$$t_{pevID,k}^{minCharge} = ceil\left(\frac{SoC_{pev_{ID}}^{max} - SoC_{pev_{ID},k}}{\left|P_{pev_{ID}}^{MIN}\right| \cdot \frac{\eta_{ch}^{pev_{ID}} \cdot T_s}{v_{pevs,k}}}\right) \tag{3.109}$$

2. Priority evaluation:

- Calculate the margin time that PSM has to charge each PEV, namely $\Delta t_{EV_{ID},k}^{ch}$, by using (3.110).

$$\Delta t_{EV_{ID},k}^{ch} = t_{pevID,k}^{connection} - t_{pevID,k}^{minCharge} \tag{3.110}$$

- Calculate the power-sharing weight defined by (3.111).

$$\omega_{ID} = \begin{cases} \dfrac{\Delta t_{EV_{ID}}^{ch}}{\sum_{ID} \Delta t_{EV_{ID}}^{ch}} \cdot \delta_{EV_{ID}}^{disA}, & if\ P_{EVpark,k}^{ch} > 0\ (discharge) \\ \dfrac{1/\Delta t_{EV_{ID}}^{ch}}{\sum_{ID} 1/\Delta t_{EV_{ID}}^{ch}}, & if\ P_{EV,k}^{ref} < 0\ (charge) \\ 1, & if P_{pevs,k}^{ref} = 0\ (iddle) \end{cases} \tag{3.111}$$

3. Power reference assignation:

- Determine the power reference of each PEV ($P_{pev_{ID},k}$) based on the power sharing weight (ω_{ID}), using (3.112). Intuitively when charging ($P_{pevs,k}^{ref} < 0$), $P_{pev_{ID},k}^{ref}$ will be more important for PEVs that has a small margin time $\Delta t_{EV_{ID},k}^{ch}$. Controversially, when discharging ($P_{pevs,k}^{ref} > 0$), $P_{pev_{ID},k}^{ref}$ will be more intense for PEVs that has a large margin time $\Delta t_{EV_{ID},k}^{ch}$.

$$P_{pev_{ID},k}^{ref} = P_{pevs,k}^{ref} \cdot \omega_{ID} \tag{3.112}$$

- Upper and lower boundary $P_{pev_{ID},k}^{ref}$ according to the limitations in the power rate and PEV storage capacity, by applying the equations (3.113) and (3.114).

$$P_{pev_{ID},k}^{ref} = \max\left(-P_{pev_{ID}}^{MIN}; \frac{SoC_{pev_{ID},k} - SoC_{pev_{ID}}^{max}}{\frac{\eta_{ch}^{pev_{ID}} \cdot T_s}{v_{pevs,k}}}; P_{pev_{ID},k}^{ref}\right), if\ charging \tag{3.113}$$

$$P_{pev_{ID},k}^{ref} = \min\left(P_{pev_{ID}}^{MAX}; \frac{SoC_{pev_{ID},k} - SoC_{pev_{ID}}^{min}}{\frac{T_s}{v_{pevs,k} \cdot \eta_{dis}^{pev_{ID}}}}; P_{pev_{ID},k}^{ref}\right), if\ discharging \tag{3.114}$$

- Verify whether the power reference coming from the TMPC is completely shared among all PEVs, by assessing the condition of (3.115) and (3.116). If the accuracy of the power-sharing is satisfactory, the algorithm stops and PSM sends the power reference $P_{pev_{ID},k}$ to the real system and execute *Maximum power boundaries definition* step (i.e. step 5); otherwise, it implements the *Retry* state.

$$P_{pevs,k} \neq \sum_{ID=1}^{N_{PEV}} P_{pev_{ID},k} \Rightarrow Retry \tag{3.115}$$

$$P_{pevs,k} = \sum_{ID=1}^{N_{PEV}} P_{pev_{ID},k} \Rightarrow \begin{matrix} Maximum\ power \\ boundaries\ definition \end{matrix} \tag{3.116}$$

4. **Retry:**
   - Identify which PEVs are not fully charged or fully discharged after the application of $P_{pev_{ID},k}$ ($\delta_{pev_{ID}}^{fullyCharged} \neq 0$ and $\delta_{pev_{ID}}^{fullyDischarged} \neq 0$), following (3.117) and (3.118).

$$\delta_{pev_{ID}}^{fullyCharged} = \begin{cases} 1, & if\ \ SoC_{pev_{ID},k} + \left|P_{pev_{ID},k}\right| \cdot \dfrac{\eta_{ch}^{pev_{ID}} \cdot T_s}{v_{pevs,k}} \geq SoC_{pev_{ID}}^{max}\ \ and\ P_{pev_{ID},k} < 0 \\ 0, & otherwise \end{cases} \tag{3.117}$$

$$\delta_{pev_{ID}}^{fullyDischarged} = \begin{cases} 1, if\ \ SoC_{pev_{ID},k} + \left|P_{pev_{ID},k}\right| \cdot \dfrac{T_s}{v_{pevs,k} \cdot \eta_{dis}^{pev_{ID}}} \leq SoC_{pev_{ID}}^{min}\ \ and\ P_{pev_{ID},k} > 0 \\ 0, \quad otherwise \end{cases} \tag{3.118}$$

   - Update the availability of PEVs. Only the PEVs that are not fully charged when the PEV parking is charging and that are not fully discharged when it is discharging will participate in the redispatch process.

$$\delta_{pev_{ID},k}^{available} = \begin{cases} \left(1 - \delta_{pev_{ID}}^{fullyCharged}\right) \cdot \delta_{pev_{ID},k}^{available}, & if\ P_{pev_{ID},k} < 0 \\ \left(1 - \delta_{pev_{ID}}^{fullyCharged}\right) \cdot \delta_{pev_{ID},k}^{available}, & if\ P_{pev_{ID},k} > 0 \end{cases} \tag{3.119}$$

   - Update the power reference $P_{pevs,k}^{ref}$. Calculate the remaining power reference that was not assigned to any PEV, using equation (3.120).

$$P_{pevs,k}^{ref} = P_{pevs,k}^{ref} - \sum_{ID=1}^{N_{PEV}} P_{pev_{ID},k} \cdot \left(1 - \delta_{pev_{ID},k}^{available}\right) \tag{3.120}$$

   - Repeat the steps 2 and 3 if the number of retries is smaller than a predefined threshold, namely $MaxNumRetries$; otherwise, execute step 5.

5. **Maximum power boundaries definition:**
   - Determine the maximum discharging ($P_{pevs,k+1}^{MAX}$) and charging ($P_{pevs,k+1}^{MIN}$) power rate for the PEV parking for the next step $k+1$, considering that the power $P_{pev_{ID},k}$ will be applied at instant k, by implementing the equations (3.121) – (3.123).

$$\begin{aligned} SoC_{pev_{ID},k+1} = SoC_{pev_{ID},k} &- P_{pev_{ID},k} \cdot \left(P_{pev_{ID},k} > 0\right) \cdot \frac{T_s}{v_{pevs,k} \cdot \eta_{dis}} \\ &- P_{pev_{ID},k} \cdot \left(P_{pev_{ID},k} < 0\right) \cdot \frac{\eta_{ch} \cdot T_s}{v_{pevs,k}} \end{aligned} \tag{3.121}$$

$$P_{pevs,k+1}^{MIN} = -\sum_{ID=1}^{ID=N_{PEV}} \min\left(-P_{pev_{ID}}^{MIN}; \frac{SoC_{pev_{ID}}^{max} - SoC_{pev_{ID},k+1}}{\frac{\eta_{ch}^{pev_{ID}} \cdot T_s}{v_{pevs,k}}}\right), if\ charging \quad (3.122)$$

$$P_{pevs,k+1}^{MAX} = \sum_{ID=1}^{ID=N_{PEV}} \min\left(P_{pev_{ID}}^{MAX}; \frac{SoC_{pev_{ID},k+1} - SoC_{pev_{ID}}^{min}}{\frac{T_s}{v_{pevs,k} \cdot \eta_{dis}^{pev_{ID}}}}\right), if\ discharging \quad (3.123)$$

3.6 Conclusion

In the view of providing a global understanding of the whole hierarchical building energy management system, this chapter describes the five control units that compose the proposed controller, notably the two model predictive controllers in cascade, the two data-driven modules and the power-sharing module. Since the core of the designed BEMS is the MPC structure, special attention was drawn on its design, by highlighting its internal linear model and its fundamental constraints to keep the safe operation of the BMG, while respecting the limitations imposed by the French grid code.

The linear equations in the form of state representation to estimate the total energy stored in batteries pack, PEV batteries and hydrogen tank were extensively detailed by pointing out its main input parameters and indicating how to embed them into the two-level hierarchical MPC. Furthermore, a brief introduction of the two MPCs cost function was provided, as well as their input and output signals to interact with other adjunct modules in the hierarchical architecture, including the data-driven units. In the following chapters, these two data-oriented modules to enhance the precision of the BMG state estimation and to adjust the EMPC cost function to assure the minimum marks of annual self-consumption at minimum costs will be further detailed.

Chapter 4 Real-time model identification

4.1 Introduction

Energy Storage Systems (ESS) are key elements for enabling the design of MGs in buildings, specially to deal with the stochastic behaviour of renewable energy resources and to promote peak shifting. However, inaccuracies in the mathematical models of ESS due to temperature and ageing effects may reduce the performance of an MPC structure. Although the MPC have proved their robustness against environmental disturbances even with simplified plant model [37], [49], [117], [184]–[186], there is a lack in evaluating its performance under environmental changes, such as temperature, electric devices ageing and model parameters inaccuracy.

In the literature [37], [49], ESS models in MPC architecture are usually composed of time-invariant parameters derived from manufacture's technical specification. However, based on more realistic models of Li-ion batteries [204], electrolysers [223] and fuel cells [205], the efficiency during their charge or discharge, their nominal voltage and other critical inherent parameters change according to the intensity of the current, equipment age and temperature.

Concerning batteries, the voltage variation can be around 10% of nominal voltage when they are fully charged and discharged [213], [224]. Moreover, at the end of their life, batteries can lose from 10% to 20% of their initial capacity [213]. On the other hand, regarding PEM electrolysers and fuel cells, the cells overpotential are very sensitive to temperature and the level of cells degradation [223],[205],[219]. The cell voltage is directly correlated to the temperature in the case of electrolysers and inversely correlated in fuel-cell configuration [217]. The voltage offset in PEM technology affects the round-trip efficiency, once the chemical hydrogen reaction is mainly dependent on the current flowing through the PEM cells, following Faraday's law of electrolysis [219]. Therefore, this implies a different hydrogen flow for the same amount of delivered power, depending on the operating temperature and their degradation level. Consequently, additional uncertainties on $i_{t,k+1}^{bat}$ and LoH_{k+1} estimation arise with static-parameter models, which may result in under or overuse of ESSs.

To face these uncertainties, there are several techniques to estimate better the intrinsic parameters of batteries, PEMFC and PEME. In the case of batteries, Arrhenius equation [225], or models devised from technical specifications [226] are usually adopted. Concerning hydrogen ESS, models based on physical structure of the PEMFC can result in a very accurate model [218]. Still, it is too complex to be embedded in MPC prediction as it requires a considerable number of parameters that are usually unknown or hard to be measured. In contrast, in [207], it is proposed a simple PEM electrolyser model by fitting sample measurements to a logarithmic equation, but its parameters are static for a single temperature and may be inaccurate for long-term operation. Moreover, these modelling types require

beforehand model calibration, which can lead to uncertainties throughout the entire life of batteries, PEMFC and PEME.

In front of this problem, to tackle model inaccuracies due to ageing effects, [227] reviewed some linear and non-linear models capable of emulating the batteries ageing and hydrogen ESS models and summarized some common health-conscious energy management strategies to prolong the lifespan of ESS. However, the prognostic in MPC strategies reviewed in this paper are resumed to constraining the batteries' SoC and limiting the number of start-up and shut-down of hydrogen ESS. The model inaccuracy due to the ESS ageing seems to be usually neglected when designing MPC.

With the technological advance in telecommunication, strategies based on data analysis have been increasingly implemented in the early years. The most pertinent algorithms to deal with batteries inaccuracy are incremental analysis of the voltage and capacity to estimate the state of health of batteries [224], [228], Kalman filter estimator [229] and other machine learning methods [213]. Concerning hydrogen ESS, in [230], it was reviewed some important model observer that would enable the EMS to anticipate PEMFC model changes.

In this perspective, aiming at reinforcing the MPC robustness, a data-driven algorithm for Real-Time Model Identification (RTMI) of Lithium-ion batteries and hydrogen ESS was designed to empower the two-level Hierarchical Model Predictive Controller (HMPC) described in Chapter 3 with more accurate state estimation. Envisaging to make maximum use of BMG resources without overexploiting them, the objective of the RTMI algorithm is to enhance the prediction of the energy stored in the batteries pack and the hydrogen tank (i.e. $i_{t,k+1}^{bat}$, and LoH_{k+1}) continuously and automatically without demanding a complex mathematical model. Remarkably, the RTMI does not deal with the model inaccuracy of the PEV batteries because it is considered that a similar module is embedded in each PEV so that the charging station provides accurate values concerning its battery parameters.

The proposed RTMI implements a dynamic algorithm to identify in real-time the model parameters of f_{bat}, f_{els} and f_{fc} of equations (3.58) and (3.85) continuously based on the measurements and past information of the plant. This module aims to identify accurate values of ESS models, without needing a thoughtful pre-modelling step, which can strengthen the flexibility and robustness of the controller.

Therefore, this chapter is structured as follows. The iterative process for identifying f_{bat} in real-time is detailed in section 4.2, whereas the algorithm to tackle the uncertainties in the hydrogen ESS model is explained in section 4.3. Finally, the conclusions on the advantages and disadvantages of the proposed approach are summarized in section 4.4.

4.2 Detail of the RTMI algorithm for batteries

The RTMI algorithm to deal with the batteries model inaccuracy is divided into two folds. The first part of the algorithm is to enhance $i_{t,k+1}^{bat}$ estimation by identifying the parameters of f_{bat}, namely θ-parameters of equation (3.58) composed of θ_{cc}, θ_{dc}, θ_{dd} and θ_{cd}. The second part of the algorithm is to identify the maximum and minimum boundaries of the batteries' capacity, namely $i_{t_{bat},k}^{max}$ and $i_{t_{bat},k}^{min}$ that define the inequality constraints (3.96) in the HMPC.

These two portions of the algorithm were designed based on the discharge curve of batteries, in which its allure is shown in Fig. 4.1 for different cell temperature T_{cell}. The θ-parameters are adjusted so that the quadruple ($i_{t,k-1}^{bat}$, $P_{bat,k-1}$, $\Delta i_{t,k}^{bat}$,v_k) computed by the HMPC approaches as much as possible to the real ($i_{t,k-1}^{meas}$, $P_{bat,k-1}^{meas}$, $\Delta i_{t,k}^{meas}$, v_k^{meas}) measured between $k-1$ and k.

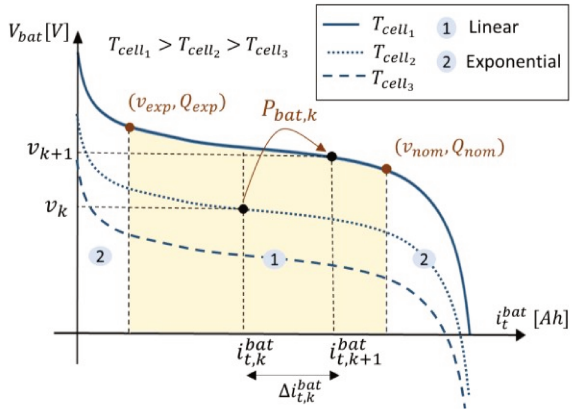

Fig. 4.1: Discharge curves of a Li-ion battery under temperature cell variations.

Notably, the validity of the linear model of equation (3.58) is conditional to the batteries operation inside the linear zone limited by Q_{exp} and Q_{nom} (i.e. $Q_{exp} \leq i_t^{bat} \leq Q_{nom}$) as shown in Fig. 4.1, where Q_{exp} is the battery charge at the battery exponential voltage (v_{exp}) and Q_{nom} is the battery charge at the nominal voltage (v_{nom}). Since the batteries voltage rises abruptly for charge bellow Q_{exp} and sharply drop for charge over Q_{nom}, the proposed linear model of (3.58) is only accurate inside the linear zone. The voltage variation in the linear area does not harm the precision of the batteries state estimation because it follows a linear tendency that is compensated by including $i_{t,k}^{bat}$ in the formulation of (3.58). Consequently, to guarantee the validity of the model, RTMI updates $i_{t_{bat},k}^{max}$ and $i_{t_{bat},k}^{min}$ to limit the operation of the batteries within this linear zone. In other words, $i_{t_{bat},k}^{max}$ tends to approach to Q_{nom}, whereas $i_{t_{bat},k}^{min}$ converges to Q_{exp}.

The θ-parameters are calculated based on an interactive and real-time algorithm, as shown in Fig. 4.2. Synchronized with the HMPC, the RTMI module acquires a new measurement point, composed by the battery current (i) and voltage (v). From the current measurement, it is possible to calculate the integral of the current defined by $i_t = \int i \, dt$.

To improve the robustness against cell temperature (T_{cell}) variations, the RTMI identifies a linear model for a temperature range defined a priori. Without any temperature sensor, the RTMI algorithm estimates the cell temperature $\hat{T}_{cell}$ using the voltage v and i_t measurements. Consequently, the RTMI sends daily to HMPC only the θ-parameters corresponding to the most likely temperature for the next day, which is the average battery temperature of the previous day (T_{avg}).

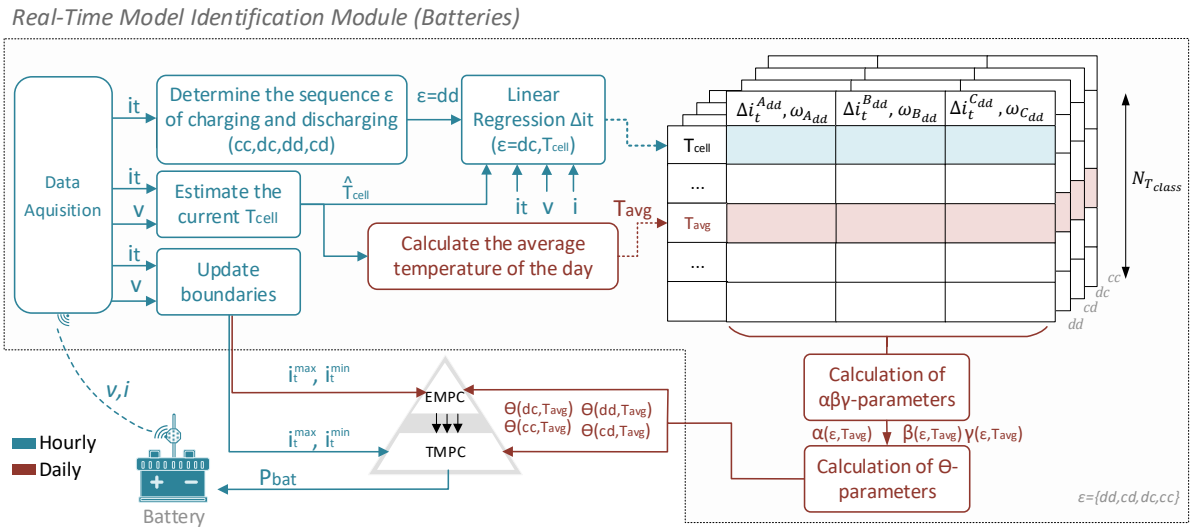

Fig. 4.2: Real-Time model identification of the parameters for Li-ion battery model.

As detailed in the following subsections, the RTMI algorithm is divided into three steps, namely: classification, updating, and identification of the limits for charging and discharging the batteries.

4.2.1 *Step 1: Classification of data measurements by temperature interval*

As depicted in Fig. 4.3a, v is directly correlated to T_{cell}. This effect in the battery voltage impacts the batteries round-trip efficiency, reducing the accuracy of the classic model defined by (3.32). Higher voltage when charging the batteries or lower voltages when discharging them implies a loss of efficiency, since the storage energy variation ($\Delta i_{t,k}^{bat}$) is mainly dependent on the current flowing through the batterie cells (equation (3.36)). Therefore, aiming to improve the robustness against T_{cell} disturbance, the RTMI fits a linear model for each temperature ranges using classified measurements points based on the estimation of $\hat{T}_{cell}$.

The RTMI algorithm estimates the temperature interval from v measurements. Fig. 4.3a shows that T_{cell} mainly involves a vertical offset in the batteries discharge curve, but almost does not affect the slope of v with respect to i_t. In this way, the maximum amplitude of v (Δv_{MAX} defined by (4.1)) due to the full charges ($i_t^{bat} = i_t^{min}$) and discharges ($i_t^{bat} = i_t^{max}$) of the batteries is almost unchanged, resulting in a quasi-constant slope along different T_{cell}, as depicted in Fig. 4.3b.

$$\Delta v_{MAX} = v\left(i_t^{min}\right) - v(i_t^{max}) \tag{4.1}$$

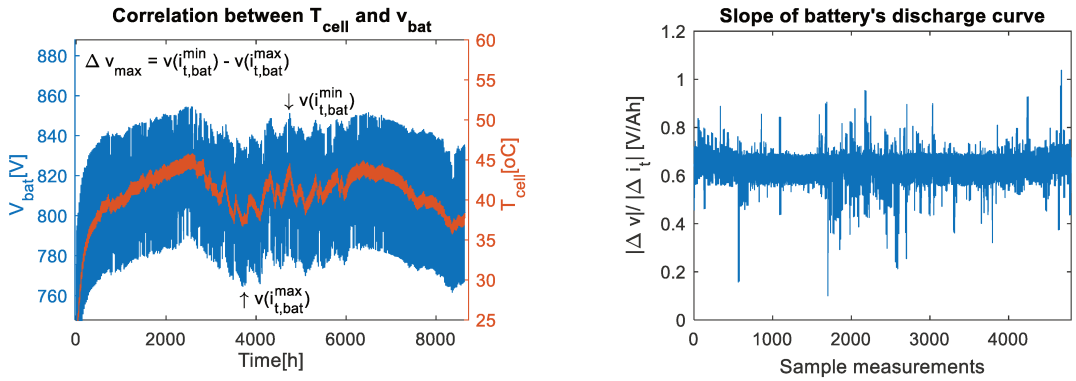

Fig. 4.3: One-year simulation of the BMG with $SoC_{max} = 80\%$ and $SoC_{min} = 20\%$ (a) Battery voltage and cell temperature correlation. (b) Slope of the battery discharge curve.

Consequently, when the batteries operate for the first time, the BEMS will force two charges and discharges of the batteries to determine the slope of the discharge curve ($\frac{dv}{di_t}$). Indeed, only one charge-discharge cycle is enough to identify $\frac{dv}{di_t}$, but it is more judicious to measure it at least twice. It is important to highlight that the estimation of $\frac{dv}{di_t}$ takes as hypothesis that the variation of cell temperature during a complete charging-discharge cycle is negligible. For this reason, it is wise to force the BEMS to discharge and charge the batteries continuously below their maximum current, in order to reduce the effects of temperature. Therefore, to avoid huge variations in the batteries' cell temperature during the RTMI initialisation step, the charging and discharging power rate are set up to 20% of batteries' maximum power rate, which is 12 kW according to Table 2.1.

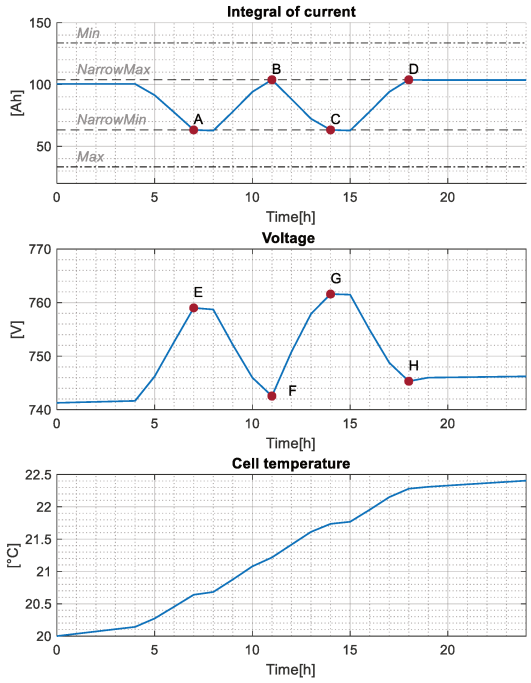

Fig. 4.4: Two forced charge-discharge cycles to identify the slope $\left|\frac{dv}{dt}\right|$ of Lithium-ion batteries.

The two first charges and discharges enable BEMS to determine the points A to H indicated in Fig. 4.4, where their coordinates are summarized in Table 4.1. Remarkably, these two charge-discharge cycles are limited to narrow boundaries $i_{t,k}^{NarrowMin}$ and $i_{t,k}^{NarrowMax}$, defined by (4.2) and (4.3), respectively. This reduction of the original boundaries $i_{t,k}^{Min}$ and $i_{t,k}^{Max}$ is to guarantee that during the two cycles the batteries are likely to operate in the linear zone. Therefore, $\frac{dv}{di_t}$ can be estimated by calculating the average of the two $\frac{dv}{di_t}$ measures, through the equation (4.4).

$$i_{t,k}^{NarrowMin} = i_{t,k}^{Min} + 0.3\left(i_{t,k}^{Max} - i_{t,k}^{Min}\right) \tag{4.2}$$

$$i_{t,k}^{NarrowMin} = i_{t,k}^{Max} - 0.3\left(i_{t,k}^{Max} - i_{t,k}^{Min}\right) \tag{4.3}$$

$$\frac{dv}{di_t} = \frac{1}{2}\left(\frac{v_{bat}^{min1} - v_{bat}^{max1}}{i_{t,bat}^{min1} - i_{t,bat}^{max1}} + \frac{v_{bat}^{min2} - v_{bat}^{max2}}{i_{t,bat}^{min2} - i_{t,bat}^{max2}}\right) \tag{4.4}$$

Table 4.1: Measurement points of battery voltage ($\boldsymbol{v}$) and integral ($\boldsymbol{i_t}$) of current for estimating the slope $\frac{\boldsymbol{dv}}{\boldsymbol{di_t}}$

Measurement	$\boldsymbol{t_1}$	$\boldsymbol{t_2}$	$\boldsymbol{t_3}$	$\boldsymbol{t_4}$
Voltage (v_{bat}^{meas})	$A = (t_1, v_{bat}^{min1})$	$B = (t_2, v_{bat}^{max1})$	$C = (t_1, v_{bat}^{min2})$	$D = (t_2, v_{bat}^{max2})$
Battery charge (i_t^{bat})	$E = (t_1, i_{t,bat}^{min1})$	$F = (t_2, i_{t,bat}^{max1})$	$G = (t_1, i_{t,bat}^{min2})$	$H = (t_2, i_{t,bat}^{max2})$

Once calculated $\frac{dv}{di_t}$, it is possible to determine the classifications of RTMI measurements through voltage measurement (v). The temperature classes are divided by the lines $\vec{s}_{T_{class}}$ defined by the equation (4.5) and shown in Fig. 4.5, where $T_{class} \in \mathbb{Z}$ is the identification number for a specific temperature class. The lines $\vec{s}_{T_{class}}$ are outspread from a voltage interval Δv_{class} which is chosen a priori regarding the desired precision, the computing resources and the RTMI convergence time.

$$\vec{s}_{T_{class}}: v = \frac{dv}{di_t} \cdot i_t^{bat} + T_{class} \cdot \Delta v_{class} \tag{4.5}$$

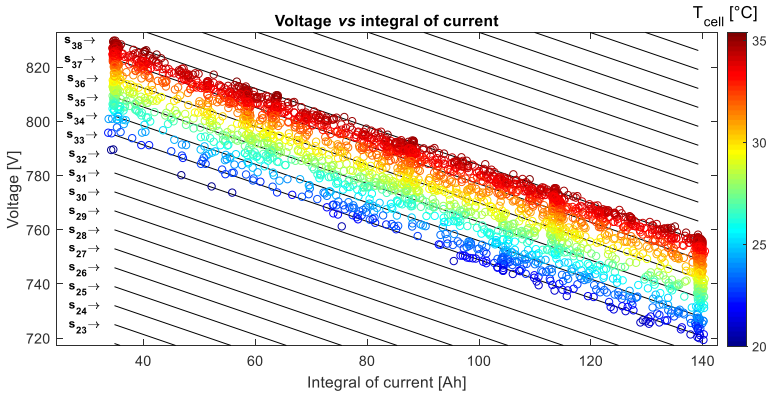

Fig. 4.5: Linear boundaries $\vec{s}_{T_{class}}$ separating the measurement points of voltage and integral of current under different battery cell temperature.

Therefore, knowing the nominal battery voltage (v_{nom}) and its maximum tolerance (tol), it is possible to determine the number of temperature classes (N_{Tclass}) and the value of Δv_{class}. For example,

considering a battery of $Q_{nom} = 167Ah, V_{nom} = 720V$ with tolerance $tol = 30\%$, the value of Δv_{class} can be calculated following the algorithm detailed in Table 4.2.

Table 4.2: Algorithm to define the boundaries of the temperature classes.

1. Calculate the maximum voltage allowed based on the given value of tol:
$$v_{max} = v_{nom} \cdot (1 + tol) = 720 \cdot (1 + 0.3) = 936V$$

2. Calculate the value of Δv_{class} separating two consecutive classes. It depends on the desired model accuracy and the convergency of the algorithm. This value can be, for instance, 1% of battery nominal voltage.
$$\Delta v_{class} = \frac{v_{nom}}{100} = \frac{720}{100} = 7.2\ V$$

3. Calculate the total number of temperature classes ($N_{T_{class}}$):
$$N_{T_{class}} = ceil\left(\frac{v_{max}}{\Delta v_{T_{class}}}\right) = 130\ classes$$

4. Based on the equation of $\vec{s}_{T_{class}}$ (equation (4.5)), $\forall\ i_t^{bat} \in \left[i_t^{min}, i_t^{max}\right]$ and $T_{class} \in \{0; N_{T_{class}}\}$:
$$v_{max}^{T_{class}}\left(i_t^{bat}\right) = \frac{dv}{di_t} \cdot i_t^{bat} + T_{class} \cdot \Delta v_{class}$$
$$v_{min}^{T_{class}}\left(i_t^{bat}\right) = \frac{dv}{di_t} \cdot i_t^{bat} + (T_{class} - 1) \cdot \Delta v_{class}$$

As a result, a measurement $M = \left(i_{t,k-1}^{bat}, P_{bat,k-1}, \Delta i_{t,k}^{bat}, v_{k-1}^{bat}\right) = \left(i_t^M, P_{bat}^M, \Delta i_t^M, v^M\right)$ belongs to T_{class}, if and only if, the voltage v^M is in between the lines $\vec{s}_{T_{class}}$ and $\vec{s}_{T_{class}+1}$. In other words, the class T_{class} must satisfy the condition of (4.6).

$$v_{min}^{T_{class}}(i_t^M) \leq\ v^M \leq v_{max}^{T_{class}}(i_t^M) \tag{4.6}$$

4.2.2 *Step 2: Updating the values of the batteries model parameters*

Once determined which class of temperature the measurement M belongs to, it is possible to adjust the θ-parameter of this respective T_{class}. As shown in Fig. 4.2, θ-parameters is calculated from the intermediate parameters α_ε, β_ε and γ_ε, named $\alpha\beta\gamma$-parameters. As presented previously in Chapter 3, $\alpha\beta\gamma$-parameters defines the equation (4.7) that can be interpreted as a plan π_ε that is active depending on the status $\varepsilon = \{cc, dc, dd, cd\}$, as illustrated in Fig. 4.6.

$$\begin{aligned}\Delta \mathrm{i_t} = {} & \alpha_{cc}P_{cc,k} + \beta_{cc}i_{t,k-1}^{bat} + \gamma_{cc}\delta_{cc,k} + \\ & \alpha_{cd}P_{cd,k} + \beta_{cd}i_{t,k-1} + \gamma_{cd}\delta_{cd,k} + \\ & \alpha_{dd}P_{dd,k} + \beta_{dd}i_{t,k-1} + \gamma_{dd}\delta_{dd,k} + \\ & \alpha_{dc}P_{dc,k} + \beta_{dc}i_{t,k-1} + \gamma_{dc}\delta_{dc,k}\end{aligned} \tag{4.7}$$

The plan π_ε covers the feasible zone of operation of the batteries, which corresponds to the limits of the HMPC (equations (4.8) – (4.10)) extended in 20%. Remarkably, the plan π_ε can be determined by identifying three pivot points, namely A_ε, B_ε and C_ε, in which their coordinates are one of the four extremities of the enlarged zone, as shown in Table 4.3. The third dimension of the pivot points (i.e. z-coordinate), referring to $\Delta i_t^{A_\varepsilon}$, $\Delta i_t^{B_\varepsilon}$ and $\Delta i_t^{C_\varepsilon}$ are initialized with the values calculated using the standard model defined by (3.32), as specified in Table 4.3.

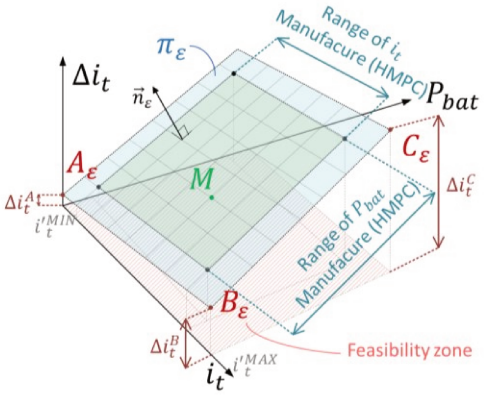

Fig. 4.6: Model perspective with the three pivot points for predicting the variation of the battery charge (Δi_t).

$$i_{t,bat}^{min} \leq i_t \leq i_{t,bat}^{max} \tag{4.8}$$

$$0 \leq P_{bat} \leq P_{bat}^{max}, if\ \varepsilon = \{cd, dd\} \tag{4.9}$$

$$P_{bat}^{min} \leq P_{bat} \leq 0, if\ \varepsilon = \{cc, dc\} \tag{4.10}$$

Table 4.3: Coordinates of the three pivot points.

Pivot point	Discharging ($\boldsymbol{\varepsilon = \{cd, dd\}}$)	Charging ($\boldsymbol{\varepsilon = \{dc, cc\}}$)
$\boldsymbol{A_\varepsilon}$	$P_{bat}^{A_\varepsilon} = -0.2 \cdot \left(P_{bat}^{max} - P_{bat}^{min}\right)$ $i_t^{A_\varepsilon} = i_{t,bat}^{min} - 0.2 \cdot \left(i_{t,bat}^{max} - i_{t,bat}^{min}\right)$ $\Delta i_{t,0}^{A} = \frac{T_s}{Q_{nom} v_{nom} \eta_{dis}} \cdot P_{bat}^{A_\varepsilon}$	$P_{bat}^{A_\varepsilon} = 0.2 \cdot \left(P_{bat}^{max} - P_{bat}^{min}\right)$ $i_t^{A_\varepsilon} = i_{t,bat}^{max} + 0.2 \cdot \left(i_{t,bat}^{max} - i_{t,bat}^{min}\right)$ $\Delta i_{t,0}^{A} = \frac{\eta_{ch} T_s}{Q_{nom} v_{nom}} \cdot P_{bat}^{A_\varepsilon}$
$\boldsymbol{B_\varepsilon}$	$P_{bat}^{B_\varepsilon} = -0.2 \cdot \left(P_{bat}^{max} - P_{bat}^{min}\right)$ $i_t^{B_\varepsilon} = i_{t,bat}^{min} - 0.2 \cdot \left(i_{t,bat}^{max} - i_{t,bat}^{min}\right)$ $\Delta i_{t,0}^{B} = \frac{T_s}{Q_{nom} v_{nom} \eta_{dis}} \cdot P_{bat}^{B_\varepsilon}$	$P_{bat}^{B_\varepsilon} = 0.2 \cdot \left(P_{bat}^{max} - P_{bat}^{min}\right)$ $i_t^{B_\varepsilon} = i_{t,bat}^{max} + 0.2 \cdot \left(i_{t,bat}^{max} - i_{t,bat}^{min}\right)$ $\Delta i_{t,0}^{B} = \frac{\eta_{ch} T_s}{Q_{nom} v_{nom}} \cdot P_{bat}^{B_\varepsilon}$
$\boldsymbol{C_\varepsilon}$	$P_{bat}^{C_\varepsilon} = P_{bat}^{max} + 0.2 \cdot \left(P_{bat}^{max} - P_{bat}^{min}\right)$ $i_t^{C_\varepsilon} = i_{t,bat}^{min} - 0.2 \cdot \left(i_{t,bat}^{max} - i_{t,bat}^{min}\right)$ $\Delta i_{t,0}^{C} = \frac{T_s}{Q_{nom} v_{nom} \eta_{dis}} \cdot P_{bat}^{C_\varepsilon}$	$P_{bat}^{C_\varepsilon} = P_{bat}^{min} - 0.2 \cdot \left(P_{bat}^{max} - P_{bat}^{min}\right)$ $i_t^{C_\varepsilon} = i_{t,bat}^{max} + 0.2 \cdot \left(i_{t,bat}^{max} - i_{t,bat}^{min}\right)$ $\Delta i_{t,0}^{C} = \frac{\eta_{ch} T_s}{Q_{nom} v_{nom}} \cdot P_{bat}^{C_\varepsilon}$

By using the coordinates of these three pivot points, the plan π_ε can be determined using principles of analytical geometry. By calculating the cross product of two non-linear dependent vectors that belong to the plane π_ε and dividing it by its norm, it is possible to determine the vector orthonormal to the plan π_ε, named $\vec{n}_\varepsilon = \langle a, b, c \rangle$. Therefore, the general equation of the plan π_ε can be calculated through $\vec{n}_\varepsilon$ and a point belonging to the plan π_ε, as defined in equation (4.11) for the point A_ε. The coordinates of the orthonormal vector $\vec{n}_\varepsilon$ can be calculated using the vectors $\overrightarrow{A_\varepsilon B_\varepsilon}$ and $\overrightarrow{A_\varepsilon C_\varepsilon}$, as specified in equation (4.12).

$$a \cdot \left(P_{bat} - P_{bat}^{A_\varepsilon}\right) + b \cdot \left(i_t - i_t^{A_\varepsilon}\right) + c \cdot \left(\Delta i_t - \Delta i_t^{A_\varepsilon}\right) = 0 \tag{4.11}$$

Where,

$$\vec{n}_\varepsilon = \langle a, b, c \rangle = \frac{\overrightarrow{A_\varepsilon B_\varepsilon} \times \overrightarrow{A_\varepsilon C_\varepsilon}}{\left\| \overrightarrow{A_\varepsilon B_\varepsilon} \times \overrightarrow{A_\varepsilon C_\varepsilon} \right\|} \tag{4.12}$$

Therefore, $\alpha\beta\gamma$-parameters can be determined following equations (4.13) – (4.15).

$$\alpha_\varepsilon = \frac{a}{c} \tag{4.13}$$

$$\beta_\varepsilon = \frac{b}{c} \tag{4.14}$$

$$\gamma_\varepsilon = -\frac{a}{c} \cdot P_{bat}^{A_\varepsilon} - \frac{b}{c} \cdot i_t^{A_\varepsilon} - \Delta i_t^{A_\varepsilon} \tag{4.15}$$

The update of $\alpha\beta\gamma$-parameters consists of adjusting the z-coordinates of the pivot points A_ε, B_ε and C_ε (i.e. $\Delta i_t^{A_\varepsilon}$, $\Delta i_t^{B_\varepsilon}$ and $\Delta i_t^{C_\varepsilon}$) as soon as a new measurement M is acquired. In this way, the xy-coordinates, referring to $P_{bat}^{A_\varepsilon}$, $P_{bat}^{B_\varepsilon}$, $P_{bat}^{C_\varepsilon}$, $i_t^{A_\varepsilon}$, $i_t^{B_\varepsilon}$and $i_t^{C_\varepsilon}$ are kept constant.

The utmost advantage of the RTMI algorithm is the non-dependency on the storage of the past measurements. The knowledge of the previous measures is stored in dynamic confidence weights, named $\omega_{A_\varepsilon,k}$, $\omega_{B_\varepsilon,k}$ and $\omega_{C_\varepsilon,k}$. Notably, only a set of parameters are stored in the memory. As shown in Fig. 4.2, all data can be structure into a unique matrix with dimension $N_{T_{class}} \times 3 \times 4$, where the number of rows refers to the number of cell temperature classes ($N_{T_{class}}$), the number of columns corresponds to the three parameters $\Delta i_t^{A_\varepsilon}$, $\Delta i_t^{B_\varepsilon}$ and $\Delta i_t^{C_\varepsilon}$ and their associated confidence weights ω_{A_ε}, ω_{B_ε} and ω_{C_ε}, and its third dimension refers to the four battery status $\varepsilon = \{cc, dc, dd, cd\}$.

Starting from small values – typically between 0.1 and 1.0 – these confidence weights grow with the acquisition of new measurements. For the first iteration, the pivot points are initialized according to Table 4.3, where the parameters given by the technical specification of the batteries and using the classical model defined by (3.32) are used. Thereafter, the values of $\Delta i_{t,k}^{A_\varepsilon}$, $\Delta i_{t,k}^{B_\varepsilon}$ and $\Delta i_{t,k}^{C_\varepsilon}$ are updated so that the plan $\pi_{\varepsilon,k+1}$ approaches to the new measurement M. To achieve this, an intermediate plan ϕ_ε defined by the intermediate pivot points A'_ε, B'_ε and C'_ε, with z-coordinates equal to z_A, z_B and z_C is used, as shown in Fig. 4.7. These z-coordinates are calculated through the optimisation of the cost function defined by (4.16). The plan ϕ_ε contains the point M and is determined to make z_A, z_B and z_C as close as possible to $\Delta i_{t,k}^{A_\varepsilon}$, $\Delta i_{t,k}^{B_\varepsilon}$ and $\Delta i_{t,k}^{C_\varepsilon}$.

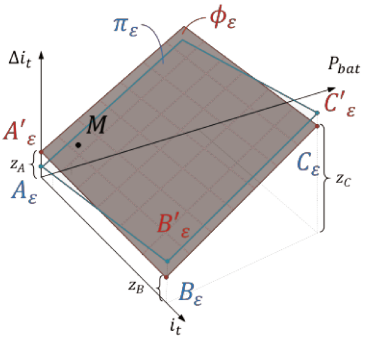

Fig. 4.7: Intermediate plan ϕ_ε to update the z-coordinates of the three pivot points.

$$z_A, z_B, z_C = \arg\left(\min_{z_A,z_B,z_C} n_{A,k}\left(\Delta i_{t,k}^{A} - z_A\right)^2 + n_{B,k}\left(\Delta i_{t,k}^{B} - z_B\right)^2 + n_{C,k}\left(\Delta i_{t,k}^{C} - z_C\right)^2\right) \tag{4.16}$$

Subject to

$$M \in A'_\varepsilon B'_\varepsilon C'_\varepsilon;\ z_A, z_B, z_C \geq 0$$

Intuitively, in equation (4.16), the high value of $n_{A,k}$ and low values of $n_{B,k}$ and $n_{C,k}$ lead z_A to approach to $\Delta i_{t,k}^{A}$ faster than z_B and z_C to $\Delta i_{t,k}^{B}$ and $\Delta i_{t,k}^{C}$, whereas balanced values of $n_{A,k}$, $n_{B,k}$ and $n_{C,k}$ result in a fair variation among z_A, z_B and z_C. The weights of (4.16) are calculated with regard to the normalized distance between the measure M and the respective intermediate pivot point projected on the plan $xy = P_{bat} \times i_t$ (i.e. operator $\|\cdot\|_{xy}$), as can be visualized in Fig. 4.8.

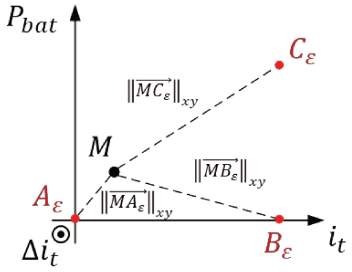

Fig. 4.8: Projected distances of the pivot points and the measurement point onto the plan P_{bat} *vs* i_t.

The weighting based on the geometric distance $\|\cdot\|_{xy}$ assumes that the nearer the measure M is to a pivot point, the more confident is its coordinates with respect to this pivot point. For instance, if a measure M is near to the pivot point A_ε and far from the other two – as shown in Fig. 4.8 – this means that the coordinates of A_ε should be close to the coordinates of M to obtain the highest model precision. Controversially, since the pivot points B_ε and C_ε are far from M, the true coordinates of B_ε and C_ε cannot be deducted with certainty only from the observations of M. Consequently, the z-coordinates of A_ε should be moved more drastically toward M than the z-coordinates of B_ε and C_ε, which results in $n_{A,k} < n_{B,k} \cong n_{c,k}$. Therefore, the weights of (4.16) are calculated using (4.17) – (4.19).

$$n_{A,k} = \frac{\|\overline{MA_\varepsilon}\|_{xy}}{\|\overline{MA_\varepsilon}\|_{xy} + \|\overline{MB_\varepsilon}\|_{xy} + \|\overline{MC_\varepsilon}\|_{xy}} \tag{4.17}$$

$$n_{B,k} = \frac{\|\overline{MB_\varepsilon}\|_{xy}}{\|\overline{MA_\varepsilon}\|_{xy} + \|\overline{MB_\varepsilon}\|_{xy} + \|\overline{MC_\varepsilon}\|_{xy}} \tag{4.18}$$

$$n_{C,k} = \frac{\|\overline{MC_\varepsilon}\|_{xy}}{\|\overline{MA_\varepsilon}\|_{xy} + \|\overline{MB_\varepsilon}\|_{xy} + \|\overline{MC_\varepsilon}\|_{xy}} \tag{4.19}$$

Once determined the intermediary plan ϕ_ε, $\Delta i_{t,k}^{A}$, $\Delta i_{t,k}^{B}$ and $\Delta i_{t,k}^{C}$, the confidence weights $\omega_{A,k}$, $\omega_{B,k}$ and $\omega_{C,k}$ are updated following equations (4.20) – (4.23), in the order of compilation. For the sake of simplicity, it will only be detailed the updating process of the pivot point A_ε, but it is important to highlight that similar equations are used for B_ε and C_ε.

$$\omega_{A,k+1} = \omega_{A,k} + \frac{\frac{1}{\|\overline{MA}\|_{xy}}}{\frac{1}{\|\overline{MA}\|_{xy}} + \frac{1}{\|\overline{MB}\|_{xy}} + \frac{1}{\|\overline{MC}\|_{xy}}} \tag{4.20}$$

$$\omega_{inertia,k}^{A} = \sigma\left(\omega_{A,k+1} - \omega_{A,k}\right) \leq \omega_{A,k+1} \tag{4.21}$$

$$\Delta i_{t,k+1}^{A} = \frac{\Delta i_{t,k}^{A} \cdot \omega_{inertia,k}^{A} + z_A \cdot \omega_{A,k+1}}{\omega_{inertia,k}^{A} + \omega_{A,k+1}} \tag{4.22}$$

$$\omega_{A,k+1} = \omega_{A,k+1} - \tau_{decay} \cdot \left(\omega_{A,k+1} - \omega_{min}\right) \tag{4.23}$$

Firstly, the confidence weight $\omega_{A,k}$ is updated using (4.20). The closer M is to the A_ε, the more reliable the value of z_A calculated from (4.16) is. Consequently, $\omega_{A,k+1}$ is inversely proportional to the distance between the pivot point A_ε and the measurement M, and it is normalised according to the distance from other pivot points (i.e. B_ε and C_ε). To improve the robustness against measurement noise, the updated $\Delta i_{t,k+1}^{A}$is a weighted value between the previous $\Delta i_{t,k}^{A}$ and the new fitted z_A. The inertial factor $\omega_{inertia,k}^{A}$ and the confidence weight $\omega_{A,k+1}$ handle the ponderation among these two variables, as defined in (4.22). The equilibrium amongst $\omega_{inertia,k}^{A}$ and $\omega_{A,k+1}$ control the convergence time of $\Delta i_{t,k+1}^{A}$ to z_A. This balance can be manually set by tuning the value of σ, which indicates the importance of the new measurement regarding the previous value. Notably, $\omega_{inertia,k}^{A}$ is upper limited by $\omega_{A,k+1}$, as specified in (4.21), to restrict the convergence time to a scale of two. Since the charge/discharge curve of batteries changes according to the level of degradation, the confidence weight $\omega_{A,k+1}$ gradually decreases with a time constant τ_{decay} until a minimum value ω_{min} which is equal to the starting value, as specified in (4.23).

With the new coordinates of A_ε, B_ε and C_ε, $\alpha\beta\gamma$-parameters are calculated using (4.13) – (4.15)(4.15) and the θ-parameters are determined by using (3.55) and (3.56), that are repeated bellow.

$$\theta_\varepsilon = \alpha_\varepsilon + \frac{1}{P_{bat}^{MAX}} \cdot \left(\gamma_\varepsilon + \frac{(i_t^{MAX} + i_t^{MIN}) \cdot \beta_\varepsilon}{2} \right), \text{if } \varepsilon = [cd, dd] \tag{4.24}$$

$$\theta_\varepsilon = \alpha_\varepsilon + \frac{1}{P_{bat}^{MIN}} \cdot \left(\gamma_\varepsilon + \frac{(i_t^{MAX} + i_t^{MIN}) \cdot \beta_\varepsilon}{2} \right), \text{if } \varepsilon = [cc, dc] \tag{4.25}$$

4.2.3 *Step 3: Identification of the limits for charging and discharging the batteries*

As mentioned before and illustrated in Fig. 4.1, the batteries must operate between points Q_{exp} and Q_{nom}. To achieve this, the strategy consists of adjusting $i_{t,bat}^{max}$ and $i_{t,bat}^{min}$ of HMPC constraints to reduce the variations of the slope $\frac{\Delta v}{\Delta i_t}$. According to Fig. 4.9, while i_t is inside the linear zone, the slope $\frac{\Delta v}{\Delta i_t}$ is quasi-constant, because v is linearly dependent on i_t. However, when operating outside this zone, $\frac{\Delta v}{\Delta i_t}$ is not constant because v is non-linear regarding i_t.

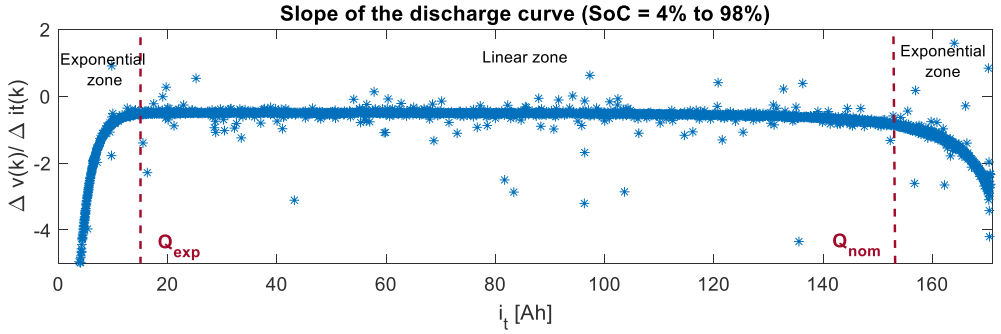

Fig. 4.9: The slope of the discharge curve as a function of i_t.

Based on this phenomenon, the developed algorithm for identifying the actual boundaries of i_t divides the temporal graphs into two zones, named $zone\ A$ and $zone\ B$, as illustrated in Fig. 4.10. The

zone A, indicated by the red dots, represents the range where the batteries operate in the linear zone very likely. On the other hand, the *zone B*, outlined by the blue dots, is the zone for which the battery can be either in the linear or non-linear region. Therefore, as shown in Fig. 4.11, *zone A* comprehends the range of the limits of i_t at the previous iteration (i.e. $i_{t,bat,k-1}^{min}$ and $i_{t,bat,k-1}^{max}$) reduced in 20%, whereas *zone B* is its complementary region.

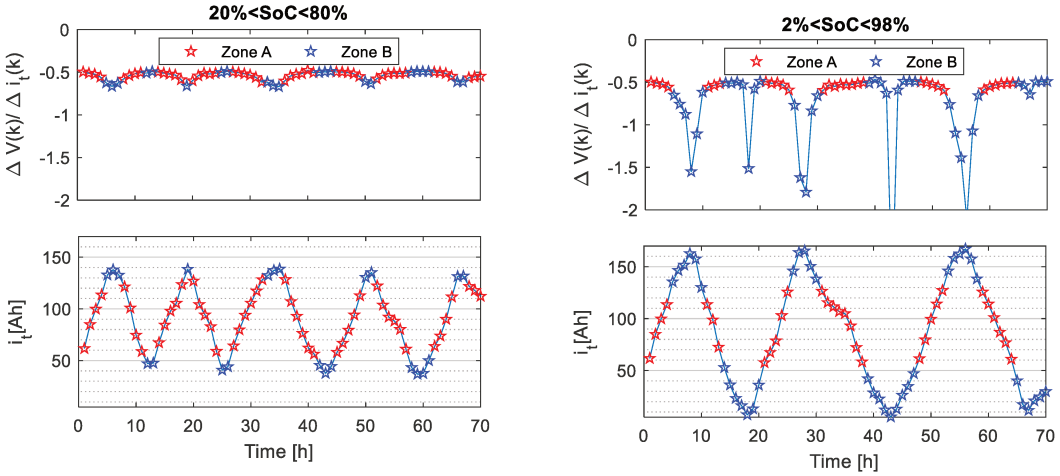

Fig. 4.10: Temporal evolution of the slope when operating (a) in the linear zone and (b) in the non-linear zone.

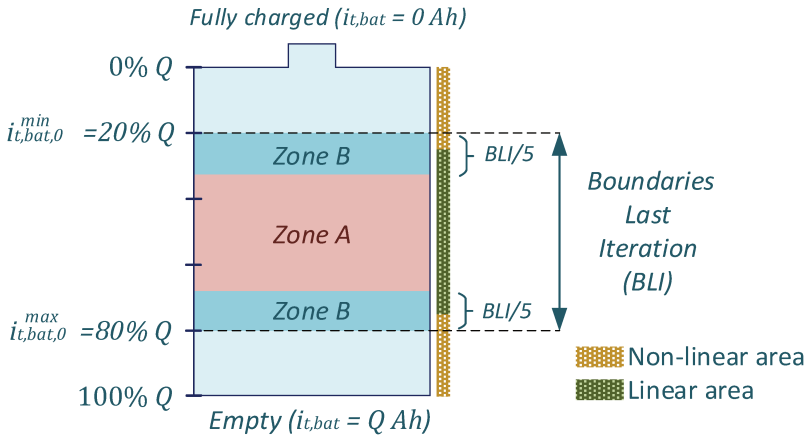

Fig. 4.11: Visualization of the definition of *zone A* and *zone B* with regard the predefined boundaries at $k = 0$ ($i_{t,0}^{min}$ and $i_{t,0}^{max}$).

Remarkably, the oscillation of the slope is more intense when zone B is in the non-linear zone (Fig. 4.10b) than when it is inside the linear range (Fig. 4.10a). As a result, to determine whether zone B corresponds to the linear or non-linear range, the average of the absolute difference between each $\left|\frac{\Delta v}{\Delta i_t}\right|$ measured inside *zone B* (m_{up}) and those measured inside *zone A* (m_{down}) are constant compared, through the mean deviations ϑ_{up} and ϑ_{down} calculated as detailed in Fig. 4.12.

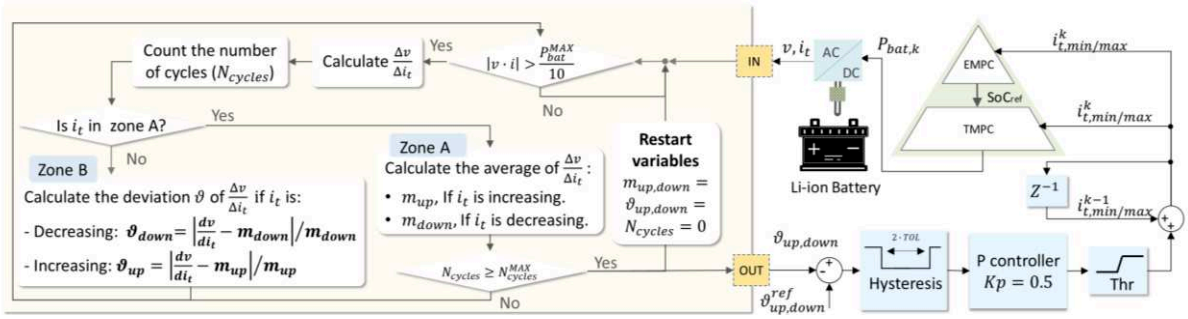

Fig. 4.12: Algorithm for identifying the i_t limits to guarantee the operation of the batteries inside the linear zone.

These deviations ϑ_{up} and ϑ_{down} are monitored by means of a proportional controller with hysteresis at its input to maintain them within the range $\vartheta_{up,down}^{ref} \pm Tol$. The values of $Tol \cong 2\%$ and $\vartheta_{up,down}^{ref} \cong 10\%$ were manually regulated, but they can be re-adjusted to reduce the oscillations or increase the response time of $i_{t,bat}^{min}$ and $i_{t,bat}^{max}$. If the i_t boundaries are modified more than 10% of the previous values, the feasibility zone of Fig. 4.6 is readjusted accordingly and the confidence values ω_{A_ε} , ω_{B_ε}, ω_{C_ε} are reset to ω_{min}.

4.2.4 *Evaluation of the performance of RTMI of batteries model*

Aiming to evaluate the impact of RTMI of batteries model on the performance of the BEMS, the BMG of sizing described in Chapter 2 was simulated for one year in MATLAB Simulink® under several scenarios. Since the goal of the RTMI is to enhance the state estimation of the MPC for long prediction horizons, only the precision of the $i_{t,k+1}^{bat}$ estimated by EMPC was assessed. To highlight the error between the day-ahead $i_{t,k+1}^{bat}$ calculated by the EMPC and the real one, the TMPC in these scenarios was considered a perfect router. Consequently, instead of optimising its cost function defined by (3.93), it does implement the control variables determined by EMPC. In this manner, it is possible to decouple the effect of TMPC and emphasize only the impact of the errors in EMPC batteries charge estimation on the BMG performance

To show the robustness of the algorithm against parameter inaccuracies from technical specifications, uncertainties to the values of the batteries' capacity (Q) were added on the HMPC parameter. Therefore, three values of Q were simulated, namely Q_{80}, Q_{100} and Q_{120}, corresponding to 80%, 100% and 120% of the actual capacity (167 Ah, shown in Table 2.1), respectively. Furthermore, scenarios with two battery ageing levels have been considered, particularly when the batteries are new and when they are in their half-life, i.e. when their capacity is degraded to 90% of their nominal value [213]. An additional simulation considering the case without the installation of batteries was considered to have a reference for the comparison between the case studies.

To identify the advantages and drawbacks of employing RTMI, the EMPC with and without the RTMI were compared based on three metrics, notably the self-consumption rate (τ_{sc}), the coverage rate (τ_c) and the final level of degradation of batteries. The self-consumption rate was calculated through (4.26), whereas the coverage rate by means of (4.27). The level of degradation of batteries was measured by the equivalent full battery cycles that are provided by the Simulink model [214].

$$\tau_{sc} = \frac{Total\ energy\ \ produced\ from\ RES\ that\ is\ consummed\ locally}{Total\ energy\ produced\ from\ RES\ locally} = 1 - \frac{\sum_k P_{grid,k}^{injected}}{\sum_k P_{pv,k}} \tag{4.26}$$

$$\tau_c = \frac{Total\ energy\ self-consumed}{Total\ energy\ consumed\ locally} = 1 - \frac{\sum_k P_{grid,k}^{import}}{\sum_k P_{cons,k}} \tag{4.27}$$

Where,

- $P_{grid,k}^{injected}$ is the power injected into the grid at instant k.
- $P_{grid,k}^{import}$ is the power imported from the grid at instant k.
- $P_{pv,k}$ is the power generated by the PV panels at instant k.
- $P_{cons,k}$ is the power consumed by the building at instant k.

Notably, in these simulations, the cost function of the EMPC optimiser is a simplified one that aims to reduce the grid energy exchange (P_{grid}^{import} and $P_{grid}^{injected}$). Consequently, the EMPC optimise daily ($T_s^{EMPC} = 24h$) the cost function defined by (4.28) and determine the batteries power references P_{bat}^{ref} that will be strictly followed by the power converter of the battery pack.

$$P_{bat,k}^{ref} = \arg\left(\min_{P_{bat,k}^{ref}} \sum_{k=1}^{N_h^{EMPC}=48} P_{grid,k}^{import} + P_{grid,k}^{injected}\right) \tag{4.28}$$

The graphs of Fig. 4.13 show that, in all cases of study, the cumulative error of the predicted batteries charge ($i_{t,k+1}^{bat}$) using the EMPC equipped with the RTMI module is 2 to 3 times lower than using the conventional EMPC with static battery parameters. The conventional model is defined by (3.32), where the static parameters Q, v_{bat}^{nom}, η_{ch} and η_{dis} are equal to 167Ah, 720V, 97% and 99%, respectively. The graph of Fig. 4.13b points out that the level of degradation of the batteries has a huge impact on the predictions made by the classic EMPC, especially when the battery capacity is overestimated (case with Q_{120}). In contrast, with the RTMI module, cumulative errors are kept under control in all scenarios.

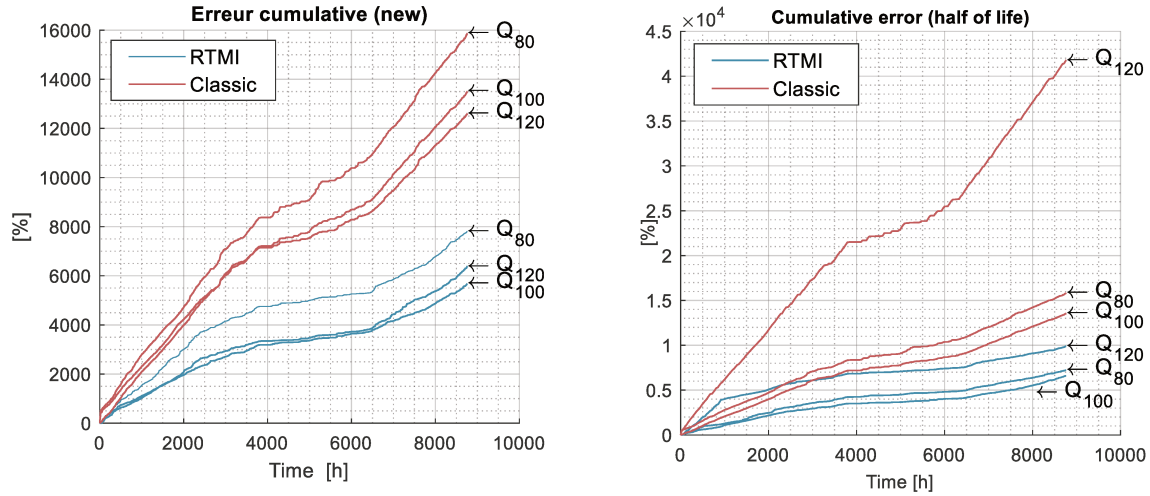

(a) (b)

Fig. 4.13: Cumulative error when predicting the state of charge of the batteries. (a) Case without battery degradation. (b) Case with battery degradation.

To better visualize, in Fig. 4.14, the batteries charge estimation with and without RTMI is shown in a time scale of 5 days. It can be noted that although the EMPC updates the batteries state estimation at each $T_s^{EMPC} = 24h$, the error when employing RTMI remains below 2% all along the predicted horizon. On the other hand, without RTMI (classic approach), the state estimation error varies from 3% to 8%. The discontinuity at 48h highlights the cumulative error that the classic EMPC has committed since the last update at 24h. At each $T_s^{EMPC} = 24h$, the i_t^{bat} estimation is corrected by measuring i_t^{meas}, making RTMI and classic predictions equals to i_t^{meas}.

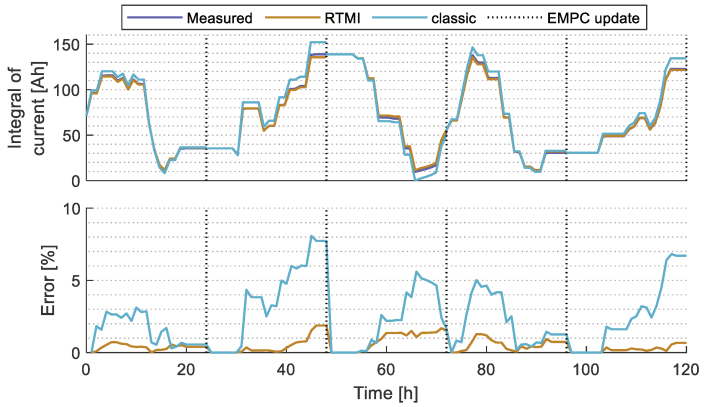

Fig. 4.14: Comparison between the real and estimated SoC using the classic model and the proposed dynamic model within the EMPC sampling time of 24 hours (marked by the vertical lines *EMPC update*).

To assess the impact of better estimating the batteries capacity on the annual BMG energy autonomy, τ_{sc} and τ_c with and without RTMI were compared. According to the graphs of Fig. 4.15a and Fig. 4.15b, τ_{sc} and τ_c are always greater when using the RTMI algorithm than not using it. This result reflects the ability of the RTMI module to identify the real capacities of the batteries, thus avoiding their underuse. For this reason, the differences are most noticeable when the batteries are underestimated, i.e. in the case with Q_{80}. It is possible to note that even subject to parametric imprecisions on the actual capacitance Q, the EMPC equipped with the RTMI module can ensure almost the same τ_{sc} and τ_c. On the other hand, the classical MPC is not robust against uncertainties in the value of Q. As shown in Fig. 4.15, τ_{sc} and τ_c are reduced when batteries are underestimated. Similarly, τ_{sc} and τ_c are increased when they are overestimated.

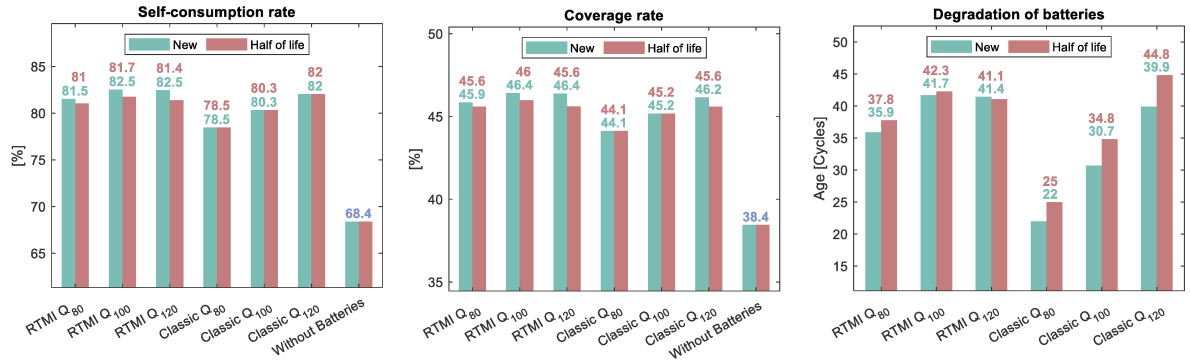

Fig. 4.15: Comparison of the performance of the MPC with and without the RTMI module. Simulation results of a year of operation of the microgrid under different levels of degradation of the batteries and inaccuracies in the estimation of the real capacity of the batteries. (a) Self-consumption rate (τ_{sc}). (b) Coverage rate (τ_c). (c) Variation in battery age. Notes: The building energy consumption is equivalent to 241.85 MWh/year, and the PVs energy generation is about 135.95 MWh/year.

Fig. 4.15a and Fig. 4.15b also show that the energy autonomy of the building is exactly the same as with the conventional EMPC on different levels of battery degradation. As the EMPC without RTMI has no knowledge about the state-of-health of the batteries, the charging and discharging instructions are the same in both ageing scenarios (i.e. new and half of life). In fact, from the point of view of the classic EMPC, the parameters of the battery models, as well as the limits of the SoC are static throughout the life of the microgrid and therefore τ_{sc} and τ_c remain unchanged.

However, the difference is remarkable in the rate of degradation of the batteries, as shown in Fig. 4.15c. Over a period of one year of operation, the batteries were degraded 13% faster in the scenario where the batteries start with half of their life than in the case where they are new. The reason behind this phenomenon is that since the classic EMPC does not monitor the DoD of the batteries, they will be discharged as if they were not degraded. Consequently, the DoD is deeper with the classic EMPC in the cases where the batteries are initially degraded, since the $i_{t,bat}^{max}$, $i_{t,bat}^{min}$ and Q_{nom} are under estimated, as illustrated in Fig. 4.16a.

On the other hand, looking at Fig. 4.16b, with the EMPC equipped with the RTMI algorithm, the $i_{t,bat}^{max}$ and $i_{t,bat}^{min}$ are monitored to ensure the operation of the batteries in the linear zone, that is, between $Q_{exp}$and Q_{nom} As a result, indirectly the RTMI module guarantees a quasi-constant degradation rate, as shown in Fig. 4.15c. The deviation of the degradation rate between the cases where batteries are initially new and in their half-life is always less than 5.5%. This is because the RTMI module changes the limits of $i_{t,bat}^{max}$ and $i_{t,bat}^{min}$ to values corresponding to the same DoD regardless of the level of degradation of the batteries.

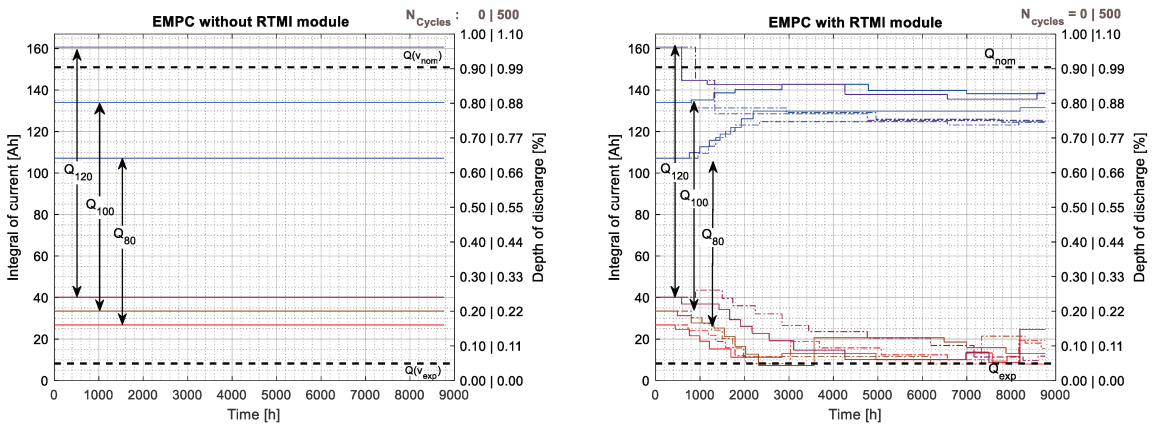

(a) (b)

Fig. 4.16: Estimation of maximum (blue) and minimum (red) limits of the integral current using the MPC with imprecisions on the rated capacity (Q_{80}, Q_{100} and Q_{120}). In dashed lines, the cases with the batteries initially degraded; and in continuous lines, the cases with new batteries. (a) EMPC controller without RTMI. (b) EMPC controller with RTMI.

In the same way, by estimating more precisely $i_{t,bat}^{max}$ and $i_{t,bat}^{min}$, τ_{sc} and τ_c are also more constant with the RTMI module than with the classic EMPC, when the controllers are subject to different intensities of imprecision of Q. However, due to the degradation level, the batteries lose their capacity, and the RTMI algorithm reduces the limits of $i_{t,bat}^{max}$and $i_{t,bat}^{min}$, which causes a reduction of the order of 1% in τ_{sc} and τ_c.

Beyond the regulation of the DoD, according to [226] and [229], the temperature of the cells is one of the most impacting factors on the state-of-health of batteries, which requires regulation of their temperature. One advantage when using the RTMI algorithm is that the variations in battery cell temperatures are indirectly monitored through the classification by temperature level (T_{class}) explained in section 4.2.1. With the processing of voltage and current integral measurements data, the T_{class} represents an image of the temperature variation as shown in Fig. 4.17. This information can be used by the MPC controller to regulate the temperature of the batteries and extend their lifespan.

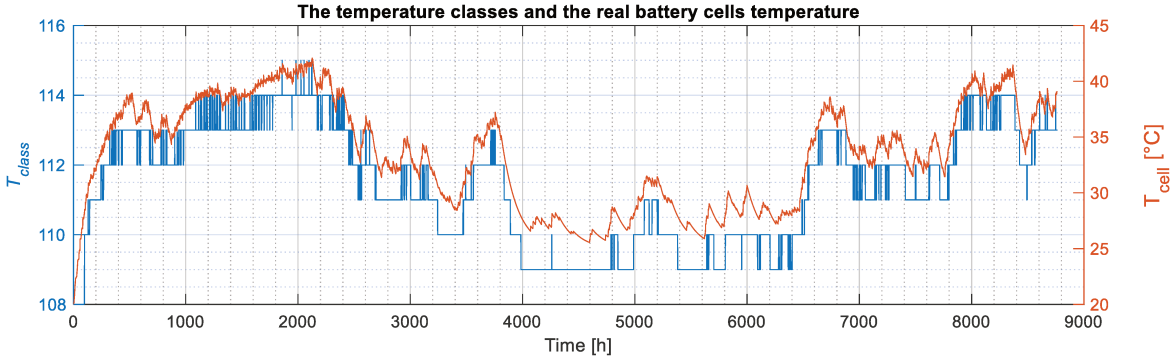

Fig. 4.17: Correlation between the T_{class} classes determined by the ITRM algorithm and the temperature of the battery cells measured (simulation Q_{100}).

4.3 Detail of the RTMI algorithm for hydrogen energy storage energy

The RTMI algorithm to improve the LoH state estimation is also based on an iterative update process, in which the parameters of functions f_{els} and f_{fc} presented in Chapter 3 (equation (3.85)) are tuned to approach the linear model as much as possible to the real measurements. To implement it, at each TMPC sampling time ($T_s^{TMPC} = 1h$), the RTMI module acquires the tank pressure (P_{tank}), the current (i_{els} and i_{fc}) and voltage (v_{els} and v_{fc}) at fuel cells and electrolysers branches, as shown in Fig. 4.18.

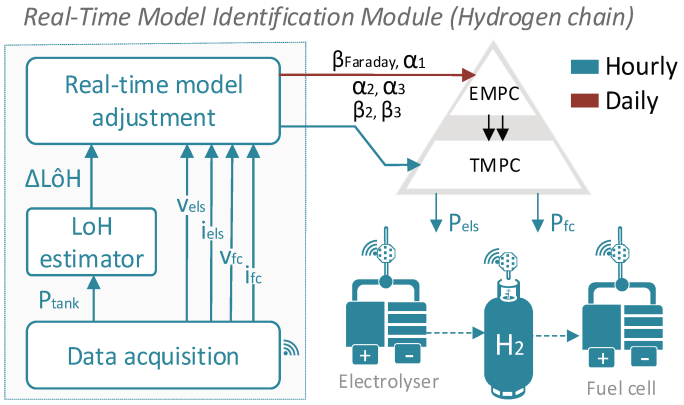

Fig. 4.18: Real-Time model identification of the parameters for a hydrogen storage system model.

Firstly, the tank pressure ($P_{tank,k}$) is used for estimating the pressure variation regarding the last measurement at $k-1$, as detailed in equation (4.29).

$$\Delta P_{tank,k} = P_{tank,k} - P_{tank,k-1} \tag{4.29}$$

Subsequently, with $\Delta P_{tank,k}$ measurement together with the voltage (v_{els} and v_{fc}) and current (i_{fc} and i_{els}), two iterative tuning process are implemented to identify the parameters of f_{els} and f_{fc} defined in (3.85) and repeated in (4.30) and (4.31). The first one resides in determining the angular coefficients $\beta_{Faraday}^{els}$ and $\beta_{Faraday}^{fc}$ linking the current ($i_{els,k}$ or $i_{fc,k}$) to the variation of tank pressure (ΔLoH_k). The second part of the algorithm consists of identifying the parameters α_{fc}^{zone1}, α_{fc}^{zone2}, α_{fc}^{zone3}, β_{fc}^{zone2}, β_{fc}^{zone3}, α_{els}^{zone1}, α_{els}^{zone2}, α_{els}^{zone3}, β_{els}^{zone2}, and β_{els}^{zone3}, linking the current flowing throughout the stacks (i_{els} of i_{fc}) and its corresponding active power ($P_{els,k}$ or $P_{fc,k}$).

$$f_{els}(P_{els}) = \frac{\beta_{Faraday}^{els}}{P_{tank}^{max}}\left(\frac{P_{els,k}^{zone1}}{\alpha_{els}^{zone1}} + \frac{P_{els,k}^{zone2}}{\alpha_{els}^{zone2}} + \frac{P_{els,k}^{zone3}}{\alpha_{els}^{zone3}} - \frac{\beta_{els}^{zone2}\cdot\delta_{els,k}^{zone2}}{\alpha_{els}^{zone2}} - \frac{\beta_{els}^{zone3}\cdot\delta_{els,k}^{zone3}}{\alpha_{els}^{zone3}}\right) \tag{4.30}$$

$$f_{fc}(P_{fc}) = \frac{\beta_{Faraday}^{fc}}{P_{tank}^{max}}\left(\frac{P_{fc,k}^{zone1}}{\alpha_{els}^{zone1}} + \frac{P_{fc,k}^{zone2}}{\alpha_{fc}^{zone2}} + \frac{P_{fc,k}^{zone3}}{\alpha_{fc}^{zone3}} - \frac{\beta_{fc}^{zone2}\cdot\delta_{fc,k}^{zone2}}{\alpha_{fc}^{zone2}} - \frac{\beta_{fc}^{zone3}\cdot\delta_{fc,k}^{zone3}}{\alpha_{fc}^{zone3}}\right) \tag{4.31}$$

Remarkably, the maximum pressure of the hydrogen tank (P_{tank}^{max}) is specified by the manufacture, and it is dependent on the tank temperature. However, since the temperature is considered constant, P_{tank}^{max} is also assumed constant. Therefore, P_{tank}^{max} is considered as an input parameter. The following two subsections explain in detail these two iterative algorithms.

4.3.1 *Dynamic identification of the parameter linking the stack current and ΔLoH_k*

The combination of Faraday's law of electrolysis with the ideal gas law enables associating the current flowing through the stack and the variation of the tank pressure, as defined in (4.32). One advantage of the RTMI algorithm is that instead of attributing static values for calculating $\beta_{Faraday}^{els,fc}$, it is determined automatically thanks to a dynamic update process.

$$\Delta P_{tank,k} = \left(\frac{R\cdot T_{tank}}{V_{tank}}\right)\cdot\frac{N_{cells}^{els,fc}}{2\cdot F}\cdot T_s^{TMPC}\cdot 3600\cdot i_{els,fc} = \beta_{Faraday,k}^{els,fc}\cdot i_{els,fc} \tag{4.32}$$

To identify the constant parameter $\beta_{Faraday,k}^{els}$ and $\beta_{Faraday,k}^{fc}$ in real-time, the pressure and current measurement are used. The sample measurement composed by the triple $M_k = \left(\Delta P_{tank,k}^{meas}, i_{els,k}^{meas}, i_{fc,k}^{meas}\right)$ permits to calculate $\beta_{Faraday,k}^{meas}$, by using (4.33) if the PEM electrolyser is active, and (4.34) in the case where the fuel cell is operating.

$$\beta_{Faraday,k}^{meas,els} = \frac{\Delta P_{tank,k}^{meas}}{i_{els,k}^{meas}}, \qquad if\ i_{els,k} \neq 0\ and\ i_{fc,k} = 0 \tag{4.33}$$

$$\beta_{Faraday,k}^{meas,fc} = \frac{\Delta P_{tank,k}^{meas}}{i_{fc,k}^{meas}}, \qquad if\ i_{els,k} = 0\ and\ i_{fc,k} \neq 0 \tag{4.34}$$

With the instantaneous value of $\beta_{Faraday,k}^{meas,els}$ and $\beta_{Faraday,k}^{meas,fc}$, the estimated value of $\beta_{Faraday,k}^{els}$ and $\beta_{Faraday,k}^{els}$ are updated through a weighted average between the last estimation and the current measurement, as specified in equation (4.35) for the electrolyser and (4.36) for the fuel cell.

$$\beta_{Faraday,k}^{els} = \frac{\omega_{els,k} \cdot \beta_{Faraday,k}^{els} + \Delta\omega_{els} \cdot \beta_{Faraday,k}^{meas,els}}{\omega_{els,k} + \Delta\omega_{els}} \tag{4.35}$$

$$\beta_{Faraday,k}^{fc} = \frac{\omega_{fc,k} \cdot \beta_{Faraday,k}^{fc} + \Delta\omega_{fc} \cdot \beta_{Faraday,k}^{meas,fc}}{\omega_{els,k} + \Delta\omega_{fc}} \tag{4.36}$$

The variables $\omega_{els,k}$ and $\omega_{fc,k}$ are confidence weights that grow with the acquisition of new measurements and are reduced with the time according to a constant time τ_{els}^{min} and τ_{fc}^{min}, whereas the static parameters $\Delta\omega_{els}$ and $\Delta\omega_{fc}$ are the variation of the confidence weights between two consecutive iterations. Therefore, similarly to the case of batteries, the weights $\omega_{els,k}$ and $\omega_{fc,k}$ are updated as soon as a new measurement M_k is acquired following the equations (4.37) and (4.38). Subsequently, at each iteration, the confidence weights are reduced at pace defined by (4.39) and (4.40).

$$\omega_{els,k} = \omega_{els,k} + \Delta\omega_{els}, \qquad if\ i_{els,k} \neq 0\ and\ i_{fc,k} = 0 \tag{4.37}$$

$$\omega_{fc,k} = \omega_{fc,k} + \Delta\omega_{fc}, \qquad if\ i_{els,k} = 0\ and\ i_{fc,k} \neq 0 \tag{4.38}$$

$$\omega_{els,k} = \omega_{els,k} - \tau_{decay}^{els} \cdot \left(\omega_{els,k} - \omega_{els}^{min}\right) \tag{4.39}$$

$$\omega_{fc,k} = \omega_{fc,k} - \tau_{decay}^{fc} \cdot \left(\omega_{fc,k} - \omega_{fc}^{min}\right) \tag{4.40}$$

With the purpose of assessing the performance of the algorithm, the hydrogen chain of the Simulink simulator explained in Chapter 2 was simulated for 100 hours, resulting in the curves shown in Fig. 4.19. While either the electrolysers or the fuel cell have never been used before the estimation of $\beta_{Faraday,k}^{els}$ and $\beta_{Faraday,k}^{fc}$ assume the values given by the manufacture, which follow the equations (4.41) and (4.42).

$$\beta_{Faraday}^{els,theoretical} = \left(\frac{R \cdot T_{tank}}{V_{tank}}\right) \cdot \frac{N_{cells}^{els}}{2 \cdot F} \cdot T_s^{TMPC} \cdot 3600 \tag{4.41}$$

$$\beta_{Faraday}^{fc,theoretical} = -\left(\frac{R \cdot T_{tank}}{V_{tank}}\right) \cdot \frac{N_{cells}^{fc}}{2 \cdot F} \cdot T_s^{TMPC} \cdot 3600 \tag{4.42}$$

In the graphs of Fig. 4.19c and Fig. 4.19d, the initial theoretical values of $\beta_{Faraday}^{els,theoretical}$ and $\beta_{Faraday}^{fc,theoretical}$ possess 30% of error regarding the real values. However, after few samples, $\beta_{Faraday,k}^{els}$ and $\beta_{Faraday,k}^{fc}$ approaches to the real values indicated by black dashed lines. In Fig. 4.19e, it is possible to observe that the weights $\omega_{els,k}$ and $\omega_{fc,k}$ grow with acquisition of new measurements and decrease with time, as expected. Notably, in this simulation, $\tau_{els}^{min} = \tau_{fc}^{min} = 0.1$ and $\Delta\omega_{els} = \Delta\omega_{els} = 1$, but these values can be adjusted according to the required robustness against measurement noise and convergence time. Finally, Fig. 4.20 shows that the identification of $\beta_{Faraday,k}^{els}$ and $\beta_{Faraday,k}^{fc}$ is very accurate, since the measurement points are aligned to the model lines.

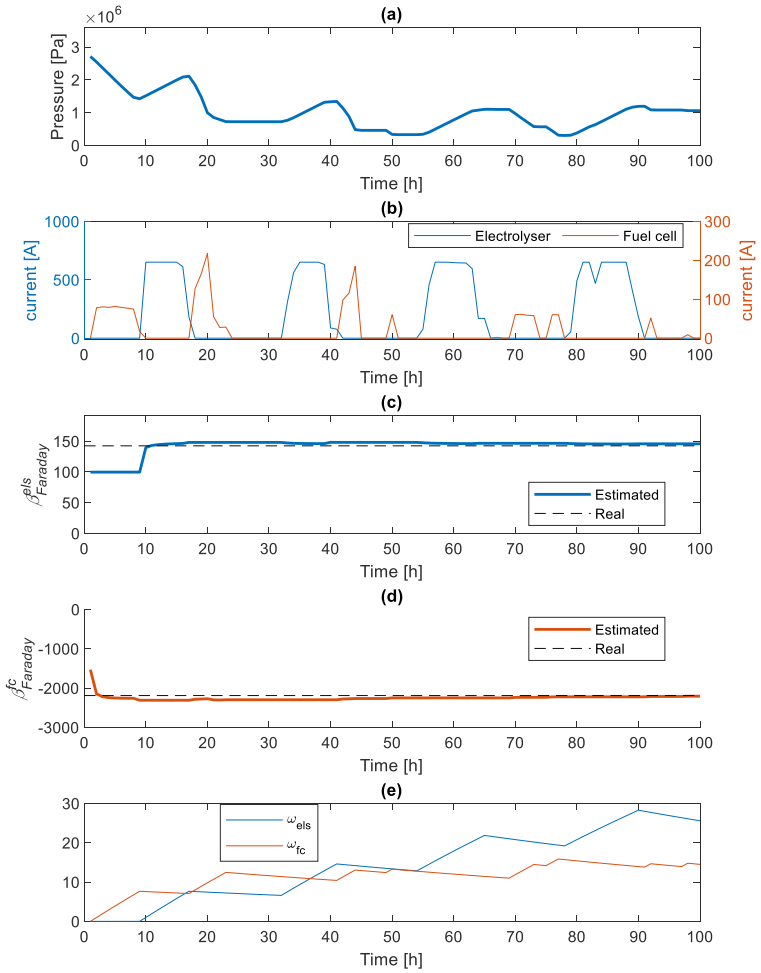

Fig. 4.19: Simulation results of the hydrogen chain operation for 100 hours assessing the RTMI algorithm for estimating the relationship between current and the variation of the tank pressure. (a) Tank pressure. (b) Fuel cells and electrolyser power. (c) Angular coefficient linking the current and the positive variation of tank pressure due to hydrogen gas production by electrolysers. (d) Angular coefficient linking the current and the negative variation of tank pressure due to hydrogen gas consumption by fuel cells. (e) Evolution of confident weights of electrolyser and fuel cells.

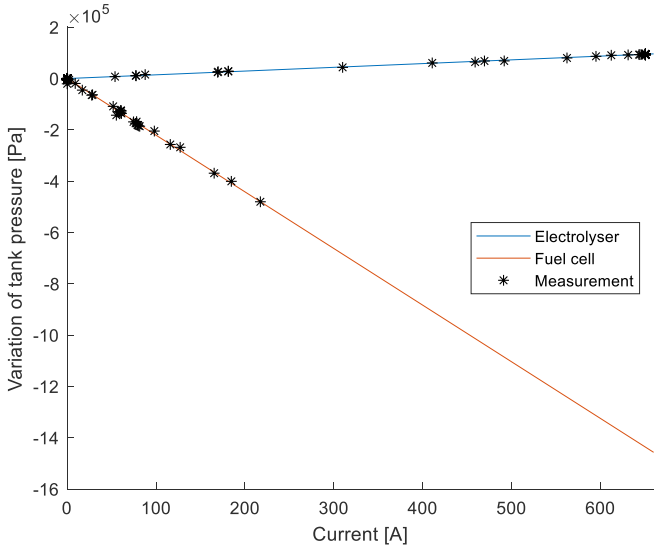

Fig. 4.20: Comparison of the final linear model and the real measurements.

4.3.2 *Linear regression between current and power*

To enhance the MPC state estimation, the power references assigned to the PEMFC and PEME are divided into three zonal powers according to their power intensity. Therefore, as explained in Chapter 3, a different linear model is assigned to each zonal power. The identification of their angular coefficients (α_{fc}^{zone1}, α_{fc}^{zone2}, α_{fc}^{zone3}, α_{els}^{zone1}, α_{els}^{zone2} and α_{els}^{zone3}) and their linear coefficients (β_{fc}^{zone2}, β_{fc}^{zone3}, β_{els}^{zone2}, and β_{els}^{zone3}) are also identified in real-time.

Without storing any past measurement, the algorithm relies only on the present measurements of current and voltage of fuel cells and electrolysers and on three points coordinates with their corresponding weights, namely A, B and C. These three points are the vertexes of the intersection between the power zones and the linear model, as shown in Fig. 4.21a. Therefore, as summarized in Table 4.4, their y-coordinates are fixed and dependent on the maximum power rate of PEME (P_{els}^{max}) and PEMFC (P_{fc}^{max}), whereas their x-coordinates are determined by the RTMI.

Table 4.4: Coordinates of the vertices points A, B and C.

	Electrolyser		**Fuel cell**	
Vertex point	x-coordinate (current)	y -coordinate (power)	x-coordinate (current)	y -coordinate (power)
A	$A_x^{els} = i_{els}^{A}$	$A_y^{els} = \frac{1}{3} \cdot P_{els}^{max}$	$A_x^{fc} = i_{fc}^{A}$	$A_y^{fc} = \frac{1}{3} \cdot P_{fc}^{max}$
B	$B_x^{els} = i_{els}^{B}$	$B_y^{els} = \frac{2}{3} \cdot P_{els}^{max}$	$B_x^{fc} = i_{fc}^{B}$	$B_y^{fc} = \frac{2}{3} \cdot P_{fc}^{max}$
C	$C_x^{els} = i_{els}^{C}$	$C_y^{els} = P_{els}^{max}$	$C_x^{fc} = i_{fc}^{C}$	$C_y^{fc} = P_{fc}^{max}$

Although only the algorithm to determine the fuel cell parameters will be detailed, it is important to highlight that a similar algorithm is applied to electrolysers. At the first iteration, the coordinates of vertex A, B and C are initialised so that the three vertex points are aligned with the first non-null measure M_k, as illustrated in Fig. 4.21a. Therefore, if the first point $M_k = \left(i_{els,k}^{meas}, i_{fc,k}^{meas}, v_{els,k}^{meas}, v_{fc,k}^{meas} \right)$, in which $i_{els,k}^{meas} = 0$ and $i_{fc,k}^{meas} \neq 0$, then the x-coordinates A_x^{fc}, B_x^{fc} and C_x^{fc} is equal to $\frac{P_{fc}^{max} \cdot i_{fc,k}^{meas}}{3 \cdot \Delta P_{tank,k}^{meas}}$, $\frac{2 \cdot P_{fc}^{max} \cdot i_{fc,k}^{meas}}{3 \cdot \Delta P_{tank,k}^{meas}}$ and $\frac{P_{fc}^{max} \cdot i_{fc,k}^{meas}}{\Delta P_{tank,k}^{meas}}$, respectively.

Subsequently, for the next iterations, the vertexes are updated according to the location of the measurement M_k. If the point M_k belongs to a specific power zone, then one of the vertexes limiting this power zone will be modified. For instance, if the M_k is in zone3, as shown in Fig. 4.21b or Fig. 4.21c, either the vertexes B or C will be modified. The upper vertex (i.e. point C) will be updated, if M_k is nearer to the vertex C than vertex B, as shown in Fig. 4.21b. On the opposite case, the lower vertex (i.e. point B) will be modified if the point M_k is nearer to vertex B than vertex C, as illustrated in Fig. 4.21c.

The update of the upper vertex C is implemented by (4.43), which corresponds to a weighted dynamic average between the last estimation of the angular coefficient of the line $\overline{BC}$ (i.e. $\alpha_{fc,k}^{zone3}$) and the new measured $\alpha_{fc,meas,k}^{zone3}$. The variable $\alpha_{fc,meas,k}^{zone3}$ is the angular coefficient of the line $\overline{BM_k}$ that is calculated through (4.44), whereas $\omega_{fc,k}^{zone3}$ is the confidence weight of the estimation of $\alpha_{fc,}^{zone3}$. The

term $\Delta\omega_{fc}$ indicates the importance of the new measurement regarding the current estimation of α_{fc}^{zone3}. Both $\omega_{fc,k}^{zone3}$ and $\Delta\omega_{fc}$ are initialised to a small value, named ω_0, which is typically in the order of 0.1. The weight $\omega_{fc,k}^{zone3}$ grows with the acquisition of measurements close to the vertex C, following equation (4.45). To deal with the ageing of the PEMFC, at each sampling time ($T_s^{TMPC} = 1h$), the confident weights decreases with time with a constant time $0.01 \leq \tau_{decay} \leq 0.05$, as defined in (4.46).

$$\alpha_{fc,k+1}^{zone3} = \frac{\omega_{fc,k}^{zone3} \cdot \alpha_{fc,k}^{zone3} + \Delta\omega_{fc} \cdot \alpha_{fc,meas,k}^{zone3}}{\omega_{fc,k} + \Delta\omega_{fc}} \tag{4.43}$$

$$\alpha_{fc,meas,k}^{zone3} = \frac{C_{y,k}^{fc} - v_{fc,k}^{meas}}{C_{x,k}^{fc} - i_{fc,k}^{meas}} \tag{4.44}$$

$$\omega_{fc,k}^{zone3} = \omega_{fc,k}^{zone3} + \Delta\omega_{fc} \tag{4.45}$$

$$\omega_{fc,k}^{zone3} = \omega_{fc,k}^{zone3} - \tau_{decay} \cdot \left(\omega_{fc,k}^{zone3} - \omega_0\right) \tag{4.46}$$

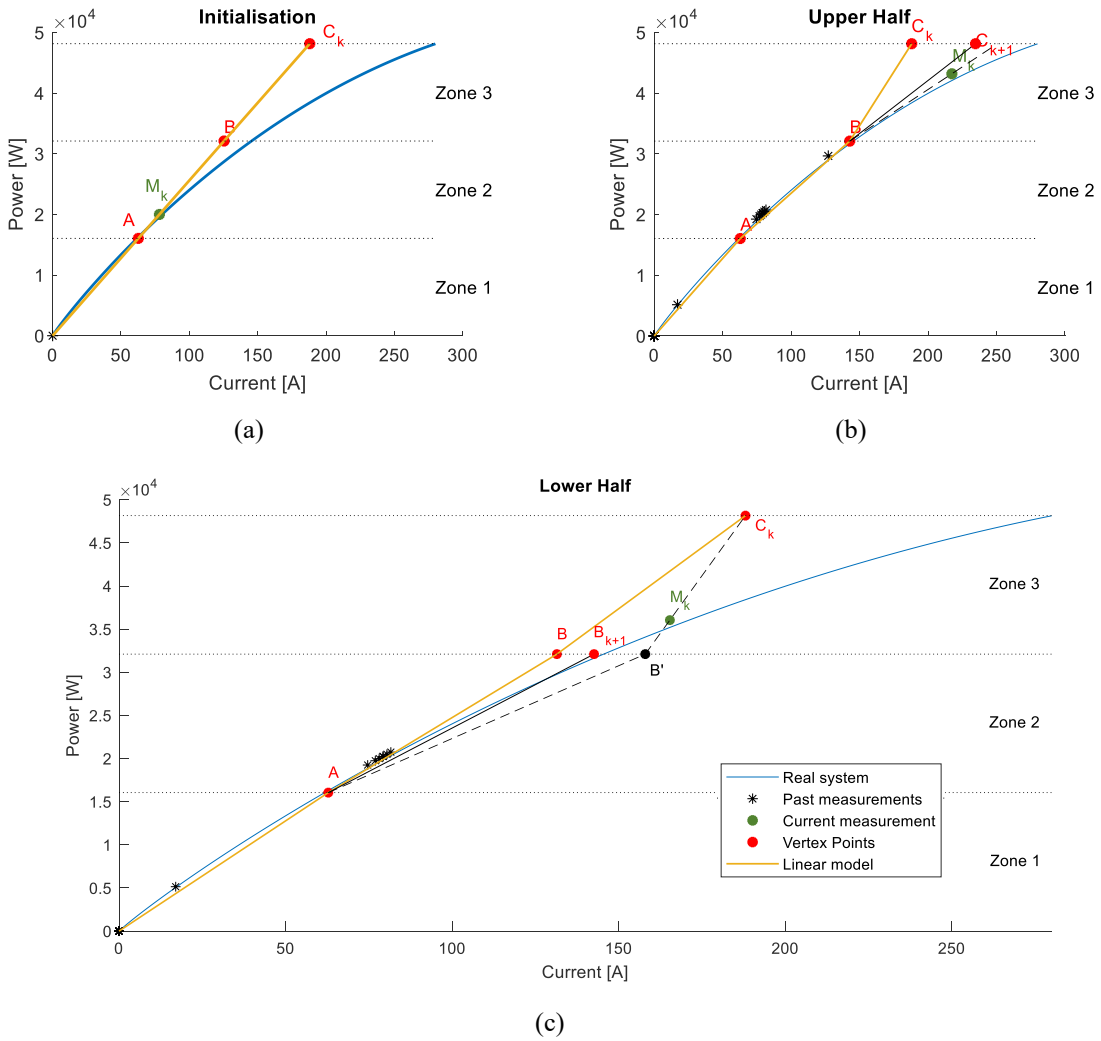

Fig. 4.21: Detail of the fuel cell RTMI. (a) Initialisation step. (b) Update step when the measurement point is near to the upper vertex of limiting the power zone. (c) Update step when the measurement point is near to the lower vertex limiting the power zone

On the opposite scenario, if the point M_k belongs to zone3 and it is nearer to vertex B than vertex C, the x-coordinate of the vertex B is modified. Firstly, as shown in Fig. 4.21c, an intermediate point $B' = \left(B'_x, B'_y\right)$ is determined. This point B' corresponds to the intersection between $\overline{BM_k}$ and the line dividing the zone 2 and zone 3. Subsequently, the point B is updated similarly to the upper vertex. Firstly, the angular coefficient of line $\overline{AB'}$, namely $\alpha^{zone2}_{fc,meas,k}$, is calculated through equation (4.47). Thereafter, the same update process of the upper vertex is applied to the lower vertex, following equations (4.48) – (4.50).

$$\alpha^{zone2}_{fc,meas,k} = \frac{B'_y - A^{fc}_{y,k}}{B'_x - A^{fc}_{x,k}} \tag{4.47}$$

$$\alpha^{zone2}_{fc,meas,k} = \frac{\omega^{zone2}_{fc,k} \cdot \alpha^{zone2}_{fc,k} + \Delta\omega_{\mathrm{fc}} \cdot \alpha^{zone2}_{fc,meas,k}}{\omega_{fc,k} + \Delta\omega_{\mathrm{fc}}} \tag{4.48}$$

$$\omega^{zone2}_{fc,k} = \omega^{zone2}_{fc,k} + \Delta\omega_{\mathrm{fc}} \tag{4.49}$$

$$\omega^{zone2}_{fc,k} = \omega^{zone2}_{fc,k} - \tau_{decay} \cdot \left(\omega^{zone3}_{fc,k} - \omega_0\right) \tag{4.50}$$

Aiming to evaluate the performance of the proposed algorithm, the hydrogen chain was simulated for 100 hours, obtaining the linear models shown in Fig. 4.22. According to Fig. 4.22a, the fuel cell final linear model for low and medium power rates (i.e. zone1 and zone2) is very accurate, but for high power (i.e. zone3), the error is much more important. This is because few points were used to identify the line $\overline{BC}$. The model accuracy would increase if more points were acquired in the zone3. Controversially, as shown in Fig. 4.22b, all electrolyser power zones were explored in a balanced fashion. Consequently, after 100 hours of operation (i.e. 41 samples), the final electrolyser model is very accurate for all the three power zones.

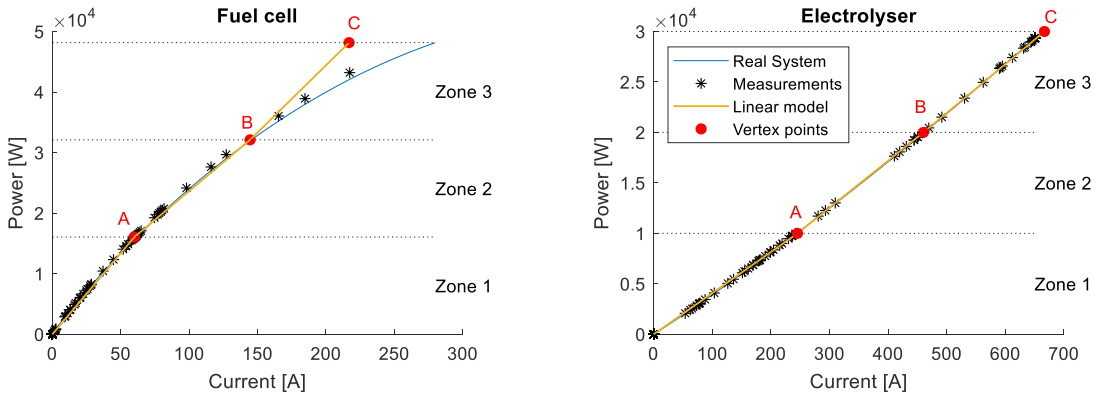

(a) (b)

Fig. 4.22: Accuracy of the final linear model after 100 hours of simulation (37 samples for fuel cells and 41 samples for electrolysers). (a) Fuel cell. (b) Electrolyser.

Fig. 4.23 shows that the identification of x-coordinates of the vertexes A, B and C attained a stable value only with very few samples. After 20 hours (or 10 samples) of PEMFC operation, the vertexes were modified less than 3%. Additionally, as expected the weights ω^{zone1}_{fc}, ω^{zone1}_{fc} and ω^{zone1}_{fc} grow when the fuel cell is operating and decreases when the fuel cell is in the idle mode.

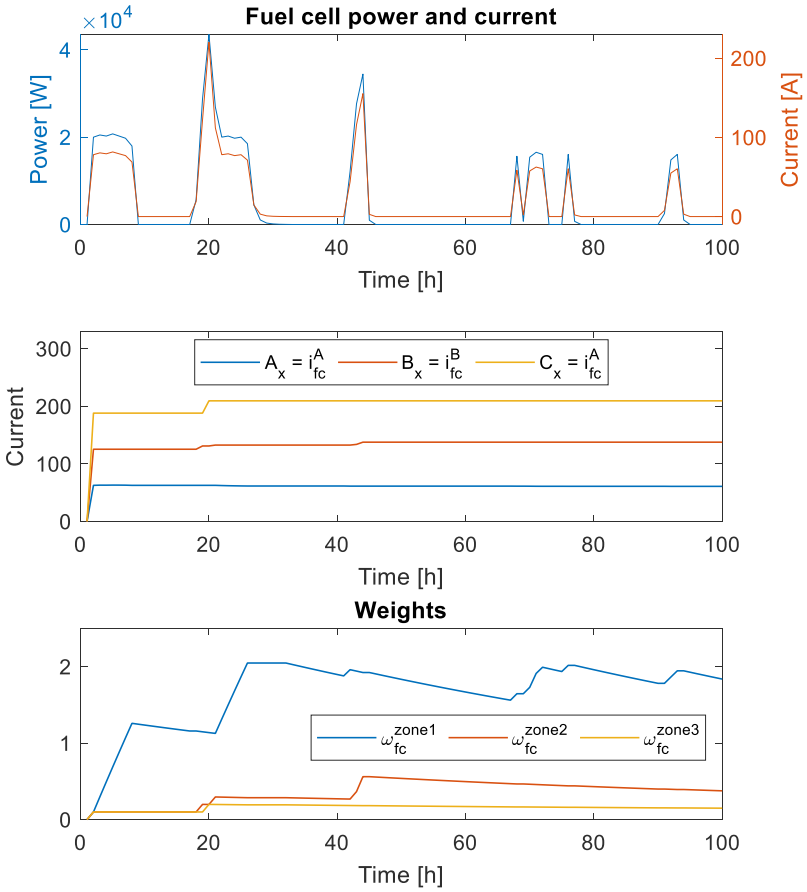

Fig. 4.23: Temporal evolution of the identification of the x-coordinates of the vertexes of power vs current curve in fuel cells.

After having identified the coordinates of the three vertexes, the angular and linear coefficients of the PEME and PEMFC model are calculated using equations (4.51) – (4.53), where the index i refers to either electrolysers (els) or fuel cells (fc). The final values of the parameters of the linear models are summarized in Table 4.5. Finally, by replacing the estimations of $\beta^i_{Faraday,k}$ and α_i^{zone1}, α_i^{zone2}, α_i^{zone3}, β_i^{zone2} and β_i^{zone3} in equations (4.30) and (4.31), the equations f_{els} and f_{fc} can be determined.

$$\alpha_i^{zone1} = \frac{A_y^i}{A_x^i} \tag{4.51}$$

$$\alpha_i^{zone2} = \frac{B_y^i - A_y^i}{B_y^{fc} - A_x^i}; \beta_i^{zone2} = \frac{P_i^{max}}{3} \cdot \left(1 - \frac{\alpha_i^{zone2}}{\alpha_i^{zone1}}\right) \tag{4.52}$$

$$\alpha_i^{zone3} = \frac{C_y^i - B_y^i}{C_y^i - B_x^i}; \beta_i^{zone3} = \frac{2 \cdot P_i^{max}}{3} \cdot \left(1 - \frac{\alpha_i^{zone3}}{\alpha_i^{zone2}}\right) + \frac{\alpha_i^{zone3} \cdot \beta_i^{zone2}}{\alpha_i^{zone2}} \tag{4.53}$$

Table 4.5: Final values of the electrolyser and fuel cells linear model after 100 hours of operation.

	Electrolyser		**Fuel cell**	
Power zone	Angular coefficient (α_{els})	Linear coefficient (β_{els})	Angular coefficient (α_{fc})	Linear coefficient (β_{fc})
Zone 1	$\alpha_{els}^{zone1} = 41.1$	–	$\alpha_{fc}^{zone1} = 266.6$	–
Zone 2	$\alpha_{els}^{zone2} = 45.6$	$\beta_{els}^{zone2} = 1081.6$	$\alpha_{fc}^{zone2} = 212.7$	$\beta_{fc}^{zone2} = 2023.6$
Zone 3	$\alpha_{els}^{zone3} = 49.5$	$\beta_{els}^{zone3} = -6799.3$	$\alpha_{fc}^{zone3} = 213.8$	$\beta_{fc}^{zone3} = -92.12$

4.3.3 *Evaluation of the performance of RTMI of hydrogen energy storage system*

To assess the performance of the RTMI algorithm for LoH state estimation, the proposed linear model was confronted with the common linear model found in the literature [37]. The classic linear model is defined by equation (4.54), where ς_{els} is the electrolyser hydrogen consumption rate in kWh/Nm^3, ς_{fc} is the fuel cell hydrogen production rate in Nm^3/kWh, and V_{tank} is the normal tank volume. These parameters are usually specified on the manufacture's datasheet, which results in 0.63 kWh/Nm^3, 4.18 Nm^3/kWh and 224 Nm^3, respectively.

$$LOH_{k+1} = LOH_k + \frac{P_{els,k} \cdot T_s}{\varsigma_{els} \cdot V_{tank} \cdot 1000} - \frac{\varsigma_{fc} \cdot P_{fc,k} \cdot T_s}{V_{tank} \cdot 1000} \tag{4.54}$$

The accuracy of these two linear models (classic *vs* RTMI) was compared to the real LoH measures (LoH_k^{meas}) by calculating the error defined by (4.55). The term $\widehat{LoH_k}$ refers to the estimated LoH calculated by the MPC. To emphasise the state estimation error, the lower MPC performing the tracking MPC was deactivated, and only the EMPC was running. In this manner, the power references determined by the EMPC are followed strictly by the fuel cells and electrolysers power converters.

$$error(\%) = \left|\widehat{LoH_k} - LoH_k^{meas}\right| \tag{4.55}$$

Under these conditions, the operation of fuel cells and electrolysers was simulated for 10 days. As a result, Fig. 4.24 shows that the RTMI algorithm identified a linear model that is more accurate than the common linear model found in the literature. Remarkably, the accuracy would be more important if there were errors in the parameters of fuel cell and electrolyser classic models. As shown in Fig. 4.25, the error when using the RTMI is lower than the classic model since the first hours of operation. In the long term, the RTMI increases the precision of the one-day-ahead state estimation up to ten times regarding the classic linear model after less than 1 day of operation.

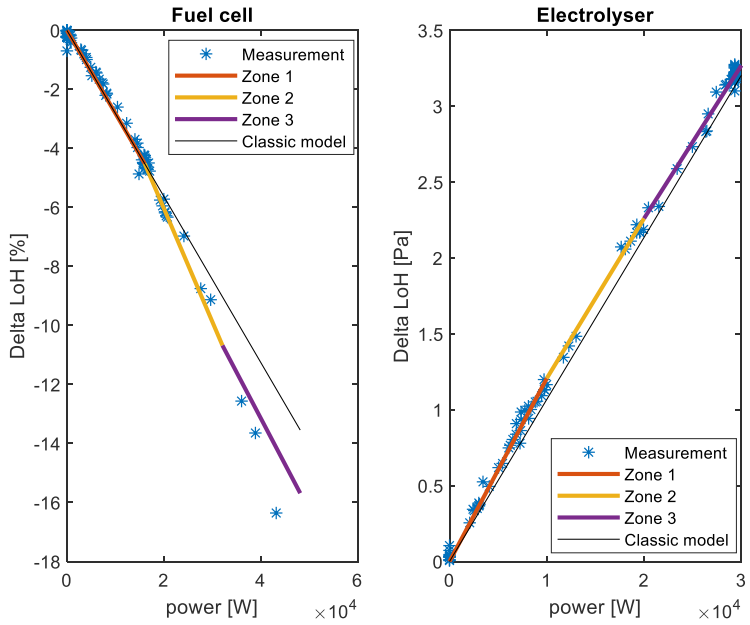

Fig. 4.24: Comparison between the linear model determined by the RTMI algorithm, the classic model and the real measurement, after 200 hours of operation.

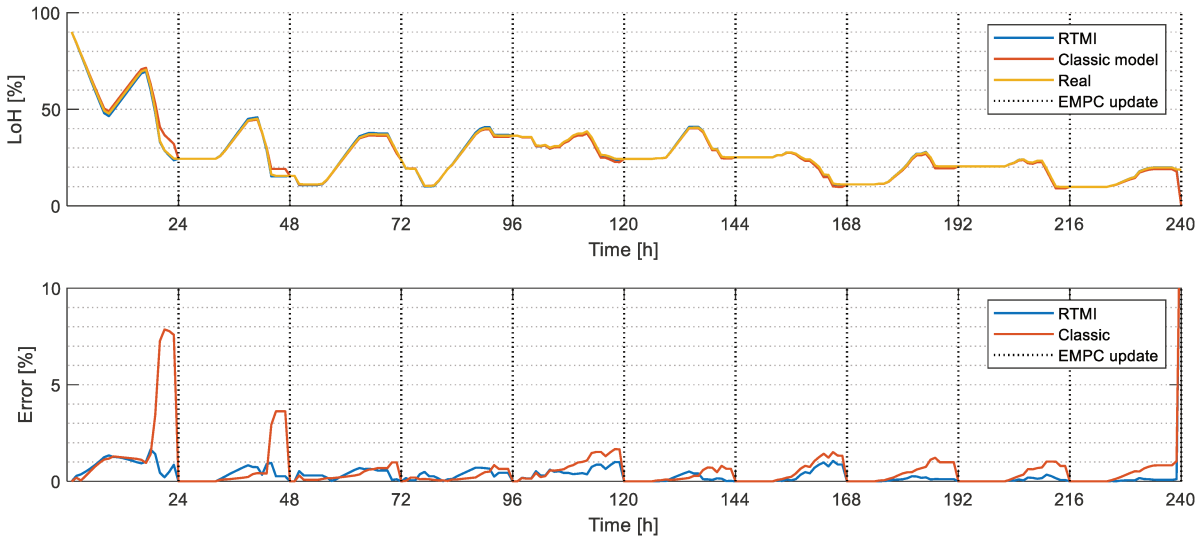

Fig. 4.25: Comparison between the real and estimated LoH using the classic model and the proposed dynamic model within the EMPC time sample of 24 hours (marked by the vertical lines *EMPC update*).

4.4 Conclusions

Aiming to develop a generic energy management system for BMGs, a real-time algorithm was designed to enable BMGs to adapt to external changes, such as the effect of temperature in batteries, ESS ageing and modelling inaccuracies without increasing the complexity of the controller. The simulation results indicate that the integration of real-time parameter identification algorithm into the MPC structure can improve the BMG performance and extend battery life, hence it can reduce maintenance costs. By relying on measurement data, the RTMI algorithm increases the accuracy of battery states of charge estimation by up to 3 times, whereas the precision of the LoH estimation was enhanced in up to 10 times. In addition, the new algorithm synchronized with the controller's sampling period can identify the actual capacity of the installed batteries and the real hydrogen consumption and production rates, which allow their better exploitation.

The simulation results showed that a better estimate of the state-of-charge and the capacity of the batteries, allows the controller to have more information concerning the variations in temperature of the batteries' cells and about their degradation. A correlation was found between the depth of discharge of the batteries and the building coverage and self-consumption rates. All this information provided by the new algorithm allows the controller to make more reliable decisions, especially to find a good compromise between the energy autonomy of the buildings and the level of degradation of the batteries.

As future steps, it is envisaged to use the estimation of temperature variation in batteries'cell and rated capacity to slow down the battery degradation. Furthermore, it is intended to enhance the RTMI of hydrogen ESS by compensating its temperature variation through the division in temperature classes as implemented in the case of RTMI of batteries. Additionally, the robustness of the algorithm against both ambient temperature oscillation and measurement noise are needed to be evaluated before implementing it in real systems.

Chapter 5 The MicroGrid cost estimator

5.1 Introduction

One of the greatest weakness of MPC is its dependence on reliable cost function definition. When dealing with hybrid ESS, the MPC's objective function is usually designed as a multi-objective one, as in [117], [184], [185]. The trade-off between batteries and hydrogen chain is often handled by weighted factors in the MPC's cost function that are usually tuned through a trial and error approach. These weighted factors are often assigned following a priority order to reduce, in all circumstances, the total imports and exports of grid energy and prioritizing the use of batteries over the hydrogen chain. This clearly diminishes the generality of the controller and might prevent the MPC to accomplish its objectives if these weighted factors in the cost function are not well-tuned or under unexpected changes in the plant model.

The multi-objective MPC's cost function can be normalised to overcome this problem by converting each cost function term into the same physical unit, such as the local currency for economic optimisations, as adopted in [37], [186]. To determine a balanced use of the hybrid ESS, the degradation cost of batteries, electrolysers, and fuel cells, as well as the electricity price, are often integrated. Nonetheless, these optimisations are limited to the MPC's horizon and consider neither the seasonality along the year nor the long-term objectives, such as the requirement concerning the building annual self-consumption rate.

To tackle this weakness of an MPC structure, the MG cost estimator was designed to adjust the cost function of the HMPC daily based on data analysis. The objective of the algorithm is to determine optimal parameters for the HMPC cost function to handle the trade-off between maximising the annual self-consumption rate and minimising the total BMG operating cost, without needing to tune any parameter. To achieve this, in synchronism with the HMPC presented in Chapter 3, the MG cost estimator adjusts the cost function of the upper level of the HMPC (i.e. EMPC), to satisfy the required marks of the annual self-consumption rate imposed by the grid code at minimum cost. The MG cost estimator also allows the building EMS to figure out a balanced use of batteries and hydrogen chain, through the estimation of their End of Life (EoL) and the assessment of their capacity in reducing the BMG injection and maximising the total BMG revenue.

By analysing both the day-ahead and the last year power imbalance prediction data, it estimates the average behaviour of the hierarchical EMS when it is subjected to similar conditions of daily power imbalance. This average behaviour enables the MG cost estimator to calculate the expected annual BMG cost and the expected annual self-consumption rate. The expected annual BMG cost defines the EMPC cost function that is minimised at least once a day, whereas the expected annual self-consumption rate is embedded into EMPC formulation through an inequality constraint, forcing it to be

higher than the required marks imposed by the grid code. To explain the main operation of the MG cost estimator, the expected annual BMG cost is detailed in section 5.2, whereas the algorithm to calculate the expected annual self-consumption rate is explained in section 5.3. Subsequently, section 5.4 describes the initialization of the whole MG cost estimator algorithm. The validation and performance of the proposed algorithm are demonstrated in section 5.5. Finally, section 5.6 provides a summary of the algorithms, and it concludes this chapter by pointing out future steps for improvement.

5.2 Estimation of the expected annual building microgrid cost

The expected annual BMG cost is estimated daily and embedded into the six π-cost terms composing the EMPC cost function defined by equation (3.91), namely $\pi_{grid,k}$, $\pi_{els,k}^{deg}$, $\pi_{fc,k}^{deg}$, $\pi_{bat,k}^{deg}$, $\pi_{sc,k}$ and $\pi_{sc,k}^{pen}$. The next four subsections explain in detail how these π-costs are determined, while subsection 5.2.5 summarises the cost function of EMPC.

5.2.1 *Electricity cost*

The term $\pi_{grid,k}$ refers to the annual electricity cost and it is estimated from both the electricity price and the total energy deficit of the previous year. Since the energy[3] deficit ($E_{deficit,k}$), defined by (5.1), can be covered either by purchasing electricity from the grid or discharging the ESS, the total energy imported can be calculated from (5.2). Therefore, the annual electricity cost can be estimated through (5.3), where $\pi_{elec,k}$ is the last-year electricity price for the hour k.

$$E_{deficit,k} = \begin{cases} T_s^{TMPC} \cdot \left(P_{cons,k} - P_{pv,k}\right) \Leftrightarrow P_{cons,k} > P_{pv,k} \\ 0 \Leftrightarrow P_{cons,k} \leq P_{pv,k} \end{cases} \tag{5.1}$$

$$E_{grid,k}^{import} = E_{deficit,k} - \left|E_{fc,k}\right| - \left|E_{bat,k}^{dis}\right| \tag{5.2}$$

$$\pi_{grid}^{annual} = \sum_{k=1}^{365} \pi_{elec,k} \cdot \left(E_{deficit,k} - \left|E_{fc,k}\right| - \left|E_{bat,k}^{dis}\right|\right) \tag{5.3}$$

Remarkably, the minimisation of π_{grid}^{annual} can be guaranteed by periodic minimizations over the overlap periods of EMPC horizon. Since $E_{deficit,k}$ is an uncontrollable variable from the point of view of EMPC, the minimisation of (5.3) can be assured by minimising (5.4) daily, for k ranging from 1 to 48 hours.

$$\pi_{grid,k} = \pi_{elec,k} \cdot T_s^{EMPC} \cdot \left(-\left|P_{fc,k}\right| - \left|P_{bat,k}^{dis}\right|\right) \tag{5.4}$$

5.2.2 *Costs due to the degradation of energy storage devices*

The cost due to the degradation of ESS includes $\pi_{bat,k}^{deg}$, $\pi_{els,k}^{deg}$ and $\pi_{fc,k}^{deg}$, referring to the deterioration cost of batteries, electrolysers and fuel cells, respectively. From experimental curves provided by the manufactures, the ESS degradation level can be estimated. In the case of batteries, the loss of nominal

[3] The relationship between power (P) and energy (E) is ruled by $E = P \cdot T_s^{TMPC}$, where T_s^{TMPC} is the smallest timestamp of the hierarchical control structure.

capacity, which follows an exponential trend depending on the number of cycles and the depth of discharge [214], can be used to measure their degradation level. Concerning PEM electrolysers and PEM fuel cells, the voltage offset is used for assessing their EoL [215]. However, the approximation given by technical specifications is usually a non-linear function that can differ from the real degradation rate. Therefore, this complicates the design of linear models and introduces undesirable errors in estimating of the EoL of ESSs.

To deal with this problem, the authors of [226] and [186] proposed linear models based on expected values. Particularly, in [186], the degradation is estimated through the expected capacity loss in the case of batteries, and the expected degradation in fuel cells and electrolysers based on a factor proportional to their power operation. Nonetheless, these linear models are still dependent on static parameters that need to be manually assigned.

In this thesis, similar linear models of [186] were implemented and updated daily based on real-time measurements to overcome this dependency on reliable technical specifications. The battery maximum capacity is estimated daily from the non-linear model existent in the Simulink® SimPower-Systems library. However, in real applications, this estimation can be implemented through data-driven algorithms such as those reviewed in [213], [224], in which the real capacity can be evaluated from voltage and current measurements.

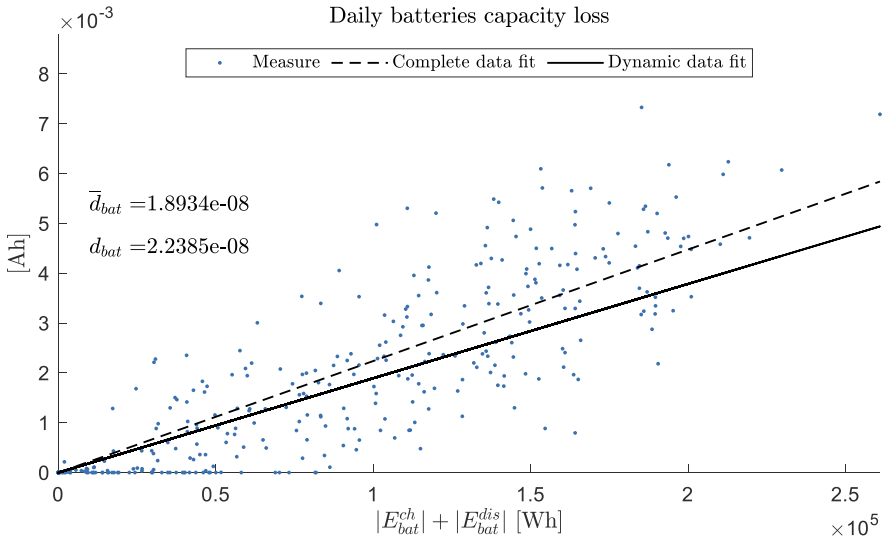

Fig. 5.1: Linear regression *vs* dynamic average approximations of the daily capacity loss of batteries.

It is therefore possible to linearly correlate batteries energy to the loss of batteries capacity, named ΔQ_{bat}. For that, the ratio $d_{bat,k}$ linking the energy used for charging and discharging the batteries to its respective $\Delta Q_{bat,k}$can be calculated daily, through equations (5.5) and (5.6). Calculated as explained in Appendix III, the dynamic average $\bar{d}_{bat,k}$ of all past measured $d_{bat,k}$ determines the model of batteries degradation. The graph in Fig. 5.1 shows the dynamic average ($\bar{d}_{bat}$) and the complete linear regression (d_{bat}) of these measurements $d_{bat,k}$, after a one-year simulation in MATLAB Simulink®. Contrary to complete linear regression, the dynamic average algorithm updates $\bar{d}_{bat,k}$ as soon as a new ΔQ_{bat} is

acquired, thus avoiding the storage of past measurements. Comparing the final linear approximations, the dynamic average $\bar{d}_{bat,k}$ represents a fair estimation of the complete linear regression.

$$\Delta Q_{bat,k} = \left| Q_{bat,k} - Q_{bat,k+24} \right| \tag{5.5}$$

$$d_{bat,k} = \frac{\Delta Q_{bat,k}}{\sum_{k}^{k+24} \left| P_{bat,k}^{ch} \right| \cdot T_s^{TMPC} + \left| P_{bat,k}^{dis} \right| \cdot T_s^{TMPC}} \tag{5.6}$$

Therefore, given that it is recommended to replace the battery packs when they lose 20% of their initial capacity (Q_{bat}) [213], the cost of employing the batteries in the current day can be expressed as in (5.7), where C_{bat} is the capital cost of batteries in €.

$$\pi_{bat,k}^{deg} = \frac{\bar{d}_{bat,k} \cdot T_s^{TMPC} \cdot C_{bat}}{0.2 \cdot Q_{bat}} \cdot \left(P_{bat,k}^{ch} + P_{bat,k}^{dis} \right) \tag{5.7}$$

Analogously, the degradation cost of PEM electrolysers and PEM fuel cells are estimated from the voltage offset after operating them. According to [220], the degradation rate in electrolysers and fuel cells is around $3\,\frac{\mu V}{h}$ per each cell at nominal operation, which corresponds to approximately 20 years of lifespan if they are operated for on average 6 hours per day. Generally, fuel cells and electrolysers must be replaced when they lose 10% of their efficiency, which represents 10% of voltage offset for the same operation condition [219]. Therefore, at the end of each day, the voltage degradation is correlated to the total energy demanded for this day, by calculating the ratio d_i, given by (5.8) and(5.9), where the index i refers to either the fuel cells or the electrolysers. Since fuel cells Simulink® model does not consider the voltage degradation yet, this phenomenon was modelled based on [215]. The modelling of the degradation of PEMFC and PEME cells was detailed in Chapter 2 on page 90.

$$\Delta v_{i,k} = \left| v_{i,k} - v_{i,k+24} \right| \tag{5.8}$$

$$d_i = \frac{\Delta v_{i,k}}{\sum_{k}^{k+24} |P_i|} \tag{5.9}$$

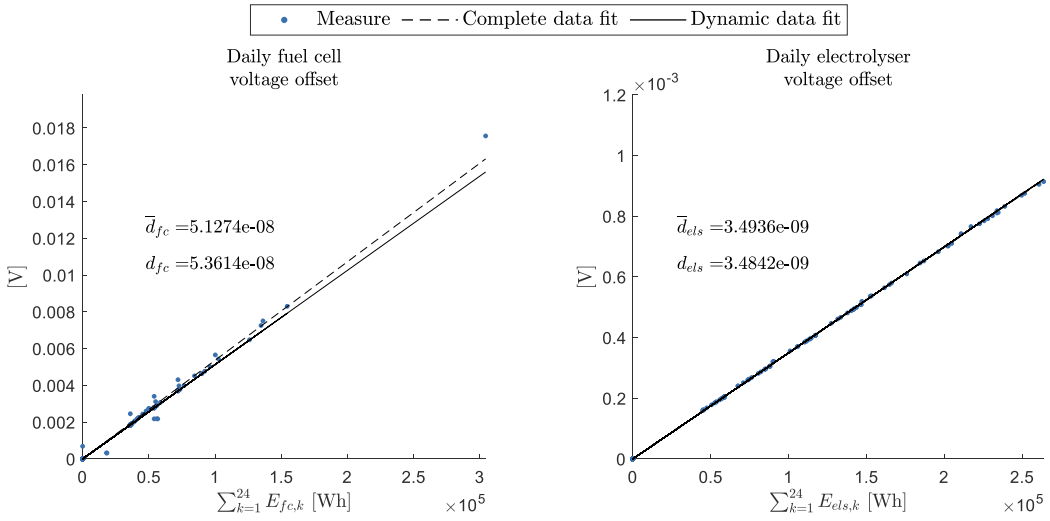

Fig. 5.2: Linear regression *vs* dynamic average approximations of voltage degradation in fuel cells and electrolysers.

The dynamic average $\bar{d}_i$ over all previous measured d_i enables the controller to estimate the EoL of electrolysers and fuel cells, as shown in Fig. 5.2. When the offset voltage attains 10% of the initial

voltage v_i^{init} (i.e. without any degradation), PEMFC and PEME are totally degraded and must be replaced. Therefore, using equation (5.10), the degradation cost of fuel cells and electrolysers during the EMPC horizons can be defined as a proportion of their capital cost in € (C_{fc} or C_{els}).

$$\pi_{i,k}^{deg} = \frac{\bar{d}_{i,k} \cdot C_i}{0.1 \cdot v_i^{init}} \cdot P_i \tag{5.10}$$

5.2.3 *Grid reward for self-consuming electricity*

Although the grid code for individual prosumers is still being developed, some financial incentives have already been established. Particularly, the French Energy Regulation Commission (ERC or *Commission de regulation de l'énergie* in French) limits the total energy injection in BMGs with capacity over or equals to 100 kWc by imposing required marks of the self-consumption rate at the end of the year [12]. The annual self-consumption rate (τ_{sc}^{annual}) measures the percentage of renewable energy that is produced and consumed locally. As expressed in (5.11), the self-consumed energy (E_{sc}) is equal to the difference between the energy generated by the PV panels ($E_{pv,k}$) and the energy injected ($E_{grid,k}^{injected}$). Deducted from the power balance of equation (3.94) on page 125, $E_{grid,k}^{injected}$ corresponds to the part of the energy surplus that was not stored in the ESS, as specified in (5.12). Consequently, τ_{sc}^{annual} is the ratio calculated in (5.14).

$$E_{sc,k} = E_{pv,k} - E_{grid,k}^{injected} \tag{5.11}$$

$$E_{grid,k}^{injected} = T_s^{TMPC} \cdot \left(P_{surplus,k} - \left|P_{els,k}\right| - \left|P_{bat,k}^{ch}\right|\right) \tag{5.12}$$

$$P_{surplus,k} = \begin{cases} P_{pv,k} - P_{cons,k} \Leftrightarrow P_{pv,k} > P_{cons,k} \\ 0 \Leftrightarrow P_{pv,k} \leq P_{cons,k} \end{cases} \tag{5.13}$$

$$\tau_{sc}^{annual} = \frac{\sum_{k=1}^{365} E_{sc,k}}{\sum_{k=1}^{365} E_{pv,k}} = \frac{T_s^{TMPC} \cdot \left(\sum_{k=1}^{365} P_{pv,k} - P_{surplus,k} + \left|P_{els,k}\right| + \left|P_{bat,k}^{ch}\right|\right)}{T_s^{TMPC} \cdot \left(\sum_{k=1}^{365} P_{pv,k}\right)} \tag{5.14}$$

To financially encourage the self-consumption beyond the minimum threshold imposed by ERC, a mechanism of reward and penalty has been established, in which the internal load matching is favoured, and the injection is penalised. The additional income [12] for the annual self-consumed energy is calculated according to (5.15), which is dependent on both the value of the premium P in €/MWh and the PV installed capacity P_{pv}^{inst}. The value of P is determined by an auction among multiple neighbouring buildings willing to inject energy into the main grid. In the BMG understudy, P is worth 20 €/MWh and P_{pv}^{inst} equals to 100 kWc. Moreover, the BMG revenue is penalised according to the maximum power injected in a year ($P_{maxInjected}$). This foster BMGs to inject constant and low power rate to relive the unpredictability of energy management among neighbouring BMGs.

$$\pi_{sc}^{annual} = 10^{-6} \cdot \left(\sum_{k=1}^{365} (P+5) \cdot E_{sc,k} + P \cdot E_{grid,k}^{injected} - 12 \cdot E_{pv,k} \cdot \frac{P_{maxInjected}}{P_{pv}^{inst}}\right) \tag{5.15}$$

The estimation of the maximum power injected at the end of the EMPC horizon ($P_{maxInjected,k=N_h^{EMPC}}$) is calculated using equations (5.16) – (5.21). As convention, $P_{grid}^{injected}$ and

$P_{maxInjected}$ are negative variables and are lower limited by P_{grid}^{Min} as in (5.16). The value of P_{grid}^{Min} is defined according to the maximum power rate supported by the AC-DC interlinking converter, connecting the BMG to the main grid. At each EMPC sampling time, the real maximum power injected ($P_{maxInjected}^{meas}$) is measured by the smart meter and transmitted to EMPC. This value is assigned to the $P_{maxInjected,k=0}$, which is the first element of the EMPC horizon, as defined in (5.17). The $P_{maxInjected,k}$ for the next periods (i.e. for $k > 0$) depends on the expected $P_{grid,k}^{injected}$ as written in (5.18). The auxiliary variables $P_{grid,k}^{negVar}$ and $P_{grid,k}^{posVar}$ are used to evaluate whether the injected power decreased or increased with respect to the last estimation of the maximum injected power. If $P_{grid,k}^{injected}$ is bigger than the estimated maximum power injected at instant k ($P_{maxInjected,k}$), then $P_{grid,k}^{negVar} < 0$, $P_{grid,k}^{posVar} = 0$, and $\delta_{grid,k}^{up_{Injection}}$ in equation (5.20) is equal to 1. Consequently, according to (5.19), $P_{maxInjected,k+1}$ will be increased by the factor $P_{grid,k}^{negVar}$. On the contrary, if $P_{grid,k}^{injected}$ is smaller than $P_{maxInjected,k}$, then $P_{maxInjected,k+1} = P_{maxInjected,k}$, since $P_{grid,k}^{negVar} = 0$.

$$P_{grid}^{Min} \leq P_{grid,k}^{injected}, P_{maxInjected,k} \leq 0 \tag{5.16}$$

$$P_{maxInjected,k=0} = P_{maxInjected}^{meas} \tag{5.17}$$

$$P_{maxInjected,k} = P_{grid,k}^{injected} + P_{grid,k}^{negVar} + P_{grid,k}^{posVar}\big|_{k>0} \tag{5.18}$$

$$P_{maxInjected,k+1} = P_{maxInjected,k} + P_{grid,k}^{negVar}\big|_{k>0} \tag{5.19}$$

$$\delta_{grid,k}^{up_Injection} \cdot P_{grid}^{Min} \leq P_{grid,k}^{negVar} \leq 0, \qquad \delta_{grid,k}^{up_Injection} \in \mathbb{Z} \tag{5.20}$$

$$0 \leq P_{grid,k}^{posVar} \leq \left(1 - \delta_{grid,k}^{up_{Injection}}\right) \cdot P_{grid}^{Max}, \qquad \delta_{grid,k}^{up_{Injection}} \in \mathbb{Z} \tag{5.21}$$

By combining (5.11) – (5.15), the maximisation of the bonus for self-consuming electricity (π_{sc}^{annual}) can be guaranteed by periodic optimisations of equation (5.22) within the EMPC horizon, where the variable β_{scPen}^{EMPC} is defined by equation (5.23). The complete reasoning for deducting (5.22) is explained in Appendix IV. Hence, depending on the maximum power injected in the past ($P_{maxInjected}^{meas}$), β_{scPen}^{EMPC} can be equal to zero or not. It is worth zero if the maximum expected injected power ($P_{maxInjected,k=N_h^{EMPC}}$) is smaller than $P_{maxInjected}^{meas}$. This is because it is not worthy try to reduce the maximum injected power ($P_{maxInjected,k=N_h^{EMPC}}$) if it is already known that the maximum available energy – which is equal to the estimated energy surplus for the next 24 hours ($T_s^{EMPC} = 24h$) – is smaller than $P_{maxInjected}^{meas}$.

$$\pi_{sc,k} = 5 \cdot 10^{-6} \cdot T_s^{TMPC} \cdot \left(\left|P_{els,k}\right| + \left|P_{bat,k}^{ch}\right|\right) - \beta_{scPen}^{EMPC} \cdot P_{maxInjected,k=N_h^{EMPC}} \tag{5.22}$$

$$\beta_{scPen}^{EMPC} = \begin{cases} 0, & if\ P_{maxInjected}^{meas} \leq \max\left(P_{surplus,[0,T_s^{EMPC}]}\right) \\ \dfrac{12 \cdot 10^{-6} \cdot \sum_{i=1}^{365} E_{pv,i}}{P_{pv}^{inst}}, & otherwise \end{cases} \tag{5.23}$$

5.2.4 *Grid penalization for not attaining the marks of self-consumption*

The French ERC requires a predefined mark of self-consumption ($\tau_{sc}^{required}$) at the end of the year, which limits BMGs to inject energy to the grid according to their annual energy consumption and annual PV energy generation. To force BMGs to respect this restriction, the premium P of equation (5.15) is reduced by 2% per percentage point of the gap between the required self-consumption rate and the real one attained by the BMG [12]. For instance, if the required mark is $\tau_{sc}^{required} = 80\%$ and the BMG attained only 70%, the premium P in the next year will be reduced in $2 \times (80\% - 70\%) = 20\%$. On the contrary, if the annual self-consumption rate is above $\tau_{sc}^{required}$, the premium factor P remains the same as the last year.

To avoid this grid penalisation and ensure the BMG profitability for the upcoming years, the objective function and constraints of EMPC were designed to force the expected annual self-consumption rate – named $\hat{\tau}_{sc}^{annual}$ – to be greater than $\tau_{sc}^{required}$. Hence, as expressed in (5.24), if $\hat{\tau}_{sc}^{annual}$ is below $\tau_{sc}^{required}$, the BMG has to virtually pay for a fraction of ESSs capital cost and the annual electricity bill of the expected deficit using the maximum electricity price in the previous year. Remarkably, this virtually over taxation is to force the BMG to attain $\tau_{sc}^{required}$ in all circumstance. The fraction of this virtual penalisation depends on the gap between $\tau_{sc}^{required}$ and $\hat{\tau}_{sc}^{annual}$, which is defined by a slack variable λ_{sc} that ranges from 0 to 1 and a binary variable δ_{sc}^{pen}. Both λ_{sc} and δ_{sc}^{pen} are worth zero when the BMG are likely to attain $\tau_{sc}^{required}$ (i.e. $\hat{\tau}_{sc}^{annual} \geq \tau_{sc}^{required}$) and they are different than zero in the opposite case. This logic is expressed in (5.26) – (5.28), where $\hat{\tau}_{sc}^{annual}$ is the expected annual self-consumption rate that will be explained in section 5.3.

$$\pi_{sc,k}^{pen} = \left(C_{bat} + C_{fc} + C_{els} + max\left(\pi_{elec,k=[1,365]}\right) \cdot \sum_{i=1}^{365} P_{deficit,i} \right) \cdot \left(\delta_{sc}^{pen} + \lambda_{sc}\right) \tag{5.24}$$

$$0 \leq \lambda_{sc} \leq 1, \qquad \lambda_{sc} \in \mathcal{R} \tag{5.25}$$

$$\hat{\tau}_{sc}^{annual} + \lambda_{sc} \geq \tau_{sc}^{required} \tag{5.26}$$

$$0 \leq \hat{\tau}_{sc}^{annual} \leq 1 \tag{5.27}$$

$$\lambda_{sc} - \delta_{sc}^{pen} \leq 0, \qquad \delta_{sc}^{pen} \in \{0,1\} \tag{5.28}$$

5.2.5 *Summary of the estimation of the building microgrid operation cost*

After calculating the six π-costs, it is possible to define the parameters of EMPC cost function that is updated by the MG cost estimator daily. Therefore, based on the six π-costs, the EMPC optimises daily the cost function defined by (3.91), where J_k^{EMPC} is determined through (5.29). All β parameters in equation (5.29) are summarized in Table 5.1 with the related equations that were discussed previously.

$$
\begin{aligned}
J_k^{EMPC} = & \beta_{grid}^{EMPC}\left(P_{fc,k} + P_{bat,k}^{dis}\right) \\
& + \beta_{fcDeg}^{EMPC} \cdot P_{fc} \\
& - \beta_{elsDeg}^{EMPC} \cdot P_{els} \\
& + \beta_{batDeg}^{EMPC} \cdot \left(-P_{bat,k}^{ch} + P_{bat,k}^{dis}\right) \\
& + 5 \cdot 10^{-6} \cdot T_s^{TMPC} \cdot \left(P_{els,k} + P_{bat,k}^{ch}\right) \\
& + \beta_{maxInjected}^{EMPC} \cdot P_{maxInjected,k=N_h^{EMPC}} \\
& + \beta_{scPen}^{EMPC} \cdot \left(\lambda_{sc} + \delta_{sc}^{pen}\right)
\end{aligned}
\tag{5.29}
$$

Table 5.1: Summary of the parameters that the MG cost estimator sends to the EMPC daily to update its cost function.

Parameter	Value	Related equation
$\boldsymbol{\beta_{grid}^{EMPC}}$	$-\pi_{elec,k} \cdot T_s^{EMPC}$	(5.4)
$\boldsymbol{\beta_{fcDeg}^{EMPC}}$	$\frac{\bar{d}_{fc,k} \cdot C_{fc} \cdot T_s^{EMPC}}{0.1 \cdot v_{fc}^{init}}$	(5.10)
$\boldsymbol{\beta_{elsDeg}^{EMPC}}$	$\frac{\bar{d}_{els,k} \cdot C_{els} \cdot T_s^{EMPC}}{0.1 \cdot v_{els}^{init}}$	(5.10)
$\boldsymbol{\beta_{batDeg}^{EMPC}}$	$\frac{\bar{d}_{bat,k} \cdot T_s^{TMPC} \cdot C_{bat}}{0.2 \cdot Q_{bat}}$	(5.7)
$\boldsymbol{\beta_{maxInjected}^{EMPC}}$	$\begin{cases} 0, & if\ P_{maxInjected}^{meas} \leq \max\left(P_{surplus,[0,N_h^{EMPC}]}\right) \\ \frac{12 \cdot 10^{-6} \cdot \sum_{i=1}^{365} E_{pv,i}}{P_{pv}^{inst}}, & otherwise \end{cases}$	(5.23)
$\boldsymbol{\beta_{scPen}^{EMPC}}$	$\left(C_{bat} + C_{fc} + C_{els} + max\left(\pi_{elec,k=[1,365]}\right) \cdot \sum_{i=1}^{365} P_{deficit,i}\right)$	(5.24)

5.3 Details of the algorithm for estimating the annual self-consumption rate

Aiming to operate the BMG at minimum cost, but at the same time guarantee the required annual marks of self-consumption imposed by French grid operators, the MG cost estimator calculates the expected annual self-consumption rate ($\hat{\tau}_{sc}^{annual}$) using both the prediction data of the previous year and the average behaviour of HMPC. The estimation process contains three main steps that is implemented once a day. Firstly, the last-year prediction data are classified into four classes using the k-means algorithm. Secondly, the average of HMPC control variables are assigned to each k-means class, and the expected annual self-consumption rate is calculated using this average and the results from k-means classification. Finally, $\hat{\tau}_{sc}^{annual}$ is integrated into the two-days ahead horizon of EMPC. The following three subsections detail these three steps.

5.3.1 *Classification of prediction data using k-means algorithm*

K-means algorithm aims to partition n observations into K clusters in which each observation belongs to the cluster with the nearest mean called centroid [231]. The MG cost estimator uses the k-means algorithm to classifies the annual prediction data of PV power generation and building power consumption into four classes, representing the four seasons. These classes distinguish the annual

dataset with respect to the five normalised features retrieved from the daily prediction data, named x_1, x_2, x_3, x_4 and x_5, as illustrated in Fig. 5.3.

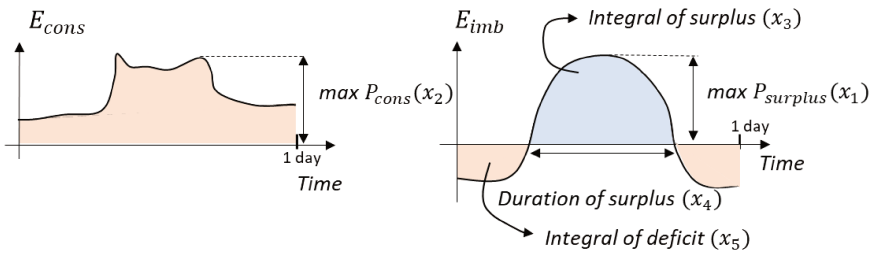

Fig. 5.3: The five features for k-means classification.

The normalization of these five features is computed with respected their maximum value of the entire dataset, following equations (5.30) – (5.34), where $i = 24 \cdot N, k = 24 \cdot N \mid N \in \mathbb{N} \cap [0,365]$. Therefore, based on the raw net power imbalance, each day is assigned to one class among $K = \{1,2,3,4\}$. Hence, by definition, each k-means class contains $n_K = \{n_1, n_2, n_3, n_4\}$ observations, where $n_1 + n_2 + n_3 + n_4 = 365\ days$.

$$x_1 = \frac{\max\left(P_{surplus,[k,k+24]}\right)}{\max\left(P_{surplus,[1,365]}\right)} \tag{5.30}$$

$$x_2 = \frac{\max\left(P_{cons,[k,k+24]}\right)}{\max\left(P_{cons,[1,365]}\right)} \tag{5.31}$$

$$x_3 = \frac{\sum_{k=1}^{24} P_{surplus,k}}{\max\left(\sum_{i=1}^{24} P_{surplus,i}\right)} \tag{5.32}$$

$$x_4 = \frac{\sum_{k=1}^{k+24}(P_{surplus,k} > 0)}{\max\left(\sum_{i=1}^{24}(P_{surplus,i} > 0)\right)} \tag{5.33}$$

$$x_5 = \frac{\sum_{k=1}^{k+24} P_{deficity,k}}{\max\left(\sum_{i=1}^{i+24} P_{deficit,i}\right)} \tag{5.34}$$

After applying the k-means algorithm, the layout of these five normalised features of the dataset of a public building is shown in the graphs of Fig. 5.4, and in Fig. 5.5 of the dataset of the residential building[4]. Observing the maximum and minimum values of the graphs in Fig. 5.6 and Fig. 5.7, it is possible to conclude that daily profiles sharing a similar portion of data are grouped into distinct k-means classes.

The black points in Fig. 5.4 and Fig. 5.5 are the four centroids of the four k-means classes. The centroids are the barycentre of the disposal of the data points in the space. They can also be interpreted as the average of all data points belonging to a specific class. Therefore, the nearest power imbalance profile to a specific centroid can be considered the most probable profile in the k-means class. In Fig. 5.8, it is possible to observe that the closest profile to the centroid is very similar to the average of all profiles belonging to a specific class.

[4] The dataset used in the k-means classification is the same as those presented in section 2.3 in Chapter 2 on page 51.

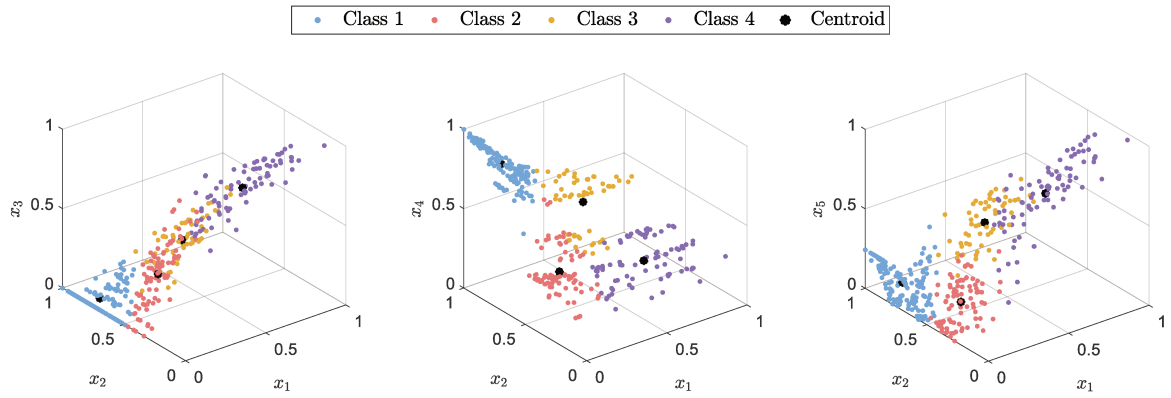

Fig. 5.4: K-means classification of the one-year power imbalance data prediction of the public building.

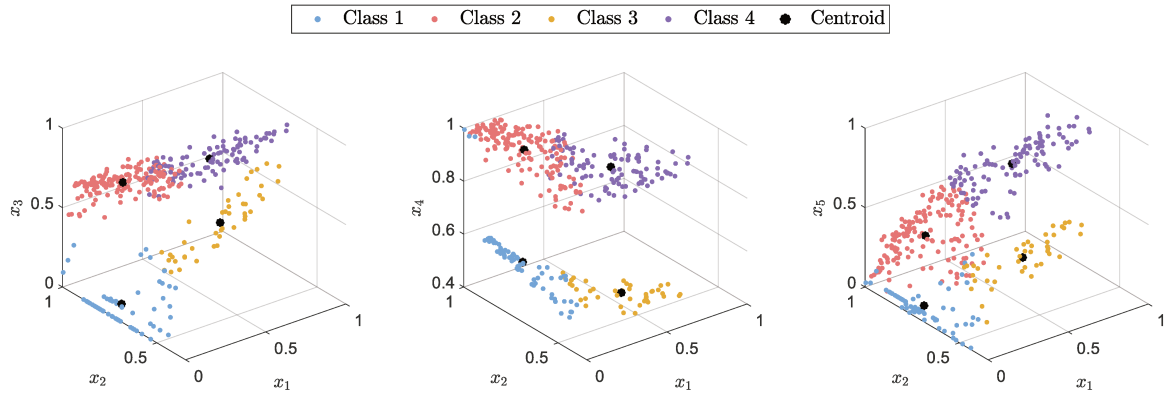

Fig. 5.5: K-means classification of the one-year power imbalance data prediction of the residential building.

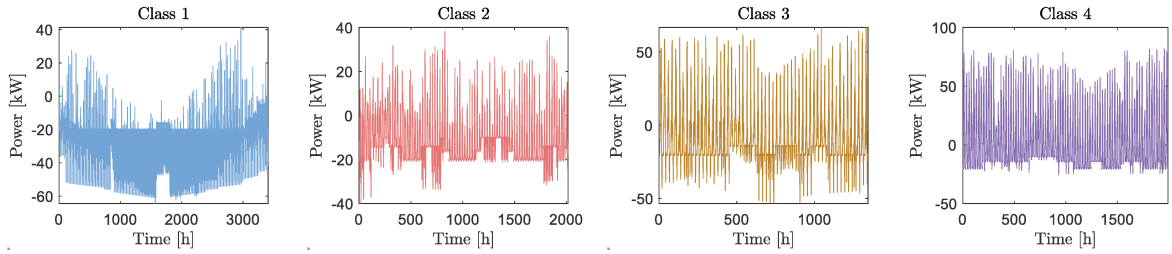

Fig. 5.6: Annual power imbalance data prediction of the public building classified into four classes.

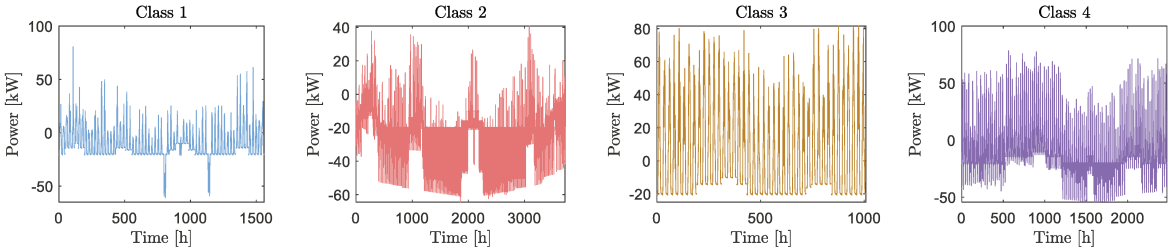

Fig. 5.7: Annual power imbalance data prediction of the residential building classified into four classes.

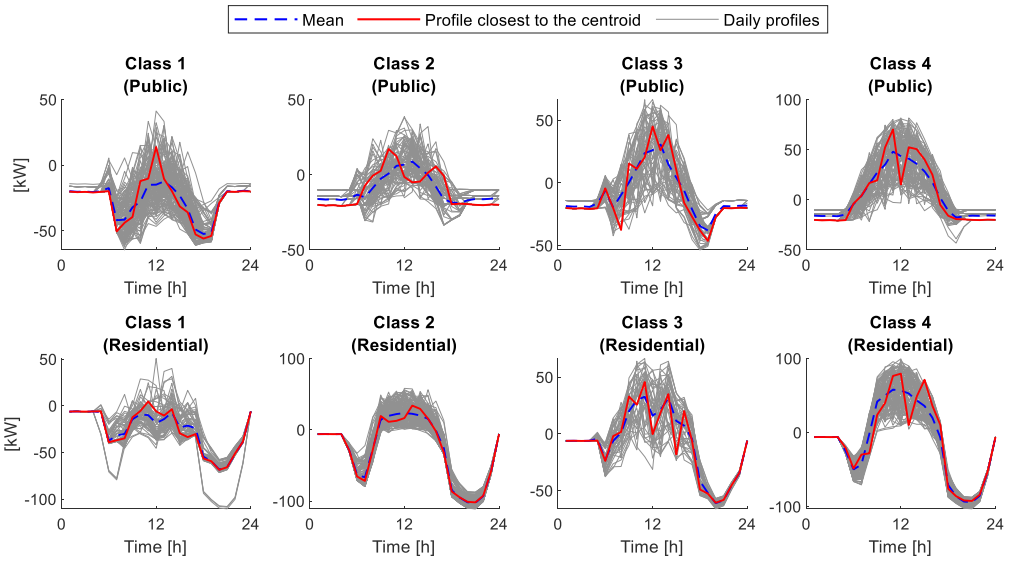

Fig. 5.8: The nearest profiles to the four centroids in the dataset of the residential and public building.

The position of the centroids also permits us to classify any generic profile into one of the four k-means classes. Considering that the coordinates of the four centroids $\mathbb{C}_K$ is equal to $\left(x_1^{\mathbb{C}_K}, x_2^{\mathbb{C}_K}, x_3^{\mathbb{C}_K}, x_4^{\mathbb{C}_K}, x_5^{\mathbb{C}_K}\right)$, where $K \in \{1,2,3,4\}$ is one of the four k-means class. Therefore, a generic profile ρ, in which its coordinates (i.e. features) equal to $\left(x_1^{\rho}, x_2^{\rho}, x_3^{\rho}, x_4^{\rho}, x_5^{\rho}\right)$, belongs to class K, if and only if, the distance between $\mathbb{C}_K$ and ρ is the smallest one for all $K \in \{1,2,3,4\}$. In other words, the profile ρ belongs to k-means class K, if and only if, the condition of equation (5.35) is satisfied.

$$\rho \in \mathbb{C}_K \Leftrightarrow \sum_{i=1}^{5}\left(x_i^{\rho} - x_i^{\mathbb{C}_K}\right)^2 \leq \sum_{i=1}^{5}\left(x_i^{\rho} - x_i^{\mathbb{C}_M}\right)^2, \forall M \in \{1,2,3,4\} \tag{5.35}$$

Therefore, every midnight the community aggregator sends to the building EMS the prediction data referring to the power generation for the next two days (horizon of 48 hours). Analogously, the building power consumption is estimated locally, through the data measurements acquired by the smart meter. With these data, it is possible to estimate the two days-ahead power imbalance and to identify the five normalised features of these two day-ahead, named ρ_{today} and $\rho_{tomorrow}$, which are defined by equations (5.36) and (5.37), respectively. Subsequently, by applying the condition of (5.35) for each of these days, it is possible to determine K_{today} and $K_{tomorrow}$, which are the k-means classes that the profiles ρ_{today} and $\rho_{tomorrow}$ belong to, respectively.

$$\rho_{today} = \left(x_1^{\rho_{today}}, x_2^{\rho_{today}}, x_3^{\rho_{today}}, x_4^{\rho_{today}}, x_5^{\rho_{today}}\right) \tag{5.36}$$

$$\rho_{tomorrow} = \left(x_1^{\rho_{tomorrow}}, x_2^{\rho_{tomorrow}}, x_3^{\rho_{tomorrow}}, x_4^{\rho_{tomorrow}}, x_5^{\rho_{tomorrow}}\right) \tag{5.37}$$

To enhance the precision over time, the position of the four centroids $\mathbb{C}_K$ are updated every midnight using updated data. For that, the data prediction of the current day replaces the data prediction of the corresponding day in the last year, as shown in Fig. 5.9. Therefore, the size of the dataset is constant, and the accuracy of the classification is enhanced when approaching the end of the year.

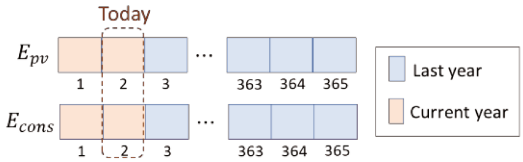

Fig. 5.9: Replacement of previous year data prediction by the recent one.

5.3.2 *The estimation of the average behaviour of the hierarchical MPC*

According to equation (5.14), the self-consumption depends on the annual $E_{pv,k}$, $E_{surplus,k}$, $E_{els,k}$ and $E_{bat,k}^{ch}$. Consequently, it is possible to estimate $\hat{\tau}_{sc}^{annual}$ by using equation (5.38), where $\hat{E}_{pv}$, $\hat{E}_{surplus}$, $\hat{E}_{els}$, $\hat{E}_{bat}^{ch}$ are the estimated values of annual E_{pv}, $E_{surplus}$, E_{els} and E_{bat}^{ch}, respectively.

$$\hat{\tau}_{sc}^{annual} = 1 - \frac{\hat{E}_{surplus} - \left|\hat{E}_{bat}^{ch}\right| - \left|\hat{E}_{els}\right|}{\hat{E}_{pv}} \tag{5.38}$$

Considering that the current day is the day D, then $\hat{E}_{pv}$ and $\hat{E}_{surplus}$ can be calculated from the combination of the prediction data of the previous year and those of the current year, using equations (5.39) and (5.40). Therefore, the estimation of $\hat{E}_{pv}$ and $\hat{E}_{surplus}$ are continuously enhanced by the replacement process described in Fig. 5.9.

$$\hat{E}_{pv} = \sum_{k=1}^{365} E_{pv,k} = \underbrace{\sum_{k=1}^{D-1} E_{pv,k}^{this_year}}_{\substack{Measured\ by \\ sensors}} + \underbrace{\sum_{k=D}^{365} E_{pv,k}^{last_year}}_{\substack{Estimated\ by \\ previous\ year \\ prediction\ data}} \tag{5.39}$$

$$\hat{E}_{surplus} = \sum_{k=1}^{365} E_{surplus,k} = \underbrace{\sum_{k=1}^{D-1} E_{surplus,k}^{this_year}}_{\substack{Measured\ by \\ sensors}} + \underbrace{\sum_{k=D}^{365} E_{surplus,k}^{last_year}}_{\substack{Estimated\ by \\ previous\ year \\ prediction\ data}} \tag{5.40}$$

Likewise, $\hat{E}_{els}$ and $\hat{E}_{bat}^{ch}$ can be estimated through equations (5.41) and (5.42), respectively. Notably, $E_{els,k}$ and $E_{bat,k}^{ch}$ of the prior period $[1; D-1]$ are measured variables, since they are collected by the sensors in the electrolysers' and batteries' DC-DC power converters. On the other hand, the outcome of k-means classification is used to calculate the expected values concerning the future partition of $\hat{E}_{els}$ and $\hat{E}_{bat}^{ch}$ (i.e. those corresponding to the future periods $[D; 365]$). Taking as hypothesis that the HMPC will determine similar control variables when subjected to similar conditions of raw power imbalance prediction data, the classified expected value of the daily energy assigned to batteries and electrolysis reflects a fair approximation to calculate the future partition of $\hat{E}_{bat}^{ch}$ and $\hat{E}_{els}$.

$$\hat{E}_{els} = \sum_{k=1}^{365} E_{els,k} = \underbrace{\sum_{k=1}^{D-1} E_{els,k}}_{\substack{Measured\ by \\ sensors}} + \underbrace{\sum_{k=D}^{365} E_{els,k}}_{\substack{Estimated\ through \\ k-means}} \tag{5.41}$$

$$\hat{E}_{bat}^{ch} = \sum_{k=1}^{365} E_{bat,k}^{ch} = \underbrace{\sum_{k=1}^{D-1} E_{bat,k}^{ch}}_{Measured\ by\ sensors} + \underbrace{\sum_{k=D}^{365} E_{bat,k}^{ch}}_{Estimated\ through\ k-means} \tag{5.42}$$

To validate this hypothesis, the power references of batteries and electrolysers, which were determined by the HMPC during one-year simulation, were collected and classified using the k-means algorithm described in subsection 5.3.1. The graphs of Fig. 5.10 and Fig. 5.11 confirm the validity of this hypothesis because there is a pattern in E_{els} and E_{bat}^{ch} according to each k-means class.

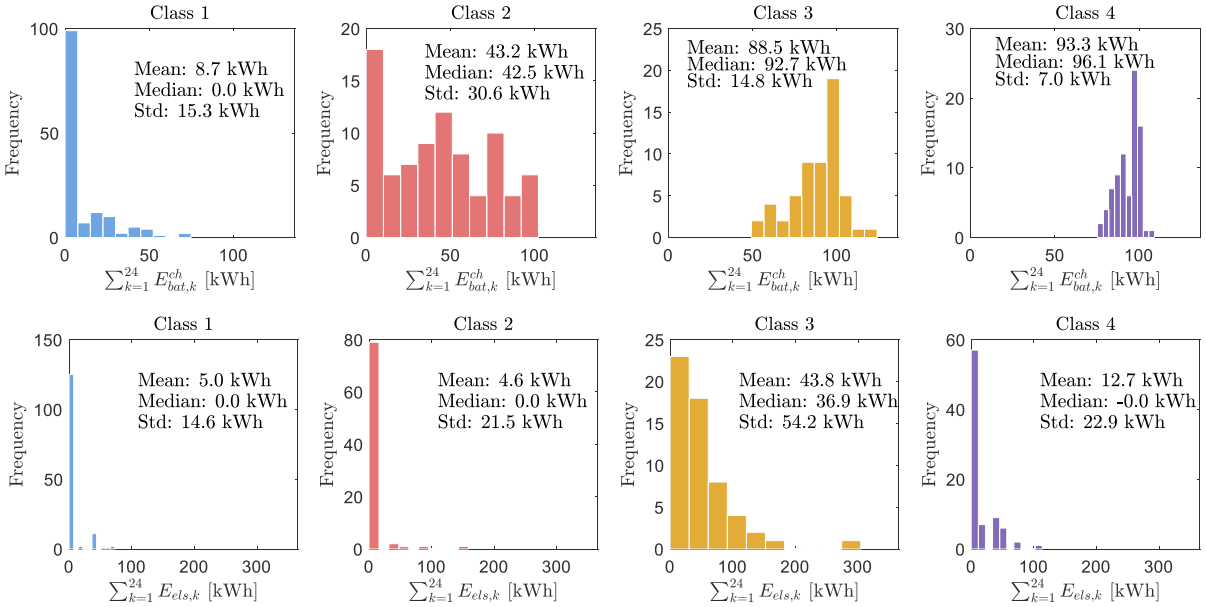

Fig. 5.10: Histogram with the statistical data of the daily energy assigned to charge the batteries (E_{bat}^{ch}) and operate the electrolysers (E_{els}) in each k-means class in the public building.

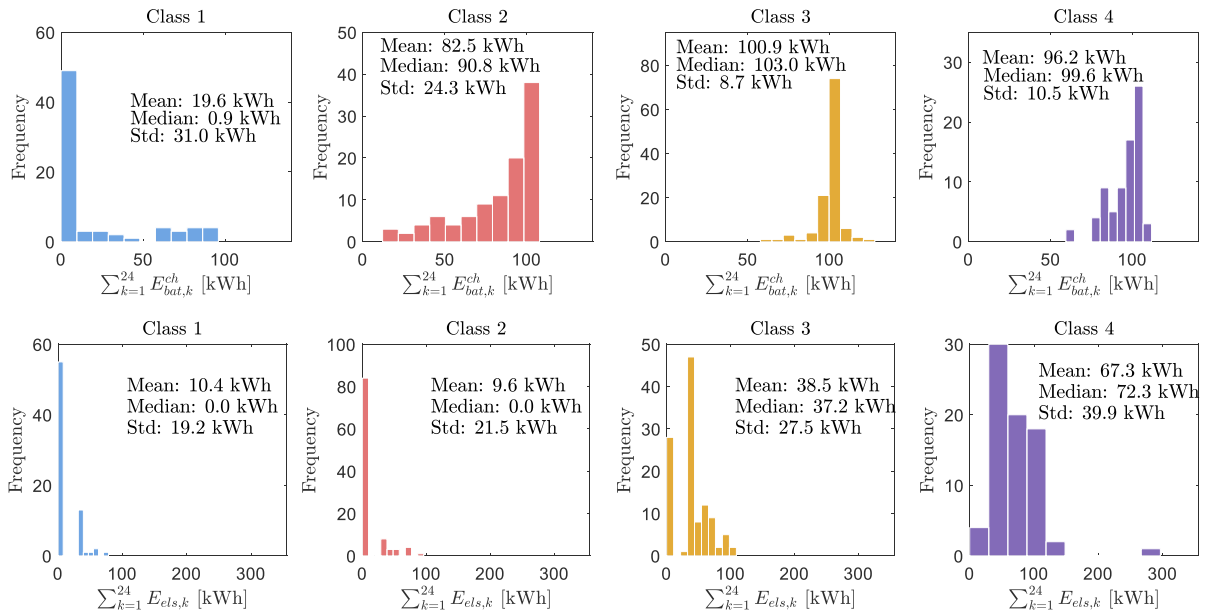

Fig. 5.11: Histogram with the statistical data of the daily energy assigned to charge the batteries (E_{bat}^{ch}) and operate the electrolysers (E_{els}) in each k-means class in the residential building.

In other words, given that the current day D belongs to the k-means class K (i.e. $c_K = K$), then it is likely that the batteries will be charged equivalently to $\bar{E}^{ch}_{bat|K}$, which is the average energy for charging the batteries given that day D belongs to class K. Analogously, the energy assigned to electrolysers will be on average equals to $\bar{E}_{els|K}$. Therefore, $\bar{E}^{ch}_{bat|K}$ and $\bar{E}_{els|K}$ are determined using (5.43) and (5.44), respectively.

$$\bar{E}^{ch}_{bat|K} = E\left(\sum_{i=1}^{24} E^{ch}_{bat,i} \middle| c_K = K\right) \Rightarrow \bar{E}^{ch}_{bat|K}\big|_{i+1} = \frac{\left(N_K \cdot \bar{E}^{ch}_{bat|K}\big|_i\right) + \sum_{i=1}^{24} E^{ch}_{bat,i}}{N_K + 1} \tag{5.43}$$

$$\bar{E}_{els|K} = E\left(\sum_{i=1}^{24} E_{els,i} \middle| c_K = K\right) \Rightarrow \bar{E}_{els|K}\big|_{i+1} = \frac{\left(N_K \cdot \bar{E}_{els|K}\big|_i\right) + \sum_{i=1}^{24} E_{els,i}}{N_K + 1} \tag{5.44}$$

The conditional expected value (i.e. $E(\cdot|\cdot)$) is calculated through the dynamic average of the total daily energy assigned to batteries and electrolysers ($\sum_{i=1}^{24} E^{ch}_{bat,i}$ and $\sum_{i=1}^{24} E_{els,i}$) after k-means classification. Remarkably, the dynamic average can be computed using the algorithm explained in Appendix III or the right side of equations (5.43) and (5.44), where N_K is the number of times that the class K has appeared from the beginning of the year until the current day D. Hence, each k-means class K, which is already identified by its centroid $\mathbb{C}_K$ and the number of observations n_K, is also associated with the average energy used to charge the batteries ($\bar{E}^{ch}_{bat|K}$) and to operate the electrolysers ($\bar{E}_{els|K}$), as shown in Fig. 5.12.

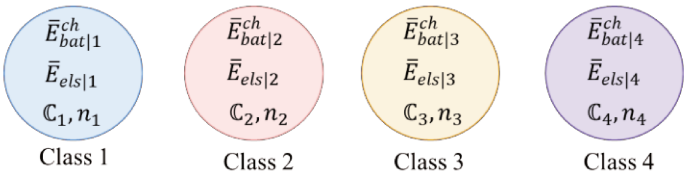

Fig. 5.12: Structure of the information associated with each k-means class.

Therefore, $\bar{E}^{ch}_{bat|K}$ and $\bar{E}_{els|K}$ combined with the expected number of days belonging to class K in the future (n_K^{future}) enables to estimate the annual $\hat{E}^{ch}_{bat}$ and $\hat{E}_{els}$. Deducted from (5.41) and (5.42), $\hat{E}^{ch}_{bat}$ and $\hat{E}_{els}$ are the union of all conditional expected values through all four k-means classes, as expressed in (5.45) and (5.46).

$$\hat{E}^{ch}_{bat} = \sum_{i=1}^{365} E^{ch}_{bat,i} = \sum_{i=1}^{D-1} E^{ch}_{bat,i} + \sum_{K=1}^{4} \left(n_K^{future} \cdot \bar{E}^{ch}_{bat|K}\right) \tag{5.45}$$

$$\hat{E}_{els} = \sum_{i=1}^{365} E^{ch}_{els,i} = \sum_{i=1}^{D-1} E_{els,i} + \sum_{K=1}^{4} \left(n_K^{future} \cdot \bar{E}_{els|K}\right) \tag{5.46}$$

The n_K^{future} is estimated from the total number of observations n_K of a given class $K \in \{1,2,3,4\}$ and the total number of observations in the past n_k^{past}, as expressed in (5.47). To summarize, Fig. 5.13 recapitulates all steps and the related equations used to estimate the annual self-consumption rate.

$$n_K = n_K^{past} + n_K^{future}, \forall K \in \{1,2,3,4\} \tag{5.47}$$

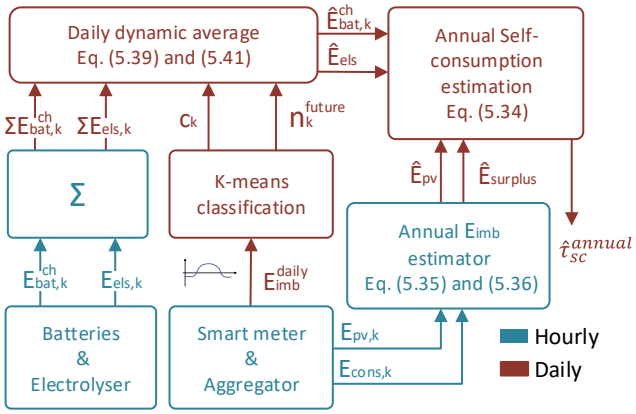

Fig. 5.13: Estimation of the expected annual self-consumption rate based on power imbalance prediction data.

5.3.3 *Integration of the annual expected self-consumption rate into the formulation of the Economic Model Predictive Control*

To integrate $\hat{\tau}_{sc}^{annual}$ into the EMPC optimisation process, the equation (5.38) is adapted to be compliant with the two-day-ahead horizon of EMPC. By combining (5.45) with (5.47) and considering that the current day (day D) belongs to the class K_{today} and the following day (day $D+1$) belongs to the class $K_{tomorrow}$, the expected energy used for charging batteries in a year can be calculated using (5.48). Likewise, for the electrolysers, the expected energy used to generate hydrogen in a year is estimated through (5.49).

$$\hat{E}_{bat}^{ch} = \sum_{i=1}^{D-1} E_{bat,i}^{ch} + \underbrace{\sum_{\substack{K=1 \\ K\neq K_{today} \\ K\neq K_{tomorrow}}}^{4} n_K^{future} E\left(\sum_{i=1}^{24} E_{bat,i}^{ch} \middle| K\right)}_{\alpha_{sc-bat}^{const}} + n_{K_{today}}^{future} E\left(\sum_{i=1}^{24} E_{bat,i}^{ch} \middle| K_{today}\right) + n_{K_{tomorrow}}^{future} E\left(\sum_{i=1}^{24} E_{bat,i}^{ch} \middle| K_{tomorrow}\right) \tag{5.48}$$

$$\hat{E}_{els} = \sum_{i=1}^{D-1} E_{els,i} + \underbrace{\sum_{\substack{K=1 \\ K\neq K_{today} \\ K\neq K_{tomorrow}}}^{4} n_K^{future} E\left(\sum_{i=1}^{24} E_{els,i} \middle| K\right)}_{\alpha_{sc-els}^{const}} + n_{K_{today}}^{future} E\left(\sum_{i=1}^{24} E_{els,i} \middle| K_{today}\right) + n_{K_{tomorrow}}^{future} E\left(\sum_{i=1}^{24} E_{els,i} \middle| K_{tomorrow}\right) \tag{5.49}$$

Since the EMPC horizon comprehends only days D and $D+1$ (i.e. today and tomorrow), the actions of EMPC will impact only the third and the fourth terms of equation (5.48) and (5.49), whereas the first and the second terms are constant from the perspective of EMPC. For simplicity, these constant terms are named as α_{sc-bat}^{const} for batteries and α_{sc-els}^{const} for electrolysers. Therefore, the expected $\hat{\tau}_{sc}^{annual}$ within the EMPC horizon ranging from 1 to 48 hours is calculated as (5.50).

$$\hat{\tau}_{sc}^{annual} = \beta_{sc}^{const} + \beta_{sc}^{today} \cdot \left(\sum_{i=1}^{24} \left(P_{bat,i}^{ch} + P_{els,i}\right)\right) + \beta_{sc}^{tomorrow} \cdot \left(\sum_{i=25}^{48} \left(P_{bat,i}^{ch} + P_{els,i}\right)\right) \tag{5.50}$$

Where β_{sc}^{const}, β_{sc}^{today} and $\beta_{sc}^{tomorrow}$ are parameters that change their values according to the current power imbalance profile, $n_{K_{today}}^{future}$ and $n_{K_{tomorrow}}^{future}$. Therefore, these parameters are calculated using (5.51) – (5.53). These parameters are sent to the EMPC daily to be embedded into the inequality constraint (5.26) that can be rewritten as expressed in (5.54).

$$\beta_{sc}^{const} = 1 - \frac{\sum_{i=1}^{365} E_{surplus,i} - \alpha_{sc-bat}^{const} - \alpha_{sc-els}^{const}}{\sum_{i=1}^{365} E_{pv,i}} \tag{5.51}$$

$$\beta_{sc}^{today} = \frac{n_{K_{today}}^{future} \cdot T_s^{TMPC}}{\sum_{i=1}^{365} E_{pv,i}} \tag{5.52}$$

$$\beta_{sc}^{tomorrow} = \frac{n_{K_{tomorrow}}^{future} \cdot T_s^{TMPC}}{\sum_{i=1}^{365} E_{pv,i}} \tag{5.53}$$

$$\beta_{sc}^{const} + \beta_{sc}^{today} \cdot \left(\sum_{i=1}^{24} \left(P_{bat,i}^{ch} + P_{els,i} \right) \right) + \beta_{sc}^{tomorrow} \cdot \left(\sum_{i=25}^{48} \left(P_{bat,i}^{ch} + P_{els,i} \right) \right) + \lambda_{sc} \geq \tau_{sc}^{required} \tag{5.54}$$

5.4 Initialisation of the microgrid cost estimator algorithm

As explained in the previous sections, the MG cost estimator is an iterative algorithm that evolves along the time. The current estimations of the degradation rate of ESS, total MG operation cost and annual self-consumption rate rely on the estimation of the previous iteration and recent data measurements. For instance, as expressed in equations (5.7) and (5.10), the degradation rate of ESS is computed through the dynamic average of $\bar{d}_{bat}$, $\bar{d}_{fc}$ and $\bar{d}_{fc}$, which are dependent on their values in the last iteration. Likewise, (5.43) and (5.44) use the previous estimation of $\bar{E}_{bat|K}^{ch}$ and $\bar{E}_{els|K}$ to update their current values. For this reason, it is necessary to initialise the MG cost estimator algorithm with reliable values to ensure that the algorithm has operate adequately since the first days of activity.

Hence, as shown in Fig. 5.14, on the first day of BMG operation, the MG cost estimator runs the k-means algorithm with the estimated power imbalance dataset of the current year, which is the power imbalance dataset of the previous year. This enables the MG cost estimator to determine the four most probable profiles in the year, which are the closest daily power imbalance profiles to the centroids. Afterwards, the MG cost estimator makes a request to the EMPC control layer. It asks the EMPC to determine the control variables – especially P_{bat}^{ch} and P_{els} – for the four most probable profiles of the prediction power imbalance in the year. In this step, the EMPC determines the control variables of these four most probable profiles using the simplified cost function defined by (5.55), since it has no information about the original cost function (equation (5.29)). In this formulation, the EMPC minimises the energy grid exchange (or maximise the self-consumption rate) without considering the inequality constraint (5.54).

$$SoC_{ref}, LoH_{ref} = \arg\left(\min_{SoC_{ref}, LoH_{ref}} \sum_{k=1}^{N_h^{EMPC}=48} \left| P_{grid,k}^{import} \right| + \left| P_{grid,k}^{injected} \right| \right) \tag{5.55}$$

As soon as the MG cost estimator receives the control variables for each of the four daily profiles, it can compute β_{sc}^{const}, β_{sc}^{today} and $\beta_{sc}^{tomorrow}$ of equations (5.51) – (5.53), respectively. On the

contrary, all cost function parameters defined by (5.54) cannot be determined by this process. Notably, only β_{grid}^{EMPC}, $\beta_{maxInjected}^{EMPC}$ and β_{scPen}^{EMPC} at this point is calculable because these parameters depend only on the electricity price, power imbalance prediction data and capital cost of ESS. The BMG knows all this information since the first instant of operation. Controversially, until the ESS is not operated, the MG cost estimator cannot determine the ESS degradation cost parameters, i.e. β_{fcDeg}^{EMPC}, β_{elsDeg}^{EMPC} and β_{batDeg}^{EMPC}.

Therefore, the EMPC in the first day will send to the real BMG the power references determined by the optimization of (5.55). Then, on the second day, the MG cost estimator will have acquired enough current and voltage measurements at batteries, PEM electrolysers and PEM fuel cells branches to estimate β_{fcDeg}^{EMPC}, β_{elsDeg}^{EMPC} and β_{batDeg}^{EMPC}. Afterwards, the MG cost estimator sends a signal to EMPC, indicating that all the parameters of the cost function (5.29) and constraint (5.54) are initialized. As a result, the initialisation process finishes and the EMPC starts operating with the more complex cost function (equation (5.29)) and with the inequality constraint (5.54). Fig. 5.14 summarises the initialization process of the MG cost estimator.

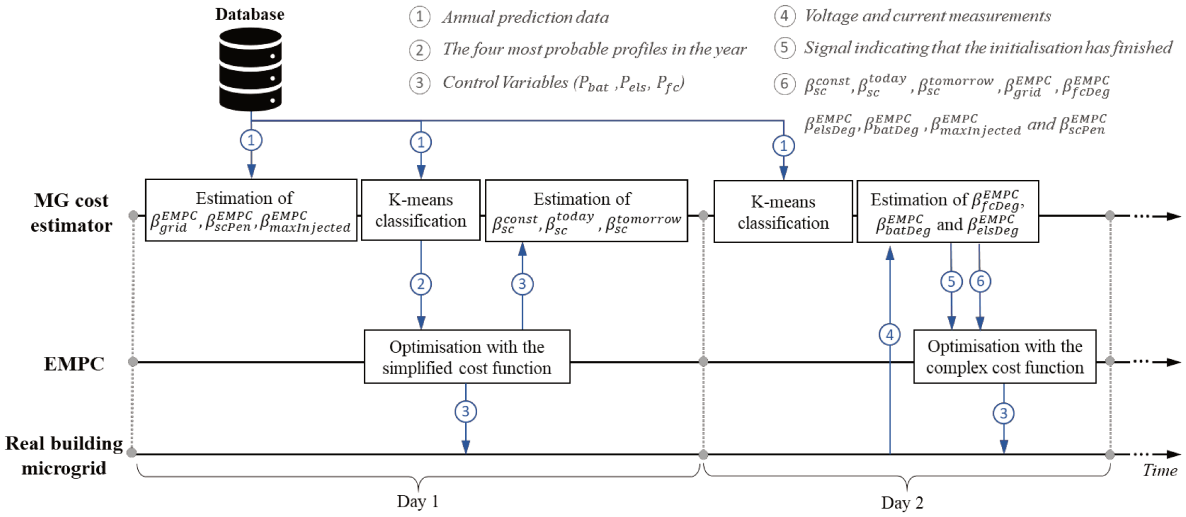

Fig. 5.14: Initialisation process of the MG cost estimator algorithm.

5.5 Validation of the microgrid cost estimator algorithm

The MG cost estimator forecasts both the expected BMG annual operating cost and the expected annual BMG self-consumption rate. To verify whether these two estimations are properly implemented, these two expected values were compared to the real values attained by BMG after one-year simulation. Therefore, section 5.5.1 describes the validation of the estimation of the annual self-consumption rate, whereas section 5.5.2 presents the validation of the estimation of the annual BMG operating cost.

5.5.1 *Validation of the estimation of the annual self-consumption rate*

The validation of the algorithm to estimate the annual self-consumption rate was conducted with the dataset of both a residential and a public building presented in Chapter 2 in section 2.3. The objective is to verify whether the algorithm can be accurate even under different situations, such as different

power imbalance data prediction and distinct ESS installation. For this reason, it was also evaluated situations in which the BMG is equipped with either only batteries or hybrid storage devices.

As explained previously in section 5.3.1, the first step to estimate $\hat{\tau}_{sc}^{annual}$ is to classify the daily power imbalance profiles. Fig. 5.15 shows the classification of the public and residential building dataset obtained after one-year simulation. Since the simulation started in the summer, the first and last 100 – 120 days in the year are assigned to classes $\mathbb{C}_3$ and $\mathbb{C}_4$ in both types of building, whereas in between 120th day and 270th day the classes $\mathbb{C}_1$ and $\mathbb{C}_2$ are more frequent. This distribution is expected because, according to the classification shown in Fig. 5.8, the classes $\mathbb{C}_3$ and $\mathbb{C}_4$ refer to daily power imbalance profiles with maximum power more than 50 kW, in contrast to less than 40 kW of classes $\mathbb{C}_1$ and $\mathbb{C}_2$. Consequently, it is expected that $\mathbb{C}_3$ and $\mathbb{C}_4$ will be assigned to summer days, while $\mathbb{C}_1$ and $\mathbb{C}_2$ to winter days. Therefore, the distribution of the k-means classes confirms that the classification is well implemented.

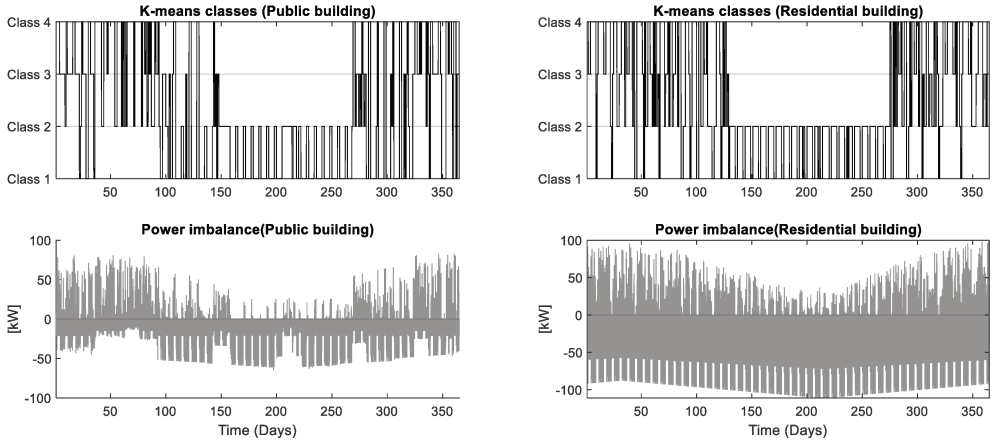

Fig. 5.15: K-means classes assigned to the daily power imbalance profiles in public and residential buildings.

Depending on the k-means classification, β_{sc}^{const}, β_{sc}^{today} and $\beta_{sc}^{tomorrow}$ of equations (5.51) – (5.53) are updated daily using recent data measurements. Fig. 5.16 shows the evolution of their values over time. Although only the simulation results of the BMG equipped with hybrid ESS are shown, it is important to highlight that similar graphs are obtained in the case where only batteries are installed. In Fig. 5.16, it is possible to observe that β_{sc}^{today} and $\beta_{sc}^{tomorrow}$ decrease over time. As expressed in equations (5.52) and (5.53), β_{sc}^{today} and $\beta_{sc}^{tomorrow}$ depend on $n_{K_{today}}^{future}$ and $n_{K_{tomorrow}}^{future}$, respectively. Hence, β_{sc}^{today} and $\beta_{sc}^{tomorrow}$ are proportional to the number of times the profiles K_{today} and $K_{tommorrow}$ are likely to be repeated until the end of the year, i.e. $n_{K_{today}}^{future}$ and $n_{K_{tomorrow}}^{future}$. According to the replacement process described in Fig. 5.9 and equation (5.47), $n_{K_{today}}^{future}$ and $n_{K_{tomorrow}}^{future}$ tend to decrease to zero, while n_k^{past} tend to increase up to 365 when approaching the year-end. On the last day of the year, $n_{K_{today}}^{future}$ and $n_{K_{tomorrow}}^{future}$ will be equal to zero, making the values of β_{sc}^{today} and $\beta_{sc}^{tomorrow}$ equal to zero as well.

These two variables indicate the impact of the current and following days (i.e. today and tomorrow) on the final annual self-consumption rate. High values of β_{sc}^{today} and $\beta_{sc}^{tomorrow}$ indicate that similar days to their associate k-means profile will be repeated many times, and thus the actions of HMPC in these days are very important to increase the annual self-consumption rate. On the other hand, low values of β_{sc}^{today} and $\beta_{sc}^{tomorrow}$ indicate that the impact of these days is almost insignificant to change the final annual self-consumption rate.

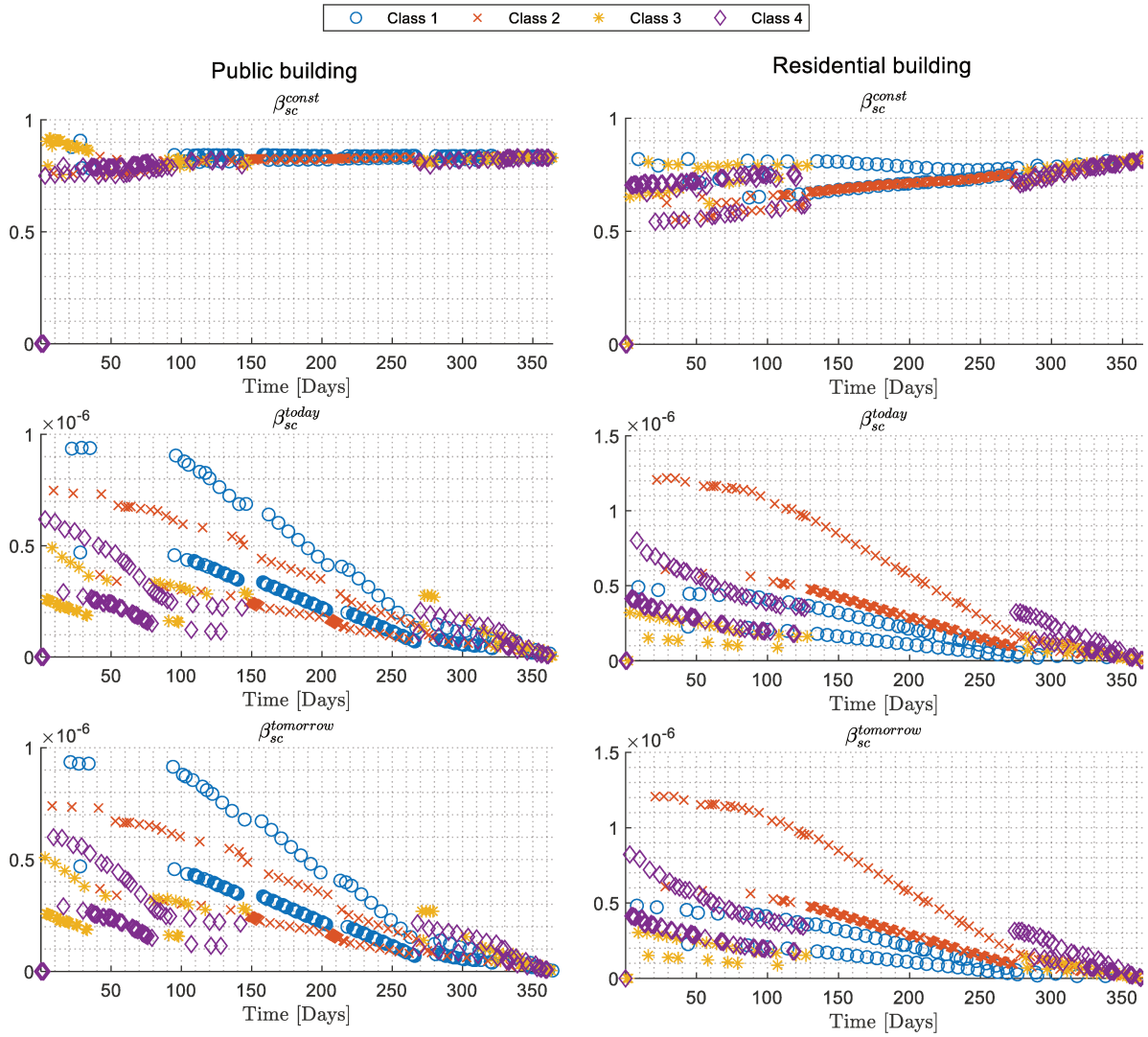

Fig. 5.16: Evolution of β_{sc}^{const}, β_{sc}^{today} and $\beta_{sc}^{tomorrow}$ parameters according to the four k-means classes after simulation with hybrid energy storage system in public and residential building.

On the other hand, over time, β_{sc}^{const} converges to the final annual self-consumption rate. As expressed in equation (5.51), β_{sc}^{const} correspond to the part of self-consumption estimation that the EMPC has no action. This is because it is composed of past control variables (i.e. $E_{els,k}$ and $E_{bat,k}^{ch}$ for $k \in [1, D-1]$), and future actions that does not cover its current horizon (i.e. $K \neq K_{today}$ and $K \neq K_{tomorrow}$). Therefore, β_{sc}^{const} indicates the expected annual self-consumption rate that the BMG is going to attain if HMPC does not operate its ESS (i.e. $\sum_{k=1}^{N_h^{EMPC}} P_{bat,k}^{ch} = 0$ and $\sum_{k=1}^{N_h^{EMPC}} P_{els,k} = 0$) in all

future days similar to K_{today} and $K_{tomorrow}$, and continues to operate similarly in other k-means daily profiles not covering its horizon ($K \neq K_{today}$ and $K \neq K_{tomorrow}$).

In Fig. 5.16, it is also possible to note that sometimes, for the same class, β_{sc}^{today} and $\beta_{sc}^{tomorrow}$ commutes between two values. The reason behind this phenomenon is because, when the classification of the two consecutive days belongs to the same class (i.e. $K_{today} = K_{tomorrow}$), the estimation of $\hat{\tau}_{sc}^{annual}$ through equation (5.54) is modified slightly. Since in this case, $\beta_{sc}^{today} = \beta_{sc}^{tomorrow}$ and β_{sc}^{const} includes estimation values of three classes instead of two, β_{sc}^{today} and $\beta_{sc}^{tomorrow}$ are worth half of their original values, following equation (5.56).

$$\beta_{sc}^{today} = \beta_{sc}^{tomorrow} = \frac{1}{2} \cdot \frac{n_{K_{tomorrow}}^{today} \cdot T_s^{TMPC}}{\sum_{i=1}^{365} E_{pv,i}} = \frac{1}{2} \cdot \frac{n_{K_{tomorrow}}^{tomorrow} \cdot T_s^{TMPC}}{\sum_{i=1}^{365} E_{pv,i}} \tag{5.56}$$

By using β_{sc}^{const}, β_{sc}^{today} and $\beta_{sc}^{tomorrow}$ parameters sent by the MG cost estimator daily, the EMPC computes the estimated $\hat{\tau}_{sc}^{annual}$ defined by equation (5.54). Fig. 5.17 shows the accuracy of the estimation of $\hat{\tau}_{sc}^{annual}$ from the perspective of EMPC when only batteries are installed in both public and residential buildings. Computed using equation (5.57), the error of $\hat{\tau}_{sc}^{annual}$ with respect the actual final τ_{sc}^{annual} is on average -0.4% in public buildings and 0.2% in residential buildings. At the beginning of the year, $\hat{\tau}_{sc}^{annual}$ is more inaccurate than at the end of the year. In public buildings the error is up to 4.2%, in contrast to 10.7% in residential buildings.

$$Error(\%) = \tau_{sc}^{annual} - \hat{\tau}_{sc}^{annual} \tag{5.57}$$

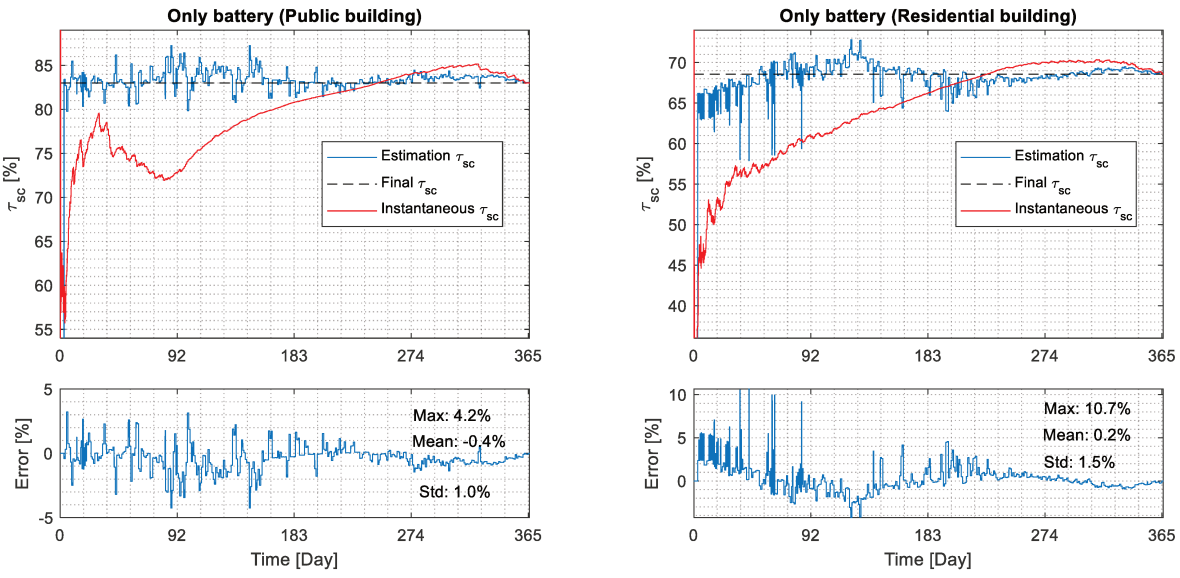

Fig. 5.17: Accuracy of the annual self-consumption prediction in public and residential building microgrids with only batteries.

Similarly, in the case of hybrid ESS, the accuracy of the algorithm is shown in Fig. 5.18 for public buildings, and Fig. 5.19 for residential ones. Since the algorithm for estimating the annual self-consumption is more complex when using hybrid ESS than the case where only batteries are installed, the algorithm's performance was evaluated using four different situations. Aiming to assess the

flexibility and accuracy of the algorithm, these four simulation conditions distinguish from each other depending on:

- The capital cost of fuel cells and electrolysers (*Today Price* or *Suitable Price*)
- The presence or not of data prediction error (*Without noise* or *With noise*)
- Limiting or not the use of hydrogen ESS (*Hard constraint* or *Soft constraint*)

Table 5.2: Simulation conditions for assessing the performance of the self-consumption estimation in building microgrids equipped with hybrid energy storage system.

Condition name	Description
Suitable Price	The capital cost of fuel cells (C_{fc}) and electrolysers (C_{els}) of equations (5.7) and (5.10) are equal to: • Residential buildings: $C_{fc} = 10\,000$ € and $C_{els} = 18\,750$ € • Public buildings: $C_{fc} = 30\,000$ € and $C_{els} = 18\,750$ € The values of C_{fc} in public and residential buildings were chosen based on the technical-economic analysis conducted in Chapter 6.
Today Price	The capital cost of fuel cells (C_{fc}) and electrolysers (C_{els}) of equations (5.7) and (5.10) correspond to their current capital cost, being equal to 18 750€ [220] and 150 000€ [219], respectively.
Without noise	The annual power imbalance prediction data used in the k-means classification are the same as those used in the MG simulator.
With noise	The annual power imbalance prediction data used in the k-means classification are different from those used in the MG simulator. The real power imbalance was multiplied by a random gaussian factor with a variance of 30%, and it was shifted in time randomly up to $3h$.
Hard constraint	Electrolysers and fuel cells can operate only if there is enough energy to run them near to their nominal power (P_{fc}^{nom} and P_{els}^{nom} in Table 2.1) for at least 2 hours. Therefore, the two following inequality constraints are embedded in the EMPC formulation: $\sum_{k=1}^{2} \delta_{fc,k} \cdot \min\left(T_s^{TMPC} \cdot P_{fc}^{nom}, -E_{deficit,k}\right) \leq \sum_{k=1}^{2} E_{fc,k}^{zone1} + E_{fc,k}^{zone1} + E_{fc,k}^{zone3}$ $\sum_{k=1}^{2} E_{els,k}^{zone1} + E_{els,k}^{zone1} + E_{els,k}^{zone3} \leq -\sum_{k=1}^{2} \delta_{els,k} \cdot \min\left(T_s^{TMPC} \cdot P_{els}^{nom}, E_{surplus,k}\right)$
Soft Constraint	There are no constraints to operate fuel cells and electrolysers so that the hydrogen chain is free to operate according to BMG needs.

The description of each of these conditions is detailed in Table 5.2. Particularly, the case with different hydrogen capital cost (*Today Price* or *Suitable Price*) was evaluated because one of the greatest barrier for installing fuel cells and electrolysers in building microgrids is their high investment cost ($C_{fc} + C_{els}$) and uncertain return of investment [220]. Hence, the designed EMPC cost function (equation (5.29)) consider C_{fc} and C_{els} to reduce their operation cost. As a result, the usage of hydrogen

storage and the annual self-consumption rate are impacted by different values of C_{fc} and C_{els}. Therefore, to verify whether the MG cost estimator can estimate correctly the annual self-consumption rate even when different strategies are adopted by EMPC, the cases *Today Price* and *Suitable Price* were included to validate the algorithm.

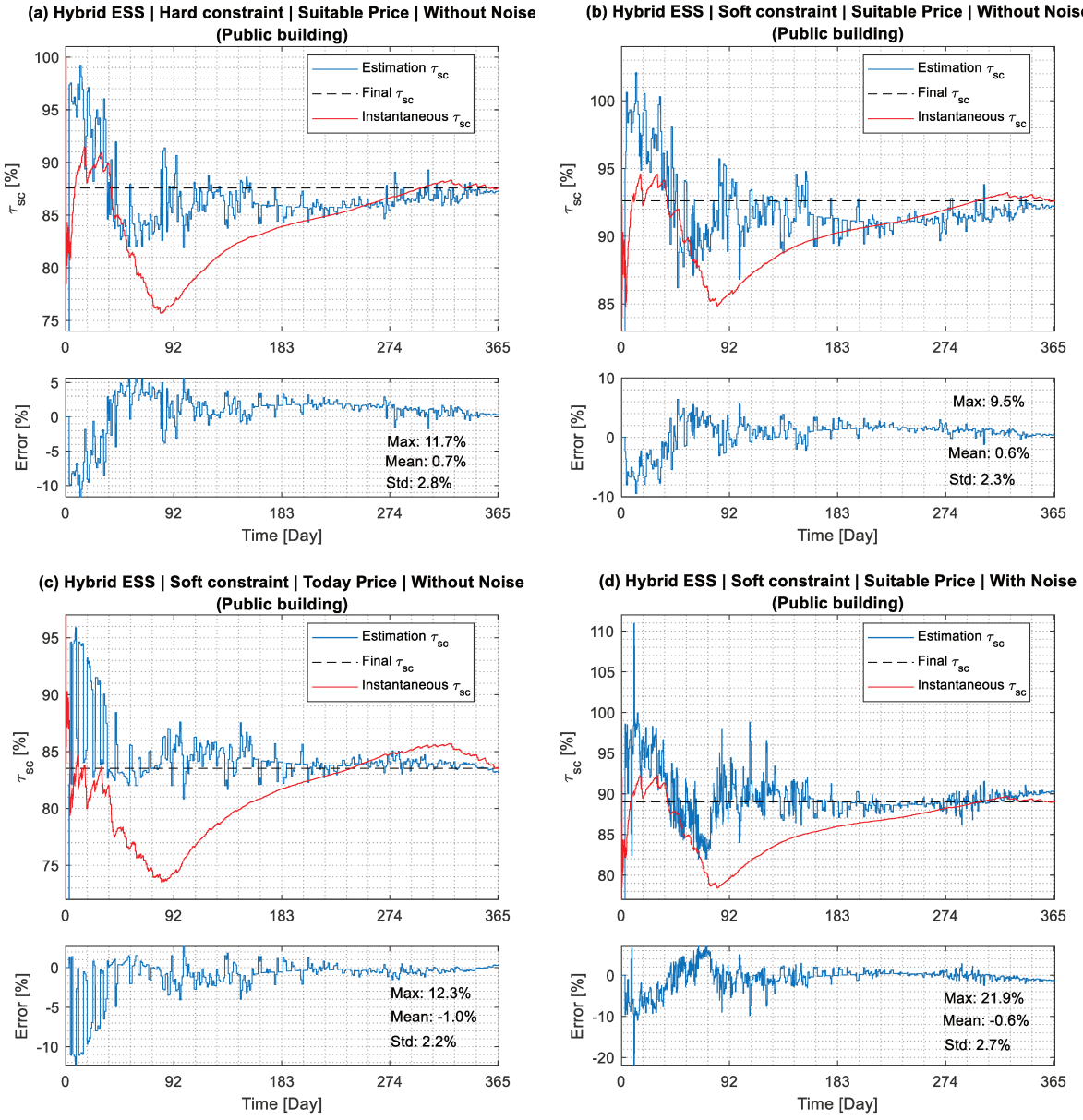

Fig. 5.18: Accuracy of the annual self-consumption prediction with the dataset of the public building microgrid with hybrid energy storage system.

By observing the graphs in Fig. 5.18, in public buildings, the average error ranges from 0.6% to 1.0%. In contrast, in residential buildings, the average error is slightly higher than public buildings, ranging between 0.3 to 5.4%, as shown in Fig. 5.19. These curves demonstrate that, despite subject to different conditions, the algorithm is on average highly accurate. It enables EMPC to estimate whether the BMG is capable or not of satisfying the required self-consumption rate ($\tau_{sc}^{required}$) since the first days of operation. For instance, when the hydrogen ESS is more affordable (condition *Suitable Price*

and in Fig. 5.18(a)(b)(d) and Fig. 5.19(a)(b)(d)), EMPC is aware that the BMG is going to attain τ_{sc} in between 85% and 90%. On the other hand, with the current hydrogen capital cost, the BMG tries to reduce its total operating cost by reducing the degradation cost of its ESS, especially the expenses with fuel cells and electrolysers. Consequently, the expected and real self-consumption rate reduce to on average 80% – 85%, as shown in Fig. 5.18(c) and Fig. 5.19(c).

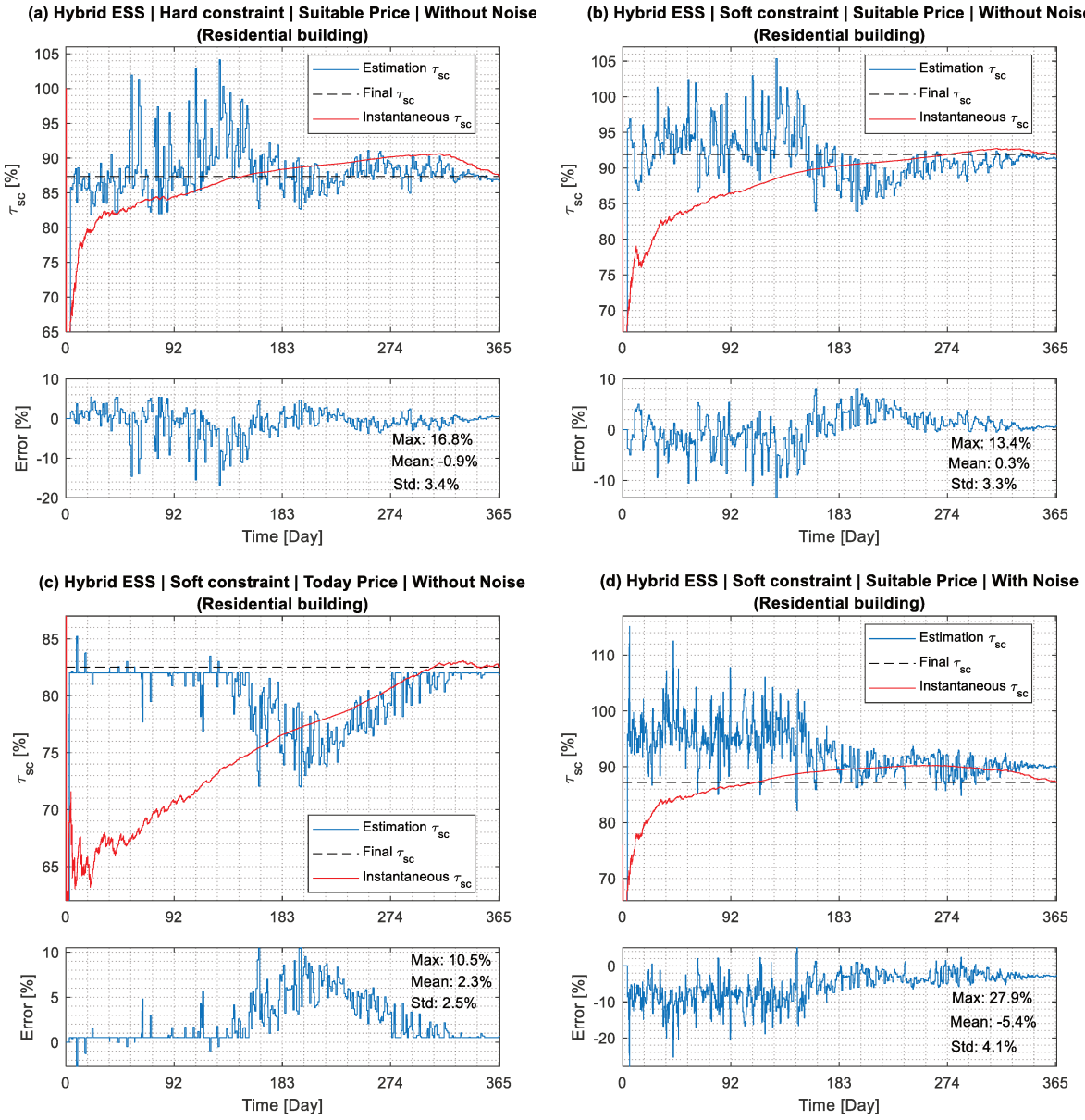

Fig. 5.19: Accuracy of the annual self-consumption prediction with the dataset of the residential building microgrid with hybrid energy storage system.

Particularly, the curve in Fig. 5.19c is mostly lower limited by 82%. This is because, in residential buildings with high hydrogen ESS capital, the EMS will try to reduce the use of fuel cells and electrolysers to decrease their degradation cost (π_{fc}^{deg} and π_{els}^{deg}) and to guarantee $\hat{\tau}_{sc}^{annual} \geq \tau_{sc}^{required}$

at minimum BMG operating cost. Since in all simulations, $\tau_{sc}^{required}$ was set up to 82%[5], $\hat{\tau}_{sc}^{annual}$ in the condition of Fig. 5.19c tends to be equal to 82%. This phenomenon is more evident in residential buildings than public buildings (Fig. 5.18c) because residential buildings have very low internal load matching with PV power generation as shown in Fig. 5.8 (or Fig. 2.9 and Fig. 2.10b).

According to Fig. 5.19c and Fig. 5.15, $\hat{\tau}_{sc}^{annual} \cong 82\%$ at classes $\mathbb{C}_3$ and $\mathbb{C}_4$, which correspond to power imbalance profiles of summer days. When the BMG disposes of a lot of energy surplus, the BMG has more liberty to use its ESS. On the contrary, during winter days, the operation of ESS is limited to the tight periods of surplus. Consequently, in k-means classes $\mathbb{C}_3$ and $\mathbb{C}_4$, $\hat{\tau}_{sc}^{annual} \cong 82\%$, whereas in k-means classes $\mathbb{C}_1$ and $\mathbb{C}_2$, $\hat{\tau}_{sc}^{annual} \neq 82\%$. As a result, during the winter, the precision of $\hat{\tau}_{sc}^{annual}$ is harmed by the standard deviation of $\sum_{k=1}^{24} E_{bat,k}^{ch}$ and $\sum_{k=1}^{24} E_{els,k}$ shown in Fig. 5.11, which impedes the residential BMG to keep $\hat{\tau}_{sc}^{annual}$ above 82%.

The graphs of Fig. 5.18d and Fig. 5.19d demonstrate that even subjected to intense data prediction error, $\hat{\tau}_{sc}^{annual}$ could remain accurate enough in both type of buildings. On average, the error of the estimation was kept below 6%. However, the estimation variates more intensely with data prediction inaccuracy. The maximum error is 21.9% in public buildings and 27.9% in residential ones when prediction data errors are introduced, compared to 12.3% in public buildings and 16.8% in residential buildings in the case with perfect data prediction.

5.5.2 *Validation of the estimation of the annual microgrid operating cost*

Defined as in equation (5.58), the MG operating cost is the sum of the degradation cost of ESS (π_{els}^{deg}, π_{fc}^{deg} and π_{bat}^{deg}) and the electricity bill (π_{grid}) discounted by the self-consumption reward (π_{sc}). Therefore, to verify whether the equations presented previously and summarised in Table 5.1 are correct or not, the estimation of both the annual ESS degradation cost and annual electricity bill were compared to real values attained by the BMG after one-year simulation.

$$\underset{operating\ cost}{Annual\ MG} = \pi_{els}^{deg} + \pi_{fc}^{deg} + \pi_{bat}^{deg} + \pi_{grid} - \pi_{sc} \tag{5.58}$$

The estimation of the annual MG operating cost is implemented using k-means classification, following the same reasoning presented in section 5.3. On each day D, the precision of the annual MG operating cost increases by the acquisition of recent data measurements, following the equations (5.59) – (5.63), where $\hat{\pi}_{els}^{deg}$, $\hat{\pi}_{fc}^{deg}$, $\hat{\pi}_{bat}^{deg}$, $\hat{\pi}_{sc}$ and $\hat{\pi}_{grid}$ are estimated values of $\pi_{els,365}^{deg}$, $\pi_{fc,365}^{deg}$, $\pi_{bat,365}^{deg}$, $\pi_{sc,365}$ and $\pi_{grid,365}$ at the end of the year, respectively.

$$\hat{\pi}_{els,D}^{deg} = \underbrace{\frac{\beta_{elsDeg,D}^{EMPC}}{\bar{d}_{els,D}} \sum_{i=1}^{D} \left| v_{els,i} - v_{els,1} \right|}_{\substack{Measured\ by \\ sensors}} + \underbrace{\sum_{K=1}^{4} n_K^{future} \cdot \beta_{elsDeg,D}^{EMPC} \cdot \bar{E}_{els|K}}_{\substack{Estimated\ through \\ k-means}} \tag{5.59}$$

[5]Although the French grid code requires only 80%, $\tau_{sc}^{required}$ was set up to 82%. The margin of 2% is to increase the robustness of the algorithm and to ensure that the BMG are going to respect the grid requirement.

$$\hat{\pi}_{fc,D}^{deg} = \underbrace{\frac{\beta_{fcDeg,D}^{EMPC}}{\bar{d}_{fc,D}} \sum_{i=1}^{D} \left| v_{fc,i} - v_{fc,1} \right|}_{\substack{Measured\ by \\ sensors}} + \underbrace{\sum_{K=1}^{4} n_K^{future} \cdot \beta_{fcDeg,D}^{EMPC} \cdot \bar{E}_{fc|K}}_{\substack{Estimated\ through \\ k-means}} \tag{5.60}$$

$$\hat{\pi}_{bat,D}^{deg} = \underbrace{\frac{\beta_{fcDeg,D}^{EMPC}}{\bar{d}_{bat,D}} \sum_{i=1}^{D} \left| Q_{bat,i} - Q_{bat,1} \right|}_{\substack{Measured\ by \\ sensors}} + \underbrace{\sum_{K=1}^{4} n_K^{future} \cdot \beta_{batDeg,D}^{EMPC} \cdot \left(\left| \bar{E}_{fc|K} \right| + \left| \bar{E}_{bat|K}^{dis} \right| \right)}_{\substack{Estimated\ through \\ k-means}} \tag{5.61}$$

$$\hat{\pi}_{sc,D} = 10^{-6} \left(-5 \cdot \underbrace{\left(\underbrace{\sum_{i=1}^{D} E_{grid,i}^{injected}}_{\substack{Measured\ by \\ sensors}} + \underbrace{\sum_{i=D+1}^{365} E_{surplus,i} - \sum_{K=1}^{4} n_K^{future} \cdot \left(\bar{E}_{bat|K}^{ch} + \bar{E}_{els|K} \right)}_{\substack{Estimated\ through \\ k-means}} \right)}_{Estimated\ annual\ energy\ injected\ into\ the\ grid} + \sum_{i=1}^{365} E_{pv,k} \right) \cdot \left(P + 5 - 12 \frac{P_{maxInjected,D}}{P_{pv}^{inst}} \right) \tag{5.62}$$

$$\hat{\pi}_{grid,D} = \underbrace{\sum_{i=1}^{D} E_{grid,k}^{injected} \cdot \pi_{elec,i}}_{\substack{Measured\ by \\ sensors}} + \underbrace{\sum_{i=D+1}^{365} E_{deficit,i} \cdot \pi_{elec,i} - \sum_{K=1}^{4} n_K^{future} \cdot mean(\pi_{elec}) \cdot \left(\bar{E}_{bat|K}^{dis} + \bar{E}_{fc|K} \right)}_{\substack{Estimated\ through \\ k-means}} \tag{5.63}$$

Therefore, each of these π-cost terms comprise two parts: the past and future partitions. The past segment is composed of data measurements that were acquired during the days before the current day D, i.e. from the first day of BMG operation in the year until the day $D-1$ ($[1; D-1]$). On the other hand, the future partition refers to coming days ($[D; 365]$) and they are estimated through the classified dynamic average of HMPC behaviour ($\bar{E}_{els|K}$, $\bar{E}_{fc|K}$, $\bar{E}_{bat|K}^{ch}$ and $\bar{E}_{bat|K}^{dis}$) and the number of observations in the future days (n_K^{future} defined by equation (5.47)). The values of $\bar{E}_{els|K}$ and $\bar{E}_{bat|K}^{ch}$ are determined through equations (5.43) and (5.44). Likewise, $\bar{E}_{fc|K}$ and $\bar{E}_{bat|K}^{dis}$ are estimated through similar equations to (5.43) and (5.44).

Therefore, by measuring daily the energy used in batteries, fuel cell and electrolyser (e.g. Fig. 5.20 and Fig. 5.21) and through the k-means classification shown in Fig. 5.15, it is possible to calculate their classified dynamic average ($\bar{E}_{bat|K}^{ch}$, $\bar{E}_{bat|K}^{dis}$, $\bar{E}_{fc|K}$ and $\bar{E}_{els|K}$). The evolution in time of $\bar{E}_{bat|K}^{ch}$, $\bar{E}_{bat|K}^{dis}$, $\bar{E}_{fc|K}$ and $\bar{E}_{els|K}$ during the one-year simulation is shown in Fig. 5.22 for public buildings, and Fig. 5.23 and for residential buildings.

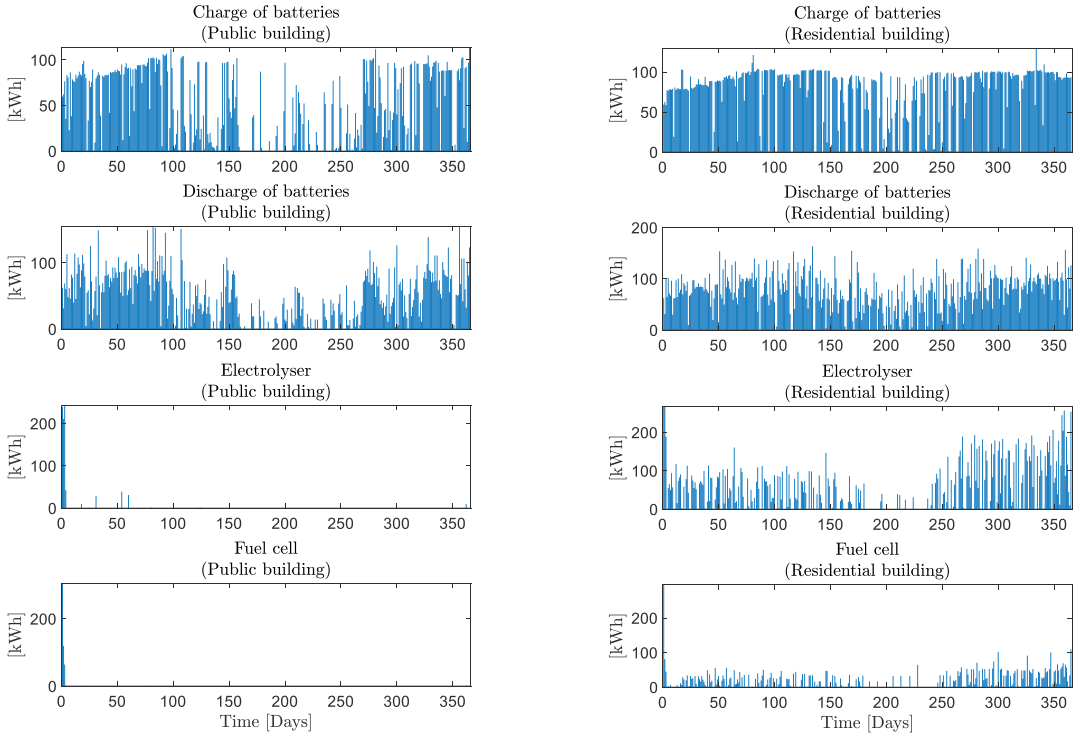

Fig. 5.20: Use of energy storage devices per day in public and residential buildings (simulation case: *Today Price*, *Soft Constraint*, *Without noise*).

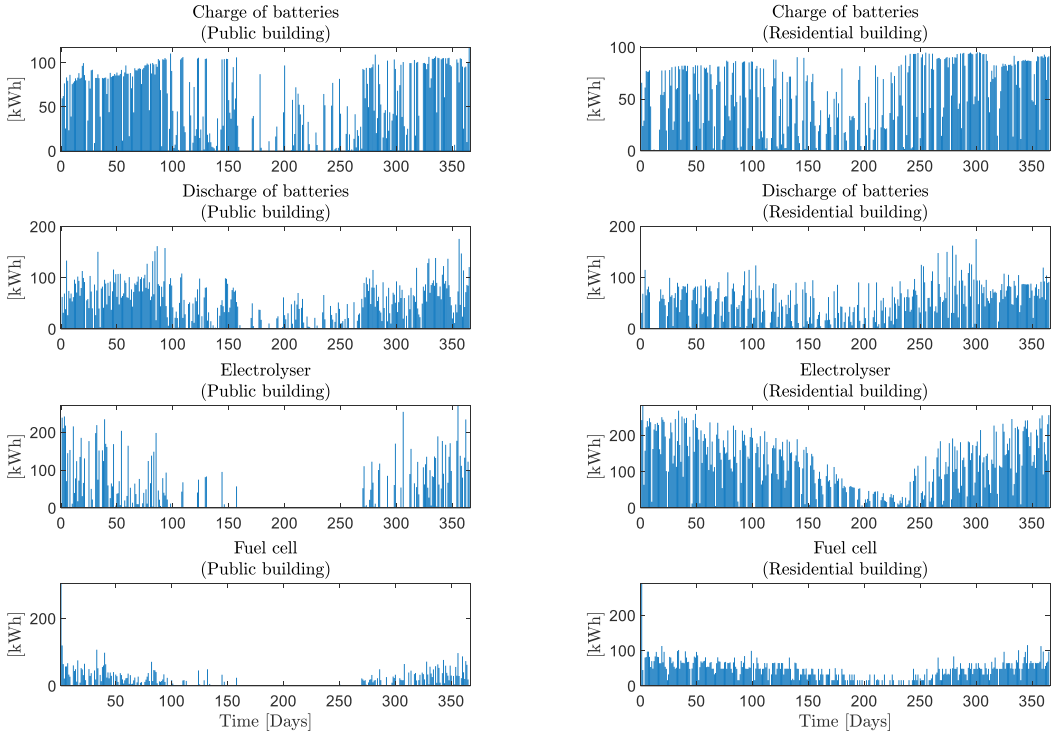

Fig. 5.21: Use of energy storage devices per day in public and residential buildings (simulation case: *Suitable Price*, *Soft Constraint*, *Without noise*).

The simulation results shown in Fig. 5.20 refers to the case *Today Price*, while the results in Fig. 5.21 refers to the case *Suitable Price.* In both cases, at the beginning of the year, the use of fuel cells and electrolysers is more intense than at the end of the year. This is because, when the BMG starts operating, the building EMS has no information about the cost to operate hydrogen ESS. Consequently, it uses fuel cells and electrolysers as much as possible to reduce grid energy injection. However, with time, the building EMS gradually becomes aware of the high costs of hydrogen ESS and the potential of each of its distributed resources in contributing to satisfy $\tau_{sc}^{required}$. Therefore, as shown in Fig. 5.20 and Fig. 5.21, after less than 5 days, the building EMS regulates the use of batteries, electrolysers and fuel cells so that $\bar{E}_{bat|K}^{ch}$, $\bar{E}_{bat|K}^{dis}$, $\bar{E}_{fc|K}$ and $\bar{E}_{els|K}$ become more steady in the long term (Fig. 5.22 and Fig. 5.23).

Particularly, as shown in the left graphs of Fig. 5.20, with high hydrogen storage capital (case *Today Price*), the public building EMS stops operating fuel cells and electrolysers after few days. As shown in Fig. 5.17, the public BMG can attain $\tau_{sc}^{required}$ only operating batteries, which is less expensive than the hydrogen ESS. On the other hand, in the scenario where the fuel cells are more affordable (left graphs of Fig. 5.21), the public building EMS operates the hydrogen ESS because it is more economic advantageous[6]. Consequently, as shown in Fig. 5.22, the average use of electrolysers and fuel cells in public buildings with low fuel cell capital cost (*Suitable Price*) are non-null (e.g. $\bar{E}_{fc|4} \cong 100\ kWh$ and $\bar{E}_{els|4} \cong 20\ kWh$), compared to null values ($\bar{E}_{fc|K} \cong \bar{E}_{els|K} \cong 0\ kWh$) in the case *Today Price*.

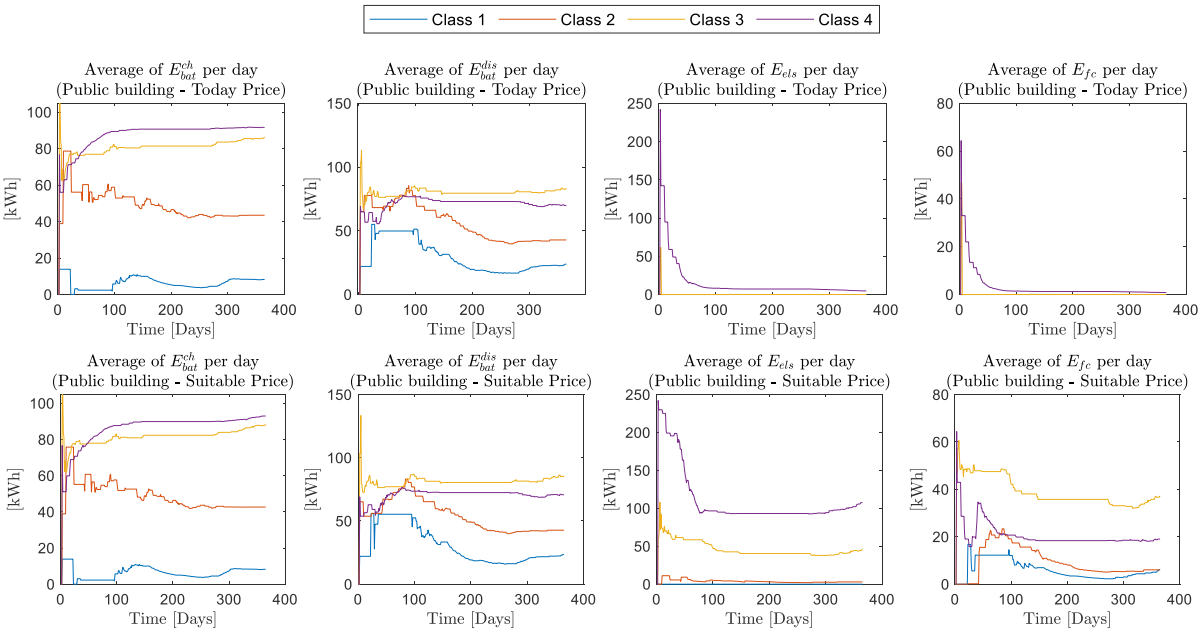

Fig. 5.22: Classified dynamic average of the total energy assigned to each energy storage system in the public building microgrid (simulation cases: *Today Price*, *Soft Constraint*, *Without noise* & *Suitable Price*, *Soft Constraint*, *Without noise*).

[6] Further analysis of hydrogen affordability is conducted in Chapter 6

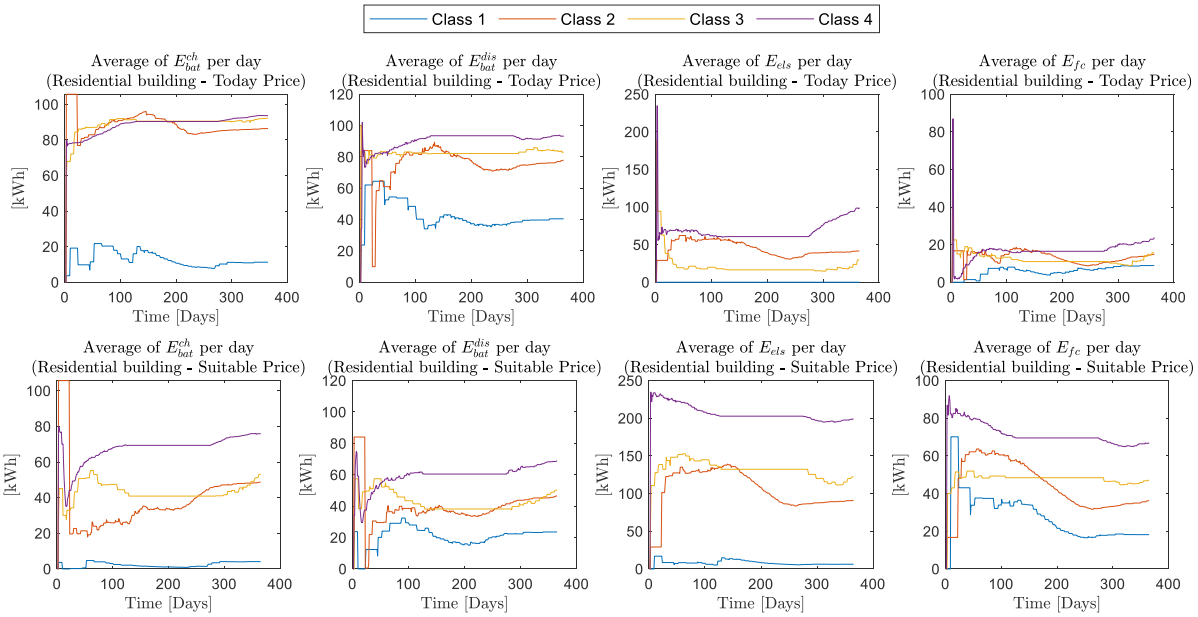

Fig. 5.23: Classified dynamic average of the total energy assigned to each energy storage system in the residential building microgrid. (simulation cases: *Today Price*, *Soft Constraint*, *Without noise* & *Suitable Price*, *Soft Constraint*, *Without noise*).

Similar phenomenon happens in residential buildings. Comparing the results of the right side of Fig. 5.20 with the right-side graphs in Fig. 5.21, the operation of fuel cell and electrolyser are more intense with low capital costs (*Suitable Price* scenario Fig. 5.21) than high ones (*Today Price* scenario Fig. 5.20). Nevertheless, contrary to the public building, the residential one cannot satisfy $\tau_{sc}^{required}$ only with batteries, as shown in Fig. 5.17. Consequently, in both *Today Price* and *Suitable Price* scenarios, the residential building microgrid had to use the hybrid ESS to respect $\tau_{sc}^{required}$. These results demonstrate that the MG cost estimator can figure out a balanced use of hybrid ESS without tunning any parameter manually. Additionally, this new algorithm kept highly accurate even when subject to different MG configurations.

However, as shown in Fig. 5.22 and Fig. 5.23, the algorithm of classified dynamic average has a very slow response time. Although fuel cells and electrolysers have stopped to be used since the 5th day of operation, their corresponding average values ($\bar{E}_{fc|K}$ and $\bar{E}_{els|K}$) take around ten times longer (about 50th days) to converge to the new pattern. On the one hand, this inertia can be advantageous to enhance the robustness of the algorithm. On the other hand, it can harm the precision of the MG cost estimator. The inertia of the algorithm can be reduced by additional data treatment. For instance, by supervising the frequency of the daily measurements, it is possible to detect whether a great deal of recent data measurements is very different from the past average values (e.g. $\bar{E}_{bat|K}^{ch}$, $\bar{E}_{bat|K}^{dis}$, $\bar{E}_{fc|K}$ or $\bar{E}_{els|K}$) and then to modified the classified average accordingly. Nevertheless, this improvement will be implemented lately as future work.

Hence, by combining the estimated average behaviour of the HMPC with the equations (5.59) – (5.63), it is possible to assess the accuracy of the estimation of annual BMG costs. The graphs of from Fig. 5.24 to Fig. 5.26 compare the estimated values ($\hat{\pi}_{els}^{deg}$, $\hat{\pi}_{fc}^{deg}$, $\hat{\pi}_{bat}^{deg}$, $\hat{\pi}_{sc}$ and $\hat{\pi}_{grid}$) with the final values attained by the BMG on the 365th day in the year, which are indicated by black dashed lines. It

is possible to observe that using the MG cost estimator algorithm, the building EMS can have an impression of the annual BMG expenses since the first days of operation. Therefore, by minimizing daily the cost function defined by (5.29), EMPC does minimise the expected annual MG costs. Additionally, this algorithm has demonstrated flexible and robust to operate in different microgrid configurations with distinct ESS capital costs.

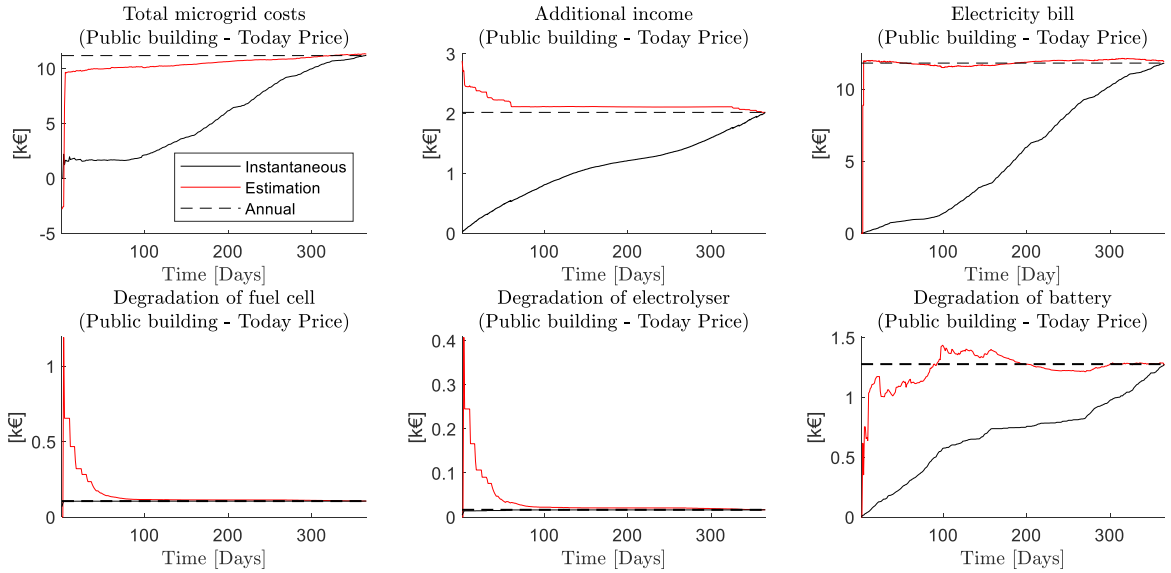

Fig. 5.24: Comparison between the total microgrid expenses estimated by the MG cost estimator (red curves), the real values attained by the public building after one-year simulation (black dashed curves) and instantaneous real values (continuous black curves). The simulation refers to the case *Today Price*, *Without Noise*, *Soft Constraint.*

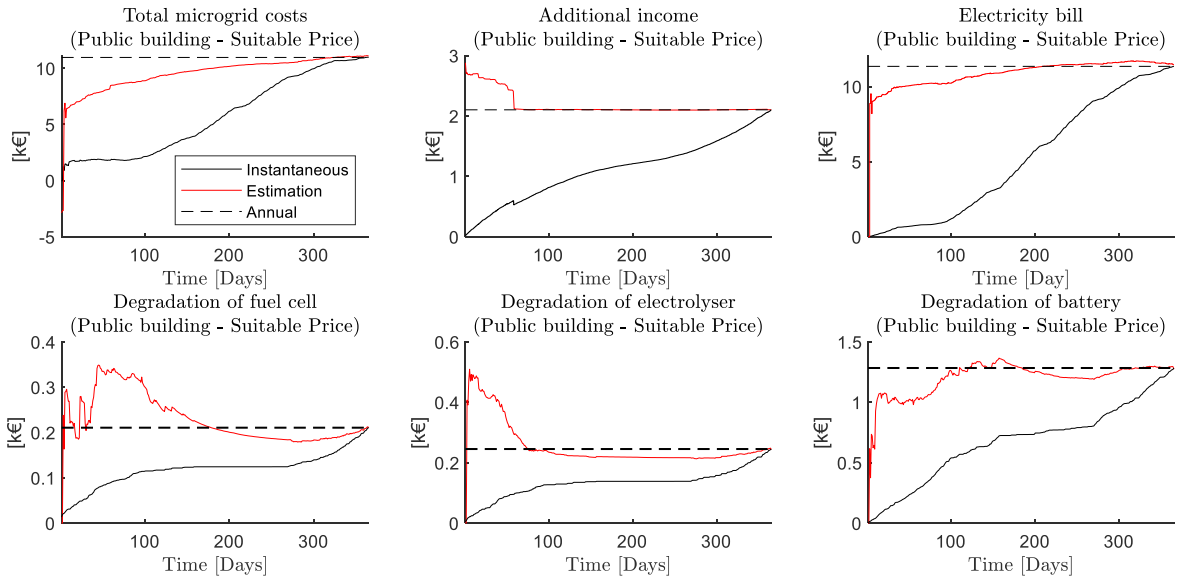

Fig. 5.25: Comparison between the total microgrid expenses estimated by the MG cost estimator (red curves), the real values attained by the public building after one-year simulation (black dashed curves) and instantaneous real values (continuous black curves). The simulation refers to the case *Suitable Price*, *Without Noise*, *Soft Constraint*.

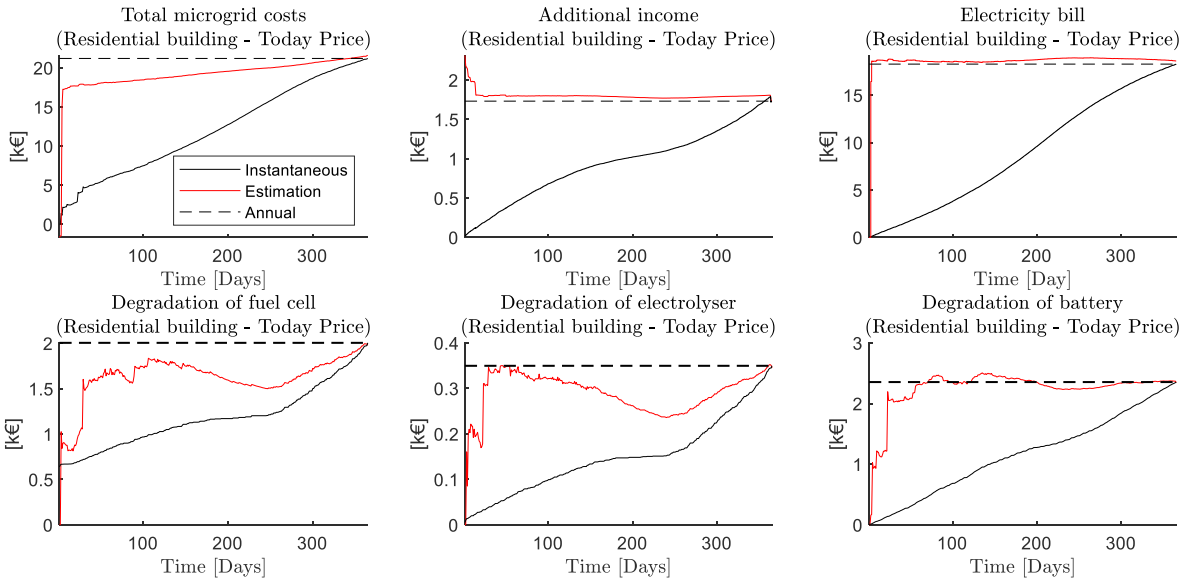

Fig. 5.26: Comparison between the total microgrid expenses estimated by the MG cost estimator (red curves), the real values attained by the residential building after one-year simulation (black dashed curves) and instantaneous real values (continuous black curves). The simulation refers to the case *Today Price*, *Without Noise*, *Soft Constraint.*

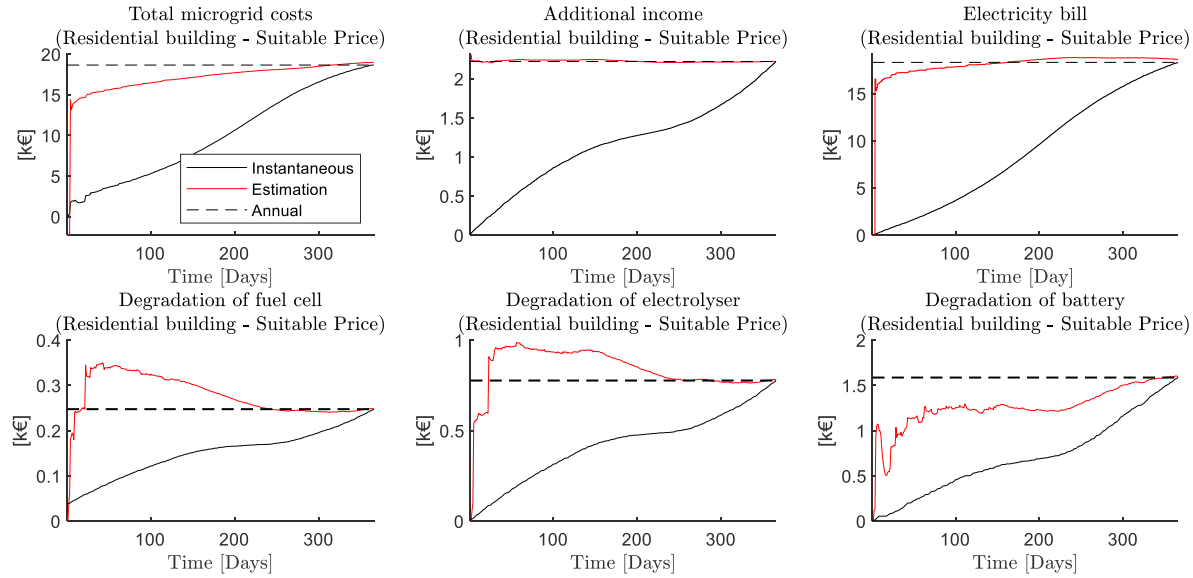

Fig. 5.27: Comparison between the total microgrid expenses estimated by the MG cost estimator (red curves), the real values attained by the residential building after one-year simulation (black dashed curves) and instantaneous real values (continuous black curves). The simulation refers to the case *Suitable Price*, *Without Noise*, *Soft Constraint.*

5.6 Conclusion

One of the greatest challenges in designing an energy management system for building microgrids equipped with hydrogen storage and batteries is the trade-off between using storage systems. Aiming to tackle this issue, the two-level Hierarchical Model Predictive Controller (HMPC) presented in Chapter 3 was empowered with the MG cost estimator. This innovative control strategy aims to increase the flexibility of the power flow controller by enabling it to adapt to different energy storage

installations (i.e. hybrid or non-hybrid) and different type of buildings (i.e. residential or public) automatically. This data-driven algorithm aims to determine optimal parameters for the HMPC to handle the trade-off between maximising the annual self-consumption rate and minimising the building microgrid's total cost, without needing to tune any parameter.

The simulation results demonstrate that the MG cost estimator can forecast the annual self-consumption rate with an average error of up to 5% in residential and public buildings. Likewise, the MG cost estimator makes the HMPC aware of the annual BMG expenses since the first days of operation. All this valuable information empowers the HMPC to make wiser decisions in exploiting the BMG distributed resources. In the next chapter, the energy and economic aspects of the whole hierarchical building energy management system will be evaluated. The proposed hierarchical controller will be compared to other conventional strategies found in the literature.

As future work, the response time of the MG cost estimator needs to be improved to enable it to adapt to abrupt changes in the system, such as changes in the vacation days or increase in the power consumption. Furthermore, the inclusion of the benefits and drawbacks of exploiting the batteries of electric vehicles on behalf of BMG needs to be embedded in the MG cost estimator.

Chapter 6 Simulation results

6.1 Introduction

This chapter aims to demonstrate the performance of the designed hierarchical EMS in satisfying, at minimal expenditure, the annual self-consumption rate required by the French grid regulator. To evaluate the capabilities of HMPC (Chapter 3) empowered with both the MG cost estimator (Chapter 5) and RTMI module (Chapter 4) in managing the BMG resources to achieve these two primary objectives, it was compared to a conventional HMPC and a traditional rule-based (RB) strategy. For the sake of clarity, these three controllers are abbreviated as HMPC-kmeans, HMPC, and RB, respectively. In section 6.2, the input parameters and the conditions of simulation tests are explained. Thereafter, in section 6.3, HMPC and RB control strategies are detailed. Afterward, the metrics for comparing are presented in section 6.4, while the performance of each control strategy is discussed in section 6.5.

As concluded in Chapter 5, the MG cost estimator cannot yet estimate the impact of electric vehicles on the total BMG operating cost and on the annual self-consumption rate. Consequently, since in section 6.5 the three controllers are compared to evaluate the performance of MG cost estimator, the electric vehicles are not present in the simulations detailed in section 6.5. Therefore, section 6.6 discusses the potentials of exploiting the batteries of PEVs on behalf of the BMG with a simplified cost function. The objective of these simulations is to identify scenarios where PEV batteries could be better exploited to support the BMG needs without damaging the welfare of PEV's owners. Finally, section 6.6 presents the conclusions obtained from the developed work.

6.2 The input parameters and conditions of simulation tests

The building's hierarchical EMS receives hourly from the community aggregator the prediction data for the next 48 hours concerning PV power generation, the building's power consumption, and the ongoing electricity price of a BMG of sizing specified in Table 2.1. These data predictions are the same as those used in the BMG simulator presented in section 2.3 in Chapter 2. In the ideal scenario, the data read from the CSV files are routed to both the BMG simulator and the HMPC directly. Controversially, in the scenario with data prediction inaccuracy, the HMPC's input data are conditioned by the functions *Add noise 1* and *Add noise 2* before arriving at MG cost estimator and HMPC, as shown in Fig. 6.1. Because annual and daily prediction data errors are different from each other, two different functions are used to emulate the prediction data errors. These two functions will be detailed in section 6.5.4, where the robustness of the whole hierarchical EMS against uncertainties in power imbalance will be evaluated.

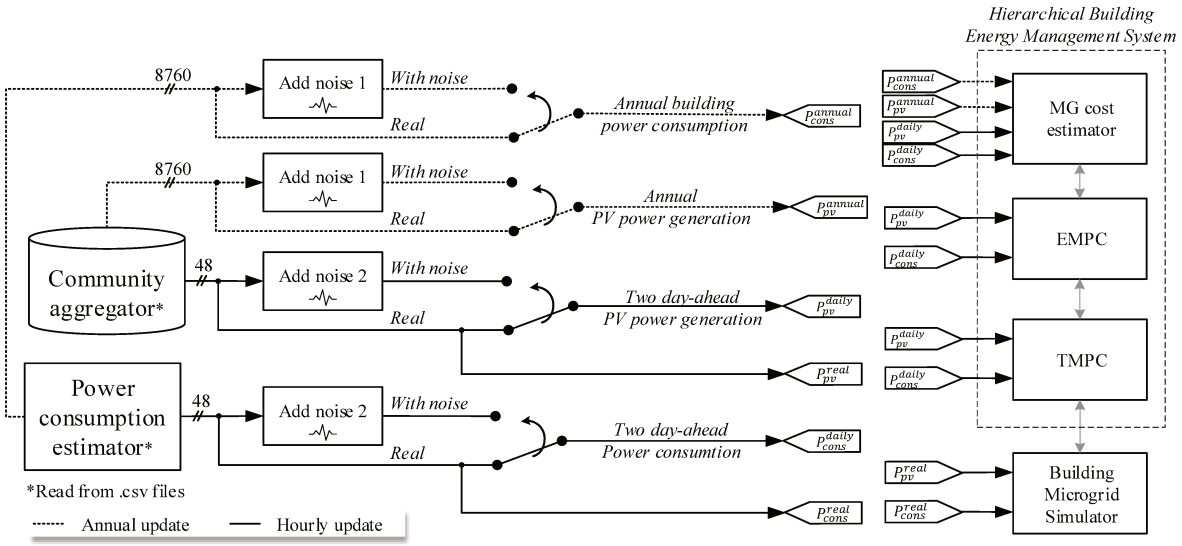

Fig. 6.1: Structure of the input prediction data that are processed by the hierarchical building energy management system depending on the simulation cases (with prediction data error or ideal case).

Additionally, all data input are streaming vectors with a resolution of one hour. Consequently, the daily prediction data contains 48 values, whereas the annual dataset vector is of size 8760. To compare the three power flow control strategies, a one-hour resolution was set up as a compromise between computation burden and accuracy. However, in real applications, the prediction data resolution may be smaller than 1 hour, which will require the pre-processing of raw prediction data to conceive reliable one-hour resolution data for the HMPC. Besides that, with the increase in the prediction data resolution, TMPC and RTMI update times must be faster than one hour to compensate for fast power imbalance variability. This will require the inclusion of filters and pre-processing data measurements, such as moving average or finite impulse response filters.

6.3 The conventional hierarchical model predictive controller and the rule-based controller

Since the objective is to demonstrate the capabilities and effectiveness of a feasible strategy to consider both energy and economic aspects in the optimisation of the BMG power flow without needing to tune any parameter in the HMPC-kmeans cost function, the HMPC and RB have a classical design considering only maximising the self-consumption rate, which is the utmost objective of the building EMS. The RB consists of a set of if-else logic that can be easily applied in real systems. This controller serves as a basis to identify the performance of the proposed controller. On the other hand, the HMPC, which is the first version of the designed hierarchical control structure [15], is a smarter control structure that takes its decisions based on prediction data but it optimises only the BMG's energy aspects and ignores economic ones. The comparison with HMPC aims to verify whether it is important to consider both economic and energy aspects when optimising the power flow. Furthermore, it allows evaluating whether the MG cost estimator does reduce the BMG operation cost or not.

In this regard, the HMPC architecture is the same as HMPC-kmeans except that it only contains the RTMI module and the two MPC layers. Therefore, HMPC does not include the MG cost estimator module as HMPC-kmeans does, which leads its EMPC to be designed differently: it penalises any grid

energy exchange, as expressed in equation (6.1). In this formulation, instead of considering ESS capital costs, ESS efficiency, electricity price, and self-consumption additional income, HMPC decides between batteries and hydrogen storage based only on their electric efficiency that is embedded in the internal ESS models.

$$SoC_{ref}, LoH_{ref} = \arg\left(\min_{SoC_{ref},LoH_{ref}} \sum_{k=1}^{N_h^{EMPC}=48} \left|E_{grid,k}^{import}\right| + \left|E_{grid,k}^{injected}\right|\right) \quad (6.1)$$

On the other hand, the RB strategy was adapted from [86], in which the use of batteries is prioritised over fuel cells and electrolysers. The use of batteries is favoured over the use of hydrogen storage because the current capital cost of fuel cells and electrolysers is much higher, and their efficiency is much lower than batteries. In the RB strategy, the hydrogen ESS is controlled using the principle of hysteresis, as detailed in Fig. 6.2.

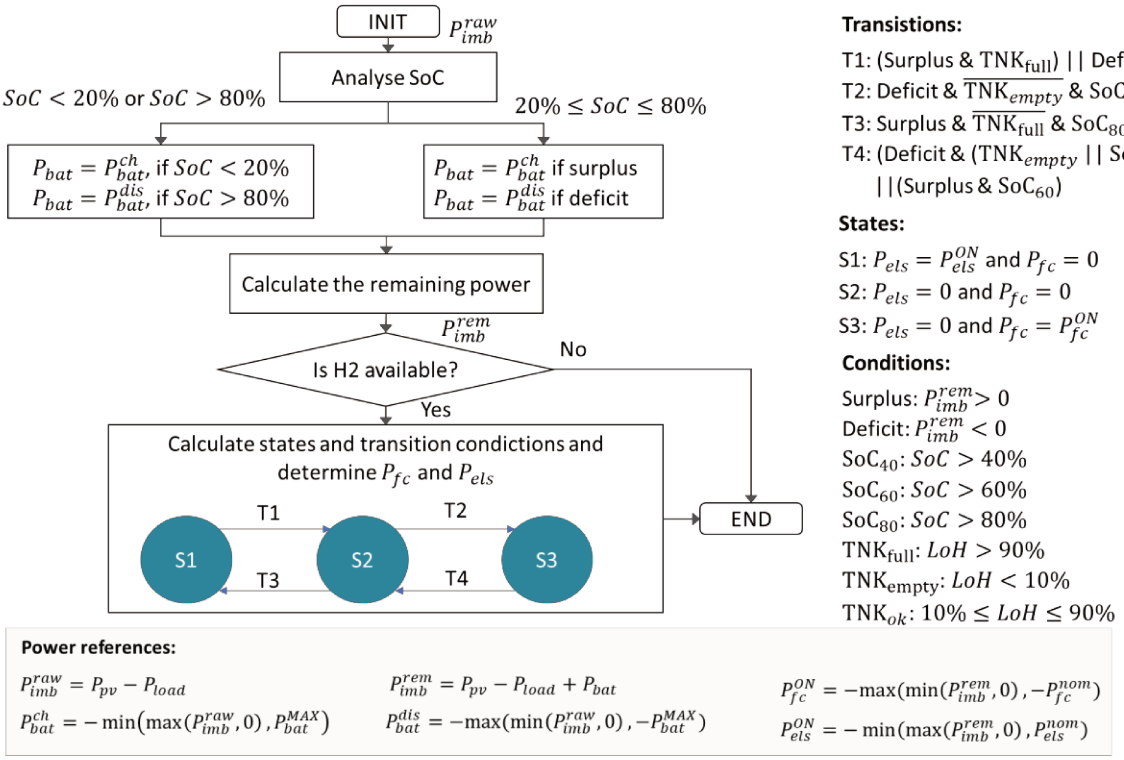

Fig. 6.2: The logic of the rule-based controller with its transitions, conditions, and states to operate building microgrids with hybrid or non-hybrid energy storage systems.

6.4 The metrics for comparison and overview of the simulation cases

Through one-year simulations in MATLAB Simulink®, the economic and energy outcomes of public and residential BMGs are evaluated to assess four important aspects:

- the impact of ESS installation
- the impact of hydrogen ESS capital costs
- the impact of constraining the use of hydrogen ESS at a nominal power rate
- the impact of power imbalance prediction data error

To evaluate these four aspects, eight metrics were created, namely the annual self-consumption rate (M_1), the coverage rate (M_2), the total MG cost (M_3), the degradation cost of batteries (M_4), electrolyser (M_5) and fuel cells (M_6), the cost of purchasing electricity (M_7), and the additional income for self-consumption (M_8). The equations used for calculating these metrics are summarised in Table 6.1, with the related equations that were discussed previously.

Particularly, the coverage rate (τ_c) refers to the percentage of the annual energy consumption that was supplied by renewable energy generated locally. In other words, the annual coverage rate is calculated through equation (6.2), which is worth 100% if the BMG does not purchase electricity from the grid ($\sum_{k=1}^{365} E_{grid}^{import} = 0$). The coverage rate indicates not only the energy autonomy of the building but also how clean the energy consumed by the building is. Consequently, it is desired that the coverage rate is as high as possible because it means that BMG is self-sufficient and has low electricity expenses.

$$\tau_c = \frac{\substack{Production\ of\ renewable \\ energy\ self-\ consummed}}{Annual\ energy\ consummed} = 100\left(1 - \frac{\sum_{k=1}^{365} E_{grid,k}^{import}}{\sum_{k=1}^{365} E_{cons,k}}\right)\ [\%] \tag{6.2}$$

Table 6.1: Metrics for comparing the performance of controllers.

Annual metrics	Equation	Related equation
M_1 – Self-consumption rate [%]	$100\left(1 - \frac{\sum_{k=1}^{365} E_{grid,k}^{injected}}{\sum_{k=1}^{365} E_{pv,k}}\right)$	(5.14)
M_2 – Coverage rate [%]	$100\left(1 - \frac{\sum_{k=1}^{365} E_{grid}^{import}}{\sum_{k=1}^{365} E_{cons,k}}\right)$	(6.2)
M_3 – Total MG cost [€]	$\pi_{bat}^{annual} + \pi_{els}^{annual} + \pi_{fc}^{annual} + \pi_{grid}^{annual} - \pi_{sc}^{annual}$	(5.58)
M_4 – Batteries cost (π_{bat}^{annual}) [€]	$C_{bat}\frac{\lvert Q_{bat,365} - Q_{bat,0}\rvert}{0.2 \cdot Q_{bat,0}}$	(5.7)
M_5 – Electrolyser cost (π_{els}^{annual}) [€]	$C_{els}\frac{\lvert v_{els,365} - v_{els,0}\rvert}{0.1 \cdot v_{els,0}}$	(5.10)
M_6 – Fuel cells cost (π_{fc}^{annual}) [€]	$C_{fc}\frac{\lvert v_{fc,365} - v_{fc,0}\rvert}{0.1 \cdot v_{fc,0}}$	(5.10)
M_7 – Electricity cost (π_{grid}^{annual}) [€]	$\sum_{k=1}^{365} \pi_{elec,k} \cdot E_{grid,k}^{import}$	(5.3)
M_8 – Additional income (π_{sc}^{annual}) [€]	$5 \cdot 10^{-6} \cdot \left(\sum_{k=1}^{365} (P+5) \cdot E_{sc,k} + P \cdot E_{grid,k}^{injected} - 12 \cdot E_{pv,k} \cdot \frac{P_{maxInjected}}{P_{pv}^{inst}}\right)$	(5.15)

The performance of HMPC and HMPC-kmeans will be compared with the RB strategy by using the relative difference defined by (6.3). Therefore, each of the eight metrics (M_1 to M_8) of HMPC and HMPC-kmeans will be presented as a relative percentage of RB metrics shown in Table 6.2 for a public building and Table 6.3 for a residential building. Nonetheless, the absolute values of the simulation presented in this chapter are summarized in Appendix 0. The degradation cost of batteries (M_4), electrolysers (M_5) and fuel cells (M_6) was calculated using the current capital costs (C_{bat}, C_{els} and C_{fc}) presented in Table 6.4.

$$\substack{relative \\ difference\ (\%)} = 100 \cdot \frac{M_i^{HMPC} - M_i^{RB}}{M_i^{RB}}, \forall i \in [1;7] \tag{6.3}$$

Table 6.2: One-year simulation results of the rule-based controller in the public building.

ESS	Self-consumption (M_1^{RB})	Coverage (M_2^{RB})	Total MG cost (M_3^{RB})	Battery cost (M_4^{RB})	Electrolyser cost (M_5^{RB})	Fuel cell cost (M_6^{RB})	Electricity cost (M_7^{RB})	Additional income (M_8^{RB})
Battery	79.7%	43.2%	11819 €	1456 €	0 €	0 €	12220 €	1857 €
Hybrid	92.9%	45.8%	12307 €	1456 €	292 €	1247 €	11723 €	2410 €
Without ESS	69.6%	37.7%	11660 €	0 €	0 €	0 €	13451 €	1791 €

Table 6.3: One-year simulation results of the rule-based controller in a residential building.

ESS	Self-consumption (M_1^{RB})	Coverage (M_2^{RB})	Total MG cost (M_3^{RB})	Battery cost (M_4^{RB})	Electrolyser cost (M_5^{RB})	Fuel cell cost (M_6^{RB})	Electricity cost (M_7^{RB})	Additional income (M_8^{RB})
Battery	62.2%	25.6%	20888 €	2586 €	0 €	0 €	19766 €	1463 €
Hybrid	86.7%	27.9%	22362 €	2586 €	541 €	2267 €	19058 €	2090 €
Without ESS	47.3%	20.2%	20047 €	0 €	0 €	0 €	21413 €	1366 €

Table 6.4: Current cost of ESS equipment.

ESS equipment	CAPEX*	Sizing	Cost (€) *
Battery [232]	500 (€/kWh)	120 kWh	$C_{bat} = 60\,000$
Electrolyser [217], [219]	750 (€/kW)	25 kW	$C_{els} = 18\,750$
Fuel cell [219]	7500 (€/kW)	20 kW	$C_{fc} = 150\,000$

*The cost includes installation expenses and ESS purchase

CAPEX: capital expenditure

6.5 Comparison between RB, HMPC, and HMPC-kmeans

The following four subsections detail the impact of the four aspects on the BMG's overall performance when using RB, HMPC, or HMPC-kmeans. Using the eight metrics presented in section 6.4, the three control strategies will be compared to determine an affordable and durable BMG operation.

6.5.1 *Impact of installing an energy storage system*

Due to the power consumption profile disposal, self-consumption and coverage rate in residential buildings are strictly inferior to public buildings in all scenarios shown in Table 6.2 and Table 6.3. Observing Fig. 2.9 and Fig. 2.10b, residential buildings have a peak of consumption when PV arrays do not generate any power and almost do not consume any energy when PV panels are generating. Controversially, by analysing Fig. 2.9 and Fig. 2.10a, the power consumption in public buildings almost superposes the solar irradiation profiles. Consequently, without ESS, in residential buildings, only 47% of the energy generated by PVs is consumed locally, compared to almost 70% in public buildings. Similarly, without ESS, only 20% of residential building power consumption are supplied by PVs, compared to 38% in public buildings. This also highlights the role of ESS installation, in which the self-consumption rate is drastically increased in residential buildings, while in public buildings, the role of ESS is somewhat less relevant.

According to RB results in Table 6.2 and Table 6.3, the BMG's first year of operation with only batteries is more expensive than the scenario without ESS. This is due to the additional cost created by the degradation of batteries, which represents about 12% of total MG expenditure. Nonetheless, without ESS, the BMG cannot guarantee the minimum mark of self-consumption of 80% ($\tau_{sc}^{required} = 80\%$ in equation (5.26)). Consequently, despite being less expensive in the first year, the self-consumption BMG without ESS will suffer more severe grid penalisation in the long term.

To evaluate the impact of the installation of ESS in the BMG revenue in the long term, it was estimated the total savings brought by batteries and hydrogen ESS for the next 25 years. The savings in the year y are calculated using equation (6.4) for batteries and equation (6.5) for hybrid ESS. In these formulations, the total savings of ESS installation correspond to the differences in the electricity bill (metric M_7), in the additional income for self-consumption (metric M_8) and the Operation and Maintenance (O&M) cost of batteries ($O\&M_{bat}$), fuel cells ($O\&M_{fc}$) and electrolysers ($O\&M_{fc}$). In this study, it is considered that $O\&M_{bat}$ is equal to 1200 €/year (i.e. 10€/year/kWh installed [233]), while $O\&M_{fc}$ is equal to 0.26€/kWh (i.e. 0.013€/kWh/kW installed) [234] and $O\&M_{els}$ is equal to 0€/kWh/kW installed. Remarkably, $O\&M_{els}$ is equal to zero because its operating costs are already included into the electricity consumed to generate hydrogen and to turn on the gas compressor [235] and its maintenance is already embedded in $O\&M_{fc}$.

$$S_{bat,y} = \left(M_{7,y}^{bat} - M_{8,y}^{bat} + O\&M_{bat,y}\right) - \left(M_{7,y}^{without} - M_{8,y}^{without}\right) \tag{6.4}$$

$$S_{hybrid,y} = \left(M_{7,y}^{hybrid} - M_{8,y}^{hybrid} + O\&M_{bat,y} + O\&M_{els,y} + O\&M_{fc,y}\right) - \left(M_{7,y}^{without} - M_{8,y}^{without}\right) \tag{6.5}$$

In this analysis, it is considered that the premium factor P equals 20 €/MWh in the first year and it is reduced by $2 \times \left(\tau_{sc}^{required} - M_1\right)\%$ p.a. [12], if $M_1 < \tau_{sc}^{required}$. Furthermore, it assumes that the electricity price doubles every 10 years [236] and that PV panels lose 10% of their efficiency over 10 years [237]. On the other hand, it is considered that the building energy consumption for the next 25 years is the same as the first year. According to [1], this is reasonable because buildings' energy consumption per square meter will be reduced in the future due to buildings' envelope's refurbishment and improvement in electric appliance efficiency. Nonetheless, considering that the building's infrastructure will be the same for the next years, the annual building energy consumption can be assumed to be the same throughout the upcoming years. Despite these assumptions, this analysis satisfies the objective of assessing the relative capabilities of the EMS algorithms in managing the BMG power flow under different conditions.

Based on these assumptions, the cumulative savings brought by ESS installation minus its investment cost are shown in Fig. 6.3. All curves in Fig. 6.3 starts at negative values corresponding to the purchase cost of ESS. Therefore, it starts with $-C_{bat}$ in the case where only batteries are installed, and with $-C_{hybrid} = -C_{bat} - C_{fc} - C_{els}$ in the case where hybrid ESS are installed. Since all curves in the case where only batteries are installed cross the abscissa axis[7], the batteries installation is more

[7] Except for rule-based controller, where the return of investment is a little more than 25 year, but close to 25 years.

profitable than not installing them within the horizon of 25 years. On the other hand, the investment in hybrid ESS is not compensated within 25 years, since the red curves do not cross the abscissa axis, even though hydrogen ESS savings are higher than the case without ESS.

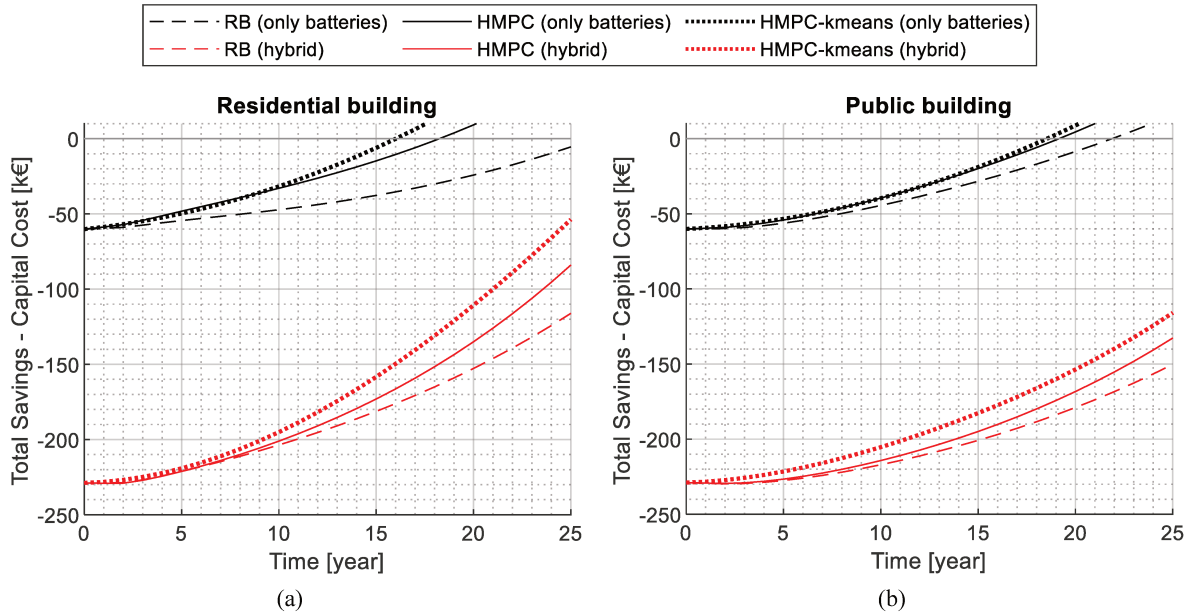

(a) (b)

Fig. 6.3: Estimation for the next 25 years of the annual building microgrids operation cost, considering the grid penalisation for not satisfying the required self-consumption rate of 80%. (a) Public building. (b) Residential building.

It is possible that within a longer horizon, the hybrid ESS investment may be paid back, but this is not the focus of this study. The savings from batteries and hydrogen ESS installation come mainly from reducing the electricity bill and the increase in the additional income due to self-consumption, as detailed in Fig. 6.4.

The results in Table 6.2 and Table 6.3 demonstrate that hybrid ESS has the potential to be more profitable in the first year of BMG operation with simple controllers as RB, if its capital cost are reduced (decrease M_5 and M_6). Hydrogen ESS can decrease the expenses with electricity (metric M_7) and increase the additional income due to self-consumption (metric M_8). However, its current capital cost and O&M is too high to make its installation worthwhile without financial incentives such as the self-consumption additional income (e.g. without penalization of P factor). Considering that the high hydrogen ESS capital cost is the main challenge for their application, in section 6.5.2, a suitable hydrogen ESS capital cost that would make its installation advantageous from the first year of BMG operating will be investigated.

The RB controller results indicate that BMG profitability is sensitive to the profile of energy consumption and may change with different ESS sizing. This highlights the need for a flexible EMS capable of adapting to many different situations, without demanding exhaustive tests. In this regard, HMPC and HMPC-kmeans were designed and compared to the RB results through the relative differences (equation (6.3)) of the eight metrics presented in section 6.4. These results are shown in Fig. 6.5 and Fig. 6.6. Remarkably, the variable $\tau_{sc}^{80\%}$ indicates the minimum relative difference of self-consumption (metric M_1) to satisfy $\tau_{sc}^{required}$ of 80%. In other words, the relative difference of M_1 must be above $\tau_{sc}^{80\%}$ to avoid reduction in P factor.

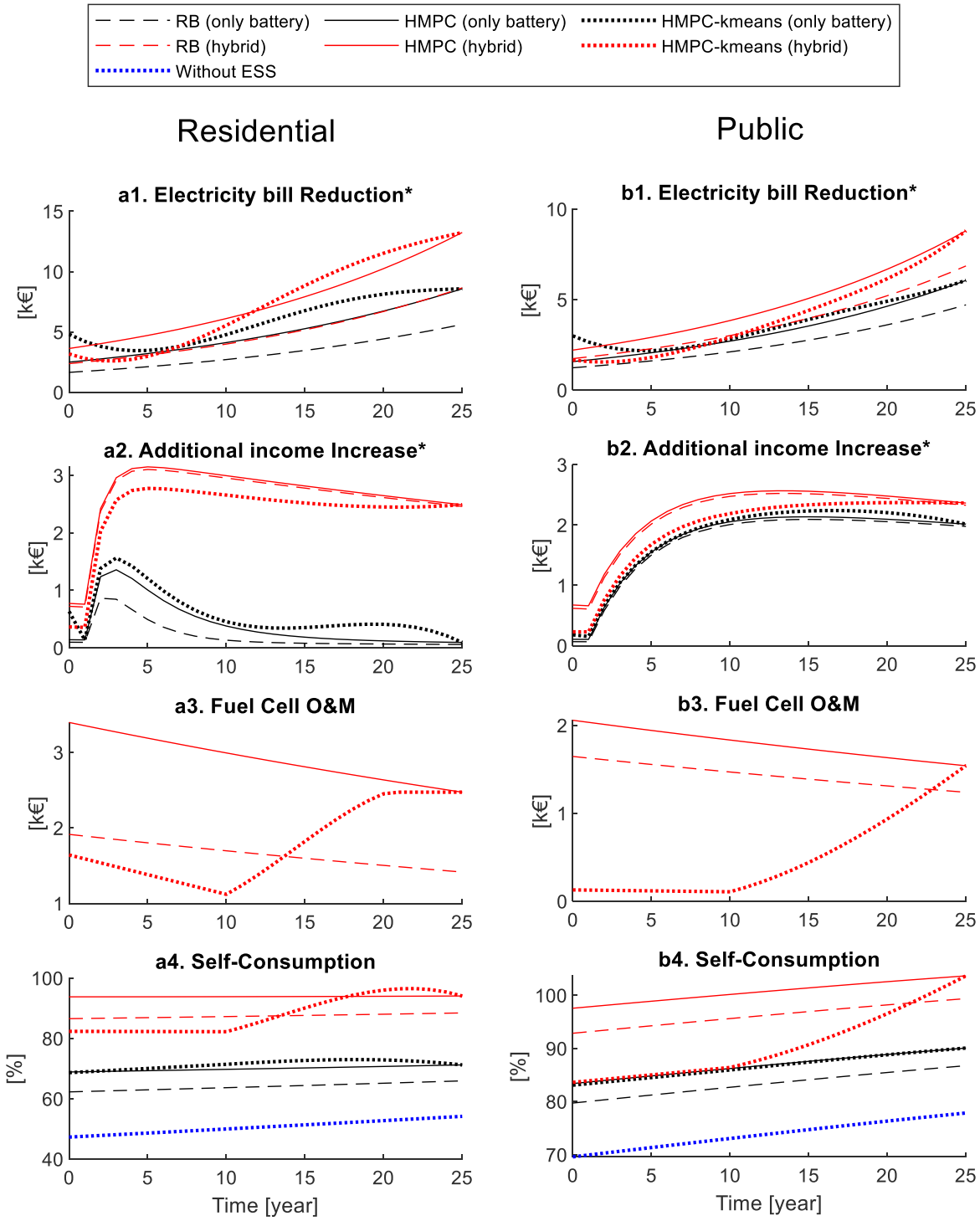

Fig. 6.4: Detail of estimating the building expenses for the next 25 years depending on the energy management system and the type of building. Obs.: *The graphs *Electricity Bill Reduction* and *Additional Income Increase* are calculated with respect the case 'without ESS'.

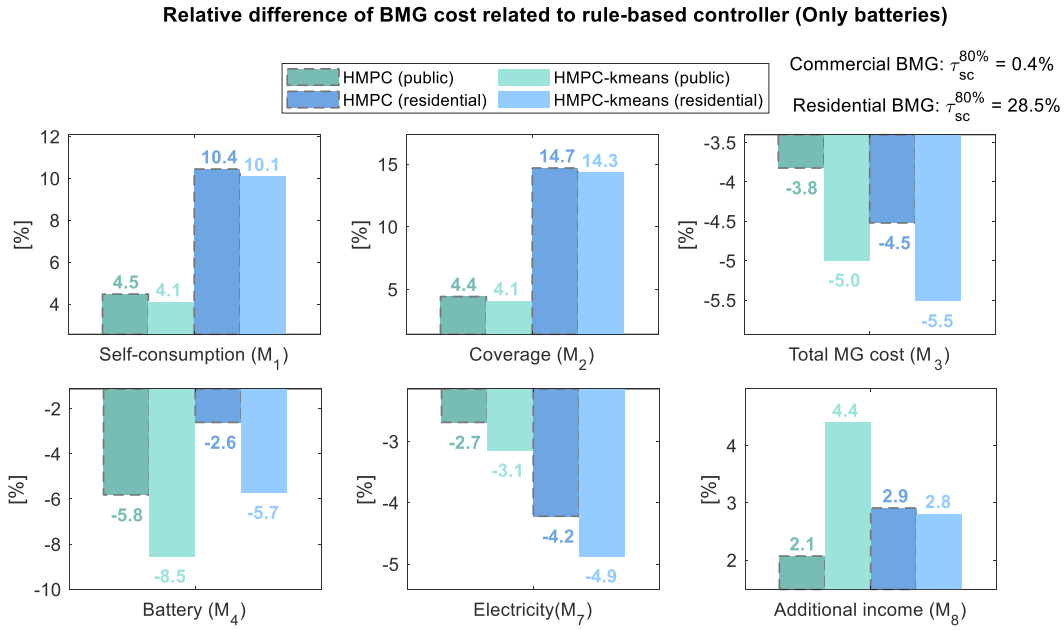

Fig. 6.5: Comparison of the first-year performance of the three control strategies when only batteries are installed.

Regarding the results of Fig. 6.5 where only batteries are installed, both HMPC and HMPC-kmeans have a higher self-consumption and coverage rates than RB. Particularly, both HMPC and HMPC-kmeans achieved similar annual self-consumption rates in the public building (around $1.04 \times 79.7 \cong 83\%$) and the residential building (around $1.10 \times 62.2 \cong 68\%$)), but HMPC-kmeans guarantees cheaper BMG operating cost. Compared to HMPC, HMPC-kmeans can save $\frac{(5-3.8)}{100} \times 11819 \cong 142$ € in public buildings and $\frac{(5.5-4.5)}{100} \times 20888 \cong 209$ € in residential buildings in the first year of operation.

In the long term, the graphs in Fig. 6.3 show that the cumulative savings of HMPC-kmeans are very similar to HMPC in public buildings, which are higher than RB: about 10k€ on the horizon of 15 years. These savings come mainly from the reduction in electricity purchase in the case of public buildings (Fig. 6.4b2) and both electricity expenses and the additional income in the case of residential buildings (Fig. 6.4a1 and Fig. 6.4a2). Since neither RB, nor HMPC, nor HMPC-kmeans attained $\tau_{sc}^{required}$ with only batteries in the residential building, the additional income gradually reduces up to the value of the case without ESS, making the graphs in Fig. 6.4a2 tend to zero. Therefore, after 15 years, the main savings come from only reducing the electricity bill, as shown in Fig. 6.4a1.

According to Fig. 6.6, HMPC-kmeans with hybrid ESS in the public building reduces by about 9% of the total MG cost (metric M_3) compared to the simple RB in the first year. Despite degrading the annual self-consumption by 10%, it could maintain the self-consumption rate above $\tau_{sc}^{required}$, since $-10\% = M_1^{HMPCkmeans} \geq \tau_{sc}^{80\%} = -14\%$. As consequence, the additional income when using HMPC-kmeans is smaller than using RB or HMPC (Fig. 6.4b2), but the factor P is not penalised in the long term. The same behaviour happens in the residential building, where the self-consumption was kept around $82\% > \tau_{sc}^{required}$ and the additional income is lower than RB and HMPC. Hence, the savings when using HMPC-kmeans comes especially from the $O\&M_{fc}$ and the degradation costs of

ESS. The hydrogen ESS is almost not exploited in public buildings in the first 10 years (Fig. 6.4b3) and they are used about 12% less than RB and about 52% less than HMPC in residential buildings (Fig. 6.4a3 and metrics M_5 and M_6 in Fig. 6.6). Notably, during the first 10 years in residential buildings (Fig. 6.4a3), HMPC-kmeans reduces the use of fuel cells because PV panels lose their efficiency, making the total raw energy surplus in the upcoming years lower than the first year. Consequently, fuel cells do not need to be run as much as the first year to satisfy $\tau_{sc}^{required}$.

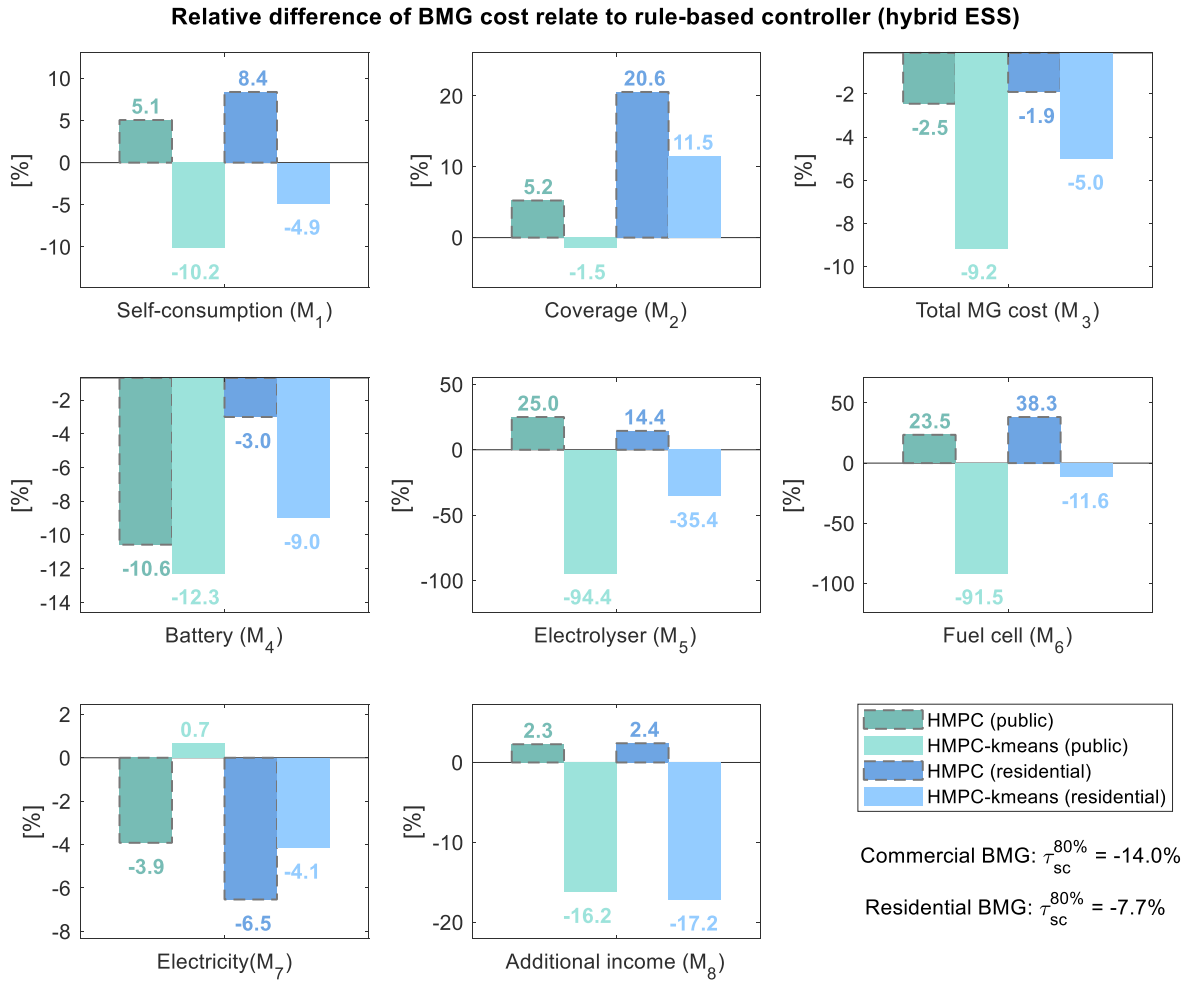

Fig. 6.6: Comparison of the first-year performance of the three control strategies when batteries and hydrogen ESS are installed.

However, this scenario change in the future, especially after 10 years from today. With the increase in the electricity price, HMPC-kmeans prefers to use the hydrogen ESS to cover the building's internal deficit rather than purchase electricity from the grid. This demonstrates that the MG cost estimator, along with the estimation of the expected annual self-consumption can handle the trade-off between the grid requirements and BMG expenditures. As an example, the first-year results shown in Fig. 6.7a reveal that HMPC-kmeans identifies that the BMG can satisfy $\tau_{sc}^{required}$ with only batteries, which is cheaper than the hydrogen chain.

Controversially, HMPC uses hydrogen ESS whenever it can, which leads it to attain a self-consumption rate 17% higher in public buildings and 14% higher in residential buildings (Fig. 6.6,

metric M_1) than HMPC-kmeans, but with total operating cost about 7% higher in public buildings and 3% higher in residential buildings (Fig. 6.6, metric M_3). According to Fig. 6.3, HMPC with hybrid ESS results in fewer savings than HMPC-kmeans, even though it attained a higher self-consumption rate (Fig. 6.4a4 and Fig. 6.4b4). This leads us to conclude that the additional income due to the self-consumption premium does not encourage the use of fuel cells and electrolysers enough because it is more advantageous not to use the hydrogen ESS than foster self-consumption. Although HMPC attained higher self-consumption marks than both RB and HMPC-kmeans, its operating cost is still higher than HMPC-kmeans and nearly the same as RB.

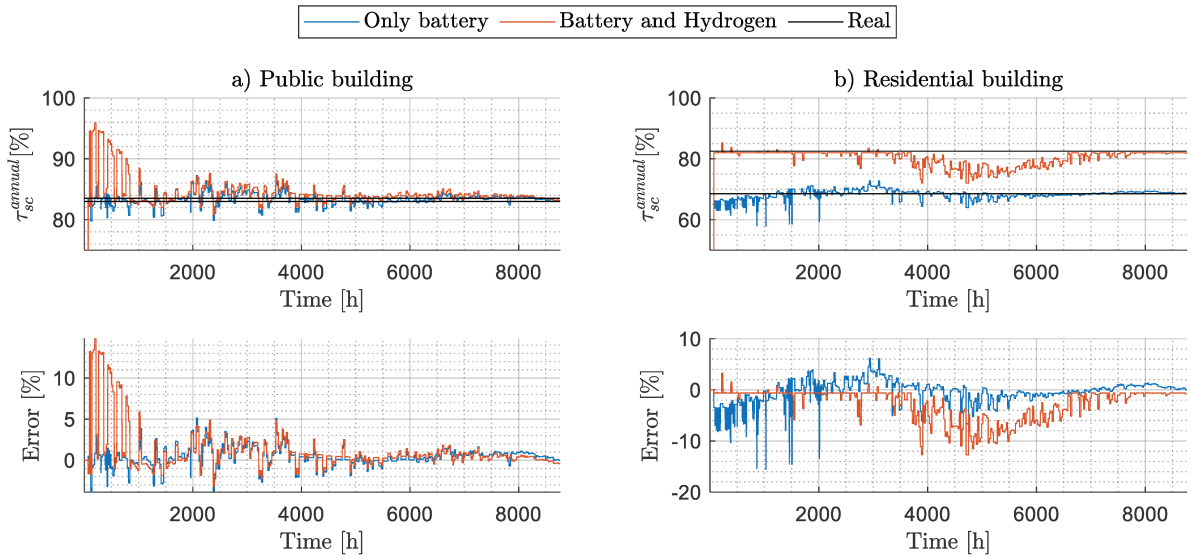

Fig. 6.7: Accuracy of the annual self-consumption prediction implemented by HMPC-kmeans.

Likewise, in the scenario of residential buildings, HMPC-kmeans with hybrid ESS provides the cheapest BMG operating cost while satisfying $\tau_{sc}^{required}$. As shown in Fig. 6.6, the total BMG operating cost with HMPC-kmeans in the residential building is reduced by 5% compared to RB. This is because HMPC-kmeans uses the hydrogen ESS only when necessary, instead of whenever there is an energy surplus or energy deficit. As concluded previously, residential BMG cannot attain $\tau_{sc}^{required}$ with only batteries (Fig. 6.5, all $M_1 < \tau_{sc}^{80\%} = 28.5\%$). Consequently, as shown in Fig. 6.7b, through the expected self-consumption estimation handled by the inequality constraint of equation (5.26), HMPC-kmeans identifies that it is necessary to use the hydrogen chain to accomplish the primordial objective of annual self-consumption rate; otherwise it will be virtually penalised by π_{sc}^{pen} of equation (5.24). However, hydrogen ESS is much more expensive than batteries. Therefore, hydrogen ESS is used only to attain the minimum $\tau_{sc}^{required}$. As a result, HMPC-kmeans degrades 35% less electrolysers and 12% less fuel cells compared to RB and much less than HMPC (metrics M_5 and M_6 of Fig. 6.6).

6.5.2 *Impact of hydrogen ESS capital costs*

Since one of the greatest challenges of hydrogen ESS market accessibility is its high investment cost, a suitable capital cost that would become hydrogen ESS cost-effective was investigated. This economic analysis was conducted using the scenario of the first year of BMG operating, which

corresponds to the current capital costs and electricity prices. According to [220], the capital cost of fuel cells is nowadays significantly higher than the cost of the entire PV-battery systems, which leads the use of fuel cells highly dependent on public policies to financially support their investment or major technological breakthroughs to reduce their capital cost.

However, the capital cost of fuel cells depends on the size of the equipment (usually in kW) and the annual manufacturing rate [238], which make future and current fuel cell capital costs (C_{fc}) very uncertain. Although many studies [220] [13] indicate that it will tend to decrease in the future, projections for C_{fc} depend on the manufacturing process which introduces high divergences in fuel cell prices, especially for small ones (some price ranges are provided in [220] and [13]).

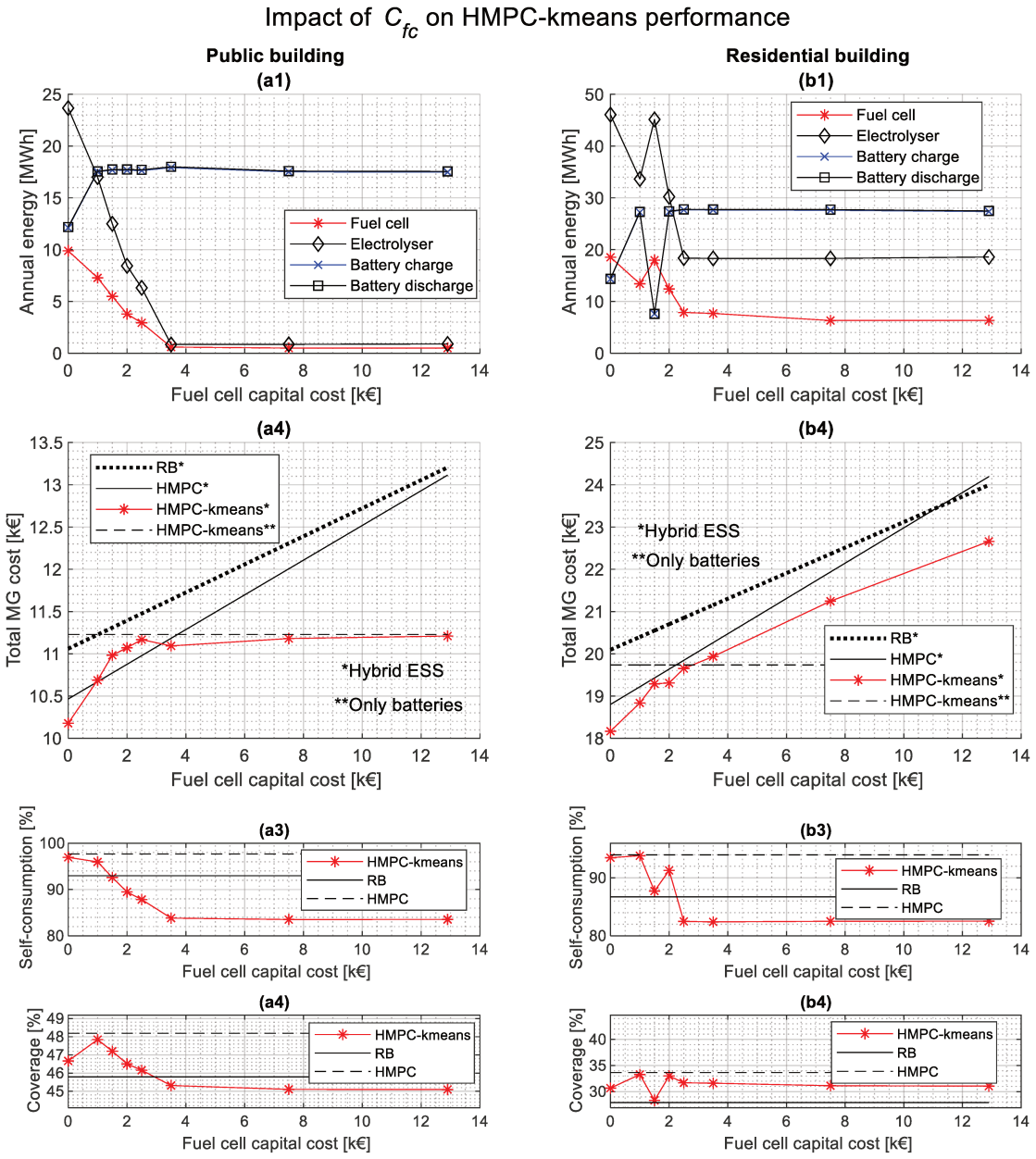

Fig. 6.8: Impact of fuel cells capital cost on the building microgrids performance. (a) Public building. (b) Residential building.

Therefore, aiming to evaluate the impact of hydrogen ESS capital costs on annual BMG operating cost, the sensitivity of HMPC-kmeans to variations in C_{fc} was assessed. Fig. 6.8a1 reveals that, from the perspective of HMPC-kmeans, the use of hydrogen ESS starts being profitable in public buildings when C_{fc} is below 3500 €/kW, which represents a decrease of 53% of the adopted current $C_{fc} \cong 7500\ €/kW$ (Table 6.4). Regarding the curves in Fig. 6.8b1, HMPC-kmeans in residential buildings starts using hydrogen ESS to increase the self-consumption rate when C_{fc} is inferior to 2500 €/kW, which is lower than in public buildings.

By correlating the use of ESS with the total MG cost with HMPC-kmeans (Fig. 6.8a1 and Fig. 6.8a2 for public buildings; Fig. 6.8b1 and Fig. 6.8b2 for residential buildings), it is possible to note that the use of fuel cells rises when the total MG cost with only batteries is smaller than the scenario with hybrid ESS. This highlights that HMPC-kmeans can adapt according to C_{fc} guaranteeing higher annual self-consumption rates (Fig. 6.8a3 and Fig. 6.8b3) and higher annual coverage rates (Fig. 6.8a4 and Fig. 6.8b4) when C_{fc} is cheaper. This mechanism provides cheaper BMG operating cost than RB in all circumstances (Fig. 6.3a2 and Fig. 6.3b2) and HMPC for high C_{fc} (above 2500 €/kW in residential and above 3500 €/kW in public buildings).

Nonetheless, at cheap C_{fc}, HMPC is very close to the performance of HMPC-kmeans and in some situations, HMPC outperforms HMPC-kmeans (Fig. 6.8a2 and Fig. 6.8b2). According to Fig. 6.8a1 and Fig. 6.8b1, at small fuel cell prices, HMPC-kmeans increases hydrogen ESS use and reduces the use of batteries, regulating the trade-off of exploiting hybrid ESS. Remarkably, in the residential building, the trade-off between batteries and hydrogen ESS is more obvious, as shown in Fig. 6.8b1 for 1000 €/kW and 2000 €/kW. When fuel cells and electrolysers become as competitive as batteries, there will be an oscillation in the tendency of ESS utilisation and the self-consumption rate.

Among the three control strategies studied, HMPC with hybrid ESS guaranteed the highest self-consumption rate but the highest BMG operating cost with the current capital cost (Fig. 6.5 and Fig. 6.6). For this reason, the condition for HMPC to be profitable was investigated. As HMPC is insensitive to C_{fc}, the hydrogen ESS would be advantageous if the economic savings of its installation were greater than its cost. In other words, to guarantee the hydrogen ESS profitability, the equation (6.6) must be respected.

$$\underbrace{\pi_{fc,hybrid}^{annual} + \pi_{els,hybrid}^{annual}}_{\substack{Amortised\ Investiment\ cost\ of \\ hydrogen\ storage}} < \underbrace{\left(-\pi_{grid,hybrid}^{annual} - \pi_{bat,hybrid}^{annual} + \pi_{sc,hybrid}^{annual} - O\&M_{fc}\right)}_{Annual\ income\ of\ the\ scenario\ with\ hybrid\ ESS} - \underbrace{\left(-\pi_{grid,onlyBAT}^{annual} - \pi_{bat,onlyBAT}^{annual} + \pi_{sc,onlyBAT}^{annual}\right)}_{Annual\ income\ of\ the\ scenario\ with\ only\ batteries} \quad (6.6)$$

In the formulation of equation (6.6), the difference between the annual income of the scenario with hybrid ESS and the annual income of the scenario with only batteries defines the total benefit created by the installation of hydrogen storage. Therefore, to guarantee the system profitability, the amortised investment cost of hydrogen storage ($\pi_{fc,hybrid}^{annual} + \pi_{els,hybrid}^{annual}$), must be inferior to their total benefit.

By dividing equation (6.6) it into three major expenses – namely electricity bill savings, battery degradation savings, and self-consumption additional income – it is obtained the equation (6.7). Notably, the factors m_{elec} and m_{sc} are positive scalar variables that can be adjusted to make the inequality (6.7) valid or non-valid. The scalar variable m_{elec} adjusts the current electricity price, whereas the scalar variable m_{sc} modifies the current French self-consumption additional income. Therefore, the scenario using the current electricity price is when m_{elec} is equal to 1. Similarly, when m_{sc} equals 1, the scenario understudy refers to the current French self-consumption.

$$\begin{aligned}\pi_{fc,hybrid}^{annual} + \pi_{els,hybrid}^{annual} \\ < \underbrace{m_{elec}\left(\pi_{grid,onlyBAT}^{annual} - \pi_{grid,hybrid}^{annual}\right)}_{Electricity\ bill\ savings} + \underbrace{\pi_{bat,onlyBAT}^{annual} - \pi_{bat,hybrid}^{annual}}_{Battery\ degradation\ savings} \\ + \underbrace{m_{sc}\left(\pi_{sc,hybrid}^{annual} - \pi_{sc,onlyBAT}^{annual}\right)}_{\substack{Self-consumption \\ additional\ income}} - O\&M_{fc}\end{aligned} \tag{6.7}$$

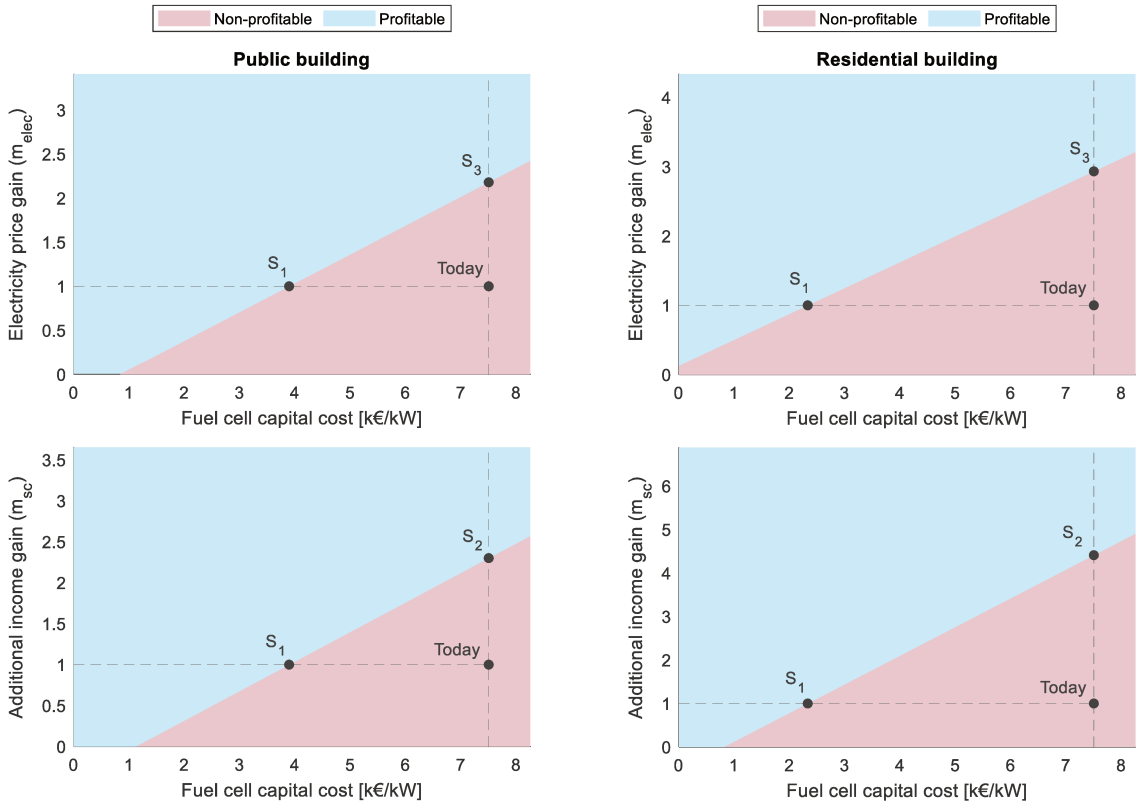

Fig. 6.9: Economic analysis of hydrogen ESS installation in public and residential BMGs to estimate three possible affordable scenarios for fuel-cell in building microgrids.

Hence, by adjusting the values of the scalar variables (m_{elec} and m_{sc}), it is possible to identify non-profitable and profitable zones, as shown in Fig. 6.9. The non-profitable zone is when the inequality (6.7) is not respected, whereas the profitable zone is the opposite case. The point $Today$ refers to the current fuel cell capital cost (7500 €/kW), current electricity price ($m_{elec} = 1$), and current self-consumption policy ($m_{sc} = 1$). As concluded previously and shown in Fig. 6.9, the current scenario makes the use of fuel cells by means HMPC non-profitable in both residential and public buildings. The

graphs in Fig. 6.9 is also straightforward to identify possible scenarios (i.e. values of C_{fc}, m_{elec} and m_{sc}) that would make fuel cells more worthwhile to be installed in public and residential. Three possible scenarios are given as example:

- **Scenario 1 (point S1):** The capital cost of fuel cells must be reduced by at least 48% in public buildings ($C_{fc} < 3892$ €/kW) and 69% in residential buildings ($C_{fc} < 2328$ €/kW).
- **Scenario 2 (point S2):** Self-consumption additional income must be increased by 230% in public buildings and 441% in residential buildings. For this, the equation (5.15) for the additional income must be modified accordingly.
- **Scenario 3 (point S3):** The price of electricity 218% in public buildings and 293% in residential buildings.

6.5.3 *Impact of operating the hydrogen ESS at a nominal power rate*

Operating PEM electrolysers and PEM fuel cells close to their nominal power rate can enhance power-to-gas or gas-to-power conversion efficiency and extend the lifetime of ESS devices [215]. However, the benefits of operating hydrogen ESS at nominal power may not be enough to cover the drawbacks of constraining the use of hydrogen ESS, which may result in the non-profitable operating of the BMG. Depending on the ESS capital cost, public financial incentives, electricity price, and internal power consumption profiles, fuel cells and electrolyser operating at nominal power may prevent the BMG to attain major objectives, such as minimising the whole operating cost or maximising the self-consumption rate. Therefore, to evaluate the impact of limiting the use of hydrogen ESS at nominal power, two additional scenarios were assessed: a scenario with hard constraints and another with soft constraints. To highlight the impact of constraining the use of hydrogen ESS, these two scenarios consider that the hydrogen ESS capital cost is zero, leading HMPC-kmeans to use fuel cells and electrolysers.

The hard constraints scenario consists of embedding into EMPC the constraints (6.8) and (6.9). In this manner, electrolysers and fuel cells can operate only if there is enough energy to run them near to their nominal power (P_{fc}^{nom} and P_{els}^{nom} in Table 2.1) for at least 2 hours. On the other hand, these constraints do not exist in the scenario with soft constraints, so that the hydrogen chain is free to operate according to BMG needs.

$$\sum_{k=1}^{2} \delta_{fc,k} \cdot \min\left(T_s^{TMPC} \cdot P_{fc}^{nom}, -E_{deficit,k}\right) \leq \sum_{k=1}^{2} E_{fc,k}^{zone1} + E_{fc,k}^{zone1} + E_{fc,k}^{zone3} \tag{6.8}$$

$$\sum_{k=1}^{2} E_{els,k}^{zone1} + E_{els,k}^{zone1} + E_{els,k}^{zone3} \leq -\sum_{k=1}^{2} \delta_{els,k} \cdot \min\left(T_s^{TMPC} \cdot P_{els}^{nom}, E_{surplus,k}\right) \tag{6.9}$$

According to the graphs in Fig. 6.10, limiting the use of the hydrogen chain reduces the capacity of the BMG to attain higher marks of self-consumption, which increases the total MG cost. Hard constraints result in a reduction of 7% of self-consumption in public buildings, whereas in residential buildings it is decreased by 2% when using HMPC. This is because the hydrogen chain is less exploited in the scenario with hard constraints than with soft constraints, which minimises the capacity of shifting the load toward periods of surplus and obliges the BMG to inject into the grid. For this reason, the total

annual degradation of hydrogen ESS (third and fourth lines of graphs of Fig. 6.10) is considerably lower with hard constraints than with soft constraints.

By observing the power flow of these two scenarios with HMPC (Fig. 6.11), the reduction of the hydrogen ESS total degradation is mainly because the hydrogen ESS is not used at all in certain circumstances, rather than because it is operated at a nominal power rate. According to Fig. 6.10, the fuel cell and electrolyser degradation rate (fifth and sixth lines of graphs of Fig. 6.10) with hard or soft constraints are nearly the same, which is in line with the conclusion of [215]. As shown in Fig. 6.11, the fuel cells and electrolysers are not used because the power imbalance is lower than their respective nominal power, while under soft constraints, the hydrogen ESS can cover most of the raw power imbalance. This is because hard constraints prevent the use of fuel cells if the energy deficit is lower than its nominal power ($P_{fc}^{nom} = 20kW$) and restrain the use of electrolysers if the energy surplus is lower than its nominal power ($P_{els}^{nom} = 25kW$).

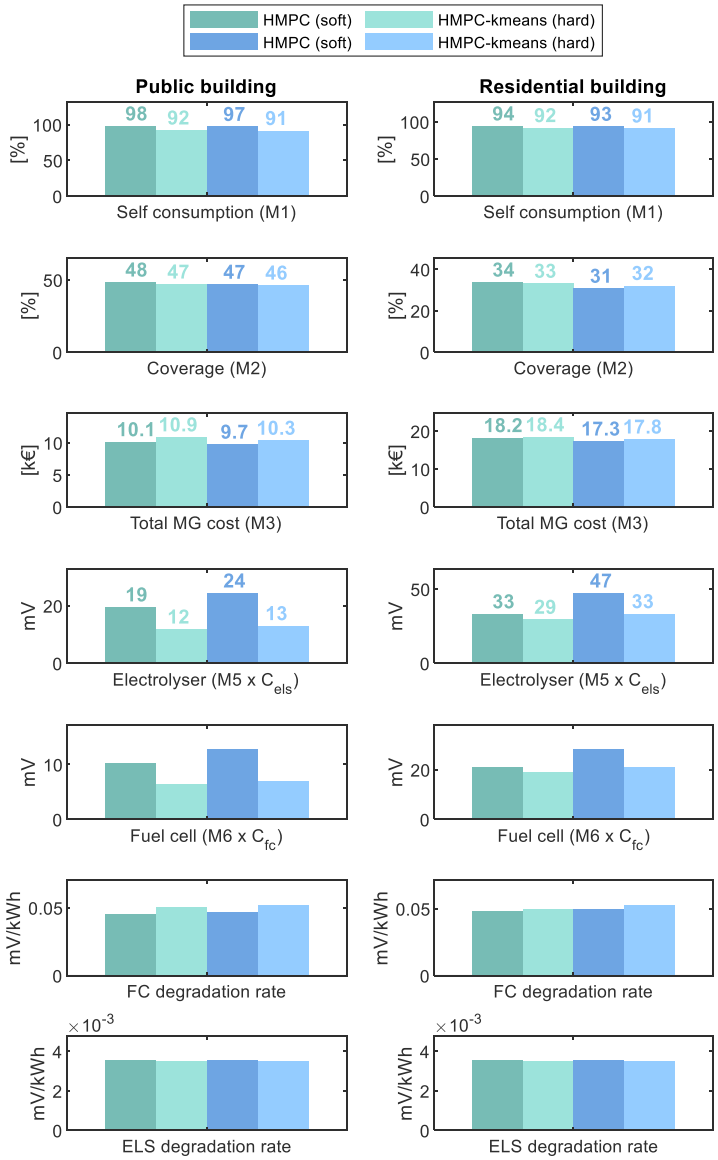

Fig. 6.10: Performance of the conventional Hierarchical Model Predictive Controller (HMPC) and proposed hierarchical model prediction controller (HMPC-kmeans) with soft and hard constraints for operating hydrogen storage.

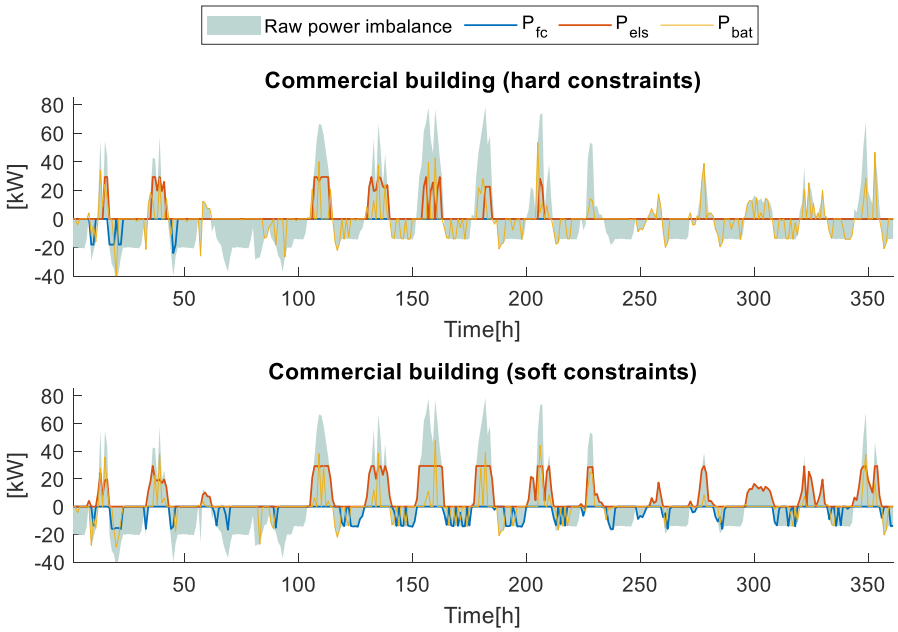

Fig. 6.11: Impact of hard and soft constraints in the operation of electrolysers and fuel cells in the public building, when using the conventional Hierarchical Model Predictive Controller (HMPC).

To overcome this problem, there are two solutions: either the hydrogen chain should be sized according to the most likely minimum power consumption and minimum power generation, or the controller should be designed with soft constraints. Given that the power imbalance in BMG is very unpredictable, it is recommended to use soft constraints rather than hard constraints. Since the power imbalance of buildings is very seasonal, it is difficult to assign minimum operating power (P_{fc}^{nom} and P_{els}^{nom}) without losing performance or profitability during the entire year.

6.5.4 *Impact of power imbalance prediction data error*

Aiming to demonstrate the robustness of the proposed HMPC-kmeans against the stochasticity in power imbalance, scenarios with prediction data error were analysed. For this, the real power imbalance was modified by two functions, *Add noise 1* and *Add noise 2* that were briefly introduced in section 6.2. The function *Add noise 1* modifies the annual prediction data used by the MG cost estimator, whereas *Add noise 2* disturbs the two day-ahead prediction data used in both MG cost estimator, EMPC and TMPC.

The real annual power imbalance (x_{real}^{annual}) is scaled by a uniformly distributed random value of interval [0,0.3], named ρ_1. The noise amplitude can be either positive or negative depending on a second random standard Gaussian distributed value of mean $\mu_1 = 0$ and standard deviation $\sigma_1 = 1$, named ϑ_1. Additionally, the annual dataset was shifted in time up to ± 3 hours. Mathematically interpreting, the disturbed annual dataset ($x_{disturbed}^{annual}$) is updated once a year by applying equation (6.10), where amp_{noise_1} and Δ_{noise_1} are defined by (6.11) and (6.12), respectively.

$$x_{disturbed,k}^{annual} = amp_{noise_1} \cdot x_{real,k+\Delta_{noise_1}}^{annual}, \quad \forall k \in [1,365] \tag{6.10}$$

$$amp_{noise_1} = 1 + sign(\vartheta_1) \cdot \rho_1 \tag{6.11}$$

$$\Delta_{noise_1} = floor\big(3 \cdot \rho_1 \cdot sign(\vartheta_1)\big) \tag{6.12}$$

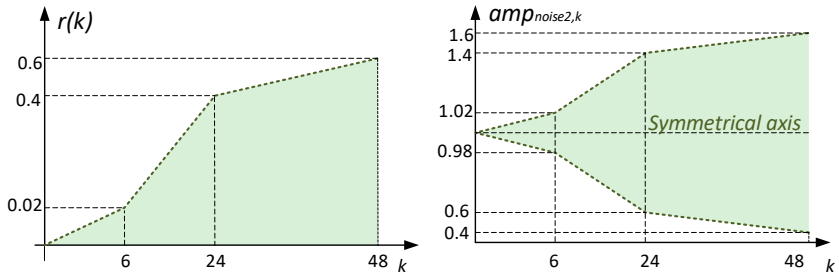

Fig. 6.12: Distribution of the time-variant random factors to emulate the error in the two day-ahead prediction data.

Similarly, the error introduced into the two day-ahead power imbalance prediction data follows equation (6.13), where amp_{noise_2} and Δ_{noise_2} are calculated through equations (6.14) and (6.15), respectively. The variable ϑ_2 is a standard Gaussian random variable of mean $\mu_2 = 0$ and standard deviation $\sigma_2 = 1$, whereas the factor $\rho_{2,k}$ is a uniformly distributed random variable in the interval of $[0, r(k)]$, where $r(k)$ is a non-linear function defined as shown in the left graph in Fig. 6.12, leading amp_{noise2} to have a shape as shown in the right graph in Fig. 6.12. Additionally, the real prediction data is shifted in time randomly up to ten times $r(k)$, i.e. up to 6 hours. The random variable $r(k)$ was defined as shown in Fig. 6.12 to mimic the rising of prediction error along the MPC horizon. As a result, the error in the amplitude of the signal increases over time, detaining 0% of errors at the current time and attaining up to 60% of errors 48 hours ahead. It is important to remark that the same two day-ahead prediction data errors are introduced in both EMPC and TMPC layers. The comparison between the real and the predicted two day-ahead power imbalance is shown in Fig. 6.13, whereas

Table 6.5 compares the real and disturbing annual prediction data.

$$x^{daily}_{disturbed,k} = amp_{noise_2} \cdot x^{daily}_{real,k+\Delta_{noise_2}}, \quad \forall k \in [1,48] \tag{6.13}$$

$$amp_{noise_1,k} = 1 + sign(\vartheta_2) \cdot \rho_{2,k} \tag{6.14}$$

$$\Delta_{noise_1,k} = floor\left(10 \cdot \rho_{2,k} \cdot sign(\vartheta_2)\right) \tag{6.15}$$

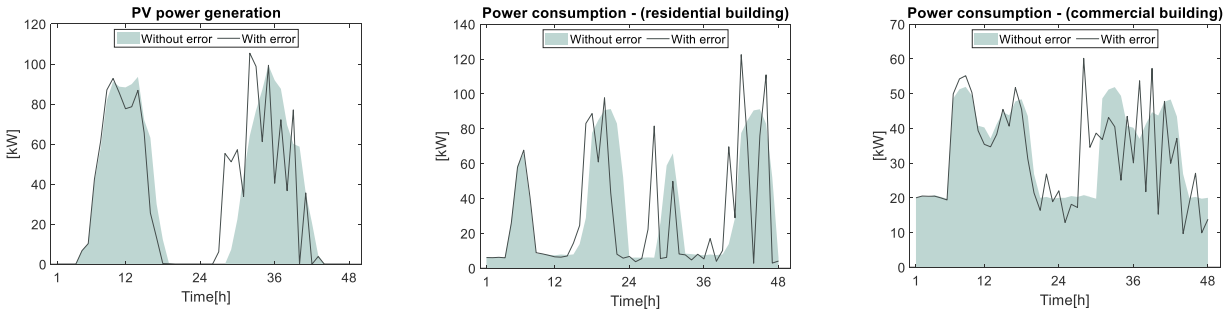

Fig. 6.13: Prediction data with and without error along the Economic Model Predictive Control horizon of 48 hours.

Table 6.5: Comparison between real and disturbing annual dataset.

		Real dataset	Disturbed dataset
Photovoltaic power generation	Average (MWh)	131.0	126.5
	Maximum (kWh)	107.1	126.0
	Minimum (kWh)	0.0	0.0
Residential building power consumption	Average (kWh)	307.1	307.0
	Maximum (kWh)	111.0	140.7
	Minimum (kWh)	5.9	4.2
Public building power consumption	Average (kWh)	241.9	241.8
	Maximum (kWh)	64.5	82.7
	Minimum (kWh)	9.6	7.0

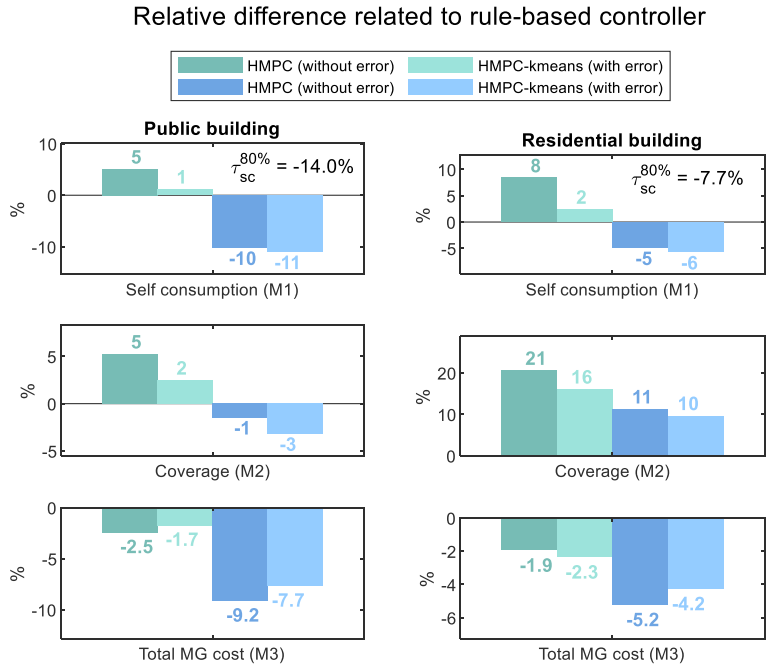

Fig. 6.14: Comparison of the first-year outcomes of the three control strategies with the hybrid energy storage system when subjected to prediction data error.

By analysing the results of Fig. 6.14, although errors in the prediction data harm the performance of both HMPC and HMPC-kmeans, they satisfy the required self-consumption[8] ($M_1 \geq \tau_{sc}^{80\%}$) and they still outperforming the RB in the economic aspects (metric M_3). With prediction data errors, HMPC assured an annual self-consumption rate of 89% in residential building (i.e. 94% in the public building), compared to 94% (i.e. 98%) in the ideal scenario. Likewise, the errors in prediction data damage the HMPC-kmeans. In the ideal scenario, HMPC-kmeans guaranteed an annual self-consumption of 83% in public buildings and 84% in residential ones. On the other hand, with data prediction inaccuracy, the annual self-consumption decreased to 82% in public buildings and 83% in residential ones.

The self-consumption rate using HMPC and HMPC-kmeans approaches the values attained by RB. In residential buildings, self-consumption is degraded by 6%, compared to 4% in public buildings. Despite this considerable reduction, HMPC-kmeans can still ensure nearly the same operating cost (results of Fig. 6.6), which is 9% lower in public buildings and 5% lower in residential buildings than RB.

[8] The absolute values of the simulation results are available in the Appendix 0 on page 238.

6.6 Performance of the power-sharing module and potentials of exploring the batteries of electric vehicles

The simulation results discussed up to this point do not include the Plug-in Electric Vehicles (PEV) parking. This is because the simulations conducted in the previous section were to assess the performance of the MG cost estimator, that currently does not yet handle the effects of PEV parking. Hence, aiming to analyse the potential of using the batteries of electric vehicles on behalf of the BMG, subsection 6.6.1 evaluates the performance of the Power-Sharing Module (PSM) presented in Chapter 3 in section 3.5. Subsequently, subsection 6.6.2 analyses different scenarios of PEV exploitation that would be beneficial for both the BMG and electric vehicles' owners. One of the analysis assesses whether it is advantageous to allow discharging PEVs to supply the building demand. This analysis includes identifying a type of remuneration that should be addressed to PEV's owners to encourage them to allow discharging their vehicles when they are plugged in the BMG. Finally, subsection 6.6.3 gives some directives in how the MG cost estimator should be adapted to comprise the effects of PEVs on annual BMG expenses and annual self-consumption rate.

Since in the simulations of this section the MG cost estimator is disabled, EMPC is conceived with a simplified cost function. As a result, instead of considering both energy and economic aspects, the upper MPC only maximises the self-consumption rate by penalising all grid energy exchanges. Like the traditional HMPC in section 6.5, it optimises the objective function defined by (6.1) at least once a day. The effects of PEV parking in the annual self-consumption and the economic benefits of exploiting them will be evaluated in the scenario where only batteries are installed. Although the proposed EMS with PEV parking operates properly with hybrid (i.e. batteries and hydrogen ESS) and non-hybrid ESS (i.e. only batteries), in this thesis only the results with the non-hybrid configuration will be shown. Considering that the objective is to evaluate the contribution of PEV batteries, simulations with only Li-ion battery pack is enough to identify their potentials. Consequently, in this section, the PEV parking and Li-ion batteries are managed by the hierarchical controller composed of EMPC with a simplified cost function, TMPC, PSM, and RTMI.

6.6.1 *Performance of the Power-sharing module*

The PSM operates as a router of energy with the objective to assure that all PEV are charged up to $SoC = 80\%$ using renewable energy before their departure time. As explained in section 3.5, the upper levels of the hierarchical controller consider the PEV parking as a huge battery with a capacity that varies according to the number of plugged PEV. Therefore, both EMPC and TMPC do not have any information about the SoC of each PEV, but only the average SoC of the entire PEV parking, named $\widehat{SoC}$. Hence, it is up to PSM to determine the portion of power that needs to be destinated to each plugged PEV to assure that they are fully charged (i.e. up to $SoC = 80\%$) before their scheduled departure time.

Therefore, to evaluate whether PSM operates correctly, six scenarios were evaluated by using the BMG of sizing specified in Table 2.1. As summarized in Table 6.6, these scenarios are the combination of the type of building, the presence or not of errors in the prediction data, and whether the PEV's

owners have authorised the BMG to discharge PEV's batteries. In residential buildings, all PEV is connected during non-business hours, which is mostly between 5 PM to 8 AM. On the other hand, in public buildings, all PEV is connected during business hours, which correspond to periods predominantly between 7 AM to 6 PM. During weekends, PEVs in residential buildings are always connected to the BMG, whereas in public buildings they are never plugged.

Table 6.6: Summary of the simulation cases to evaluate the impact of plug-in electric vehicles.

Case ID	Type of building	Prediction data error			PEV connection		Discharging	
		Power imbalance	Initial SoC	Departure and Arrival time	Business hours	Non-business hours	Allowed	Not allowed
1	Residential					✓	✓	
2	Residential	✓	✓	✓		✓	✓	
3	Residential					✓		✓
4	Public				✓		✓	
5	Public	✓	✓	✓	✓		✓	
6	Public				✓			✓

In the ideal scenario – corresponding to cases 1, 3, 4, and 6 – all PEV connects to the BMG as planned and specified in their schedule table (similar to Table 3.1). Furthermore, there is no error in the power imbalance prediction data, and all PEV arrives every day with $SoC = 40\%$. On the contrary, with the purpose to test the limits of the entire hierarchical controller (i.e. EMPC, TMPC, and PSM), scenarios with prediction data error were evaluated (cases 2 and 5). The errors include inaccuracies in the power imbalance, in the energy that PEV batteries have stored at the moment that they are plugged in the BMG (named 'Initial SoC' in Table 6.6), and the planned departure and arrival time.

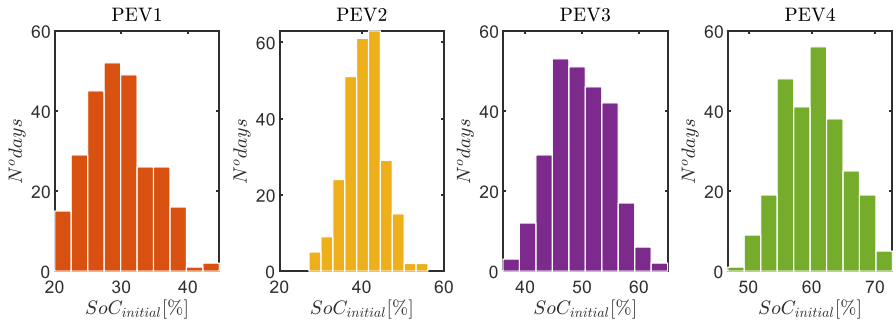

Fig. 6.15: Initial state-of-charge of the four plug-in electric vehicles in the simulations with prediction data error.

The noise in the power imbalance is generated by the function *add noise 2* explained previously in section 6.5.4. Similarly, the noise in initial SoC follows a Gaussian distribution of standard deviation $\sigma_{pev} = 0.05$ and mean $\mu_{pev_{ID}}$ that depends on the user behaviour. It was considered four types of users. Consequently, four mean values were used, namely 30%, 40%, 50%, and 60%. The histogram in Fig. 6.15 shows the initial SoC distribution of each of the four PEV profiles during a one-year simulation.

The noise in the departure and arrival times was emulated similarly to the function *add noise 2*. The idea is to mimic that the departure and arrival times are more uncertain when they are far from happening. Hence, the uncertainty gradually reduces when approaching the real PEV disconnection or connection time. Therefore, the real arrival and departure times ($t^{real}_{arrival}$ and $t^{real}_{departure}$) are scaled by a uniformly distributed random value of interval $[0, r_{pev}(t)]$, named ρ_{pev}, as expressed in equations

(6.16) and (6.17). The variable ϑ_{pev} is a random standard Gaussian distributed variable of mean $\mu_{pev} = 0$ and standard deviation $\sigma_{pev} = 1$, whereas $r_{pev}(t)$ is defined as shown in Fig. 6.16. As a result, imprecisions in the arrival and departure times are bounded to 4 hours. The graphs in Fig. 6.17 compares the real and disturbing arrival and departure times of a PEV connected to the public building. It is possible to observe that the error is bigger when the PEV departure or arrival is far from happening.

$$t_{real,k}^{disturbed} = \left(1 + sign\left(\vartheta_{pev}\right) \cdot \rho_{pev}\right) \cdot t_{arrival,k}^{real}, \quad \forall k \in [1,365] \tag{6.16}$$

$$t_{real,k}^{disturbed} = \left(1 + sign\left(\vartheta_{pev}\right) \cdot \rho_{pev}\right) \cdot t_{arrival,k}^{real}, \quad \forall k \in [1,365] \tag{6.17}$$

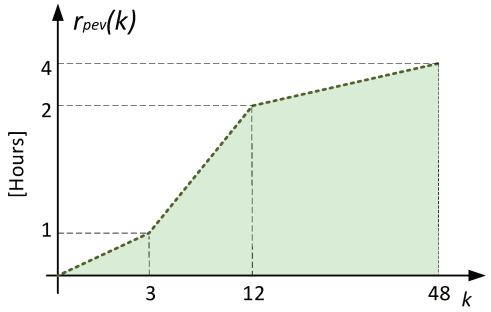

Fig. 6.16: Boundary of the time-variant random factor ρ_{pev} to emulate the error in arrival and departure time of plug-in electric vehicles.

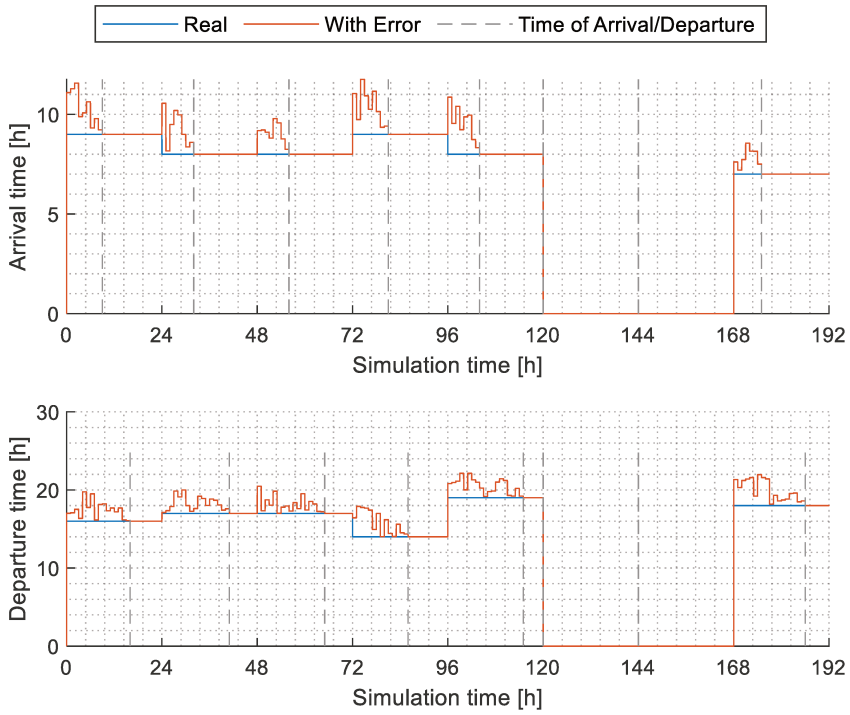

Fig. 6.17: Comparison between the real and disturbing arrival and departure time of the plug-in electric vehicle 1 in a public building.

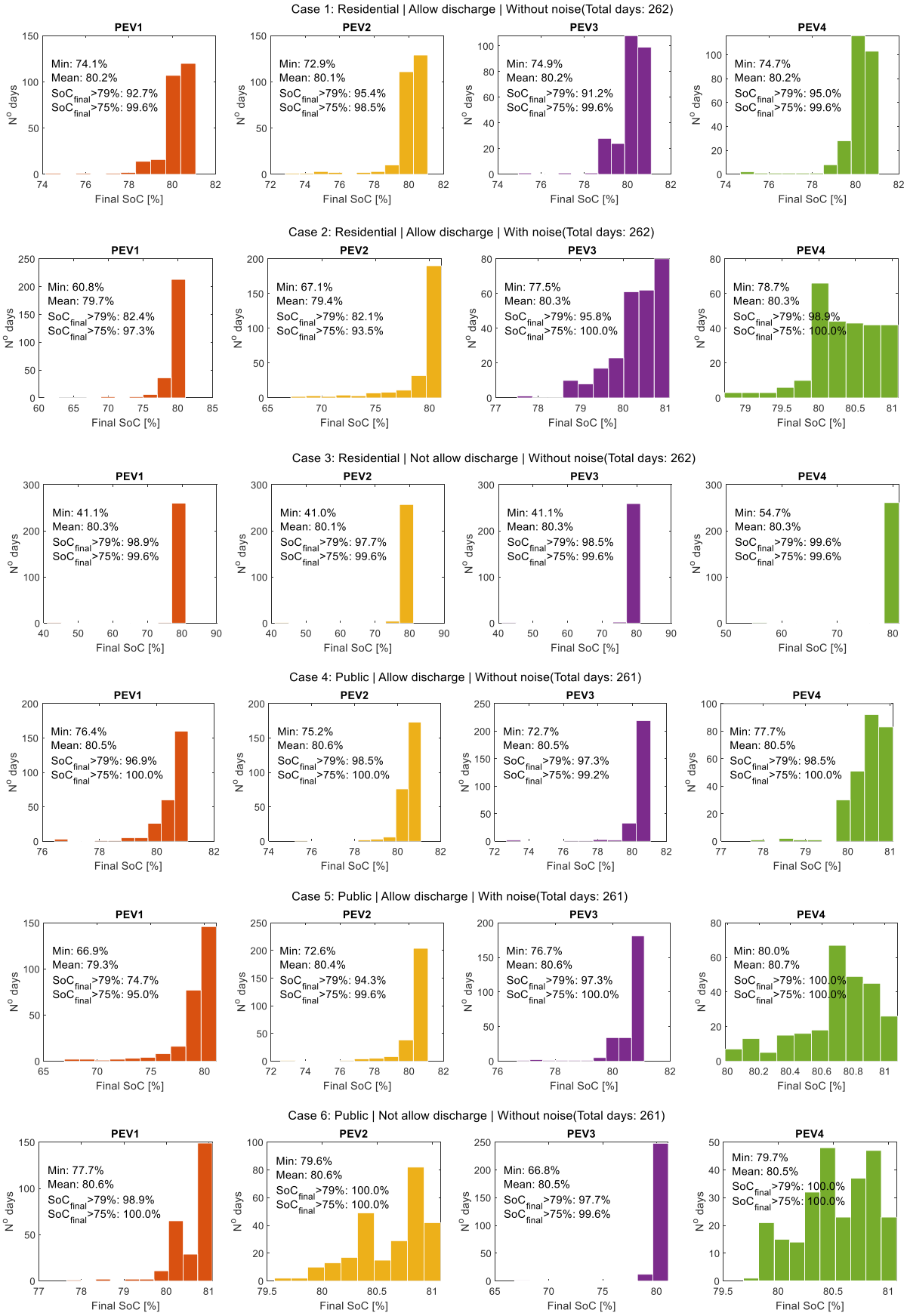

Fig. 6.18: State-of-charge of the four plug-in electric vehicles before disconnecting from the building.

Aiming to verify whether PSM is capable of charging all the PEVs before their disconnection, the distribution of the SoC of the four PEVs just before their departure time – named 'final SoC' or SoC_{final} – is shown in Fig. 6.18. It is possible to observe that, in all simulation cases, the hierarchical controller assured on average that more than 99% of PEVs are fully charged to $SoC_{final} \geq 75\%$ and more than 95% of PEVs to $SoC_{final} \geq 79\%$. Even when subjected to intensive prediction data inaccuracies – corresponding to cases 5 and 6 – the combination of HMPC and PSM guaranteed that most of PEVs were charged very close to 80%.

One of the particularities of HMPC design is that the SoC of PEV are kept most of the time softly constrained (equation (3.95)), except at the moment of their departure time, where SoC_{pev} is forced to be 80% (equation (3.100)). The HMPC was formulated in this manner to allow PEV's batteries to support the BMG energy needs under the condition to be charged before disconnecting. Therefore, with the purpose to check whether the PEVs are preferably charged when there is a surplus of energy and discharged to cover the building energy deficit, the PEV's power references were superposed to the raw net power imbalance ($P_{cons} - P_{pv}$), as shown in Fig. 6.20 for public buildings and Fig. 6.22 and Fig. 6.24 for residential buildings. These figures and the evolution of the SoC of each of the four PEVs and Li-ion batteries pack, that are shown in Fig. 6.19, Fig. 6.21, and Fig. 6.23, allow observing that PEV's batteries are preferably charged and discharged to avoid energy injection and to reduce electricity purchase.

According to these graphs, load matching is more frequent in the public building (Fig. 6.20) than in the residential building (Fig. 6.22). This is because, in public buildings, PEVs are predominantly connected when there is an energy surplus (negative power imbalance). Consequently, PEVs can be used to absorb the surplus of energy generated by PV panels directly. Conversely, in residential buildings, PEVs are mostly connected during periods of energy deficit (positive power imbalance) and disconnected from the BMG when PV panels start producing energy. Hence, the residential BMG usually must purchase electricity from the grid to charge its PEVs.

Still, due to the building's power imbalance profile, PEVs in public buildings are often prevented from being discharged because they are plugged in the BMG when there is no energy deficit. Consequently, according to the inequality constraint (3.105), they cannot be discharged except to charge the Li-ion battery pack. Due to efficiency issues and a short period in which PEV stay plugged in BMG, the hierarchical controller prefers not to discharge PEV's batteries to charge the battery pack.

Conversely, in residential buildings, PEVs can be discharged more frequently, especially during the weekend because they stay plugged in the BMG for long periods. As shown in Fig. 6.21, PEVs actively reduce the grid energy exchange on Sundays and Saturdays. Nonetheless, if the PEV's owners have not authorized the discharge of their PEVs, the load matching during weekends is less intensive, as shown in Fig. 6.24. In order to verify the economic and energy effects of PEV's owner authorization, section 6.6.2 analyses the advantages and drawbacks of discharging PEV's batteries from the perspective of both BMG and PEV's owners.

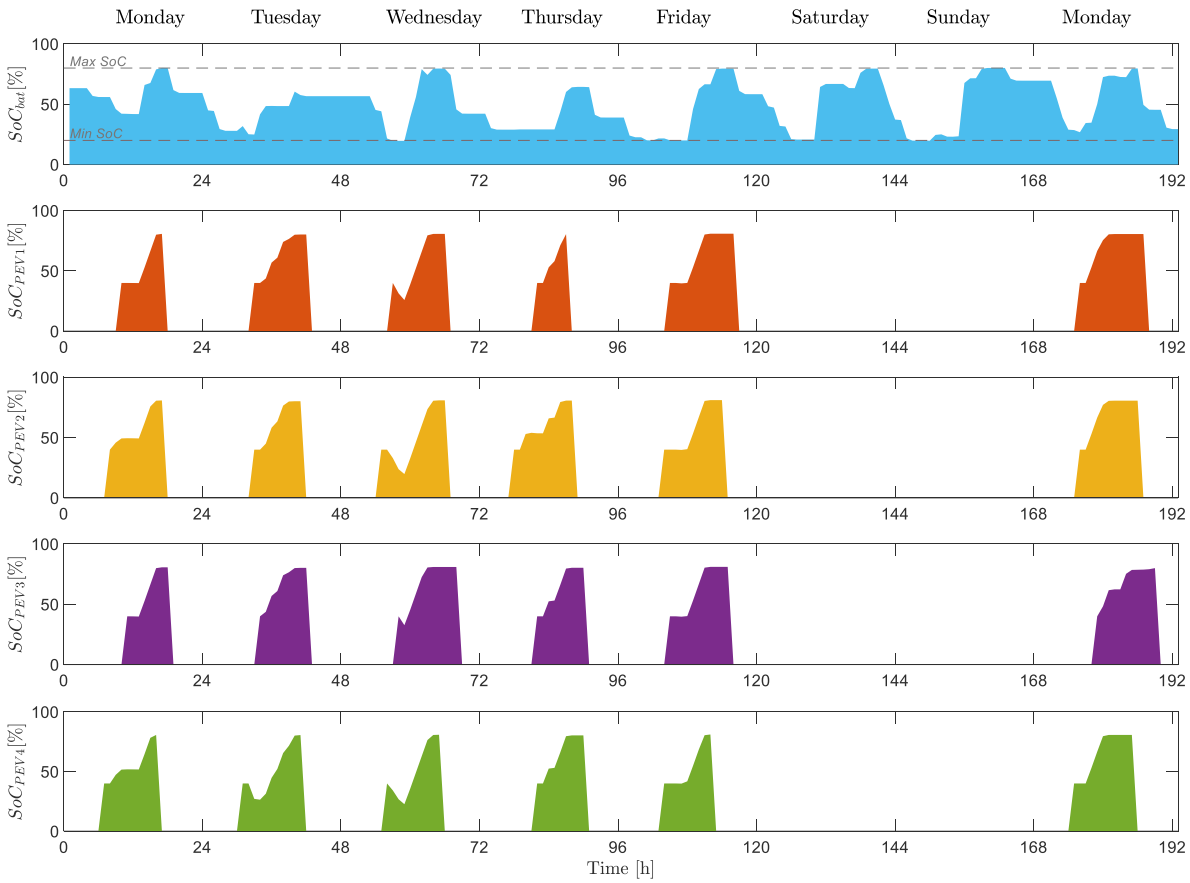

Fig. 6.19: State of charge of the four plug-in electric vehicles in the public building (case 4).

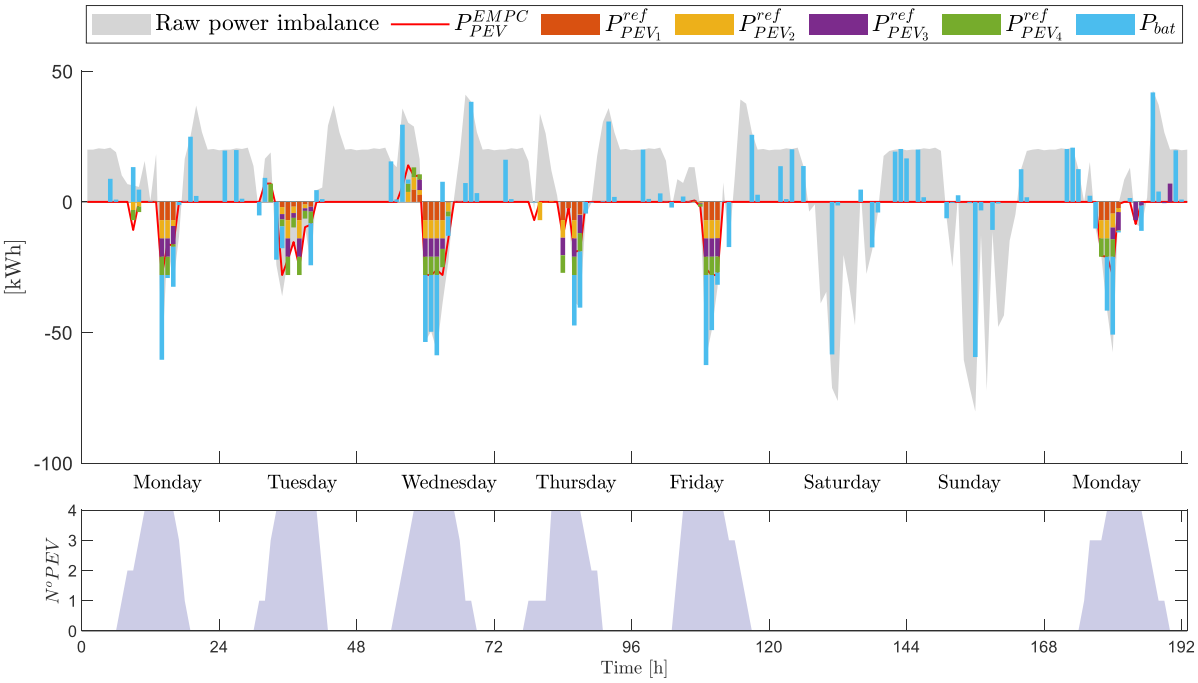

Fig. 6.20: Power references determined by the Economic MPC control layer (P_{PEV}^{EMPC}) that was shared by the PSM to guarantee that all plug-in electric vehicles in the public building are charged before their departure time (case 4).

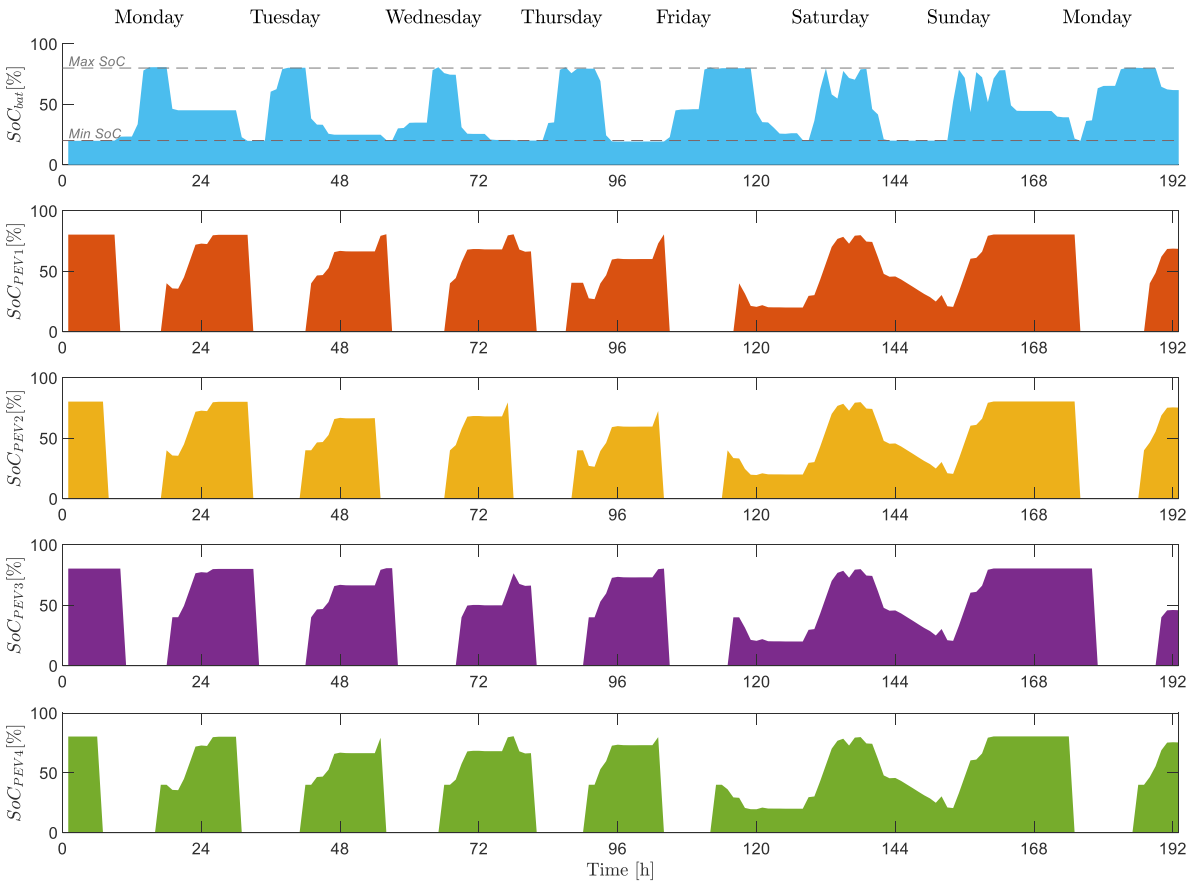

Fig. 6.21: State of charge of the four plug-in electric vehicles in the residential building (case 1).

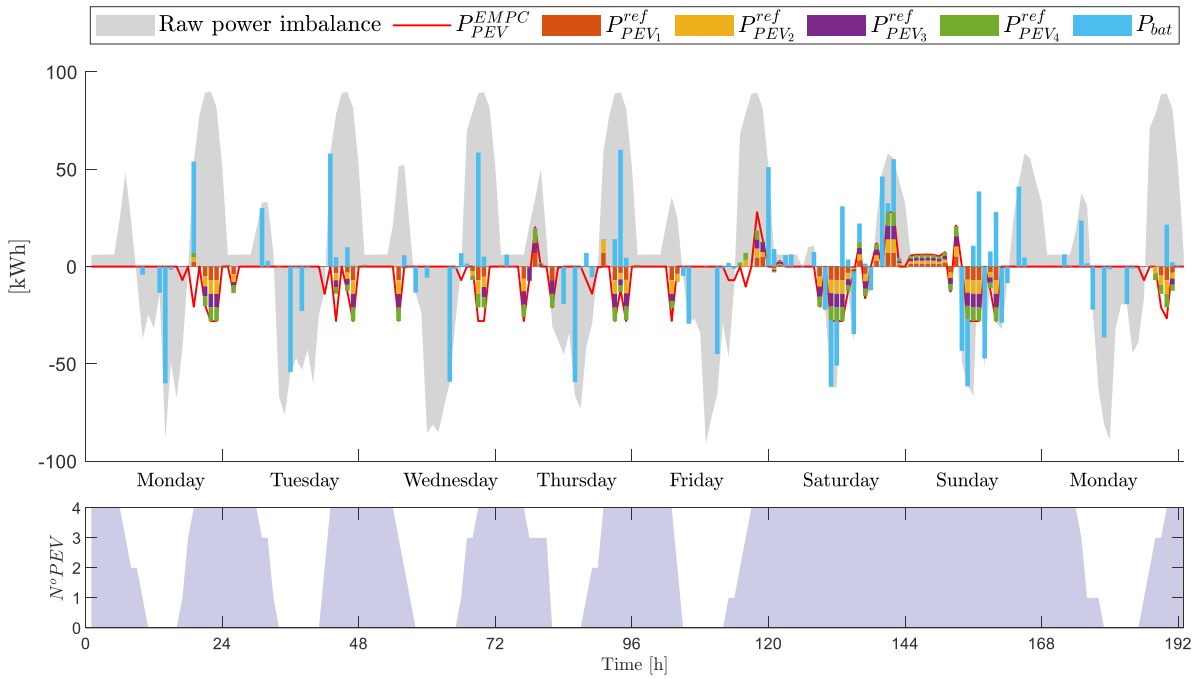

Fig. 6.22: Power references determined by the Economic MPC control layer (P_{PEV}^{EMPC}) that was shared by the PSM to guarantee that all plug-in electric vehicles in the residential building are charged before their departure time (case 1).

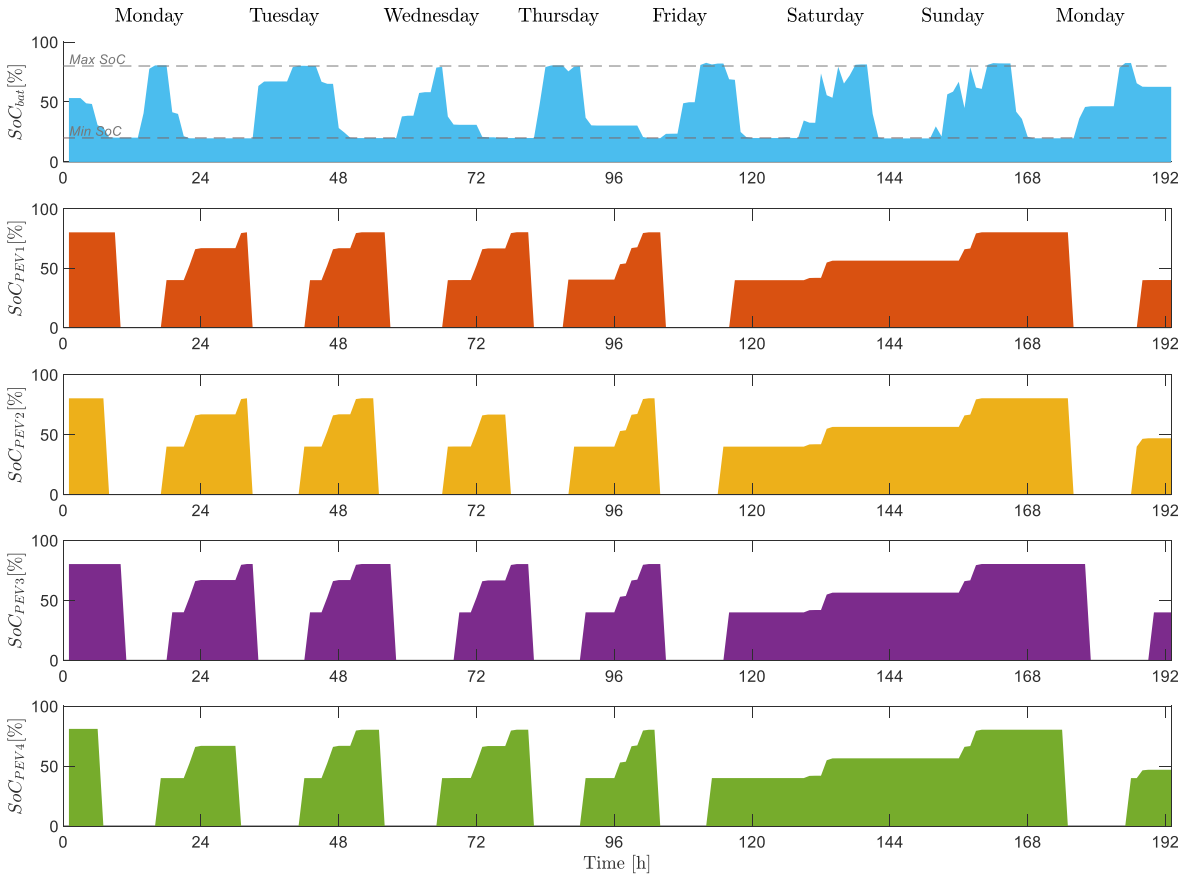

Fig. 6.23: State of charge of the four plug-in electric vehicles in the residential building (case 3).

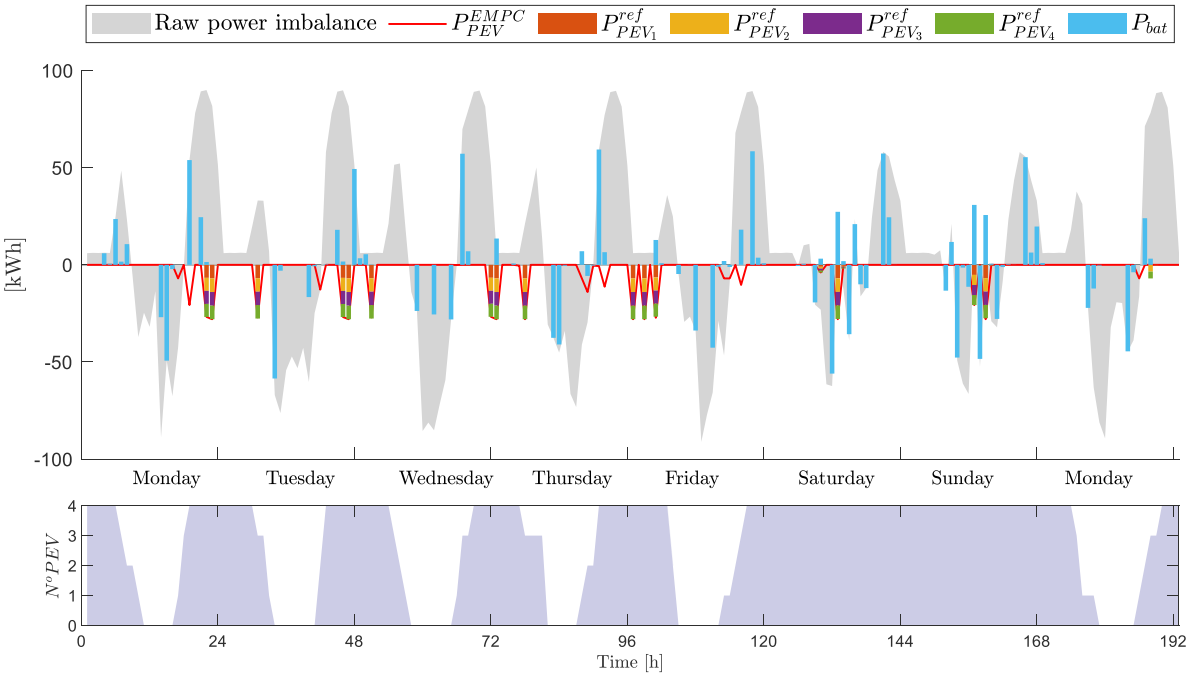

Fig. 6.24: Power references determined by the Economic MPC control layer (P_{PEV}^{EMPC}) that was shared by the PSM to guarantee that all plug-in electric vehicles in the residential building are charged before their departure time (case 3).

In Fig. 6.20, Fig. 6.22, and Fig. 6.24, it is possible to observe that sometimes Li-ion batteries pack are used to charge PEVs, but they are not enough to provide all energy required to charge the entire PEV parking. By observing the SoC of the battery pack (first graphs in Fig. 6.19, Fig. 6.21 and Fig. 6.23), the batteries are fully charged ($SoC_{bat} = 80\%$) and fully discharged ($SoC = 20\%$) once a day. Due to the chosen size of batteries, they are not capable of shifting the BMG energy surplus to charge completely the PEV's batteries. These results indicate that it is necessary to figure out a compromise between the sizing of ESSs, PEVs profiles, and annual raw net power imbalance to take full advantage of the batteries available in PEV parking.

By comparing the EMPC's power reference – named P_{PEV}^{EMPC} in Fig. 6.20, Fig. 6.22, and Fig. 6.24 – with the sum of power reference of each PEV ($\sum_{i=1}^{4} P_{pev_i}^{ref}$), it is possible to observe that most of the time PSM follows the EMPC power reference. However, there are divergences between the upper and lower control layer decisions in some situations, even though there were no prediction data errors. These divergences are because EMPC considers that the total energy stored in the PEV parking is equally shared among the four PEVs, and it assumes that all PEVs can absorb and deliver up to $E_{PEV}^{MAX} = 7kWh$. Nevertheless, these hypotheses are not always satisfied. Since the four PEV connect and disconnect at different time, the PSM will share the total power reference P_{pevs}^{TMPC} to assure that all PEVs are charged before their departure time. Consequently, PSM will charge firstly PEVs that will be disconnected sooner, which will not necessarily guarantee that all PEVs have the same SoC every time.

Moreover, the upper layers (EMPC and TMPC) ignore that some PEVs are fully charged or fully discharged. As a result, EMPC considers that PEVs are never fully charged and can always absorb up to $7kWh$. Likewise, EMPC assumes that PEVs are never empty so that they can always supply up to $7kWh$, as specified in inequality constraints (3.23) – (3.25). These divergences are corrected by the TMPC that updates the P_{PEV} maximum and minimum boundaries in the first element of its horizon, by P_{pevs}^{MIN} and P_{pevs}^{MAX} sent by the PSM hourly, as described in equations (3.122) and (3.123). Hence, the power reference sent by TMPC is equal to the sum of all power references calculated by PSM ($\sum_{i=1}^{4} P_{pev_i}^{ref}$), which are sometimes different from those calculated by EMPC. Despite these divergences, the whole hierarchical controller satisfied the objective of charging PEVs properly, as shown in the results in Fig. 6.18. The cooperation of PSM with HMPC simplifies the design of EMPC and TMPC because instead of estimating the SoC of each PEV, HMPC estimates only the average energy stored in the whole PEV parking.

6.6.2 *Potentials of exploring the batteries of electric vehicles*

Once validated that the PSM operates as expected, in this subsection, the potentials of exploring the batteries of PEVs will be analysed. Therefore, the ideal scenarios presented in the last subsection and summarized in Table 6.6 will be assessed by comparing some Key Performance Indicators (KPI), including the annual self-consumption rate, the coverage rate, the annual electricity purchased, the annual degradation of PEV's batteries, and the contribution of PEVs in reducing the grid energy dependency.

Firstly, aiming to evaluate whether it is interesting or not to discharge PEV batteries to support the BMG energy needs, the case where PEVs can be discharged (cases 1 and 4) were compared to the case where PEVs cannot be discharged (cases 3 and 6). These two scenarios were also confronted with the case where only batteries are installed, named 'Without PEV'. The comparison to the case without PEV parking aims to verify the consequences of having or not a PEV parking. The graphs in Fig. 6.25 show some economic and energy KPIs obtained after a one-year simulation that compare these three simulation cases in public and residential buildings.

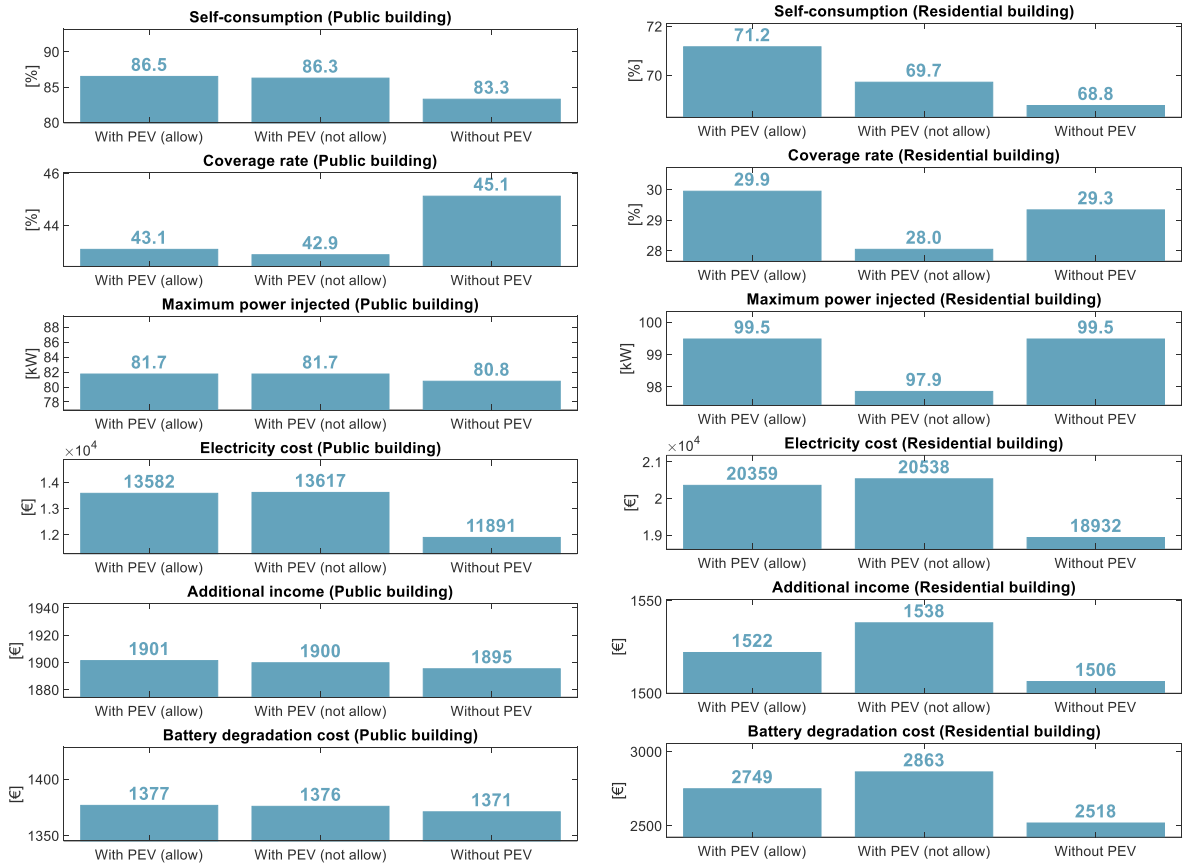

Fig. 6.25: Comparison of the economic and energy key performance indicators of residential and public building microgrids when plug-in electric vehicles are allowed and not allowed to be discharged. The indicators are compared to the case where only batteries are installed, named 'without PEV'.

According to the results shown in Fig. 6.25, from the point of view of the BMG, the discharging of PEVs implies a reduction in the annual electricity bill of 35 €/year in public buildings and 179 €/year. On the other hand, the additional annual income due to self-consumption is almost the same in the public and residential buildings. As defined by equation (5.15), the additional income is higher if the total energy self-consumed (E_{sc}) – or the self-consumption rate – is higher. Moreover, the additional income is greater if the maximum power injected ($P_{maxInjected}$) is lower. Consequently, although in residential buildings the annual self-consumption rate was higher when allowing the PEV discharging, the additional income was lower due to the increase in the maximum power injection (third row in Fig. 6.25). By comparing the degradation cost of batteries (sixth-row Fig. 6.25), it is possible to note that the PEV parking in residential buildings reduces the use of Li-ion batteries pack, decreasing its degradation cost by 114 €/year. On the other hand, in public buildings, the Li-ion batteries were used

as much when discharging PEVs as when avoiding discharging them, keeping its degradation practically the same in both cases.

Therefore, the total savings when allowing the PEV discharging – being equal to the sum of electricity and batteries degradation costs minus the additional income – are 35 €/year in public buildings and 282 €/year in residential ones. Despite being more advantageous in discharging PEVs than not discharging them, these savings are insignificant compared to the total BMG expenses. Hence, this leads us to conclude that allowing or not discharging PEVs' batteries does not impact the performance of BMG significantly. As already discussed in the previous section, due to the power imbalance profile and sizing of the battery pack, in public buildings, PEVs can be rarely discharged. Consequently, the differences in the KPIs when authorising or not their discharging are very minimal. Likewise, in residential buildings, the effects of discharging PEVs are also negligible, but more important than in public ones.

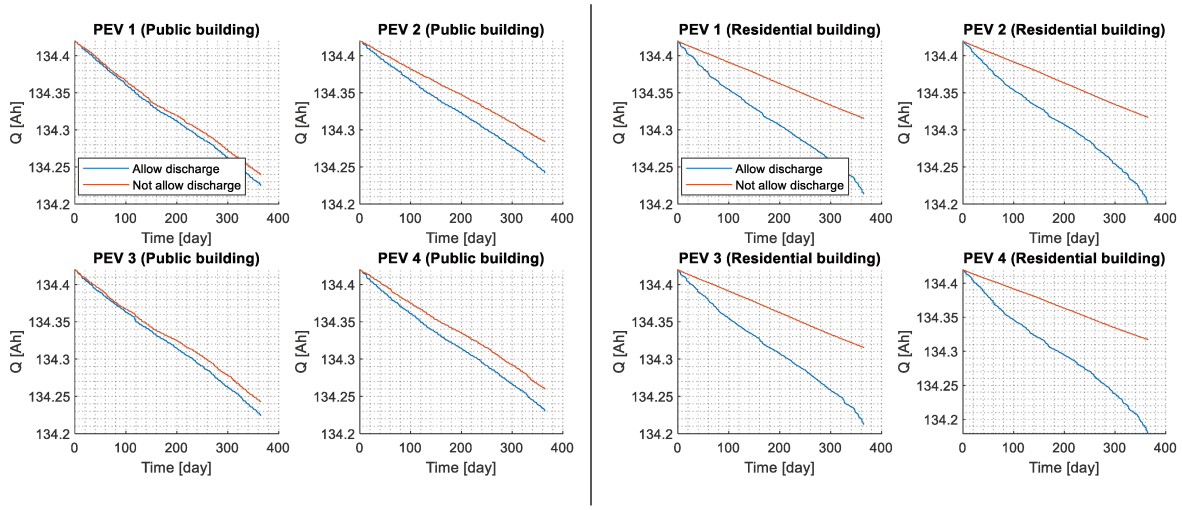

Fig. 6.26: Comparison of the level of degradation of batteries of plug-in electric vehicles when they are allowed and not allowed to be discharged.

From the perspective of the PEV's owners, the discharging of their PEV's batteries increases the degradation rate of PEV's batteries. As shown in Fig. 6.26, the maximum capacity of PEV's batteries (Q) at the end of the year is smaller when allowing discharging them than not allowing it. According to the website of Renault [239], the current price of batteries of Renault Zoe® costs on average 8100 € depending on the country. Taking this value to estimate the equivalent cost of allowing discharging the PEV's batteries from the perspective of PEV's owners, the additional loss of batteries' capacity of 26 mAh/year in public buildings and 115 mAh/year in residential buildings mean on average 7.91 €/year for each PEV's owner in public buildings and 34.57 €/year in residential ones. These costs are lower than the total savings made by the BMG when allowing the PEV's discharge. Considering the hypothesis that the BMG would refund the degradation provoked by the additional degradation cost of PEV's batteries, the BMG would make only 3.36 €/year as profit in public buildings and 143.72 €/year in residential ones. Therefore, the differences between both sides when allowing or not the discharging of PEV's batteries are very small. From the perspective of PEV's users, the discharging of their PEV's batteries may be seen as a disadvantage because their batteries would be degraded faster than usual, without contributing substantially to the performance of the BMG or the use of renewable energy.

Still concerning the results shown in Fig. 6.25, it is possible to note that having PEV parking installed in the BMG increases the electricity expenses on average 1708.50 €/year in the public building and 1516.50 €/year in the residential building. This is because, despite all, PEV is still a load that consumes energy. As a result, on average, the daily energy demand in Wh required by the PEV parking is given by the equation (6.18). Therefore, in the ideal scenario in which $\widehat{SoC}_{initial} = 40\%$, having a PEV parking of four Renault Zoe® represents an increase of 83.2 kWh/day in the building's power consumption. Since PEVs connect 260 days/year in public buildings and 261 days/year in residential ones (Fig. 6.18), the PEV parking means an increase in about 21.6 MWh/year in the annual building energy consumption. With the sizing of the BMG and the connection profile of PEVs, the public BMG has to purchase electricity to charge its PEVs, which increases the total electricity costs by 14% and reduces the coverage rate by 2% points regarding the case without PEV parking. Similarly, in residential buildings, it increases electricity expenses by 8%. However, depending on the PEV's discharging authorisation, the coverage rare increases 0.6% point when allowing discharging and decreases by about 1% point when not allowing it.

$$\hat{E}_{pevs}^{ch} = N_{PEV} \cdot \left(SoC_{pev}^{MAX} - \widehat{SoC}_{initial}\right) \cdot Q_{nom}^{pev} \cdot V_{nom}^{pev} \tag{6.18}$$

It is important to highlight that these conclusions were drawn from the simulation of the BMG of sizing specified in Table 2.1, in which only four PEVs are available. In order to verify whether the results would be the same if the PEV parking were more significant, scenarios with twenty and forty PEVs were also evaluated. It is noteworthy that the BMG simulator is the same as this presented in Chapter 2, which implies that only four batteries model of Simulink SimPowerSystem library were used. The emulation of twenty and forty PEVs was implemented by increasing the capacity of Simulink batteries model. In other words, in the simulation of twenty PEVs, the capacity ($Q_{pev_{ID}}^{nom}$) and maximum power rate ($P_{pev_{ID}}^{MAX}$) of each PEV were multiplied by five, whereas in the simulation of forty PEVs they were multiplied by ten. These simulations assume that five PEVs out of twenty (or ten PEVs out of forty) arrive and depart simultaneously.

The main results obtained from the simulations with different sizes of PEV parking are shown in Table 6.7, where it is possible to note that the higher the number of PEVs is, the lower the annual coverage rate. This is because with a larger PEV parking, the building energy demand increases, but due to the PEVs' connection profiles, they are mostly charged with the energy provided by the main grid. As shown in Table 6.7, with the enlargement of PEV parking, the charging of PEV with energy coming directly from PV panels is limited to 5.9 MWh/year in residential buildings and 13.5 MWh/year in public ones. Likewise, with more PEVs, the Li-ion battery pack is discharged more frequently to charge the PEV's batteries, i.e. $E_{pevs}^{ch,bat}$ is higher. Nonetheless they are limited to discharge up to 6.3 MWh/year in residential buildings and 2.6 MWh/year in public ones. For this reason, the total energy imported from the main grid tends to increase, and the coverage rate tends to decrease with the enlargement of the PEV parking.

Table 6.7: Results of the one-year simulation of the residential and public building microgrid with different sizing of the parking of plug-in electric vehicles.

	Residential building				**Public building**			
	Only batteries	**4 PEV**	**20 PEV**	**40 PEV**	**Only batteries**	**4 PEV**	**20 PEV**	**40 PEV**
PV power generated (E_{pv})*	131.0							
Power consumption without PEV (E_{cons})*	307.2				241.9			
Raw energy surplus ($E_{surplus}$)*	69.0				39.8			
Raw energy deficit ($E_{deficit}$)*	245.3				150.7			
Self-consumption rate (τ_{sc}) (%)	68.7	71.1	71.7	71.4	83.3	86.5	88.8	88.8
Coverage rate (τ_c) (%)	29.3	29.9	27.6	25.1	45.1	43.0	33.3	25.6
Grid energy import (E_{grid}^{import})*	217.1	234.2	314.2	416.4	132.7	150.3	234.9	342.3
Grid energy injection ($E_{grid}^{injection}$)*	40.9	37.8	36.9	37.4	21.9	17.7	14.6	14.7
Energy to charge batteries (E_{bat}^{ch})*	28.3	28.9	27.3	28.0	18.1	15.8	9.6	10.4
Energy to discharge batteries (E_{bat}^{dis})*	28.3	29.1	27.5	28.3	18.1	15.8	9.6	10.5
Energy to charge PEVs (E_{pev}^{ch})*	0	27.1	126.6	249.0	0	22.2	109.4	218.1
- from grid ($E_{pev}^{ch,grid}$)*	0	19.4	113.6	236.8	0	14.5	94.3	202.0
- from PV panels ($E_{pev}^{ch,pv}$)*	0	3.7	5.8	5.9	0	6.6	13.3	13.5
- from batteries ($E_{pev}^{ch,bat}$)*	0	4.0	7.2	6.3	0	1.1	1.8	2.6
Energy to discharge PEVs (E_{pev}^{dis})*	0	5.4	18.3	32.7	0	0.9	3.0	3.2

* Annual values in MWh

Following the same reasoning, the self-consumption rate rises with the increase of the number of PEVs, but it is limited to around 71% in residential buildings and 89% in public buildings. As expressed in equations (5.11) and (5.14), the self-consumption rate is higher if the total grid energy export is lower. Furthermore, due to the inequality constraint (3.104) and the grid code for small prosumers, the BMG can inject into the grid only the energy surplus, which is equal to 69 MWh/year in residential BMG and 39.8 MWh/year in public ones. Since the objective functions of EMPC were designed to reduce the injection through the use of battery pack and PEV batteries (equation (6.1)), the battery pack avoid injecting approximately E_{bat}^{ch} and the PEV parking reduces the injection in $E_{pev}^{ch,pv}$. This means up to 28 MWh/year in residential building and up to 23 MWh/year in residential buildings. Consequently, the annual grid energy injection is saturated to 37 MWh/year in residential buildings and about 14.7 MWh/year in public buildings.

These results reveal that the enlargement of PEV parking can increase the self-consumption rate but there is a saturation in this tendency. Consequently, there is an optimal number of PEVs that a BMG can have to increase the annual self-consumption rate without rising too much the electricity expenses or reducing drastically the coverage rate. To determine the value of the optimal sizing of a PEV parking, it is necessary to anticipate the saturation of charging the PEVs from PV panels and batteries. This depends on the connection and disconnection profiles of each PEV, the estimated $\widehat{SoC}_{initial}$ and the annual raw net power imbalance. The next subsection analyses these profiles and gives some directives on how to use this analysis to adapt the MG cost estimator (Chapter 5) to operate with PEVs.

6.6.3 *Directives to adapt the MG cost estimator to operate with the electric vehicles*

Regarding the PEV parking, the main objective of the hierarchical controller is to charge the PEV batteries with the energy coming from renewable energy provided either by the PV panels or by the discharge of battery packs. As concluded in the last subsection, the charging of PEV's batteries with

green energy – named $E_{pevs}^{ch,green}$ – reduces the annual energy injection and reduces the electricity bill. Therefore, it is of prime interest of the BMG to maximise the charging of PEVs with renewable energy ($E_{pevs}^{ch,green}$). The relationship between the energy used to charge PEV with renewable energy ($E_{pevs}^{ch,green}$) and the annual self-consumption rate (τ_{sc}) is given by (6.19), in which the charging of PEV parking with renewable energy generated locally ($E_{pevs}^{ch,green}$) increases τ_{sc}. This formulation is deducted similarly to equation (5.14) for the case of a BMG without a PEV parking explained in Chapter 5.

$$\tau_{sc} = 1 - \frac{E_{surplus} - E_{bat}^{ch} - E_{pevs}^{ch,green}}{E_{pv}} \tag{6.19}$$

Likewise, by discharging PEV's batteries, the BMG will reduce electricity bill because the energy provided by PEV's batteries (E_{pevs}^{dis}) will feed the building's local energy demand, avoiding purchasing energy from the main grid. Consequently, similarly to equation (5.3), the electricity cost can be estimated through equation (6.20), in which E_{pevs}^{dis} counterbalances the energy required to charge PEV that is not supplied by PV panels and batteries – named $E_{pevs}^{ch,NotGreen}$. In other words, $E_{pevs}^{ch,NotGreen}$ is the energy imported from the external grid that is used to charge PEVs.

$$\pi_{grid}^{annual} = \sum_{k=1}^{365} \pi_{elec,k} \cdot \left(E_{deficit,k} - \left|E_{pevs,k}^{dis}\right| + \left|E_{pevs,k}^{ch,NotGreen}\right| - \left|E_{bat,k}^{dis}\right|\right) \tag{6.20}$$

Hence, the MG cost estimator needs to calculate the energy used to charge PEVs that comes from renewable energy ($E_{pevs}^{ch,green}$), the energy used to charge PEVs that comes from the external grid ($E_{pevs}^{ch,NotGreen}$) and the energy used to discharge PEVs (E_{pevs}^{dis}) to estimate the impact of PEV parking on the annual self-consumption rate and the total MG operating cost. In the case of allowing the discharging of PEV's batteries, the refund to be addressed to PEV's owner must also be estimated by forecasting the degradation of PEV batteries provoked by the discharging while they are connected to the BMG. This estimation can be implemented similarly to the degradation cost of Li-ion battery packs that is given by equation (5.7).

To estimate $E_{pevs}^{ch,green}$, $E_{pevs}^{ch,NotGreen}$ and E_{pevs}^{dis}, the MG cost estimator must consider not only the raw net power imbalance but also the connection and disconnection table of PEVs. As explained in the previous subsection, depending on the raw net power imbalance and the connection profile of PEVs, $E_{pevs}^{ch,green}$ and E_{pevs}^{dis} can be saturated. This saturation can be visualised in Fig. 6.27 and Fig. 6.28, where the total energy used to charge PEVs in each daily connection must be matched by the daily surplus of energy. However, depending on the raw net power imbalance, the complete PEV load matching is impossible. By using the equation (6.18) and the estimated value of the average PEV's initial SoC ($\widehat{SoC}_{initial}$) – that can be deducted by calculating the average of the SoC of each PEV when it plugs in the BMG – in the ideal scenario (cases 3 and 6), the daily energy required to charge the PEV parking ($\hat{E}_{pevs}^{ch}$) is equal approximately to 83 kWh both in the public and residential buildings. Consequently, to calculate $E_{pevs}^{ch,green}$, it is necessary to estimate the likelihood of fitting $\hat{E}_{pevs}^{ch}$ with the raw energy surplus. This can be calculated by the k-means classification to identify the four most probable profiles of raw

net power imbalance and superpose it to the energy demand of PEVs $\hat{E}_{pevs}^{ch}$ with the availability of PEVs ($N_{pev} \times E_{pev_{ID}}^{MAX}$), where $N_{PEV,k}$ is the number of PEV connected at time k, and $E_{pev_{ID}}^{MAX} = 7kWh$ is the maximum energy that PEV's batteries can provide per hour. In this manner, it is possible to calculate $\hat{E}_{pevs}^{ch,green}$ and $\hat{E}_{pevs}^{ch,notGreen} = \hat{E}_{pevs}^{ch} - \hat{E}_{pevs}^{ch,green}$.

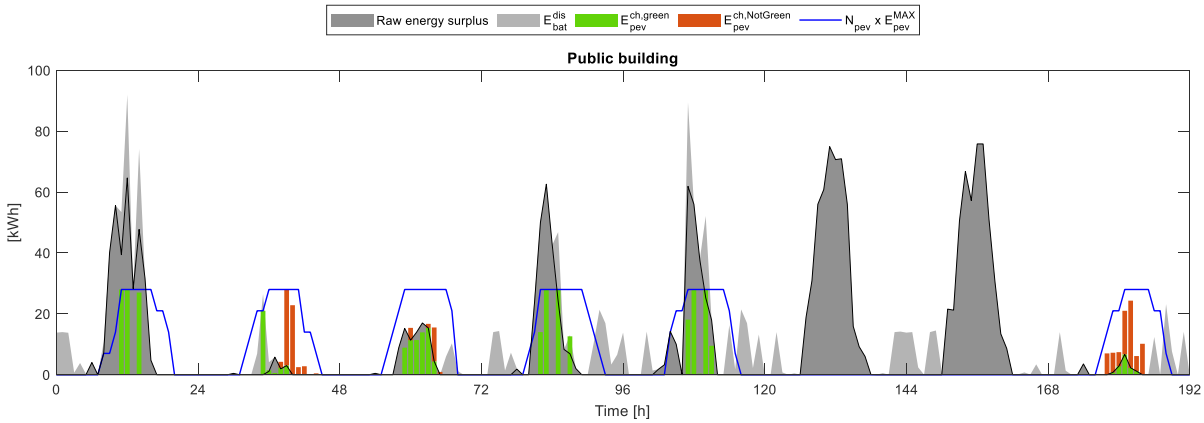

Fig. 6.27: Visualisation of the effects of the disposal of raw net power imbalance and the connection profile of plug-in vehicles on the charging of electric vehicles' batteries with renewable energy in public buildings considering the ideal case (case 6).

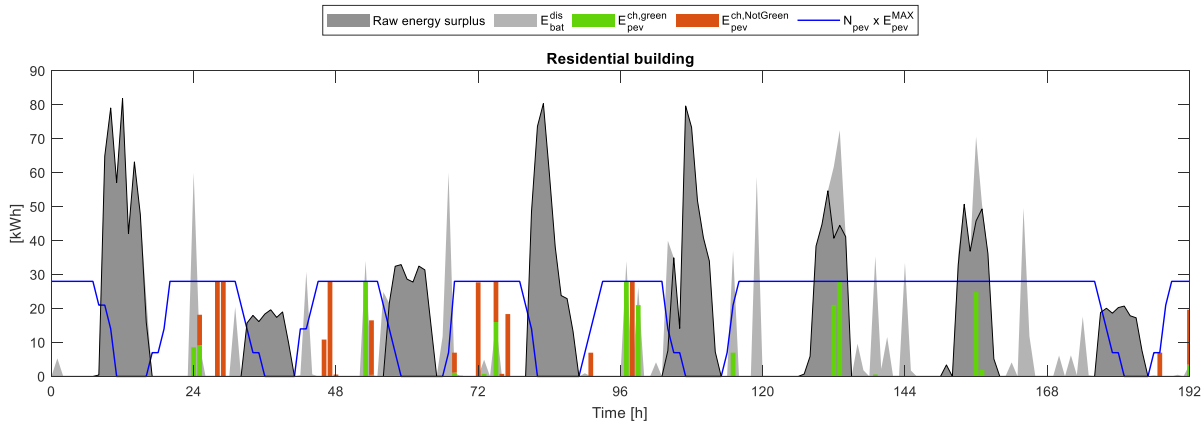

Fig. 6.28: Visualisation of the effects of the disposal of raw net power imbalance and the connection profile of plug-in vehicles on the charging of electric vehicles' batteries with renewable energy in residential buildings (case 3).

The optimal sizing of PEV parking can be calculated from the values of $\hat{E}_{pevs}^{ch,green}$ and $\hat{E}_{pevs}^{ch,notGreen}$, that depends on the estimated energy surplus and size of building ESS. The idea is to maximise $\hat{E}_{pevs}^{ch,green}$ by covering $\hat{E}_{pevs}^{ch,notGreen}$ with the energy provided by batteries. Therefore, one solution would be setting up the desired number of PEVs (i.e. $\hat{E}_{pevs}^{ch}$) and increasing the size of batteries accordingly to reduce $\hat{E}_{pevs}^{ch,notGreen}$. Another solution would be setting up the size of batteries and calculating the number of PEVs to cover as much as possible the energy surplus by $\hat{E}_{pevs}^{ch,green}$.

6.7 Conclusion

Aiming to evaluate the performance of the whole hierarchical controller, this chapiter assesses its capabilities in handle different building microgrid configurations, including distinct power imbalance

profiles and several types of Energy Storage Systems (ESS). Since the hierarchical controller empowered with the MicroGrid cost estimator presented in Chapter 5 does not yet include the effects of batteries available in the electric vehicle parking, the simulation results were divided twofold. The first part evaluated the performance of the MicroGrid cost estimator in tackling the problems related to the design of a hierarchical energy management system capable of managing a hybrid energy storage system to satisfy the required self-consumption rate imposed by the grid code at minimum cost. Meanwhile, the second partition deals with the potentials of using the electric vehicle's batteries on behalf of the building microgrid. Besides aiming to evaluate the effectiveness of the power-sharing module presented in Chapter 3, this second partition evaluates the capabilities of the proposed hierarchical controller in increasing the annual self-consumption rate while assuring that all electric vehicles are charged before their departure time.

In the first partition, through simulations using the dataset of both a public and a residential building, the HMPC empowered with the two data-driven modules was confronted with a traditional rule-based and a conventional HMPC. The simulations were carried out in MATLAB Simulink® to assess four important aspects of these three controllers: the impact of ESS installation, the impact of hydrogen storage capital costs, the impact of constraining the use of hydrogen storage at nominal power, and the impact of errors in the prediction data.

Considering all simulation scenarios, the proposed HMPC – named HMPC-kmeans – identifies the most suitable storage device to be run daily to guarantee the required self-consumption rate at minimum cost. Compared to the rule-based controller, the proposed controller reduced the building microgrid's total operating cost by up to 5% in residential buildings and up to 9% in non-residential buildings in the first year of operation. To highlight the importance of considering not only energy aspects but also economic ones in power flow optimisation, the proposed controller was compared to another HMPC that contains a cost function that maximises only the self-consumption rate. The comparison with the conventional HMPC aims at evaluating the capabilities of the proposed HMPC-kmeans in handling conflicting objectives and verifying whether it does reduce the BMG operating cost. The result simulation indicates that although the proposed strategy guaranteed a self-consumption rate from 5% to 17% lower than the conventional HMPC, the proposed strategy satisfied the required self-consumption rate with an annual operating cost between 1% and 7% lower.

The results also revealed that the current French grid reward for self-consumption is not enough to encourage fuel cells and electrolysers with their current capital cost. Hydrogen storage is still very costly to be profitable to be integrated into building microgrids. Since the proposed HMPC calculates its control actions that maximise the expected annual self-consumption rate and minimises the expected annual operation cost, it runs fuel cells and electrolysers only when it is strictly necessary. As a result, the hydrogen chain is almost unused in the scenario where the microgrid can satisfy the minimum requirements of self-consumption rate with only batteries. On the other hand, the rule-based controller and the conventional HMPC operate the hydrogen chain as much as possible to maximise the self-consumption rate, but they ignore the economic aspects, resulting in higher operating costs. Although this result was drawn in French grid policy scenario, it can be exploitable in other countries. Based on

the results obtained, three possible scenarios to make fuel cells profitable were suggested, which can be useful to other applications that target encouraging self-consumption in buildings.

Furthermore, it was verified that constraining the use of hydrogen chains around their nominal power restrain the capacity of the building microgrid to attain a higher annual self-consumption rate. Due to the stochasticity in the power imbalance, it is difficult to determine an optimal minimum power threshold to operate fuel cells and electrolysers, without degrading the system's profitability. Consequently, making the use of hydrogen chain free not only allows the BMG to increase the self-consumption rate by up to 6.5% and reduce total costs by up to 7% but also reduces the complexity of the controller's design.

In the second part of this chapter, the potentials of using electric vehicle batteries while they stay plugged in the building microgrid were assessed. Since the HMPC empowered by the MicroGrid cost estimator in this set of simulations was disabled, the potentials of exploiting their batteries on behalf of the building microgrid were evaluated through the use of a simplified hierarchical controller that minimises the grid energy exchange and ignores the economic aspects. Considering the dataset of a common residential and public building, the simulations conducted with electric vehicles aimed to assess the impact of having or not an electric vehicle parking and their contribution in increasing the annual self-consumption rate. The simulation results revealed that the cooperation among the three control layers of the hierarchical control structure reduces the complexity of the design of the model predictive controller, while guaranteeing electric vehicles' state-of-charge over 75% even when subjected to data prediction inaccuracies.

Besides reducing the complexity of the controller's design, the combination of control units operating with long and short horizons, allowed the controller to use the batteries of plug-in electric vehicles to reduce the grid energy dependency. This strategy decreases the annual energy injection by up to 7% in residential buildings and up to 32% in public ones, compared to the scenario where only batteries are installed. It was constated through six different simulation scenarios that the proposed HMPC preferably charge electric vehicles during periods of surplus and discharge them during energy deficit.

Nonetheless, due to the raw net power imbalance, sizing of battery packs, and the daily connection and disconnection profiles of electric vehicles, the charging of electric vehicles from renewable energy is saturated to 10% of annual photovoltaic energy generation (or 13 MWh/year) in residential buildings and about 12% (or 16 MWh/year) in public ones. This means about 10% to 14% of total parking energy demand of 20 vehicles are supplied with renewable energy, whereas only 4% to 8% with 40 vehicles. Consequently, with the enlargement of the electric vehicle parking, the annual self-consumption rate is saturated to 72% in residential buildings and 89% in public ones. Electric vehicle parking also results in a considerable increase in the total energy purchased from the grid. Depending on the number of electric vehicles, the entire parking means an increase of the total grid energy purchase in about 17 MWh/year for parking of 4 vehicles and up to 209 MWh/year for parking of 40 vehicles, representing an increase in about 5% and 61% of the building annual power consumption, respectively.

In this chapter, a thoughtful analysis was conducted to verify the effectiveness, robustness, and flexibility of the proposed hierarchical building energy management system. However, further

development needs to be implemented before deploying it in real applications. For this reason, the most important conclusions drawn from this Ph.D. thesis and the perspectives for future work are provided in the next and final chapter.

Chapter 7 Conclusions and perspectives

The research conducted in this Ph.D. thesis aims at providing an in-depth analysis of how renewable energy sources can be integrated into buildings. The installation of both roof-top photovoltaic panels and electric energy storage systems in building environments can assist the energy transition toward zero-carbon energy, especially because buildings represent nowadays more than 40% of electric energy consumed worldwide [1]. This innovative grid topology, also known as Building MicroGrid (BMG), allows taking advantage of free solar energy that is usually unexploited while enabling final energy consumers to become active players in the electrical grid. However, significant efforts are needed to restructure the entire centralised fossil-based electrical grid toward a distributed and zero-carbon power system.

One of the greatest challenges is to design a reliable energy management system capable of managing all-electric components inside the microgrid so that it operates as efficiently as possible without harming the main grid stability. Within this context, a comprehensive literature review on the paramount requirements for building microgrids and on the most relevant control strategies to tackle these paradigms were discussed in Chapter 1. This thoughtful analysis on the topic of hierarchical control structure for building microgrids allows identifying two main open-ended research fields restraining the breakthroughs of renewable energy in buildings. The first one is the difficulty in design a robust energy management system capable of handling efficiently unpredictability in renewable energy generation and dwelling occupancy. The second obstacle for BMG development is the lack of well-established rules for grid interoperability between small prosumers and the external grid, which complicates the design of an energy management system that can be functional in real applications.

Among the possible solutions to interconnect BMGs to the electrical grid, the concepts of community aggregator and self-consumption rate have emerged as a feasible approach that avoids radical changes into the current grid structure. Compared to the novel peer-to-peer grid configuration, the grid division into energy clusters managed by a local community aggregator is a more conservative approach. Its operation is similar to the traditional electricity market but with a smaller capacity. Hence, some features already well-implemented into the conventional electric grid can be adapted for this new configuration.

Besides this dilemma in selecting a suitable grid topology for forthcoming BMGs, it was also identified some restrictions on the level of its energy management system. Most of the control strategies reported in the literature were developed to manage the power flow of an electric system with a specific microgrid sizing. However, several types of buildings exist, such as residential, industrial, commercial, and public buildings. Therefore, their power demand profile can differ considerably from each other as well as the sizing of their microgrid electric devices. Consequently, the concept of BMGs would be easily overspread if their energy management system was more flexible and simpler to be designed to

the point that electric components could be just plugged and played into the microgrid without needing a laborious pre-setting step.

By comparing the most relevant control strategies to deal with power flow optimisation – including deterministic, metaheuristic, stochastic, predictive control, and artificial intelligence algorithms – Model Predictive Control (MPC) structure was identified as the most suitable approach to handle the major barriers of BMGs mentioned above. The capacity to consider prediction data and periodic optimisations over a sliding window is the main strength of an MPC structure that leads it to be highly appreciated not only for academic but also for industrial applications. The foremost advantage of using MPC structure in microgrids is the inclusion of forecast data of power generation and power consumption into its decision-making process. Compared to other algorithms, MPC is an intuitive control structure that is highly robust with low effort, since it usually relies on simplified linear models.

On this ground, Chapter 3 provided a complete framework to design a hierarchical MPC adept to be implemented in real BMGs. All this labour in detailing the whole hierarchical controller that is compliant with the French grid code concerning the self-consumption rate is one of the contributions of this Ph.D. thesis. Although the controller was designed considering the French grid policy, it can be adapted to other applications by modifying a set of parameters or by including other constraints following similar reasoning detailed in Chapter 3.

Targeting to tackle the main barriers identified in Chapter 1, the proposed controller that is composed mainly of two MPC layers in cascade was enhanced by two data-driven modules, named Real-Time Model Identification (RTMI) and MicroGrid cost estimator. Presented in Chapter 4 and Chapter 5 respectively, these two adjunct control units aim to improve the flexibility of the MPC structure to foster the plug-and-play aspect of BMGs. Thanks to these two data-oriented modules, the building energy management system can adapt itself according to continuous data measurements to accomplish its objectives as effectively as possible without demanding rigorous design steps or many human interventions.

The RTMI module faces the uncertainties arisen from the imprecision of the modelling of energy storage devices. Since one of the weaknesses of MPC is the high dependency on trustful internal models that usually need to be pre-tuned throughout exhaustive tests, the RTMI module was designed to determine automatically the parameters that enable MPC to predict the state-of-charge of Li-ion battery packs and the level-of-hydrogen of the tank more accurately. Through simulations using the BMG simulator developed in MATLAB Simulink® (Chapter 2), RTMI has proved more accurate than conventional modelling approaches found in the literature. It can enhance the batteries' state-of-charge estimation up to three times and improve up to ten times the accuracy of the estimation of the level-of-hydrogen stored in the tank.

The improvement in MPC's internal model provided by RTMI algorithm also enables the controller to take more reliable decisions and avoid overexploiting the energy storage systems. Compared to the conventional modelling method, the RTMI degrades 13% less the batteries in their half-life. This is because the RTMI module changes the limits of maximum and minimum state-of-charge of batteries to values corresponding to the same depth of discharge regardless of their level of degradation or intensity of parameter imprecisions. The simulation results showed that a better estimation of the state-of-charge

and the capacity of the batteries also allowed the controller to have more information concerning the variations in temperature of the batteries' cells, which can be straightforward to retard the degradation rate of batteries and extend their lifespan. Furthermore, a correlation was found between the depth of discharge of the batteries and the building coverage and self-consumption rates: the deeper the depth of discharge, the higher the coverage and self-consumption rate. All this information provided by the new algorithm allows MPC to take more reliable decisions, especially to find a wise compromise between the energy autonomy of buildings and the level of degradation of batteries.

Concerning the hydrogen energy storage system, RTMI algorithm handles the non-linear behaviour of hydrogen flow in electrolysers and fuel cells in real-time. However, it does not yet compensate for temperature variation as the RTMI for batteries does. Hence, as the next steps, it is necessary to include the temperature into the iterative algorithm through the division in temperature classes as implemented in RTMI for batteries. Furthermore, the robustness of RTMI algorithm against both ambient temperature variation and measurement noise needs to be evaluated before implementing it in real applications.

The second MPC module extension, named MicroGrid cost estimator, was designed to automatically determine adequate weights for the upper MPC's cost function. Relying only on power imbalance data prediction and local measurements, this adjunct module also sets up key constraints parameters that assure that the building microgrid satisfies the required annual self-consumption rate at minimum operating cost. Since economic and energy aspects of BMGs are competing objectives that are hard to be balanced, the designed MicroGrid cost estimator determines autonomously adequate parameters to the hierarchical MPC to relieve the trade-off between these two conflicting goals.

Unfortunately, the self-consumed energy maximisation does not necessarily imply the most cost-effective configuration for BMGs. Due to the solar power generation and building inherent power consumption profiles, the increase of self-consumption rate requires more intensive use of energy storage devices. Nevertheless, according to the simulation conducted in Chapter 6, with a simplified rule-based controller, the use of energy storage devices might be unaffordable, since batteries represent about 12% of total annual building microgrid operating cost, while a hybrid energy storage system means about 25%. Within this context, in France, a mechanism of economic reward and penalty has been established to encourage buildings to install energy storage devices to attain high marks of the self-consumption index. Nonetheless, further analysis is needed to verify whether this energy policy is in line with the current and future costs of BMG's piece of equipment, such as the cost of batteries, fuel cells, electrolysers, and plug-in electric vehicle parking.

Aiming to provide a technical-economic analysis and to propose a feasible strategy to consider both energy and economic aspects in the optimisation of the BMG power flow without needing to tune any parameter, the performance of the MicroGrid cost estimator was assessed by comparing it to a well-established rule-based controller and a conventional hierarchical MPC. Through simulations, the hierarchical controller empowered with the MicroGrid controller can determine which energy storage device must be run daily based only on the estimation of the annual self-consumption rate and the annual microgrid operation costs. Besides reducing the complexity of controller design, the real-time analysis implemented by MicroGrid cost estimator decreases the total building expenditure because it avoids

grid penalisation regarding the annual self-consumption rate and reduces the degradation and maintenance of energy storage devices. Although the proposed hierarchical controller guaranteed a self-consumption rate from 5% to 17% lower than the conventional hierarchical MPC, the proposed strategy satisfied the required self-consumption rate with an annual operating cost between 1% and 7% lower.

The simulation results in Chapter 6 also highlight that the current policy for encouraging self-consumption in France is not enough to make the installation of hydrogen energy storage system worthwhile. The high capital cost of fuel cells, low round-trip efficiency of hydrogen conversion, and expensive operation and maintenance costs of the entire hydrogen chain are the main factors that lead to the installation of hydrogen energy storage systems in buildings non-profitable. Three possible scenarios to make the use of fuel cells advantageous were identified based on three mechanisms: increase of electricity price, reduction of fuel cell capital cost, and increase of the additional income due to self-consumption rate. These three future scenarios can be useful for projects willing to promote self-consumption and the installation of hydrogen storage in buildings.

Last but not least, the potentials of shifting in time the charging of batteries of plug-in electric vehicles to reduce the energy grid dependency were evaluated in the last section of Chapter 6. Plug-in electric vehicles are elastic loads that must be fulfilled within a pre-defined schedule. Consequently, to enhance the internal load matching, the BMG is of primary interest to charge electric vehicles at periods of energy surplus and discharge them during periods of energy deficit. By combining the strengths of MPC and the Power Sharing Module described in Chapter 3, the whole hierarchical controller guaranteed that plug-in electric vehicles are charged over a state-of-charge of 75% even under inaccuracy in the prediction data.

One of the advantages of the design of an additional control unit to handle the particularities of the electric vehicle parking is the reduction of hierarchical MPC's design complexity. Instead of estimating the state-of-charge of each plug-in electric vehicle, the two MPC in cascade estimates only the average energy stored in the entire parking. Therefore, it is up to the Power Sharing Module to determine the share of energy that must be addressed to each plug-in electric vehicle to charge them before their scheduled departure. Besides simplifying the controller's design, the cooperation of the Power Sharing Module with the hierarchical MPC allowed the controller to use the batteries of plug-in electric vehicles to reduce the grid energy dependency, by decreasing the annual energy injection by up to 7% in residential buildings and up to 32% in public ones, compared to the scenario where only batteries are installed.

It was constated through simulations that the proposed hierarchical controller charges and discharges electric vehicle batteries to reduce grid energy exchange. Nonetheless, due to the raw net power imbalance, size of battery packs, and the daily connection and disconnection profiles of electric vehicles, the charging of electric vehicles from renewable energy is saturated to 10% of annual photovoltaic energy generation (or 13 MWh/year) in residential buildings and about 12% (or 16 MWh/year) in public ones. This means about 10% to 14% of the total parking power demand of 20 vehicles are supplied with renewable energy, whereas only 4% to 8% with 40 vehicles. Consequently, with the enlargement of the electric vehicle parking, the annual self-consumption rate is saturated to 72% in residential buildings and 89% in public ones. Electric vehicle parking also results in a

considerable increase in the total energy purchased from the grid. Depending on the number of electric vehicles, the entire parking means an increase of the total grid energy purchase in about 17 MWh/year for parking of 4 vehicles and up to 209 MWh/year for parking of 40 vehicles, representing an increase in about 5% and 61% of the building annual power consumption, respectively.

In summary, the main contributions of the hierarchical building energy management system developed during this Ph.D. thesis can be outlined by the six points stated below:

- **Maximisation of the self-consumption rate at minimum cost following the French grid code**. This is assured by the hierarchical MPC (Chapter 3) and MicroGrid cost estimator (Chapter 5).
- **Technical-economic analysis for hydrogen energy storage system market accessibility.** The affordability of hydrogen storage in BMGs was assessed in Chapter 6.
- **Daily assessment of degradation rate of batteries, electrolysers, and fuel cells.** The degradation rate models of energy storage systems are detailed in Chapter 2, whereas their end-of-life estimation is implemented by the MicroGrid cost estimator (Chapter 5).
- **Real-time identification of the energy storage systems model.** It is implemented by the Real-Time Model Identification (RTMI) module explained in Chapter 4.
- **Estimation of annual self-consumption and building operation cost based on power imbalance data processing.** It is implemented by the MicroGrid cost estimator presented in Chapter 5.
- **Assessment of the potentials of exploiting batteries of plug-in electric vehicles on behalf of building microgrids.** The coordination of charging-discharging of electric vehicles is assured by the hierarchical MPC and the power-sharing module presented in Chapter 3. The effectiveness of this control strategy is evaluated in Chapter 6.

Despite these worthy contributions, some improvements in the proposed hierarchical controller need to be implemented before deploying it in real applications. First, the performance of the proposed hierarchical MPC with more severe prediction data errors, such as changes in vacation days needs to be evaluated. The simulations in Chapter 6 were limited to prediction data noises centred in zero. This means that the average of the annual raw net power imbalance in the ideal case and the scenario with data prediction errors are likely the same. Since the MicroGrid cost estimator relies on the average behaviour of hierarchical MPC and considering that the k-means classification is based on average values, the proposed hierarchical controller remains highly robust against errors with a mean around zero. To better evaluate the performance of the whole energy management system, it is needed to evaluate it when subjected to dataset error with bias. In other words, it is necessary to evaluate cases with datasets with non-zero noise disturbances. This will verify the robustness of the controller to handle events that approach real applications.

Still concerning future works, the impact and contribution of plug-in electric vehicles on the estimated annual self-consumption rate and annual BMG expenses need to be integrated into the algorithm of the MicroGrid cost estimator. For instance, the use of the schedule table with the expected arrival and departure time together with the estimation of the initial state-of-charge of electric vehicles' batteries are fundamental to forecast the total annual charging and discharging energy that electric vehicles parking can provide to the microgrid. In this thesis, some directives to estimate their impact on

the total microgrid expenses and annual self-consumption rate were provided but it is needed to further develop it to make it feasible in real applications.

Additionally, the robustness of the Power Sharing Module (Chapter 3 and Chapter 6) against unexpected disconnection and connection of electric vehicles needs to be assessed. Although in this thesis, the simulations with electric vehicles considered uncertainties in the connection and disconnection schedule times, it was assumed that the electric vehicles' schedule is updated hourly. Consequently, over time, the hierarchical energy management system becomes gradually more confident with electric vehicles' departure and arrival times. However, this mechanism does not necessarily reflect the real behaviour of plug-in electric vehicles since they can disconnect and connect to the BMG whenever they want. Consequently, it is essential to certify that the proposed Power Sharing Module can handle unexpected electric vehicle connections and disconnections to guarantee the whole system reliability.

Finally, suggestions for further research also arise from the limitations of the scale of the building microgrid. Expanding the technical-economic analysis to the context of collective self-consumption would be a valuable development. The installation of energy storage devices in buildings could be more affordable in the scenario where multiple building microgrids share the same electric resources. Besides reducing the total investment cost per building, the cooperation among neighbouring buildings might attain a higher index of the self-consumption rate, since the degree of freedom of the entire system rises.

The main concern of collective self-consumption is to guarantee the whole system's performance while maximising the welfare of all BMGs belonging to the same community. In this thesis, the proposed hierarchical controller deals with only the interest of a unique building and partially ignores the major interests of the external grid. Self-consumption is also a primary objective of the community microgrid, which is indirectly managed through the day-ahead electricity price broadcast and the self-consumption additional income incentive. Therefore, when dealing with collective self-consumption, the problem lies in defining these key demand-side signals, i.e. the grid community internal price and financial grid policy. The difficulty resides in maintaining the interest of selfish individual buildings while achieving the whole community's objective. In the literature, game theory has been a promising strategy to deal with multiple prosumers interaction to achieve the collective equilibrium despite heterogenous, rational and independent individuals [240]–[242]. Therefore, it would be interesting to orient future research toward the design of the community aggregator intelligence.

Additionally, it is needed to extrapolate the analysis conducted in simulation to real systems. Further investigation is required to deal with possible concerns related to communication latency, limitations in the computation resources, noise measurements, and resilience against faults. It is therefore vital that future research considers all the economic and technical peculiarities of real applications to make possible the integration of renewable energy sources in the building environment in the foreseeable future.

List of publications

	Publication	Chapter
I.	D. Y. Yamashita, I. Vechiu, and J.-P. Gaubert, "A review of hierarchical control for building microgrids," *Renewable and Sustainable Energy Reviews*, vol. 118, p. 109523, Feb. 2020, doi: 10.1016/j.rser.2019.109523.	Chapter 1
II.	D. Y. Yamashita, I. Vechiu, and J.-P. Gaubert, "Hierarchical Control Structure for Optimising Building Microgrid Self-consumption," in 2019 International Conference on Smart Energy Systems and Technologies (SEST), Porto, Portugal, Sep. 2019, pp. 1–6, doi: 10.1109/SEST.2019.8849054.	Chapter 3
III.	D. Yassuda Yamashita, I. Vechiu, and J.-P. Gaubert, "Real-time Parameters Identification of Lithium-ion Batteries Model to Improve the Hierarchical Model Predictive Control of Building MicroGrids," in 22nd European Conference on Power Electronics and Applications (EPE '20 ECCE Europe), Lyon, Sep. 2020.	Chapter 3 Chapter 4
IV.	D. Yassuda Yamashita, I. Vechiu, and J.-P. Gaubert, "Two-level hierarchical model predictive control with an optimised cost function for energy management in building microgrids," *Applied Energy*, vol. 285, p. 116420, Mar. 2021, doi: 10.1016/j.apenergy.2020.116420.	Chapter 4 Chapter 5 Chapter 6
V.	D. Y. Yamashita, I. Vechiu, and J.-P. Gaubert, "Identification en temps réel des paramètres des batteries pour améliorer le contrôle par modèle prédictif des micro-réseaux dédiés aux bâtiments," in Symposium de Génie Electrique (SGE 2020), Jul. 2021, p. 8. (Accepted paper and available online soon)	Chapter 4
VI.	D. Y. Yamashita, I. Vechiu, and J.-P. Gaubert, "Hierarchical Coordination of a Vehicle-to-Grid System to Improve Self-consumption in Building Microgrids," in 2021 International Conference on Smart Energy Systems and Technologies (SEST), Vaasa, Finland, Sep. 2021. (Accepted abstract)	Chapter 6

Appendix

I. Calculation of hydrogen utilisation rate in PEMFC

The hydrogen utilization U_{H_2} is the ratio between hydrogen consumed by the PEMFC (equation (2.22) and (2.23)) and the hydrogen flowing across the PEMFC ($\dot{N}_{H2}$, defined by equation (A.I.1)). Notably, x_{H_2} is the nominal composition of hydrogen which is worth 99.95% as specified in Table 2.6. Therefore, U_{H_2} is calculated using (A.I.2).

$$\dot{N}_{H2} = \dot{N}_{fuel} \cdot x_{H_2} \tag{A.I.1}$$

$$U_{H_2} = \frac{\dot{n}_{H_2cons}^{stack}\left|_{\frac{mol}{s}}\right.}{\dot{n}_{H_2cons}^{stack}\left|_{\frac{mol}{s}}\right.} = \frac{\dot{N}_{H_2cons}^{stack}\left|_{\frac{l}{min}}\right.}{\dot{N}_{H2}\left|_{\frac{l}{min}}\right.} \ [\%] \tag{A.I.2}$$

To calculate the ratio U_{H_2}, it is necessary to adapt the units firstly because $\dot{n}_{H_2cons}^{stack}$ in (2.23) is in mol/s, while $\dot{N}_{fuel}$ and $\dot{N}_{H2}$ are in l/min. To pass from mol/s to l/min, it is used the ideal gas law defined by equation (A.I.3), where $n_{H_2cons}^{cell}$ is the number of moles of hydrogen consumed by one PEMFC cell and V_{H_2} is the hydrogen gas volume at the pressure P_f and temperature T_{fc}, both in SI system.

$$P_f \cdot V_{H_2} = n_{H_2cons}^{cell} \cdot R \cdot T_{fc} \tag{A.I.3}$$

By deriving in time (A.I.3), it is obtained (A.I.4).

$$\dot{n}_{H_2cons}^{cell} = \frac{d}{dt} n_{H_2cons}^{cell} = \frac{d}{dt}\left(\frac{P_f \cdot V_{H_2}}{R \cdot T_{fc}}\right) [mol/s] \tag{A.I.4}$$

The designed PEMFC and hydrogen tank models assume that their temperature and pressure are maintained constant thanks to its ancillary system. Therefore, the equation (A.I.4) is simplified to (A.I.5).

$$\dot{n}_{H_2cons}^{cell} = \frac{d}{dt} n_{H_2cons}^{cell} = \frac{P_f}{R \cdot T_{fc}} \frac{dV_{H_2}}{dt} \ [mol/s] \tag{A.I.5}$$

The term $\frac{dV_{H_2}}{dt}$ is the hydrogen consumed by PEMFC in m^3/s. Therefore, to transform $\dot{n}_{H_2cons}^{cell}$ in mol/s to m^3/s, it is necessary to use the (A.I.6) deducted from (A.I.5).

$$\frac{\dot{n}_{H_2cons}^{cell}}{\dot{N}_{H_2cons}^{cell}} = \frac{P_f}{R \cdot T_{fc}} \left[\frac{mol}{m^3}\right] \tag{A.I.6}$$

Using the principles of dimensional analysis, it is obtained (A.I.7) and (A.I.8).

$$\dot{N}_{H_2cons}^{cell} \left[\frac{l}{min}\right] = \dot{n}_{H_2cons}^{cell} \left[\frac{mol}{s}\right] \times \left[\frac{60s}{1\ min}\right] \times \left[\frac{R \cdot T_{fc}}{P_f} \frac{m^3}{mol}\right] \times \left[\frac{1000\ l}{m^3}\right] \tag{A.I.7}$$

$$\dot{N}_{H_2cons}^{stack}\left|_{\frac{l}{min}}\right. = \dot{n}_{H_2cons}^{stack}\left|_{\frac{mol}{s}}\right. \frac{60000 \cdot R \cdot T_{fc}}{P_f} \tag{A.I.8}$$

From the Faraday's law of electrolysis (equations (2.22) and (2.23)), the hydrogen consumption of $\dot{N}_{H_2cons}^{stack}$ implies a current of $i_{fc}^{stack} = i_{fc}^{cell}$ defined by (A.I.9).

$$i_{fc}^{cell} = \frac{2 \cdot F}{\dot{n}_{H_2cons}^{cell}} = \frac{2 \cdot F \cdot \dot{N}_{H_2cons}^{cell} \cdot P_f}{60000 \cdot R \cdot T_{fc}} \quad \text{(A.I.9)}$$

Therefore, by combining (A.I.6) with (A.I.8) and (A.I.9), the hydrogen utilization is defined as in (A.I.10). Consequently, to obtain a hydrogen utilization of $U_{H_2} = 100\%$, it is needed to set the fuel flow as specified in (A.I.11).

$$U_{fc} = \frac{\dot{N}_{H_2cons}^{stack}}{\dot{N}_{H2}} = \frac{\dot{N}_{H_2cons}^{cell}}{\frac{\dot{N}_{H2}}{N_{cell}}} = \frac{\frac{60000 \cdot R \cdot T_{fc} \cdot i_{fc}^{cell}}{2 \cdot F \cdot P_f}}{\frac{\dot{N}_{fuel} \cdot x_{H_2}}{N_{cell}}} \quad \text{(A.I.10)}$$

$$\dot{N}_{fuel} = \frac{60000 \cdot R \cdot T_{fc} \cdot N_{cell}}{2 \cdot F \cdot x_{H_2} \cdot P_f} \; [l/min] \quad \text{(A.I.11)}$$

II. Analytical equations for calculating the linear parameters of the hydrogen chain linear model

The parameters α_{fc}^{zone1}, α_{fc}^{zone2}, α_{fc}^{zone3}, β_{fc}^{zone2}, β_{fc}^{zone3}, α_{els}^{zone1}, α_{els}^{zone2}, α_{els}^{zone3}, β_{els}^{zone2}, and β_{els}^{zone3} of the developed linear model of hydrogen energy storage system can be deducted from the analytical equation of the theoretical non-linear equation of power *vs* current curves of PEM electrolysers and PEM fuel cells. The following two subsections describe how to determine these α_s and β_s parameters for PEME and PEMFC, respectively.

a) Electrolyser parameters

Concerning the PEM electrolysers, their power generated is defined by (A.II.1), where v_{els} is the voltage in Volts of the PEME stack and I_{els} is the current flowing across the PEME cells in Ampere.

$$P_{els} = v_{els} \cdot i_{els} \quad \text{(A.II.1)}$$

According to [206], the voltage v_{els} is expressed by (A.II.2).

$$v_{els} = N_{cell}^{els} \cdot (v_{oc} + v_{act} + v_{ohm} + v_{con}) \quad \text{(A.II.2)}$$

Where,

- N_{cell}^{els} is the number of cells of the electrolysers;
- v_{oc} is the open circuit voltage;
- v_{act} is the activation overpotential:
- v_{ohm} is the ohmic overpotential; and
- v_{con} is the concentration overpotential.

The electrolyser voltage is dependent on many intrinsic parameters, including the concentration of the hydrogen and oxygen in the cathode and anode side, as well as the temperature, the PEM membrane physical characteristics and electrolyse plates. All these parameters increase the complexity of modelling v_{els}. In front of this problem, the authors in [207] validated a simplified mathematical model of PEM electrolyser with experimental data. Their proposed model is approximated by the equation (A.II.3), in which v_{els} is defined by three terms: constant, logarithmic and ramp components. In this

formulation, U_{rev}, P_1 and P_2 are determined by fitting this equation to the polarization curve of the PEME experimental data for a given temperature T, whereas A is the membrane active area, F is the Faraday constant and R is the ideal gas constant.

$$v_{els} = N_{cell}^{els} \cdot \left(\underbrace{U_{rev}}_{Constant} + \underbrace{\frac{RT}{F} ln\left(\frac{i_{els}}{A \cdot P_1}\right)}_{Logarithmic} + \underbrace{\frac{P_2 i_{els}}{A}}_{Ramp} \right) \tag{A.II.3}$$

Therefore, by combining (A.II.1) to (A.II.3) the power consumed by the PEME can be calculated using (A.II.4).

$$P_{elz} = v_{elz} \cdot i_{els} = N_{cells} \left(U_{rev} + \frac{RT}{F} \cdot \ln\left(\frac{i_{els}}{A \cdot P_1}\right) + P_2 \cdot \frac{i_{els}}{A} \right) \cdot i_{elz} \tag{A.II.4}$$

By linearizing (A.II.4) at the operating point $\left(v_{els}^0, i_{els}^0\right)$, it is obtained.

$$\begin{aligned} P_{elz} \cong & \left(U_{rev} + \frac{RT}{F} \cdot \ln\left(\frac{i_{els}^0}{A \cdot P_1}\right) + P_2 \cdot \frac{i_{els}^0}{A} \right) \cdot N_{cells} \cdot i_{els}^0 \\ & + N_{cells} \left[U_{rev} + \frac{RT}{F} \left(\ln\left(\frac{i_{els}^0}{A \cdot P_1}\right) + \frac{1}{A \cdot P_1} \right) + \frac{2 \cdot P_2}{A} i_{els}^0 \right] \cdot (i_{elz} - i_{els}^0) \end{aligned} \tag{A.II. 5}$$

Therefore, α_{els}^{zone1}, α_{els}^{zone2}, α_{els}^{zone3}, β_{els}^{zone2}, and β_{els}^{zone3} can be calculated using the generic equations (A.II.6) – (A.II.8) for a linearization point i_{els}^0. Notably, this linearization point depends on the zonal power.

$$P_{els} \cong \alpha_{els} \cdot i_{els} + \beta_{els} \tag{A.II.6}$$

$$\alpha_{els} = N_{cells} \left[U_{rev} + \frac{RT}{F} \left(ln\left(\frac{i_{els}^0}{A \cdot P_1}\right) + \frac{1}{A \cdot P_1} \right) + \frac{2 \cdot P_2}{A} i_{els}^0 \right] \tag{A.II.7}$$

$$\beta_{els} = -N_{cells} \cdot i_{els}^0 \left[\frac{RT}{F} \left(\frac{1}{A \cdot P_1} \right) + \frac{P_2}{A} i_{els}^0 \right] \tag{A.II.8}$$

b) Fuel cells parameters

The power consumed by the PEMFC is defined by (A.II.9), where v_{fc} is the voltage of the PEMFC in Volts and i_{fc} is the current flowing across its cells in Ampere.

$$P_{fc} = v_{fc} \cdot i_{fc} \tag{A.II.9}$$

Based on [205], v_{fc} is defined by (A.II.10),where v_{oc} is the open circuit voltage, v_{act} and v_{ohm} are the activation and ohmic overpotentials, respectively.

$$v_{fc} = N_{cells}^{fc} \cdot (v_{oc} + v_{act} - v_{ohm}) \tag{A.II.10}$$

Where,

$$v_{oc} = k_c \cdot E_n \tag{A.II.11}$$

$$v_{ohm} = R_{ohm} \cdot i_{fc} \tag{A.II.12}$$

$$v_{act} = A \cdot ln\left(\frac{A \cdot i_0}{i_{fc}}\right) \tag{A.II.13}$$

In equations (A.II.11) – (A.II.13), k_c is a voltage constant at nominal condition of operation, R_{ohm} is the cell PEMFC internal resistance, N_{cells}^{fc} is the number of cells in the PEMFC stack, A is the membrane active area, and i_0 is the exchange current. To obtain the PEMFC linear equation, the PEMFC power defined by (A.II.14) is linearized using first-order Taylor approximation at the point of operation i_{fc}^0 as specified in (A.II.15).

$$P_{fc} = N_{cells}^{fc} \cdot \left(k_c \cdot E_n + R_{ohm} \cdot i_{fc} + A \cdot ln\left(\frac{A \cdot i_0}{i_{fc}}\right)\right) \cdot i_{fc} \tag{A.II.14}$$

$$P_{fc}(i_{fc}) \cong P_{fc}(i_{fc}^0) + \frac{d}{dt} P_{fc}(i_{fc})\Big|_{i_{fc}=i_{fc}^0} (i_{fc} - i_{fc}^0) \tag{A.II.15}$$

Therefore, α_{fc}^{zone1}, α_{fc}^{zone2}, α_{fc}^{zone3}, β_{fc}^{zone2}, and β_{fc}^{zone3} can be calculated using the generic equations (A.II.16) – (A.II.18) for a linearization point i_{fc}^0. Notably, this linearization point depends on the zonal power P_{fc}^{zone1}, P_{fc}^{zone2} and P_{fc}^{zone3}.

$$P_{fc} \cong \alpha_{fc} \cdot i_{fc} + \beta_{fc} \tag{A.II.16}$$

$$\alpha_{fc} = k_c \cdot E_n - 2 \cdot R_{ohm} \cdot i_{fc}^0 - N_{cells} \cdot A\left(1 + \ln\left(i_{fc}^0\right)\right) \tag{A.II.17}$$

$$\beta_{fc} = R_{ohm} \cdot \left(i_{fc}^0\right)^2 + i_{fc}^0 \cdot N_{cells}^{fc} \cdot A\left(1 + \ln\left(i_{fc}^0\right) + ln\left(\frac{i_0}{i_{fc}^0}\right)\right) \tag{A.II.18}$$

III. Dynamic average algorithm

Let be x_i a measurement point acquired at instant i and $\bar{x}_N$ the dynamic average of all N past measurement points from $t = 0$ to $t = i$. Therefore, $\bar{x}_{N+1}$ can be calculated only using the current measure x_i and the total number of updates N, as specified in the following equations in order of compilation:

$$\bar{x}_{N+1} = N \cdot \bar{x}_N + x_i \tag{A.III.1}$$

$$N = N + 1 \tag{A.III.2}$$

$$\bar{x}_{N+1} = \bar{x}_{N+1}/N \tag{A.III.3}$$

IV. Calculation of the premium for self-consuming electricity (additional income)

The premium for self-consuming electricity in French regions are defined by (A.IV.1).

$$\pi_{sc}^{annual} = 10^{-6} \cdot \left(\sum_{k=1}^{365} (P + 5) \cdot E_{sc,k} + P \cdot E_{grid,k}^{injected} - 12 \cdot E_{pv,k} \cdot \frac{P_{maxInjected}}{P_{pv}^{inst}} \right) \tag{A.IV.1}$$

The energy self-consumed ($E_{sc,k}$) is calculated from (A.IV.2).

$$E_{sc,k} = E_{pv,k} - E_{grid,k}^{injected} \tag{A.IV.2}$$

By replacing (A.IV.2) in (A.IV.1), and knowing that $E_{grid,k}^{injected}$ is calculated from (5.12), π_{sc}^{annual} can be calculated following (A.IV.3).

$$\pi_{sc}^{annual} = 10^{-6} \cdot \left(\sum_{k=1}^{365} 5 \cdot \left(\left| E_{els,k} \right| + \left| E_{bat,k}^{ch} \right| \right) - 5 \cdot E_{surplus,k} + (P+5) \cdot E_{pv,k} - 12 \cdot E_{pv,k} \cdot \frac{P_{maxInjected}}{P_{pv}^{inst}} \right) \tag{A.IV.3}$$

Since $E_{surplus,k}$ is uncontrolled by the EMPC because it is dependent on weather conditions and building internal consumption, the maximization of π_{sc}^{annual} is guaranteed by optimizing (A.IV.4).

$$\pi_{sc}^{annual} = 10^{-6} \cdot \left(\sum_{k=1}^{365} 5 \cdot \left(\left| E_{els,k} \right| + \left| E_{bat,k}^{ch} \right| \right) - 12 \cdot E_{pv,k} \cdot \frac{P_{maxInjected}}{P_{pv}^{inst}} \right) \tag{A.IV.4}$$

V. Absolute values of the simulation of Chapiter 6

a. Rule-based controller

Table A.V.1: One-year simulation results of the rule-based controller in the public building.

ESS	Self-consumption (M_1^{RB})	Coverage (M_2^{RB})	Total MG cost (M_3^{RB})	Battery cost (M_4^{RB})	Electrolyser cost (M_5^{RB})	Fuel cell cost (M_6^{RB})	Electricity cost (M_7^{RB})	Additional income (M_8^{RB})
Battery	79.7%	43.2%	11819 €	1456 €	0 €	0 €	12220 €	1857 €
Hybrid[a,b]	92.9%	45.8%	12307 €	1456 €	292 €	1247 €	11723 €	2410 €
Without ESS	69.6%	37.7%	11660 €	0 €	0 €	0 €	13451 €	1791 €

[a]Soft constraint [b]C_{fc}, C_{els} in Table 6.4

Table A.V.2: One-year simulation results of the rule-based controller in a residential building.

ESS	Self-consumption (M_1^{RB})	Coverage (M_2^{RB})	Total MG cost (M_3^{RB})	Battery cost (M_4^{RB})	Electrolyser cost (M_5^{RB})	Fuel cell cost (M_6^{RB})	Electricity cost (M_7^{RB})	Additional income (M_8^{RB})
Battery	62.2%	25.6%	20888 €	2586 €	0 €	0 €	19766 €	1463 €
Hybrid[a,b]	86.7%	27.9%	22362 €	2586 €	541 €	2267 €	19058 €	2090 €
Without ESS	47.3%	20.2%	20047 €	0 €	0 €	0 €	21413 €	1366 €

[a]Soft constraint [b]C_{fc}, C_{els} in Table 6.4

b. Conventional Hierarchical Model Predictive Controller (HMPC)

Table A.V.3: One-year simulation results of the HMPC controller in the public building.

ESS	Self-consumption (M_1^{RB})	Coverage (M_2^{RB})	Total MG cost (M_3^{RB})	Battery cost (M_4^{RB})	Electrolyser cost (M_5^{RB})	Fuel cell cost (M_6^{RB})	Electricity cost (M_7^{RB})	Additional income (M_8^{RB})
Battery[a]	83.3%	45.1%	11367 €	1371 €	0 €	0 €	11891 €	1895 €
Hybrid[a,c,f]	97.7%	48.2%	12005 €	1301 €	364 €	1540 €	11263 €	2465 €
Hybrid[a,d,e]	91.9%	46.8%	10851 €	1309 €	0 €	0 €	11544 €	2002 €
Hybrid[b,c,f]	94.0%	46.9%	12093 €	1096 €	313 €	1330 €	11544 €	2190 €
Without ESS	69.6%	37.7%	11660 €	0 €	0 €	0 €	13451 €	1791 €

[a]Without noise [b]With noise [c]Soft constraint [d]Hard constraint [e]$C_{fc} = C_{els} = 0$€ [f]C_{fc}, C_{els} in Table 6.4

Table A.V.4: One-year simulation results of the HMPC controller in the residential building.

ESS	Self-consumption (M_1^{RB})	Coverage (M_2^{RB})	Total MG cost (M_3^{RB})	Battery cost (M_4^{RB})	Electrolyser cost (M_5^{RB})	Fuel cell cost (M_6^{RB})	Electricity cost (M_7^{RB})	Additional income (M_8^{RB})
Battery[a]	68.8%	29.3%	19944 €	2518 €	0 €	0 €	18931 €	1506 €
Hybrid[a,c,f]	94.0%	33.7%	21936 €	2508 €	619 €	3135 €	17813 €	2140 €
Hybrid[a,d,e]	91.6%	33.1%	18382 €	2517 €	0 €	0 €	17989 €	2124 €
Hybrid[b,c,f]	88.8%	32.4%	21844 €	2420 €	532 €	2789 €	18158 €	2056 €
Without ESS	47.3%	20.2%	20047 €	0 €	0 €	0 €	21413 €	1366 €

[a]Without noise [b]With noise [c]Soft constraint [d]Hard constraint [e]$C_{fc} = C_{els} = 0$€ [f]C_{fc}, C_{els} in Table 6.4

c. Hierarchical Model Predictive Controller with the MG Cost Estimator (HMPC-kmeans)

Table A.V.5: One-year simulation results of the HMPC-kmeans controller in the public building.

ESS	Self-consumption (M_1^{RB})	Coverage (M_2^{RB})	Total MG cost (M_3^{RB})	Battery cost (M_4^{RB})	Electrolyser cost (M_5^{RB})	Fuel cell cost (M_6^{RB})	Electricity cost (M_7^{RB})	Additional income (M_8^{RB})
Battery[a]	83.0%	45.0%	11229 €	1332 €	0 €	0 €	11836 €	1939 €
Hybrid[a,c,f]	83.5%	45.1%	11180 €	1277 €	16 €	105 €	11801 €	2019 €
Hybrid[a,d,e]	91.2%	46.1%	10327 €	1156 €	0 €	0 €	11586 €	2415 €
Hybrid[b,c,f]	82.7%	44.3%	11361 €	1053 €	40 €	171 €	11996 €	1901 €
Without ESS	69.6%	37.7%	11660 €	0 €	0 €	0 €	13451 €	1791 €

[a]Without noise [b]With noise [c]Soft constraint [d]Hard constraint [e]$C_{fc} = C_{els} = 0$€ [f]C_{fc}, C_{els} in Table 6.4

Table A.V.6: One-year simulation results of the HMPC-kmeans controller in the residential building.

ESS	Self-consumption (M_1^{RB})	Coverage (M_2^{RB})	Total MG cost (M_3^{RB})	Battery cost (M_4^{RB})	Electrolyser cost (M_5^{RB})	Fuel cell cost (M_6^{RB})	Electricity cost (M_7^{RB})	Additional income (M_8^{RB})
Battery[a]	68.5%	29.2%	19737 €	2438 €	0 €	0 €	18804 €	1505 €
Hybrid[a,c,f]	82.5%	31.1%	21245 €	2353 €	349 €	2004 €	18269 €	1731 €
Hybrid[a,d,e]	91.2%	32.0%	17813 €	1875 €	0 €	0 €	1860 €	2122 €
Hybrid[b,c,f]	81.8%	30.6%	21417 €	2038 €	385 €	2148 €	18593 €	1747 €
Without ESS	47.3%	20.2%	20047 €	0 €	0 €	0 €	21413 €	1366 €

[a]Without noise [b]With noise [c]Soft constraint [d]Hard constraint [e]$C_{fc} = C_{els} = 0$€ [f]C_{fc}, C_{els} in Table 6.4

References

[1] "Perspective for the clean energy transition 2019 - the critical role of buildings," International Energy Agency, Apr. 2019.

[2] IEA-IRENA (International Renewable Energy Agency), "Perspectives for the Energy Transition: Investment Needs for a Low-Carbon Energy System," 2017.

[3] Y. Guo, M. Pan, and Y. Fang, "Optimal Power Management of Residential Customers in the Smart Grid," *IEEE Transactions on Parallel and Distributed Systems*, vol. 23, no. 9, pp. 1593–1606, Sep. 2012, doi: 10.1109/TPDS.2012.25.

[4] M. A. F. Ghazvini, P. Faria, H. Morais, Z. Vale, and S. Ramos, "Stochastic framework for strategic decision-making of load-serving entities for day-ahead market," in *2013 IEEE Grenoble Conference*, Jun. 2013, pp. 1–6, doi: 10.1109/PTC.2013.6652394.

[5] D. Zhang, N. Shah, and L. G. Papageorgiou, "Efficient energy consumption and operation management in a smart building with microgrid," *Energy Conversion and Management*, vol. 74, pp. 209–222, Oct. 2013, doi: 10.1016/j.enconman.2013.04.038.

[6] Y. Wang, Y. Li, Y. Cao, Y. Tan, L. He, and J. Han, "Hybrid AC/DC microgrid architecture with comprehensive control strategy for energy management of smart building," *International Journal of Electrical Power & Energy Systems*, vol. 101, pp. 151–161, Oct. 2018, doi: 10.1016/j.ijepes.2018.02.048.

[7] T. M. Lawrence *et al.*, "Ten questions concerning integrating smart buildings into the smart grid," *Building and Environment*, vol. 108, pp. 273–283, Nov. 2016, doi: 10.1016/j.buildenv.2016.08.022.

[8] M. Tavakoli, F. Shokridehaki, M. Marzband, R. Godina, and E. Pouresmaeil, "A two stage hierarchical control approach for the optimal energy management in commercial building microgrids based on local wind power and PEVs," *Sustainable Cities and Society*, vol. 41, pp. 332–340, Aug. 2018, doi: 10.1016/j.scs.2018.05.035.

[9] A. Lüth, J. M. Zepter, P. Crespo del Granado, and R. Egging, "Local electricity market designs for peer-to-peer trading: The role of battery flexibility," *Applied Energy*, vol. 229, pp. 1233–1243, Nov. 2018, doi: 10.1016/j.apenergy.2018.08.004.

[10] D. I. Chatzigiannis, G. A. Dourbois, P. N. Biskas, and A. G. Bakirtzis, "European day-ahead electricity market clearing model," *Electric Power Systems Research*, vol. 140, pp. 225–239, Nov. 2016, doi: 10.1016/j.epsr.2016.06.019.

[11] R. Luthander, J. Widén, D. Nilsson, and J. Palm, "Photovoltaic self-consumption in buildings: A review," *Applied Energy*, vol. 142, pp. 80–94, Mar. 2015, doi: 10.1016/j.apenergy.2014.12.028.

[12] Commission de Régulation de l'Energie, "Cahier des charges de l'appel d'offres portant sur la réalisation et l'exploitation d'Installations de production d'électricité à partir d'énergies renouvelables en autoconsommation et situées en métropole continentale." Dec. 26, 2019.

[13] D. Y. Yamashita, I. Vechiu, and J.-P. Gaubert, "A review of hierarchical control for building microgrids," *Renewable and Sustainable Energy Reviews*, vol. 118, p. 109523, Feb. 2020, doi: 10.1016/j.rser.2019.109523.

[14] D. Y. Yamashita, I. Vechiu, and J. P. Gaubert, "Hierarchical Control Structure for Optimising Building Microgrid Self-consumption," in *2019 International Conference on Smart Energy Systems and Technologies (SEST)*, Porto, Portugal, Sep. 2019, pp. 1–6, doi: 10.1109/SEST.2019.8849054.

[15] D. Yassuda Yamashita, I. Vechiu, and J.-P. Gaubert, "Real-time Parameters Identification of Lithium-ion Batteries Model to Improve the Hierarchical Model Predictive Control of Building MicroGrids," presented at the 2020 22nd European Conference on Power Electronics and Applications (EPE '20 ECCE Europe), Lyon, Sep. 2020, doi: 10.23919/EPE20ECCEEurope43536.2020.9215878.

[16] D. Yassuda Yamashita, I. Vechiu, and J.-P. Gaubert, "Two-level hierarchical model predictive control with an optimised cost function for energy management in building microgrids," *Applied Energy*, vol. 285, p. 116420, Mar. 2021, doi: 10.1016/j.apenergy.2020.116420.

[17] R. Teodorescu, M. Liserre, and P. Rodriguez, *Grid Converters for Photovoltaic and Wind Power Systems*. John Wiley & Sons, 2011.

[18] M. Nemati, M. Braun, and S. Tenbohlen, "Optimization of unit commitment and economic dispatch in microgrids based on genetic algorithm and mixed integer linear programming," *Applied Energy*, vol. 210, pp. 944–963, Jan. 2018, doi: 10.1016/j.apenergy.2017.07.007.

[19] R. Herranz, A. M. S. Roque, J. Villar, and F. A. Campos, "Optimal Demand-Side Bidding Strategies in Electricity Spot Markets," *IEEE Transactions on Power Systems*, vol. 27, no. 3, pp. 1204–1213, Aug. 2012, doi: 10.1109/TPWRS.2012.2185960.

[20] T. L. Vandoorn, J. C. Vasquez, J. D. Kooning, J. M. Guerrero, and L. Vandevelde, "Microgrids: Hierarchical Control and an Overview of the Control and Reserve Management Strategies," *IEEE Industrial Electronics Magazine*, vol. 7, no. 4, pp. 42–55, Dec. 2013, doi: 10.1109/MIE.2013.2279306.

[21] Z. Cheng, J. Duan, and M.-Y. Chow, "To Centralize or to Distribute: That Is the Question: A Comparison of Advanced Microgrid Management Systems," *IEEE Industrial Electronics Magazine*, vol. 12, no. 1, pp. 6–24, Mar. 2018, doi: 10.1109/MIE.2018.2789926.

[22] D. E. Olivares *et al.*, "Trends in Microgrid Control," *IEEE Transactions on Smart Grid*, vol. 5, no. 4, pp. 1905–1919, Jul. 2014, doi: 10.1109/TSG.2013.2295514.

[23] J. M. Guerrero, J. C. Vasquez, J. Matas, L. G. de Vicuna, and M. Castilla, "Hierarchical Control of Droop-Controlled AC and DC Microgrids; A General Approach Toward Standardization," *IEEE Transactions on Industrial Electronics*, vol. 58, no. 1, pp. 158–172, Jan. 2011, doi: 10.1109/TIE.2010.2066534.

[24] J. W. Simpson-Porco, Q. Shafiee, F. Dorfler, J. C. Vasquez, J. M. Guerrero, and F. Bullo, "Secondary Frequency and Voltage Control of Islanded Microgrids via Distributed Averaging," *IEEE Transactions on Industrial Electronics*, vol. 62, no. 11, pp. 7025–7038, Nov. 2015, doi: 10.1109/TIE.2015.2436879.

[25] M. Savaghebi, A. Jalilian, J. C. Vasquez, and J. M. Guerrero, "Secondary Control Scheme for Voltage Unbalance Compensation in an Islanded Droop-Controlled Microgrid," *IEEE Transactions on Smart Grid*, vol. 3, no. 2, pp. 797–807, Jun. 2012, doi: 10.1109/TSG.2011.2181432.

[26] D. Wang, J. Qiu, L. Reedman, K. Meng, and L. L. Lai, "Two-stage energy management for networked microgrids with high renewable penetration," *Applied Energy*, vol. 226, pp. 39–48, Sep. 2018, doi: 10.1016/j.apenergy.2018.05.112.

[27] Y. Liu *et al.*, "Coordinating the operations of smart buildings in smart grids," *Applied Energy*, vol. 228, pp. 2510–2525, Oct. 2018, doi: 10.1016/j.apenergy.2018.07.089.

[28] L. Romero Rodríguez, J. Sánchez Ramos, Mc. Guerrero Delgado, J. L. Molina Félix, and S. Álvarez Domínguez, "Mitigating energy poverty: Potential contributions of combining PV and building thermal mass storage in low-income households," *Energy Conversion and Management*, vol. 173, pp. 65–80, Oct. 2018, doi: 10.1016/j.enconman.2018.07.058.

[29] S. Baldi, A. Karagevrekis, I. T. Michailidis, and E. B. Kosmatopoulos, "Joint energy demand and thermal comfort optimization in photovoltaic-equipped interconnected microgrids," *Energy Conversion and Management*, vol. 101, pp. 352–363, Sep. 2015, doi: 10.1016/j.enconman.2015.05.049.

[30] B. Aluisio, M. Dicorato, G. Forte, G. Litrico, and M. Trovato, "Integration of heat production and thermal comfort models in microgrid operation planning," *Sustainable Energy, Grids and Networks*, vol. 16, pp. 37–54, Dec. 2018, doi: 10.1016/j.segan.2018.05.004.

[31] D. Leskarac, M. Moghimi, J. Liu, W. Water, J. Lu, and S. Stegen, "Hybrid AC/DC Microgrid testing facility for energy management in commercial buildings," *Energy and Buildings*, vol. 174, pp. 563–578, Sep. 2018, doi: 10.1016/j.enbuild.2018.06.061.

[32] Y. Riffonneau, S. Bacha, F. Barruel, and S. Ploix, "Optimal Power Flow Management for Grid Connected PV Systems With Batteries," *IEEE Transactions on Sustainable Energy*, vol. 2, no. 3, pp. 309–320, Jul. 2011, doi: 10.1109/TSTE.2011.2114901.

[33] S. Conti, R. Nicolosi, S. A. Rizzo, and H. H. Zeineldin, "Optimal Dispatching of Distributed Generators and Storage Systems for MV Islanded Microgrids," *IEEE Transactions on Power Delivery*, vol. 27, no. 3, pp. 1243–1251, Jul. 2012, doi: 10.1109/TPWRD.2012.2194514.

[34] J. Song *et al.*, "System design and policy suggestion for reducing electricity curtailment in renewable power systems for remote islands," *Applied Energy*, vol. 225, pp. 195–208, Sep. 2018, doi: 10.1016/j.apenergy.2018.04.131.

[35] N. N. A. Bakar, M. Y. Hassan, M. F. Sulaima, M. N. Mohd Nasir, and A. Khamis, "Microgrid and load shedding scheme during islanded mode: A review," *Renewable and Sustainable Energy Reviews*, vol. 71, pp. 161–169, May 2017, doi: 10.1016/j.rser.2016.12.049.

[36] M. C. Argyrou, P. Christodoulides, and S. A. Kalogirou, "Energy storage for electricity generation and related processes: Technologies appraisal and grid scale applications," *Renewable and Sustainable Energy Reviews*, vol. 94, pp. 804–821, Oct. 2018, doi: 10.1016/j.rser.2018.06.044.

[37] F. Garcia-Torres and C. Bordons, "Optimal Economical Schedule of Hydrogen-Based Microgrids With Hybrid Storage Using Model Predictive Control," *IEEE Transactions on Industrial Electronics*, vol. 62, no. 8, pp. 5195–5207, Aug. 2015, doi: 10.1109/TIE.2015.2412524.

[38] B. Zhao, X. Zhang, J. Chen, C. Wang, and L. Guo, "Operation Optimization of Standalone Microgrids Considering Lifetime Characteristics of Battery Energy Storage System," *IEEE Transactions on Sustainable Energy*, vol. 4, no. 4, pp. 934–943, Oct. 2013, doi: 10.1109/TSTE.2013.2248400.

[39] A. C. Luna, N. L. Diaz, M. Graells, J. C. Vasquez, and J. M. Guerrero, "Mixed-Integer-Linear-Programming-Based Energy Management System for Hybrid PV-Wind-Battery Microgrids: Modeling, Design, and Experimental Verification," *IEEE Transactions on Power Electronics*, vol. 32, no. 4, pp. 2769–2783, Apr. 2017, doi: 10.1109/TPEL.2016.2581021.

[40] A. Chaouachi, R. M. Kamel, R. Andoulsi, and K. Nagasaka, "Multiobjective Intelligent Energy Management for a Microgrid," *IEEE Transactions on Industrial Electronics*, vol. 60, no. 4, pp. 1688–1699, Apr. 2013, doi: 10.1109/TIE.2012.2188873.

[41] N. Sasidharan and J. G. Singh, "A resilient DC community grid with real time ancillary services management," *Sustainable Cities and Society*, vol. 28, pp. 367–386, Jan. 2017, doi: 10.1016/j.scs.2016.10.007.

[42] L. T. D. Santos, M. Sechilariu, and F. Locment, "Day-ahead microgrid optimal self-scheduling: Comparison between three methods applied to isolated DC microgrid," Oct. 2014, pp. 2010–2016, doi: 10.1109/IECON.2014.7048778.

[43] L. Wang, Z. Wang, and R. Yang, "Intelligent Multiagent Control System for Energy and Comfort Management in Smart and Sustainable Buildings," *IEEE Transactions on Smart Grid*, vol. 3, no. 2, pp. 605–617, Jun. 2012, doi: 10.1109/TSG.2011.2178044.

[44] M. Marzband, E. Yousefnejad, A. Sumper, and J. L. Domínguez-García, "Real time experimental implementation of optimum energy management system in standalone Microgrid by using multi-layer ant colony optimization," *International Journal of Electrical Power & Energy Systems*, vol. 75, pp. 265–274, Feb. 2016, doi: 10.1016/j.ijepes.2015.09.010.

[45] J. Shen, C. Jiang, Y. Liu, and X. Wang, "A Microgrid Energy Management System and Risk Management Under an Electricity Market Environment," *IEEE Access*, vol. 4, pp. 2349–2356, 2016, doi: 10.1109/ACCESS.2016.2555926.

[46] A. S. Jacob, R. Banerjee, and P. C. Ghosh, "Sizing of hybrid energy storage system for a PV based microgrid through design space approach," *Applied Energy*, vol. 212, pp. 640–653, Feb. 2018, doi: 10.1016/j.apenergy.2017.12.040.

[47] H. Jia, Y. Mu, and Y. Qi, "A statistical model to determine the capacity of battery–supercapacitor hybrid energy storage system in autonomous microgrid," *International Journal of Electrical Power & Energy Systems*, vol. 54, pp. 516–524, Jan. 2014, doi: 10.1016/j.ijepes.2013.07.025.

[48] H. Ren, Q. Wu, W. Gao, and W. Zhou, "Optimal operation of a grid-connected hybrid PV/fuel cell/battery energy system for residential applications," *Energy*, vol. 113, pp. 702–712, Oct. 2016, doi: 10.1016/j.energy.2016.07.091.

[49] P. R. C. Mendes, L. V. Isorna, C. Bordons, and J. E. Normey-Rico, "Energy management of an experimental microgrid coupled to a V2G system," *Journal of Power Sources*, vol. 327, pp. 702–713, Sep. 2016, doi: 10.1016/j.jpowsour.2016.07.076.

[50] V. Lešić, A. Martinčević, and M. Vašak, "Modular Energy Cost Optimization for Buildings with Integrated Microgrid," *Applied Energy*, pp. 14–28, Jul. 2017.

[51] M. Pereira, D. Limon, T. Alamo, L. Valverde, and C. Bordons, "Economic model predictive control of a smartgrid with hydrogen storage and PEM fuel cell," in *IECON 2013 - 39th Annual Conference of the IEEE Industrial Electronics Society*, Nov. 2013, pp. 7920–7925, doi: 10.1109/IECON.2013.6700456.

[52] J. Soares, M. Silva, T. Sousa, Z. Vale, and H. Morais, "Distributed energy resource short-term scheduling using Signaled Particle Swarm Optimization," *Energy*, vol. 42, no. 1, pp. 466–476, Jun. 2012, doi: 10.1016/j.energy.2012.03.022.

[53] F. A. Mohamed and H. N. Koivo, "Online management genetic algorithms of microgrid for residential application," *Energy Conversion and Management*, vol. 64, pp. 562–568, Dec. 2012, doi: 10.1016/j.enconman.2012.06.010.

[54] V. N. Coelho *et al.*, "Multi-objective energy storage power dispatching using plug-in vehicles in a smart-microgrid," *Renewable Energy*, vol. 89, pp. 730–742, Apr. 2016, doi: 10.1016/j.renene.2015.11.084.

[55] X. Jin, J. Wu, Y. Mu, M. Wang, X. Xu, and H. Jia, "Hierarchical microgrid energy management in an office building," *Applied Energy*, vol. 208, pp. 480–494, Dec. 2017, doi: 10.1016/j.apenergy.2017.10.002.

[56] A. Hermelink *et al.*, "Towards nearly zero-energy buildings Definition of common principles under the EPBD," Energy Performance of Buildings Directive, Final Report, 2013.

[57] I. Sartori, A. Napolitano, and K. Voss, "Net zero energy buildings: A consistent definition framework," *Energy and Buildings*, vol. 48, pp. 220–232, May 2012, doi: 10.1016/j.enbuild.2012.01.032.

[58] "Panel distribution." http://www.zebra-monitoring.enerdata.eu/nzeb-activities/panel-distribution.html (accessed Jun. 26, 2019).

[59] L. Belussi *et al.*, "A review of performance of zero energy buildings and energy efficiency solutions," *Journal of Building Engineering*, vol. 25, p. 100772, Sep. 2019, doi: 10.1016/j.jobe.2019.100772.

[60] W. Pan and K. Li, "Clusters and exemplars of buildings towards zero carbon," *Building and Environment*, vol. 104, pp. 92–101, Aug. 2016, doi: 10.1016/j.buildenv.2016.04.027.

[61] "Building profiles | Zero Carbon Hub." http://www.zerocarbonhub.org/building-profiles (accessed Jun. 14, 2019).

[62] S. S. S. Baljit, H.-Y. Chan, and K. Sopian, "Review of building integrated applications of photovoltaic and solar thermal systems," *Journal of Cleaner Production*, vol. 137, pp. 677–689, Nov. 2016, doi: 10.1016/j.jclepro.2016.07.150.

[63] "Pixel Building: Australia's First Carbon Neutral Building is Now Complete!" https://inhabitat.com/pixel-building-australias-first-carbon-neutral-building-is-now-complete/ (accessed Jun. 14, 2019).

[64] Q. S. Li, Z. R. Shu, and F. B. Chen, "Performance assessment of tall building-integrated wind turbines for power generation," *Applied Energy*, vol. 165, pp. 777–788, Mar. 2016, doi: 10.1016/j.apenergy.2015.12.114.

[65] "Powervault battery storage," *EDF Energy*. https://www.edfenergy.com/for-home/battery-storage (accessed Jun. 27, 2019).

[66] "Solar Battery Storage: Including Tesla Powerwall, LG Chem, Powervault," *Naked Solar*. https://nakedsolar.co.uk/storage/ (accessed Jun. 27, 2019).

[67] S. Bracco, F. Delfino, F. Pampararo, M. Robba, and M. Rossi, "The University of Genoa smart polygeneration microgrid test-bed facility: The overall system, the technologies and the research

challenges," *Renewable and Sustainable Energy Reviews*, vol. 18, pp. 442–459, Feb. 2013, doi: 10.1016/j.rser.2012.10.009.

[68] D. Arcos-Aviles, J. Pascual, F. Guinjoan, L. Marroyo, P. Sanchis, and M. P. Marietta, "Low complexity energy management strategy for grid profile smoothing of a residential grid-connected microgrid using generation and demand forecasting," *Applied Energy*, vol. 205, pp. 69–84, Nov. 2017, doi: 10.1016/j.apenergy.2017.07.123.

[69] R. Gupta, A. Bruce-Konuah, and A. Howard, "Achieving energy resilience through smart storage of solar electricity at dwelling and community level," *Energy and Buildings*, vol. 195, pp. 1–15, Jul. 2019, doi: 10.1016/j.enbuild.2019.04.012.

[70] H. Mahmood, D. Michaelson, and J. Jiang, "A Power Management Strategy for PV/Battery Hybrid Systems in Islanded Microgrids," *IEEE Journal of Emerging and Selected Topics in Power Electronics*, vol. 2, no. 4, pp. 870–882, Dec. 2014, doi: 10.1109/JESTPE.2014.2334051.

[71] Y. Wang, H. Jiang, L. Zhou, and P. Xing, "An Improved Adaptive Droop Control Strategy for Power Sharing in Micro-Grid," in *2016 8th International Conference on Intelligent Human-Machine Systems and Cybernetics (IHMSC)*, Aug. 2016, vol. 01, pp. 50–53, doi: 10.1109/IHMSC.2016.97.

[72] A. Bidram and A. Davoudi, "Hierarchical Structure of Microgrids Control System," *IEEE Transactions on Smart Grid*, vol. 3, no. 4, pp. 1963–1976, Dec. 2012, doi: 10.1109/TSG.2012.2197425.

[73] T. V. Vu, S. Paran, F. Diaz-Franco, T. El-Mezyani, and C. S. Edrington, "An Alternative Distributed Control Architecture for Improvement in the Transient Response of DC Microgrids," *IEEE Transactions on Industrial Electronics*, vol. 64, no. 1, pp. 574–584, Jan. 2017, doi: 10.1109/TIE.2016.2607681.

[74] F. Alam, M. Ashfaq, S. S. Zaidi, and A. Y. Memon, "Robust droop control design for a hybrid AC/DC microgrid," Aug. 2016, pp. 1–6, doi: 10.1109/CONTROL.2016.7737547.

[75] U. B. Tayab, M. A. B. Roslan, L. J. Hwai, and M. Kashif, "A review of droop control techniques for microgrid," *Renewable and Sustainable Energy Reviews*, vol. 76, pp. 717–727, Sep. 2017, doi: 10.1016/j.rser.2017.03.028.

[76] V. Verma and G. G. Talpur, "Decentralized Master-Slave operation of microgrid using current controlled distributed generation sources," in *2012 IEEE International Conference on Power Electronics, Drives and Energy Systems (PEDES)*, Dec. 2012, pp. 1–6, doi: 10.1109/PEDES.2012.6484502.

[77] G. G. Talapur, H. M. Suryawanshi, A. B. Shitole, R. R. Deshmukh, and M. S. Ballal, "Master-slave control based reliable micro-Grid with back-to-back voltage source converter as master DG," Oct. 2017, pp. 310–315, doi: 10.1109/IECON.2017.8216056.

[78] L. K. Vedulla and M. K. Mishra, "PSO based power sharing scheme for an islanded DC microgrid system," in *IECON 2017 - 43rd Annual Conference of the IEEE Industrial Electronics Society*, Oct. 2017, pp. 392–397, doi: 10.1109/IECON.2017.8216070.

[79] C. D. Korkas, S. Baldi, I. Michailidis, and E. B. Kosmatopoulos, "Occupancy-based demand response and thermal comfort optimization in microgrids with renewable energy sources and energy storage," *Applied Energy*, vol. 163, pp. 93–104, Feb. 2016, doi: 10.1016/j.apenergy.2015.10.140.

[80] L. Damiano and D. Dougan, "ANSI/ASHRAE Standard 62.1-2016," in *Encyclopedia of Energy Engineering and Technology - 3 Volume Set (Print Version)*, B. Capehart, Ed. CRC Press, 2016, pp. 50–62.

[81] M. Killian and M. Kozek, "Implementation of cooperative Fuzzy model predictive control for an energy-efficient office building," *Energy and Buildings*, vol. 158, pp. 1404–1416, Jan. 2018, doi: 10.1016/j.enbuild.2017.11.021.

[82] G. S. Pavlak, G. P. Henze, and V. J. Cushing, "Optimizing commercial building participation in energy and ancillary service markets," *Energy and Buildings*, vol. 81, pp. 115–126, Oct. 2014, doi: 10.1016/j.enbuild.2014.05.048.

[83] E. Rokrok, M. Shafie-khah, and J. P. S. Catalão, "Review of primary voltage and frequency control methods for inverter-based islanded microgrids with distributed generation," *Renewable*

and Sustainable Energy Reviews, vol. 82, pp. 3225–3235, Feb. 2018, doi: 10.1016/j.rser.2017.10.022.

[84] B. Bendib, H. Belmili, and F. Krim, "A survey of the most used MPPT methods: Conventional and advanced algorithms applied for photovoltaic systems," *Renewable and Sustainable Energy Reviews*, vol. 45, pp. 637–648, May 2015, doi: 10.1016/j.rser.2015.02.009.

[85] Z. Cui and L. Song, "Improvement of maximum power point tracking for a new wind power system," in *2018 13th IEEE Conference on Industrial Electronics and Applications (ICIEA)*, May 2018, pp. 1665–1670, doi: 10.1109/ICIEA.2018.8397977.

[86] H. Yu, S. Niu, Y. Zhang, and L. Jian, "An integrated and reconfigurable hybrid AC/DC microgrid architecture with autonomous power flow control for nearly/net zero energy buildings," *Applied Energy*, vol. 263, p. 114610, Apr. 2020, doi: 10.1016/j.apenergy.2020.114610.

[87] M. Marzband, M. Javadi, S. A. Pourmousavi, and G. Lightbody, "An advanced retail electricity market for active distribution systems and home microgrid interoperability based on game theory," *Electric Power Systems Research*, vol. 157, pp. 187–199, Apr. 2018, doi: 10.1016/j.epsr.2017.12.024.

[88] R. Lu, S. H. Hong, and X. Zhang, "A Dynamic pricing demand response algorithm for smart grid: Reinforcement learning approach," *Applied Energy*, vol. 220, pp. 220–230, Jun. 2018, doi: 10.1016/j.apenergy.2018.03.072.

[89] M. A. Hossain, H. R. Pota, S. Squartini, F. Zaman, and J. M. Guerrero, "Energy scheduling of community microgrid with battery cost using particle swarm optimisation," *Applied Energy*, vol. 254, p. 113723, Nov. 2019, doi: 10.1016/j.apenergy.2019.113723.

[90] M. F. Zia, E. Elbouchikhi, and M. Benbouzid, "Microgrids energy management systems: A critical review on methods, solutions, and prospects," *Applied Energy*, vol. 222, pp. 1033–1055, Jul. 2018, doi: 10.1016/j.apenergy.2018.04.103.

[91] Y. Guo, M. Pan, Y. Fang, and P. P. Khargonekar, "Decentralized Coordination of Energy Utilization for Residential Households in the Smart Grid," *IEEE Transactions on Smart Grid*, vol. 4, no. 3, pp. 1341–1350, Sep. 2013, doi: 10.1109/TSG.2013.2268581.

[92] G. Kyriakarakos, D. D. Piromalis, A. I. Dounis, K. G. Arvanitis, and G. Papadakis, "Intelligent demand side energy management system for autonomous polygeneration microgrids," *Applied Energy*, vol. 103, pp. 39–51, Mar. 2013, doi: 10.1016/j.apenergy.2012.10.011.

[93] S. Cheikh-Mohamad, M. Sechilariu, F. Locment, and Y. Krim, "PV-Powered Electric Vehicle Charging Stations: Preliminary Requirements and Feasibility Conditions," *Applied Sciences*, vol. 11, no. 4, p. 1770, Feb. 2021, doi: 10.3390/app11041770.

[94] Y. Chen, P. Xu, J. Gu, F. Schmidt, and W. Li, "Measures to improve energy demand flexibility in buildings for demand response (DR): A review," *Energy and Buildings*, vol. 177, pp. 125–139, Oct. 2018, doi: 10.1016/j.enbuild.2018.08.003.

[95] N. Sujitha and S. Krithiga, "RES based EV battery charging system: A review," *Renewable and Sustainable Energy Reviews*, vol. 75, pp. 978–988, Aug. 2017, doi: 10.1016/j.rser.2016.11.078.

[96] S. Moussa, M. J.-B. Ghorbal, and I. Slama-Belkhodja, "Bus voltage level choice for standalone residential DC nanogrid," *Sustainable Cities and Society*, vol. 46, p. 101431, Apr. 2019, doi: 10.1016/j.scs.2019.101431.

[97] J. Decuir and P. Michael, "Draft IEEE standard for DC microgrids for rural and remote electricity access applications," in *2017 IEEE Conference on Technologies for Sustainability (SusTech)*, Phoenix, AZ, USA, Nov. 2017, pp. 1–5, doi: 10.1109/SusTech.2017.8333510.

[98] "IEEE Standard for Interconnection and Interoperability of Distributed Energy Resources with Associated Electric Power Systems Interfaces," *IEEE Std 1547-2018 (Revision of IEEE Std 1547-2003)*, pp. 1–138, Apr. 2018, doi: 10.1109/IEEESTD.2018.8332112.

[99] G. Van den Broeck, J. Stuyts, and J. Driesen, "A critical review of power quality standards and definitions applied to DC microgrids," *Applied Energy*, vol. 229, pp. 281–288, Nov. 2018, doi: 10.1016/j.apenergy.2018.07.058.

[100] "IEEE Recommended Practice for 1 kV to 35 kV Medium-Voltage DC Power Systems on Ships," IEEE. doi: 10.1109/IEEESTD.2010.5623440.

[101] "IEEE Standard for the Specification of Microgrid Controllers," IEEE. doi: 10.1109/IEEESTD.2018.8340204.

[102] S. Marzal, R. Salas, R. González-Medina, G. Garcerá, and E. Figueres, "Current challenges and future trends in the field of communication architectures for microgrids," *Renewable and Sustainable Energy Reviews*, vol. 82, pp. 3610–3622, Feb. 2018, doi: 10.1016/j.rser.2017.10.101.

[103] H. R. Baghaee, M. Mirsalim, G. B. Gharehpetian, and H. A. Talebi, "Unbalanced harmonic power sharing and voltage compensation of microgrids using radial basis function neural network-based harmonic power-flow calculations for distributed and decentralised control structures," *Transmission Distribution IET Generation*, vol. 12, no. 7, pp. 1518–1530, 2018, doi: 10.1049/iet-gtd.2016.1277.

[104] A. M. dos Santos Alonso, D. I. Brandao, T. Caldognetto, F. P. Marafão, and P. Mattavelli, "A selective harmonic compensation and power control approach exploiting distributed electronic converters in microgrids," *International Journal of Electrical Power & Energy Systems*, vol. 115, p. 105452, Feb. 2020, doi: 10.1016/j.ijepes.2019.105452.

[105] L. Meng, F. Tang, M. Savaghebi, J. C. Vasquez, and J. M. Guerrero, "Tertiary Control of Voltage Unbalance Compensation for Optimal Power Quality in Islanded Microgrids," *IEEE Transactions on Energy Conversion*, vol. 29, no. 4, pp. 802–815, Dec. 2014, doi: 10.1109/TEC.2014.2363687.

[106] L. Meng *et al.*, "Distributed Voltage Unbalance Compensation in Islanded Microgrids by Using a Dynamic Consensus Algorithm," *IEEE Transactions on Power Electronics*, vol. 31, no. 1, pp. 827–838, Jan. 2016, doi: 10.1109/TPEL.2015.2408367.

[107] R. Teodorescu, M. Liserre, and P. Rodríguez, *Grid Converters for Photovoltaic and Wind Power Systems*. Chichester, UK: John Wiley & Sons, Ltd, 2011.

[108] V. Nasirian, S. Moayedi, A. Davoudi, and F. L. Lewis, "Distributed Cooperative Control of DC Microgrids," *IEEE Transactions on Power Electronics*, vol. 30, no. 4, pp. 2288–2303, Apr. 2015, doi: 10.1109/TPEL.2014.2324579.

[109] Z. Guo, H. Jiang, Y. Zheng, and S. Li, "Distributed model predictive control for efficient operation of islanded microgrid," in *2017 Chinese Automation Congress (CAC)*, Oct. 2017, pp. 6253–6258, doi: 10.1109/CAC.2017.8243904.

[110] J. Liu, M. J. Hossain, J. Lu, F. H. M. Rafi, and H. Li, "A hybrid AC/DC microgrid control system based on a virtual synchronous generator for smooth transient performances," *Electric Power Systems Research*, vol. 162, pp. 169–182, Sep. 2018, doi: 10.1016/j.epsr.2018.05.014.

[111] R. Azim *et al.*, "A comparative analysis of intelligent classifiers for passive islanding detection in microgrids," in *2015 IEEE Eindhoven PowerTech*, Eindhoven, Netherlands, Jun. 2015, pp. 1–6, doi: 10.1109/PTC.2015.7232369.

[112] A. Emadi and H. Afrakhte, "A reference current perturbation method for islanding detection of a multi-inverter system," *Electric Power Systems Research*, vol. 132, pp. 47–55, Mar. 2016, doi: 10.1016/j.epsr.2015.11.002.

[113] E. J. Agnoletto, R. V. A. Neves, R. F. Bastos, R. Q. Machado, and V. A. Oliveira, "Fuzzy secondary controller applied to autonomous operated AC microgrid," in *2016 European Control Conference (ECC)*, Jun. 2016, pp. 1788–1793, doi: 10.1109/ECC.2016.7810550.

[114] J. Rocabert, A. Luna, F. Blaabjerg, and P. Rodríguez, "Control of Power Converters in AC Microgrids," *IEEE Transactions on Power Electronics*, vol. 27, no. 11, pp. 4734–4749, Nov. 2012, doi: 10.1109/TPEL.2012.2199334.

[115] M. U. Younus, S. ul Islam, I. Ali, S. Khan, and M. K. Khan, "A survey on software defined networking enabled smart buildings: Architecture, challenges and use cases," *Journal of Network and Computer Applications*, vol. 137, pp. 62–77, Jul. 2019, doi: 10.1016/j.jnca.2019.04.002.

[116] P. Tian, X. Xiao, K. Wang, and R. Ding, "A Hierarchical Energy Management System Based on Hierarchical Optimization for Microgrid Community Economic Operation," *IEEE Transactions on Smart Grid*, vol. 7, no. 5, pp. 2230–2241, Sep. 2016, doi: 10.1109/TSG.2015.2470551.

[117] L. Valverde, C. Bordons, and F. Rosa, "Integration of Fuel Cell Technologies in Renewable-Energy-Based Microgrids Optimizing Operational Costs and Durability," *IEEE Transactions on Industrial Electronics*, vol. 63, no. 1, pp. 167–177, Jan. 2016, doi: 10.1109/TIE.2015.2465355.

[118] M. Molina-Solana, M. Ros, M. D. Ruiz, J. Gómez-Romero, and M. J. Martin-Bautista, "Data science for building energy management: A review," *Renewable and Sustainable Energy Reviews*, vol. 70, pp. 598–609, Apr. 2017, doi: 10.1016/j.rser.2016.11.132.

[119] J.-S. Chou and N.-S. Truong, "Cloud forecasting system for monitoring and alerting of energy use by home appliances," *Applied Energy*, vol. 249, pp. 166–177, Sep. 2019, doi: 10.1016/j.apenergy.2019.04.063.

[120] Y. Guan, J. C. Vasquez, and J. M. Guerrero, "Hierarchical controlled grid-connected microgrid based on a novel autonomous current sharing controller," Sep. 2015, pp. 2333–2340, doi: 10.1109/ECCE.2015.7309988.

[121] M. H. Cintuglu, T. Youssef, and O. A. Mohammed, "Development and Application of a Real-Time Testbed for Multiagent System Interoperability: A Case Study on Hierarchical Microgrid Control," *IEEE Transactions on Smart Grid*, vol. 9, no. 3, pp. 1759–1768, May 2018, doi: 10.1109/TSG.2016.2599265.

[122] C.-X. Dou and B. Liu, "Multi-Agent Based Hierarchical Hybrid Control for Smart Microgrid," *IEEE Transactions on Smart Grid*, vol. 4, no. 2, pp. 771–778, Jun. 2013, doi: 10.1109/TSG.2012.2230197.

[123] M. Nassourou, V. Puig, J. Blesa, and C. Ocampo-Martinez, "Economic model predictive control for energy dispatch of a smart micro-grid system," in *2017 4th International Conference on Control, Decision and Information Technologies (CoDIT)*, Apr. 2017, pp. 0944–0949, doi: 10.1109/CoDIT.2017.8102719.

[124] F.-J. Heredia, M. D. Cuadrado, and C. Corchero, "On optimal participation in the electricity markets of wind power plants with battery energy storage systems," *Computers & Operations Research*, vol. 96, pp. 316–329, Aug. 2018, doi: 10.1016/j.cor.2018.03.004.

[125] L. Meng, E. R. Sanseverino, A. Luna, T. Dragicevic, J. C. Vasquez, and J. M. Guerrero, "Microgrid supervisory controllers and energy management systems: A literature review," *Renewable and Sustainable Energy Reviews*, vol. 60, pp. 1263–1273, Jul. 2016, doi: 10.1016/j.rser.2016.03.003.

[126] M. W. Khan, J. Wang, M. Ma, L. Xiong, P. Li, and F. Wu, "Optimal energy management and control aspects of distributed microgrid using multi-agent systems," *Sustainable Cities and Society*, vol. 44, pp. 855–870, Jan. 2019, doi: 10.1016/j.scs.2018.11.009.

[127] N. Rezaei and M. Kalantar, "Stochastic frequency-security constrained energy and reserve management of an inverter interfaced islanded microgrid considering demand response programs," *International Journal of Electrical Power & Energy Systems*, vol. 69, pp. 273–286, Jul. 2015, doi: 10.1016/j.ijepes.2015.01.023.

[128] K. Mason, J. Duggan, and E. Howley, "Multi-objective dynamic economic emission dispatch using particle swarm optimisation variants," *Neurocomputing*, vol. 270, pp. 188–197, Dec. 2017, doi: 10.1016/j.neucom.2017.03.086.

[129] L. Meng, "Hierarchical Control for Optimal and Distributed Operation of Microgrid Systems," Aalborg University, 2015.

[130] E. De Santis, A. Rizzi, and A. Sadeghian, "Hierarchical genetic optimization of a fuzzy logic system for energy flows management in microgrids," *Applied Soft Computing*, vol. 60, pp. 135–149, Nov. 2017, doi: 10.1016/j.asoc.2017.05.059.

[131] L. Meng, T. Dragicevic, J. Roldán-Pérez, J. C. Vasquez, and J. M. Guerrero, "Modeling and Sensitivity Study of Consensus Algorithm-Based Distributed Hierarchical Control for DC Microgrids," *IEEE Transactions on Smart Grid*, vol. 7, no. 3, pp. 1504–1515, May 2016, doi: 10.1109/TSG.2015.2422714.

[132] L. Ren, Y. Qin, B. Wang, P. Zhang, P. B. Luh, and R. Jin, "Enabling Resilient Microgrid Through Programmable Network," *IEEE Trans. Smart Grid*, vol. 8, no. 6, pp. 2826–2836, Nov. 2017, doi: 10.1109/TSG.2016.2589903.

[133] X. Feng, A. Shekhar, F. Yang, R. E. Hebner, and P. Bauer, "Comparison of Hierarchical Control and Distributed Control for Microgrid," *Electric Power Components and Systems*, vol. 45, no. 10, pp. 1043–1056, Jun. 2017, doi: 10.1080/15325008.2017.1318982.

[134] N. Rahbari-Asr, Y. Zhang, and M. Y. Chow, "Cooperative distributed scheduling for storage devices in microgrids using dynamic KKT multipliers and consensus networks," in *2015 IEEE Power Energy Society General Meeting*, Jul. 2015, pp. 1–5, doi: 10.1109/PESGM.2015.7286376.

[135] T. Sousa, T. Soares, P. Pinson, F. Moret, T. Baroche, and E. Sorin, "Peer-to-peer and community-based markets: A comprehensive review," *Renewable and Sustainable Energy Reviews*, vol. 104, pp. 367–378, Apr. 2019, doi: 10.1016/j.rser.2019.01.036.

[136] C. Long, J. Wu, Y. Zhou, and N. Jenkins, "Peer-to-peer energy sharing through a two-stage aggregated battery control in a community Microgrid," *Applied Energy*, vol. 226, pp. 261–276, Sep. 2018, doi: 10.1016/j.apenergy.2018.05.097.

[137] A. Etxeberria, I. Vechiu, H. Camblong, and J.-M. Vinassa, "Comparison of three topologies and controls of a hybrid energy storage system for microgrids," *Energy Conversion and Management*, vol. 54, no. 1, pp. 113–121, Feb. 2012, doi: 10.1016/j.enconman.2011.10.012.

[138] Q. Tabart, I. Vechiu, A. Etxeberria, and S. Bacha, "Hybrid Energy Storage System Microgrids Integration for Power Quality Improvement Using Four-Leg Three-Level NPC Inverter and Second-Order Sliding Mode Control," *IEEE Trans. Ind. Electron.*, vol. 65, no. 1, pp. 424–435, Jan. 2018, doi: 10.1109/TIE.2017.2723863.

[139] I. Vechiu, O. Curea, and H. Camblong, "Transient Operation of a Four-Leg Inverter for Autonomous Applications With Unbalanced Load," *IEEE Trans. Power Electron.*, vol. 25, no. 2, pp. 399–407, Feb. 2010, doi: 10.1109/TPEL.2009.2025275.

[140] A. Etxeberria, I. Vechiu, H. Camblong, S. Kreckelbergh, and S. Bacha, "Operational limits of a three level neutral point clamped converter used for controlling a hybrid energy storage system," *Energy Conversion and Management*, vol. 79, pp. 97–103, Mar. 2014, doi: 10.1016/j.enconman.2013.12.008.

[141] A. Sheikh, T. Youssef, and O. Mohammed, "AC Microgrid Control Using Adaptive Synchronous Reference Frame PLL," in *2017 Ninth Annual IEEE Green Technologies Conference (GreenTech)*, Mar. 2017, pp. 46–51, doi: 10.1109/GreenTech.2017.13.

[142] A. Etxeberria, I. Vechiu, S. Baudoin, H. Camblong, and S. Kreckelbergh, "Control of a Vanadium Redox Battery and supercapacitor using a Three-Level Neutral Point Clamped converter," *Journal of Power Sources*, vol. 248, pp. 1170–1176, Feb. 2014, doi: 10.1016/j.jpowsour.2013.10.021.

[143] A. J. Babqi and A. H. Etemadi, "MPC-based microgrid control with supplementary fault current limitation and smooth transition mechanisms," *Transmission Distribution IET Generation*, vol. 11, no. 9, pp. 2164–2172, 2017, doi: 10.1049/iet-gtd.2016.1387.

[144] S. Jupin, I. Vechiu, and G. Tapia-Otaegui, "Universal switched state-space representation for model predictive control of power converters," *Electric Power Systems Research*, vol. 180, p. 106120, Mar. 2020, doi: 10.1016/j.epsr.2019.106120.

[145] J. Mongkoltanatas, D. Riu, and X. LePivert, "H infinity controller design for primary frequency control of energy storage in islanding MicroGrid," in *2013 15th European Conference on Power Electronics and Applications (EPE)*, Sep. 2013, pp. 1–11, doi: 10.1109/EPE.2013.6634714.

[146] H. Han, X. Hou, J. Yang, J. Wu, M. Su, and J. M. Guerrero, "Review of Power Sharing Control Strategies for Islanding Operation of AC Microgrids," *IEEE Transactions on Smart Grid*, vol. 7, no. 1, pp. 200–215, Jan. 2016, doi: 10.1109/TSG.2015.2434849.

[147] A. E. M. Bouzid, P. Sicard, H. Chaoui, A. Cheriti, M. Sechilariu, and J. M. Guerrero, "A novel Decoupled Trigonometric Saturated droop controller for power sharing in islanded low-voltage microgrids," *Electric Power Systems Research*, vol. 168, pp. 146–161, Mar. 2019, doi: 10.1016/j.epsr.2018.11.016.

[148] K. D. Brabandere, B. Bolsens, J. V. den Keybus, A. Woyte, J. Driesen, and R. Belmans, "A Voltage and Frequency Droop Control Method for Parallel Inverters," *IEEE Transactions on Power Electronics*, vol. 22, no. 4, pp. 1107–1115, Jul. 2007, doi: 10.1109/TPEL.2007.900456.

[149] X. Lu, X. Yu, J. Lai, Y. Wang, and J. M. Guerrero, "A Novel Distributed Secondary Coordination Control Approach for Islanded Microgrids," *IEEE Transactions on Smart Grid*, vol. 9, no. 4, pp. 2726–2740, Jul. 2018, doi: 10.1109/TSG.2016.2618120.
[150] T. L. Vandoorn, J. D. M. De Kooning, B. Meersman, and L. Vandevelde, "Review of primary control strategies for islanded microgrids with power-electronic interfaces," *Renewable and Sustainable Energy Reviews*, vol. 19, pp. 613–628, Mar. 2013, doi: 10.1016/j.rser.2012.11.062.
[151] P. P. Vergara, J. C. López, L. C. P. da Silva, and M. J. Rider, "Security-constrained optimal energy management system for three-phase residential microgrids," *Electric Power Systems Research*, vol. 146, pp. 371–382, May 2017, doi: 10.1016/j.epsr.2017.02.012.
[152] D. Tenfen and E. C. Finardi, "A mixed integer linear programming model for the energy management problem of microgrids," *Electric Power Systems Research*, vol. 122, pp. 19–28, May 2015, doi: 10.1016/j.epsr.2014.12.019.
[153] F. Garcia Torres, "Advanced Control of Renewable Energy Microgrids with Hybrid Energy Storage System," PHD thesis, Seville, Spain, 2015.
[154] C. Eid *et al.*, "Market integration of local energy systems: Is local energy management compatible with European regulation for retail competition?," *Energy*, vol. 114, pp. 913–922, Nov. 2016, doi: 10.1016/j.energy.2016.08.072.
[155] M. A. Fotouhi Ghazvini, S. Ramos, J. Soares, R. Castro, and Z. Vale, "Liberalization and customer behavior in the Portuguese residential retail electricity market," *Utilities Policy*, vol. 59, p. 100919, Aug. 2019, doi: 10.1016/j.jup.2019.05.005.
[156] N. P. Yu, C. C. Liu, and J. Price, "Evaluation of Market Rules Using a Multi-Agent System Method," *IEEE Transactions on Power Systems*, vol. 25, no. 1, pp. 470–479, Feb. 2010, doi: 10.1109/TPWRS.2009.2030379.
[157] T. Gomez *et al.*, "European Union Electricity Markets: Current Practice and Future View," *IEEE Power and Energy Magazine*, vol. 17, no. 1, pp. 20–31, Jan. 2019, doi: 10.1109/MPE.2018.2871739.
[158] "XBID Launch Information Package." Feb. 2018, [Online]. Available: https://www.nordpoolgroup.com/globalassets/download-center/xbid/xbid-launch-information-package.pdf.
[159] "Capacity Allocation & Congestion Management." https://www.entsoe.eu/network_codes/cacm/ (accessed Sep. 05, 2020).
[160] "Bidding zone - a cornerstone of market-based electricity trading - Emissions-EUETS.com." https://www.emissions-euets.com/internal-electricity-market-glossary/375-bidding-zone (accessed Sep. 06, 2020).
[161] "Bidding Zones Literature Review," p. 14, 2014.
[162] "Day-ahead electricity market - Emissions-EUETS.com." https://www.emissions-euets.com/internal-electricity-market-glossary/1468-day-ahead-electricity-market (accessed Sep. 06, 2020).
[163] "Intraday electricity market - Emissions-EUETS.com." https://www.emissions-euets.com/internal-electricity-market-glossary/1486-intraday-electricity-market (accessed Sep. 06, 2020).
[164] "Non-frequency ancillary services - Emissions-EUETS.com." https://www.emissions-euets.com/internal-electricity-market-glossary/1821-non-frequency-related-ancillary-services (accessed Sep. 06, 2020).
[165] "Standard Contracts - Emissions-EUETS.com." https://www.emissions-euets.com/standard-contracts-remit (accessed Sep. 06, 2020).
[166] J. Hu, R. Harmsen, W. Crijns-Graus, E. Worrell, and M. van den Broek, "Identifying barriers to large-scale integration of variable renewable electricity into the electricity market: A literature review of market design," *Renewable and Sustainable Energy Reviews*, vol. 81, pp. 2181–2195, Jan. 2018, doi: 10.1016/j.rser.2017.06.028.
[167] A. Saez and I. Martinez, "Optimal sizing and control of energy storage systems for the electricity markets participation of intelligent photovoltaic power plants," p. 224.

[168] M. Doostizadeh and H. Ghasemi, "A day-ahead electricity pricing model based on smart metering and demand-side management," *Energy*, vol. 46, no. 1, pp. 221–230, Oct. 2012, doi: 10.1016/j.energy.2012.08.029.

[169] E. Perez, H. Beltran, N. Aparicio, and P. Rodriguez, "Predictive Power Control for PV Plants With Energy Storage," *IEEE Transactions on Sustainable Energy*, vol. 4, no. 2, pp. 482–490, Apr. 2013, doi: 10.1109/TSTE.2012.2210255.

[170] N. B. De Nadai, A. C. Z. de Souza, J. G. C. Costa, C. A. M. Pinheiro, and F. M. Portelinha, "A secondary control based on fuzzy logic to frequency and voltage adjustments in islanded microgrids scenarios," Jun. 2017, pp. 1–6, doi: 10.1109/PTC.2017.7981212.

[171] H. Kakigano, Y. Miura, and T. Ise, "Distribution Voltage Control for DC Microgrids Using Fuzzy Control and Gain-Scheduling Technique," *IEEE Transactions on Power Electronics*, vol. 28, no. 5, pp. 2246–2258, May 2013, doi: 10.1109/TPEL.2012.2217353.

[172] S. Wang, F. Guo, and R. Sharma, "Two-level prediction-based reactive power coordination and voltage restoration strategy for microgrid," in *2017 IEEE Power Energy Society General Meeting*, Jul. 2017, pp. 1–5, doi: 10.1109/PESGM.2017.8274626.

[173] J. Hu, Y. Xu, K. W. Cheng, and J. M. Guerrero, "A model predictive control strategy of PV-Battery microgrid under variable power generations and load conditions," *Applied Energy*, vol. 221, pp. 195–203, Jul. 2018, doi: 10.1016/j.apenergy.2018.03.085.

[174] Y. del Valle, G. K. Venayagamoorthy, S. Mohagheghi, J.-C. Hernandez, and R. G. Harley, "Particle Swarm Optimization: Basic Concepts, Variants and Applications in Power Systems," *IEEE Transactions on Evolutionary Computation*, vol. 12, no. 2, pp. 171–195, Apr. 2008, doi: 10.1109/TEVC.2007.896686.

[175] A. Lorestani and M. M. Ardehali, "Optimization of autonomous combined heat and power system including PVT, WT, storages, and electric heat utilizing novel evolutionary particle swarm optimization algorithm," *Renewable Energy*, vol. 119, pp. 490–503, Apr. 2018, doi: 10.1016/j.renene.2017.12.037.

[176] Y. K. Wu, C. Y. Lee, L. C. Liu, and S. H. Tsai, "Study of Reconfiguration for the Distribution System With Distributed Generators," *IEEE Transactions on Power Delivery*, vol. 25, no. 3, pp. 1678–1685, Jul. 2010, doi: 10.1109/TPWRD.2010.2046339.

[177] D. Peng, H. Qiu, H. Zhang, and H. Li, "Research of Multi-objective optimal dispatching for microgrid based on improved Genetic Algorithm," Apr. 2014, pp. 69–73, doi: 10.1109/ICNSC.2014.6819602.

[178] R. Velik and P. Nicolay, "Grid-price-dependent energy management in microgrids using a modified simulated annealing triple-optimizer," *Applied Energy*, vol. 130, pp. 384–395, Oct. 2014, doi: 10.1016/j.apenergy.2014.05.060.

[179] C. Wang, J. Xia, and W. Yan, "Optimal operation of microgrid based on chaotic simulated annealing particle swarm algorithm," in *2016 IEEE PES Asia-Pacific Power and Energy Engineering Conference (APPEEC)*, Oct. 2016, pp. 2374–2378, doi: 10.1109/APPEEC.2016.7779909.

[180] J. N. Bharothu, M. Sridhar, and R. S. Rao, "Modified adaptive differential evolution based optimal operation and security of AC-DC microgrid systems," *International Journal of Electrical Power & Energy Systems*, vol. 103, pp. 185–202, Dec. 2018, doi: 10.1016/j.ijepes.2018.05.003.

[181] N. Tiwari and L. Srivastava, "Generation scheduling and micro-grid energy management using differential evolution algorithm," Mar. 2016, pp. 1–7, doi: 10.1109/ICCPCT.2016.7530218.

[182] J. Zhang, Y. Wu, Y. Guo, B. Wang, H. Wang, and H. Liu, "A hybrid harmony search algorithm with differential evolution for day-ahead scheduling problem of a microgrid with consideration of power flow constraints," *Applied Energy*, vol. 183, pp. 791–804, Dec. 2016, doi: 10.1016/j.apenergy.2016.09.035.

[183] G. Lou, W. Gu, Y. Xu, M. Cheng, and W. Liu, "Distributed MPC-Based Secondary Voltage Control Scheme for Autonomous Droop-Controlled Microgrids," *IEEE Transactions on Sustainable Energy*, vol. 8, no. 2, pp. 792–804, Apr. 2017, doi: 10.1109/TSTE.2016.2620283.

[184] M. Petrollese, L. Valverde, D. Cocco, G. Cau, and J. Guerra, "Real-time integration of optimal generation scheduling with MPC for the energy management of a renewable hydrogen-based microgrid," *Applied Energy*, vol. 166, pp. 96–106, Mar. 2016, doi: 10.1016/j.apenergy.2016.01.014.

[185] P. Velarde, L. Valverde, J. M. Maestre, C. Ocampo-Martinez, and C. Bordons, "On the comparison of stochastic model predictive control strategies applied to a hydrogen-based microgrid," *Journal of Power Sources*, vol. 343, pp. 161–173, Mar. 2017, doi: 10.1016/j.jpowsour.2017.01.015.

[186] F. J. Vivas, F. Segura, J. M. Andújar, and J. J. Caparrós, "A suitable state-space model for renewable source-based microgrids with hydrogen as backup for the design of energy management systems," *Energy Conversion and Management*, vol. 219, p. 113053, Sep. 2020, doi: 10.1016/j.enconman.2020.113053.

[187] E. Kuznetsova, Y.-F. Li, C. Ruiz, E. Zio, G. Ault, and K. Bell, "Reinforcement learning for microgrid energy management," *Energy*, vol. 59, pp. 133–146, Sep. 2013, doi: 10.1016/j.energy.2013.05.060.

[188] R. Leo, R. S. Milton, and S. Sibi, "Reinforcement learning for optimal energy management of a solar microgrid," in *2014 IEEE Global Humanitarian Technology Conference - South Asia Satellite (GHTC-SAS)*, Trivandrum, India, Sep. 2014, pp. 183–188, doi: 10.1109/GHTC-SAS.2014.6967580.

[189] W. Liu, P. Zhuang, H. Liang, J. Peng, and Z. Huang, "Distributed Economic Dispatch in Microgrids Based on Cooperative Reinforcement Learning," *IEEE Transactions on Neural Networks and Learning Systems*, vol. 29, no. 6, pp. 2192–2203, Jun. 2018, doi: 10.1109/TNNLS.2018.2801880.

[190] P. Kofinas, A. I. Dounis, and G. A. Vouros, "Fuzzy Q-Learning for multi-agent decentralized energy management in microgrids," *Applied Energy*, vol. 219, pp. 53–67, Jun. 2018, doi: 10.1016/j.apenergy.2018.03.017.

[191] I. Goroohi Sardou, M. Zare, and E. Azad-Farsani, "Robust energy management of a microgrid with photovoltaic inverters in VAR compensation mode," *International Journal of Electrical Power & Energy Systems*, vol. 98, pp. 118–132, Jun. 2018, doi: 10.1016/j.ijepes.2017.11.037.

[192] M. Tavakoli, F. Shokridehaki, M. Funsho Akorede, M. Marzband, I. Vechiu, and E. Pouresmaeil, "CVaR-based energy management scheme for optimal resilience and operational cost in commercial building microgrids," *International Journal of Electrical Power & Energy Systems*, vol. 100, pp. 1–9, Sep. 2018, doi: 10.1016/j.ijepes.2018.02.022.

[193] L. Bianchi, M. Dorigo, L. M. Gambardella, and W. J. Gutjahr, "A survey on metaheuristics for stochastic combinatorial optimization," p. 50.

[194] M. Marzband, M. Ghadimi, A. Sumper, and J. L. Domínguez-García, "Experimental validation of a real-time energy management system using multi-period gravitational search algorithm for microgrids in islanded mode," *Applied Energy*, vol. 128, pp. 164–174, Sep. 2014, doi: 10.1016/j.apenergy.2014.04.056.

[195] M. Marzband, S. S. Ghazimirsaeid, H. Uppal, and T. Fernando, "A real-time evaluation of energy management systems for smart hybrid home Microgrids," *Electric Power Systems Research*, vol. 143, pp. 624–633, Feb. 2017, doi: 10.1016/j.epsr.2016.10.054.

[196] L. Suganthi, S. Iniyan, and A. A. Samuel, "Applications of fuzzy logic in renewable energy systems – A review," *Renewable and Sustainable Energy Reviews*, vol. 48, pp. 585–607, Aug. 2015, doi: 10.1016/j.rser.2015.04.037.

[197] M. Zachar and P. Daoutidis, "Energy management and load shaping for commercial microgrids coupled with flexible building environment control," *Journal of Energy Storage*, vol. 16, pp. 61–75, Apr. 2018, doi: 10.1016/j.est.2017.12.017.

[198] C. Zhang, J. Wu, Y. Zhou, M. Cheng, and C. Long, "Peer-to-Peer energy trading in a Microgrid," *Applied Energy*, vol. 220, pp. 1–12, Jun. 2018, doi: 10.1016/j.apenergy.2018.03.010.

[199] K. Zhou, S. Yang, and Z. Shao, "Energy Internet: The business perspective," *Applied Energy*, vol. 178, pp. 212–222, Sep. 2016, doi: 10.1016/j.apenergy.2016.06.052.

[200] B. V. Mathiesen *et al.*, “Smart Energy Systems for coherent 100% renewable energy and transport solutions,” *Applied Energy*, vol. 145, pp. 139–154, May 2015, doi: 10.1016/j.apenergy.2015.01.075.
[201] “Integrated Demand Response for Multi-Energy Load Serving Entity,” presented at the 2018 International Conference on Smart Energy Systems and Technologies (SEST), 2018.
[202] “Pré-étude de dimensionnement d’une installation photovoltaïque avec stockage pour l’alimentation en autoconsommation raccordé réseau du nouveau bâtiment de l’ESTIA3.” Dec. 14, 2018.
[203] M. Z. Hossain, N. A. Rahim, and J. a/l Selvaraj, “Recent progress and development on power DC-DC converter topology, control, design and applications: A review,” *Renewable and Sustainable Energy Reviews*, vol. 81, pp. 205–230, Jan. 2018, doi: 10.1016/j.rser.2017.07.017.
[204] O. Tremblay and L.-A. Dessaint, “Experimental Validation of a Battery Dynamic Model for EV Applications,” *World Electric Vehicle Journal*, vol. 3, no. 2, pp. 289–298, Jun. 2009, doi: 10.3390/wevj3020289.
[205] S. M. Njoya, O. Tremblay, and L.-A. Dessaint, “A generic fuel cell model for the simulation of fuel cell vehicles,” in *2009 IEEE Vehicle Power and Propulsion Conference*, Dearborn, MI, Sep. 2009, pp. 1722–1729, doi: 10.1109/VPPC.2009.5289692.
[206] Z. Abdin, C. J. Webb, and E. MacA. Gray, “Modelling and simulation of a proton exchange membrane (PEM) electrolyser cell,” *International Journal of Hydrogen Energy*, vol. 40, no. 39, pp. 13243–13257, Oct. 2015, doi: 10.1016/j.ijhydene.2015.07.129.
[207] R. García-Valverde, N. Espinosa, and A. Urbina, “Simple PEM water electrolyser model and experimental validation,” *International Journal of Hydrogen Energy*, vol. 37, no. 2, pp. 1927–1938, Jan. 2012, doi: 10.1016/j.ijhydene.2011.09.027.
[208] M. V. Naik and P. Samuel, “Analysis of ripple current, power losses and high efficiency of DC–DC converters for fuel cell power generating systems,” *Renewable and Sustainable Energy Reviews*, vol. 59, pp. 1080–1088, Jun. 2016, doi: 10.1016/j.rser.2016.01.029.
[209] “JRC Photovoltaic Geographical Information System (PVGIS) - European Commission.” https://re.jrc.ec.europa.eu/pvg_tools/en/tools.html#MR (accessed Mar. 05, 2020).
[210] S. Lee, D. Whaley, and W. Saman, “Electricity Demand Profile of Australian Low Energy Houses,” *Energy Procedia*, vol. 62, pp. 91–100, 2014, doi: 10.1016/j.egypro.2014.12.370.
[211] L. H. Saw, K. Somasundaram, Y. Ye, and A. A. O. Tay, “Electro-thermal analysis of Lithium Iron Phosphate battery for electric vehicles,” *Journal of Power Sources*, vol. 249, pp. 231–238, Mar. 2014, doi: 10.1016/j.jpowsour.2013.10.052.
[212] S. Ma *et al.*, “Temperature effect and thermal impact in lithium-ion batteries: A review,” *Progress in Natural Science: Materials International*, vol. 28, no. 6, pp. 653–666, Dec. 2018, doi: 10.1016/j.pnsc.2018.11.002.
[213] Y. Li *et al.*, “Data-driven health estimation and lifetime prediction of lithium-ion batteries: A review,” *Renewable and Sustainable Energy Reviews*, vol. 113, p. 109254, Oct. 2019, doi: 10.1016/j.rser.2019.109254.
[214] N. Omar *et al.*, “Lithium iron phosphate based battery – Assessment of the aging parameters and development of cycle life model,” *Applied Energy*, vol. 113, pp. 1575–1585, Jan. 2014, doi: 10.1016/j.apenergy.2013.09.003.
[215] C. Rakousky *et al.*, “Polymer electrolyte membrane water electrolysis: Restraining degradation in the presence of fluctuating power,” *Journal of Power Sources*, vol. 342, pp. 38–47, Feb. 2017, doi: 10.1016/j.jpowsour.2016.11.118.
[216] C. Wang, “Modelling and control of hybrid wind/photovoltaic/fuel cell distributed generation systems,” p. 402, 2006.
[217] C. Lamy, “From hydrogen production by water electrolysis to its utilization in a PEM fuel cell or in a SO fuel cell: Some considerations on the energy efficiencies,” *International Journal of Hydrogen Energy*, vol. 41, no. 34, pp. 15415–15425, Sep. 2016, doi: 10.1016/j.ijhydene.2016.04.173.

[218] Z. Abdin, C. J. Webb, and E. MacA. Gray, "PEM fuel cell model and simulation in Matlab–Simulink based on physical parameters," *Energy*, vol. 116, pp. 1131–1144, Dec. 2016, doi: 10.1016/j.energy.2016.10.033.
[219] A. Buttler and H. Spliethoff, "Current status of water electrolysis for energy storage, grid balancing and sector coupling via power-to-gas and power-to-liquids: A review," *Renewable and Sustainable Energy Reviews*, vol. 82, pp. 2440–2454, Feb. 2018, doi: 10.1016/j.rser.2017.09.003.
[220] D. Parra, L. Valverde, F. J. Pino, and M. K. Patel, "A review on the role, cost and value of hydrogen energy systems for deep decarbonisation," *Renewable and Sustainable Energy Reviews*, vol. 101, pp. 279–294, Mar. 2019, doi: 10.1016/j.rser.2018.11.010.
[221] E. F. Camacho and C. Bordons, *Model predictive control*. London ; New York: Springer, 2004.
[222] Enedis l'électricité en réseau, "Conditions de raccordement des Installations de stockage." Oct. 2017.
[223] Z. Abdin, C. J. Webb, and E. MacA. Gray, "Modelling and simulation of a proton exchange membrane (PEM) electrolyser cell," *International Journal of Hydrogen Energy*, vol. 40, no. 39, pp. 13243–13257, Oct. 2015, doi: 10.1016/j.ijhydene.2015.07.129.
[224] X. Li, C. Yuan, X. Li, and Z. Wang, "State of health estimation for Li-Ion battery using incremental capacity analysis and Gaussian process regression," *Energy*, vol. 190, p. 116467, Jan. 2020, doi: 10.1016/j.energy.2019.116467.
[225] L. Su *et al.*, "Path dependence of lithium ion cells aging under storage conditions," *Journal of Power Sources*, vol. 315, pp. 35–46, May 2016, doi: 10.1016/j.jpowsour.2016.03.043.
[226] G. Cardoso, T. Brouhard, N. DeForest, D. Wang, M. Heleno, and L. Kotzur, "Battery aging in multi-energy microgrid design using mixed integer linear programming," *Applied Energy*, vol. 231, pp. 1059–1069, Dec. 2018, doi: 10.1016/j.apenergy.2018.09.185.
[227] M. Yue, S. Jemei, R. Gouriveau, and N. Zerhouni, "Review on health-conscious energy management strategies for fuel cell hybrid electric vehicles: Degradation models and strategies," *International Journal of Hydrogen Energy*, vol. 44, no. 13, pp. 6844–6861, Mar. 2019, doi: 10.1016/j.ijhydene.2019.01.190.
[228] X. Pichon, A. Collet, D. Riu, and J. C. Crebier, "State of charge estimation at battery level from multiple cells management," in *2015 Tenth International Conference on Ecological Vehicles and Renewable Energies (EVER)*, Monte Carlo, Mar. 2015, pp. 1–7, doi: 10.1109/EVER.2015.7112977.
[229] Z. Song *et al.*, "The sequential algorithm for combined state of charge and state of health estimation of lithium-ion battery based on active current injection," *Energy*, vol. 193, p. 116732, Feb. 2020, doi: 10.1016/j.energy.2019.116732.
[230] H. Yuan, H. Dai, X. Wei, and P. Ming, "Model-based observers for internal states estimation and control of proton exchange membrane fuel cell system: A review," *Journal of Power Sources*, vol. 468, p. 228376, Aug. 2020, doi: 10.1016/j.jpowsour.2020.228376.
[231] M. E. Celebi, *Partitional Clustering Algorithms*. Springer, 2014.
[232] S. K. Kim, K. H. Cho, J. Y. Kim, and G. Byeon, "Field study on operational performance and economics of lithium-polymer and lead-acid battery systems for consumer load management," *Renewable and Sustainable Energy Reviews*, vol. 113, p. 109234, Oct. 2019, doi: 10.1016/j.rser.2019.06.041.
[233] P. L. Denholm, R. M. Margolis, and J. D. Eichman, "Evaluating the Technical and Economic Performance of PV Plus Storage Power Plants," NREL/TP--6A20-68737, 1376049, Aug. 2017. doi: 10.2172/1376049.
[234] "Catalog of CHP Technologies," U.S. Environmental Protection Agency Combined Heat and Power Partnership, Mar. 2015.
[235] G. Glenk and S. Reichelstein, "Economics of converting renewable power to hydrogen," *Nat Energy*, vol. 4, no. 3, pp. 216–222, Mar. 2019, doi: 10.1038/s41560-019-0326-1.
[236] E. Panos and M. Densing, "The future developments of the electricity prices in view of the implementation of the Paris Agreements: Will the current trends prevail, or a reversal is ahead?," *Energy Economics*, vol. 84, p. 104476, Oct. 2019, doi: 10.1016/j.eneco.2019.104476.

[237] Dualsun, “Warrant terms of photovoltaic panels of Dualsun.” Nov. 01, 2017, [Online]. Available: https://dualsun.com/en/.
[238] W. Blvd and A. Va, “Manufacturing Cost Analysis of Stationary Fuel Cell Systems,” p. 123, 2012.
[239] “The price of an electric car battery,” *Easy Electric Life*, May 28, 2020. https://easyelectriclife.groupe.renault.com/en/day-to-day/charging/what-is-the-price-of-an-electric-car-battery/ (accessed Dec. 17, 2020).
[240] A. Paudel, K. Chaudhari, C. Long, and H. Beng Gooi, “Peer-to-Peer Energy Trading in a Prosumer-Based Community Microgrid: A Game-Theoretic Model,” *IEEE Transactions on Industrial Electronics*, vol. 66, no. 8, p. 11, 2019.
[241] N. Liu, X. Yu, C. Wang, C. Li, L. Ma, and J. Lei, “Energy-Sharing Model With Price-Based Demand Response for Microgrids of Peer-to-Peer Prosumers,” *IEEE Trans. Power Syst.*, vol. 32, no. 5, pp. 3569–3583, Sep. 2017, doi: 10.1109/TPWRS.2017.2649558.
[242] P. Aristidou, A. Dimeas, and N. Hatziargyriou, “Microgrid Modelling and Analysis Using Game Theory Methods,” in *Energy-Efficient Computing and Networking*, vol. 54, N. Hatziargyriou, A. Dimeas, T. Tomtsi, and A. Weidlich, Eds. Berlin, Heidelberg: Springer Berlin Heidelberg, 2011, pp. 12–19.